DTIC FILE COPY

①

AD-A214 578

59th
Shock and Vibration
Symposium

Volume I

DTIC
ELECT
NOV 07 1989
S   D

Proceedings of a conference sponsored by
The Department of Defense and
The Department of Energy
held in Albuquerque, New Mexico
October 18-20, 1988

89 11 06 037

DISCLAIMER NOTICE

59th
Shock and Vibration
Symposium

Volume I

Proceedings of a conference sponsored by
The Department of Defense and
The Department of Energy
held in Albuquerque, New Mexico
October 18-20, 1988

Sandia National Laboratories

SYMPOSIUM MANAGEMENT

Host Representatives:
Mr. David O. Smallwood - Sandia National Laboratories
Mr. Rodney G. Galloway - Air Force Weapons Laboratory

Contract Management:

Mr. David O. Smallwood - Sandia National Laboratories

SYMPOSIUM MANAGER

Henry C. Pusey
4193 Sudley Road
Haymarket, VA 22069

REGISTRATION MANAGER

Sallie C. Pusey

59TH SYMPOSIUM PROGRAM COMMITTEE

Lt. C-M Carlin, USN
Defense Nuclear Agency
SPWE
6801 Telegraph Road
Alexandria, VA 22310

Rodney G. Galloway
U.S. Air Force
AFWL/NTES
Kirtland AFB, NM 87117-6008

J. Scott Milne
NASA/GSFC
M/C 302
Greenbelt, MD 20771

Jerome Pearson
U.S. Air Force
AFWAL/FIBG
Wright-Patterson AFB, OH 45433

John A. Robinson
U.S. Army Combat Systems Test Act.
STECS-EN-EV
Aberdeen Proving Ground, MD 21005

Lt. Col. Al Schenker
Defense Nuclear Agency
TTST
Kirtland AFB, NM 87115-5000

David O. Smallwood
Sandia National Laboratories
Division 7544
P.O. Box 5800
Albuquerque, NM 87185

Rudolph H. Volin
Naval Research Laboratory
Code
Wash. DC 20375

COMPILATION OF PROCEEDINGS

Henry C. Pusey
Sallie C. Pusey

PRODUCTION OF PROCEEDINGS

Vibration Institute

PREFACE

Hosted by Sandia National Laboratories and the Air Force Weapons Laboratory, the 59th Shock and Vibration Symposium is a continuation of the series of symposia sponsored by the former Shock and Vibration Information Center (SVIC). As was true of the 58th Symposium in 1987, this conference was organized in response to the continuing needs of the shock and vibration technical community. Because these symposia provide the only annual forum for the interchange of certain defense- and space-related information, they are expected to continue on an annual basis while a permanent solution for the sharing of such information is being sought

The response to the Call-for-Papers for the 59th Symposium was very gratifying; a large percentage of the more than 130 papers proposed were accepted. The final program included an Opening Session and three Plenary Sessions as well as 14 unclassified and four controlled-access technical sessions. Responsibility for preparation and distribution of the Proceedings for the 59th Shock and Vibration Symposium has been shared by Sandia National Laboratories and the Air Force Weapons Laboratory (AFWL). All technical papers for public release have been published by Sandia in four volumes. Volumes I, II, and III are to be distributed to registrants at the Symposium; Volume IV is to be mailed to qualified individuals after the Symposium. All technical papers requiring controlled access are to be published by AFWL and mailed to qualified recipients as soon as possible following the Symposium. Outstanding support from representatives from Sandia and AFWL and the enthusiastic cooperation of authors and speakers have helped greatly in attaining these goals.

The reader will note that each volume of the Proceedings contains a Table of Contents for all four volumes; however, the contents of Volume IV as of this writing are subject to change. The contents of the limited access Proceedings published by AFWL will be arranged in a similar way. Any questions relating to post-symposium availability may be addressed to me or to an appropriate Host Representative. It is anticipated that the unlimited Proceedings will be available from the National Technical Information Service and that the controlled-access Proceedings will be available from the Defense Technical Information Center.

Any success that the 59th Symposium may enjoy is the result of a team effort, and certain members of that team deserve special recognition. Host Representatives Dave Smallwood and Rod Galloway are to be applauded for providing the outstanding support that made the Symposium possible. The Interagency Program Committee is to be congratulated for a superb technical program. In addition, the Vibration Institute deserves credit for their work on producing the Proceedings. And my wife Sallie deserves very special thanks for keeping track of endless details and managing the registration. Finally, I offer my sincere personal thanks to all authors and speakers for their cooperation in meeting the necessary deadlines.

Henry C. Pusey
Symposium Manager

TABLE OF CONTENTS
Papers Appearing in Volume I

Papers Appearing in Volume II

Papers Appearing in Volume III

MACHINERY VIBRATION

VIBRATION CONTROL

AIRBLAST

GUNS AND PROJECTILES

Papers Expected to Appear in Volume IV

FEATURED PAPERS

VIBROACOUSTIC PAYLOAD ENVIRONMENT PREDICTION SYSTEM (VAPEPS)

DYNAMIC MEASUREMENT

DYNAMIC CRITERIA

MODAL APPLICATIONS

FEATURED PAPERS

DEVELOPMENT TESTING AT SANDIA

Mr. Del M. Olson
Director of Development Testing
Sandia National Laboratories
Albuquerque, NM 87185

Sandia National Laboratories maintains an extensive development
test capability including, but not limited to, explosive, climatic,
electromagnetic, thermal, mechanical shock, vibration, and static
environments. These facilities are briefly described.

BACKGROUND

Sandia National Laboratories was established in 1945 and operated by the University of
California until 1949, when President Truman Asked AT&T to assume the operation as an
"opportunity to perform an exceptional service in the National Interest." Today AT&T
Technologies, Inc. continues to operate Sandia for the Department of Energy on a no-profit,
no-fee basis. The Labs' responsibility is national security programs in defense and energy,
with primary emphasis on nuclear weapon research and development. Sandia also does a
limited amount of work for the Department of Defense and other federal agencies on a non-
interference basis.

Sandia National Laboratories is one of the nation's largest research and development
engineering facilities. About 7200 persons are employed in Albuquerque, about 1100 in
Livermore CA, and about 100 at the Tonopah Test Range, the Nevada Test Site, Kauai Test
Facility, and elsewhere.

About 60 percent of Sandia's research and development effort involves the weaponization of
nuclear explosives for national defense; the remainder involves energy programs and advanced
military technologies. About 30 percent of Sandia's operating budget is from federal agency
reimbursables. Sandia does not manufacture or assemble weapons, this work is performed by
other contractors. After the weapons reach stockpile, Sandia quality assurance evaluators
periodically obtain representative samples and test them in laboratory and field exercises to
ensure that they continue to operate safely and reliably.

Sandia operates a broad range of facilities, many of them unique. They are used for a wide
variety of projects, ranging from basic materials research, to the design of specialized
parachutes. Development testing is an integral part of our activities and the facilities include
state-of-the-art equipment for environmental testing, radiation research, combustion research,
and computing.

DEVELOPMENT TESTING

Sandia National Laboratories has an exceptional range of testing facilities that in many
instances have been designed and built here and are not readily available anywhere else,
especially in one easily accessible location. Although designed and built for the Department of
Energy, these facilities give Sandia a unique capability to assist government agencies and their
contractors who have development testing projects requiring state-of-the-art skills and
facilities. Through special arrangements, Sandia can make its facilities available for such
projects. Some of these facilities are briefly described below. Many of Sandia's test facilities
are located in remote locations to facilitate the testing of items with explosives or other
hazardous materials.

Aerial Cable Facility: Steel cables stretched between mountain peaks are used to free-drop payloads as heavy as 3000 lb from heights of 600 ft. Impact velocities of up to 190 ft/s can be achieved in free fall; 1000:1 s using a rocket pull down technique.

Centrifuges: Centrifuges range from spinners capable of spinning a 350 kg test item up to 40,000 rpm, a high-onset centrifuge with a 10" radius which can reach 2000 g in 1.4 second, a 35 ft radius outdoor centrifuge, to a 29 ft radius below-ground centrifuge with a capacity of 1.6 million g-lb.

Climatic Test Facilities: Sandia maintains a large number of chambers and ovens for simulating a wide range of environmental conditions. Exposures are made to combinations of temperature, thermal shock, humidity, and altitude, as well as salt-fog and rain. Items as large as 8 ft in diameter and 30 feet long can be accommodated.

Electromagnetic Environments Simulator. This facility is capable of producing continuous wave electric fields over the frequency range of 4 MHz to 10 GHz and fields of 100,000 V/m.

Explosive Testing: Explosive testing takes many forms at Sandia including blast testing using shock tubes and explosively driven flyer plates. Shock tubes up to 19 ft in diameter are available. Flyer plates have achieved velocities up to 14,000 ft/s.

Field Testing: Two field ranges are used by Sandia; the Tonopah Test Range in central Nevada is used for flight and trajectory studies, and high altitude rocket and reentry body studies, and the Kauai Test Facility in Hawaii has a rocket launching capability for high-altitude scientific research and reentry vehicle studies. In addition field tests operations are conducted world wide supported by a substantial inventory of test equipment.

Fuel Fire Facility: The Aircraft Fuel Fire Simulation Facility, designed and built by Sandia, represents a major advance in fire testing with jet fuel.

Horizontal Actuator: The facility consists of an 18 in. pneumatic actuator with a 92 ft track. The actuator can directly generate 700,000 lb of force. Larger forces and a variety of pulse shapes can be generated using multiple sleds.

Large-Scale Melt Facility: The melt facility helps engineers understand and predict events during a reactor-core meltdown. During full scale testing, temperatures above 3000 K are produced.

Laser Tracker: Sandia's laser tracker with a three-radians-per-second slew rate is unique among tracking instruments and is ideally suited for measuring trajectories of high performance rocket systems or other high velocity projectiles.

Light-Initiated High Explosive (LIHE) Facility: This facility developed at Sandia permits the remote spraying of explosives onto complex surface shapes and detonating the explosives with a flash of light. Impulse levels from 10 to more than 10,000 taps can be achieved.

Lightning Simulator: The lightning simulator duplicates the characteristics of severe natural lightning currents in a controlled laboratory environment. The facility can produce up to 4 strokes per flash with currents rising to a peak of 200,000 amps.

Modal Testing: Sandia conducts state-of-the-art modal tests on items ranging from components weighing a few ounces to 100 m tall vertical axis wind turbines. Tests are run in both the laboratory and at field locations.

Nondestructive Testing: NDT methods used at Sandia include x-radiograph, ultrasonics, computer aided radiography and ultrasonics, radiographic image analysis, laser interferometry, and others.

Photometrics: The equipment encompasses slow- to ultra-high-speed camera and video systems, most of which can be mounted on unique tracking platforms. Radiometric equipment covers the untraviolet through the near infared spectrum.

Radiant Heat Facility: Sandia's Radiant Heat Facility provides laboratory simulation of high temperature environments and acquires and records the responses of test items to these environments. Up to 5 MW of power can be used to simulate a wide variety of heat sources including solar, reentry heating, and fires.

Rocket Sled Facility: Sandia has two rocket sleds; a 10,000 ft narrow gage track for high-velocity requirements, and a shorter standard railroad gage track used to simulate transportation and other relative low velocity (up to about 300 mph) accidents.

Shock Testing: In addition to the facilities described elsewhere for conducting mechanical shock tests, Sandia has several conventional shock machines, air guns, and actuators. Sandia pioneered developments in reverse Hopkinson bar testing, pyrotechnic shock simulation, and water entry simulations.

Structural Testing: Sandia has static test frames capable of testing items up to 200 in long with loads up to 500,000 lb. Several Universal Test Machines are available for conducting tests from a few ounces to 600,000 lb. Pressure vessels are available for conducting pressure tests of items up to 40 inches in diameter and 10 ft long. Items 18 inches in diameter and 15 ft long can be tested to 16,000 psi. These facilities are equipped with extensive instrumentation for measuring strain, displacement, load, pressure, and other quantities.

Vibration Testing: Sandia conducts vibration tests on components, subsystems, and entire systems using a number of modern shakers systems with state-of-the-art digital control systems. Available shakers range from 1 lb force to 40,000 lbs. Sandia has been a leader in implementing digital controls for shock, sine, random, and multiple input random testing.

Water Impact Facility: Sandia maintains a 50 ft deep pond used in conjunction with a 300 ft drop tower and air powered guns to provide testing for water-entry and water impact studies.

CONCLUSIONS

As the above list illustrates, Sandia maintains an extensive development testing capability. The combination of unique environmental requirements, low production numbers, high reliability and safety requirements, and the difficulty of full scale tests requires Sandia to continually strive to provide the most realistic simulations possible. This effort has resulted in a unique national asset which can be made available to qualified users. Further information about the capability or availability of any of these facilities can be acquired by contacting Sandia National Laboratories, Development Testing Directorate, Albuquerque, New Mexico (505) 844-8007.

THE QUEST FOR $\omega = \sqrt{K/M}$:
NOTES ON THE DEVELOPMENT OF VIBRATION ANALYSIS

Neville F. Rieger
Stress Technology Incorporated
1800 Brighton-Henrietta Town Line Road
Rochester, NY 14623

ABSTRACT

The origins of vibration analysis are traced through the achievements of pioneers such as Galileo, Mariotte, Newton, and Leibnitz, and of developers like the Bernoullis, Euler, d'Alembert, and Lagrange. Necessary conditions for the development of the single degree theory are deduced, and some possible originators of the formula and theory are proposed.

INTRODUCTION

Mystery surrounds the origin of the formula $\omega = \sqrt{K/M}$ which is commonly used to calculate frequency of vibration of a single degree system[1]. The name of the person who first recognized the significance of this formula is not known, nor is that of the originator of the familiar theory for vibrations of a single degree system. The formula and its related theory are fundamental aspects of all modern vibration textbooks, and both are in daily use by vibration engineers. The fact that so little is known about the origins of both is an intriguing blank in the history of engineering. This paper outlines some of the research conducted by the author in his quest for the origin of the formula and its theory.

The development of vibration knowledge may be classified into four phases. In the first phase (1564-1727) fundamental knowledge was developed on mechanics, on the concepts of dynamics, on the differential and integral calculus; and the theory of differential equations was begun. In the second phase (1687-1787) the structure of modern mathematics was established and greatly developed by scientists who were also intrigued by problems of oscillation of strings. The third phase (1787-1850) saw the development of general theories of elasticity and of vibration theory, with supporting experiments. The fourth phase (1872-1934) includes the work of scholars of vibration, and their development of analysis methodologies from the vibration knowledge which had evolved over three centuries.

GENIUS AWAKENING (1564-1727)

Galileo GALILEI (1564-1642) was born in Pisa where his father was an established musician and composer. At nineteen he enrolled at the University of Pisa to study medicine. Under the guidance of the mathematician Ricci, he studied geometry

---

[1] ω is circular frequency of vibration, K is stiffness, and M is mass.

and natural phenomena, and in 1584 he considered the regularity with which a pendulum oscillates. As the story goes, these studies began with his observations of the great lamp of Pisa Cathedral, swinging in a cross-breeze. Galileo's later writings show that he understood the laws of the pendulum. He was also the first to propose that the pendulum could be used as a basis for precise timekeeping. According to a plaque at the entrance to the Leaning Tower in Pisa, his initial studies of falling objects were made from the Tower in 1586.

Instead of pursuing medical studies, Galileo moved to Florence where he studied mathematics and mechanics. In Florence he wrote on hydrostatics and on the center of mass of solids, and invented the hydraulic balance. Based on the merit of these writings, he was appointed Professor of Mathematics at the University of Pisa in 1589, and in 1592 he moved to the University of Padova to teach geometry and astronomy. In Padova he conducted his famous studies of uniformly accelerated motion, around 1594.

Galileo had heard of the invention of the telescope in 1609, and was quick to advocate its military importance in a letter to the Doge of Venice (1609). In 1609 he built his first telescope, and with it he became the first person to study the motions of celestial bodies. His firm belief in the Copernican model of the solar system, led him to write a book on his astronomical researches, 'Sidereus Nuncius,' containing drawings of Jupiter's moons. He was summoned to Rome in 1616 and again in 1633, where he was forced to recant his teachings. During the last eight years of his life Galileo prepared his greatest work 'Discourses and Mathematical Demonstrations Concerning Two New Sciences,' which contains most of his discoveries, including the pendulum laws. He recognized that the period of oscillation was proportional to the square root of the length, but does not appear to have known explicitly of the mathematical formula. That discovery was made by Huygens, who published it in 1673.

Abbe Marin MERSENNE (1588-1648) was a French mathematician and theologian, and a close friend of René Descartes (1596-1650). In his mature years he wrote several books on mathematics and natural philosophy, such as 'La Verité dans les Sciences' (1625). On music and musical instruments he wrote 'Harmonie Universelle' (1637). Mersenne stated his laws of vibrating strings in his book 'Harmonicorum Liber' (1636), and made the first direct determination of the frequency of vibration of a musical sound. He also worked on the geometric relations which describe cycloidal curves.

Fr. Edme MARIOTTE (1620-1684) was a Prior of St. Martin-sous-Beaune in Dijon, France. Mariotte in 1664 was the independent co-discoverer of the gas law PV = Constant, which was first presented by Robert Boyle in England in 1662. During the construction of the Palace of Versailles by Louis XIV Mariotte was in charge of the design of the extensive water supply system for the gardens and fountains. The elevation of water to a great height required the development of a suitable pressure vessel, the strength of which Mariotte developed by proof-testing. He measured the growth in vessel circumference under pressure, and found that a proportional relationship exists between circumferential growth and pressure head, i.e., between force F and displacement K, $F = K\delta$, where K is the stiffness of the body. This discovery and its publication (1678) were made independently of Hooke's discovery of the force-displacement law (1660) and its statement (1676). This proportional relationship is of course indispensible to the expression $\omega = \sqrt{K/M}$. The Hooke-Mariotte discovery therefore provides an earliest possible date (1676) for the frequency relationship.

In 1673, Mariotte suggested to Leibnitz, his pupil, that Leibnitz should solve a problem involving the vibrations of a compound pendulum. A picture of this pendulum is shown in figure 1. The challenge was for Leibnitz to determine the period of oscillation of the pendulum. Leibnitz claimed to have found the solution, but did not supply it in his reply to Mariotte.

Christiaan HUYGENS (1629-1695) knew of the correspondence between his father and Galileo while Galileo was spending his final years in Arcetri and studying problems of precise navigation. Later, with his own (much improved) telescopes Huygens observed and solved the riddle of Saturn's rings, which had puzzled Galileo forty years before. Huygens went to Paris in 1655 where he studied under Pascal and knew of Mariotte. Huygens invented the isochronous or cycloidal pendulum, and with it he developed a clock movement which kept accurate time. He made many contributions including the center of oscillation, the postulation of centrifugal force, and Huygens' principle. His portrait is shown in figure 2.

Isaac NEWTON (1642-1727) in 1665, at twenty-three years of age, formulated ideas on universal gravitation and the calculus. His great work 'Principia Mathematica de Philosophie Naturailis' which contains the statement of the laws of motion was published by the Royal Society of London in 1687. Figure 3 shows Newton at about sixty years of age. The title page of the 'Principia' is shown in figure 4, and the page with the first two laws of motion is shown in figure 5. This epochal work is written in three parts, and the style is similar to that of Greek geometry. Geometrical proofs are used throughout, and it has been suggested that Newton chose this format for ease of understanding. In use however, Newton's notation was less convenient than that chosen by Leibnitz. This convenience led to the more rapid development of the calculus in Europe than in Britain, during the subsequent century.

The Principia discusses central forces on bodies, motion through a resisting medium, motion of a pendulum, wave theory, motion of planets, and universal gravitation. Newton's greatest achievements were the creation of the differential and integral calculus, the universal theory of gravitation, the principles of optics, and the corpuscular theory of light (1684). He was also the first to solve a differential equation, in 1676.

Gottfried Wilhelm LEIBNITZ (1646-1716), German philosopher, statesman, and mathematician was first noted for his construction of an early calculating machine in 1673, which he presented to the Royal Society of London. In 1675 he independently developed the first energy methods for the study of dynamics. In 1676 he became librarian, then councillor (1678) to the Duke of Braunschweig-Luneburg, where he worked as an engineer on mechanical devices, on the improvement of education, and on various geology problems while continuing his work on mathematics and on metaphysics. In 1684 his book 'Nova Methodus pro Maximum et Minimus,' was published containing an exposition of his differential calculus. A portrait of Leibnitz painted ca. 1700 is shown in figure 6.

THE CENTURY OF THE CALCULUS (1687-1787)

Jacob (1654-1705), Johann (1667-1748) and Nikolaus (1687-1759) BERNOULLI were three founding brothers of a famous family of scientists and mathematicians which originated in Basel, Switzerland. The mathematicians of this family are shown in the chart of figure 7. Jacob Bernoulli studied experimental physics in Basel and in 1687 became Professor of Mathematics at Basel University. He wrote on summation of infinite series, and corresponded with Leibnitz on problems of the calculus. He

established the initial concepts of the Calculus of Variations in his study of the isoperimetric problem. Using his variational calculus he discovered the form of the catenary, and of the isochrone. In 1696 he formulated and solved the brachystochrone problem, and offered this as a problem to the best mathematicians of Europe by letter, giving six months for solution. Newton's response is best known: he solved the problem overnight, and communicated the solution anonymously to Johann Bernoulli, who quickly recognized, with admiration, the author of that solution by his style.

Johann Bernoulli was also fascinated with problems and possibilities of the new mathematics, and he obtained the tautochrone curve using the variational calculus. Johann had three sons who also became mathematicians, Nikolaus IV (1695-1726), Daniel (1700-1782), and Johann II (1710-1790). Daniel Bernoulli's famous book 'Hydrodynamica' which contains Bernoulli's theorem was published in 1738. In 1742 he suggested in a letter to Euler that the differential equation for the deflected form of the elastica could be obtained by minimizing the integral of the square of the curvature taken along the length. This task was subsequently completed by Euler and the solution for the deflected forms of the Elastica was published in 1744. This solution is the basis for the well-known Bernoulli-Euler theory for deflection of slender beams. Daniel Bernoulli also suggested to Euler in 1748 a procedure for obtaining the differential equation for vibrations of slender beams. A portrait of Daniel Bernoulli is shown in figure 8.

Johann II (1710-1790) succeeded his father to the Chair of Mathematics in Basel. His son Jacob II (1759-1789) also became Professor of Mathematics at the Academy of St. Petersburg, where he followed the works of his uncle and teacher, Daniel. He studied Chladni's experimental work on vibrations of plates, and sought a theoretical explanation for the nodal patterns.

Brook TAYLOR (1685-1731) was an English mathematician and a contemporary of Newton, whose best-known achievements were the development of the Taylor's Series, and the early development of the Calculus of Finite Differences. His portrait is shown in figure 9. He found the formula for the center of oscillation (c.g.) of a compound pendulum which gave the correct period. Taylor is mentioned by R. B. Lindsay as the first person to achieve 'a strictly dynamical solution to the problem of the vibrating string.' To do this, Taylor assumed that the string was made up of many identical particles along its length, and that the nature of vibration modes was such that every particle reached its maximum amplitude at the same time. Using this form and Newton's second Law of Motion together with the Difference Calculus, Taylor obtained a formula for the frequency of vibration of a vibrating string which was in agreement with the experimental results of Mersenne.

Leonhard EULER (1707-1783) was a Swiss mathematician who made voluminous contributions to the development of applied mathematics and to engineering analysis. He was born in Basel, and was a student of Johann Bernoulli. At the age of twenty, in 1727, he became an Associate of the Imperial Academy of St. Petersburg. In 1733 he obtained the first solution for the second-order differential equation with constant coefficients. This effort was possibly motivated by a desire to solve the wave equation which had been obtained but not solved by Daniel Bernoulli in 1723. In 1736 he obtained and demonstrated the expression for minimizing a curve. In 1741, tired of the intrigues of St. Petersburg he joined the Imperial Academy of Berlin, and he published his famous work on beam deflection (1744), and his work with D. Bernoulli on the lateral vibrations of bars (St. Petersburg, 1751), during his tenure in Berlin. According to A.E.H. Love (Cambridge, 1927) the fourth-order equation vibration equation was obtained 'by variation of the function they

(Bernoulli and Euler) had previously used for the work done in (static) bending. They determined the functions we should now call Normal Functions, and the equation we should now call the Period Equation, in the six cases which arise according to whether the ends (of the bar) are free, clamped, or pinned' (Love 1927). The method therefore is due in concept to D. Bernoulli, and the execution was performed by Euler. Later studies by this talented pair included an attempt to develop a theory for the tones of a bell. Euler's later researches on beams initiated the theory of elastic stability of columns and his well-known ductility formula (1757).

In 1759 Euler returned to the St. Petersburg Academy, and around 1767, he became totally blind. A portrait of Euler around this time is shown in figure 10. Despite this loss of sight, his productivity continued at a high level. His memory appears to have been uncommonly acute, and his ability for mental computation was phenomenal. He introduced the symbols e, π, and i into common mathematical parlance, and the identity $e^{i\pi} + 1 = 0$ bears his name. He wrote two textbooks on the calculus (1755, 1770). These textbooks have guided the format of mathematical texts to the present day.

Was Euler the first person to find $\omega = \sqrt{K/M}$? This feat would have been possible after 1733, when the solution to the second-order equation became available. Euler, D. Bernoulli, and d'Alembert, who were in relatively close communication for those days, avidly investigated problems of mechanics and dynamics of continua. However, it appears that particle dynamics per se did not intrigue them.

Jean Le Rond D'ALEMBERT (1717-1783) was admitted to the French Academy of Sciences in 1741, and published his best-known work 'Traite de Dynamique' in 1743. This work contains his famous principle of dynamics. D'Alembert studied the vibrations of strings in 1747, and published his work on this topic in a memoir to the Berlin Academy in 1750. This is the first published work to contain the equation and solution for the motion of a string treated as a continuum, i.e., the wave equation, although this equation had been obtained without publication by D. Bernoulli in 1723. D'Alembert's solution to this equation was achieved by separation of the variables, a procedure devised by Johann Bernoulli in 1696. This procedure was successfully applied to the vibrating string independently by both d'Alembert and Euler. His portrait is shown in figure 11.

Joseph Louis LAGRANGE (1736-1813) was acknowledged as the greatest mathematician of his age. His principal accomplishment was the generalization of Newtonian mechanics, for which he devised a straightforward procedure for obtaining the equations of motion, Lagrange's equation. His book 'Mecanique Analytique' (1788) contains these achievements. At twenty-three years of age he extended the earlier work of d'Alembert, and generalized the solution to the vibrating string. In this study, the string was again considered as a system of identical particles, for which he obtained the equations of motion, and demonstrated that the number of independent modes is equal to the number of particles. He showed that in the limit, the result for the frequencies agreed precisely with those achieved earlier by d'Alembert and Euler for the continuum model of the string. Lagrange's solution for the discrete particle model appears to be the closest any analyst has come to finding the single degree theory, up to that time. A portrait is shown in figure 12 of Lagrange around the year 1787.

THE ERA OF THE ELASTICIANS (1787-1850)

Ernst Florens CHLADNI (1756-1827) studied the modal patterns of vibrating plates, and first published his results at Leipzig in 1787. These results greatly stimulated the mathematicians to further apply those techniques which had succeeded with strings, beams, and rods to the analysis and explanation of plate vibrations. Chladni gave a more complete account of his work in his book 'Die Akustik' also published in Leipzig, in 1802, in which he documents his researches on plates, with dates of their original publication. A copy of the title page of Chladni's book with his portrait is given in figure 13.

Sophie GERMAIN (1776-1831) wrote three memoirs to explain the modal patterns Chladni had reported in his book 'Die Akustik,' for which she was awarded a Prize by the French Academy in 1816. The gold medal which accompanied this prize is shown in figure 14. In these memoirs, she first obtained the equation for deflection of the mid-surface of a thin rectangular plate, and in later work she established the equation for the normal vibrations of such a plate.

Baron Augustin-Louis CAUCHY (1789-1857) worked on the mathematical theory of wave propagation for which he was awarded the Prize of the Institute de France in 1816. He also contributed extensively to the theory of stresses in solids.

Simon Denis POISSON (1781-1840) contributed to the development of the theory of elasticity, and is memorialized by his contributions to the generalization of the stress-strain law of elasticity into three dimensions, which required among other concepts, the introduction of Poisson's well-known Ratio.

Claude-Louis Henri NAVIER (1785-1836) was the first mathematician to investigate the general equations of equilibrium and vibration of elastic solids. He developed a 'molecular' theory of solids in which the mass and elastic properties of the solid were concentrated at certain material points. He determined the equations of motion of these 'molecule' points, and took the variation of the work done by the forces acting on the molecule in a small displacement. This procedure gave the differential equations of motion and the boundary conditions at the surface of the body.

THE SCHOLARS OF VIBRATION (1872-1934)

John William STRUTT, LORD RAYLEIGH (1841-1919) in 1877 published the first edition of his famous treatise, 'The Theory of Sound.' His first paper on gases was presented to the British Association for the Advancement of Science in 1882, and he won the Nobel Prize for the isolation of argon in 1904. Rayleigh was a prolific writer and became Chancellor of Cambridge University in 1908, a post which he held until his death in 1919. Rayleigh's portrait of this period is shown in figure 15. The theory of vibration as taught today for a single-degree system appears in 'The Theory of Sound,' Volume 1, Chapter 3, pages 44-50: see figure 16. The formula for the period $p = 2\pi \sqrt{M/K}$ appears on page 44 of the Dover edition (1946).

The Ukrainian-born Stephen TIMOSHENKO (1878-1972) published the first edition of his famous book on the Theory of Elasticity in St. Petersburg in 1913. He left his homeland in 1918 for the United States, and he worked for the Westinghouse Electric and Manufacturing Company in Pittsburgh from 1923 to 1927. Timoshenko solved vibration problems, collected vibration literature, and taught courses on vibration analysis at the Westinghouse Night School during this period. His course notes were first published in 1928 by the D. Van Nostrand Company under the title

'Vibration Problems in Engineering.' This was the first U.S. book on vibration analysis, and it was the first English-language vibration text written with a practical orientation. Timoshenko virtually established the science of engineering mechanics in the United States through his writings and through his students.

Jan Pietr DEN HARTOG (1899-   ) worked initially in association with Timoshenko at Westinghouse. Timoshenko's book 'Vibration Problems' mentions work performed by Den Hartog during this period. In 1934 Den Hartog began his teaching career at Harvard, and at M.I.T. in 1944. The first edition of his lucid textbook 'Mechanical Vibrations' was published in 1934.

WHO WAS FIRST?

What can be concluded with regard to the probable origins of $\omega = \sqrt{K/M}$ from the lives of the earliest pioneers? First, we know that their discoveries came at a time when there were strong commercial incentives for the development of mechanical devices such as chronometers, efficient pumps, and steam engines. Second, the correspondence between Galileo and Huygens' father in Leyden, and between Galileo and Mersenne was significant because it provided inspiration and fertile ground for the genius of Huygens to grow. Huygens went to Paris to study. Paris was the intellectual center of Europe during the reign of Louis XIV, under his finance minister, Colbert. Studying with Mersenne, Huygens must have heard of Galileo's suggestion to use the pendulum for timekeeping, and of Mersenne's work on the cycloidal curves. To put such pieces of information together into a working device would have required precisely those intellectual and mechanical skills which Huygens possessed. He created the first chronometer by introducing the cycloidal, i.e., isochronous escapement. A later version of the escapement mechanism is shown in his book 'Horologium Oscilatorium.' Did Huygens meet Mariotte in Paris? Very likely. Were Mariotte's questions to Leibnitz concerning the compound escapement inspired by Huygens' cycloidal pendulum? Such a mathematical analysis was conceptually within the ability of the twenty-seven year old Leibnitz, though the calculus involved would not have evolved from him until 1684. Further, the solution of the simultaneous second-order differential equations involved would also have had to wait a further sixty years for Euler's contribution. Leibnitz had received his doctorate at twenty years of age, and was on cordial terms with Mariotte and Newton.

Prior to Galileo there were no concepts of mass or motion as we now understand these terms. The few earlier writers who had studied the positions of celestial bodies (Ptolemy, Copernicus) had drawn conclusions concerning orbital motion. Aristotle in his 'Physics' states that particles travel in straight lines. To believe otherwise, i.e., parabolic motion, was to deny the great credibility given to Aristotle by Aquinas. Aristotle further states that the medium drives the projectile. Such 'Physics' as existed prior to Galileo was apparently understood in much different terms to those we believe today.

Galileo's major contributions to dynamics were to coordinate the concepts of displacement and velocity, and to introduce the new concept of acceleration. Expressed in modern terms, these concepts bring us to the brink of the differential calculus. They provide a reason for the discovery of the calculus thirty years after the publication of Galileo's book. In order to explain the results of his experiments in 1594 with falling weights, Galileo did three things: First, he devised the concept of acceleration. Second, he applied the scientific method - he devised a theory to explain his experimental observations. Third, using this theory he expressed his results in analytical form - the expressions for the laws of accelerating motion. At the time of Galileo, any one of these innovations would be

sufficient to demonstrate his creative brilliance. All three, together, gave birth to the new science of dynamics, and changed forever the way in which science itself was understood.

Newton continued from where Galileo left off. By realizing the principles which lay behind Galileo's dynamical ideas, he conceived the differential calculus, and by inferring the reciprocity of the differential relations, he was then able to devise the principles of the integral calculus. These two mighty discoveries appear to have taken place immediately following his graduation from Cambridge, in the plague years of 1665 and 1666, when he was back in Woolsthorpe. The concept of universal gravitation also occurred to him during the same period. Prior to this time there was no explanation for how the observed orbital motions of the moon about the earth, and of the planets about the sun, could occur.

Given Galileo's concepts of motion and (by this time) of mass, Newton deduced that it was the mass property which provided the attraction, and the motion property which provided the equilibrium. Thus Newton unified and explained the planetary motions, and introduced the concept of universal gravitation with the inverse-square law, and further showed that these ideas were in accordance with the principle of centrifugal action, given by Huygens in 1655. These achievements together with the three Laws of Motion are given in the 'Principia,' Volume 2.

By the year 1700 the concepts of mass and of acceleration were both well accepted, though not yet in the same use as engineers employ them today. There were several reasons for this. First, the development of mathematics itself was the primary interest of mathematicians such as Johann Bernoulli, Newton, and Taylor. Of these, Taylor was the only one who put the mathematical discoveries to use for vibration analysis, with his discrete-particle solution of the string problem. Secondly, energy methods were being developed very enthusiastically around this time in Europe, and their proponents saw in them great promise for the discovery of general laws of dynamical systems. Thirdly, the field of differential equations remained to be appreciated, solved, and formalized. However, this path apparently led to solutions for specific problems in dynamics, rather than to general principles, and this was possibly less interesting to pioneers such as Newton and Leibnitz, whose major interest in applied dynamics lay in celestial mechanics. And lastly, the early mathematicians continued to be fixated on the discovery of analytical forms for special curves. Galileo, Mersenne, and Huygens worked on their cycloids; Newton and Halley sought expressions for planetary orbits; Johann Bernoulli, and Leibnitz developed analytic forms for the Brachystochrone and Tautochrone; and D. Bernoulli and Euler solved the Elastica. Evidently, the development of single degree of freedom dynamics would have to wait until a talented but less ambitious mathematician with engineering interests appeared on the scene.

D. Bernoulli, Euler, and d'Alembert were mathematicians with less general interests. This can be discerned from the specific types of problems which they studied, without detracting in any way from the greatness of their prodigious contributions. Most of our basic mathematical tools, and many other procedures, are due to them. Furthermore, engineering dynamics owes much to what must have been a very close and fortuitous intellectual friendship between Daniel Bernoulli and Leonhard Euler, and to some extent with d'Alembert also, throughout their long, active lives. Bernoulli first brought his strong mathematical skill and fine practical insight to the problem of the uniform vibrating string, in 1723. Euler's solution to the second-order differential equation (1733) may have been an outgrowth of their earlier collaboration on this work, as colleagues in St. Petersburg. The concept of Separation of Variables had been contributed by Johann Bernoulli in 1696,

and it is easy to speculate that these two steps were utilized by Daniel Bernoulli and Euler, during their time together (1726-1730), in semi-isolation in St. Petersburg. Nonetheless, despite the continuing correspondence between these two after Bernoulli returned to Basel, the solution to the wave equation was not first published by them, but rather by d'Alembert in 1750. Was d'Alembert in touch with Bernoulli from Paris, between 1733 and 1751? Quite likely, but his solution for axial and torsional vibrations of a uniform continuum does not mention any earlier work on the vibrating string by Bernoulli and Euler, even though d'Alembert's work was published by the Berlin Academy in 1750, while Euler was in Berlin.

It seems that the pendulum problem may have served most significantly to direct the minds of the mathematicians toward dynamics. Following Leibnitz, Johann Bernoulli began to work on problems of particle dynamics: as noted, the Brachystochrone problem (path of steepest descent), was solved by Newton, overnight, in 1696. Brook Taylor's solution to the vibrating string problem in 1714 using particle dynamics and the difference calculus preceded the early development of the wave equation by Daniel Bernoulli. The first solution to the wave equation was obtained by Euler and by d'Alembert, apparently independent of each other, around 1749. D'Alembert published his work in 1750 at the Berlin Academy, and Bernoulli published another result in 1755 in the Memoirs of the same Institution. Considering that the method of separation of variables was available from the work of Johann Bernoulli in 1694-97, it is not surprising that methods for solving differential equations of the second-order with constant coefficients soon became available from Euler, with contributions by d'Alembert, between 1733 and 1736.

The solution to the wave equation in its most general form was given by Lagrange in an extensive memoir to the Berlin Academy in 1759, while Lagrange was still residing in Turin. This generalization was made by reverting to a multi-particle model of a string, similar to that used by Taylor. It is this use of the particle model, and by observing that Lagrange's solution shows the number of modes is equal to the number of particles which comprise the string, which suggests that Lagrange may also have been the originator of the single degree of freedom theory. This thought may be pursued by a reading of Lagrange's memoir (1759), and by studying his famous book 'Mecanique Analytique' (1788).

The specific reason for Chladni's (1787) interest in the vibration of plates is not known. It can be surmised that acoustically-excited patterns of plates (or of surfaces, possibly of the sea?) somehow led to Chladni's interest, as the title of his book 'Die Akustik' suggests. Was this a two-dimensional extrapolation of the preceding interest in strings? In any case, Chladni's results stimulated the great French analysts to seek a solution to the plate problem. Their efforts lasted for half a century. Amongst other things, this resulted in Sophie Germain's derivation (1815) of the plate equation, and the general equations of elasticity for plates and solids by Cauchy (1810), Navier (1822-29), Poisson (1831), and others.

If the single degree theory and $\omega = \sqrt{K/M}$ was developed during the Era of the Elasticians, this event has not been widely recognized. Nor is it evident that it occurred during the Century of the Calculus, when the emphasis was on mathematical development, and on the wave equation. And how could it have occurred during the Age of Genius when neither the equations, nor many of the mathematical concepts were available? It therefore appears that although Brook Taylor may have come surprisingly close with his early result for the single degree system, in 1714, his interest lay mainly in explaining the string vibrations. All things considered, Lagrange's interest in the development of equations for discrete systems makes him a likely originator of the single degree theory, and hence of the result $\omega = \sqrt{K/M}$.

CLUES FROM THE CLASSICAL TEXTS

The first textbook on the dynamics of physical systems is the unified presentation by Lagrange 'Mecanique Analytique' (1788). This book contains the development from fundamentals of Lagrange's Principle, with applications. This work is a mathematical treatise, in which geometrical aspects are presented in analytical terms, in the tradition of Descartes, through the introduction and use of Lagrange's procedure. The generalized presentation given is thereby applicable to any physical system.

The first English text to address the subject of vibration is Rayleigh's 'Theory of Sound.' This book is the work of a mathematical physicist, and it shows that the vibration problems of interest to Rayleigh were not viewed in the same manner as they would be today. Rayleigh saw vibration in relation to acoustics alone: he states that 'Without our ears we should hardly care much more about vibrations than without eyes we should care about light,' (Preface, 'Theory of Sound' Volume 1, page xxxiv, 1877). The 'Theory of Sound' is a full compendium of physical knowledge on acoustics and vibrations, together with the mathematics of these subjects, rigorously presented. It is a treatise, not a beginner's textbook. Apparently, Rayleigh was not acquainted with reciprocating steam engine vibrations, nor propeller or paddle wheel vibrations in ships, nor overhead factory lineshaft vibrations, nor shaft whirling (Rankine, 1869), nor the vibrations nor noise of bridges as the steam trains of the day passed over them; and despite related disasters, nor of the Brighton and Menai Straits suspension bridge collapses.

Certain European and Russian books on vibration theory and applications may also have been published during the period 1877 to 1928, but no details of such works are known at this writing. None of the texts mentioned above contain any indication of where the original single degree theory came from, nor gives any indication of the source of $\omega = \sqrt{K/M}$.

Ninety-five years after the publication of Lagrange's book, Rayleigh devoted part of a chapter in the 'Theory of Sound' to the single degree system, in which he cited the results mentioned earlier. These results are stated with no reference to their author. Were they so well-known by 1877, or likely even so trivial in Rayleigh's mind, that there was no need to identify the original source? It seems surprising that all textbooks written since Rayleigh's time have followed his lead with the single degree theory, yet no subsequent author has thus far identified the originator of that theory.

NO SPECIFIC RESULT BUT A CLEARER PICTURE

A review of the evidence available at this time leads us to five conclusions:

1) The physics of string vibrations was understood to some degree by Pythagoras, and more completely by Galileo and Mersenne; but neither Galileo or Mersenne had the equation of the vibrating string, much less the mathematical techniques which are required to achieve a solution to this equation.

2) Taylor gave the first (approximate) solution for the lowest mode of the vibrating string in 1714. D. Bernoulli gave the wave equation for the vibrating string around 1723, but without a solution. This solution was achieved by D'Alembert and Euler between 1747 and 1750, and was generalized by Lagrange around 1759.

3) The pendulum problem was observed by Galileo in 1586. Huygens first devised the cycloidal pendulum in 1659, and obtained the formula for the frequency of oscillation of a pendulum, probably around 1673.

4) The first known publication to give single degree forced damped vibration theory was in Lord Rayleigh's 'Theory of Sound' Volume 1, in 1877.

5) It seems both probable and likely that the single degree theory was available prior to Rayleigh's book.

It is helpful to recall that the mathematical tools for analysis of the single degree system became available in the mid-eighteenth century. These tools were developed by mathematical researchers, who were seeking procedures for general systems. When Euler obtained solutions for second-order ordinary differential equations, d'Alembert immediately applied these solutions for use on partial differential equations, viz. on the wave equation.

It is possible that the single degree theory originated with Lagrange, who generalized Newtonian mechanics into a single comprehensible procedure for all of mathematical physics, and who had the mathematical tools and concepts to achieve such a solution. Could the great Lagrange have for once gazed so low as to attempt to solve the simple problem of a single oscillating particle?

The solution does not appear to have been achieved by the inspired French school of elasticians who began with Chladni, and which included Sophie Germain, Poisson, Cauchy, Navier, Lame, Kirchoff, and Boussinesq, during the years 1786 to 1850. These mathematical physicists were, again, interested in developing general formulations for elasticity, with applications to plates and shells. Vibrations of plates, shells, surfaces, and solids were also studied by the French school, and were later furthered by the English elasticians, beginning with Stokes, Rayleigh, Mitchell, and Love. Simply stated, the formidable talents of all these scientists very likely demanded something more challenging than the simple oscillator. The very simplicity of this system is the reason why the originator of the theory, and of the formula $\omega = \sqrt{K/M}$ has so far not been identified. This work is continuing.

ACKNOWLEDGEMENTS
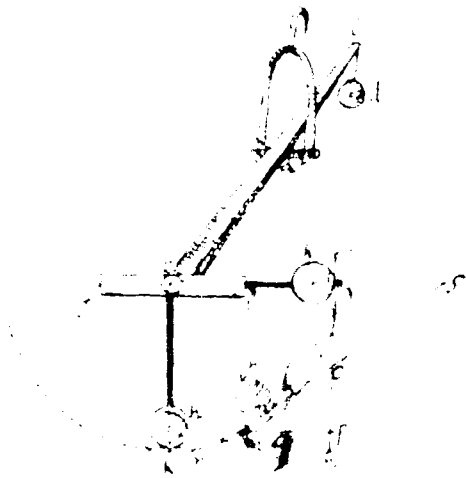
Figure 1

Figure 2   Christiaan Huygens
(1629–1695)

Figure 3   Isaac Newton
(1642–1727)

PHILOSOPHIE
NATURALIS
PRINCIPIA
MATHEMATICA

Autore JS. NEWTON, Trin. Coll. Cantab. Soc. Matheseos
Professore Lucasiano, & Societatis Regalis Sodali.

IMPRIMATUR
S. PEPYS, Reg. Soc. PRAESES.
Julii 5. 1686.

LONDINI,
Jussu Societatis Regiae ac Typis Josephi Streater. Prostat apud
plures Bibliopolas. Anno MDCLXXXVII.

Figure 4   Title Page –
Principia

AXIOMATA
SIVE
LEGES MOTUS

Figure 5   Page From Principia –
First Two Laws of
Motion

GUILL. GODEFROY LEIBNITZ

Figure 6   Gottfried Leibnitz
(1646–1716)
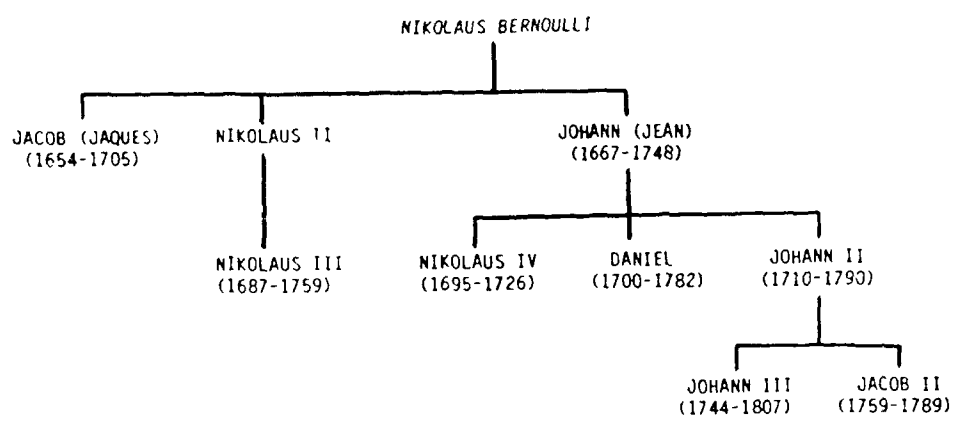
Figure 7   The Bernoullis

Figure 8   Daniel Bernoulli
(1700-1782)

Figure 9   Brook Taylor
(1685-1731)

Figure 10   Leonhard Euler
(1707–1783)

J. D'ALEMBERT
Secretaire perpetuel de l'Académie France membre
de l'Académie des Sciences &c &c

Figure 11   Jean Le Rond D'Alembert
(1717–1783)

Figure 12   Joseph Louis Lagrange
(1736-1813)
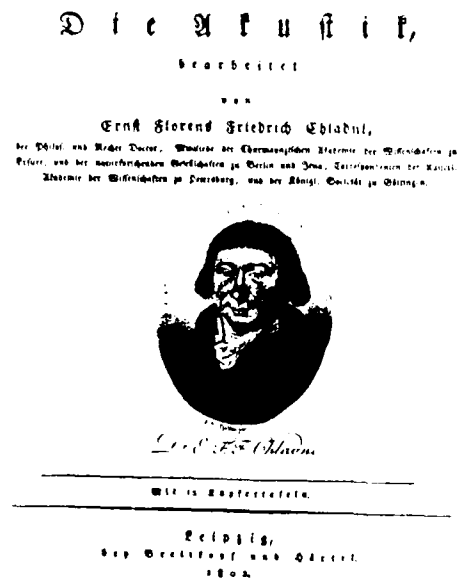
Figure 13   Ernst Florens Chladni
(1756-1827)

Figure 14   Sophie Germain
(1776-1831)

Figure 15   Lord Rayleigh
(1841-1919)

CHAPTER III.

SYSTEMS HAVING ONE DEGREE OF FREEDOM.

43. THE material systems, with whose vibrations Acoustics is concerned, are usually of considerable complication, and are susceptible of very various modes of vibration, any or all of which may coexist at any particular moment. Indeed in some of the most important musical instruments, as strings and organ-pipes, the number of independent modes is theoretically infinite, and the consideration of several of them is essential to the most practical questions relating to the nature of the consonant chords. Cases, however, often present themselves, in which one mode is of paramount importance; and even if this were not so, it would still be proper to commence the consideration of the general problem with the simplest case—that of one degree of freedom. It need not be supposed that the mode treated of is the only one possible, because so long as vibrations of other modes do not occur their possibility under other circumstances is of no moment.

44. The condition of a system possessing one degree of freedom is defined by the value of a single co-ordinate u, whose origin may be taken to correspond to the position of equilibrium. The kinetic and potential energies of the system for any given position are proportional respectively to $\dot{u}^2$ and u^2:—

$$T = \tfrac{1}{2} m\dot{u}^2, \quad V = \tfrac{1}{2} \mu u^2 \dots\dots\dots\dots\dots(1),$$

where m and μ are in general functions of u. But if we limit ourselves to the consideration of positions *in the immediate neighbourhood of that corresponding to equilibrium*, u is a small quantity, and m and μ are sensibly constant. On this understanding we

44   ONE DEGREE OF FREEDOM

now proceed. If there be no forces, either resulting from internal friction or viscosity, or impressed on the system from without, the whole energy remains constant Thus

$$T + V = \text{constant}.$$

Substituting for T and V their values, and differentiating with respect to the time, we obtain the equation of motion

$$m\ddot{u} + \mu u = 0 \dots\dots\dots\dots\dots(2)$$

of which the complete integral is

$$u = a \cos(nt - \alpha) \dots\dots\dots\dots\dots(3),$$

where $n^2 = \mu \div m$, representing a *harmonic* vibration. It will be seen that the period alone is determined by the nature of the system itself, the amplitude and phase depend on collateral circumstances. If the differential equation were exact, that is to say, if T were strictly proportional to $\dot{u}^2$, and V to u^2, then, without any restriction, the vibrations of the system about its configuration of equilibrium would be accurately harmonic. But in the majority of cases the proportionality is only approximate, depending on an assumption that the displacement u is always small—how small depends on the nature of the particular system and the degree of approximation required; and then of course we must be careful not to push the application of the integral beyond its proper limits.

But, although not to be stated without a limitation, the principle that the vibrations of a system about a configuration of equilibrium have a period depending on the structure of the system and not on the particular circumstances of the vibration, is of supreme importance, whether regarded from the theoretical or the practical side. If the pitch and the loudness of the note given by a musical instrument were not within wide limits independent, the art of the performer on many instruments, such as *the violin and pianoforte, would be revolutionized*.

The periodic time

$$\tau = \frac{2\pi}{n} = 2\pi \sqrt{\frac{m}{\mu}} \dots\dots\dots\dots(4),$$

so that an increase in m, or a decrease in μ, protracts the duration of a vibration By a generalization of the language employed in the case of a material particle urged towards a position of equilibrium by a spring, m may be called the *inertia* of the system, and

Figure 16   Pages From The Theory of Sound —
The Theory of Vibration for a
Single Degree System

STATISTICAL ENERGY ANALYSIS
AN OVERVIEW OF ITS DEVELOPMENT
AND ENGINEERING APPLICATIONS

Dr. Jerome E. Manning
Cambridge Collaborative, Inc.
689 Concord Avenue
Cambridge, MA 02138

Statistical Energy Analysis is a technique for predicting the vibration and acoustic response of complex dynamic systems. Unlike classical methods of vibration analysis, SEA is well suited for systems having a large number of modes of vibration. It is therefore often used to predict the high frequency response of structures to broadband random acoustic excitation. However, it can also be used at low frequencies and to predict narrowband vibration levels, if one is willing to adopt a statistical approach to the prediction of vibratory energy. SEA is particularly useful for design projects where complete information describing the system is not available and the predictions must be prepared in a short amount of time. In this paper an overview of SEA is presented. It is hoped that the information presented will give engineers a better understanding of this technique so that they can use it to advantage.

INTRODUCTION

The concept of a "Statistical Energy Analysis" of the vibrations of complex dynamic systems was introduced over 25 years ago. Since then SEA has slowly gained acceptance as a useful analysis procedure for vibration and acoustic problems. Although the technique has been used for a broad range of problems, there continues to be uncertainty regarding the type of problem for which it is suited and the accuracy to be expected. Certainly some of the readers of this paper will be skeptical about SEA and might say "I tried it and it didn't work!" Others may think of SEA as the answer to all their problems. Neither of these extremes is a valid assessment of the current situation. When used properly SEA can provide useful answers to very complicated dynamic problems. The general simplicity of the analysis adds greatly to its appeal. On the other hand, the inability to use SEA to obtain detailed predictions of the vibration response at specific locations and frequencies will disappoint some users. The objective of this paper is to provide the reader with an overview of SEA. It is hoped that the information presented will allow engineers to make intelligent decisions regarding the use of SEA and to know what to expect from this type of analysis.

Many questions exist regarding the use of SEA. One commonly asked question is whether SEA can be used to make predictions based only on drawings without the aid of measured data. The answer is yes with some qualifications regarding the prediction of vibration and acoustic source levels and the prediction of damping. SEA has been successfully used on many occasions to predict vibration and acoustic transfer functions. These combined with measured data to describe the source of the

vibration can be used to make absolute predictions. The prediction of damping can be a problem for any method of vibration analysis. A second commonly asked question is "What is the accuracy of SEA?" Being a statistical technique this question is harder to answer. In general, we can expect the SEA predictions of the mean vibration or acoustic level to be within 5 to 10 dB of the measured one-third-octave band or octave band levels at a specific location. Peaks in the narrow band vibration spectra are generally within 5 to 10 dB of the mean plus two standard deviations of the SEA prediction. The expected accuracy is significantly improved by comparing the SEA predictions with measured data that has been averaged over several measurement locations. We would expect a SEA model to provide predictions in this case within 5 dB of the measured data. In providing such specific estimates of the accuracy of SEA we must point out that these estimates are based on the experience of the author and that surprises can occur even for experienced SEA users.

Many of the applications of SEA are to compare the vibration or noise produced by different designs. Because SEA preserves the parameter dependence in the prediction it is often possible to predict differences as small as 1 or 2 dB. This makes SEA particularly valuable in the design process. It can be used to evaluate various design options and modifications without extensive cost.

In discussing the development and use of SEA we focus on three aspects. First, we must consider the *Statistical* aspect of the predictions. SEA treats the resonance frequencies and mode shapes of a structure or acoustic space as random variables. Although this statistical approach is common in room acoustics, vibration engineers will be less familiar with it. Since the modes are treated statistically, the SEA predictions are also statistical. We must learn how to interpret predictions of the mean and standard deviation of the vibration levels. Second, we must consider the *Energy* aspect of SEA. SEA uses dynamic energy to describe the state of a vibrating system. The use of energy variables allows the use of simple power balance equations to describe the inter-

Figure 1. Overview of SEA

action of coupled systems. It also allows a unified treatment of both structural and acoustic subsystems. However, we must learn to accept predictions of energy and to use these predicted energy levels to obtain the response or stress variables that may be of more immediate interest. Finally, we must consider the *Analysis* aspect of SEA. The dependence of SEA parameters such as modal density and coupling loss factor on geometric and material properties of the system being studied must be understood.
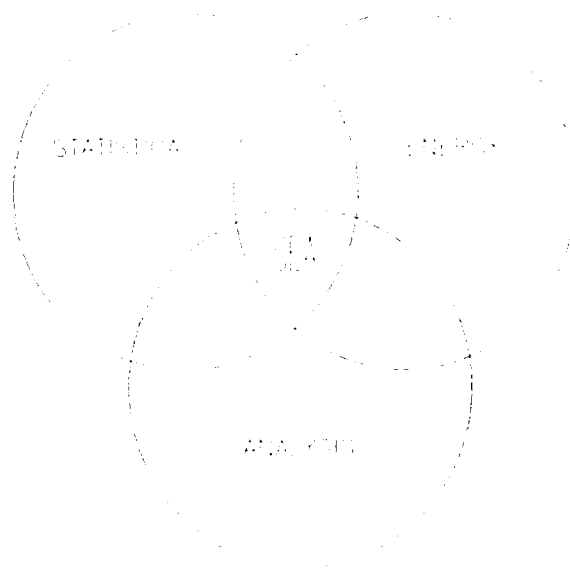
BACKGROUND TO THE DEVELOPMENT OF SEA

Historically, vibration analysis has focused on the low frequency range encompassing the first few resonance frequencies of the structure being studied. Thus, a large number of analytical and numerical techniques have been developed dealing with low frequency vibration problems. None of these techniques are particularly well suited for vibration or acoustic problems in which a large number of modes contribute to the overall response. The techniques of vibration analysis based on modal and finite element methods have been greatly enhanced over the past 10 to 20 years. Although these techniques are valid, at least in principal, for large systems with many modes, their use is often impractical, particularly when the excitation is random and distributed over the structure. The use of these techniques requires a large number of degrees of freedom and extensive computational power. Although these requirements can be met by available computers, the cost to develop, check and validate a large model can be prohibitive. SEA provides a new capability for these problems. Since the modes are treated statistically, they can be divided into a relatively small number of groups of similar modes thereby greatly reducing the number of degrees of freedom. Although the name Statistical Energy Analysis is new the concepts behind SEA have been known for a long time.

Lord Rayleigh is generally recognized for his fundamental contributions to vibration analysis and his work can be considered to be the foundation of modal analysis [1]. Interestingly, Rayleigh (with Jeans [2]) can also be credited with the ideas leading to SEA, although his applications were oriented toward the radiation of electromagnetic energy by a hot body. Following Rayleigh's approach, Nyquist [3] formulated the problem of thermal noise in an electrical circuit using an approach that is amazingly like SEA. Adopting this approach to structural vibrations we consider the vibrations of a one-dimensional structure (a beam) excited

Figure 2. Vibration Transmission from a Structure.

by a random distributed excitation, as shown in Figure 2. The beam is connected at each end to other structures which, for this example, will be considered to be similar. We consider the case where the beam has many modes of vibration. Each mode can be decomposed into two travelling waves - one travelling to the right and one travelling to the left. Thus, the vibration field in the beam can be considered in terms of a number of vibration waves with various amplitudes and phases travelling in each direction. By symmetry the energy in the right-travelling and left-travelling waves can be considered to be equal. The power incident on the right (or left) junction is given by one half the energy density in the beam times the group speed (the speed with which energy can be conducted in the beam). At the junction a fraction of the incident power is transmitted to the connected structure and the rest is reflected. The ratio of the transmitted power to the incident power is a transmission coefficient, τ, which is expressed in Equation 1 in terms of the

impedances of the structures, where Z_1 is the complex impedance of the beam, Z_2 is complex impedance of the structure connected to the right, and R_1 and R_2 are the resistances (real part of the impedances). The power transmitted from the beam, (1), to the connected structure, (2), is now given by Equation 2, where e_1 is the energy density (energy per unit length) and c_{g1} is the group speed. The energy density can be assumed to be uniformly distributed along the beam, and therefore can be expressed as the ratio of the total energy, E_1, to the length of the beam, L_1. The power transmitted can then be written as Equation 3. The quantity in brackets is recognized to be the inverse of the modal density of the beam. Thus, the power transmitted in a band of frequencies Δf can be given in terms of the modal energy, ϵ_1, by Equations 4 and 5. From this result we see that the power transmitted from the beam to the connected structure is proportional to

$$\tau_{12} = \frac{4 \, R_1 \, R_2}{|\, Z_1 + Z_2 \,|^2} \tag{1}$$

$$W_{12}^{trans} = \frac{1}{2} \, \tau_{12} \, e_1 \, c_{g1} \tag{2}$$

$$W_{12}^{trans} = \tau_{12} \, E_1 \left[\frac{c_{g1}}{2 L_1} \right] \tag{3}$$

$$W_{12}^{trans} = \tau_{12} \, \epsilon_1 \, \Delta f \tag{4}$$

$$\epsilon_1 = \frac{E_1}{n_1(f) \, \Delta f} \tag{5}$$

the modal energy and a power transmission coefficient, which can be expressed in terms of the impedances of the structures. Returning to Nyquist's formulation the beam is an electrical circuit and the terminating structures are assumed to be resistors with a resistance R. The energy of each mode in the circuit is assumed to be the same, at least statistically, according to the equipartition theorem of statistical mechanics. The modal energy is set to equal kT where k is Boltzmann's constant and T is the absolute temperature. In the absence of any sources and under the condition of thermal equilibrium the power transmitted to the resistor must be equal to the power generated by the resistor due to thermal noise. This emitted power can then be given by Equations 6 and 7. The corresponding mean-square current in the line is given by Equation 8 and the voltage required to generate this current is given by Equation 9. Combining these results we can represent the thermal noise of the resistor by a source voltage given by Equation 10. Although this formulation by Nyquist is 60 years old it continues to serve electrical circuit designers. Hopefully, SEA will also continue to serve designers 60 years from now.

In deriving the results above we have assumed a state of thermal

$$W^{emitted} = W_{12}^{trans} \tag{6}$$

$$W^{emitted} = \tau_{12} \, kT \, \Delta f \tag{7}$$

$$<i^2>_t = \frac{W^{emitted}}{R_1} \tag{8}$$

$$<v^2>_t = <i^2>_t \,|\, Z_1 + R \,|^2 \tag{9}$$

$$<v^2>_t = 4 \, R \, kT \, \Delta f \tag{10}$$

equilibrium exists so that the power transmitted equals the power returned. This is not always the case, particularly for vibration and acoustic problems. However, we can extend the above analysis so as to express the net power as the difference between modal energies

$$W_{12}^{net\ trans} = r_{12}\ \Delta f\ \left[\ \epsilon_1 - \epsilon_2\ \right] \tag{11}$$

This result, that the net power transmitted is proportional to the difference in modal energies, is the basic result underlying SEA [4]. It allows a power balance to be performed in which the power input to a system from vibration and acoustic sources is balanced with the sum of the power transferred to other connected structure and the power dissipated due to damping.

Credit for recognizing that the statistical theory used by Rayleigh, Jeans, and Nyquist had relevance to vibration problems must be given to R. H. Lyon. His paper with G. Maidanik [5], "Power Flow Between Linearly Coupled Oscillators," can be credited as being the birth of SEA, although the name had not yet been formed. Many others working in the area of vibration and acoustics must also be given credit for recognizing the importance of using a statistical approach in describing the vibrations of complex systems.

Previous to Lyon's work, Powell [6] formulated the response of a finite plate to an exciting pressure field. Powell showed that the response spectrum for the plate can be approximated by that for an infinite plate if the damping is sufficiently large as to cause modal overlap. This restriction on damping is not valid for many typical structures. However, Powell went on qualitatively and showed that the average spectral level over a band of frequencies can be approximated by the response spectral level of the infinite plate if the band encompasses many resonances of the plate. At approximately the same time, Skudrzyk [7] advanced the idea that the point impedance of an infinite panel is equal to the impedance of the finite panel if that impedance is averaged over a band of frequency. Skudrzyk also pointed out the role of the modal density as a bridge between the behavior of finite and infinite systems. Although Powell and Skudrzyk were among the first to recognize that statistics; e.g. frequency averages, could be used to advantage, others, such as Maidanik, Smith, Heckl, Bolotin, and Ungar made important contributions to the problem of understanding the behavior of coupled structures and acoustic spaces that have become a part of SEA [4].

By 1965 the basic concepts of SEA had been developed, but the technique had been applied to only a few cases. In the period from 1965 to 1975 the applications of SEA were greatly expanded. Manning [8] and Scharton [9] made early contributions by applying SEA to systems with many SEA mode groups. Others such as Crocker [10] and Fahy [11] expanded the use of SEA. The period from 1975 to 1980 saw a slow expansion of SEA applications. However, it was becoming clear that the calculation of SEA coupling loss factors was not a simple procedure. Two approaches emerged for calculating coupling loss factors: the mode approach and the wave approach. Following the mode approach coupled structures are described in terms of coupled modes with a mode-to-mode coupling factor being used for each pair of coupled modes. Following the wave approach the dynamic response of coupled structures is described in terms of travelling waves using transmission coefficients and impedance analysis to calculate a coupling loss factor. As should be expected the two approaches generally lead to the same result [12]. The original derivation by Lyon used the mode approach and this approach continues to be of interest. Those contributing to this approach include Lyon, Scharton, Ungar, Newland, and most recently Woodhouse. The derivation shown above in this paper follows the wave approach. This approach

al so continues to be of interest. Those contributing to the wave approach include
Smith, Heckl, Eichler, Fihlman, and Moore.

Although the expanding applications of SEA are important, the significant
advancement to the technique was the development of general purpose SEA software
programs. At Cambridge Collaborative, Inc. DeJong and Powell developed a general
purpose program, SEAM™, which is being marketed by that company. Although the
program has been updated and significantly improved, the basic flow of their
original modelling procedure has been preserved. Two other programs of significant
merit were developed at approximately the same time: Cosmic SEA by McDonnell Douglas
and VAPEPS by Lockheed. These software programs are available from the University
of Georgia and the Jet Propulsion Laboratory, respectively. Of the three programs
SEAM is the most extensive and has been used for the most diverse range of problems.
SEA models of ship structures, helicopters, construction equipment, automobiles,
aircraft, and space structures have been developed using SEAM. The VAPEPS program
is often used to predict payload environments for spacecraft structures and has the
important added feature of a data base, which can be used to compare and catalog
measured data.

DEVELOPING SEA MODELS

The general procedure for developing an SEA model is shown in Table I. Following this procedure there are six steps. The first three steps generally require some experience in SEA modelling in that the selection of subsystems and junctions can have a direct effect on the results obtained. Steps 4 through 6 of the procedure may require significant computations, but are generally amenable to implementation in a general purpose SEA software program. The SEAM, VAPEPS, and COSMIC-SEA programs are three examples of such software programs.

The first step of the general procedure is to identify SEA subsystems. The number of subsystems determines the number of degrees of freedom in the SEA model and the number of equations that must be solved. Each subsystem consists of a group of modes of vibration. The degree of freedom is the modal energy or average energy per mode of the group. Although it is not necessary, the identification of mode groups can be done by first substructuring the overall dynamic system into a set of coupled structures and acoustic spaces. The structures are generally represented by homogeneous beams, frames, pipes, plates, shells, and solids. Orthotropic plates and shells may be required for some models.

Step 1:	Identify SEA Subsystems
	Substructure
	Identify similar modes
Step 2:	Identify Junctions
	Point, line, and area junctions
Step 3:	Compute Power Inputs
	Impedance formulation
Step 4:	Compute SEA Parameters
	Modal densities
	Coupling factors
	Damping factors
Step 5:	Power Balance Equations
	Form matrix equation
	Solve for modal energies
Step 6:	Response Statistics
	Relate to modal energies
	Mean response
	Standard deviation

Table I. General Procedure for SEA.

The acoustic spaces are generally represented by one, two, and three dimensional spaces. The modes of each substructure are then divided into groups of similar modes. For example, the modes should be grouped according to their resonance frequencies with modes having resonances within a given one-third octave band being grouped together. The modes should also be grouped according to their direction of response. For example, the bending, longitudinal, and torsional modes of a beam should be grouped separately. In plate structures, the bending, longitudinal, and shear modes may be grouped together, although the longitudinal and shear modes are often grouped together into a single mode group because they are strongly coupled in most structures and can be expected to have the same modal energies. A simple example of substructuring and mode group identification is shown in Figures 3 and 4.

The connections between the subsystems are identified in terms of junctions. In general the junctions can be idealized as point, line, and area junctions. The type of junction and the subsystems connected at the junction determine the coupling factors between the subsystems. Two computational methods exist for determining these coupling factors: the mode approach and the wave approach. It can be shown that both approaches lead to the same coupling factor. However, in general the mode approach is more useful for systems with a fixed number of resonance frequencies while the wave approach is more useful for continuous systems. For those interested in calculating their own coupling factors there are a number of references available. Most of us, however, are content to use the coupling factors from the available software programs so that we can focus more attention on selecting SEA subsystems and junctions.

The calculation of power input from vibration and acoustic sources can be carried out either by specifying the excitation forces or by specifying the modal energy of the excited subsystem. Using the first approach, an impedance analysis is used to calculate the power input to the system. In this approach it is assumed that the excitation forces are unaffected by the vibrations of the system being excited. The source is assumed to have infinite impedance. This assumption is often not appropriate. A related procedure is to specify the vibrational displacement (or velocity or acceleration) of the source. An impedance analysis can
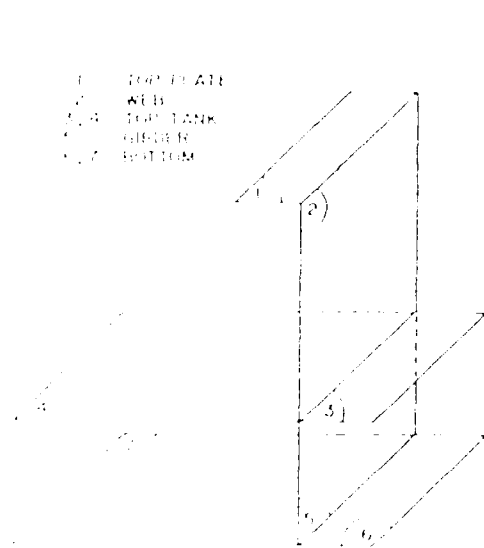
Figure 3.   Connected Plate Structure

Figure 4.   Mode Group Identification

31

still be used with the source having an zero impedance. Again this assumption may not be appropriate. Although an impedance analysis can be carried out with a finite source impedance, the second approach of specifying the modal energy of the excited subsystem is generally more useful. This is particularly true for acoustic excitation. Since the pressure acting on the structure can be affected by its response, the best procedure for specifying the source is to create a large acoustic space and to specify the modal energy of that space using Equation 13 to relate modal energy to mean-square pressure. Remember that the mean-square pressure measured on a rigid surface will be twice the mean-square pressure in Equation 13, which is the mean-square pressure away from any surfaces.

PRESENTATION OF SEA PREDICTIONS

By using SEA we obtain predictions of the modal energies of each group of modes used to describe the dynamic response of the complex system being studied. Although it is possible and perhaps desirable to develop design criteria based on vibratory energy, this has not been done. Thus, we are generally interested in predicting response variables such as acceleration, pressure, stress, displacement, etc. rather than modal energies. In addition, we are often interested in validating the SEA predictions by comparing them with measured data. Since energy cannot be measured directly but must be inferred through response measurements at specific locations, we are again interested in predicting response rather than modal energies.

To obtain response predictions from energy we use the SEA assumption that the dynamic response of the system is dominated by the resonant response of the individual modes. Thus, we can take the time-average kinetic and potential energies to be equal. In the case of structures the mean-square response velocity averaged over the spatial extent of the structure can be related to the time-average kinetic energy (which is taken to be one-half the total energy) the structure mass and the modal density,

$$<v^2>_{t,x} = \frac{n(f) \, \Delta f \, \epsilon}{M} \tag{12}$$

Similarly, for acoustic systems the mean-square pressure averaged over the spatial extent of the structure can be related to the time-average potential energy, which is taken to be one-half the total energy,

$$<p^2>_{t,x} = \frac{n(f) \, \Delta f \, \epsilon}{C_a} \tag{13}$$

where the acoustic compliance C_a is given by $V/\rho c^2$. If we define a structural compliance as V/E, where V is the structure volume and E is an extensional modulus (Youngs Modulus for beams or plates), Equation 13 can also be used to predict the mean-square stress averaged over the volume of the structure. The relationship between mean-square response and modal energy can also be expressed in terms of the drive point conductance at the measurement point as

$$<v^2(x)>_t = \frac{2}{\pi} \, \epsilon \, G_f \, \Delta f \tag{14}$$

... is the drive point conductance averaged over the frequency band Δf. It is ... the point conductance over the spatial extent of the structure. Equation 1 ... shown to be equivalent to Equation 1'. However, we can also use Equation 1 ... with the reverberant velocity and the measured point conductance to ... measured value of the modal energy.

... Figure ... shows a comparison of the SEA prediction of the transfer mobility (the amplitude at a response point divided by the applied force amplitude at an ... point) for a fluid filled piping system to the narrowband transfer ... obtained from a large finite element model. The agreement between the SEA and the finite element data is reasonably good if we average over frequency, ... the agreement at any one frequency is rather poor. Note, however, that the ... the narrowband spectrum generally fall within ... two times the standard ... In Figure ... the SEA prediction of the transfer mobility in octave bands ... compared with the finite element data. Again the comparison between the SEA mean and the finite element data is quite good, although significant deviations occur at ... frequencies. The frequency range below 500 Hz for this model encompasses the ... few resonances of the piping system. Although the SEA model is generally not ... at these low frequencies we expect the peaks in the data to be encompassed ... the SEA prediction of the mean plus two standard deviations.

An important feature of SEA is its ability to guide the development of design ... modifications. Toward this end we identify a SEA subsystem for which a design goal ... the vibration or acoustic level can be set. We then look at the power input ... connected subsystems. To calculate the power input from these subsystems the ... modal energies are combined with the SEA coupling factors to calculate the ... input from each connected subsystem. A pie chart can then be constructed as shown in Figure ... This chart is for the power input to the passenger compartment of ... automobile in the one-third-octave band centered at 250 Hz. The floor panels ... seen to be the major source of interior noise (for the operating condition considered) contributing 40% of the total power input to the space.

... Prediction Compared with   Fig 6 SEA Prediction Compared with
Narrowband Finite Element Data   Octave Band Finite Element Data
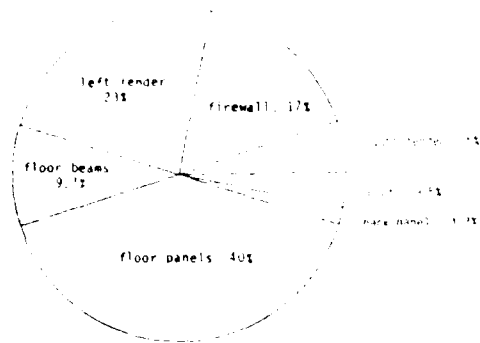
Fig. 7   Power Input to the Passenger   Fig. 8   Power Balance for the Floor Panels
         Acoustic Space
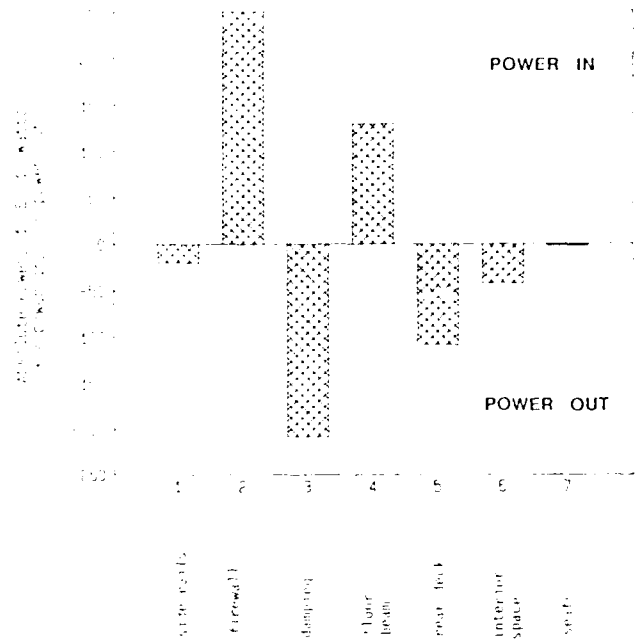
     The pie charts give an effective presentation of the power input to a subsystem
and thereby assist in identifying the primary noise sources.   However, the pie chart
does not show a complete picture of the power balance for the subsystem.   This
objective is best accomplished using bar charts.   For the example of the automobile
interior we may be interested in the power balance for the floor panels since they
were found to be the major source of interior noise.   A bar chart for the power in
and power out to connected subsystems and to damping is shown in Figure 8.   Bars
extending above the midline represent power input to the subsystem.   Bars extending
below the midline represent power dissipation or power leaving the subsystem.
Examination of these charts allows the vibration engineer to identify the subsystems
and paths of vibration transmission contributing most to the vibration or acoustic
levels.   Vibration and noise control can then focus on these important subsystems.

EXAMINATION OF SEA ASSUMPTIONS

     A key premise of SEA is that the resonance frequencies can be considered to be
random variables.   Ot immediate concern then is the assumed probability distribution
of the resonances and the influence of the assumed distribution on the SEA pre-
dictions.   Many of the basic concepts used to describe stochastic processes can be
applied to the problem of describing resonance frequencies statistically.   In most
basic reference material the stochastic process is considered to be a random
function of time.   We can make use of these references if we substitute frequency
for time.   The occurrence of a resonant frequency can be considered to be a random
"event" occurring as a function to frequency rather than time.   This allows us to
define a resonant frequency (or mode) counting function, which is a positive,
integer valued function of frequency which increments by one at each resonance

frequency.[1] Nearly all of the basic results of SEA have been obtained by assuming that the resonant frequency counting function is a Poisson Process. This assumption has been made in large part because of the extensive use of this type of random process to study such random events such as the failure of machines, noise in electron tubes, arrival of customers at a ticket window, price movements in the commodity market, and the spatial distribution of biological species. Because of this use many results are available regarding the statistical description of the resonance frequencies of the modes of a structure or acoustic space.

In a paper published in 1970 Lyon [13] discusses the influence of the assumption of that the resonance frequency counting function is a Poisson Process on the SEA predictions. He concludes that the SEA predictions of mean modal energy values are not significantly affected by the form of the probability distribution. The variance, however, was significantly affected. In many of the recent applications of SEA variance has been used to predict the peaks in the vibration or acoustic response spectra, since many design criteria are based on envelopes of the spectra rather than mean values. As a consequence we must examine in more detail the underlying assumption that the resonance frequencies can be described by a Poisson Process.

One test the validity of the Poisson assumption is to form the probability distribution for the intervals between resonance frequencies. The spacing intervals are formed by sorting the resonance frequencies in ascending order and calculating the spacing between a resonance frequency and its next neighbor. If the underlying resonance frequency counting function is Poisson the spacing intervals must be statistically independent and distributed according to an exponential distribution.

Before the development of finite element modelling it was difficult if not impossible to predict or measure the resonance frequencies of complex structures at high frequencies. Therefore in Lyon's paper examples from electromagnetic experiments are used to study the underlying frequency spacing statistics. The use of finite element models now makes it possible to study frequency spacing statistics for complex structures.

In Figure 9 we show the counting function for resonance frequencies of the interior of a large vehicle (solid line). The resonance frequencies were obtain from a finite element model of the interior space. To test whether the Poisson Process is a good model for these resonance frequencies we must compute resonance frequency spacings (the difference between adjacent resonance frequencies) and normalize the spacing so that so that the average rate of occurrence of resonance frequencies is constant over the range of frequencies being considered. The mean rate of occurrence of resonance frequencies is equal to the modal density of the system, which can be calculated by smoothing the resonance frequency counting function and differentiating with respect to frequency. Thus, we can normalize the resonance frequency spacings by multiplying each spacing by the modal density, which may be a function of frequency. A smoothed resonance frequency counting function is shown in Figure 9 (broken line). Using this smoothed function we obtain the resonance frequency spacings shown in Figure 10. These certainly look random! The normalized frequency spacings are then sorted into bins to obtain an estimate of the probability distribution function. This is shown in Figure 11 and compared to an exponential distribution.

---

[1] The term "counting function" is consistent with terminology used in describing random processes. However, in room acoustics and in several papers on SEA the term "cumulative mode count" or "mode count" is used for this function. Since Lyon[4] defines mode count differently we prefer to use the term counting function to avoid confusion.
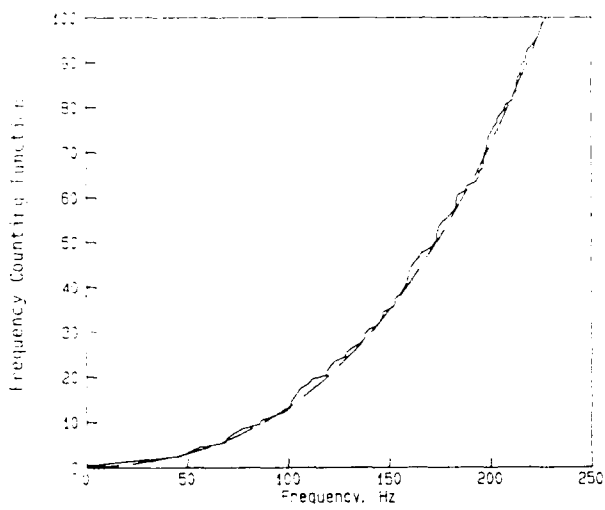
Fig. 9   Resonance Frequency Counting
         Function
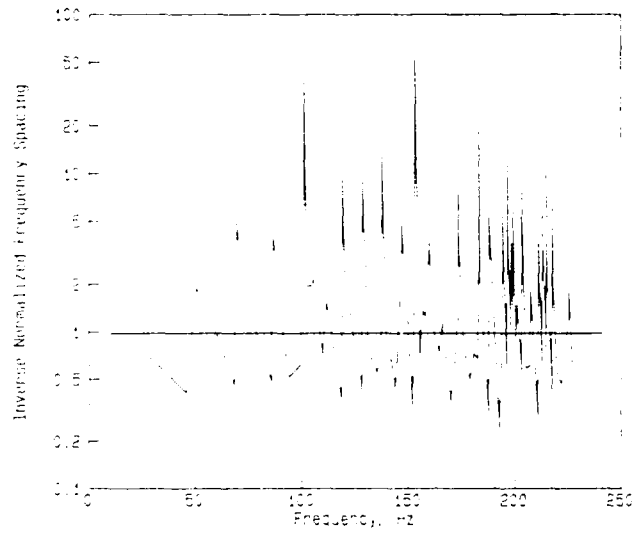
Fig. 10   Inverse Normalized Frequency
          Spacing
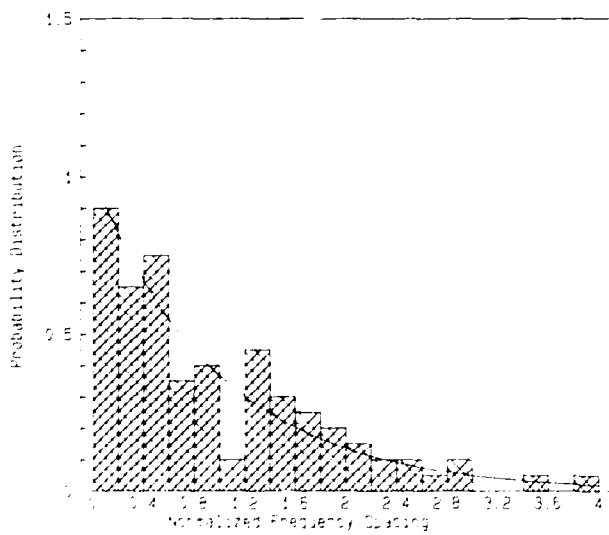
Fig. 11   Probability Distribution of the
          Frequency Spacings - Vehicle
          Interior
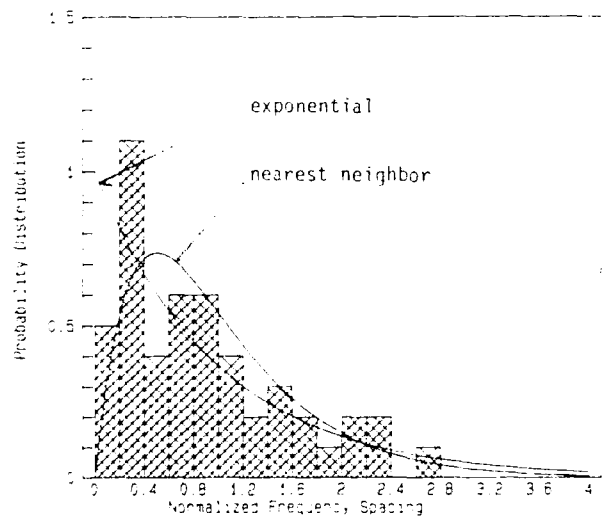
Fig. 12   Probability Distribution of the
          Frequency Spacings - Ship
          Foundation

The comparison is quite good, which suggests that the underlying process is Poisson.

The resonance frequency spacing statistics for a second case is shown in Figure 12. The resonance frequencies for this case are from a finite element model of a large ship foundation and hull structure out to a major bulkhead. A model with approximately 5,000 degrees of freedom was use to compute the first 100 resonance frequencies. In this case the probability distribution function fits a "nearest neighbor" distribution better than the exponential distribution, which suggests that the underlying process is not Poisson. Physically, the deviation from a Poisson Process may result from modal coupling which causes some degree of repulsion between adjacent resonant frequencies. Note that the nearest neighbor distribution deviates from the exponential distribution for small values of spacing, which would result from the repulsion effect.

The difference between the two cases shown suggests that the Poisson assumption may be valid for some cases and not others. The author believes this to be the case although more evidence is needed to draw definitive conclusions. The difference in the two cases studied is in the degree of modal coupling that exists. In the case of the vehicle interior the boundary conditions and cross-section of the space were taken to be uniform along its length. Thus, the underlying equations describing the acoustic pressure fluctuations are separable so that eigenvalues can be expressed as the sum of squares of the cross mode eigenvalues and the longitudinal mode eigenvalues. No modal coupling occurs. The model of the ship foundation is much more complex with plates and frames aligned in different planes. In this case the underlying equations cannot be separated and a description of the modes requires a coupling of the modes of each plate substructure in accordance with a modal synthesis technique. In other words, modal coupling occurs.

The evidence presented above suggests that further research is needed to determine the conditions under which the Poisson assumption can be used. Given the large number of finite element models that are available readers are encouraged to test the Poisson Process assumption by calculating normalized resonance frequency spacing statistics.

CONCLUSIONS

Statistical Energy Analysis can be effectively used to predict the vibration and acoustic response of complex dynamic systems. The technique is particularly useful at high frequencies or for large structures where many modes of vibration contribute to the response. In this paper we have shown that the concept behind SEA - treating resonance frequencies as random variables - is not new. However, many vibration engineers may be uncomfortable at first with a statistical approach. The key parameters in SEA are the modal density, the coupling loss factor, and the damping loss factor. The calculation of these parameters is not always simple. Fortunately, software programs such and SEAM, VAPEPS, and COSMIC-SEA take care of most if not all the calculations. This greatly aids in the development and application of SEA modeling and has made SEA a truly useful engineering prediction procedure.

In most of the SEA development to date the resonance frequencies have been assumed to be described statistically by a Poisson Process. It has been shown that this assumption may not be valid for complex systems. Although the prediction of the SEA mean is not strongly dependent on the assumed distribution of resonances, the SEA variance may be significantly changed. This is important when using SEA at low frequencies where the variance can be quite large. At these frequencies we would like to improve the SEA prediction by reducing the variance. This can be done by improving the assumption regarding the distribution of resonance frequencies.

REFERENCES

1. J.W. Strutt, Lord Rayleigh, The Theory of Sound, Vol. 1 and 2, 1877, reprinted Dover, New York, 1945.

2. The Rayleigh-Jeans radiation theory is well known in physics.

3. H. Nvquist, Phys. Rev., Vol. 32, pp. 110, 1928

4. R.H. Lyon, Statistical Energy Analysis of Dynamical Systems, M.I.T. Press, Cambridge, MA, 1975.

5. R.H. Lyon and G. Maidanik, "Power FLow Between Linearly Coupled Oscillators," J. Acoust. Soc. Am., Vol. 34, pp. 623-639, 1962.

6. A. Powell, "On the Approximation to the Infinite Solution by the Method of Normal Modes for Random Vibration," J. Acoust. Soc. Am., Vol. 30, No. 12, 1958.

7. E. Skudrzyk, "Vibration of a System with a Finite or an Infinite Number of Resonances," J. Acoust. Soc. Am., Vol. 30, No. 12, 1958.

8. J.E. Manning et al., "The Transmission of Sound and Vibration to a Shroud-Enclosed Spacecraft," NASA Contractor Report, 1966.
    also in R.H. Lyon, Random Noise and Vibration in Space Vehicles, Monograph SVM-1, Shock and Vibration Information Center, 1967.

9. T.D. Scharton, "Random Vibration of Coupled Oscillators and Coupled Structures," Sc.D. thesis, MIT Dept. of Mech. Eng., 1965.
    also R.H. Lyon and T.D. Scharton, "Vibrational Energy Transmission in a Three-Element Structure," J. Acoust. Soc. Am., Vol. 38, No. 2, 1965.

10. M.J. Crocker and A.J. Price, "Sound Transmission Using Statistical Energy Analysis," J. Sound Vib., Vol. 9, 1969.

11. F.J. Fahy, "Vibration of Containing Structures Excited by Sound in the Contained Fluid," J. Sound Vib., Vol. 10, No. 3, 1969.

12. S.H. Crandall and R. Lotz, "On the coupling Loss Factor in Statistical Energy Analysis," J. Acoust. Soc. Am., Vol. 49, No. 1, 1971.

13. R.H. Lyon, "Statistical Analysis of Power Injection and Response in Structures and Rooms," J. Acoust. Soc. Am., Vol. 45, 1969.

DATA BASES

DOE/DOD ENVIRONMENTAL DATA BANK

C. A. Davidson
Applied Mechanics Division II
Sandia National Laboratories
Albuquerque, NM 87185

ABSTRACT

The purpose of this paper is to describe an engineering analysis support activity which involves the collection, analysis, storage, and retrieval of technical environmental information. This information is at the disposal of system and component analysts for use in formulating initial conditions, forcing functions and performance requirements for numerous hardware application evaluations. This paper will describe the Engineering Environmental Data Bank system which provides this information service to many Sandia Laboratories' technical analysis efforts and other qualified programs. Its structure and data sources will be summarized.

INTRODUCTION

From the moment of its manufacture, equipment is exposed to one or more potentially adverse environments. This exposure may affect the useful life of the equipment during storage, transport, handling, and use. It has been found that it is useful to have a central store of measured environmental data available to the technical community to aid in establishing design and test criteria. Such a "Data Bank" of information was developed, began operations in 1959, and is currently being maintained at Sandia National Laboratories.

SOURCES OF INFORMATION

Environmental information for inclusion in the Data Bank is acquired from many sources. Military agencies, such as Aberdeen Proving Ground, Wright Air Development Center, Naval Ordnance Test Center, Air Force Environmental Technical Applications Center (ETAC), and Army QM R&E Center, and industrial groups, such as railroads, aircraft companies, and trucking concerns, have contributed information. A considerable portion of the information has been obtained from various project groups within Sandia Laboratories. The Data

Bank's operators not only extract information from published sources, but engage in specific research activities to obtain data not otherwise available.

The original data sources are referenced on each entry in the Data Bank.

STRUCTURE OF THE ENVIRONMENTAL BANK

Environmental data can be defined as numerical descriptions of the aggregate of all external conditions and influences affecting the development and survival of systems, subsystems, and components. For efficient collection and evaluation of these data, fourteen basic environmental categories were established and the filing system is based upon them.

Environmental Categories

1. Acceleration/time histories	8. Pressure
2. Acoustic noise	9. Radiation
3. Atmospheric contents	10. Shock
4. Biotic	11. Temperature
5. Fragmentation	12. Trajectory
6. Humidity	13. Vibration
7. Precipitation	14. Wind

For purposes of indexing and data retrieval, the data are catalogued under two major headings: Normal and Abnormal Environments.

The normal environments are those which will be encountered regularly. They are characterized by a high frequency of occurrence but relatively low intensity. The abnormal environments, on the other hand, are not encountered often. They are characterized by a low frequency of occurrence but high intensity. As an example, consider wind. At any given location there are many more hourly measurements of winds ranging from calm to 20 mph (normal) than there are of catastrophic winds ranging from 70 to 100 mph (abnormal).

Not all environments lend themselves to the normal/abnormal division. Three factors operate to limit the number of abnormal environmental levels which require consideration.

1. Some environments reach an absolute limit. For example, humidity is limited by ambient temperature; e.g., relative humidity cannot exceed 100 percent.

2. The abnormal aspects of some environments are encountered so infrequently that they are of little interest; e.g., acoustic noise of such intensity as to cause structural damage.

3. Protection against the effects of some normal environments includes protection against the abnormal; e.g., protection against entry of liquid water is effective in a cloudburst as well as during drizzle.

For these reasons, the abnormal levels of environment are considered only in the following categories.

Environmental Categories	Abnormal Manifestation Examples
Acceleration/time histories	Earthquake, vehicle collision
Fragmentation	Projectile impalement, explosion, puncture
Pressure	Explosion, immersion depth, crush
Radiation	Lightning (direct strike)
Shock	Impact (vehicle collision)
Temperature	Fire
Wind	Wind storm (tornado, hurricane, etc.)

All of the environments, in both normal and abnormal aspects, are considered from the standpoint of either input or response. Definitions are necessary to differentiate input from response data. Whether the environment can be termed _input_ or _response_ is often dependent upon the system being considered. Basically, an _input_ is defined as "the environment to which a system is exposed" and _response_ is "the reaction of components of that system to an input."

Under the input and response headings, each of the categories is further divided into the individual use phases that occur during the life of a system:

1. Handling,
2. Storage,
3. Transport,
4. Utilization, and
5. General.

The transport and utilization phases are further subdivided into the type of carrier involved; e.g., aircraft, automobile, railroad, etc. Figure 1 is a diagrammatic representation of the cataloging structure of the Environmental Data Bank.

ENVIRONMENTAL DATA BANK OPERATION

When either raw data or published information are acquired by the Data Bank, they are reviewed for engineering data content. Pertinent information is then extracted, assigned a numerical index number, collated, and microfilmed. Two forms of microfilm are currently used: aperture cards and microfiche. The data cards and/or microfiche are filed in numerical order without regard to subject. This manual technique, along with the use of a computer-aided system, makes it possible to maintain a flexible file, permits complete data retrieval, and makes publication of a current index [1] feasible.

Facilities for viewing the data and obtaining hard copy are located at the Bank site.

There is a two-part number listed after the title of a particular Data Bank entry which is the access number for the data file. The first number, e.g., 1614, is the file number. The number after the dash (-) is the number of
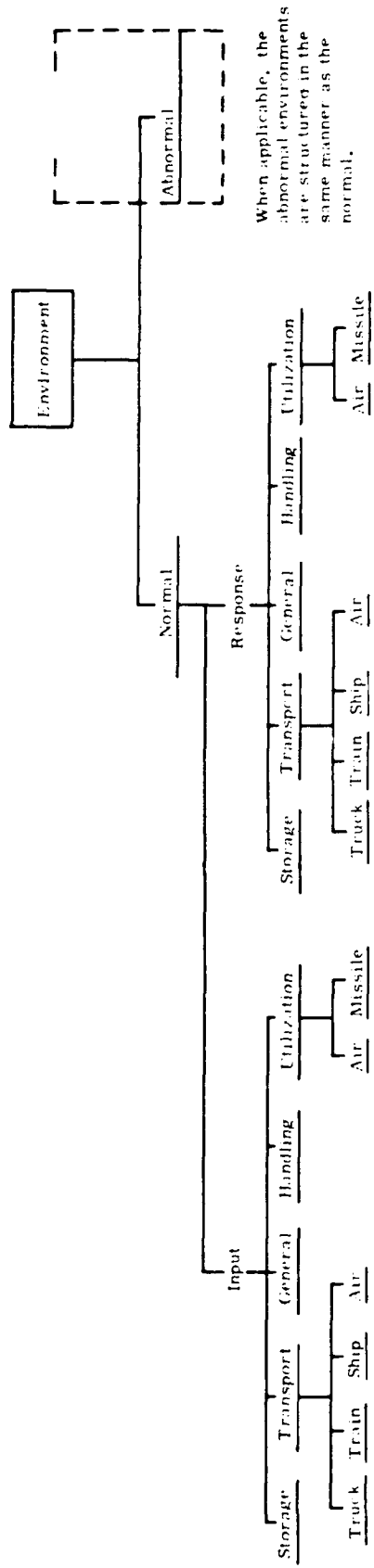
Figure 1. Cataloging Structure of the Environmental Data Bank

pages available on the subject. File numbers that contain an alphabetical prefix are summarized data. Requests for hard copies of data generally cite these two numbers. For a large data request, it is faster and more economical for the Data Bank operators to transmit the data to the requester in the form of duplicate microfilm aperture cards or duplicate microfiche.

DATA BANK OUTLOOK

The index and selected holdings of the Environmental Data Bank are in the process of being installed as part of a computerized data base management system under development at Sandia. This system, called GREEDI, is being implemented to facilitate management of and access to current and frequently used engineering data, and is discussed in detail in Reference 2. Options for upgrading hardcopy backup and reproduction equipment, which is compatible with GREEDI, are also under investigation. These changes are expected to significantly ease the indexing, filing, and retrieval burden of the data bank manager as increasingly more digitized data become available.

REFERENCE

1. Davidson, C. A., Foley, J. T., Scott, C. A., DOE/DOD Environmental Data Bank Index, SAND 85-0155, May 1985.

2. Adams, C. R., and Kephart, E. M., "GREEDI - The Computerization of the DOE/DOD Environmental Data Bank," 59th Shock and Vibration Symposium Proceedings, October 1988.

GREEDI – THE COMPUTERIZATION OF
THE DOE/DOD ENVIRONMENTAL DATA BANK[1]

Charles R. Adams
Sandia National Laboratories
Organization 1522
P.O. Box 5800
Albuquerque, NM 87185

Elisa M. Kephart
RE/SPEC Inc.
Software Engineering Division
P.O. Box 14984
Albuquerque, NM 87191

One of the major responsibilities of Sandia National Laboratories is to develop shock and vibration specifications for system mechanical, electrical, and pyrotechnic components. The data required to generate these specifications are collected from finite element analyses, from laboratory simulation experiments with hardware, and from environmental tests. The production of the component specifications requires the analysis, comparison, and continual updating of these data. Sandia National Laboratories has also maintained the DOE/DOD Environmental Data Bank for over 25 years to assist in its shock and vibration efforts as well as to maintain data for several other types of environments. A means of facilitating shared access to engineering analysis data and providing an integrated environment to perform shock and vibration data analysis tasks was required. An interactive computer code and database system named *GREEDI* (a Graphical Resource for an Engineering Environmental Database Implementation) was developed and implemented. This transformed the DOE/DOD Environmental Data Bank from a card index system into an easily accessed computerized engineering database tool that can manage data in digitized form. GREEDI was created by interconnecting the *SPEEDI* (Sandia Partitioned Engineering Environmental Database Implementation) code, and the *GRAFAID* code, an interactive X-Y data analysis tool. An overview of the GREEDI software system is presented.

INTRODUCTION

The development of shock and vibration specifications for system mechanical, electrical, and pyrotechnic components is one of Sandia National Laboratories' major responsibilities. The data required to generate these specifications are collected from finite element analyses, laboratory simulation experiments with hardware, and environmental tests. The production of the component specifications requires the analysis, comparison, and continual updating of these data. Previously, each engineer used *GRAFAID* [1], an interactive X-Y data analysis tool, to perform these tasks and to maintain his own database file copies of these data. For engineers to share data, duplicate copies of the data files had to reside on the computer, one for each engineer using the data.

Sandia National Laboratories has also maintained the DOE/DOD Environmental Data Bank [5] for over 25 years to assist in its shock and vibration effort as well as to maintain data for several other types of environments. This data bank consists of data represented in a variety of formats stored on microfiche, aperture cards, and microfilm. Computerized access to this national resource of information was desired.

A computerized database access system was developed with the following primary objectives:

1. Computerize access to the DOE/DOD Environmental Data Bank.

2. Integrate digitized X-Y data, including shock and vibration data, into a common database to eliminate the duplication of engineering analysis data.

3. Incorporate the GRAFAID data analysis and graphics capabilities into a common workspace for the production of component specifications for various types of environments and for general data analysis.

The interactive computer code and database access system *GREEDI* (a Graphical Resource for an Engineering Environmental Database Implementation) was developed and implemented. GREEDI facilitates the shared access to engineering analysis data and provides an integrated environment to perform shock and vibration data analysis tasks. It transformed the DOE/DOD Environmental Data Bank from a card index system into an easily accessed computerized engineering database tool that can accept data in digitized form. GREEDI was created by interconnecting the *SPEEDI* (Sandia Partitioned Engineering Environmental Database Implementation) [7,8] and GRAFAID codes.

An overview of the GREEDI software system is presented by respectively describing the GREEDI interconnection, the SPEEDI software, and the GRAFAID code capabilities.

GREEDI

The GREEDI code was generated by interconnecting the GRAFAID code and the SPEEDI code while maintaining the functionality of each code. The GREEDI software system including the interrelationships between the GRAFAID and the SPEEDI codes is illustrated in Figure 1. The SPEEDI partition of the GREEDI software system maintains the environmental data bank in an INGRES database and provides all of the database access including the data set indexing and the import/export of data. INGRES is a commercial relational database management system marketed by Relational Technology Inc. (RTI) [9,10] that provides the organizational base for storing and retrieving the indexing information associated with the data. SPEEDI has its own user interface into the database. The GRAFAID partition performs the data analysis and provides the graphic capabilities for the GREEDI system.

GRAFAID and SPEEDI were interconnected to make the GREEDI system by making them both callable subroutines and by providing database access to GRAFAID through a SPEEDI subroutine interface. The partitioned system was selected over a single software system because of the need to retain the GRAFAID code as a stand alone system for analysts outside of the Engineering Analysis Department and outside of Sandia National Laboratories. The GREEDI code is written in FORTRAN with embedded SQL (Structured Query Language). The ANSI FORTRAN 77 [11] and SQL [3] standards where adhered to as much as possible to maximize portability.

In the remainder of this section, a detailed description of the initiation of a GREEDI use is presented. In the next two sections, the SPEEDI and GRAFAID codes are summarized.
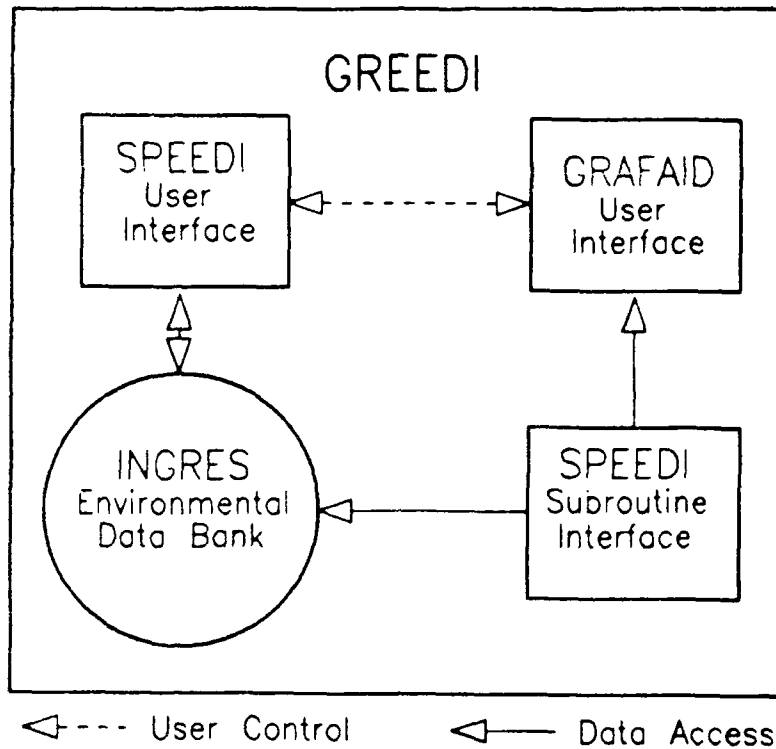
Figure 1 — GREEDI SYSTEM SCHEMATIC

Executing GREEDI

When a GREEDI session is initiated, the system starts up in the GRAFAID partition. This is indicated by a "GRAFAID>" command prompt. If the session is the first for an analyst, the operating environment is automatically initialized to the default state of the system. Otherwise, the operating environment from the analyst's last session is automatically recovered from the database. While in the GRAFAID partition, the analyst may execute any of GRAFAID's capabilities or may execute any commands that are common between GRAFAID and SPEEDI. The analyst may switch to the SPEEDI partition from any command level within the GRAFAID partition by entering the "SPEEDI" command. Presence in the SPEEDI partition is indicated by a "SPEEDI>" command prompt. Likewise, an analyst operating in the SPEEDI partition may switch to the GRAFAID partition by entering the "GRAFAID" command.

SPEEDI

The evaluation of the requirements and the design and implementation of SPEEDI was performed by RE/SPEC Inc. at the request of Sandia National Laboratories to provide centralized computer access to the DOE/DOD Environmental Data Bank. The INGRES database management system was chosen as the organizational tool for storing and retrieving the indexing information associated with the data. The access routines which compose SPEEDI were written in FORTRAN with embedded SQL calls to the INGRES database. The actual data are stored in VAX/VMS [6] direct access files which are managed by the SPEEDI software. Currently there are eighty pieces of information which the analyst can use to identify a given data set. These are referred to as *SPEEDI indexable fields*. Any attribute field which is stored in the database may become an indexable field by simply adding information about it to one of the database tables:

no modification to the SPEEDI software is necessary. In order to readily access and effectively use the data, each data set is uniquely identified by a subset of these indexable fields called the RIDDL (Record Identification and Data Definition Label). In the following sections, SPEEDI's method of data definition and identification will be discussed, and the SPEEDI command and subroutine interfaces will be described.

Data Definition and Identification

One of the most important features of the user interface to SPEEDI is the means by which the analyst identifies the data sets with which to work. In this section we will first discuss data identification and the RIDDL types available in SPEEDI for data identification. We will then present the methods and commands available for defining and using RIDDL Masks to identify data.

Data Definition Using the RIDDL. The data stored in SPEEDI's INGRES database is made up of two different sets of data. One set consists of the stable environmental data, such as the DOE/DOD Environmental Data Bank, which we refer to as the *Environmental Data Bank*. The other set consists of engineering analysis data which we call the *Analysis Data Bank*. All data in the Environmental and Analysis Data Banks are uniquely defined by a series of data attributes. There are a number of attribute fields associated with each data set entered into the database which must contain identifying information. Many fields may contain long character strings and are used strictly for maintaining historical information. Other fields are required for data identification. The RIDDL can be thought of as a shorthand specification consisting of the fields required to uniquely identify a data set stored in the database.

Some of the SPEEDI indexable fields must contain values which conform to a specific list of permitted values (the *permitted vocabulary*) for the field. This restriction is imposed to enforce consistency throughout the database. For example, "VIBR" is the permitted value associated with a vibration environment. Provided that every analyst adheres to the permitted vocabulary, a search on the "VIBR" environment will return all vibration environment entries in the database.

A RIDDL consists of a string of values for each of the RIDDL fields separated by the delimiter "/". Notice that since a field delimiter is used in the RIDDL, the analyst need not fill in the entire width of any given field. Because the types of data to be stored in the Analysis and Environmental Data Banks are so varied in origin and structure, it would be difficult and inefficient to design a single RIDDL which could be used for all data. Therefore, SPEEDI allows for multiple RIDDL types.

The type associated with each RIDDL determines the number of fields, the width of each field, the name of each field, and the ordering of the fields in the RIDDL. Each RIDDL attribute field is represented by a few (from one to twenty) characters. These fields have been chosen to include the data attributes which are expected to be used frequently in searchs of the database. In addition, enough attributes are included to uniquely identify each data set, that is, if the analyst were to select a single value from the permitted vocabulary for each field, no more than one data set would be selected from the database. Because the RIDDL is intended as a shorthand notation for the convenience of the analyst, it is desirable to minimize the number of fields included.

As data sets are processed and manipulated by analysts, it is necessary to identify them by specifying values for each and every one of the core attribute fields of the appropriate RIDDL type. In order to meet the needs of the frequent and experienced user, an approach to identifying the data has been developed which allows the analyst to create a restricted view of the database and use an abbreviated form of the RIDDL when accessing data. This method will be described in detail below.

RIDDL Types Available in SPEEDI. A core group of attributes provides a unique specification and identification, a RIDDL, for each type of data in the database. Three types of data have been identified and their corresponding RIDDL types have been implemented. These three types of data are the existing Environmental Data Bank data, test and simulation data, and

derived data. The RIDDLs designed for each of these types of data are as follows.

The DB RIDDL type is designed to provide maximal indexing capabilities on the stable Environmental Data Bank. Fourteen of the indexable fields were chosen as a key for this data. The fourteen fields which constitute the DB RIDDL type are as follows:

RTYPE	RIDDL type = "DB"
GROUP	User Group Name
OWNER	Username of Owner of the Data Set
VERSION	Integer Version Number of the Data Set
ROLE	Role of Data in the Test
PROGRAM	Program being Tested
PHASE	Phase of Life of System to which Data Pertain
CONDITION	Environmental Condition
ENVIRONMENT	Environment of Test
EVENT	Event Monitored
CARRIER	Carrier of Unit Tested
MODEL	Carrier Model
SUMMARY	Data Summary Prefix for DB RIDDLs
FILE	File Access Number for DB RIDDLs.

Although the SUMMARY and FILE fields form a unique identifier for each data set in the DOE/DOD Environmental Data Bank, these were deemed insufficient for adequate search capabilities.

Data sets are often loaded into the Analysis Data Bank from SATADEF (Standard ASCII Test Analysis Data Exchange Format) [2] tapes, so the RIDDL type tailored for analysis data, the SD RIDDL type, is based on the SATADEF header. This RIDDL consists of twenty-six of the SPEEDI indexable fields. These are necessary to provide a unique RIDDL key for each data set in the Analysis Data Bank and maximum flexibility in efficiently indexing data. These fields are as follows:

RTYPE	RIDDL Type = "SD"
GROUP	User Group Name
OWNER	Username of Owner of the Data Set
VERSION	Integer Version Number of the Data Set
ORIGIN	Origin of the Data Set
FUNCTION	Functional Description of Data
FILTER	Filter Identifier
MEASURE	Data Measured
ROLE	Role of Data in the Test
PROGRAM	Program being Tested
UNIT	Test Unit, Simulation Model, or Event Site (for natural phenomena)
PHASE	Phase of Life of System to which Data Pertain
CONDITION	Environmental Condition
ENVIRONMENT	Environment of Test
METHOD	Method of Obtaining Data
EVENT	Event Monitored
SUBEVENT	Stage of Event Tested
CARRIER	Carrier of Unit Tested
SUBCARRIER	Carrier Subgroup
MODEL	Carrier Model
EVENT AXIS	Event Axis (axis being loaded)
RUN ID	Run Identifier (test run recorded)
TRANS ID	Transducer Identifier
TRANS AXIS	Transducer Axis
ANAL ID	Analysis Run Identifier
CHANNEL	Analog to Digital Tape Channel Identifier (monitored for data)

The Analysis Data Bank also contains data sets derived from other data sets. In order to provide maximal flexibility in accessing these derived data, the DD RIDDL type has been implemented. The DD RIDDL is composed of the twenty six fields in the SD RIDDL plus a derivation name and a derivation type. In addition to the RIDDL information, the derivation parameters specific to the given derivation type and the data tags of the data sets involved in the derivation procedure are stored by SPEEDI. The DD RIDDL fields which differ from the SD RIDDL are as follows:

RTYPE	RIDDL Type = "DD"
DERIV_NAME	User Defined Derivation Name
DERIV_TYPE	Type of Derivation Used to Generate Data Set.

The RIDDL Mask and the SubRIDDL. An analyst typically uses well defined subsets of data during a particular analysis. In the context of the data attributes and the RIDDL, this implies that a subset of data must be defined by fixing the value of a particular field of the RIDDL. By fixing the values of many of the RIDDL fields, the analyst can define a manageable subset of data within which to work. Once those fields are fixed, it is no longer necessary to specify them when selecting data sets from the database. Only the subset of the RIDDL fields which are not fixed need be specified when selecting data sets. This subset of the RIDDL fields is referred to as the *subRIDDL*.

The *RIDDL Mask* is a collection of information which describes what must be specified in the analyst's subRIDDL. The Mask also defines how the subRIDDL is to be interpreted and mapped into a full RIDDL. This includes which fields are to be explicitly specified by the analyst and which are implicitly specified, the ordering of the explicit fields, and logical expressions which define values for each field.

Specifying SubRIDDLs to SPEEDI. Throughout SPEEDI the analyst specifies a subRIDDL to identify data. In the context of a particular *RIDDL Mask*, the subRIDDL will retrieve zero or more data sets which match the attributes specified in the subRIDDL. The syntax for specifying a subRIDDL provides for the use of wild card characters as well as override specification of any of the SPEEDI indexable fields.

One of the capabilities available in SPEEDI is a utility to define a RIDDL Mask. Using the *RIDDL Mask Definition Utility*, the analyst may tailor the use of the RIDDL via the following operations.

- "EXPLICIT" command states that a given field must be specified explicitly in the sub RIDDL when the Mask is active and specifies a permissible value or range of permissible values for the field using logical expressions.

- "IMPLICIT" command states that a given field need not be specified in the subRIDDL when the Mask is active and specifies a permissible value or range of permissible values for the field using logical expressions.

- "REORDER" command changes the sequence of explicit fields in the active RIDDL Mask.

To assist the analyst in using and maintaining a library of RIDDL Masks, the following operations are also available in the RIDDL Mask Definition Utility.

- "SAVE" command saves a RIDDL Mask and associates a name with it.

- "ACTIVATE" command activates a named Mask.

- "MASK" command displays the names of saved Masks or displays the definition of a Mask.

- "FIELD" command displays the permitted vocabulary for a particular field.

- "DELETE" command deletes a user defined RIDDL Mask.

- "RENAME" command renames a user-defined RIDDL Mask.

- "COPY" command copies a RIDDL Mask.

There are three RIDDL Masks intrinsic to SPEEDI for each RIDDL type. These are available to casual, new, and infrequent users as well as to serve as a starting point for user-defined Masks. They are the FULL, UNSPECIFIED, and EMPTY Masks. When the FULL Mask is active, all RIDDL fields must be specified explicitly (except the RTYPE field) and there is no restriction on the value for any field. When the UNSPECIFIED Mask is active, no RIDDL fields need be specified explicitly and no restrictions are placed on the value for any field. However, when the EMPTY Mask is active, no RIDDL fields need be specified explicitly, but no value will be assigned to the fields. The FULL and UNSPECIFIED Masks are useful for retrieving data and as a basis for new RIDDL Masks. The EMPTY Mask is provided solely as a basis for user-defined RIDDL Masks.

SPEEDI Command Interface

In addition to accessing the database through the GRAFAID partition of GREEDI, it is accessible through the SPEEDI command interface. The SPEEDI command interface controls all the types of utilities including the RIDDL Mask Definition Utility described above. The analyst can enter SPEEDI commands in three ways: from a procedure, directly in response to a SPEEDI command prompt, or as a choice from a SPEEDI menu presentation. The command prompt displayed during a SPEEDI session consists of a character string indicating the program level followed by the character ">". For example, "SPEEDI>" is the prompt at the main SPEEDI program level, and "RIDDL>" is the prompt in the RIDDL Mask Definition Utility. If SPEEDI does not have sufficient information to complete the execution of a command, the analyst will be prompted to supply that information. The types of commands available at different SPEEDI program levels is described below.

SPEEDI Global Commands. The following commands may be entered at any SPEEDI program level prompt. In addition, each SPEEDI menu level has the option "GLOBAL" which, if selected, presents the analyst with a menu of these commands.

- "SET" command modifies the operating environment of SPEEDI to suit the analyst.

- "SHOW" command displays the status of a particular operating environment feature.

- "HELP" command provides online help for SPEEDI commands.

- "DIRECTORY" command displays indexing information about data in the database.

- "EDIT" command invokes a text editor from within SPEEDI.

- "EXECUTE" command executes a previously saved SPEEDI command procedure.

- "DCL" command executes a single operating system command from within SPEEDI.

- "SPAWN" command temporarily disconnects from the GREEDI session and connects to a subprocess process. When the analyst logs out of the subprocess, control is returned to SPEEDI at the "SPEEDI-SYSTEM" environment.

- "EXIT" command terminates the SPEEDI session.

- "SAVE" command saves the current procedure and returns to the previous level.

- "QUIT" command returns to the previous program level without saving changes.

- "TOP" command returns to the top-most command procedure.

SPEEDI Program Level. Some of the commands available at the SPEEDI program level are described below. In each command where data sets are manipulated, they are identified via a subRIDDL in the context of an active Mask.

- "EXPORT" command writes a data set and appropriate identifying information to a file or device in a specified format such as SATADEF.

- "GRAFAID" command switches to the GRAFAID partition.

- "IMPORT" command loads data and identifying information into the database from a file or device in a specified format such as SATADEF.

- "RIDDL" command enters the RIDDL Mask Definition Utility.

- "TYPE" command displays a data set to the terminal or to a specified device.

SPEEDI Subroutine Interface

The GRAFAID partition of GREEDI accesses the database through the SPEEDI subroutine interface. This is a collection of software modules which allows access to the database while ensuring consistency of format and unique identification of each data set. The subroutine interface consists of routines such as the following.

- A SPEEDI initialization routine which connects to SPEEDI's INGRES database, verifies that the analyst is an authorized SPEEDI user, initializes the SPEEDI environment, and initializes or restores the analyst's session environment.

- Routines which activate and report about RIDDL Masks.

- Routines which store, retrieve, delete, and purge GRAFAID data sets, plot definitions, and plot aggregates.

- A SPEEDI end routine which saves the current session environment description (unless the analyst has entered a "QUIT" command), deletes temporary tables from the database, and disconnects from the INGRES database.

GRAFAID

The GRAFAID code was first implemented at Sandia National Laboratories in 1981 and has been under continual development since then. GRAFAID is primarily a tool for the analysis of shock and vibration data. It was developed for use on the Digital Equipment Corporation (DEC) VAX computers under the VAX/VMS operating system [6]. GRAFAID's numerous data analysis, manipulation, creation, and plotting capabilities make it a general purpose data summary and analysis tool for any X Y data. The GRAFAID features that are incorporated into the GREEDI system are briefly described in the following sections. Topics covered are the command interface, the data set definition, the active set operations, the plotting capabilities, the plot definition, and the data analysis utilities.

GRAFAID Command Interface

GRAFAID is an interactive menu and command driven code. That is, either a menu or a prompt — an explicit question to answer — is always presented to the analyst. GRAFAID corresponds with the analyst through messages accompanying the menu or prompt. In addition to directing GRAFAID operations by either making a menu selection or answering a prompt, the analyst may enter one of GRAFAID's set of unprompted commands, similar to SPEEDI's global commands. The unprompted commands constitute a powerful GRAFAID feature because they release the analyst from the rigid menu and prompt structure and give him the flexibility needed to immediately do what he wants to do.

A brief introduction to some of GRAFAID's unprompted commands is presented in the following list.

- "CONTROL/C" causes a friendly interrupt of the currently executing function.

- "END" command terminates the current menu or prompt request and returns control to the next higher menu level. If a data set utility is operational, the utility is terminated with the operand data set definition being saved in the database.

- "HARDCOPY" command sends a copy of the current GRAFAID plot to a print file for later output to a laser graphics printer or similar graphics printer.

- "HELP" command accesses GRAFAID's help library.

- "PLOT" command erases the terminal screen and then displays the current GRAFAID plot definition on the terminal screen.

- "QUIT" command terminates the current menu or prompt and returns control to the next higher menu level. If a data set utility is operational, the utility is terminated without saving any data set modifications in the database.

- "RUN" command executes one of GRAFAID's customized run functions.

- "SAVE" command saves the current version of the operand data set definition in the database if a data set utility is operational. Otherwise, the command is ignored.

- "SET" command is used to assign a new value to one of GRAFAID's operating environment parameters.

- "SHOW" command exhibits the current value of one of GRAFAID's operating environment parameters.

- "SYSTEM" command temporarily exits the GREEDI session and creates an operating system command subprocess.

- "SPEEDI" command trans... to co...... to the SPEEDI partition of the GREEDI system.

- "STOP" command terminates the GREEDI session by saving the current session environment in the database and by saving the operand data set if a data set utility is operational.

GRAFAID Data Set Definition

One of the basic entities stored in the database is the data set. It is a fundamental system entity since all of GRAFAID's operations are ultimately for the creation, manipulation, modification, or graphical display of one or more data sets. A *data set* includes a set of X-Y data pairs and a data description. The X data are real values only. The Y data may be either real or complex values. The data description consists of both textual and numeric data. It contains indexing information, data history information, data derivation parameters, and graphical plot characteristics for displaying the data. The plot characteristics include the following items:

- A *plot title* consisting of up to five lines, each having a maximum of eighty characters

- A *label* of up to forty characters for each plot axis

- The *plot axis limits* that define the data plot window; these limits include values for the minimum X, maximum X, minimum Y, and maximum Y

- An *axis scale type* specifying either a linear or logarithmic scale for each axis

- *Plot window information* specifing items such as the number of windows, the window format, and the data display type of magnitude, phase, real, or imaginary.

The data sets are indexed with the SPEEDI RIDDL described previously. A list of the data sets stored in the database may be exhibited with the "DIRECTORY" command.

GRAFAID Active Set Operations

GRAFAID's active set concept is basic to all of its data set operations. The *active set* is simply a list of data sets consisting of a subset of all data sets contained in the database. A data set must be in the active set for it to be plotted or for it to be analyzed by GRAFAID. The analyst manipulates the contents of the active set with the unprompted "SET.ACTIVE SET" command. Command options are provided for defining a completely new active set and for editing the contents of the current active set. The current contents of the active set may be displayed with the "SHOW.ACTIVE SET" command.

GRAFAID Plotting Capabilities

The plot produced by GRAFAID on the analyst's computer terminal is defined by the active set contents and by the current values of some of GRAFAID's operating environment parameters. The *GRAFAID plot definition* includes parameters that match the data set plot characteristics such as a title, axis labels, window limits, window scale formats, and so on. It also includes GRAFAID parameters that govern other aspects of a plot such as plot size, data line characteristics, grid characteristics, numerical scale format, and so on. The operating environment parameters that govern the plot display may be modified and shown with the "SET" and "SHOW" command options, respectively. A summary of the GRAFAID plotting capabilities are listed below.

- Multiple data sets may be displayed simultaneously.

- Up to five plot title lines may be displayed. Each plot title line consists of up to eighty characters and is either automatically defined by active set operations or explicitly specified by the analyst.

- An axis label of up to forty characters for each axis may be displayed. The labels are either automatically defined by active set operations or explicitly specified by the analyst.

- User defined notes may be displayed at user specified locations on the plot.

- Either linear or logarithmic axis scaling for each plot axis is displayed.

- The data are displayed in a plot window defined by numerical limits that are automatically defined by active set operations, explicitly specified by the analyst, or generated from the data in the active set.

- The plot window may be displayed with either a grid or tic numerical demarcation format.

- The data plotted may be displayed as either dashed or solid lines.

- The data plotted may be highlighted with symbol or character flags displayed along data plot lines.

- The plot text may be displayed with either hardware (terminal generated) or software generated characters.

- Terminal dependent color graphics is used to display plots on the analyst's terminal.

Plot Definition

A plot definition is an additional entity stored in the database. A plot definition consists of all GRAFAID operating environment parameters that define its plot characteristics and the active set when the plot definition is created. It is created and its database index or name is assigned with the "NAME" command. The name of a plot definition is a character string of up to 20 alphanumeric characters including interior blank characters. The "DRAW" command and its options are used to retrieve from the database a complete plot definition, a plot definition's operating system plot characteristics, or an active set associated with a plot definition. A list of the plot definitions stored in the database may be exhibited with the "DIRECTORY" command.

GRAFAID Data Analysis Utilities

GRAFAID has over two dozen utilities for data analysis, data manipulation, and data creation. The utilities generate data sets and operate on data sets that are in the active set. All data manipulation is performed in computer memory and the results are stored in the database only when the utility is exited by the analyst or when the analyst executes the unprompted "SAVE" command. The analyst may also abort a utility and discard any changes to a data set by entering the unprompted "QUIT" command. In this case, GRAFAID removes the utility operand data set from the active set and does not save the operand data set in the database. These features give the analyst total control over the integrity of the data.

The various GRAFAID utilities are presented along with a brief description in the following list.

- APPEND is used to append the data from specified data sets to an existing data set or to add data sets to create a new data set.

- CALCULATOR is for creating a data set from the result of performing mathematical functions involving constant factors and the Y data from various data sets.

- CROSS is for creating a new data set by defining its abscissa (X) values from the ordinate (Y) values from one data set and its ordinate (Y) values from the ordinate (Y) values from a second data set.

- CURSOR is for editing X-Y data pairs in a data set via input with the computer terminal's graphics cursor.

- DELETE is for deleting data sets from the database.

- DESINE is for creating a data set that is the shock spectra of a user defined decayed sine time history pulse.

- DIFFERENTIATE is for creating a data set that is the result of the numerical differentiation of data sets.

- DIGITIZER is for transferring data from a paper plot into a data set with a digitizer tablet.

- DOMAIN STATISTICS is for calculating a data set that is an a umulative average, standard deviation, or variance of the Y data values as a function of the X values for one of the data ets.

- DUPLICATE is for creating a new data set that is a copy of a data set.

- EDIT is for the input and editing of the X-Y data in a data set.

- ENVELOPE is for calculating a data set that is either a maximum or minimum envelope of multiple data sets.

- FFT is for calculating a new data set that is the Fast Fourier Transform approximation to the Fourier transform (Fourier spectra) of a data set.

- FILE is for creating a data set by reading its X-Y data pairs from an external file that has been written with either free format, formatted, or binary records.

- FILTER is for creating a data set that is the result of applying either a high pass, a low pass, or a band pass Butterworth filter to a time history data set.

- HAVERSINE is for creating a data set that is the shock spectra of a user defined Haversine time history pulse.

- INTEGRATE is for creating a data set that is the result of the integration of a data set.

- INVERT is for creating a data set from another data set by interchanging all of its X and Y data values and X and Y plot axis characteristics.

- OCTAVE is for calculating a data set that is the result of generating a histogram data set (that has its octave bin center frequencies defined approximately as a doubling of the previous bin frequency) from a power spectral density data set.

- PEAK RANK is for defining a data set that is the result of ordering the amplitudes of an input time history data set in descending order.

- PSD is for calculating the power spectral density data set from an input time history data set.

- SAMPLE is for creating a new data set by redefining the sample characteristics (including sample rate and range of data) of an input data set.

- SHOCK SPECTRA is for calculating a data set that is either the absolute acceleration or relative displacement shock response spectra of an input time history data set.

- STATISTICS is for calculating a data set that is the average, the standard deviation, or the variance of the Y data from all of the data sets in the active set.

- WINDOW is for creating a data set that is the result of applying a Hanning Window, a Hamming Window, or a Kaiser-Bessel Window (in the time domain) to an input time history data set.

SUMMARY

The GREEDI software system, an interactive computer code and database access system, was developed and implemented at Sandia National Laboratories. GREEDI facilitates shared access to engineering analysis data and provides an integrated environment with extensive graphical capabilities to perform shock and vibration data analysis tasks. It transformed the DOE/DOD Environmental Data Bank from a card index system into an easily accessed computerized engineering database tool that can manage data in digitized form.

REFERENCES

1. C. R. Adams, "GRAFAID Code User Manual Version 2.0," Report # SAND84 1725, Sandia National Laboratories, Albuquerque, NM 87185, Sept., 1985.

2. C. R. Adams, "SATADEF File Specification, Version 2.0," Memorandum, Sandia National Laboratories, Albuquerque, NM 87185, Oct. 23, 1987.

3. American National Standards Institute, Inc., "American National Standard Database Language SQL," ANSI X3.135 1986, New York, NY 10018, Oct. 16, 1986.

4. American National Standards Institute, Inc., "American National Standard Programming Language FORTRAN," ANSI X3.9 1978, New York, NY 10018, Apr. 3, 1978.

5. C. A. Davidson, "DOE/DOD Environmental Data Bank," 59th Shock and Vibration Symposium Proceedings, Oct., 1988.

6. Digital Equipment Corporation, "VAX/VMS User's Manual," Maynard, MA, 1986.

7. K. H. Haskell and E. M. Kephart, "System Guide to SPEEDI: The Sandia Partitioned Engineering Environmental Database Implementation," Report # RSI 0329, RE/SPEC Inc., Albuquerque, NM 87191, in preparation.

8. K. H. Haskell and E. M. Kephart, "Users' Guide to SPEEDI: The Sandia Partitioned Engineering Environmental Database Implementation," Report # RSI 0330, RE/SPEC Inc., Albuquerque, NM 87191, in preparation.

9. Relational Technology Inc. (RTI), "INGRES Database Administrator's Guide, Release 5.0, VAX/VMS," Alameda, CA, 1987.

10. Relational Technology Inc. (RTI), "INGRES Installation and Operations Guide, Release 5.0, VAX/VMS," Alameda, CA, August 1986, Revision Date: January 22, 1987.

A SHOCK AND VIBRATION DATABASE
FOR MILITARY EQUIPMENT

Mr. Robert A. McKinnon
U.S. Army Combat Systems Test Activity
STECS-EN-EV
Aberdeen Proving Ground, MD 21005-5059

This paper discusses the creation and utilization of a database containing shock and vibration information collected from a variety of military equipment. This information can provide designers and developers with realistic environments which their item must be capable of withstanding, so arbitrary environments are not relied upon.

INTRODUCTION

Numerous laboratory vibration test schedules have been developed in recent years for both cargo and combat vehicles in the Army's inventory. Additionally, many road shock and vibration, rail impact, drop, and firing shock tests have been conducted on a wide variety of vehicles and equipment as part of the Engineer Design Test/Development Test/Product Improvement Program (EDT/DT/PIP) testing mission. Through this total effort, a large amount of meaningful data have been gathered, processed and reported by the U.S. Army Combat Systems Test Activity (USACSTA) to meet the specific requirements of the various investigations and tests. With such a great quantity of data known to exist, numerous contacts are made to USACSTA and U.S. Army Test and Evaluation Command (TECOM) by other Government activities, program manager offices, and private contractors (involved with developmental design for Government contracts) to acquire specific data. Currently, these data exist in many data files which must be researched to obtain data for a specific request. There has been no effort to establish a complete and meaningful database to provide timely information on the shock and vibration characteristics of vehicles and equipment. Such data provide designers and developers with realistic environments the item must withstand so they do not rely on the selection of some arbitrary, and often erroneous, environment. The objective of this project was to develop a shock and vibration database for various vehicles and equipment mounted on vehicles.

DATABASE CONTENTS

The objective was to determine which types of information should be stored in the shock and vibration database in order to make the database as useful as possible.

The original project proposal suggested that the database should contain information on vehicle type, equipment type, test course, and test environment. It also suggested that the database consist of raw data, power spectral density computations, amplitude distribution analyses and shock response spectra.

Being the probable main users of this database, the USACSTA Vibration Test Branch personnel were questioned as to the types of data to be stored. The responses are summarized in Table 1.

TABLE 1. FIELD SHOCK AND VIBRATION DATABASE SUMMARY

Information To Be Stored

a. Test item(s), name, model number.

b. Carrier vehicle(s), name, model number.

c. Date of test.

d. Test Engineer.

e. Measurement locations.

f. Test courses and speeds, drop heights, or rail impact speeds with run number.

g. Raw digital data tape numbers.

h. Save tape (calibration files, etc.) numbers.

i. Analyzed data tape numbers.

j. Analyzed data file names (particularly overlay files).

k. Summarized data (rms, peak, crest factor, kurtosis).

l. Type of analyses performed.

m. Report number.

n. Sample rate of processed data.

o. Recording and analyzing data frequency ranges.

p. Data logbook volume number.

q. Types of tests performed.

r. Test item securement (loose, secured, etc.).

s. Types of data (acceleration, strain, displacement, etc.).

It was decided to include as much of the above listed data as possible with the limitation being the computer memory size.

In addition to the information listed above for field shock and vibration tests, it was determined that other testing conducted by the Vibration Test Branch should be included in the database. A second set of information for the database

to include laboratory testing was developed. As the majority of the laboratory shock and vibration tests are conducted on ammunition, the recommended database information is primarily ammunition-related. The suggested information from the Vibration Test Branch personnel is listed in Table 2.

TABLE 2. LABORATORY SHOCK AND VIBRATION DATABASE SUMMARY

Information To Be Stored

a. Test Item(s), name, model number.

b. Date of test.

c. Test personnel.

d. Types of tests performed.

e. Conditioning temperature(s).

f. Packaging of test item.

g. Report number.

h. Details of tests.

   (1) Document detailing test procedure for each test.

   (2) Vibration tests.

     (a) Vehicle(s) simulated.

     (b) Mileage simulated.

     (c) Type of Vibration Test schedule (swept sine, random, swept narrow-band random-on-random, etc.).

     (d) Test orientations.

   (3) Loose cargo tests.

     (a) Type of table surface.

     (b) Speed of table.

     (c) Test time.

     (d) Test orientations.

   (4) Drop tests.

     (a) Drop heights.

     (b) Impact surface.

(c)   Drop orientations.

(5) Shock tests.

(a)   Shock amplitude.

(b)   Pulse duration.

(c)   Transient duration.

(d)   Type of shock pulse.

(e)   Test orientations.

A database to store information that was used in the development of laboratory vibration test schedules was also deemed necessary. This would include all information pertinent to the complex development process. This database includes the information included in Table 3.

TABLE 3. LABORATORY VIBRATION SCHEDULE DATABASE SUMMARY

Information To Be Stored

a. Test item(s), name, model number.

b. Test vehicle.

c. Location of test item on vehicle.

d. Name of person developing schedule.

e. Scenario information.

   (1) Total transport distance.

   (2) Percent of distance used for schedules.

   (3) Test courses utilized.

   (4) Average speed on each 'est course.

f. Person requesting schedule.

g. Names of all computer files generated.

h. Exaggeration factor.

i. B/N exponent (Miner's Theory).

j. Number of standard deviations added for conservatism.

k. Type of vibration test schedule.

Since there are distinctly different types of information to be stored in the database, three separate databases were determined to be needed. These three databases are independent; however, limited cross-referencing should be available for data common to more than one database. Examples of these would be the test item name and the report number.

All of the information listed in Table 1 was included in the database with the exception of the following:

e. Measurement locations.

f. Test courses and speeds, drop heights, or rail impact speeds with run number.

j. Analyzed data file names (particularly overlay files).

k. Summarized data (rms, peak, crest factor, kurtosis).

Each of the above data types has a large number of possible database entries which makes the complete storage of information impractical. While not directly accessible from the database, the excepted information can be readily located by examining the logbook and data storage tapes identified through the database. The information listed in Tables 2 and 3 were all included in their respective databases.

These databases can be used to locate information on previously conducted tests more efficiently than prior to its existence. Most of the test details can be recovered directly from the databases. The actual test data, which is voluminous in most cases, can also be recovered more efficiently through the databases than in the past. Currently the test data on file at the Engineering Test Division are stored on several hundred nine-track digital tapes. The databases can direct the requester to the tapes with the desired data.

The databases will make shock and vibration environment information more readily available to designers and developers. These people can then incorporate this information into their designs in lieu of remeasuring the shock and vibration levels or selecting arbitrary levels. This can lead to savings in terms of both development time and money.

All shock and vibration test reports are now filed in ascending order by report number making it easier to find reports which have been identified by the databases. Previously, the reports were filed by the type of test item. In some cases where more than one type of item was tested and reported in a single report, locating the report was difficult. Now, the databases will provide the desired report numbers and utilizing the report will provide any detailed information that is not available in the database.

DATABASE SYSTEM SELECTION

The objective was to create or locate a database system compatible with the computer systems currently accessible by the Engineering Test Division which would provide an adequate amount of data storage space.

At the start of this investigation, the only computers available were Hewlett-Packard (HP) 1000 computer systems. The original plan was to write a series of FORTRAN computer programs which would input, edit, and retrieve the database information. An effort was started in this direction and the data input software was written. As that effort was concluding, Zenith model Z-248 personal computers (PCs) were acquired by the Engineering Test Division. Acquired at the same time was the Enable 1.15 software package.

A subset of the Enable software package is a Database Management System (DBMS). This DBMS allows up to 65,000 records with up to 254 fields which can contain up to 254 characters each. Each record is composed of fields or types of information and the information in each field is referred to as data or values. This system permits the entry of up to 65,000 test programs and 254 different types of data variables per test program [1].

At the time of acquiring the Zenith computers, it was decided to shift the database effort from the HP 1000 minicomputer to the Zenith personal computer. The reasons for the shift were the ability to immediately have a verified and usable database system. Utilization of the Enable DBMS allowed almost immediate data entry and data access. The use of the Zenith computers also allowed easier access to the database, in that these computers are located throughout the Vibration Test Branch while the HP 1000 computers are only accessible in a single location.

The Enable DBMS was selected as the database software package. The shock and vibration database has been placed into one Zenith computer system and can be transported to other systems on 5-1/4-inch floppy disks giving more people access to the database.

By using the Enable database package, the database configuration was established and the system was ready for data input in a few days. Enable also gives better portability for the information stored in the database because it can be used on any of the Zenith computers.

The Enable DBMS comes with a set of instruction manuals to aid users of this system. This precluded the need to write a set of instructions which would have been required if the HP 1000 database was selected. Overall, the Enable DBMS is fairly easy to use utilizing the manuals provided with the system.

DATABASE INPUT

The objective was to develop a systematic and timely way of entering information from past and future test programs into the database. For ease of operation, the databases require a timely method of gathering information from previously conducted shock and vibration tests as well as from future tests that will be conducted.

The first step in the data input process was to gather information from all previous shock and vibration tests. The types of information are discussed in

Tables 1 through 3. To make this effort more organized, forms were developed on which all of the test data from laboratory reports and test logbooks could be summarized. Two basic forms were developed, one for field shock and vibration tests and the other for laboratory tests. Examples of these forms are included in Figures 1 through 4. These forms differ in the types of information which are summarized. For the most part the laboratory shock and vibration tests are strictly pass-fail tests with no response vibration data measured. Approximately one-half of the field shock and vibration are also pass-fail, while the remainder have some type of response vibration measurements made. A third summary form was developed for the database on the development of laboratory vibration test schedules (figures 5 and 6).

The three types of database information summary forms were completed for most of the testing performed by the Vibration Test Branch as far back as available records permitted. Test reports and data for field shock and vibration tests dating back to 1967 have been located and are included in the database, as have the 1983 to 1988 laboratory shock and vibration tests. Data from all tests conducted prior to 1980 are limited to the information contained in the test report. This is because the magnetic data storage tapes from tests conducted prior to 1980 have been destroyed due to their incompatibility with the current data analysis system and the need for storage space for tapes from more recent projects.

Following the completion of the summary forms, each of the forms was examined and checked by the database manager for accuracy and completeness. If any discrepancies were noted, the correct information was recovered from the report and/or logbook and entered on the summary forms.

Currently, as tests are concluded and the final reports written, the appropriate database summary forms are completed. Then at biweekly intervals, the database manager examines the list of completed projects and determines if the summary forms have been completed. If the summary forms have not been completed, the database manager, either on his own or with the assistance of personnel involved with the test, completes a summary form. Completion of a summary form usually takes from 2 to 5 minutes. This procedure will continue to be used to ensure updating of the database.

Once the database summary forms have been completed, actual data entry can begin. The Enable DBMS allows for an input form to be developed. The three developed input forms, which appear on the computer terminal screen, are identical to the three summary forms. Included on the designed input forms are blank spots in the same location as the blanks on the summary forms. This allows the data entry person to simply reproduce the summary form on the computer screen by typing the information on the computer keyboard. Entering the data from a single summary form takes approximately 2 minutes.

After the completed database summary forms have been entered into the computer database, they are stored in a notebook for a historical record. These forms are essentially an additional backup of the database information. Backup copies of the database are made at periodic intervals on 5-1/4 inch floppy disks. The most appropriate time for the backup copies to be made is at the conclusion of a data entry session.

The use of the database summary forms allows any test personnel to gather all the pertinent test information on a single sheet of paper by simply filling in the

FIELD SHOCK & VIBRATION DATABASE SUMMARY FORM

SYSTEM NAME:_____
SYSTEM ACRONYM:_____

PRIME MOVER NUMBER, VERSION:_____
CARRIED ITEM NUMBER, VERSION:_____
TOWED VEHICLE(S) NUMBER, VERSION:_____
TRAILERED ITEM NUMBER, VERSION:_____

TEST ENGINEER:_____
TEST COMPLETION DATE (MONTH, YEAR):_____
REPORT NUMBER:_____
LOG BOOK NUMBER:_____
DOCUMENTATION FILE NAME:_____

PROCESSED DATA SAMPLE RATE:_____
RECORDING CUTOFF FREQUENCY (Hz):_____
DATA ANALYSIS FREQUENCY RANGES:_____

SUBTESTS (check all applicable)   ANALYSIS TYPES
_____ AIRCRAFT   _____ AMPLITUDE DISTRIBUTION
_____ WATERCRAFT   _____ STRAIN DISTRIBUTION
_____ RAIL   _____ POWER SPECTRAL DENSITY
_____ DROP   _____ RIDE QUALITY (ISO 2631-1978)
_____ ROAD   _____ ABSORBED POWER
_____ FIRING   _____ CREST FACTOR
_____ OTHER _____   _____ SKEWNESS & KURTOSIS
                                         _____ SHOCK RESPONSE SPECTRA
MEASUREMENTS   _____ SHOCK INTENSITY SPECTRA
_____ INSTALLED EQUIPMENT   _____ VIBRATION SCHEDULES
_____ LOOSE CARGO   _____ IMPULSE

                                         LIST RAW DATA TAPE NUMBERS_____
DATA TYPES   LIST SAVE TAPE NUMBERS_____
_____ ACCELERATION   LIST PROCESSED DATA TAPE NUMBERS_____
_____ STRAIN
_____ DISPLACEMENT

Figure 1.   Field Shock and Vibration Database Summary Form (Side One).

TEST COURSES

MUNSON | PERRYMAN | CHURCHVILLE

1. ____ Gravel
2. ____ 6' Washboard
3. ____ 2' Washboard
4. ____ Radial Washboard
5. ____ Belgian Block
6. ____ 3' Spaced Bump
7. ____ Imbedded Rock
8. ____ Staggered Bump
9. ____ Other Munson

11. ____ Cross-Country No. 1
12. ____ Cross-Country No. 2
13. ____ Cross-Country No. 3
14. ____ Cross-Country No. 4
15. ____ Paved
16. ____ Secondary Road 'A'
17. ____ Secondary Road 'B'

19. ____ Other Perryman

21. ____ Churchville 'A'
22. ____ Churchville 'B'
23. ____ Churchville 'C'

29. ____ Other Churchville

31. ____ Profile IV
32. ____ Spaced Ramps
33. ____ One-Inch Bumps
34. ____ Semicircular Bumps (WES)

39. ____ Other Test Courses

Figure 2. Field Shock and Vibration Database Summary Form (Side Two).

LABORATORY SHOCK & VIBRATION DATABASE SUMMARY FORM

TEST ITEM NAME: _____

TEST ITEM ACRONYM: _____

TEST ITEM CATEGORY:
(check all that apply)

TYPE

CARTRIDGES   _____
FUZES   _____
GRENADES   _____
MINES   _____
MORTARS   _____
PROJECTILES   _____   DIAMETER _____
PROPELLANTS   _____
SMALL ARMS   _____
OTHER _____

	BARE	BOXED	CONTAINER	PALLET	RACK	TEST TEMPS (°C)		
_____ LABORATORY VIBRATION	____	____	____	____	____	____	____	____
_____ LOOSE CARGO	____	____	____	____		____	____	____
_____ DROP								
_____ 46cm (1.5ft)	____	____	____	____		____	____	____
_____ 61cm (2ft)	____	____	____	____		____	____	____
_____ 76cm (2.5ft)	____	____	____	____		____	____	____
_____ 91cm (3ft)	____	____	____	____		____	____	____
_____ 1.2m (4ft)	____	____	____	____		____	____	____
_____ 1.5m (5ft)	____	____	____	____		____	____	____
_____ 2.1m (7ft)	____	____	____	____		____	____	____
_____ 3.0m (10ft)	____	____	____	____		____	____	____
_____ 12.0m (40ft)	____	____	____	____		____	____	____
_____ Other _____m	____	____	____	____		____	____	____
_____ JOLT/JUMBLE	____	____	____	____		____	____	____
_____ LABORATORY SHOCK	____	____	____	____	____	____	____	____

TEST PERSONNEL: _____   _____

_____   _____

_____   _____

REPORT NO.: _____

TEST COMPLETION DATE (MONTH,YEAR): _____

Figure 3. Laboratory Shock and Vibration Database Summary Form (Side One).

TEST DETAILS

LABORATORY VIBRATION

VIB. SCHED. NOTEBOOK NO._____

VIBRATION SCHEDULE ORIGIN:
(circle applicable documents) 810C 810D 1-2-601 4-2-602 TEST PLAN VTB OTHER_____

VEHICLES SIMULATED: _____COMPOSITE WHEELED   _____TWO-WHEELED TRAILER
MILEAGE SIMULATED: _____km   _____km
LAB TEST TIME/AXIS: _____min   _____min
EXAGGERATION FACTOR:_____   _____

OTHER VEHICLES: _____ _____ _____ _____ _____
MILEAGE SIMULATED: _____km _____km _____km _____km _____km
LAB TEST TIME/AXIS: _____min _____min _____min _____min _____min
EXAGGERATION FACTOR:_____ _____ _____ _____ _____

SCHEDULE TYPE:_____SNBROR _____RANDOM _____SINE _____SINE/RANDOM
RESPONSE DATA MEASURED: YES   NO   (circle one)

LOOSE CARGO

LOOSE CARGO SCHEDULE ORIGIN:
(circle applicable documents) 810C 810D 331A 4-2-602 TEST PLAN OTHER_____

TABLE SURFACE: _____WOOD   _____STEEL
TABLE SPEED: _____RPM
TABLE MODE: _____SYNC   _____ASYNC   _____VERTICAL
TEST TIME PER ORIENTATION:_____MINUTES   NUMBER OF ORIENTATIONS:_____

DROP

DROP SCHEDULE ORIGIN:
(circle applicable documents) 810C 810D 331A 4-2-602 TEST PLAN OTHER_____

IMPACT SURFACE:____STEEL ____PLYWOOD ____CONCRETE ____MACADAM ____SOIL
    IF SOIL: LOCATION: _____ PENETROMETER READING:_____ PRESSURE:_____kPa

LABORATORY SHOCK

SHOCK SCHEDULE ORIGIN:
(circle applicable documents) 810C 810D 331A TEST PLAN OTHER_____

SHOCK AMPLITUDE:_____g's PULSE WIDTH: _____msec   TRANSIENT DURATION:_____msec
NO. OF SHOCKS: _____
SHOCK PULSE TYPE: ____SAWTOOTH ____HALF-SINE ____TRAPEZOID ____CAT LAUNCH/ARREST LNDG
RESPONSE DATA MEASURED: YES NO (circle one)
CRT FILES FOR INPUT TO CONTROLLER:_____

Figure 4. Laboratory Shock and Vibration Database Summary Form (Side Two).

71

VIBRATION SCHEDULE DATABASE SUMMARY FORM

TEST ITEM(S): INSTALLED EQ   SECURED CARGO   SPECIFIC ITEM_____
(select one)

TEST VEHICLE:_____
(one vehicle/form)

LOCATION ON VEHICLE:_____
SCHEDULE DEVELOPER:_____
AXES RELATIVE TO: _____VEHICLE   _____ITEM

SCENARIO INFORMATION:
Total Distance:_____km
Percent of Distance used for schedules:_____%

APG Test Courses Used: Paved Belg Blk 2˚WB RWB 3˚SB Other(s)_____
(select appropriate courses)

Average Speed:_____km/hr
Exposure Time:_____hours
Exaggeration Factor:_____
Exponent (b/n):_____
Total Test Time:_____minutes

DEVELOPED FOR:_____   (POC)
_____   (ADDRESS)
_____
_____   (CITY,STATE ZIP)
_____   (TELEPHONE NO.)

DATE (MONTH, YEAR):_____

PSD FILES (lowest,highest run numbers):$_____,$_____   STORAGE TAPE:_____
                                        $_____,$_____

PSD TYPE USED: _____AV   _____SD _____PE

PKPSD FILES-Vert (lowest,highest run numbers): _____,_____
                 Tran   : _____,_____
                 Long   : _____,_____

NUMBER OF STD DEVS USED:_____

Figure 5. Laboratory Vibration Schedule Development Database Summary Form
           (Side One).

WHEELED VEHICLES

RRVIB FILES
saved from $CRRBD Vert:_____
                  Tran:_____
                  Long:_____

CRPSD FILES   PSD Storage   Plot (PSDL7) Files
(exaggerated breakpoints
from $CRPSD):   Vert:_____   _____   _____
                  Tran:_____   _____   _____
                  Long:_____   _____   _____

STORAGE TAPE NO.:_____

TRACKED VEHICLES

TEST PHASE	REMPR FILES	ACCPR FILES	PLOT (PSDL6)FILES
V01	_____	_____	_____
V02	_____	_____	_____
V03	_____	_____	_____
V04	_____	_____	_____
V05	_____	_____	_____
V06	_____	_____	_____
V07	_____	_____	_____
T01	_____	_____	_____
T02	_____	_____	_____
T03	_____	_____	_____
T04	_____	_____	_____
T05	_____	_____	_____
T06	_____	_____	_____
T07	_____	_____	_____
L01	_____	_____	_____
L02	_____	_____	_____
L03	_____	_____	_____
L04	_____	_____	_____
L05	_____	_____	_____
L06	_____	_____	_____
L07	_____	_____	_____

STORAGE TAPE NO.:_____

Figure 6. Laboratory Vibration Schedule Development Database Summary Form
           (Side Two).

several blank spaces with check marks or somewhat standardized short answers. The information is then in a format which can be quickly entered into the computer database.

Input to the database will continue as additional shock and vibration tests are completed. Currently, the database contains information on all field shock and vibration tests in which data were acquired. An effort is underway to complete the entry of all historical data from the laboratory tests and from the development of laboratory vibration schedules. All laboratory testing and vibration schedule development which have been reported since January 1983 has been entered in the database.

The data input procedure has been working well in that the amount of time required to gather and input test information is minimal. Efforts are on-going to enter the remaining historical laboratory test and vibration schedule development information into the database, and will be completed shortly. The process of entering test information from future tests will be continuous.

DATABASE OUTPUT

The objective was to provide requested shock and vibration information from the database in a timely manner and in a usable format.

Similar to the Enable DBMS input forms, report forms can also be generated. Currently there are two prepared report forms for use with each database. The one set of report forms are identical to the handwritten summary forms, and contain all of the same information. These provide the requester with all of the information stored in the database for a particular test. The other set of report forms is shorter and contains the test item name, the type of tests, the report number, and whether data were acquired during the test. Either of these two report forms can be viewed on the terminal screen or outputted to a printer. In addition to the two prepared report forms, the database information can be presented in other formats by preparing additional forms.

The shorter report form is the one which is requested the majority of the time by members of the Vibration Test Branch. This form lists most of the commonly requested database information, namely the report number, the types of tests conducted, and the types of measurements made, if any.

The longer report form has so far been used only to duplicate the handwritten summary forms and not as a tool to locate database information. This form, when used, will provide the most complete information on the test programs. In cases where database information is needed immediately (during a telephone conversation for example) simply reporting only requested data in the shorter format has been found to be the quickest method to determine if the requested information is available.

Once the database has been accessed and it indicates that the data requested are available, the database manager will note the report numbers and data tape numbers. The next step is to locate the requested information first by looking in the test reports. If the information is not recorded in the test reports then the data tapes are retrieved. If the database indicates the required information has been computed and stored on processed data tapes then these are retrieved from the tape library. The processed data tapes are then installed on the HP 1000 computer's tape drive and the requested information is then reformatted by the

computer into the desired format. The data formats usually desired are either plots or tables.

The Enable DBMS allows the user to retrieve information in almost any desired format. Currently, only two report forms have been developed; however, additional report forms will be created as the need arises.

The database information can be accessed directly using an Enable DBMS default report form. This would be done in the event information is desired quickly and precise formatting is not required. This method will list only the information specified and is most useful for retrieving a limited amount of information such as was a certain test conducted on a specified test item.

The report forms aid in the timely location of information stored in the database. The forms identify the data that are available as well as where the data can be found, usually in test reports or on magnetic data tapes.

TYPES OF AVAILABLE DATA

All of the information stored in the databases and listed in Tables 1 through 3 are readily available. Additionally, data which have been further analyzed are also available. The analyzed data include but are not limited to time history and power spectral density plots, amplitude distribution data, shock response spectrum data. Desired information can be presented in various formats as determined by the requester. Some examples of the types of data available are shown below. Figures 7 and 8 show sample time history and power spectral density plots respectively. Table 4 is a sample of summarized acceleration data.

In cases where the requested data have not been previously computed and stored on magnetic tape, the raw data tapes are retrieved and the necessary computations are made. The computed data are then outputted in the desired format and this information is then stored on properly identified processed data tapes which are annotated in the database for future use. Also available is the development of laboratory vibration test schedules for cases in which the desired measurements have been made.

In order for laboratory vibration test schedules to be developed, additional information is required. This information includes the exact mounting or storage location of the item which is to be tested in the vibration laboratory. Additionally, the types of terrain and the expected vehicle mileage on each terrain type need to be identified.

DATABASE USAGE DETERMINATION

The objectives were to devise a way to measure the usage of the shock and vibration database and to document who is utilizing the database.

In order to keep track of database usage, a data request form was developed (figure 9). This form will be completed each time the Vibration Test Branch is requested to provide shock and vibration data. The form was designed to record all information pertinent to the data requested including the name and organization of the requester. The information on these forms is used by the person accessing the database, as it contains the types of information to be searched for in the database. The information on the data request forms is then

RUN 1

ACCEL – G's

TIME (SEC)
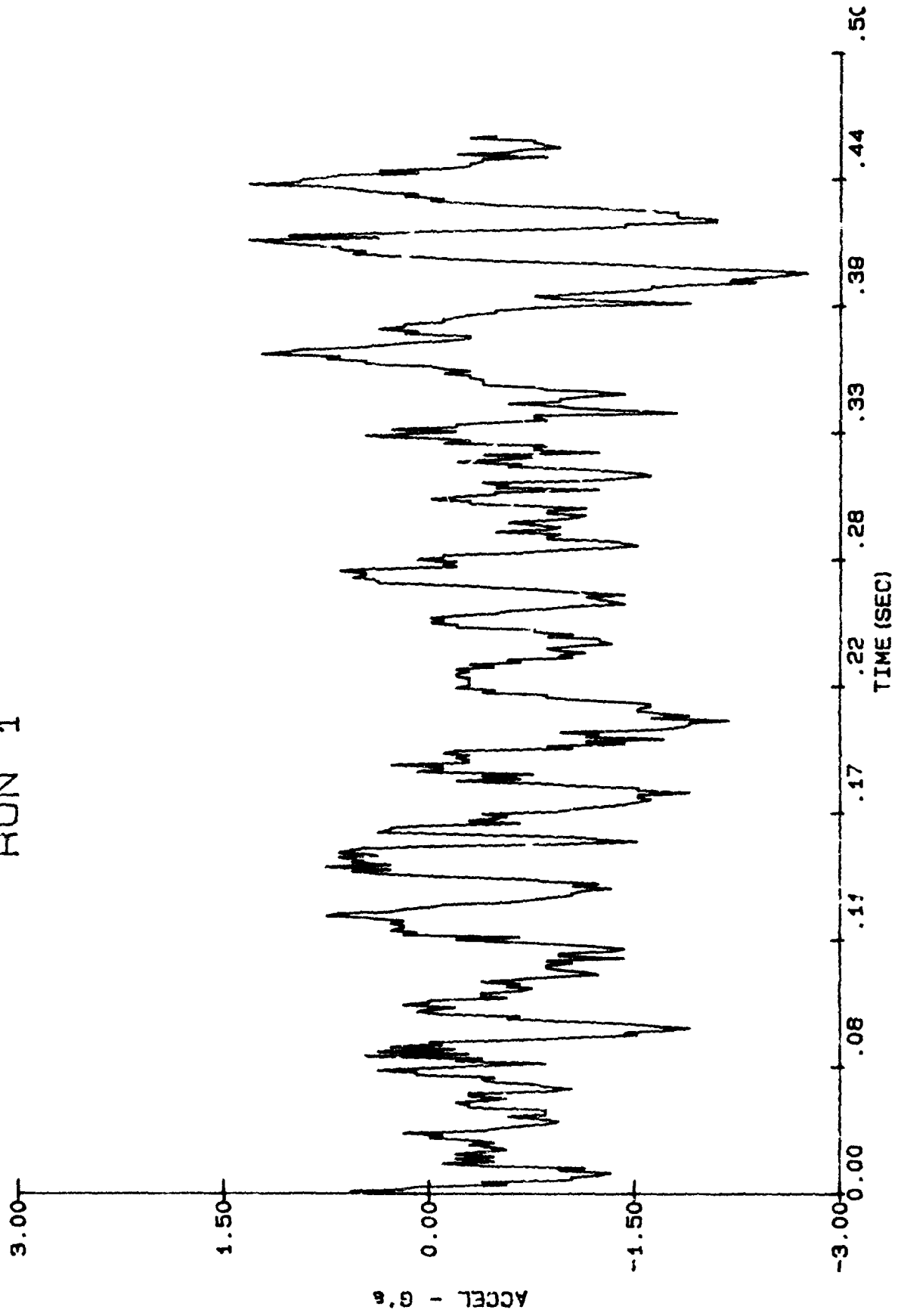
Figure 7. Typical Time History Plot.

TYPICAL TRACKED VEHICLE DATA

LOCATION 1 (L)

PSD - G SQ PER HZ

.01000
.00900
.00800
.00700
.00600
.00500
.00400
.00300
.00200
.00100
0.00000

0.00 50.00 100.00 150.00 200.00 250.00 300.00 350.00 400.00 450.00 500.00

FREQUENCY - HERTZ
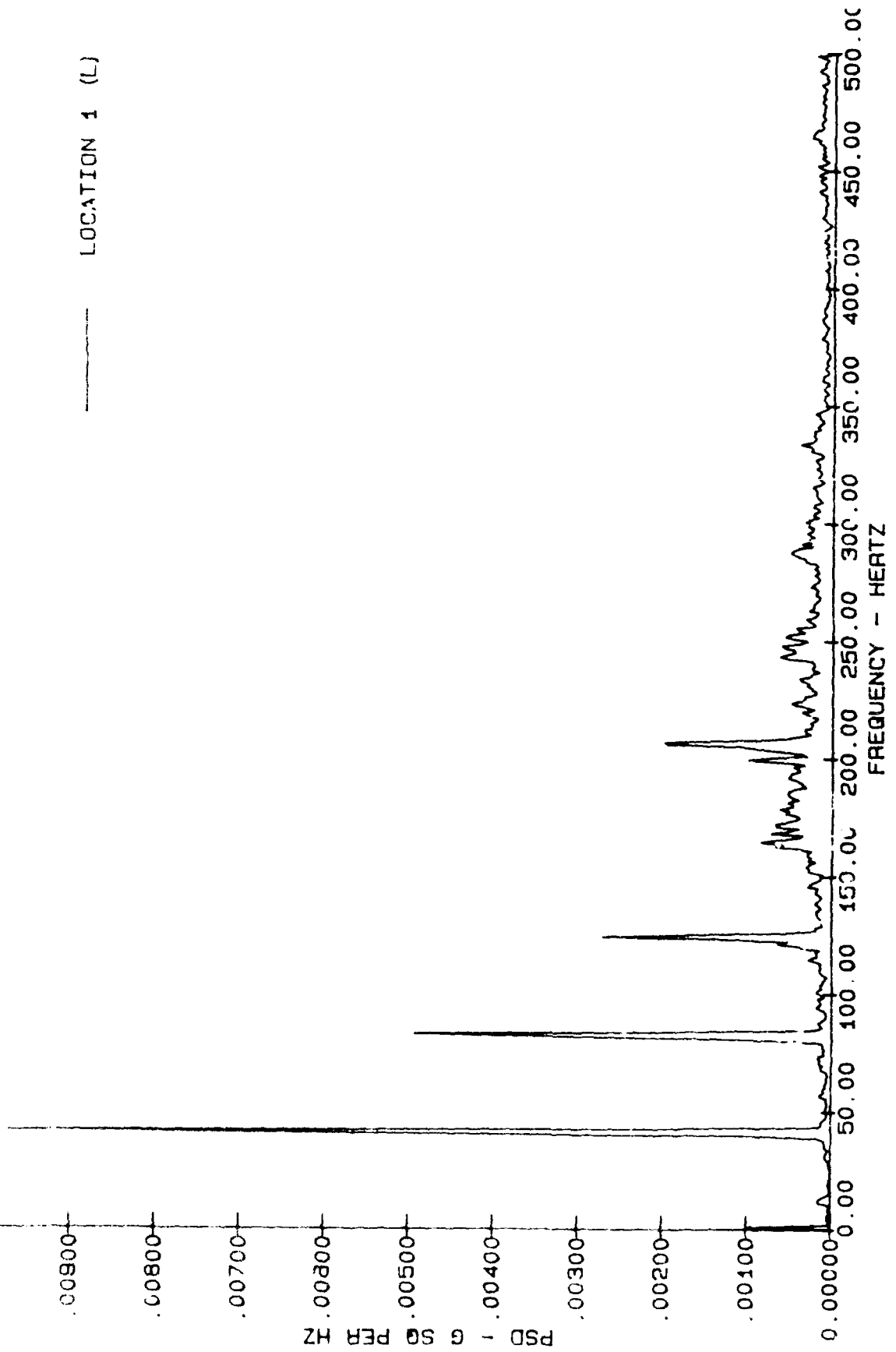
Figure 3. Typical Tracked Vehicle Power Spectral Density Plot.

Table 2. Typical Summarized Acceleration Data.

DATA REQUEST FORM

REQUESTER INFORMATION:
NAME:_____
ADDRESS:_____ (include company or
_____ organization name)

_____

PHONE NO.:_____

DATA REQUESTED

EQUIPMENT TYPE(S):_____

TEST TYPE(S):   ROAD   RAIL IMPACT   DROP   OTHER_____

TEST COURSES, SPEEDS, ETC.:_____

DATA TYPE(S):   AMPLITUDES   PSD   SRS   VIB SCHS   OTHER_____

HOW DID THE REQUESTER FIND US(circle one)?

PREVIOUS CONTACT   TEST   TECOM   USACSTA   OTHER
     WITH VTB   SPONSOR   PERSONNEL   _____

NAME OF PERSON WHO DIRECTED REQUESTER TO VTB:_____

WAS VTB ABLE TO SUPPLY DATA(circle one)? ALL   SOME   NONE

IF ADDITIONAL DATA ANALYSIS WAS REQUIRED, TIME INVOLVED:_____hours

WAS THE S&V DATABASE UTILIZED TO RECOVER DATA?   YES   NO

DATE REQUESTED:_____   DATE SENT OUT:_____

The purpose of this form is to measure the utilization of the shock and vibration
database. Your cooperation is appreciated.

                              S&V Database Committee

      Figure 5. Data Request Form.

stored in a separate database, since this information is dissimilar with the other databases. This database also utilizes the Enable DBMS.

These forms have only been utilized for a short time as the shock and vibration database is in its infancy. The forms are easy to complete and have been used successfully.

The data request forms also provide a space to document the amount of time the data recovery process took, including the time for any additional data analysis not previously performed. This will give an indication of the number of hours spent doing research and analysis on projects which are not currently funded.

Since the shock and vibration database is just getting started, its use has been limited to approximately two to three times per week. It is anticipated, based on past inquiries, that this usage will increase dramatically.

REQUESTING DATABASE INFORMATION

All requests for information must be made in writing on stationary bearing the letterhead of the requesting organization. The request must include the information desired and the purpose for requesting the information. Telephone requests may be made, however no information will be released until a follow-up letter is received. All requests for shock and vibration information should be sent to the Chief, Vibration Test Branch. The mailing address and telephone number are:

Commander
US Army Combat Systems Test Activity
ATTN: STECS-EN-EV
Aberdeen Proving Ground, MD 21005-5059
Telephone: (301) 278-3787
AUTOVON: 298-3787

After the determination is made that the requested information is available, the appropriate test director or supervisor is contacted and informed of the data request. The test director or supervisor will make the decision as to whether the information can be provided to the requester. Under no circumstances can classified test information be provided.

The letter requesting the information along with a completed Data Request Form will be retained by the Vibration Test Branch for a minimum of three years from the date of the request. The information from the Data Request Form will be entered into the Shock & Vibration Database as previously stated.

REFERENCE

1. ENABLE Data Base Management and Spreadsheet/Graphics, Zenith Data Systems Corporation, 1935.

VIBRATION DATABASE FOR
AIRCRAFT AND ITS APPLICATION

Michael T. Orth
Wright-Patterson Air Force Base
Aeronautical Systems Division
ENFSL
Dayton OH

A vibration data base is necessary for verifying
aircraft structural integrity and equipment design.
Vibration data is obtained through numerous flight
tests intended to capture maximum vibration levels and
vibration trends. The data is processed through
available software and the desired output. This paper
gives a brief description of aircraft vibration and
methods of obtaining and processing flight vibration
data in order familiarize the laymen with the correct
application of an aircraft vibration data base.

INTRODUCTION

The Loads and Dynamics Branch (ENFSL) of Aeronautical Systems Division has
acquired an extensive vibration data base for the purpose of verifying aircraft
structural integrity and equipment design. A brief discussion of aircraft
vibration along with methods of obtaining, processing and applying the data will
be provided.

Aircraft Vibration

Numerous sources induce vibration throughout an aircraft including the
aerodynamic boundary layer, turbulent air flows, acoustic fields, pressure
pulsations, unbalance of rotating equipment, acoustic cavity resonances, and
repetitive gunfire blasts. These sources produce loads small in comparison to the
inertial and aerodynamic loads used in aircraft design but can induce structural
fatigue due to the repetition (frequency) and the amplification (Q) of the
vibration levels by airframe and equipment resonances. The performance of
equipment can also be affected by vibration without fatigue failure.

To categorize the severity of the vibration, the aircraft is divided into
vibration zones each with relatively uniform vibration; an example is given in
Figure 1. Typically vibration is lowest at the nose of an aircraft and is
progressively more severe moving aft. This occurs because the aerodynamic
boundary layer begins to separate and become turbulent moving aft due to the
generation of highly disturbed flows from airflow perturbances. Airflow induced
vibration is also dependent upon variations in the vehicle's flight envelope.
Flight vibration is proportional to dynamic pressure and reaches a maximum at
approximately .9 Mach at sea level, decreasing during transonic airflow, and again
increasing after Mach 1 (Fig. 2). Vibration design criteria for high performance
airplanes are usually dominated by the vibration at .9 Mach at the lowest
allowable altitude. Maximum vibration during ground operation occurs at
initiation of ground roll when the acoustic noise of the propulsion system is a

maximum. This condition dominates the vibration criteria aft of the engines for airplanes which do not fly at high speeds at low altitude, ex. C-130 and C-17.
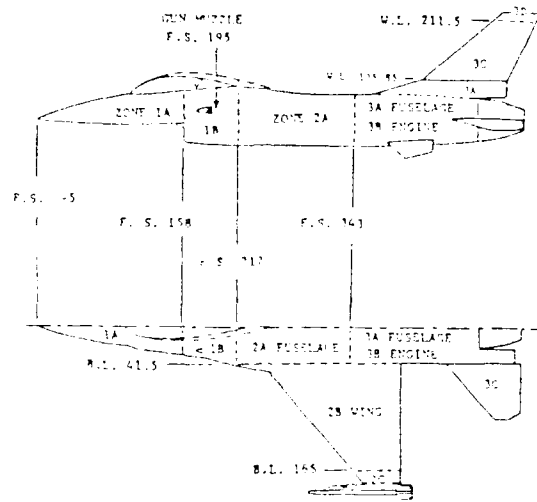
FIGURE 1. VIBRATION ZONES OF AN AIRCRAFT
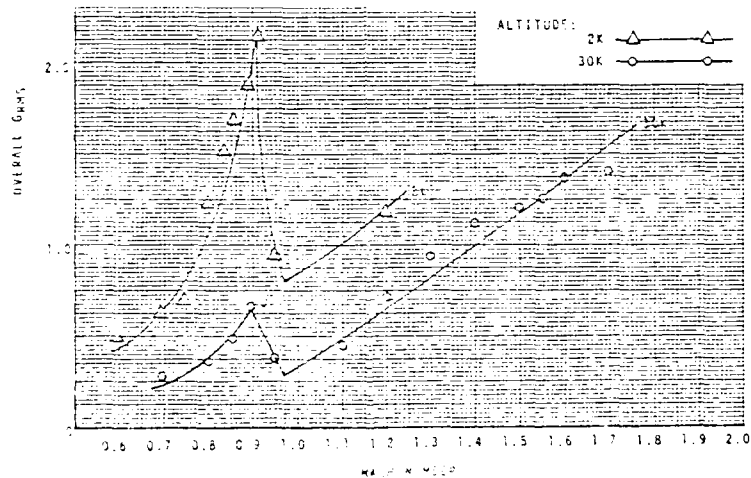
FIGURE 2. VARIATION OF FLIGHT VIBRATION WITH MACH NUMBER

DEVELOPMENT OF DATA BASE

Obtaining Data

The vibration environment for avionics equipment can be determined by measuring vibration levels during flight tests. To ensure measurement of the maximum levels and the vibration trends, many conditions in the aircraft's flight envelope must be included. Additional flight tests may also be necessary if there are modifications to the aircraft configuration which induce changes in the aerodynamic environment, flight envelope, or load paths of the vehicle.

Equipment located in the equipment bays experience vibration through load transfers at the mounts or attachment points. The vibration input to the avionics equipment is measured by instrumenting the equipment supporting structure. For

equipment directly exposed to the airflow (i.e., stores, antennas, missiles), the structural response rather than input is measured. The difference is due to the inability to measure the complex integration of pressure fields or vibration input to the surface of the external equipment.

In actual flight tests, vibration measurements will be a small part of the test program due to the expense, time constraints, and available instrumentation. The number and location of pickups, recording time, and flight test points for vibration measurements will be highly limited. Pickups will be located to record the vibration of structures supporting the most equipment. Single or double axis pickups will be used rather than tri-axial as much as possible to minimize instrumentation requirements and maximize instrumented locations. Flight test conditions will be chosen to provide the most information about the aircraft's vibration trends (load vs. g, level vs. Mach) so that data can be extrapolated to all parts of the flight envelope.

Vibration measurements from a flight test should not be confused with those of a vehicle ground vibration test (GVT). Ground vibration tests are conducted to determine the basic structural resonant frequencies, mode shapes, and structural damping characteristics of the aircraft (ref. 5). During a GVT, the vehicle is excited by arbitrary low level vibration which is not indicative of the actual flight environment. The results of a ground vibration test are used in the vehicle's flutter analysis and are not directly related to the design of avionic equipment.

Data Processing

In the 50's and early 60's, data were normally recorded on an oscillograph. The peak value and frequencies were analyzed directly from the recorded wave forms and were interpreted as sinusoidal peak values. In the 60s, and 70s, the gage signal was analyzed by sweeping the time history of the analog signal with an electric filter. The filter acted as a variable resonator to determine the frequency content of the signal and the measured amplitude was the RMS of the signal across the filter bandwidth. Because the measured amplitude is an average across a bandwidth, the accuracy of the output at a particular frequency is limited. Also, the analysis time using electric filters is lengthy because of the necessity to dwell at the increment of the record being analyzed long enough to statistically measure the variation of the signal. This was repeated at each frequency band of the analysis range. A compromise was required between accuracy (analysis bandwidth, averaging time) and cost.

With the introduction of Fast Fourier Transform (FFT) software and the availability of inexpensive digital computers, the analysis time and accuracy have been greatly reduced. An analysis is performed by digitizing the analog signal and transforming from the time domain to the frequency domain with the FFT software. The FFT produces narrow band line spectra which are mathematical representations of filter outputs centered at the frequency of each line. The vibration amplitude represents the mean square value of all components in the signal within the frequency bandwidth and is given as the measured variable (ex. acceleration, velocity, displacement) squared per Hertz (ref. 3). A plot of vibration amplitude vs. frequency is often referred to as a power spectral density (PSD) or acceleration spectral density (Fig. 3).
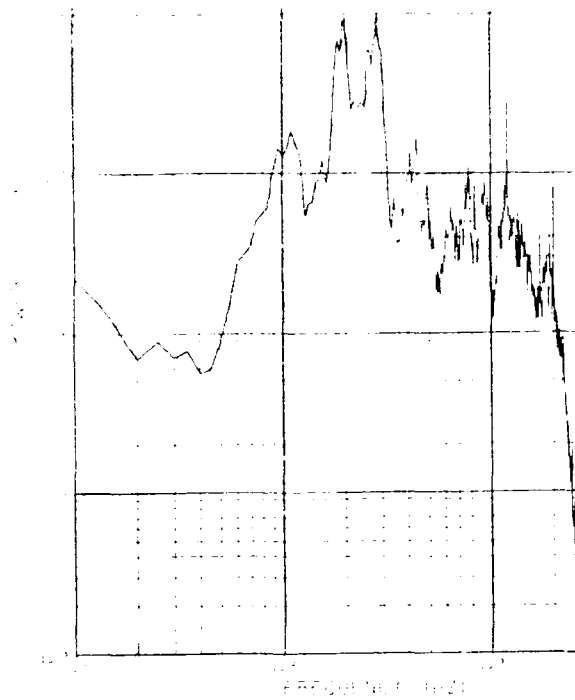
FIGURE 3.   PSD EXAMPLE

After the flight data have been analyzed and are in hard copy form, the maximum vibration levels at a particular gage can be determined by enveloping all measurements at that gage.   Further enveloping of the multiple gages within a particular zone is done to determine the maximum vibration levels within that zone (Fig. 4).
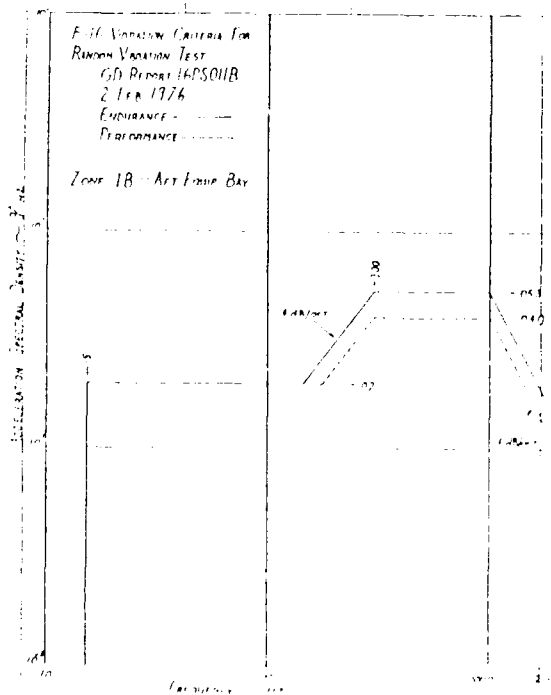

FIGURE 4.   A VIBRATION ENVELOPE

The flight vibration data that ENFSL has available is given in Table 1. The data is from numerous sources and in many forms. The data usually represents the max. "q" (max. vibration) condition in the flight envelope and does not represent a complete vibration survey throughout the aircraft.

TABLE 1: ENFSL's AVAILABLE FLIGHT VIBRATION DATA

AIRPLANES

XC-123	C-130A/B	HC-130H	EC-130Q	C-130 GUNSHIP
C-133	C-135B	RC-135S	KC-135	C-119B
C-5A	DC-10	T-43A	E-3A	SAUDI E-3
E-4B	P-3C	BOEING 747	DC/KC-10	AV-8A/B/C
F-4C/G/H	RF-4C	F-111A/E	RF-110	F-15
F/TF-15	F-16A/B/C	B-58	B-52G/H	TR-1
A-7	A-10			

HELICOPTERS

H-37A	UH-1C	OH-6A	HH-3C	HH-53	HH-60A/D
SH-60B					

MISSILES/STORES

CBU-39/40	PAVE PENNY	ALCM	RF-4C CENTERLINE TANK	
QRC-160A-1	QRC-160A-8	ALQ-71	F-15/IMV	F-14/IMV
AMRAAM	AIM-4D	FIREYE	F-16/AIM 9-L	F-15/AIM 9-L
CONDOR	SHRIKE	GBU-15	ESL-475	PAVE TACK

APPLICATION OF PROCESSED DATA

To test the performance of the equipment's design in the aircraft's vibration environment (qualification test), the equipment is vibrated on a mechanical shaker to the required zone vibration levels. It is desirable to shake the item for its' full lifetime, however, compromises of the test duration are typical. The test duration is determined through a relationship between the desired life of the equipment, the average vibration for each segment in the mission profile, the test input levels (performance levels), and the S vs N curve of the equipment material (Eq. 1) (ref. 6).

$$(W1/W2)**b = (T2/T1) \qquad\qquad Eq. 1$$
where: W = Vibration Level
T = Time
b = material constant (slope of log/log S/N
curve) typically specified as 4 for
aluminum

The test can be accelerated by selecting a shorter test duration and increasing the input level through Eq. 1. The new test level is typically referred to as an endurance level. The flight condition chosen for obtaining the endurance qualification levels may differ from those used for functional qualification. This occurs where the equipment is not required to function during a more severe environment (ref. 1). To test equipment as it is used in its

service life, the test levels and duration are continually adjusted to account for aircraft modifications. Aircraft which ENFSL has established functional and endurance vibration criteria are given in Table 2. The available data is in the form of PSDs.

TABLE 2: AIRCRAFT WITH FUNCTIONAL AND ENDURANCE VIBRATION CRITERIA

A-7	A-10	B-1B	B-52	C-5A	C-141A
KC-10	KC135	E-3A	C-130	F-5	HH-60
F-111	F-15	F-16	F-4	T-43	

Another method of testing the design of equipment in an aircraft's vibration environment is to scale the performance level with the dynamic pressure of each segment of the mission profile to obtain a varying vibration level throughout the mission (ref. 4). A test is then conducted which approximates the vibration environment for a typical mission of the aircraft. The test is repeated until a life of the aircraft has been represented. The vibration level in each segment of the mission profile is scaled using the following relationship.

$$W/W_{max} = (q^2/q_{max}^2) \times k \qquad \qquad \text{Eq. 2}$$

W = Vibration level during mission segment
W_{max} = Performance level
q = Dynamic pressure during mission segment
q_{max} = Dynamic pressure at .9 Mach and sea level
k = Transonic flow factor

The data which ENFSL have collected are in hard copy form and from a wide range of sources. ENFSL cannot provide copies of the data but can give references. The data can be reviewed in our office and a limited number of pages can be reproduced.

REFERENCES

1. J. F. Dreher, E. D. Lakin, E. A. Tolle, "Vibroacoustic Environment and Test Criteria for Aircraft Stores During Captive Flight," Shock and Vibration Bulletin 39, April 1969.

2. Svende Gade, Henrik Herlufsen, "Windows to FFT Analysis," Sound and Vibration, March 1988.

3. C. M. Harris, C. E. Crede, "Shock and Vibration Handbook," McGraw Hill, 1976.

4. M. L. Lindsley, "Vibration Design Criteria For Avionics," Aerospace Technology Conference Proceedings October 87, SAE #871768.

5. Military Specification, "Aircraft Structures, General Specification For," MIL-A-87221 (USAF) 28 February 85.

6. Military Standard, "Environmental Test Methods and Engineering Guidelines," Method 514.3 MIL-STD-810D.

VIBROACOUSTIC PAYLOAD

ENVIRONMENT PREDICTION SYSTEM

(VAPEPS)

THE IMPORTANCE OF NON-RESONANT AND INPLANE VIBRATION TRANSMISSION IN STATISTICAL ENERGY ANALYSIS

Dr. Robert E. Powell and Dr. Jerome E. Manning
Cambridge Collaborative, Inc.
689 Concord Avenue
Cambridge, MA 02138

Most of the applications of Statistical Energy Analysis (SEA) presented to date consider the interaction of resonant acoustic modes in air and bending deformation modes of beam and plate structures. However, there are many cases of practical significance where the predominant coupling mechanism between two resonant mode groups is through the non-resonant (mass-like or spring-like) dynamics of intervening structure. There are other cases where the primary coupling mechanism is through resonant inplane (compressional and shear) vibrations. This paper explores several examples of non-resonant and inplane coupling. Comparisons are made with exact simulations of two beam networks.

INTRODUCTION

Statistical Energy Analysis (SEA) is an approach to the modeling of fluid and structural dynamics that considers the responses of and interactions between resonant groups of modes. An SEA model evaluates the vibrational energy distribution among the resonant mode groups (subsystems) of a structural and/or acoustic system. The result of the analysis is the average dynamic energy of the subsystems, from which the response variables of acceleration and pressure are calculated. Because the calculation is statistical, the prediction of response can include both the expected mean value and higher moments such as the expected standard deviation. This information can be especially useful to manufacturers trying to predict how many units of a production run might be expected to exceed a certain level.

SEA methods differ from deterministic analyses such as finite elements in two fundamental aspects: the statistical description of the system itself and the use of dynamic energy and power as the system variables. The system being analyzed is assumed to be drawn from an ensemble of similar systems whose dynamic properties are known in a statistical sense [1], that is, the natural frequencies and mode shapes may be taken as random variables described by probability distributions, rather than as deterministic values. This assumption may seem unnatural to those accustomed to modal analysis of the first ten system modes, but those with experience in higher frequency testing can appreciate the inherent variability of high-order modes. The use of energy and power variables instead of displacement and force is fundamental to the grouping of "similar" modes into subsystems that are then treated as a single degree of freedom in the analysis. The energy of each mode (modal energy) in a subsystem is assumed equal due to similar excitation, damping and coupling properties. SEA's description of the state of the system by

the modal energies of the subsystems allows a natural handling of fluid/structure interaction, avoiding the change of variables to pressure or potential that is often required in finite element analysis.

A common misconception about SEA is that excitation and responses must be random noise. SEA predicts the response to pure tones of the ensemble of systems from which any single unit is drawn. As the frequency bandwidth of system excitation is decreased to zero while maintaining constant power input, the mean value energy prediction remains constant while the standard deviation prediction increases. A pure tone standard deviation includes the expected variations in response due to the excitation frequency coinciding with system resonances or anti-resonances.

This paper begins by reviewing the basic SEA equations, including the formulae commonly used to evaluate point coupling. Reasons for including coupling through non-resonant modes and inplane modes are then discussed. Two examples that illustrate these forms of coupling are examined by comparing "exact" deterministic simulations to several different SEA models. Recommendations are suggested for recognizing systems that may require non-resonant coupling or inplane mode groups.

SEA BASICS

The SEA response prediction is accomplished by the setting up and solution of a set of linear power balance equations, one for each subsystem. In the steady state, the sum of the power dissipated in a subsystem and the net power transferred from other subsystems is equal to the externally-supplied input power

$$\Pi_{diss} + \Pi_{trans} = \Pi_{in} \tag{1}$$

The input power provided by a point force F acting on a structural subsystem can be calculated from the drive point *conductance* G

$$\Pi_{in} = Re(V/F) \langle F^2 \rangle_t = G \langle F^2 \rangle_t \tag{2}$$

where the quantity in brackets is the mean-square force. The conductance of a multi-modal system, averaged over frequency, can be shown [2] to be equal to the infinite system conductance where the subsystem boundaries have been extended far from the drive point. Thus, the infinite system conductances may be used in Eq. (2) to calculate input power for an SEA model.

The power dissipated by the resonant modal response is proportional to the total energy E of the subsystem

$$\Pi_{diss} = \omega \, \eta_{diss} \, E \tag{3}$$

where ω is radian frequency and η_{diss} is the *dissipation loss factor*, which is equal to twice the critical damping ratio ζ. The total energy is the product of the *modal energy* e and the number of subsystem modes N that are excited in the frequency band $\Delta\omega$ under consideration

$$E = N e \tag{4}$$

It is helpful to introduce the *modal density* $n(\omega)$ as the average number of resonant vibration modes in a unit bandwidth

$$m(\omega) = N \dots \tag{...}$$

The modal density is simply the inverse of the average frequency spacing (in radians second) between the subsystem modes. The use of mode count becomes awkward in describing the response to pure tones, while the modal density is a continuous function that can be evaluated at the center frequency of any bandwidth. The power dissipated in a subsystem can then be expressed as

$$\Pi_{diss} = \omega \, \eta_{diss} \, N \dots = \eta_{diss} \, n(\omega) \dots$$

In the same spirit used to define the modal density, a bandwidth-independent quantity of the modal energy can be defined as the ratio of total energy to modal density

$$\hat{e} = E/n(\omega) \dots$$

where $\hat{e}$ is given the name modal power $\hat{\rho}$ in consideration of its dimensions. Modal power has physical significance, the power incident on the boundary of a two-dimensional subsystem is $\hat{\rho}/2\pi$. It is also useful in the calculation of system response after the power balance equations have been solved. The average mean-square velocity of a structural subsystem is given by [3]

$$\langle v^2 \rangle = \frac{\hat{\rho}}{\pi} \dots \tag{...}$$

The dissipated power can be described simply in terms of modal power by

$$\Pi_{diss} = \omega \, \eta_{diss} \, n(\omega) \, \hat{\rho} = \beta_{diss} \, \hat{\rho} \tag{...}$$

where β_{diss} is the dimensionless damping factor $\omega \, \eta_{diss} \, n(\omega)$.

Coupling Interactions

A basic postulate of SEA is that the net power transmitted between any two subsystems i and j is proportional to their difference in modal energy. When expressed in terms of modal power, the transmitted power is

$$\Pi_{i,j} = \beta_{i,j} \, (\hat{\rho}_i - \hat{\rho}_j) \tag{...}$$

with the non-dimensional, symmetric coupling factor β defined by

$$\beta_{i,j} = \omega \, \eta_{i,j} \, n(\omega)_i \tag{...}$$

where $\eta_{i,j}$ is the coupling loss factor from subsystem i to subsystem j and $n(\omega)_i$ is the modal density of subsystem i. Coupling loss factors are analogous to dissipation loss factors in that they represent the fraction of total energy leaving the subsystem in one cycle of vibration. One may easily draw the analogy between Eq. (...) and the Fourier equation governing thermal conduction. The heat flow power between two reservoirs (subsystems) is proportional to their difference in temperature (modal power), and to the conductivity (coupling factor) of the connection.

For subsystems connected at a point junction, the SEA coupling factor can be calculated from a transmission coefficient τ that is the ratio of transmitted to incident power [3]

$$\beta_{i;j} = \frac{1}{\pi} \frac{\tau_{i;j}}{(2 - \tau_{i;j})} \tag{12}$$

where the τ in the denominator accounts for the distortion of the field in the source subsystem when the coupling is strong ($\tau \to 1$). When the coupling takes place through the motion of a single *degree of freedom* (unidirectional translation, for example), the transmission coefficient can be expressed in terms of the impedances Z of the subsystems

$$\tau_{i;j} = \frac{4 \; Re\{Z_i\} \; Re\{Z_j\}}{\left| \sum Z_k \right|^2} \tag{13}$$

where the summation in the denominator represents the total impedance of the junction degree of freedom. When multiple degrees of freedom (such as rotational and translation velocities) transmit significant power across the junction, the average power transmitted can be approximated by the incoherent sum of the power transmitted by each degree of freedom with the others blocked.

Equation Solution

The power balance equations (Eq. (1) for each SEA subsystem) must be solved simultaneously. With the modal powers as the *unknowns*, Eqs. (9) and (10) may be substituted into Eq. (1) to write the matrix equation

$$[A] \; \{\xi\} = \{\Pi_{in}\} \tag{14}$$

where the diagonal elements of the coupling matrix $[A]$ are all positive

$$A_{i;i} = \beta_{diss} + \sum_j \beta_{i;j} \tag{15}$$

and the off-diagonal elements are symmetric, negative, and smaller in magnitude than the corresponding diagonal elements.

$$A_{i;j} = -\beta_{i;j} \tag{16}$$

After solving Eq. (14) for the modal power distribution, the response quantities of average subsystem velocities and net power flows may be calculated through Eqs. (8) and (10), respectively. Velocities may be converted into accelerations or stresses, as desired. Power flows are useful in diagnosing the transmission paths that dynamic energy follows in reaching critical components. All calculations must be repeated for each frequency band of interest, since most of the dynamic parameters will vary with frequency.

NON-RESONANT TRANSMISSION

The impedances used for calculating SEA coupling factors are typically taken to be the characteristic wave impedances of the infinite or semi-infinite systems.

When the frequency range is high enough that the (finite) subsystems have many resonant modes, it can be shown that the frequency-average impedance is equal to that of the infinite system Z_∞. There are many practical cases where the system has many nodes, but there exist small components that do not have many modes in the frequency range of interest. When two multi-modal subsystems are connected to each other through a third component, the coupling can be described in terms of the modes of the coupling element. Some of the coupling modes will be resonant in the current frequency band, and these will be modeled as an SEA subsystem with separate connections to the source and receiver subsystems. Coupling also occurs through modes with natural frequencies above and below the current band. Thus, term non-resonant coupling. This coupling represents a direct interaction between the resonant modes of the source and receiver subsystems, with a local modification of the subsystem impedances depending on the impedance of the coupling element. The subsystems and connection paths are illustrated in Fig. 1.

In many cases, the coupling contribution through non-resonant modes is negligible in comparison to the resonant contribution, and the non-resonant coupling may be omitted. However, when the coupling modes are widely spaced in frequency, are highly damped, or are only weakly excited by the source subsystem, attention must be given to the non-resonant coupling path. Non-resonant coupling can be divided further into mass-controlled and stiffness-controlled coupling, depending on the relative importance of coupling modes with natural frequencies below and above the frequency band of interest, respectively. That relative importance depends on the impedance of the coupling element compared to the source and receiver subsystems.
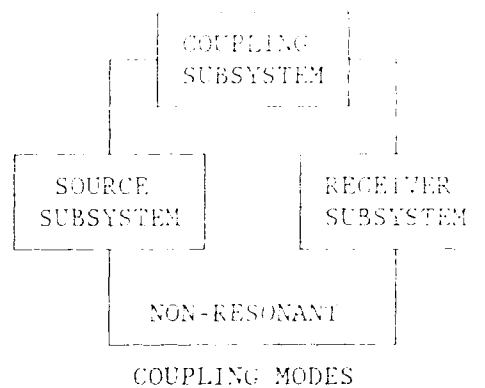

Fig. 1. SEA Model of Non-Resonant Coupling

The actual impedance of small components as seen by a junction may be significantly different from that of an infinite system with the material and cross-sectional properties of the component. At low frequencies, (near and below the first dynamic mode of the small component), the impedance seen by the junction is greatly influenced by the termination impedance at the other end of the component. The resistance (Re{Z}) especially is dominated by termination losses, and it is this resistance that needs to appear in the expression for transmission coefficient (Eq. (13)). For example, if the component is very stiff compared to its termination impedance, the junction impedance will be the complex sum of the termination impedance and the mass impedance ($j\omega M$) of the component. On the other hand, if the small component is very compliant in comparison with its termination, the effective impedance of the coupling at the junction is found by inverting the complex sum of the termination (receiver) mobility and the spring mobility of the coupling element:

$$Z_j = \frac{1}{1/Z_r + j\omega/K} = \frac{Z_r K/j\omega}{Z_r + K/j\omega} \tag{1}$$

where Z_r is the impedance of the receiver subsystem at the connection location. Note that the effective impedance magnitude is that of the spring when ωM is very

large compared to Z_r. The transmission coefficient is reduced also since $Re(Z_j)$ is attenuated for a very compliant spring.

Applications of Non-Resonant Transmission

Acousticians are familiar with the mass-law transmission loss of panels separating two acoustic spaces. This form of mass-controlled coupling is important at lower frequencies because the resonant panel modes are only weakly excited by the long-wavelength sound waves. The proper modeling of this configuration was important for early SEA applications to space payload environments [4] and architectural acoustics [5]. The use of limp mass barriers (trim panels) is also employed in commercial aircraft noise treatments. The transmission of panel vibration across a frame member is of critical importance for predicting structureborne noise in ships. Some panel modes will couple into the beam modes of the frame and thus transmit resonantly, but the panel waves transmitting energy fore/aft will tend to be normally incident on the frame and will transmit through the mass-controlled frame impedance. The structural applications of blocking masses and elastic isolators have been covered extensively from the standpoint of transmission efficiency [6], which can be used directly for SEA modeling through Eqs. (12) and (13).

The non-resonant transmission through stiffness-controlled coupling modes is encountered repeatedly in the modeling of noise control treatments. Elastomer mounts for the isolation of machinery are employed in all fields of transportation, and in the design of commercial buildings. Shipboard noise control requirements are leading to the application of hull coatings in order to decouple the hull from the external fluid. An interesting type of elastic isolation is that provided by a bubble-filled fluid layer just outside of the hull.

INPLANE TRANSMISSION

Early applications of SEA were primarily directed at the sound-structure interaction problem. Spacecraft environments and building acoustics problems had relatively short transmission paths that were well-described by acoustic modes in air and flexural (bending) modes in the structure. As SEA techniques have been applied more extensively to large-scale structureborne noise problems, the inclusion of inplane compressional and shear modes has become necessary. There are two basic reasons for the importance of inplane transmission: The high wavespeed and impedance of inplane wave types results in less attenuation with distance than occurs for flexural waves. The other factor is that design optimization for minimum weight and stress results in designs that carry gravity and operational loads through the membrane stiffness of the structural members. The dynamic loads tend to follow the static load path, which has been optimized to avoid discontinuities.

Even though the flexural waves in a structure may be more strongly excited by a source of vibrational energy, the high wavespeed and low attenuation characteristics of inplane modes leads to the inplane modal energy eventually exceeding that of the flexural modes for distant structural locations. Coupling of the inplane modes back into flexural modes occurs at asymmetrical impedance discontinuities, such as the bulkheads and frames of a ship hull. The inplane-excited flexural modes in turn radiate sound that could interfere with sonar sensors or increase the ship's radiated sound. The inplane modes often act as "carriers" of energy over long distance, although the amplitudes of the inplane modes themselves is rarely a problem. In fact, the vibration amplitudes of inplane

modes are exceedingly difficult to measure directly because the local strains and accelerations of flexural modes tend to be much higher. In spacecraft structures, the inplane modes of truss structures tend to have smaller impedance discontinuities at joints than do the flexural modes. The typical reduction in diameter of the truss members reduces the flexural rigidity more than it does the longitudinal stiffness.

Applications of Inplane Transmission

A recent application of SEA methods, including inplane modes, was reported [7] on a laboratory model of a ship foundation and hull section. This work was also cited in an article discussing inplane transmission [8]. The model described in this research was selected for an in-house SEA analysis by Cambridge Collaborative. The structure, consisting of seven welded plates, is shown in Fig. 2. The results of SEA predictions with bending-only and bending/inplane models are compared to the measurements of [7] in Fig. 3. It can be seen that the bending-only model under-predicts the vibration transmission from the top plate to the bottom plate. The inclusion of inplane mode types in this case improves the agreement with the data.
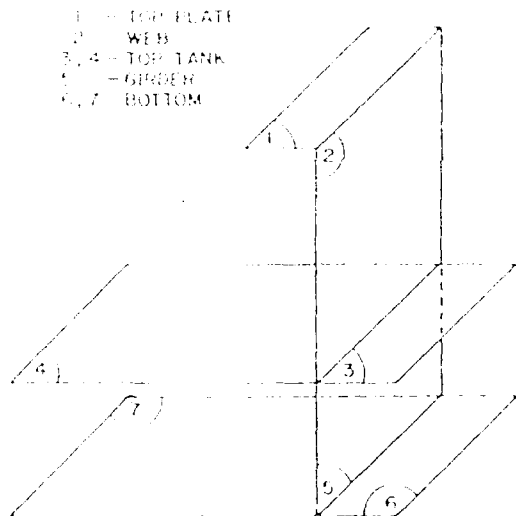
Fig. 2. Model of Ship Foundation & Hull   Fig. 3. SEA Model and Measured Data
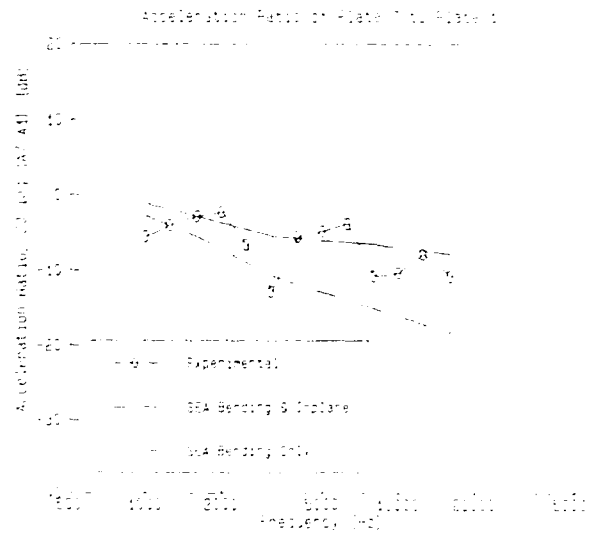
BEAM TEST CASES

A two-dimensional system consisting of three beams was chosen to demonstrate the influence of non-resonant and inplane coupling. Fig. 4 shows the configuration of the two test cases. The top and bottom beams are connected 1.5 m from an end by a vertical beam. The dimensions are summarized in Table 1. In both cases, the damping loss factor is a moderate 0.06 in the top and vertical beams, while the lower beam was assigned a high loss factor of 0.2. With excitation applied to the top beam, the high damping in the lower beam simulates coupling losses to a large

structure. Damping loss factors must be higher than coupling loss factors in an SEA model to avoid equipartition of modal energy. If the coupling away from a subsystem is stronger than its internal losses, then it will tend to have the same modal energy as its neighbors and its response becomes insensitive to coupling changes. Care must be taken in any study of SEA coupling factors to avoid equipartition.

In the first configuration (case 1), the vertical coupling beam was half the thickness of the top and bottom beams. The width and elastic properties are the same in case 1 for all of the beams, and the joints are rigid. This is a typical case where the bending modes of the vertical beam transmit resonantly. For the configuration chosen, those bending modes have dissipation losses that reduce resonant transmission into the bottom beam.

For case two, the impedance of the vertical beam was increased by making it from steel with twice the thickness of the top and bottom beams. Flexural transmission was blocked by hinges at each end of the vertical beam, simulating a thick bulkhead with stress relief at the joints.

Deterministic Analysis

A beam transmission line simulation program (TRAN3D) developed at Cambridge Collaborative was chosen to perform the "exact" analysis of the coupled beam problem. While using fewer than ten grid points, this method gives results comparable to the direct solution of a beam finite element model with a very fine mesh. In addition, the code calculates kinetic and potential energy in the elements, a valuable tool for comparing to SEA results. For each beam configuration, the model was run with a unit force excitation for 301 logarithmically-spaced frequencies from 10 Hz to 10 kHz. Results were processed for

• drive point mobility on the top beam

• bottom beam energy / input power

The energy of the bottom beam integrates the velocity distribution, smoothing the mode-to-mode variations. Normalization by
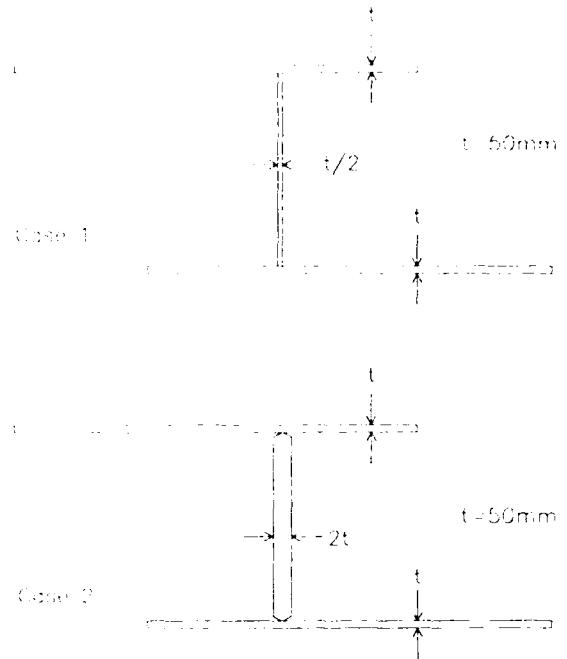
Fig. 4. Beam test case configurations

TABLE 1. BEAM DIMENSIONS

Top & Bottom Beams (Aluminum)

Length:	3.00 m
Width:	0.05 m
Thickness:	0.04 m
Density:	2.7×10^3 kg/m^3
Young's Modulus:	7.0×10^{10} Pa
Loss Factor (Top Beam):	0.06
Loss Factor (Bottom Beam):	0.2

Vertical Beam

Length:	1.5 m
Width:	0.05 m
Loss Factor (η_{diss}):	0.06

(Case 1, Aluminum)

Thickness:	0.02 m
Density:	2.7×10^3 kg/m^3
Young's Modulus:	7.0×10^{10} Pa

(Case 2, Steel)

Thickness:	0.08 m
Density:	7.8×10^3 kg/m^3
Young's Modulus:	2.0×10^{10} Pa

input power removes the resonant peaks, further smoothing the narrow band data. The smoothing of deterministic data facilitates comparison to the slowly-varying SEA predictions.

SEA Model

Simple SEA models of the beam test cases were prepared to run under Cambridge Collaborative's SEAM [9] computer code. Flexural subsystems were used for the top and bottom beams, and for the vertical beam in case 1. Inplane subsystems were used to model longitudinal modes in the vertical beam. Dimensions, material properties, and damping loss factors were identical for the deterministic and statistical analyses. Non-resonant transmission was included explicitly in the SEA model by joining the top and bottom beams only at a junction with the added impedance of the vertical beam mass. In this case, the impedance of longitudinal modes in the vertical beam was larger than the flexural impedance of the top and bottom beams, so no isolation compliance was modeled. Two junction degrees of freedom were included in the coupling through resonant modes of the vertical beam: vertical translation (force) coupling to the inplane modes, and rotation (moment) coupling to the flexural modes. The junction models were edited to eliminate selectively the bending, inplane, or non-resonant contributions to the energy of the bottom beam. All SEA models were run in third-octave bands from 10 Hz to 10 kHz.

The SEA junction impedances for the subsystem in case 1 (thin vertical beam) are plotted in Fig. 5. The top three curves are vertical force impedance magnitudes (F/V) for the inplane (Rod F), top beam (Beam F), and rigid mass (Mass F). The bottom beam is identical in impedance to the top beam. At low frequencies, the mass impedance is smaller than that of the beams. The resultant lack of mass-blocking means that the non-resonant path will be significant at lower frequencies. The first inplane mode of the vertical beam (with free-free or clamped-clamped boundaries) is at 1700 Hz, so it is questionable whether the resonant inplane subsystem should be included at low-frequencies. However, the loading effect of the beam imped-ances at the inplane boundaries will tend to reduce the frequency of the first mode. The inplane and beam bending impedances are nearly equal above 1 kHz, so the inplane transmis-sion path should be efficient at high frequencies.

Fig. 5. Junction Impedances for Case 1

The lower two curves are moment impedances for the top beam (Beam M) and the vertical beam (Rod M). There is a constant impedance mismatch of 20 dB for the moment impedances, indicating that the moment junction transmission coefficients will be small and constant with frequency.
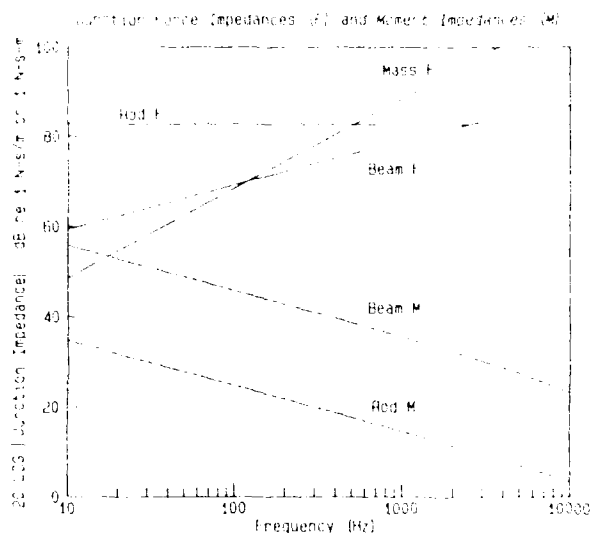
The magnitude of the drive point mobility on the top beam is shown in Fig. 6. The drive point is located halfway between the free end and the vertical beam. The thin solid curve is the simulation result, while the thick solid line is the SEA average value of the top beam subsystem mobility. The statistical nature of the SEA prediction has been indicated by the inclusion of dotted lines at plus and minus two standard deviations, as predicted by the SEA software. In general, the narrow-band peaks and dips are enveloped by the +/-2σ curves. The peak in the mobility at 13 Hz is the first mode of the coupled system.

The normalized energy in the bottom beam for a bending-only SEA model is compared to the simulation result in Fig. 7. In this SEA model, the inplane subsystem was left uncoupled, and the non-resonant junction was removed. Due to the moment impedance mismatch and moderate damping ($\eta=0.06$) in the vertical beam, the system is undercoupled and the SEA response prediction for the bottom beam is generally between 5 dB and 10 dB low.

The addition of the non-resonant junction directly coupling the vertical motion of the top and bottom beams through the mass of the vertical beam improves the agreement between deterministic and statistical analyses considerably. The energy of the bottom beam, normalized by the input power, is shown for this second SEA model in Fig. 8. The simulation results are the same as in Fig. 7. One might wonder if the further addition of inplane coupling might overpredict the transmission, especially in light of the low inplane modal density. The SEA model for case 1 with all three types of coupling is shown in Fig. 9. At low frequencies, the response is unchanged, indicating that the non-resonant path is stronger than the inplane path. At the highest frequencies the response is increased over Fig. 8 by 5 dB. Although the SEA prediction including
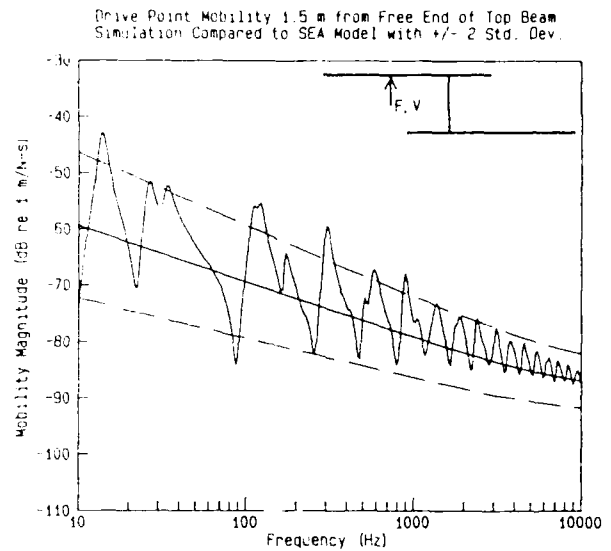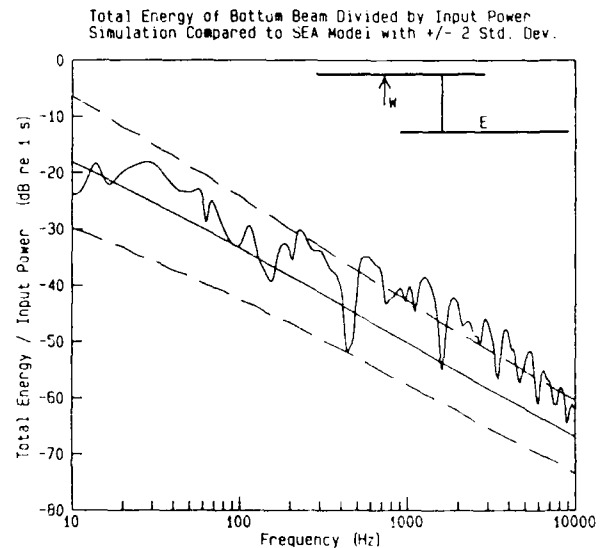

Fig. 6. Drive Point Mobility

Fig. 7. Normalized Energy in Bottom Beam with Bending-Only SEA Model (Case 1)

all three coupling paths is slightly
high, it is a conservative modeling
technique to include all possible
coupling types.

Case 2 Result Comparison

The bending path was deliberately
left out of case 2 in order to
highlight the vertical translation
coupling degree of freedom. Junction
impedances for the full SEA model are
shown in Fig. 10. The inplane (Rod)
impedance is now much greater than the
beam bending impedance over the full
frequency range. The impedance of the
mass is also greater than that of the
beams, especially at high frequencies,
so the non-resonant transmission will
decrease at higher frequencies.

The SEA model was run first with
only the non-resonant coupling (no
inplane). The energy of the bottom
beam, normalized by the input power, is
shown for the "exact" simulation and
for the SEA model with mass-coupling in
Fig. 11. The deterministic simulation
for this case appears to have two
slopes: at low frequencies the energy
is quite high, and it decreases with
frequency until a "plateau" is reached
around 1 kHz, where the slope
decreases. The SEA model with only
non-resonant coupling agrees well with
the low-frequency slope, but fails to
cross over to the lower slope at mid
frequencies. By 10 kHz, the SEA
prediction is 20 dB low.

When the resonant inplane subsystem
is coupled into the SEA model, with the
non-resonant mass coupling *removed*, the
prediction (Fig. 12) agrees well with
the simulation in the higher frequency
range. The low-frequency prediction
with inplane coupling only is slightly
low. When the non-resonant and reson-
ant inplane coupling are combined
(Fig. 13), the SEA results are in good
agreement with the deterministic
simulation across the full frequency
range. The matching of the different
slopes at different frequency ranges
suggests the utility of SEA models for
the interpretation of measured data.
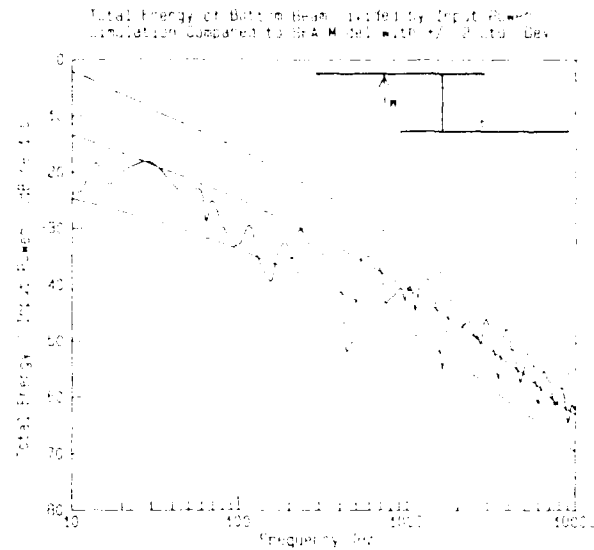
Fig. 8. Normalized Energy in Bottom Beam
for Bending and Mass-Coupled SEA
Model (Case 1)

Fig. 9. Normalized Energy in Bottom Beam
with Bending, Mass, and Inplane
Coupling (Case 1)

Fig. 10. Junction Impedances for Case 2

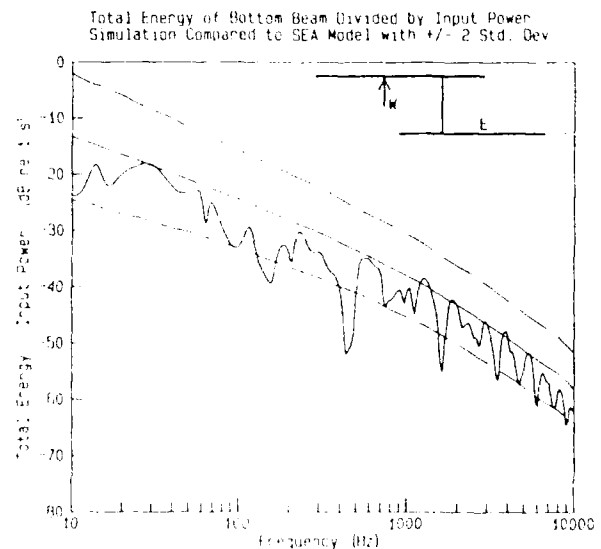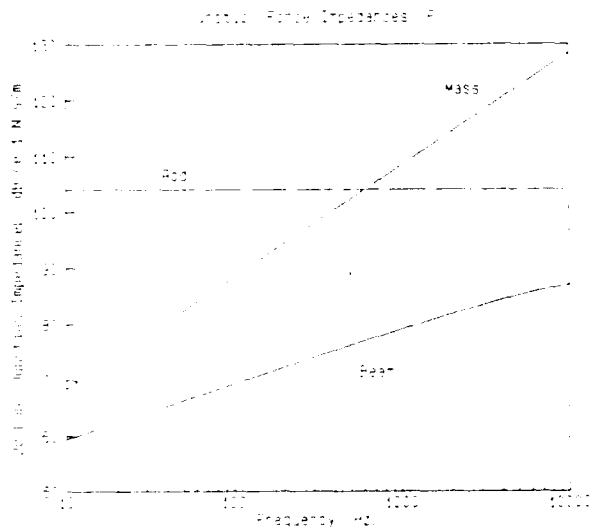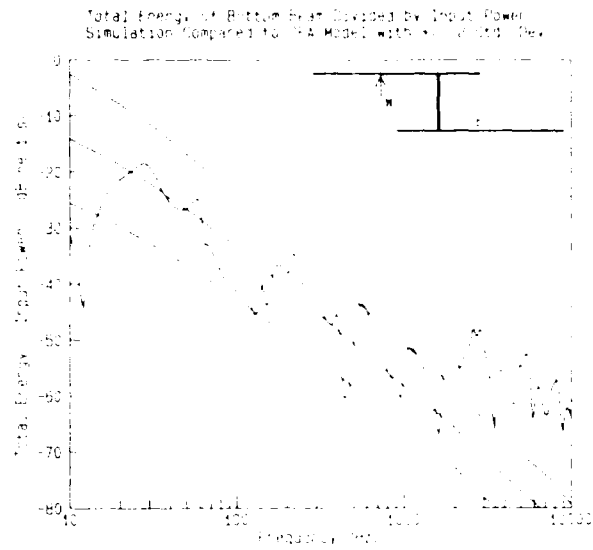Fig. 11. Normalized Energy of Bottom Beam
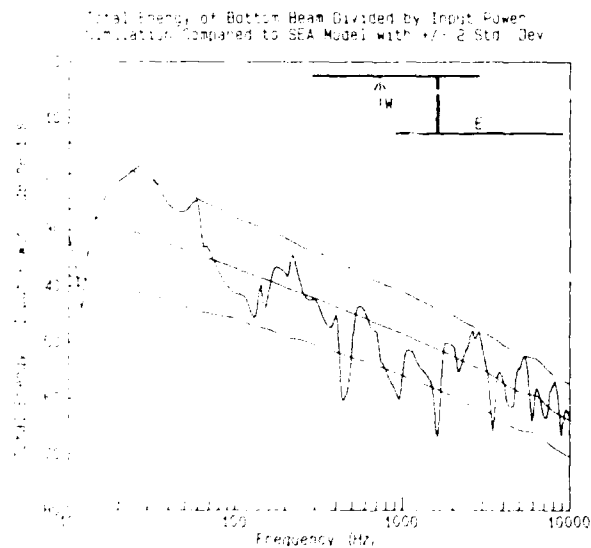with Mass Coupling Only (Case 2)

Fig. 12. Normalized Energy of Bottom
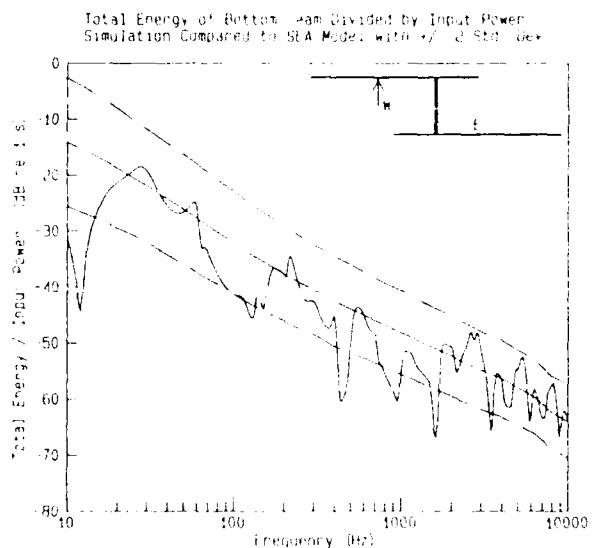Beam with Inplane Coupling
Only (Case 2)

Fig. 13. Normalized Energy of Bottom
Beam with Mass and Inplane
Coupling (Case 2)

100

CONCLUSIONS

Statistical Energy Analysis has traditionally formulated when the response of complex systems has been dominated by the resonant energy in flexural and torsional modes. Since many practical engineering structures contain small components, such as isolation mounts or short standoff supports, it is necessary to model the energy transmission through these components in terms of both resonant and nonresonant modes. When the resonant mode contribution is reduced due to a low modal density or a high damping loss factor, the non-resonant transmission is the dominant path. The contribution of inplane mode types is often ignored in SEA models, because the excitation and measured response are dominated by flexural modes. Because of their relatively high wave speeds and characteristic impedance, inplane compressional and shear modes are less subject to dissipation, radiation, and reflection losses than are bending mode types. When structureborne noise propagates over large distances, the lower attenuation per unit distance of inplane modes can result in their being the dominant path of energy travel. The SEA model of a large structure, such as a ship, space structure, or office building, should include the contributions of inplane mode groups when predicting structureborne response at large distances from the source.

This paper has demonstrated SEA modeling methods for the incorporation of non-resonant coupling into SEA analytical models. The basics of Statistical Energy Analysis were reviewed, including the description of point coupling in terms of transmission coefficients and junction impedances. Several examples were presented to demonstrate potential underprediction of response when non-resonant or inplane coupling paths are neglected. Non-resonant coupling through a mass or a spring should be included when a small component connects multi-modal subsystems that have impedances greatly higher (spring) or lower (mass) than the characteristic impedance of the component. The non-resonant path can be especially important at low frequencies or when the resonant path is highly damped. Inplane mode groups should be modeled when the structureborne response travels over distances of many wavelengths, or when the flexural path has impedance discontinuities or is isolated from noise control treatments or from radiation.

REFERENCES

1. R. H. Lyon, Statistical Energy Analysis of Dynamical Systems, p. 3, M.I.T. Press, Cambridge, MA, 1975.

   L. Cremer, M. Heckl, and E.E. Ungar, Structure-Borne Sound, Section IV.5, Second Edition, Springer-Verlag, Berlin, 1988.

2. "Statistical Energy Analysis Theoretical Manual," Cambridge Collaborative, Inc., Report No. 88-15-21610-1, Contract N00167-86-D-0193, July 1988.

   R.H. Lyon, "Random Noise and Vibration in Space Vehicles," Eq. (3.35), Monograph SVM-1, Shock and Vibration Information Center, U. S. Department of Defense, 1967.

   M.J. Crocker and A.J. Price, "Sound Transmission Using Statistical Energy Analysis," J. Sound Vib., Vol. 9, pp. 469-486, 1969.

5. Cremer, Heckl, and Ungar, IV.5, V.

   J. Tratch Jr., "Vibration Transmission Through Machinery Foundation and Ship Bottom Structure," Mech. Eng. Thesis, Mech. Eng. Dept., MIT, June 1985.

   R.H. Lyon, "In-plane Contribution to Structural Noise Transmission," Noise Control Engineering Journal, January-February 1986.

   "SEAM User's Manual," Cambridge Collaborative, Inc., Cambridge, MA, 1986.

VIBROACOUSTIC RESPONSE
USING THE FINITE ELEMENT METHOD
AND STATISTICAL ENERGY ANALYSIS

Fred L. Gloyna
General Dynamics, Convair Division
San Diego, CA 92138

A dual analytical approach is discussed for prediction of random vibration response to spatially distributed random pressure fields encountered by aerospace structures. The Finite Element Method (FEM) and Statistical Energy Analysis (SEA) are shown as complementary analysis tools and the strengths of each are combined for vibroacoustic response analysis. Spatial correlation characteristics of the excitation environments in the low frequency range are discussed as being of fundamental importance in determining random response which, when overlooked, may lead to over test at low mode order resonances.

INTRODUCTION

Aerospace structures may be exposed to extreme aeroacoustic environments such as rocket exhaust noise, near field jet engine noise, or aerodynamically induced noise. Random vibration is a structural design constraint for most aerospace vehicles. The Finite Element Method (FEM) is generally useful in determining responses in low mode order frequencies, while Statistical Energy Analysis (SEA) is valid at higher frequencies. FEM has been brought to bear on the vibroacoustic response problem, however, the complexity in describing the pressure field and applying it as a forcing function has significantly slowed application of this approach. SEA has been proven by research workers in acoustics, as well as pioneering work by R. H. Lyon, to be an analysis framework to close the gap on determining vibroacoustic response. However, the structural side of the SEA framework, particularly at lower frequencies, needs more theoretical development for modal density and coupling loss factor expressions to define energy flow along radiation and structure-borne paths. Both methods, used separately, leave large areas of uncertainty that can be reduced if the two are combined as complementary analyses.

The development of a FEM excitation model, based on the use of measured correlation data, is described for an acoustic source using test measurements, however, the format of the excitation can also be used to model turbulent boundary layer pressure fluctuations. An example of panel response to a diffuse acoustic field was available from the test data base, and both FEM and SEA were utilized to predict random vibration and compare with the test data.

Excitation Pressure Fields

The ability of a fluctuating pressure field to excite structural response is determined by both the amplitude of the power spectrum and spatial correlation characteristics. While the amplitude spectrum is commonly available by direct measurement, estimated from similar configurations, or analyzed from a rational basis, spatial correlation is usually not considered.

Three forms of environmental pressure fluctuations to which aerospace structures are exposed are turbulent boundary layer, sonic impingement from an acoustic noise source and a diffuse noise field representative of a reverberant acoustic test chamber. At high frequencies each tends to behave like a diffuse field, however, at low frequencies they have distinguishing correlation characteristics.

Turbulent boundary layer excitation is aerodynamically induced, convected at a velocity somewhat less than the airspeed and has some degree of spatial correlation in the streamwise direction, but laterally, is practically uncorrelated. Methods for predicting parameters of the fluctuating pressure field acting on the surfaces of flight vehicles due to propulsion systems and aerodynamic flow are treated in References [1,2,8].

The risk of simulating the above service environments by a reverberant field is to over-test the structure in random vibration. A diffuse sound field, as found in a reverberation chamber, tends to excite all modes of vibration and spatial correlation characteristics are isotropic [3]. A highly correlated field such as low-frequency jet noise or rocket noise is more selective, but can still excite low order modal resonances very effectively. By comparison, turbulent boundary layer pressure fields exhibit short streamwise correlation distances and even less laterally. In today's environmental testing the high intensity noise field in the reverberant chamber is intended to simulate the combined noise field and aerodynamic turbulence in flight. Low frequency vibration is dominated by overall structural modes. As a consequence of longer wavelengths at low frequencies, a reverberant field is spatially correlated and can excite all structural resonances in the low frequency range. As frequency increases, say above 1,000 Hz for aircraft fuselage structure, jet noise is much less effective at exciting structure than is the turbulent boundary layer.

Finite Element Excitation Models

Although the excitation is assumed to be from a point source, the acoustic rays to the structural surface of interest are considered to be parallel, as for a homogeneous pressure field. This is an acceptable simplification when the structural surface is a reasonable distance from the source, as suggested by Figure 1. As a consequence of assuming parallel rays to the structural surface, the model may use separation coordinates, ξ and η, rather than absolute locations to define the trace velocity and spatial decay rate on the structural plane.

The excitation field can be assumed to consist of a series of outwardly propagating acoustics plane waves incident on a panel surface at different angles of incidence. The angles are dependent on locations of effective noise sources relative to the panel. In truth, the noise source is not a point, but is distributed over a finite volume and plane waves for a particular frequency are incident on the panel over a range of three-dimensional angles of incidence. Thus traveling plane wave excitation may have many attributes of a reverberant acoustic field, particularly at high frequencies [5]. It is reasonable to model engine noise on the structure as a reverberant sound field if differences in excitation efficiency in the low frequency range are considered.

As acoustic disturbances are propagated toward the panel, phase behavior characteristics of the sound waves are projected onto the structural surface. The angle of incidence of the acoustic ray directed toward the center of the structural panel, point P, will be assumed constant for all wave fronts. Trace velocity components in the x and y directions may be derived from the phase angle spectrum of the pressure cross PSD on the panel surface.

$$V_x = \omega \xi / \Phi_x \qquad V_y = \omega \eta / \Phi_y \qquad (1)$$

Here ω is the band center frequency in radians/second and Φ is the phase angle of the cross power spectral density (XPSD) at those separation distances in radians. Lacking experimental data, the trace velocities could also be calculated from the geometry using an assumed source locations as shown in Figure 1.

$$V_x = c_0 / \sin\Psi \qquad V_y = c_0 / (\cos\Psi \sin\Theta) \qquad (2)$$

The acoustic ray travels from the point source at the speed of sound, c_0. Thus trace velocity components on the structural surface are always supersonic. If the structure is part of a moving air, raft, angular corrections can be added to compensate for the downstream vector component.

To obtain the narrow band acoustic correlation function, it is assumed that there are not two or more statistically independent noise sources. Otherwise a weighted average coherence function would have to be developed. The narrowband coherence function is a quantity defined by

$$\gamma^2(x_1, x_2, f) = |G_p(x_1, x_2, f)|^2 / [G_p(x_1, f) * G_p(x_2, f)] \le 1 \qquad (3)$$
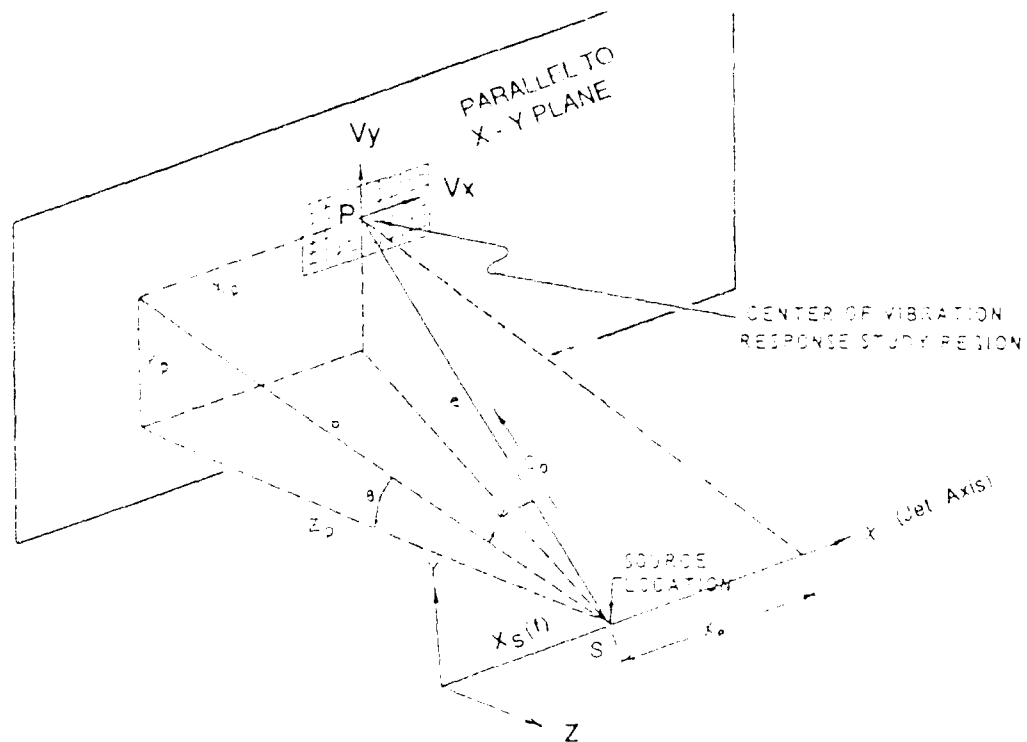

Figure 1
Acoustic Point Source Impinging on a Flat Plate

where $G_p(x_1,x_2,f)$ is the complex pressure cross power spectral density function between points x_1 and x_2, and $Gp(x_1,f)$ and $G_p(x_2,f)$ are the corresponding pressure spectral densities at locations x_1 and x_2. Since the pressure field is assumed homogeneous, the coherence function can be written in terms of separation distances, ξ and η, referencing the x and y directions respectively.

The coherence function is identical to the square of the maximum narrowband correlation coefficient. The amplitude of the correlation coefficient at a frequency ω can be represented by

$$\gamma(\xi,\eta,\omega) = e^{[-C'_x(\omega/V_x)|\xi|]} * e^{[-C'_y(\omega/V_y)|\eta|]} \qquad (4)$$

Equation (4) implies the correlation is separable in the x and y directions. Spatial decay in the x and y directions are expressed as functions of frequency, separation distance and acoustic trace velocity. Decay coefficients, C'_x and C'_y, are slowly varying functions of frequency. The form of the FEM excitation model is shown as follows:

$$G_p(\xi,\eta,\omega) = [G_p(\omega)]*[e^{-C'_x(\omega/V_x)|\xi|} e^{-C'_y(\omega/V_y)|\eta|}]*[e^{-i\omega\xi}/V_x\ e^{-i\omega\eta}/V_y] \quad (5)$$
Complex pressure   Pressure PSD   Narrowband spatial decay   Phase
excitation

The spatial decay rate characterizes the distances, ξ and η, and frequencies, ω, over which the pressure field is correlated and is important in determining how efficiently it can excite a structural panel. When it is required to perform vibroacoustic predictions of low frequency response, knowledge of the correlation characteristics of the excitation is essential.

Spatial decay rates can be evaluated experimentally using an array of flush mounted surface microphones aligned in the longitudinal and lateral directions. Cross power spectral density and coherence is calculated for a range of transducer separation distances to form the curves shown in Figure 2.
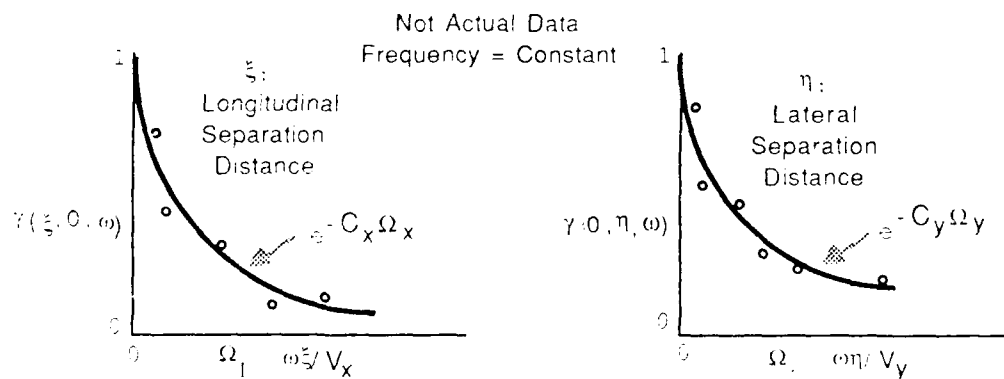

Figure 2
Spatial Decay Coefficients Defined by Curve Fit of Ordinary Coherence Data

The spatial decay study must represent the flight conditions of interest, location and relative orientation to noise sources and the curves should be developed separately for narrow

frequency ranges of interest. Response calculations assume that field properties do not change over the finite element grid system for which a XPSD matrix is generated. An example of spatial decay results from a static ground test, with a jet engine operating at take-off thrust, is shown in Table I. In this test, the location of the measurements were on the aft fuselage of an aircraft with wing mounted engines.

Table I
Example of Spatial Decay Coefficients, Jet Engine Noise

Freq Hz	Spatial Decay	
	C_x	C_y
200	.63	.18
300	.58	.14
500	.48	.08

Spatial decay rates were determined by interpreting the frequency dependent correlation properties of the ordinary coherence function, γ^2, calculated from an array of microphone measurements aligned in the longitudinal and lateral directions and the non-dimensional data plotted as in Figure 2. Lacking test data one could estimate conservative conditions for the structure in frequency and space. Apparent noise source locations can be established by acoustic ray tracing using the change in XPSD phase angle over known separation distances, assuming the sources are distributed along the jet axis.

The analytical model represents a simplification of the near-field engine noise vibroacoustic excitation environment, but provides a framework to allow analysis including the effects of spatial correlation properties. It is noted that the spatial decay rates listed do not represent recommended coefficients, but rather suggests that measurements of this type are needed to evaluate the correlation characteristics of excitation pressure fields to complement the traditional amplitude only measurements. Turbulent boundary layer simulation can be expressed in a similar format and would be additive to the excitation matrix for jet noise since the two are uncorrelated with respect to each other. Reference [1] presents methods for predicting aeroacoustic pressure fluctuations.

To obtain the force XPSD for use as the excitation in a finite element analysis, the pressure field must be discretized to a set of complex forces, each centered on a "finite element" area. The proper mathematical treatment, although not always required, is to perform a surface integration of the pressure expression, equation (5), over all pairs of finite element areas, ie, a quadratic integration. To accomplish this it is assumed that all finite elements are rectangles of the same dimensions and therefore equally spaced. In this manner, changes in spatial decay and phase within each individual finite element are included to produce an integrated complex force for the element. Thus the force representation for large elements in a coarse FEM analysis may benefit by the integration of the pressure field depending on correlation lengths.

A finer FEM idealization would suggest that simply multiplying the complex forces by the applicable areas would allow one to omit the integration (and the requirement for equally spaced grids). With turbulent boundary layer excitation correlation lengths may be short, such that many small pressure eddies may reside over a single finite element. In this case, the net force should be determined by adding incremental complex forces by surface integration over all pairs of finite elements, and the integrated expression would represent a more accurate force distribution [7]. The integrated expression is presented in the Appendix

The reverberant sound field differs from the convected fields in that all waves have been incident and reflected many times from boundaries of the enclosure over a random variation of angles[4]. The pressure field of a point in time and space is statistically related to that at another point. The energy density is based on sound waves traveling in any direction with equal probability. Depending on angle of incidence, some waves contribute more to the flow of energy into a structural specimen than others. The narrowband spatial correlation of a reverberant sound field depends on phase relationships which is also independent of direction. Thus the narrowband correlation characteristics of an ideal diffuse sound field approach randomness in a standard way [3].

The cross power spectral density of a diffuse pressure field is described as a product of the pressure PSD and narrowband spatial correlation [2].

$$G_p(\xi, \eta, \omega) \ = \ G_p(\omega) \cdot Sin(\kappa r)/(\kappa r) \tag{6}$$

The spatial analog of the frequency f is $1/\lambda$ where λ denotes the wavelength; the spatial analog of the radian frequency ω, is the wavenumber $\kappa = 2\pi/\lambda$ [1], and r is the radial distance between the two points, $r = (\xi^2 + \eta^2)^{1/2}$, independent of direction.

Finite Element Application

The overall effort for implementing the finite element method using NASTRAN [9] is shown in the Figure 3 flow diagram.
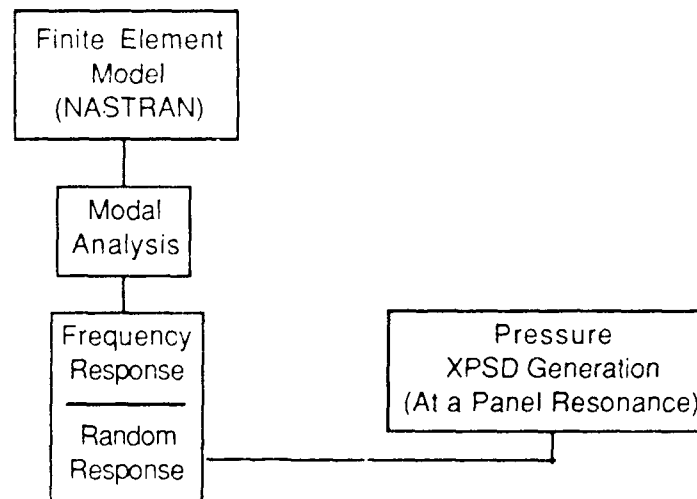

Figure 3
Flow Diagram For Finite Element Vibroacoustic Response Calculation

The NASTRAN finite element program was used to model a simply supported honeycomb panel subjected to a diffuse acoustic field. The finite element model of the panel is shown in Figure 4 indicating 45 interior grid points at a slightly elevated Z-coordinate relative to the outer perimeter of plates. The interior grid points are located on the neutral axis of a honeycomb cross section. Plate elements representing honeycomb construction connect with the outer perimeter of conventional isotropic plate elements by a transition ring of narrow aspect ratio plates.
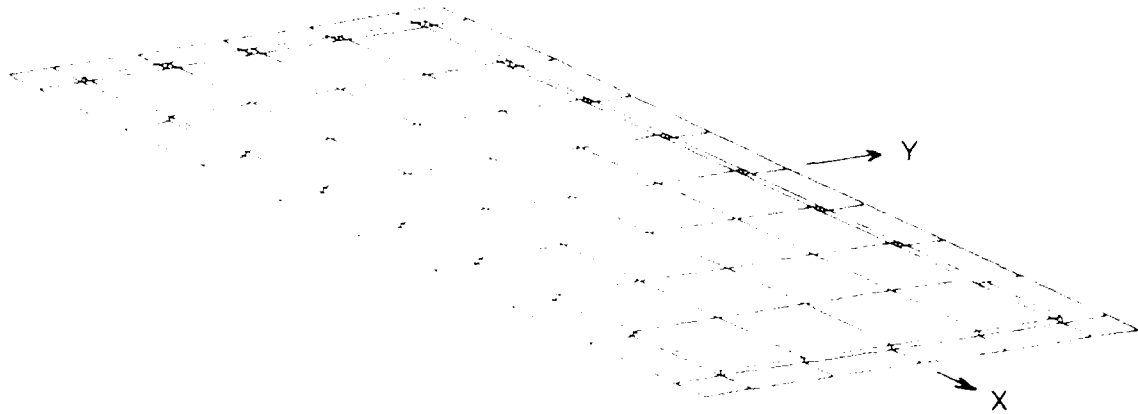
Figure 4
Finite Element Model for Honeycomb Panel

Other approaches to modeling the 3-dimensional aspects of the honeycomb panel which transitions to a solid plate near the boundary could also be acceptable or even better, however, good results were obtained in low order modes with a coarse idealization. Physical properties of the panel are defined in Table II, with the corresponding panel resonances presented in Figure 5.

Table II
Honeycomb Panel Modeling Data

Overall Panel
L_x = 38.0 in.   E = 10.5x106 psi
L_y = 15.25 in. ρ = 0.101 lb/in^2

Honeycomb Interior Section Plates
L'_x = 33.8 in   Z elevation = 0.2305 in
L'_y = 12.05 in I_c = 7.938x10^{-3} in^4
Total thickness, both face sheets = 0.065 in
Non-structural weight
(core material and bonding resin) = 6.34x10^{-3} lb/in^2

Boundary Plates
t = 0.131 in   Z elevation = 0.

Transition Plates
t = 0.131 in

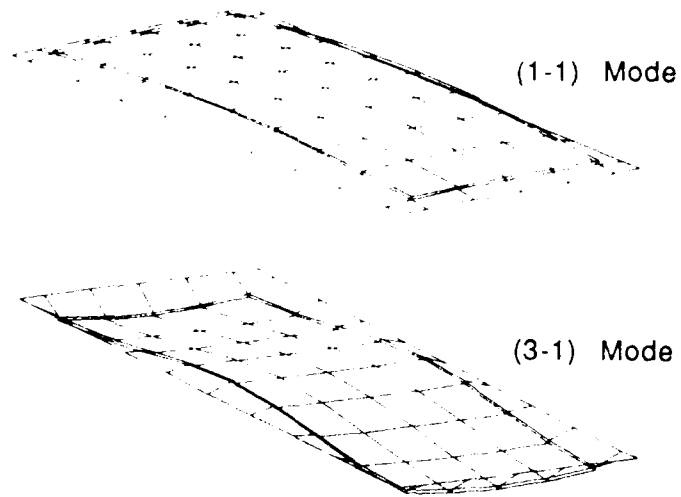| Mode Order (X,Y)	Frequency (Hz)
(1-1)	244.2
(2-1)	323.2
(1-2)	381.4
(3-1)	434.4
(2-2)	504.6
(4-1)	557.4

(1-1) Mode

(3-1) Mode

Figure 5
Modal Analysis Results, Honeycomb Panel

The excitation model will represent a diffuse acoustic environment using equation (6). It is interesting to compare the plan view of the panel from the perspective of the pressure field and structural models using a common grid array. In Figure 6(a) the structural model uses grid points to interface structural elements and as a basis for calculating distributed dynamic behavior, with fineness of the grid consistent with structural discontinuities and requirements for higher order modes. The pressure field model will distribute complex pressures (which are real in the case of diffuse excitation) to the mid points of the elements shown in Figure 6(b).

(a) Structural Idealization

(b) Pressure Field Idealization
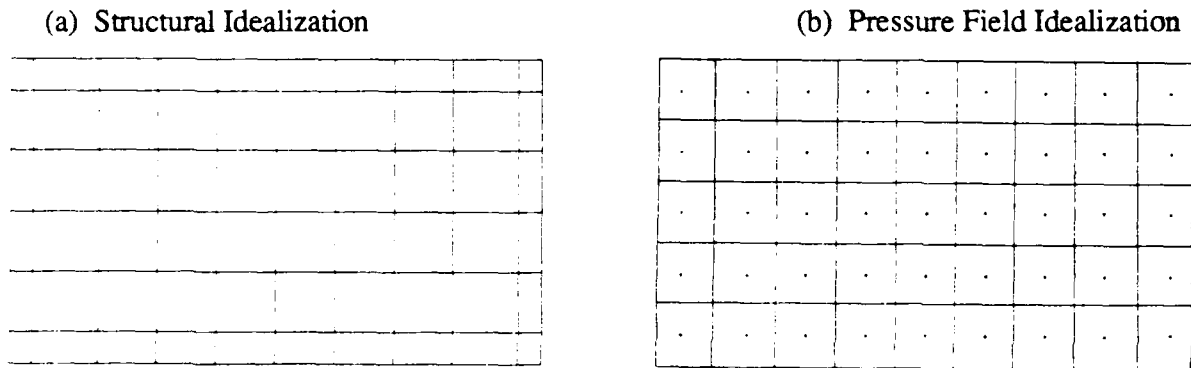
Figure 6
Plan View of Honeycomb Panel Model for Structural and Pressure Field

The cross spectral density of the reverberant field excitation was calculated in the pressure domain, ie, $(psi)^2/Hz$, for two frequencies corresponding to the (1-1) and (3-1) panel modes.

For frequencies of 244 Hz and 434 Hz the $\sin(\kappa r)/(\kappa r)$ function of equation (6) has the first sign change at a separation distance of 27 inches and 17 inches, respectively. Since the reverberant pressure field correlation lengths are long at these frequencies compared to element dimensions, there is no need for surface integration as given in the Appendix for a convected

field. Therefore, excitation forces are developed in NASTRAN by applying the surface area of each element. Pressure field calculations assumed an evenly spaced set of grids, although in the present example the outer perimeter of areas are 11% smaller along the short dimension and 1% larger on the long sides. This was done to accommodate the structural detail of the panel. The excitation at the two panel resonances were extracted from the Sound Pressure Level (SPL) spectrum shown in Figure 8.

In NASTRAN, random response analysis is treated as a data reduction procedure that is applied to the results of a frequency response analysis. It is noted that the implementation of a complex frequency dependent description of the excitation model is not well conceived in NASTRAN which can only provide solutions for a single frequency or frequency band, where the excitation is constant within that band. NASTRANs subcase facility is "used up" for calculating frequency response where a subcase is required to develop each row (and corresponding column) of the frequency response matrix, $H(\xi,\eta,f)$. Hipol and Piersol [6] bypass this part of NASTRAN and utilize the reciprocity characteristics of linear elastic structures to the maximum extent for a very efficient solution.

The upper triangular part of the excitation cross spectral density $G_p(\xi,\eta,f)$ is input as one complex number per "card" (1035 cards for a 45x45 matrix). The problem is overcome by letting computers format the data, however, each pass thru NASTRANs random response solution works with only one excitation definition. Thus response calculations for constant excitation were limited to a narrow frequency range centered about the excitation frequency.

Once the limitations in NASTRANs random response capabilities are understood the solution for acceleration spectral density is easily completed using the following expression

$$G_a(f) = H^*(f) \, G_p(f) \, H(f) \tag{7}$$

where the asterisk designates the complex conjugate. Random response calculations were made for the panel center location using two separate excitation matrices, ie, two NASTRAN runs. In each run response was calculated at frequencies slightly below and above the resonance. The response predictions are compared with test data in Figure 9. The vibration response calculated for two resonance frequency ranges agree favorably with the test results, although slightly overpredicted.

Statistical Energy Analysis

The basic approach of the Statistical Energy Analysis (SEA) is that of power flow between reverberant systems. The primary variable is energy and the energy storage elements are groups of similar modes. SEA performs energy averages in time and space and treats the vibroacoustic problem in a statistical rather than deterministic manner [11]. Under equilibrium conditions there must be a balance between energy input and output; reverberant conditions being assumed so that there is no preferred direction to complicate the averaging process.

A motivation for using SEA is that response estimates are often needed at a stage in a project where structural detail is not yet known. Instead of describing every vibration mode of a system, average values are assumed for mode shapes and the number of modes that fall within a specified frequency bandwidth. The justification for such an averaging procedure is that in practical situations it is not possible to describe the system in detail beyond the low order modes because of computational limitations, construction variations and engineering tolerances, etc. At higher frequencies, mode shapes and resonances show greater sensitivity to

small details of geometry and construction. Thus average results used over one-third octave frequency bandwidths are appropriate and SEA is concerned with vibrations considerably above the fundamental structural resonance. SEA has shown that the power radiated from a set of resonant modes is proportional to the product of energy in an "average" mode by the number of modes in the frequency band. The modes are assumed to be excited by random noise in a third octave bandwidth and the important properties of the modes will be space-time average transverse velocities.

SEA is based on power flow between interconnected elastic subsystems where each contains many modes. The SEA approach requires modes in connected subsystems to be of the type for which coupling can occur. Power flow between subsystems and energy loss due to damping and absorption is the basis of SEA and is assumed to represent the relevant physical behavior. Acoustic fields must be reverberant to meet SEA criteria.

Using the VibroAcoustic Payload Environmental Prediction System (VAPEPS), Reference [10], a system of idealized structures and acoustic spaces is modeled as a series of distinct SEA elements. Engineering judgement must be exercised to represent subsystems as SEA elements. Once defined, the flow of energy between elements, and losses within an element, are calculated for both acoustical and mechanical energy paths. The honeycomb panel vibroacoustic response is addressed using the energy flow model outlined in Figure 7, showing all important energy flow paths.
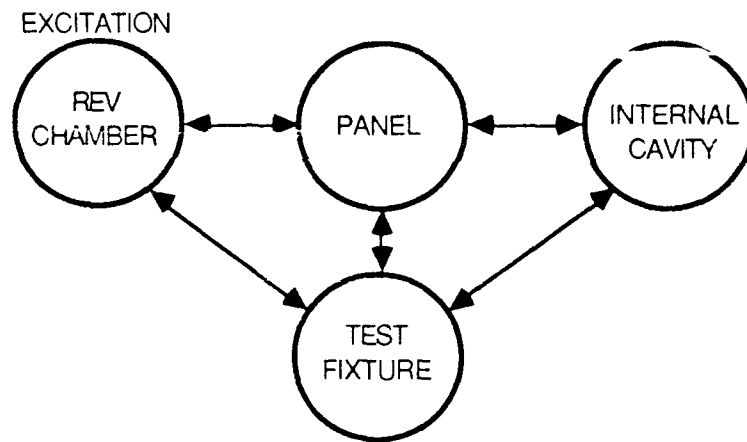

Figure 7
Four Element Model For Statistical Energy Analysis

Unlike FEM, SEA analysis includes power flow between the panel and the cylindrical test fixture (for which insufficient modeling information is available), as well as the build-up of a reverberant sound field in the internal cavity. Energy paths are indicated as two-directional arrows. Energy conservation expressions are derived by VAPEPS and organized into simultaneous equations in the form of a matrix of coupling loss factor coefficients and an energy vector. The number of equations is equal to the number of SEA elements and at least one element is named as excitation source. Either a reverberant acoustic space or structure can be named as excitation source, and, as such, sound pressure level or acceleration spectral density is specified. The excitation Sound Pressure Level spectrum is shown in Figure 8.
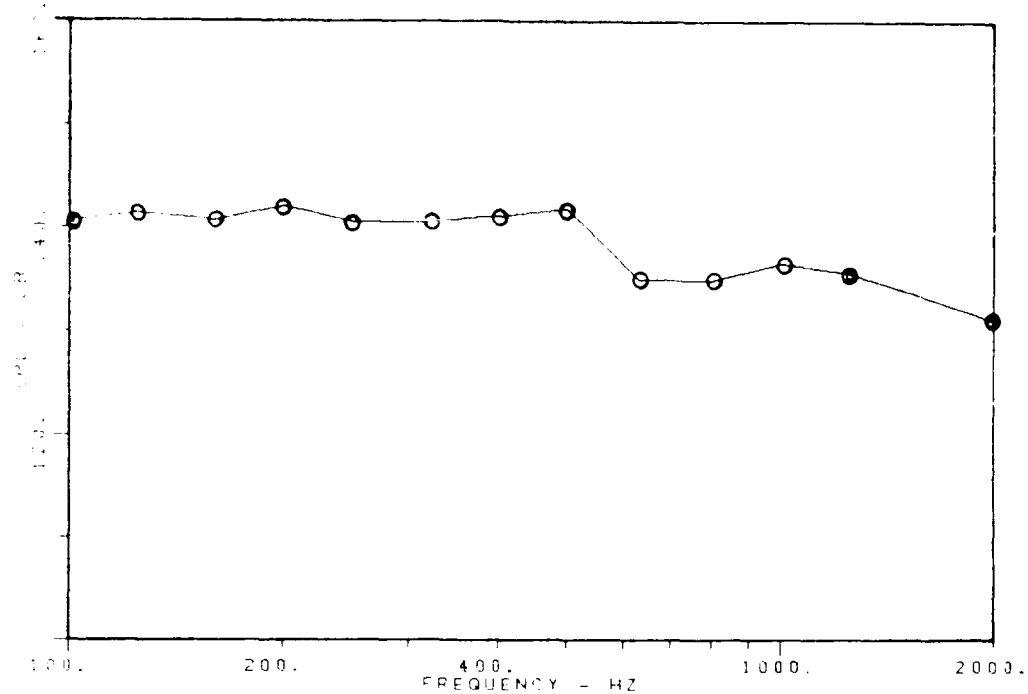
Figure 8
Reverberant Chamber Third Octave Band Noise Levels
(dB, re: .0002 dynes/cm^2)

Using VAPEPS, physical parameters of each SEA element in the model are needed to define the structure or acoustic space. Units are of the type, IN., LBF-SEC^2/IN, SEC.

Reverberant acoustic space SEA parameters:
- Mass density of air (RHO)
- Velocity of sound (CO)
- Surface area (AP)
- Absorption coefficient (AAC)

If the acoustic space is an excitation source, the volume, area and absorption coefficient have no bearing on the energy level in that element since it is sustained by an external power source.

Structural SEA parameters for flat plates and cylinders:

- Structural mass density and surface density (RHO, RHOS)
- Thickness (H)
- Diameter (if cylinder or cone) (D)
- Length (BL)
- Surface area (AP)
- Young's modulus (E)
- Damping loss factor (DLF)
- Length and width of typical (stiffened) sub-panels (ALX, ALY)
- Structural discontinuity length for "edge mode radiation" (PATA)
- Longitudinal wave speed in the structural material (CL)
- Velocity of sound in the radiation medium (CO)
- Nonstructural mass (ASMS)

113

The connection between each SEA element is explicitly identified from a wide array of possible energy path types. VAPEPS recognizes 46 types of connection.

The "equivalent plate" module in VAPEPS was used to develop stiffness parameters for a uniform homogeneous plate which is equivalent to that of the sandwich plate. Parameter input for the four element analysis is listed in Table II.

Table II
VAPEPS Parameter Input Data For SEA Elements - Honeycomb Panel

```
REVB
DESCRIPT=DIFFUSE ACOUSTIC FIELD
TYPE     =           1
RHO      = 1.120E-07 CO      = 1.320E+04 VOLUME  = 1.000E+06 AP      = 1.000E+06
AAC      = 2.000E-02

SKIN
DESCRIPT=HONEYCOMB FLAT PANEL
TYPE     =           3
RHO      = 2.485E-05 CL      = 2.100E+05 H       = 9.691E-01 AP      = 5.643E+02
ALX      = 3.700E+01 ALY     = 1.525E+01 DLF     = 4.000E-02 E       = 1.097E+06
PHTA     = 4.600E+01 RHOS    = 2.409E-05 ASMS    = 9.300E-06


FIXT
DESCRIPT=CYLINDRICAL TEST FIXTURE
TYPE     =           4
RHO      = 2.620E-04 CL      = 2.100E+05 H       = 3.750E-01 AP      = 3.700E+03
BL       = 4.000E+01 ALX     = 7.200E+01 ALY     = 6.000E+01 D       = 2.036E+01
DLF      = 2.000E-02 E       = 1.050E+07 PATA    = 1.280E+02 RHOS    = 9.830E-05
ASMS     = 0.000E+00 CO      = 1.320E+04

CAV
DESCRIPT=INTERIOR ACOUSTIC CAVITY
TYPE     =           1
RHO      = 1.120E-07 CO      = 1.320E+04 VOLUME  = 3.620E+04 AP      = 4.500E+03
AAC      = 2.000E-02
```

The vibration solution was carried out in the "SEMOD" module in VAPEPS on a DEC-VAX computer. The computer operating costs were very low. Computations ranged over all third octave band frequencies from 100 Hz to 2000 Hz and the vibration response is superimposed on Figure 9.

The low frequency limit of SEA validity is interpreted from the number of modes per one-third octave band, which can be calculated from modal density output from VAPEPS. For the present example, there are less than one mode per third octave band at frequencies below 1,000 Hz indicating results below this frequency are not valid. At least several modes in each band are preferred so that the vibration response calculated using SEA may be considered suspect at frequencies up to 1,500 Hz. Some additional VAPEPS output which is very useful provides the response contribution of each SEA element to the overall solution on the basis of energy arriving and exiting the element expressed as a percentage of the total energy of that element.
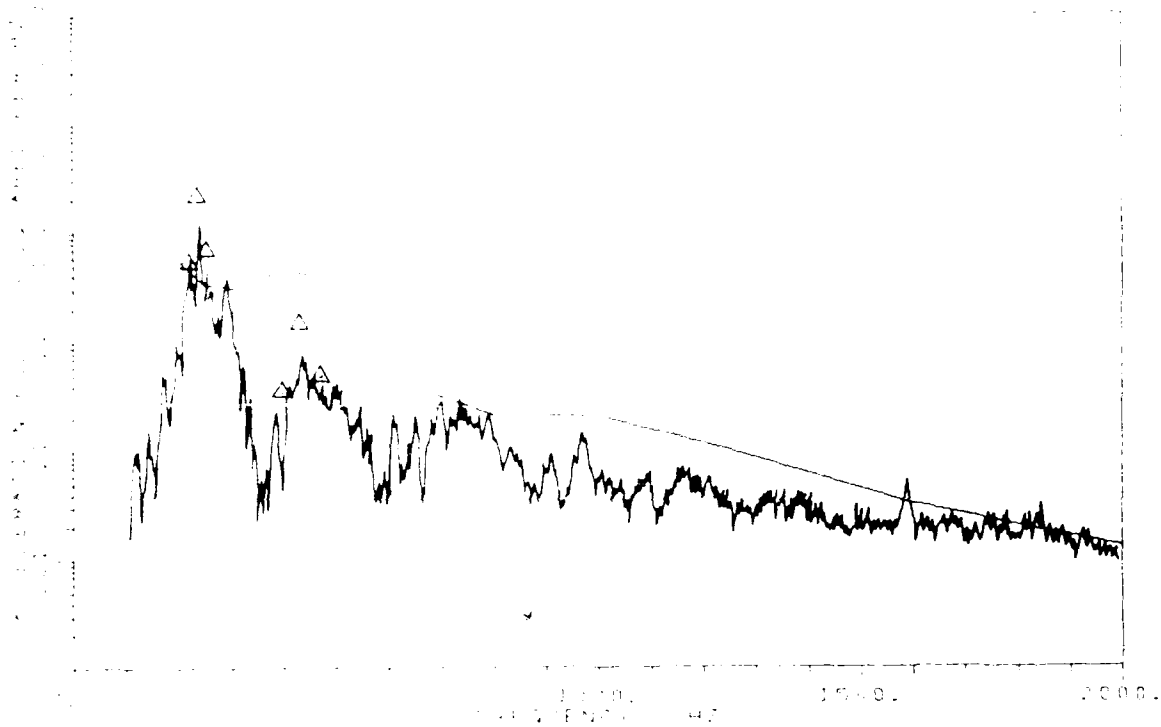
Figure 9
Predicted Vibration Response Compared to Panel Center Measurement
Δ FEM, —— SEA

Conclusions

The vibroacoustic response analysis of an example problem was demonstrated for the Finite Element Method using NASTRAN and for Statistical Energy Analysis using VAPEPS. Low frequency results from FEM can be merged with high frequency SEA results and the strengths of both approaches utilized. In the present example, the SEA response calculations below 1,000 Hz should be disregarded due to a low modal density.

The calculated response was somewhat higher than was measured, however, a dual approach for response prediction is clearly justified. Using a coarse FEM idealization of the panel structure and limiting NASTRAN calculations to low frequency resonant response, the solution was in the "small problem" category. If large scale finite element models are required, an innovation described in reference [6] may be used which maximizes the use of reciprocity to greatly improve efficiency of response calculations.

In calculating low frequency vibroacoustic response, it is important to include the correlation characteristics of the excitation pressure field. The consideration also extends to testing, where the environment simulated should exhibit similar low frequency correlation characteristics as that created in the test chamber. It is evident that the coherence properties will rarely be available to the analyst, and spatial decay may have to be conservatively estimated. Test measurements of an excitation pressure field could be designed to include correlation as well as amplitude data for the low frequency range. If the additional instrumentation leads to a better understanding of the propensity for vibroacoustic response and prevents an over-test, then the effort is justified.

References

1. Ungar, E. E., Wilby, J.F., Bliss, D. B., et al, "A Guide for the Estimation of Aeroacoustic Loads on Flight Vehicles", AFFDL-TR-76-91, Vol. I & II, Feb. 1977.

2. Cockburn, J. A. and Jolly, A. C., "Structural-Acoustic Response of an Aircraft Fuselage Excited by Random Pressure Fields", AFFDL-TR-68-2, 1968.

3. Morrow, C. T., "Point To-Point Correlation of Sound Pressures in Reverberation Chambers", Shock & Vibration Bulletin, No 39, 1969.

4. Beranek, L. L. (EJ.) Noise and Vibration Control, McGraw-Hill, 1971

5. Wilby, J. F., and Scharton, T. D., "Acoustic Transmission Through a Fuselage Sidewall", BB&N Report No. 2742, Submitted to NASA Langley Contract No. NAS1-11839, 10 July 1974

6. Hipol, P. J., and Piersol, A. G., "Efficient Implementation of Random Pressure Fields with the Finite Element Method", SAE Tech. Paper 871740, Long Beach, CA. 1987

7. Jacobs, L. D., Lagerquist, D. R., and Gloyna, F. L., "Response of Complex Structures to Turbulent Boundary Layers", J. of Aircraft, Vol 7, No 3, May-June 1970.

8. Wilby, J. F. and Gloyna, F. L., "Vibration Measurements of an Airplane Fuselage Structure," I. Turbulent Boundary Layer Excitation, II. Jet Noise Excitation, J. of Sound and Vibration (1972) 23 (4), 443-486

9. Gockel, M. A., (EJ.) MSC/NASTRAN Version 63 Handbook for Dynamic Analysis, The MacNeal-Schwendler Corp., June 1983

10. Y. A. Lee, et al, "VibroAcoustic Payload Environment Prediction System (VAPEPS)", NASA Contractor Report No. 166823, Five Volumes, Lockheed Missiles and Space Company, June 1984. Also draft revision of Volume II: User's Manual Draft, June 1987.

11. Lyon, R. H., "Statistical Energy Analysis for Designers", Part I: Basic Theory, Part II: The Engineering Application, AFFDL-TR-74-56, Sept 1974

Appendix

The pressure field excitation will be discretized to a set of complex forces, each centered on a "finite-element" size area. Consider two such plate elements, typically separated, as in Figure A1.
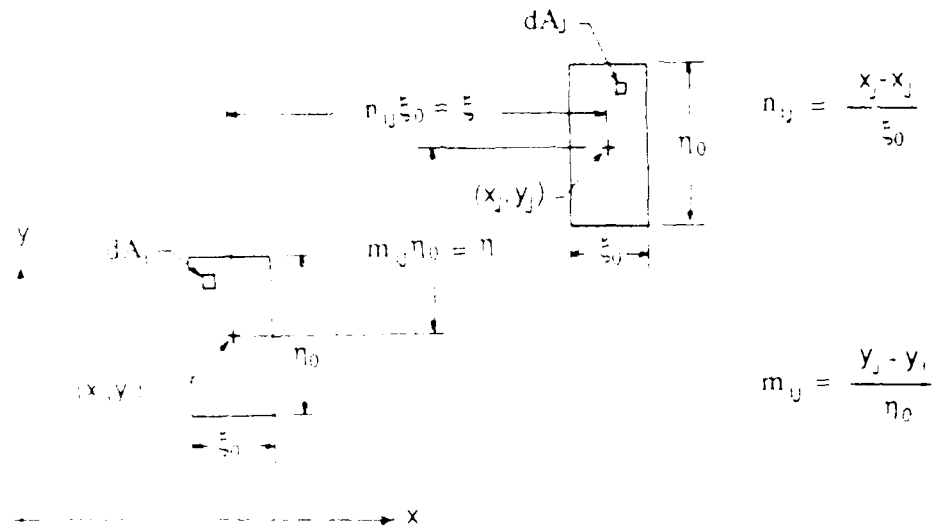

Figure A1
Typical Finite Element Pair for Surface Integration of the Pressure Field

The pressure field expression given in equation (5) can be integrated over finite element areas i and j to produce force cross PSD.

$$
G_{ij}(\xi,\eta,\omega) = G_p(\omega) \int_{-\frac{\xi_0}{2}}^{\frac{\xi_0}{2}} \int_{-\frac{\eta_0}{2}}^{\frac{\eta_0}{2}} \int_{n_{ij}\xi_0 - \frac{\xi_0}{2}}^{n_{ij}\xi_0 + \frac{\xi_0}{2}} \int_{m_{ij}\eta_0 - \frac{\eta_0}{2}}^{m_{ij}\eta_0 + \frac{\eta_0}{2}}
$$

$$
e^{-C_1|x_j - x_i|} \; e^{-C_2|y_j - y_i|} \; e^{-iC_3(X_j - X_i)} \; e^{-iC_4(Y_j - Y_i)} \; dx_i dy_i dx_j dy_j \qquad (A1)
$$

Equation (A1) was simplified by substituting C_1 thru C_4 for quantities not participating in the integration. The decay coefficients are assumed independent of separation distance. Also it is assumed the integrations in the x and y directions can be performed separately. Because of the absolute value signs in the function, two special cases are treated separately when $n_{ij} = 0$ and $m_{ij} = 0$ by revising the limits of integration. The final result of the integration is written below

$$G_p(\xi,\eta,\omega) = G_p(\omega).$$

$$\left\{ \left(\frac{1}{C_1+iC_3}\right)^2 \left[2e^{-(C_1+iC_3)|n_j|\xi_0} - e^{-(C_1+iC_3)(n_j+1)\xi_0} - e^{-(C_1+iC_3)(n_j-1)\xi_0} \right] \right\} \cdot$$

$$\left\{ \left(\frac{1}{C_2+iC_4}\right)^2 \left[2e^{-(C_2+iC_4)|m_j|\eta_0} - e^{-(C_2+iC_4)(m_j+1)\eta_0} - e^{-(C_2+iC_4)(m_j-1)\eta_0} \right] \right\} \tag{A2}$$

The following restrictions are imposed due to the absolute value signs:

(1) If $n_{ij} < 0$ replace C_1 with $-C_1$

(2) If $m_{ij} < 0$ replace C_2 with $-C_2$

(3) If $n_{ij} = 0$ replace the second term with:

$$\left\{ \left(\frac{1}{C_1-iC_3}\right)^2 \left[1 - e^{-(C_1-iC_3)\xi_0} \right] \left(\frac{1}{C_1+iC_3}\right)^2 \left[1-e^{-(C_1+iC_3)\xi_0} \right] - \xi_0 \left[\frac{1}{C_1-iC_3} + \frac{1}{C_1+iC_3} \right] \right\}$$

(4) If $m_{ij} = 0$ replace the third term with

$$\left(\frac{1}{C_2-iC_4}\right)^2 \left[1 - e^{-(C_2-iC_4)\eta_0} \right] \left(\frac{1}{C_2+iC_4}\right)^2 \left[1-e^{-(C_2+iC_4)\eta_0} \right] - \eta_0 \left[\frac{1}{C_2-iC_4} + \frac{1}{C_2+iC_4} \right]$$

STUDY OF HELIUM EFFECT ON SPACECRAFT RANDOM VIBRATION WITH VAPEPS PROGRAM

Y. Albert Lee
Space System Division
Lockheed Missiles & Space Company
Sunnyvale, CA 94086

One possible method proposed for reducing the acoustic induced random vibration environment of a shroud enclosed payload is to reduce the acoustic environment surrounding the payload by filling the shroud with helium. Acoustic tests performed on a shroud filled with air and then helium showed that while the payload acoustic environment is reduced significantly by helium, a similar trend was not evident in the payload random vibration environment. The random vibration was found to increase for some payload panels and to decrease for the other. To investigate the possible mechanisms for helium effects on sound pressure and random vibration, a statistical energy analysis, using the VAPEPS computer program, was performed. The analysis suggests a possibility of structural damping change due to helium, in addition to other effects. The damping of the equipment panel may be altered because of helium gas pumping effect at structural joints. The overall effect depends on the number of structural joints. After including this gas pumping effect, the analyses agreed well with test observations.

INTRODUCTION

During the launch and ascent phase of flight, a high level fluctuating acoustic and aerodynamic pressure environment exists on the exterior surface of a space vehicle fairing. This environment will cause the fairing to vibrate and radiate acoustic energy into the internal space enclosed by the fairing. This radiated acoustic energy will cause a payload mounted within this space to vibrate. Also, vibration will be generated by energy directly transmitted to the payload through mechanical paths that couple the payload and fairing together. It is frequently desirable to reduce this payload vibration. While there are a number of ways this could be accomplished, removing the air surrounding the payload by flooding the fairing with helium has often been discussed as a simple and cost effective way for accomplishing this. The physical properties of helium are such that the sound pressure level within the fairing will reduced with

respect to tha' which would exist for air and, therefore, hopefully also reduce that of the acoustic induced random vibration environment of the payload. To study this idea, acoustic tests [ref. 1] were performed on a payload enclosed by a fairing. Tests were performed with this fairng first filled with air and then with helium. Comparative measurements did show that the sound pressure level was reduced significantly by helium; however, these measurement did not show a clear advantage for reducing the random vibration response of the paylaod. The random vibration of certain payload panels were found to increase, while that of other panels were found to decrease.

In this paper the data obtained from these tests are reviewed, and a possible mechanism for the above described observations is proposed and explored analytically. The analysis was to predict the effect of helium on both acoustic and vibration environment using statistical energy analysis concepts. The computer code VAPEPS was employed to perform this analysis.

REVIEW OF TEST

An experimental test program [1] was performed to evaluate the effectiveness of reducing the internal sound field to obtain a payload vibration reduction. The test was performed in a reverberant acoustic chamber. As shown in Fig. 1 the test specimen was a shroud10-ft in diameter with a simulated payload installed inside and mounted to the acoustic test facility floor by a base mount fixture.
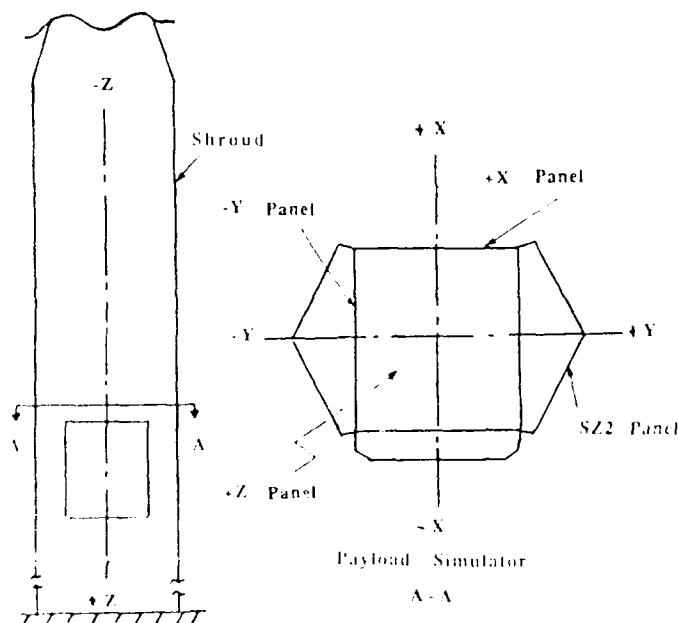

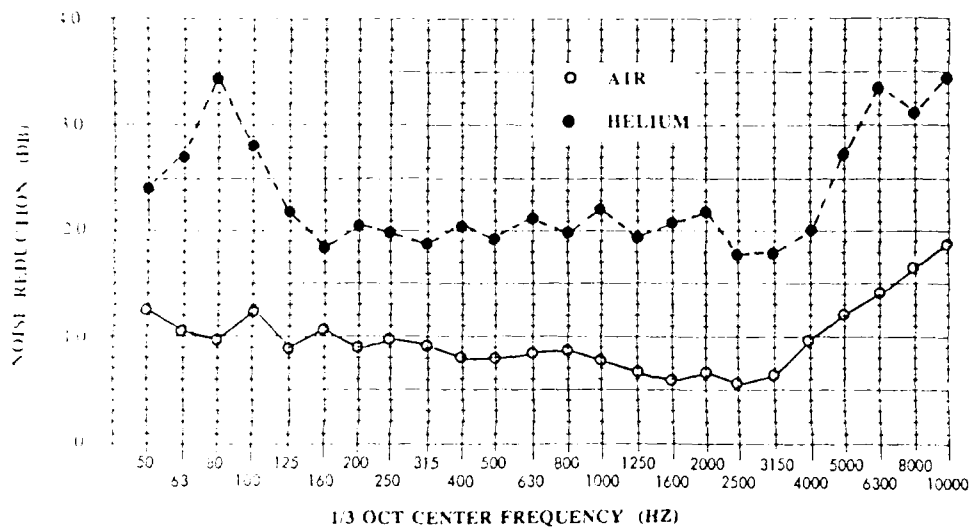Fig. 1 TEST SIMULATION (note: not to scale)

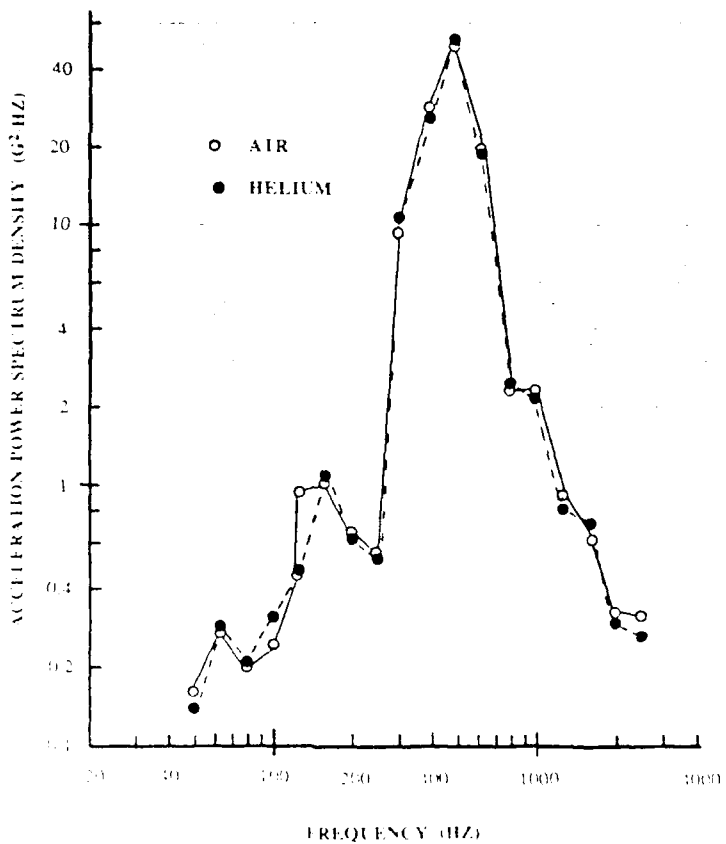Fig. 2 Typical Noise Reduciton

Fig. 3 Random vibration of Shroud

Microphones were used to measure the sound pressure level inside and outside of the shroud. Accelerometer measurements were made to define the vibration level of the shroud and the simulated payload. Fig. 2 shows a typical noise reduction of the shroud filled with air and helium. The noise reduction is the difference between spatially averaged external SPL and the internal SPL measured in the upper portion of the shroud. Similar noise reductions were found in the other portion of the shroud. Helium produced significantly more noise reduction than air. The internal sound pressure level for helium is about 10 dB or more lower than that of air over all frequencies. Fig. 3 shows the random vibration of the shroud. Helium does not significantly affect the random vibration of shroud itself. This is expected because the shroud vibration is mainly due to external acoustic field which is unchanged. Fig. 4 shows the random vibration of +Z panel. Helium is found to reduce the panel
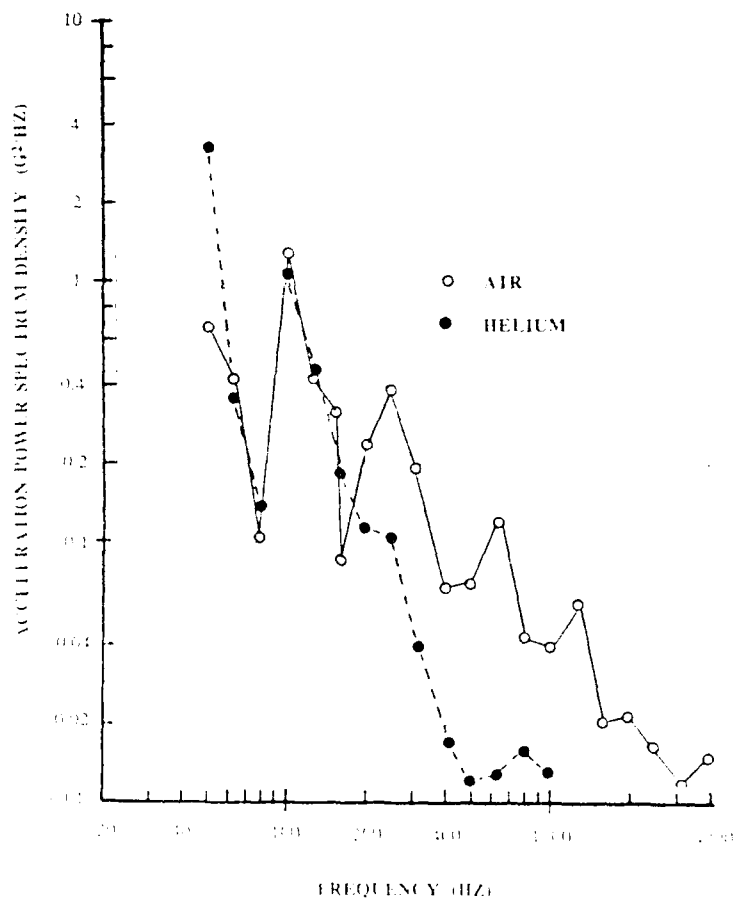
Fig. 4 Random Vibration of +Z Panel

random vibration significantly, especially in the higher frequencies. This panel is the bottom panel of the box-like payload which is mounted to the shroud at this location. It has few structural joints. It is excited by both the mechanical energy transmitted from the shroud via support structures and the internal sound pressure. The relative contribution of these two excitation source on the resulting panel vibration is unkown. Fig. 5 shows the random vibration of +X panel. This is one of the side panels. Helium is found to increase the panel random vibration level which is opposite to the helium effect found in +Z panel vibration. The fundamental structure of this panel is not too different from that of the +Z panel, except this panel has many structural joints.

Fig. 5   Random Vibration of +X Panel

The acoustic/structural coupling of +X panel and +Z panel are very similar and is not believed that this effect would account for the differences observed. This

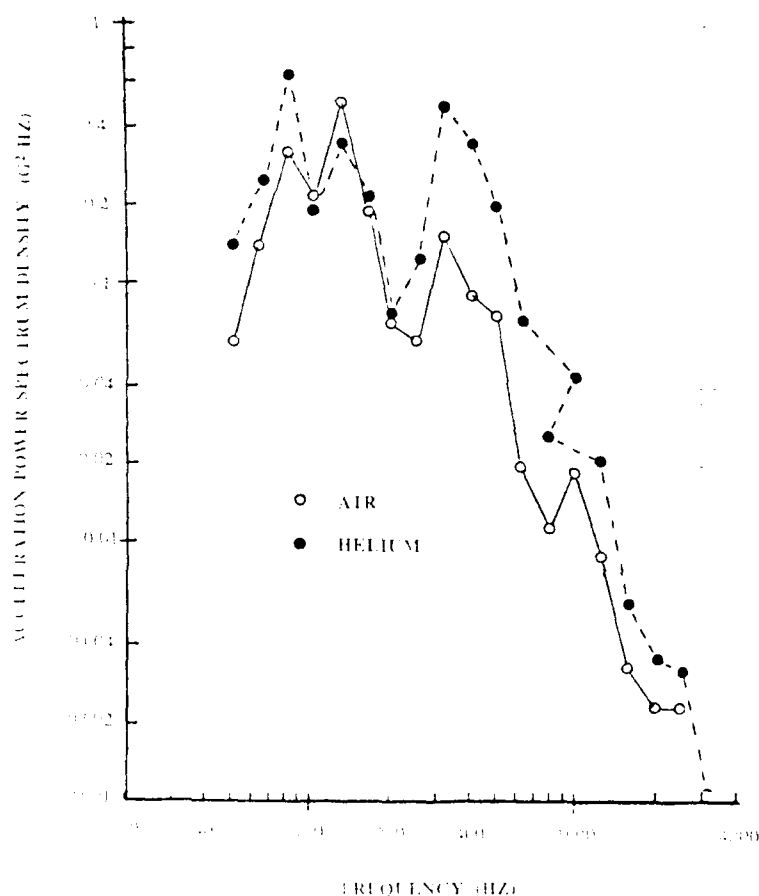leads one to wonder if the structural joints may have something to do with the helium effect on panel vibration. Fig. 6 shows the random vibrations of -Y panel. This is another side panel of the payload. It is very similar to +X panel and also has many structural joints. Again, the helium is found to increase the panel random vibration level. This finding is consistent with the measurement of +X panel. This consistency at least convinces us the findings are real and ruled out the possiblility of mistakes made in measurement or data reduction.
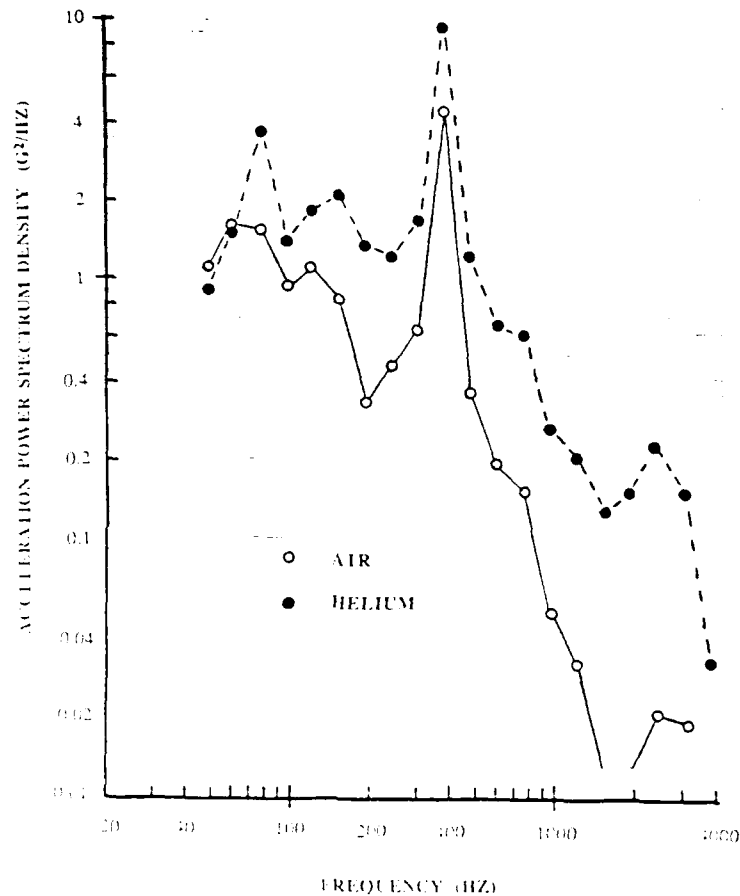
Fig. 6   Random vibration of -Y Panel

Fig. 7 shows the random vibration level for SZ2 panel which is the panel mounted on the side of payload. The original data in [1] is presented in terms of transfer function in dB between the vibration level and internal sound pressure level. Since the internal SPL is not the same for air and helium, the original transfer function data cannot be used for direct comparisons. To make a direct comparison, these data are corrected to the same external SPL by adding back the difference in noise reduction between air and helium. As seen in Fig. 7

helium is found to reduce the random vibration significantly. The SZ2 panel has few joints and its response is mainly due to acoustic excitation. These mixed results of helium on panel vibraiton have puzzled the aerospace community for some time. To understand the seemingly mysterious findings of the helium effect on panel vibration, an analytical study was performed. Hopefully, this analysis would offer a possible explanation of the helium effect on a shrouded payload.
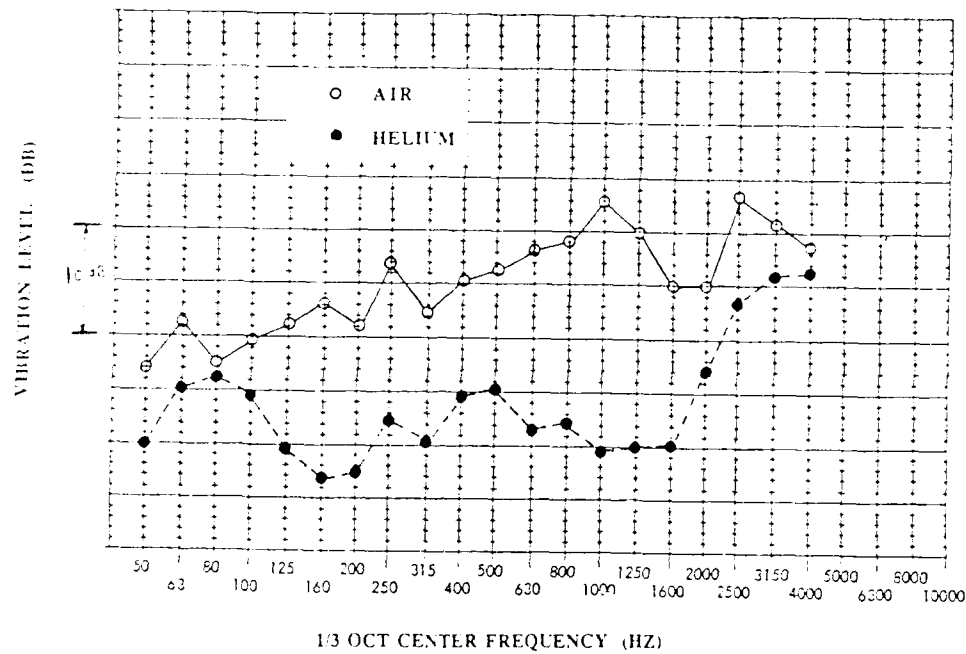
Fig. 7   Random vibration of SZ2 Panel

ANALYTICAL STUDY

SEA MODEL

To study the effect of helium on the internal sound pressure level and random vibration of payloads, Statistical Energy Analysis (SEA) were performed. The VAPEPS code [3] was used to facilitize the modelling and computation. Two Statistical Energy Analysis (SEA) Models were used and are shown in Fig. 8. These SEA models consist of 4 elements which represent the external acoustic field (CELL), cylindrical shroud (CYLN), internal acoustic field (CAV), and payload panel (PLAT). Both resonant energy transmision (solid line) and nonresonant transmission (dotted line) are included in these models. The external acoustic field is assumed to be reverberant and with a sound pressure level of 130 dB flat over the frequencies. Because of the lack of detailed

sturctural information on the test specimen in [1], the shroud in the model was arbitarily chosen to be a 200-inch diameter cylinder, 70-inch in length. The payload panel is assumed to be a 50-inch by 50-inch flat homogeneous aluminum plate of 0.2-inch in thickness. The structural properties used in the SEA model are definitely different from those of the specimen tested in [1]. The SEA model is intended to study the observed helium effects qualitatively, not quantitatively.

Model I: Acoustic Path
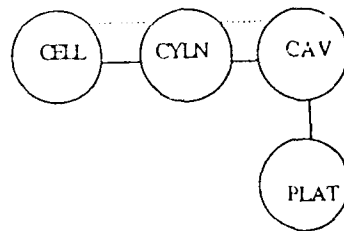
Model II: Acoustic & Mechanical Path
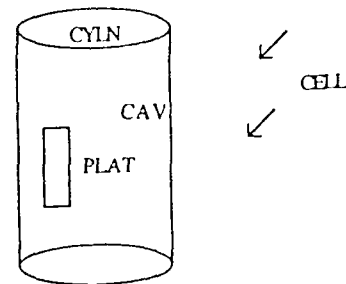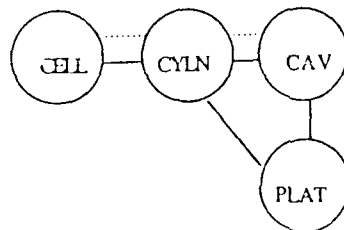
Fig. 8   Statistical Energy Analysis Model

In model I, There is no connection between the CYLN element and PLAT element. The payload panel (PLAT) is excited by the internal acoustic field only. This model is suitable in the study of SZ-2 panel which is mounted off the upper edge of the box-like payload. Its vibration is mainly due to the direct excitation of the acoustic field around it. In model II, in addition to the connection to the internal acoustic field (CAV) the PLAT element is also connected to the CYLN element. The payload panel is excited by both the internal acoustic field and the mechanical energy transmitted from the shroud (CYLN). This model is suitable in the study of +Z, +X, and -Y panels. Table 1 shows the parameters of the SEA elements used in the model. Some parameters are obvious and others are peculiar to the VAPEPS code. The meaning of each parameter in this table will be found in the VAPEPS User's Manual [3]. Table 2 describes the connecting path between elements. For the meaning of these connecting path refer to VAPEPS User's Manual [3]. Briefly, the connecting elements are specified and followed by the type of connection. For example

TABLE 1
PARAMETERS OF SEA ELEMENTS
(units: snail,   inch,   sec)

Element: CELL
TYPE =   1
RHO =   1.15E-7
AP   =   3.20E6
√   =   3.19E8
AAC =   0.02
CO   =   1.32E4

Element: CAV
TYPE =   1
RHO =   1.15E-7
AP   =   4.896E4
V   =   2.198E8
AAC =   0.02
CO   =   1.32E4

Element: CYLN
TYPE =   4
RHO =   2.54E-4
RHOS =   9.41E-5
ASMS=   0
H   =   0.375
D   =   200.
BL   =   70.
ALX =   209.
ALY =   70.
PATA=   1676.
AP   =   4.396E4
E   =   10.E6
DLF =   0.04
CL   =   2.01E5
CO   =   1.32E4

Element: PLAT
TYPE =   3
RHO =   2.54E-4
RHOS =   5.08E-5
ASMS=   0
H   =   0.2

ALX =   50.
ALY =   50.
PATA=   200.
AP   =   2.5E3
E   =   10.E6
DLF =   0.04
CL   =   2.01E5
CO   =   1.32E4

TABLE 2
CONNECTING PATH

MODEL I

CELL, CYLN, 2
CYLN, CAV, 2
CELL, CYLN, CAV, 5
CAV, PLAT, 1

MODEL II

CELL, CYLN, 2
CYLN, CAV, 2
CELL, CYLN, CAV, 5
CAV, PLAT, 1
CYLN, PLAT, 11
BJL=50.
BETA=90.

(CELL,CYLN, 2) indicates external acoustic field (CELL) is coupled to the cylinder (CYLN). In model II, the payload panel is assumed to be attached radially (parameter BETA=90.) inward to the shroud with a junction length (paramenter BJL) of 50 inches. This junction length is arbitarily chosen and will strongly influence the relative contribution of acoustic excitaiton and mechanical excitation.

STRUCTURAL DAMPING

The damping of aerospace structures made up of sheets, ribs, stringers and rivets may be due to (1) internal metal damping, (2) surface friction and plastic deformation at joints, (3) gas pumping at joints. The first two damping mechanisms are independent of the surrounding gas medium. The third one does depend on the medium. When the structure vibrates, the small structural joint gaps change accordingly. The gas is pumped in and out of the narrow gap, and causes viscous dissipation. The amount of dissipation depends on the gas properties. This mechanism is believed to be one of the reasons for the observed changes in vibration due to helium.

The theory of damping by gas-pumping is rather complicated. G. Madanik [2] derived the expression for the loss factor for the case of a vibrating panel with a stationary beam attached.

$$\eta \sim \frac{c^2\, p}{h} \, H(\theta) \tag{1}$$

Where

c = speed of sound in gas

p = rms pressure

The function $H(\theta)$ is a measure of the ease of gas flow in the gap, and

$$\theta \equiv h\, /\, \delta \tag{2}$$

$$\delta \equiv 2\, (\, \nu\, /\, \omega\,)^{1/2} \tag{3}$$

where

h = gap thickness

ν = kinematic viscosity of the gas

$$H(\theta) \sim \theta^2 \sim (\, 1/\delta\,)^2 \sim 1/\nu \qquad \text{for } \theta < 2$$

but $\nu_{helium} \sim 8 \, \nu_{air}$

and $C_{helium} \sim 2.5 \, C_{air}$

Using equations (2) & (3), equation (1) becomes

$$\eta_{helium} \sim 0.78 \, \eta_{air} \, (\, P_{helium} / \, P_{air} \,) \tag{4}$$

It is obvious that helium reduces the gas-pumping damping. Since the total structural damping is the contribution of all three mechanisms (i.e. internal friction, friction at joints, and gas pumping at joints), the overall effect of helium depends on the type of joints as well as the number of joints. When the

TABLE 3
DAMPING LOSS FACTOR DUE TO HELIUM GAS-PUMPING

FREQ (HZ)	INTERNAL SPL (AIR) (DB)	INTERNAL SPL (HELIUM) (DB)	P_{air}/P_{helium}	LOSS FAC
50	116.1	113.7	1.318	0.024
63	116.3	113.6	1.365	0.023
80	116.3	113.4	1.396	0.022
100	116.6	113.2	1.479	0.021
125	116.5	112.9	1.514	0.021
160	116.3	112.5	1.549	0.021
200	116.1	112.1	1.585	0.020
250	116.4	111.5	1.758	0.018
315	116.6	111.6	1.778	0.018
400	116.6	113.1	1.496	0.021
500	115.3	111.5	1.549	0.020
630	113.8	109.9	1.567	0.020
800	112.3	108.1	1.622	0.019
1000	111.5	106.4	1.758	0.018
1250	124.4	105.0	2.951	0.011
1600	115.6	102.8	4.365	0.007
2000	111.8	101.0	3.467	0.009
2500	108.2	99.2	2.818	0.011
3150	105.8	97.4	2.630	0.012
4000	103.1	95.4	2.427	0.013

structural pieces are fastened together with welding there is no gap between them, and there is no gas-pumping effect on damping. If the pieces are bolted together, there are significant gas-pumping effects at these joints. The damping loss factor of payload panel (PLAT) for air is assumed to be 0.04. This damping value is also used for the helium without gas-pumping at joints. In the case of helium with gas-pumping, equation (4) is used to calculate the damping loss factor for payload panel (PLAT). Table 3 shows the damping loss factor of panel due to helium gas-pumping. Since the values of P_{air}/P_{helium} are required in equation (4), the internal rms pressure (in dB) were first calculated using a SEA model. The resilts are shown in columns (2) and (3) in Table 3 for the air and the helium, respectively. The ratios of these pressure (in linear value) are calculated and shown in column (4). The damping loss factors due to helium gas-pumping are then calculated according to equation (4) and shown in column (5). These values are assumed to be the total damping loss factor of payload panel (PLAT). In other words, the gas-pumping of air and helium at joints is assumed to be the dominant over other damping mechanism.

Results of Analysis

(A) Model I - Acoustical Path Only

Fig. 9 shows the internal Sound Pressure Level (SPL) of the cylincrical cavity (CAV) predicted with SEA Model I (acoustical path only). The SPL of the
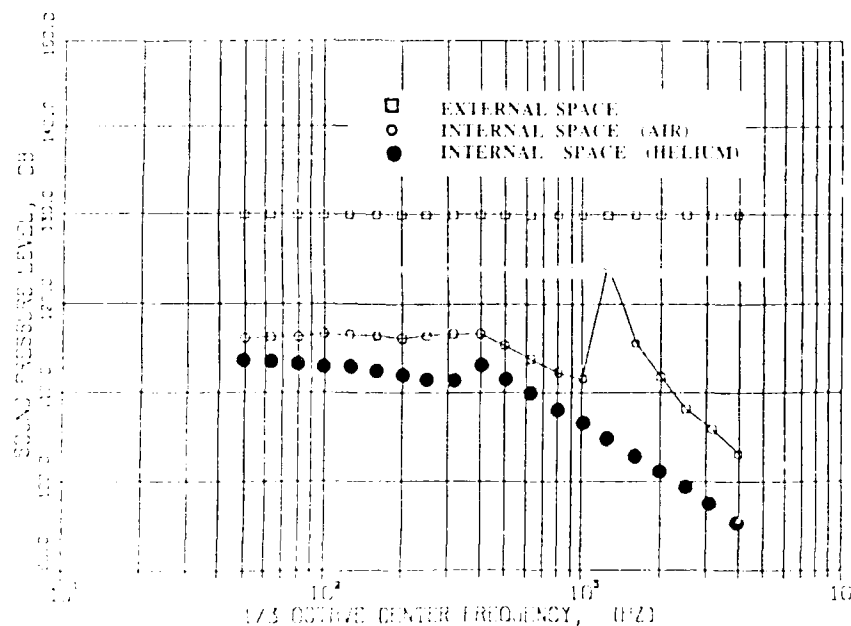

Fig. 9 Sound Pressure Level, No Gas Pumping, Acoustic Path only

reverberant chamber (CELL) is arbitrarily assumed to be 130 dB. The structural damping of the payload panel (PLAT) is assumed to be the 0.04 for both air and helium. This corresponds to the case when gas-pumping is negligible. The helium is found to reduce the internal SPL appreciably. Fig.10 shows the effect of helium on acceleration random vibration. The cylinder vibration is unchanged and the panel vibration is reduced by helium. The panel structural damping is assumed to be unchanged. This correpsonds to the case of the SZ2 panel in [1], which has very few structural joints.
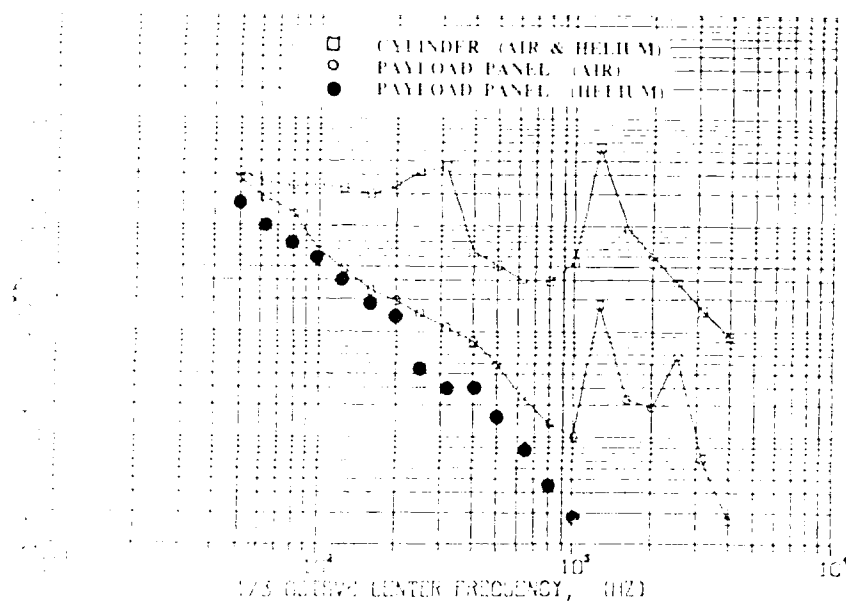
Fig. 10 Random Vibration, No Gas Pumping, Acoustic Path only

B) Model II Acoustical and Mechanical Path

Fig. 11 shows the predicted internal SPL in the cylindrical cavity (CAV) filled with air and helium, respectively. Both acoustical and mechanical paths are included in SEA model II. The SPL of reverberant chamber (CELL) is 130 dB. The structural damping of the payload panel (PLAT) is assumed to be 0.04 for air and helium. This is the case when gas-pumping is negligible. Helium is found to reduce the internal SPL appreciably. The predicted random vibration is shown in Fig. 12. The random vibration level of the cylinder is found to be unchanged. The payload panel vibration is reduced slightly in the case of helium. Since the panel structural damping is assumed to be unchanged and the excitation is mainly due to the transmitted mechanical energy from the cylinder in this model, this reduction in vibration is mainly due to the difference in radiation damping which is not much. This corresponds to the case of the +Z panel in [1], which has very few joints. The helium effect on vibration reduction is found to be the same.

When the structure has many joints, the gas-pumping effect at joints can be important in determining the overall structural damping. When this is the

Fig. 11 Sound Pressure Level, No Gas Pumping, Acoustic & Mechanical Path

Fig. 12 Random Vibration, No Gas Pumping, Acoustic & Mechanical Path

case for payload panels, the values in Table 3 should be used for the damping loss factor. Fig. 13 shows the predicted helium effect on the internal SPL.

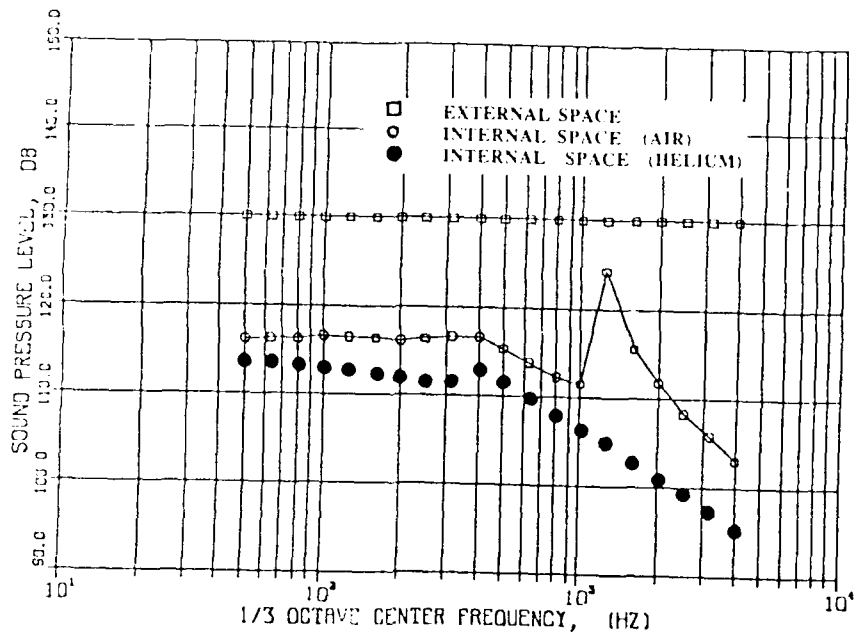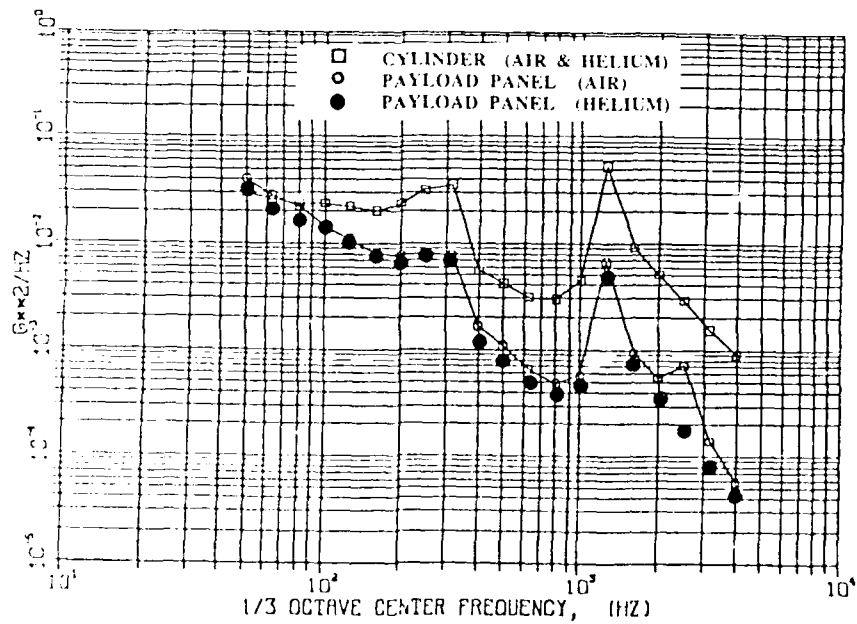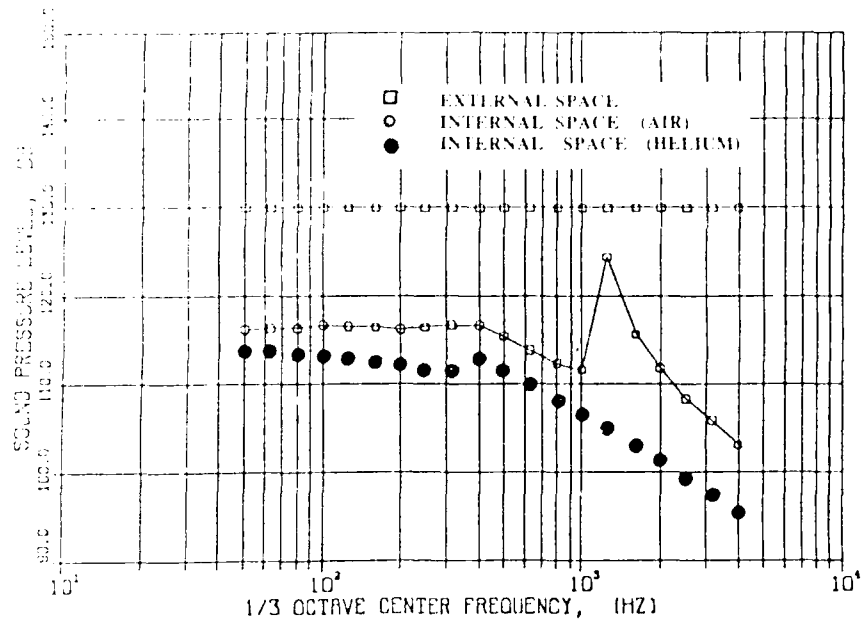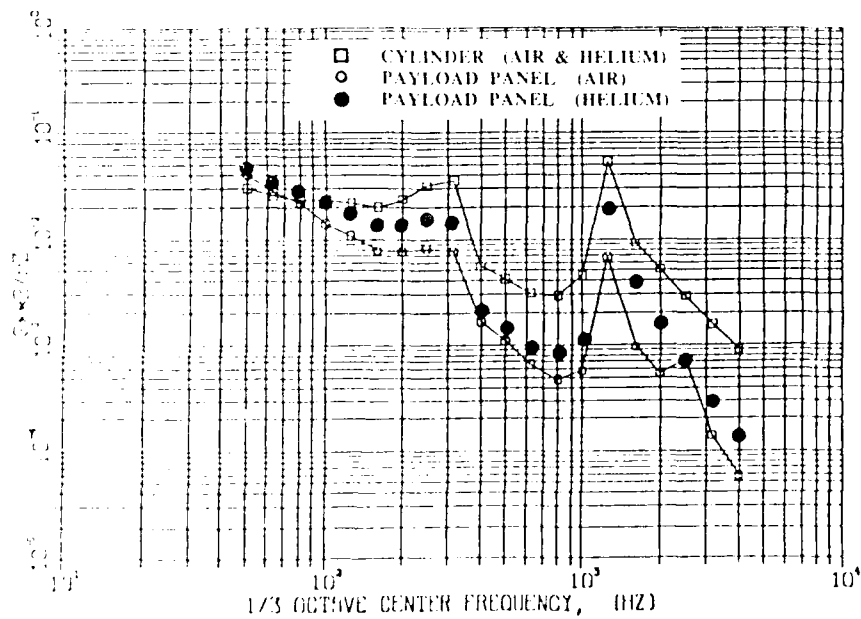Fig. 13   Sound Pressure Level, With Gas Pumping, Acoustic & Mechanical Path

Fig. 14   Random Vibration, with Gas Pumping, Acoustic & Mechanical Path

138

As in the other cases, the internal SPL is significantly reduced. Fig. 14 shows the predicted vibration level. The panel vibration is found to be increased. This is consistent with that observed for the +X panel, and -Y panel in ref. [1]. These panels have many structural joints and therefore gas pumping has a significant effect on their damping characteristics. In these cases, the reduced structural damping due to helium more than compensate for the reduced internal SPL excitation.

CONCLUSIONS

Using SEA models, the predicted effect of helium on internal sound pressure levels and payload vibration is found to be consistent with that empirically observed. Helium lowers the internal sound pressure level, however, its effect on payload vibration is more complex because of the changes in internal sound pressure level and the changes in structrual damping itself. Helium does change the acoustic/structural coupling and radiation damping, but the effect is secondary. The overall damping of a structure is due to a combination of friction and gas-pumping at joints. Joint friction is independent of the gas medium. However, the gas pumping effect is strongly dependent on medium properties. The pumping of helium at joints lowers the damping in comparison with that which exists with the air. If the internal acoustic pressure is the main excitation of the payload structure and there are few joints, helium will reduce the payload vibration mainly due to the lowered sound pressure level. Helium has little effect on the vibration of panels with few structural joints when the excitation is dominated by mechanically transmitted energy. However, when the payload has many structural joints, the structural damping will be reduced significantly by the helium. The payload vibration will depend on the relative effects of reduced structural damping and reduced sound pressure levels when it is the internal acoustics that is the dominating source of excitation. When mechanically transmitted energy is the dominant source of excitation, helium will increase the structural vibration due to reduced damping. The SEA concept, as embodied in the VAPEPS conputer code, not only provides a method for accounting for the effect of various acoustic/structural parameters on payload response, but also is a valuable tool for interpreting empirical data trends.

REFERENCES

1. "Acoustic Attenuation Test Program", Internal LMSC Test Report, Lockheed Missiles & Space Co., Sunnyvale, CA., 30 April 1976.

2.   "Energy Dissipation Associated with Gas-pumping in Structural Joints",
Madanik, G., J. of Acoustic Society of America, (40), Page 1064, Nov. 1966,

3.   "Vibroacoustic Payload Environment Prediction System (VAPEPS), Volume II:
VAPEPS USER'S REFERENCE MANUAL", NASA CR-180781, Lockheed Missiles &
Space Co., Sunnyvale, CA., 1988

VALIDATION OF LACE SPACECRAFT VIBROACOUSTIC PREDICTION MODEL

Aaron A. Salzberg
Naval Research Laboratory
Washington, DC 20375

The purpose of this paper is threefold: first, verify that the VibroAcoustic Payload Environment Prediction System (VAPEPS) , as developed by the Lockheed Missile and Space Company and monitored by the Jet Propulsion Laboratory (JPL), is a viable means of predicting spacecraft component responses to an acoustic environment; second, address the determination of important parameters in the creation of a Statistical Energy Model in order to achieve accurate results using VAPEPS; third, present a technique for deriving component random vibration test levels from these results.

INTRODUCTION

Any payload transported to space is required to survive several structurally threatening environments. Launch and ascent subject the space vehicle to an entire spectrum of vibratory loads. Structureborne, low-frequency vibrations feed energy into the lower modes of the structure, inducing large system level stresses. High-order modes, excited acoustically by engine and aerodynamic noise, fatigue components. Early and reliable prediction of these operating environments ensures a safe and efficient part design.

Several techniques are available for predicting the response of a structure to random vibratory loading. Deterministic analyses, such as the finite element method, have a proven record of successfully predicting the stresses and displacements in the low frequency regime. At higher frequencies however, the models often become complex and require large amounts of computer time.

Recently, statistical energy analysis (SEA) methods have emerged with a philosophy more suited to dealing with the high-order modes of a structure. The vibrating system is represented statistically and the response prediction based upon the average vibrational energy contained within a band of frequencies. With this method the structure is more simply modelled using its gross structural properties and the analysis performed quickly and inexpensively. [1]

The Vibroacoustic Payload Environment Prediction System (VAPEPS) was developed as a tool for determining the response of structures excited by an acoustic field. JPL, under contract to the Air Force Space Division, has since taken over development of the program,

enhancing its capabilities while promoting its industry-wide use. Although VAPEPS contains several methods for extrapolating new responses from previously tested configurations, the core of the system is a Statistical Energy MODeler, SEMOD. The following paper presents a methodology for developing an SEA model for a particular spacecraft and discusses important aspects in characterizing the specific structural elements within the constraints of the VAPEPS software. The results of the analyses were compared to experimental data measured during a system-level acoustic test of the spacecraft. The predictions were evaluated with regard to their spectral shape and overall root-mean-square accelerations (GRMS), and the valid frequency range for these predictions was defined. Since the ultimate goal is to provide the designer with an accurate random vibration environment for testing components early in the flight program, techniques were demonstrated for extracting these test spectra from VAPEPS results.

SEA MODEL

LACE

The Low-power Atmosphere Compensation Experiment satellite, LACE, is shown deployed in Figure 1; it is 96 inches high, 52 inches wide, and 52 inches deep. The satellite's primary structure is constructed from one inch thick honeycomb sandwich panels bolted to an aluminum stringer-longeron frame (see Figure 2). Each of the four side panels are composed of three smaller individual panels joined together by a longeron. The core is capped at each end, on the +Z side by the space end deck and on the -Z side by the earth end deck. The space end deck is one inch thick honeycomb as is the internal RF/Boom deck. The earth end deck is a rib-stiffened 0.125 inch thick aluminum plate. All the decks are bolted along their perimeters to the main framework. The deployable solar and sensor panels are 0.5 inch honeycomb sandwich panels bolted to locking hinges and stowed with two explosive bolts. At each corner, deployable sensor arms are attached by a hinge at one end and an explosive bolt at the other.

SEA MODEL OVERVIEW

Within the VAPEPS system, SEAMOD was used to assemble user specified elements to develop and analyze the SEA model of the structure. The structural elements, acoustic excitations, and element connections were selected and characterized through an interactive runstream and the analysis carried out using SEA methods developed by Dr. Lyon [7]. Each element was defined by its geometric configuration, material properties, and physical parameters (such as mass-loading and panel discontinuities), which dictate its response to acoustic excitations.

The primary modeling philosophy was to keep the complexity low without compromising the value of the response predictions. It was also demonstrated that exacting detail in the model gained little benefit in the predictions; this is a direct result of the statistical nature of the analysis. The primary LACE structure was represented by four stiffened plate elements welded at the edges to form the
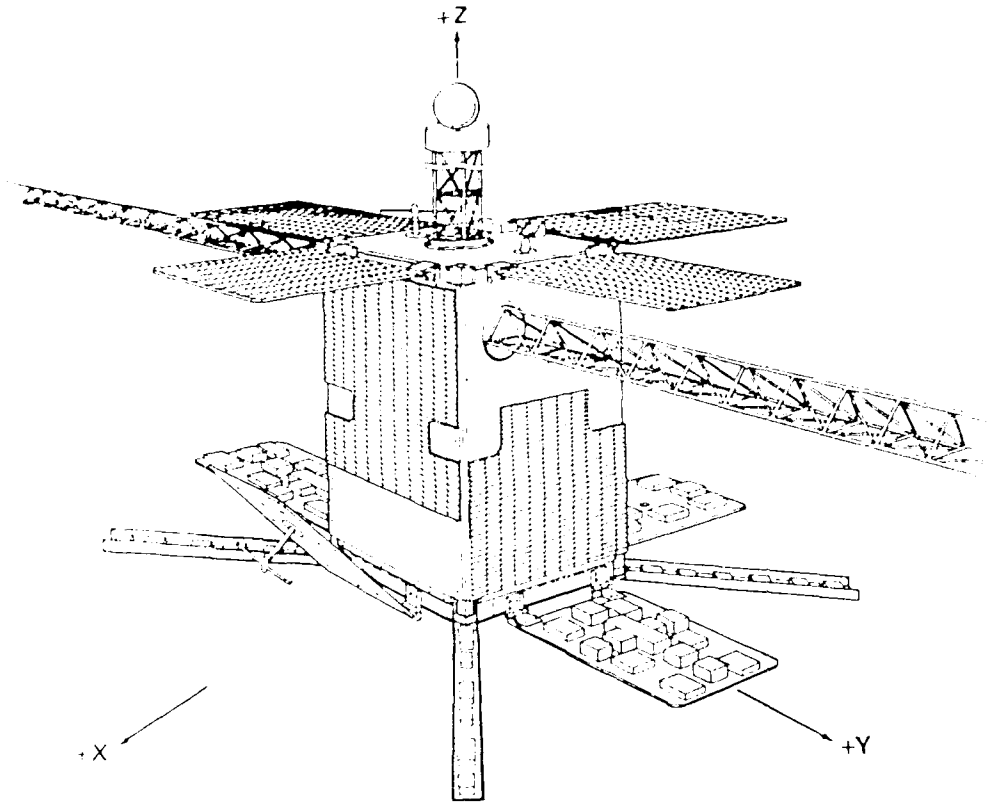
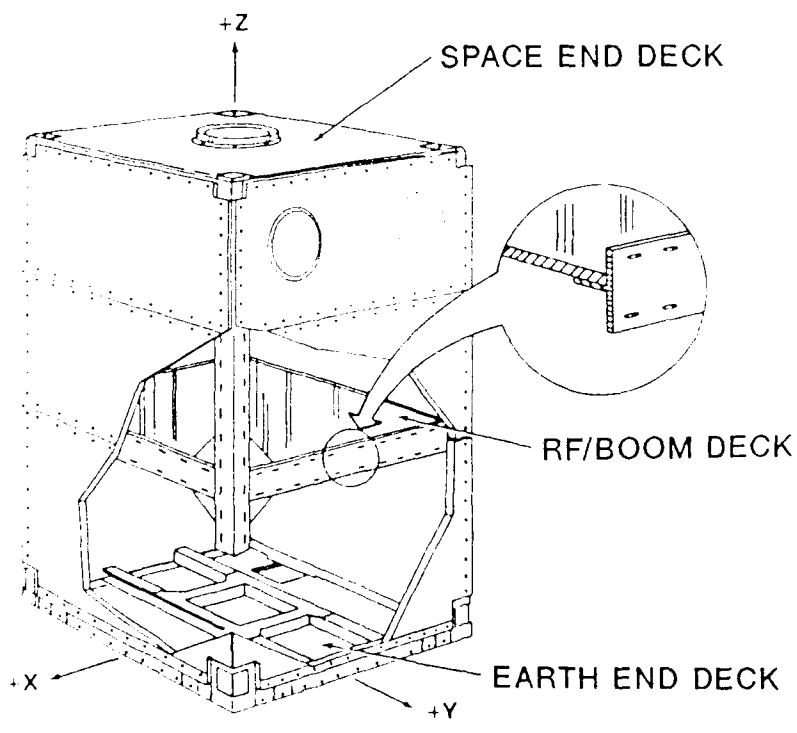Figure 1. LACE On Orbit Configuration

Figure 2. LACE Primary Structure

rectangular core. The space end and RF-Deck panels were modelled as unstiffened square plates welded on each edge to each of the four side panels. The earth end panel was a similarly attached, rib stiffened plate. The models for the enclosed and external airspaces were based on standard atmospheric conditions at room temperature.

The solar and sensor panels were represented by unstiffened plate elements connected to the primary structure through point connections. Three plate elements were welded together to form the C cross section of the sensor arm and the unit was attached to the primary structure using two point connections. The entire model was excited by specifying the sound pressure level in the external airspace acting on all external surfaces.

A flowchart of the model which contained 29 structural and acoustic elements and 69 path connections is given in Figure 3.

ELEMENT CHARACTERIZATION

Accurate prediction with VAPEPS was highly dependent on the input variables used to define a particular element. Parameter selection influenced the magnitude as well as the shape of the response spectrum.

A VAPEPS subroutine, EQPL, was used to reduce complex multi-layered panels (such as a honeycomb sandwich panel, with or without ribs) to equivalent homogeneous plates by modifying the plate stiffness, density, and thickness in order to match the dynamic characteristics of the original panel. This allowed replacement of the LACE panels with "dynamically equivalent" homogeneous plates which responded like the original panels to an acoustic excitation. EQPL was used to compute the equivalent material properties for the unstiffened honeycomb sandwich solar and sensor panels. This was repeated for the space end and RF/Boom deck panels, making the assumption that the primary truss structure did not influence the plate stiffness.

The stiffness parameters of the ribbed panels were defined for two frequency ranges, accurately representing the frequency-dependent dynamic behavior of these panels. Low-frequency excitations drove the entire panel, and the EQPL parameters for the rib-panel combination appropriately characterized the plate. However, at high frequencies, the wavelength of the bending waves traveling in the panel became smaller, and the response of the panel was dominated by the unstiffened area between the ribs. This effect was modeled by basing the plate response on the unstiffened honeycomb panel parameters at frequencies above the transition frequency f_t, as defined below, and the equivalent properties for the ribbed panel below f_t.

The frequency f_t was determined by computing the first resonant mode of the panel area between the ribs. The first mode occurred when:

$$ l = L/2 \tag{1} $$

where L = wavelength of the bending wave in the material (in), and
   l = smallest subpanel surface dimension (in).

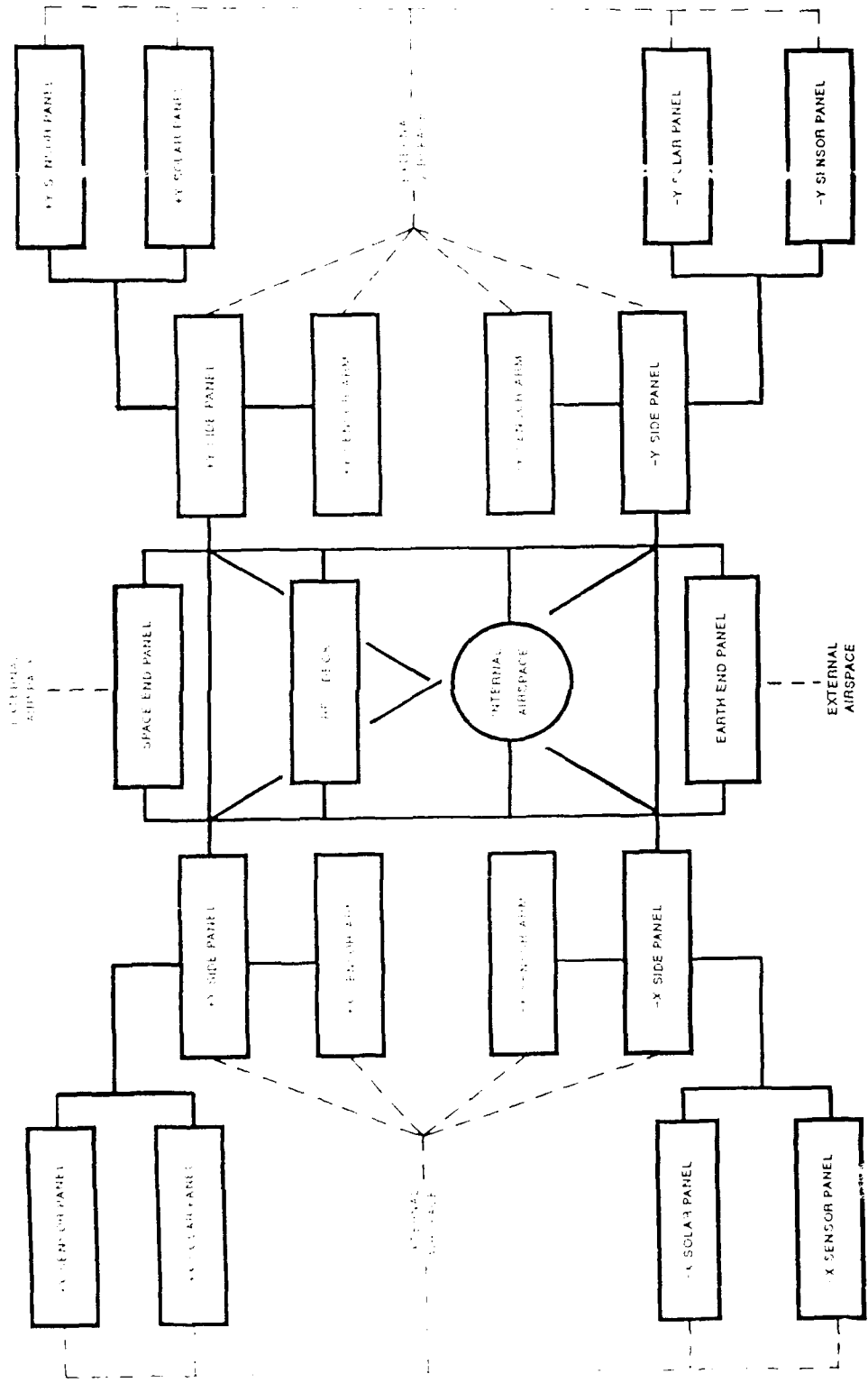The frequency f_t, computed from the bending wavespeed in metal [3] for a wavelength of 2l, was then

Figure 3. LACE SEA Model

$$f_t = (.452tC_1)/1^2 \qquad\qquad (2)$$

where t = subpanel equivalent thickness (in), and
 C_1 = longitudinal wavespeed (in/sec),

Following the above rationale, the ribbed side ana earth end panels were represented with material properties based on their stiffened parameters below f_t and unstiffened parameters above f_t. As before, the surrounding frame structure was included as a boundary condition for the plate elements, not as stiffeners.

Other input parameters that characterized the structure were not easily derived, relying on "engineering judgment". One such parameter measured the linear length of discontinuities which disrupted the bending wave pattern in the panel. This determined the radiation capabilities of a particular panel based on equations derived by Maidanik [8]. Boundary conditions, rib stiffener edges, and components with sharp corners mounted with closely spaced bolts were all considered as discontinuities of the LACE panels, and their individual lengths were added together. Another parameter, panel damping, was assumed to be the same for all the panels, varying inversely with frequency, with ten percent damping at 250 Hertz. Comparisons with the test data indicated that at high frequencies the influence of the assumed damping on the predicted plate response was excessive; therefore it was set to zero above 1000 Hertz. Lastly, components which added mass but no stiffness were considered as non-structural masses and included as a mass smeared across the panel. The ratio of the component to total panel mass was then used as part of the SEMOD calculations to scale the response.

After each panel was represented with an "equivalent" homogeneous plate element, all were assembled by specifying either weld or point connections between them. The internal air element was modeled and coupled acoustically to all internal surfaces and to the external airspace by a non-resonant connection through the side panels. The external airspace was the only excitation element, applying a specified sound pressure level to all external surfaces.

The SEMOD program computed the coupling loss factors of the model and solved the energy balance equations for each 1/3 octave band. The element response predictions were presented as mean acceleration spectral density values for each frequency band.

ACOUSTIC TEST

A system level acoustic test of the LACE spacecraft was performed at the Naval Research Laboratory's acoustic test facility. An overall sound pressure level of 147 dB was maintained for 120 seconds. The averaged microphone pressure level is shown in Figure 4. The LACE structure was instrumented with 84 accelerometers, several measuring the panel responses normal to the surface.

The data were analyzed using a GENRAD Data acquisition system, downloaded to a VAX 11/780, and read into VAPEPS for conversion into 1/3 octave band acceleration spectral densities. VAPEPS contained several routines for the manipulation and analysis of test data; one

such routine performed the conversion of narrow band test data into 1/3 octave band data.
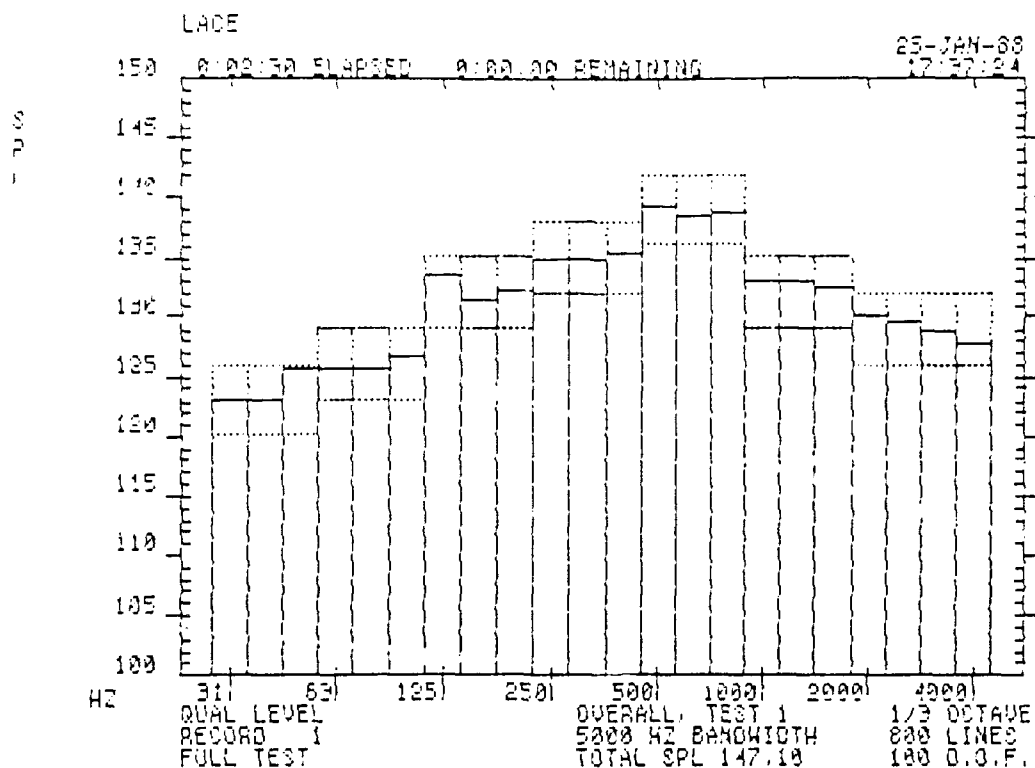
Figure 4. LACE Acoustic Test Sound Pressure Level

RESULTS

The mean-square acceleration spectral densities predicted by VAPEPS are presented along with the measured values for several elements in Figures 5 through 14.

Figures 5 through 8 show the results for the unstiffened panels. They all exhibit good or excellent agreement in the mid- to high-frequency ranges, with large discrepancies occurring at the low-frequency end. The overall GRMS levels were also accurately determined as seen in Table 1, which compares the predicted and measured GRMS values.

The results for the heavily loaded, ribbed earth end panel are shown in Figure 9. The data show considerable variability over the range of measurement points, presumably due to the complexity of the panel structure and masses. In the element representation, the material characteristics of the plate were reduced to the unstiffened case at 550 Hz as dictated by Equation (2). Good spectral correlation is seen above 130 Hz along with reasonable agreement of the overall GRMS levels.

The predictions and data for the four side panels are shown in Figures 10 through 13. Again, the data are shown to be highly dependent upon the exact measurement location, and the spectral correlations are less accurate (but good) above 100 Hz. Equation (2)

Figure 5. - X Sensor Panel: Predicted Response Versus Test Data
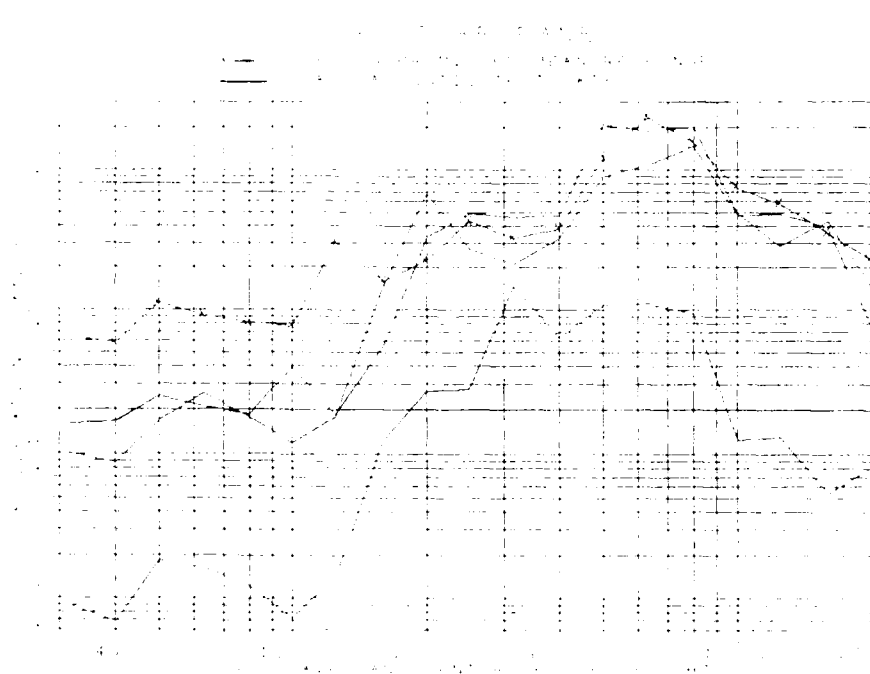
Figure 6. + X Solar Panel: Predicted Response Versus Test Data
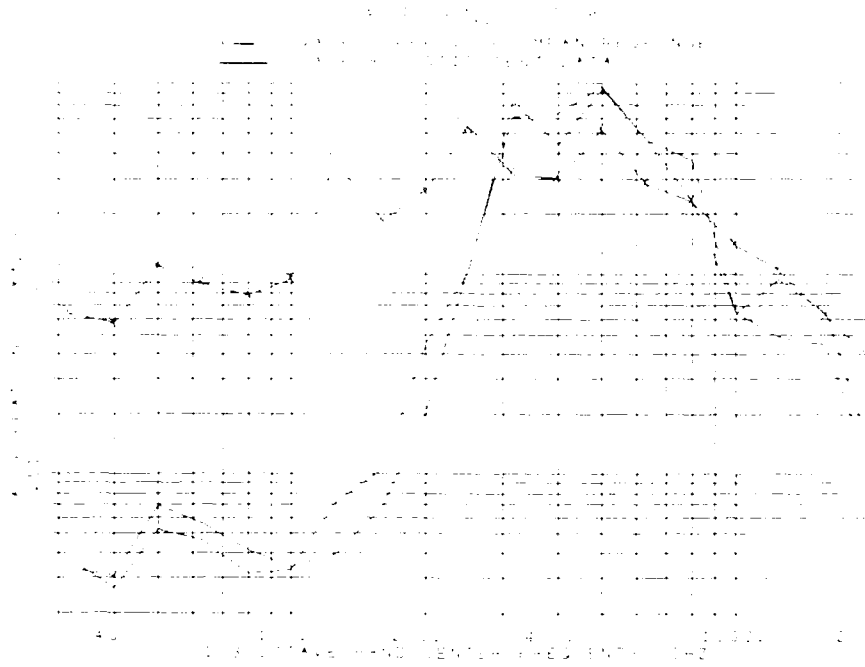
Figure 7.   Space End Deck: Predicted Response Versus Test Data

Figure 8.   RF/Boom Deck: Predicted Response Versus Test Data

Figure 9. Earth End Deck: Predicted Response Versus Test Data

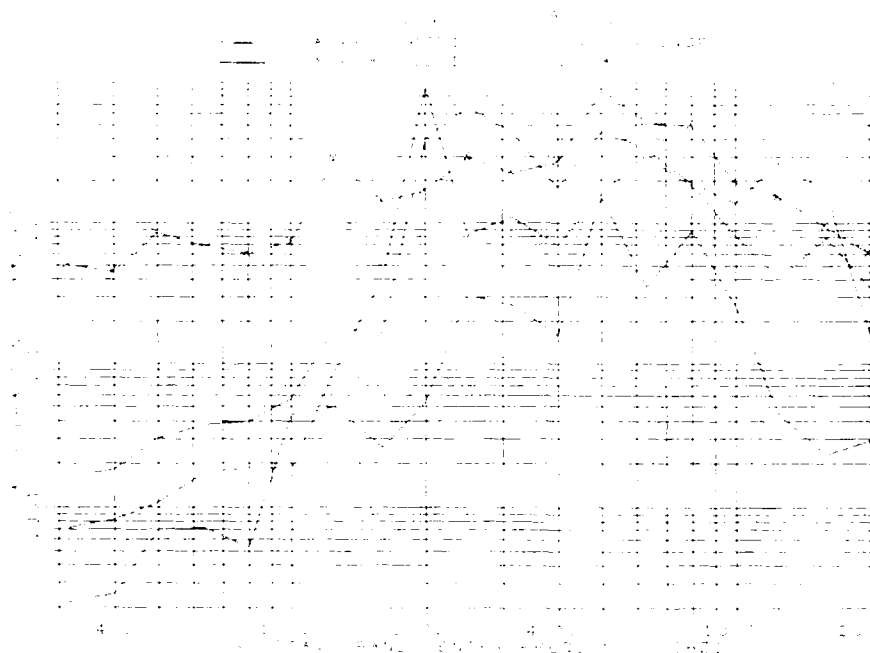Figure 10. + X Side Panel: Predicted Response Versus Test Data

Figure 11. - X Side Panel: Predicted Response Versus Test Data
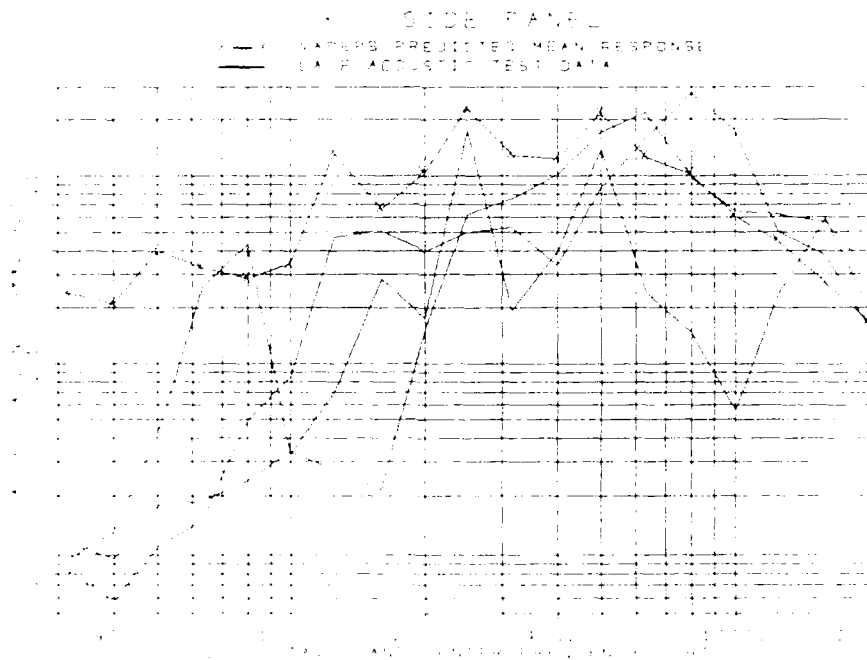
Figure 12. + Y Side Panel: Predicted Response Versus Test Data
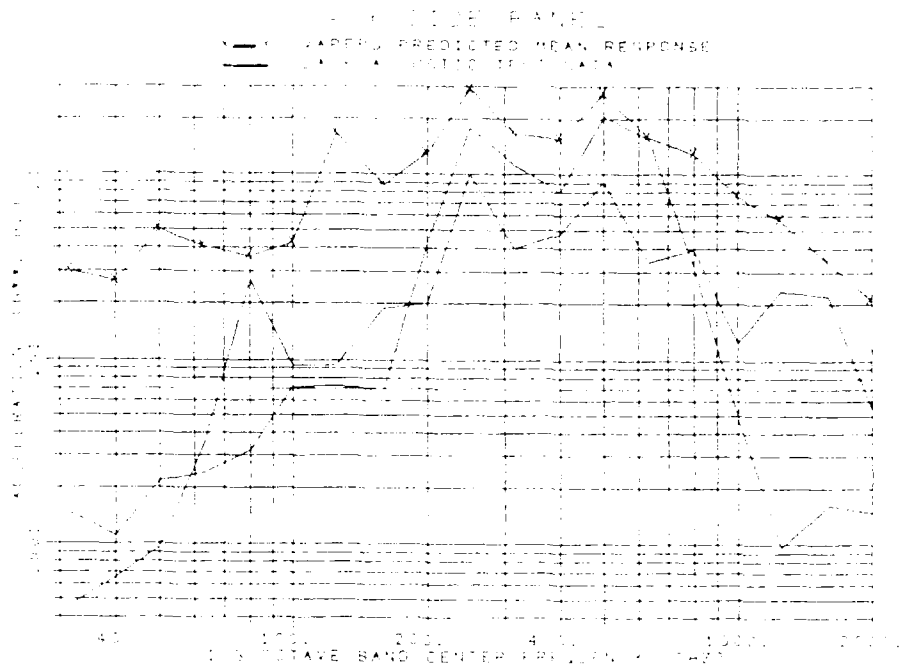
Figure 13.   - Y Side Panel: Predicted Response Versus Test Data
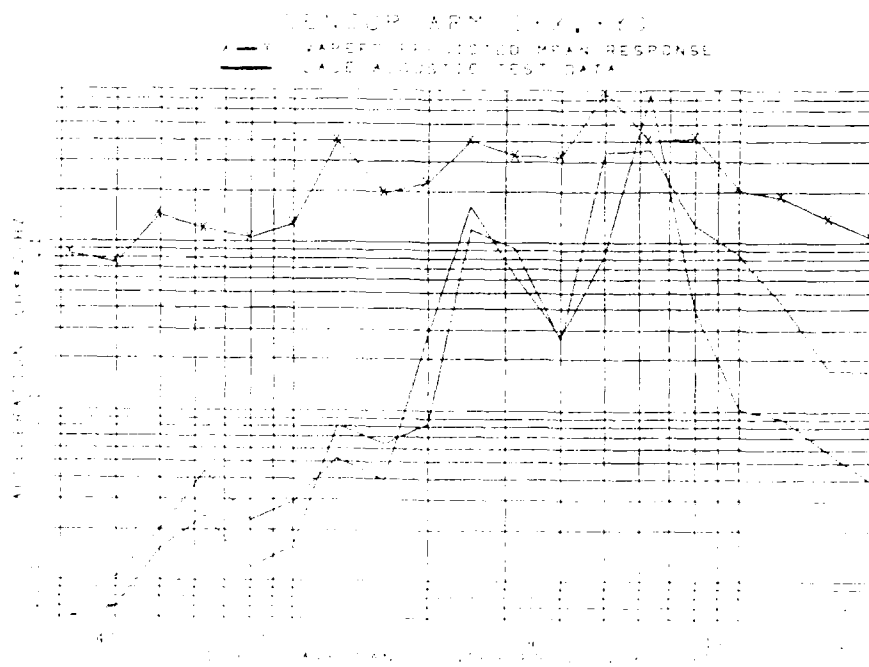
Figure 14.   Sensor Arm: Predicted Response Versus Test Data
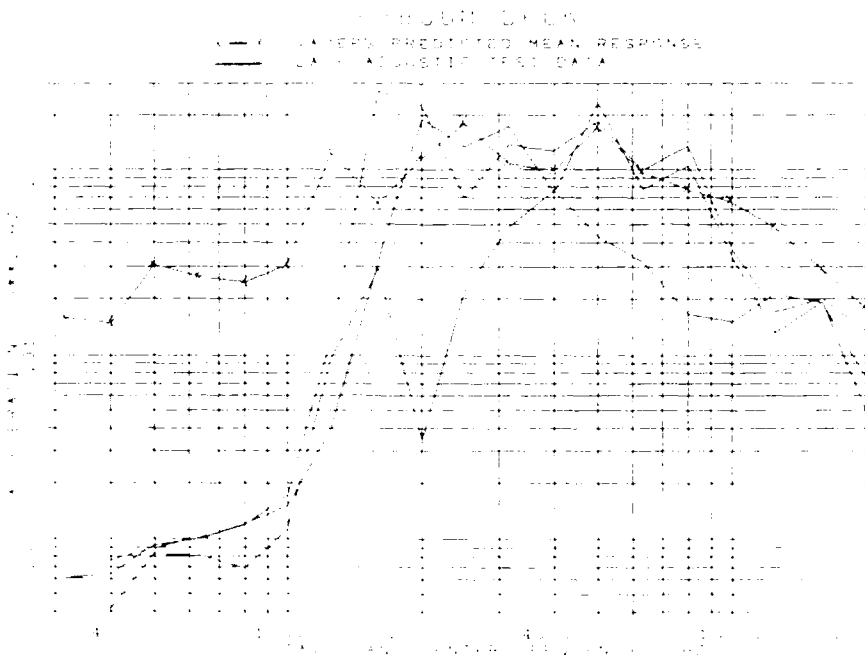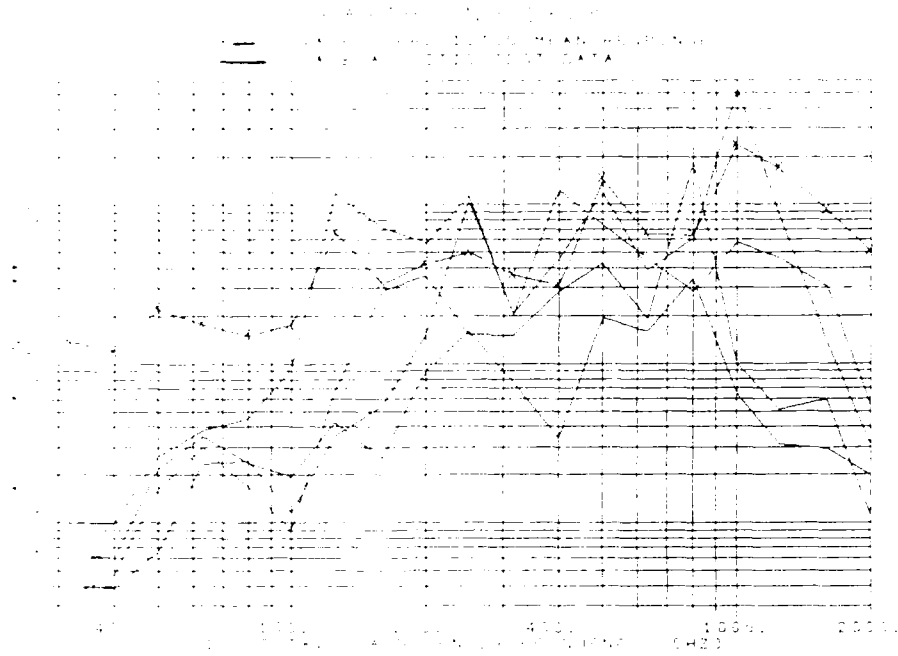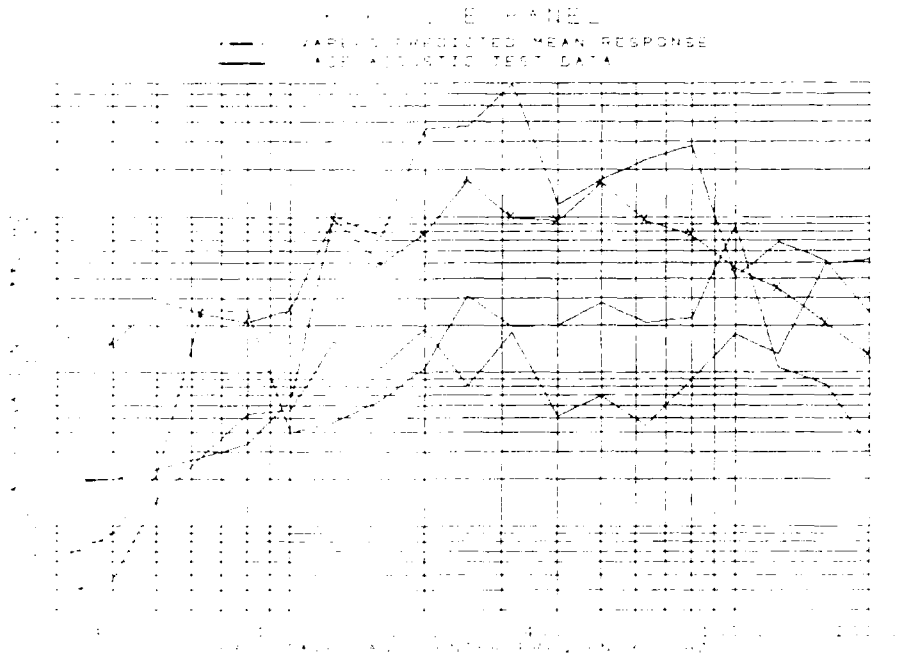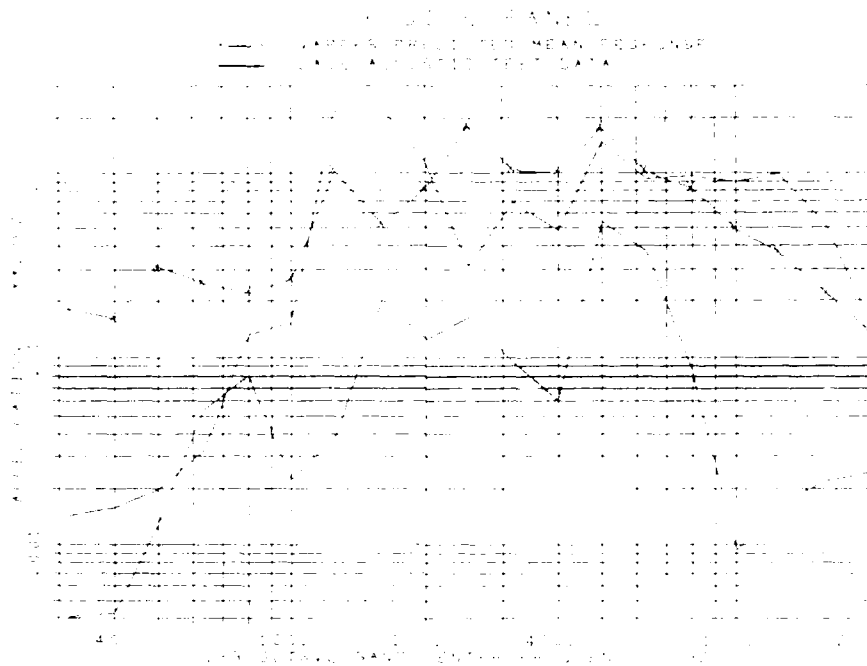
dictated a change in stiffness properties at 290 Hz. The overall GRMS
levels predicted did show good agreement with the measured values.

TABLE 1. Overall GRMS Comparison

SEA ELEMENT	LACE ACOUSTIC TEST DATA SEPARATE MEASUREMENT LOCATIONS MEAN GRMS				VAPEPS RESULTS GRMS		
					MEAN	95TH %	MEAN UNLOADED
- X SENSOR PANEL	20.5	15.4	7.3	-	24.5	53.9	43.9
+ X SOLAR PANEL	32.6	37.7	8.7	-	38.2	92.0	38.2
SPACE END DECK	20.0	-	-	-	19.1	45.9	25.8
RF BOOM DECK	6.8	10.7	11.5	-	11.6	28.0	21.4
EARTH END DECK	9.5	4.2	7.6	14.0	14.5	34.9	48.1
+ X SIDE PANEL	4.4	12.4	-	-	10.8	25.9	25.6
- X SIDE PANEL	6.6	7.0	16.4	-	11.1	26.8	25.6
+ Y SIDE PANEL	7.6	-	12.5	-	12.4	29.8	25.6
- Y SIDE PANEL	8.8	13.2	9.1	-	13.9	33.5	25.6
SENSOR ARM (+X,+Y)	9.0	12.0	-	-	23.2	55.8	57.9

The sensor arm data are shown in Figure 14, along with the
prediction. Poor correlation is seen below, and passable results
above, 500 Hz. Again the overall GRMS is given in Table 1.

In all cases it was evident that VAPEPS did not predict the low-
frequency responses accurately. A priori knowledge of where this
divergence occurs is critical in defining the frequency range over
which the predictions are valid. Two criteria can be used to
establish this low-frequency limit. VAPEPS uses Maidanik's equations
[8] for computing the radiated energy from an acoustically excited
panel. These expressions are valid only when

$$1/2 \quad k_p l < 1 \tag{3}$$

where k_p = wavenumber of acoustic field (2*PI/L, 1/in), and
l = smallest panel dimension (in).

From here, a lower frequency limit can be computed based on the
validity of the theoretical equations governing the response.
Secondly, statistical energy analysis is valid only in frequency bands
which contain at least one structural mode. This establishes a low
frequency boundary by requiring that

$$n \Delta f > 1 \tag{4}$$

where n = the modal density (modes/frequency band, 1/Hz), and
Δf = the frequency bandwidth (Hz).

Table 2 gives the low-frequency limits for several elements using both

techniques. Comparing the limits to the earlier graphs demonstrates the effectiveness of selecting the higher of the two frequencies as a low-frequency boundary. In all cases, except for the narrow sensor arm, equation (4) is the limiting factor.

TABLE 2. Low Frequency Limits

SEA ELEMENT	LOWER LIMITING FREQUENCY (HZ)	
	EQUATION (3)	EQUATION (4)
SOLAR AND SENSOR PANELS	73	200
SPACE END DECK	85	315
EARTH END DECK	85	500
RF/BOOM DECK	85	315
SIDES	85	200
SENSOR ARM	450	250

It should be noted that the measured data are influenced by local mass-loading effects, as well as the spatial variation of the response due to certain boundary conditions. These affect the spectral distribution and magnitude of the measured responses, and should be considered when comparing the data to the mean-value predictions based on a smeared-mass approximation.

DEVELOPING COMPONENT RANDOM VIBRATION TEST SPECTRA

A random vibration test is a simulation of the vibratory environment that a particular component may be exposed to and often the only test used to qualify the design. Therefore it is appropriate to discuss how test spectra can be determined using the VAPEPS predictions.

Figure 15 shows the Earth end panel narrow band test data plotted with the predicted response from VAPEPS. Looking at the data, it can be seen that basing a test specification on the mean value predicted response may create an undertest condition by underpredicting the peak responses and the localized mass loading effects.

A proposed method for bounding the narrow band peaks was to use a 95th percentile response based upon a log-normal distribution and the predicted mean response. [9] However, this yielded extremely conservative and potentially damaging GRMS levels in several cases. (Table 1) Another approach was to define a specification using the worst-case panel response, (ie. the largest GRMS), as an upper bound. For any panel, this could be determined by setting the non-structural mass to zero and executing the SEA model.

The mean square spectral acceleration for the unloaded earth end panel is also shown in Figure 15. This is the result obtained by setting the non-structural mass for the earth end element to zero and resolving the energy balance equations, determining a new response. Although it does not completely bound the peaks, it does cover the

possible variations of responses due to local mass loading effects in a "total energy" sense; see Table 1. In most cases it also provides reasonable GRMS levels, allowing component test spectra to be based on a constant energy approach, to be derived. With the limits established, other influencing factors and engineering judgment can be used to derive appropriate test levels. [6]

Localized environments for specific components can also be calculated by scaling the unloaded response using a factor, proposed by Barrett [2], which ratios the component and structure weights. In either case, random vibration test specifications can be generated for general or component-specific applications using the VAPEPS predictions.
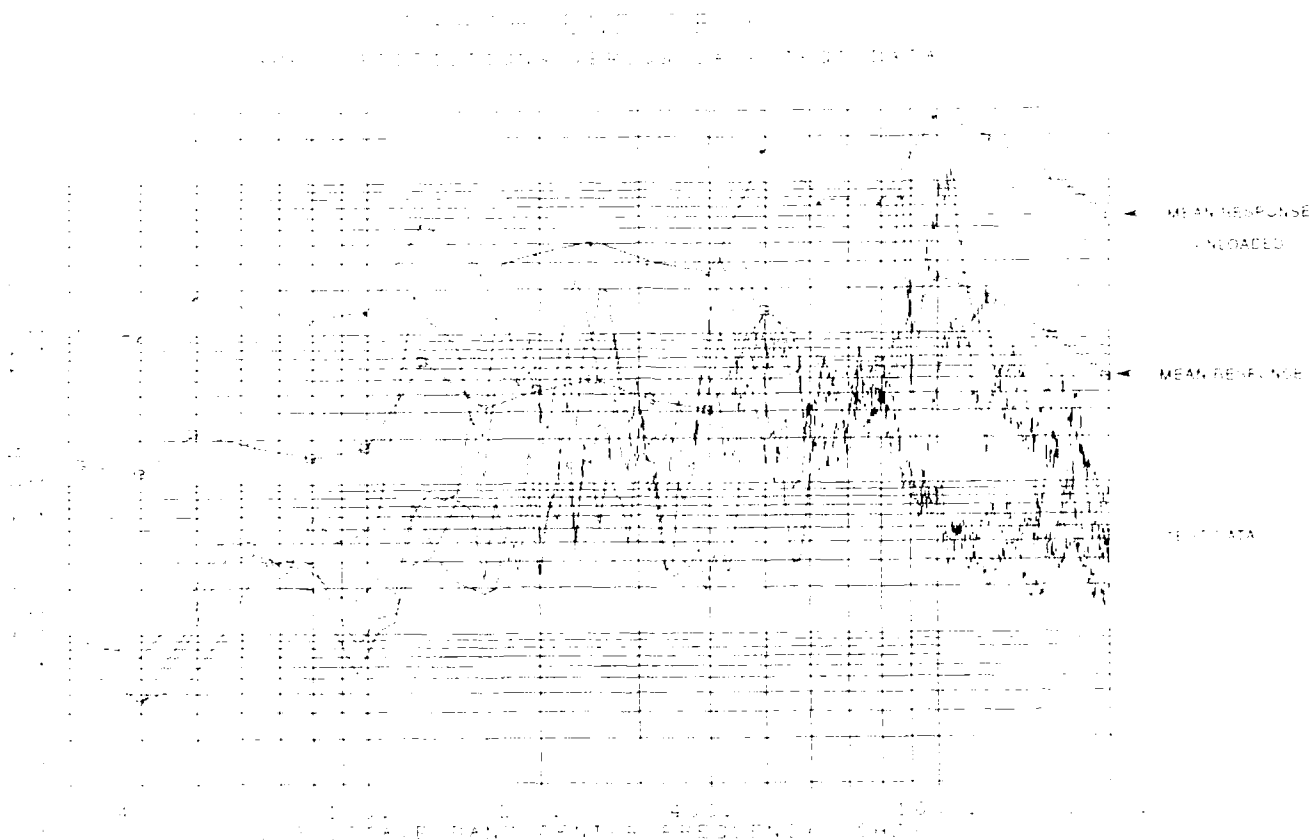
Figure 15. Earth End Panel Predicted Responses Versus Narrow Band Test Data

CONCLUSIONS

The feasibility of SEA techniques for analyzing the high-frequency response of structures, and in particular their application to acoustics, has been demonstrated several times before. [4],[5] The results of this study indicate that the VAPEPS software can be used without much modification, to set up and execute vibroacoustic models with good results.

In the case of the LACE satellite model, the damping and

stiffness were tailored to represent more accurately the dynamic behavior of the actual vehicle. Reducing the high-frequency damping was very effective in raising the responses above 1000 Hz, resulting in better agreement with the test data. Separating the material properties of the ribbed panels into two frequency ranges allowed better characterization of the response mechanisms taking place in the panel, and dramatically improved the spectral and overall correlations. Both modifications were easily achieved within the VAPEPS environment.

The capabilities of SEA at low frequencies were limited, but the range in which the results are applicable were easily determined. Good results were achieved with only one structural mode in the band of interest, which is important for models of smaller, less complex structures.

With a small amount of manipulation, the results from VAPEPS can be used to bound the response spectra and aid in the derivation of random vibration test spectra for components. Component masses, "engineering judgment", and program philosophies will all affect the final specification, but VAPEPS can be used to establish initial guidelines.

The VibroAcoustic Payload Environment Prediction System (VAPEPS) is clearly a valuable asset to the aerospace community. It is interactive, easy to use, and (based on this study) accurate. Control of the entire model is in the hands of the user; the ability to control and tailor parameter inputs at any point in the analysis is excellent.

Research is still continuing in several areas; for example, mass stiffening, coupling loss factors, and damping. Hopefully, the results will expand VAPEPS prediction capabilities and reduce the significant role that "engineering judgment" has in the developement of the models. At present, it can be concluded that VAPEPS can provide accurate environmental predictions and provide the needed data for developing reasonable vibroacoustic component test specifications.

ACKNOWLEDGEMENTS

REFERENCES

1. J.S. Archer, "Structural Vibration Prediction", NASA SP-8050, June 1970

2. Robert E. Barrett, "Techniques For Predicting Localized Vibratory Environments of Rocket Vehicles," NASA TN D-1836, October 1963

3.	Leo L. Beranek, <u>Noise and Vibration Control</u>, McGraw-Hill Book Company, New York, 1971, pp. 271-357

4.	B. Clarkson,R. J. Cummins, D. Eaton, J. Vessaz, "Prediction of High-Frequency Structural Vibrations Using Statistical Energy Analysis (SEA)", <u>ESA Journel</u> 1981, Vol. 5, pp. 127-152

5.	F. J. Fahey, "Statistical Energy Analysis - A Critical Review", Presented at Colloquium of the Commission Acoustique W51 du Counceil International du Batiment, Liverpool, England, October 1973

6.	J. Judkins, S. Ranaudo, "Spacecraft Internal Vibration Response accelerations System Level Versus Component Level", <u>Journal of Environmental Sciences</u>, pp. 17-23, November/December 1987

7.	Richard H. Lyon, <u>Statistical Energy Analysis of Dynamical Systems</u>, MIT Press, Cambridge Massachesetts, 1975

8.	Gideon Maidanik, "Response of Ribbed Panels to Reverberant Acoustic Fields," <u>Journal of the Acoustical Society of America</u>, Vol. 34, No. 6, pp. 809-826, June 1962

9.	"VibroAcoustic Payload Environment Prediction System (VAPEPS)", From VAPEPS workshop notes, Jet Propulsion Laboratory, Semptember 1987

COMPARISON OF VAPEPS PREDICTIONS
WITH IUS VIBROACOUSTIC DATA

Clark J. Beck
Boeing Aerospace
Seattle, Washington

ABSTRACT

The Vibroacoustic Payload Environment Prediction System (VAPEPS) was used to predict acoustic and vibration environments for an Inertial Upper Stage (IUS) vehicle. The predictions were made with the VAPEPS Statistical Energy Modeler (SEMOD). The step-by-step analysis procedure is described in this paper, and an example prediction is presented. The predictions are compared with vibroacoustic test environments measured on the IUS. Conclusions and recommendations are presented relative to use of VAPEPS SEMOD.

INTRODUCTION

This paper contains vibration and noise predictions from the VAPEPS SEMOD computer program. The predictions are compared with measured vibration and acoustic data.

A description of the step-by-step analysis procedures is presented. The description includes: model definition; equivalent plate calculation; SEMOD input; SEMOD execution; SEMOD output; and model revision.

SEMOD was used to predict the vibration levels of loaded and unloaded structure. The effects of damping on acoustic and noise environments were investigated. The effect of configuration change was evaluated by conducting analyses with different combinations of elements and connecting paths between the elements.

The IUS Development Test Vehicle (DTV) was the subject of the SEMOD analysis. A large number of vibroacoustic measurements are available from this vehicle. Comparisons of IUS DTV measurements with the SEMOD results provide an evaluation of the predictor.

Conclusions and recommendations are presented relative to the use of VAPEPS SEMOD.

ANALYSIS PROCEDURE

The SEMOD part of VAPEPS version 5.2 was used to perform the analysis. The analysis procedure is shown in Figure 1.
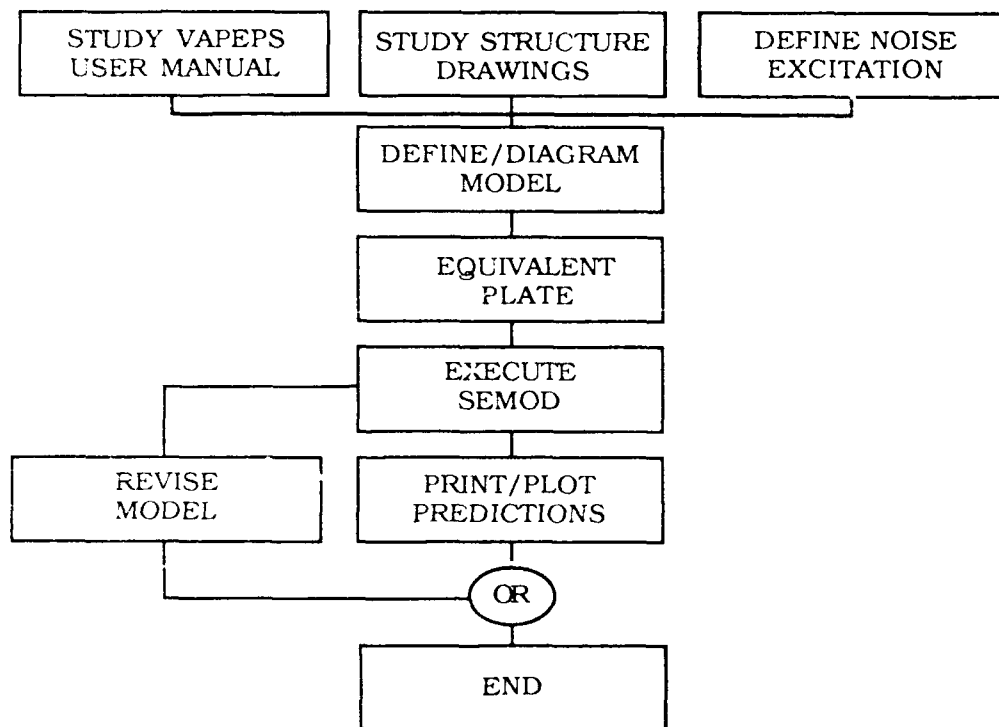
Fig. 1   Analysis procedure

STRUCTURE DESCRIPTION

The Inertial Upper Stage (IUS) Development Test Vehicle was the subject of the VAPEPS analysis. The DTV interstage cylindrical structure and Equipment Support Section (ESS) conical structure are shown in Figure 2. The lower interface of the interstage attaches to a solid rocket motor (SRM 1). A second solid rocket motor (SRM 2) is located inside the conical structure. Figure 3 is a photograph of SRM 2 and the equipment deck. Figure 4 shows the vehicle dimensions and the relationship between the various DTV elements.
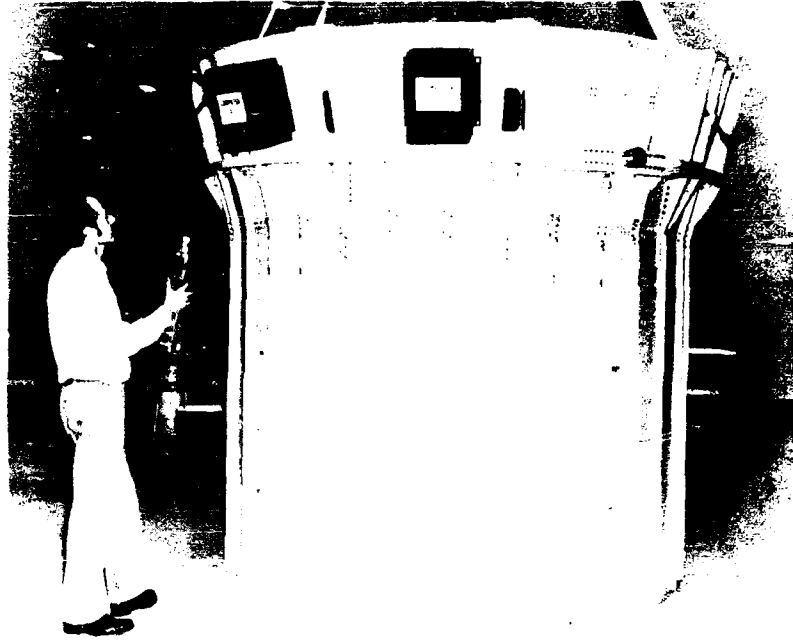
Fig. 2   DTV Interstage and Equipment Support Section
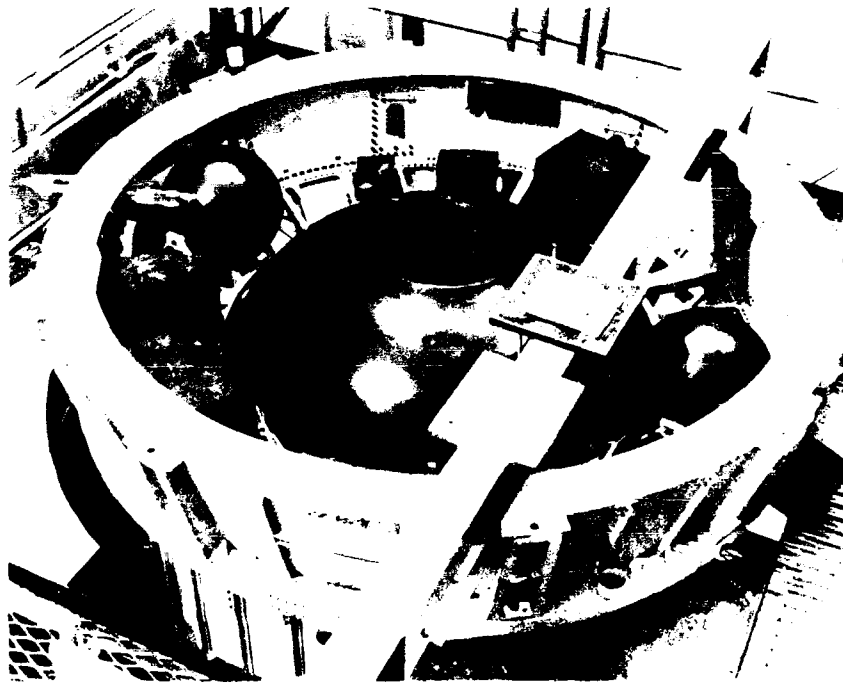
Fig. 3   SRM 2 and Equipment Deck
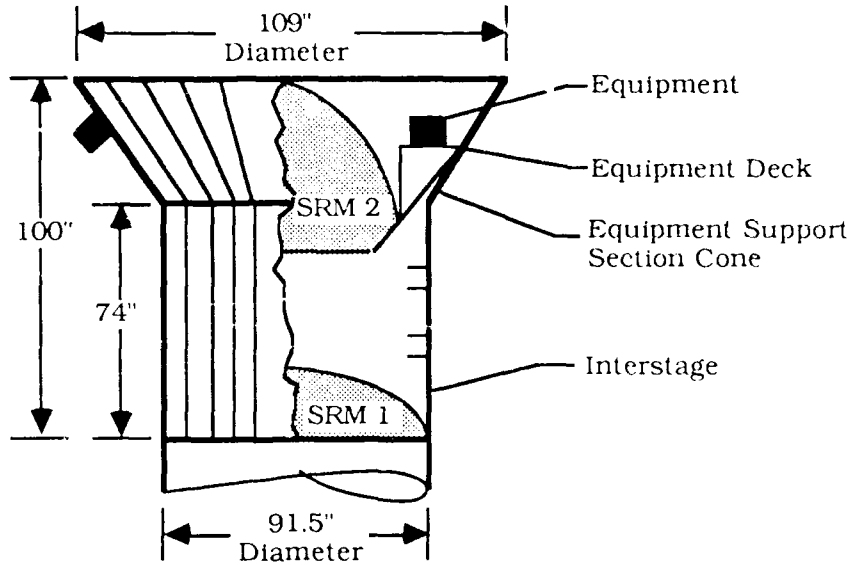
Fig. 4 DTV Configuration and Dimensions

ACOUSTIC NOISE EXCITATION

The DTV has been subjected to acoustic noise tests in a reverberation test cell. The cell is 16 feet wide, 24 feet long and 20 feet high. The test cell noise levels are shown in Table 1. The one-third octave band sound pressure levels are used as the excitation element in the SEMOD model.

Table 1 Acoustic Noise Excitation

One-third Octave Band	
Center Frequency (HZ)	Sound Pressure Level (DB REF .00002 N/M2)
50	126.8
63	130.9
80	131.5
100	132.5
125	132.0
160	133.4
200	132.0
250	132.9
315	134.5
400	135.4
500	133.0
630	133.3
800	133.3
1,000	132.5
1,250	131.2
1,600	130.3
2,000	128.9
OVERALL	144.7

EXAMPLE PREDICTION

VAPEPS User's Manual

The first step in conducting a SEMOD prediction is to study section 11 of the VAPEPS User's Manual, reference. Section 11 describes SEMOD and the information required for SEMOD input. The Equivalent Plate command is also used in this example. This command is described in section 3.51 of the Users's Manual.

Vehicle Drawings

The SEMOD and Equivalent Plate input requirements are obtained from vehicle assembly and detail part drawings. The acoustic test cell dimensions are also required.

Define/Diagram Model

The model must be defined and expressed in terms of a SEMOD diagram. It is not necessary to model the entire vehicle. In fact it is sometimes helpful to predict the responses of a part of the vehicle and evaluate the predictions before adding another part. This example is for the DTV interstage. The interstage configuration details and the associated SEMOD diagram are shown in Figure 5.

ELNAME
    EXTA = Acoustic Test Cell
    INST = Interstage Cylinder
    INTA = Interstage Cavity
PATHNAME
    EXTA, INST, Connection Type 2
    INST, INTA, Connection Type 2
    EXTA, INST, INTA Connection Type 5
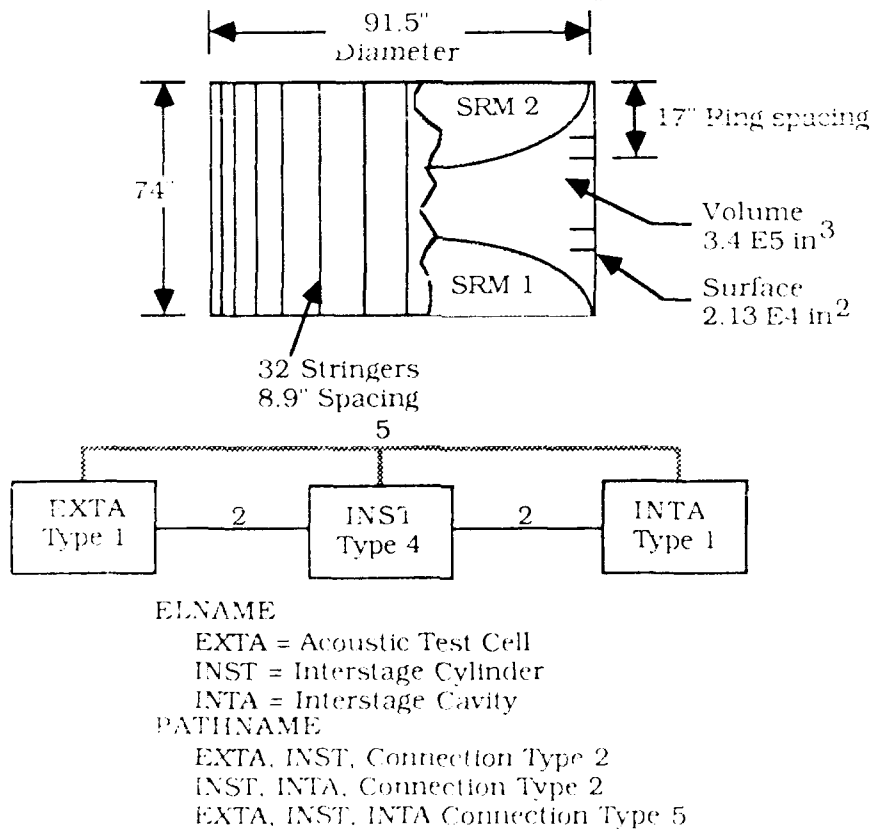
Fig. 5   DTV Interstage and SEMOD Diagram

Equivalent Plate

The interstage (INST) described in Figure 5 is a cylindrical shell consisting of a skin, lengthwise stiffeners and ring stiffeners. This configuration must be reduced to an equivalent plate for SEMOD input. The VAPEPS command, RUN=EQPL, is used to determine the equivalent plate. Figure 6 presents the interstage structure details for input to RUN=EQPL. Table 2 shows the RUN=EQPL command procedure file. Annotations are provided on the file to help the reader understand the procedure. Table 3 presents the output file, EQPL.OUT. The boxed numbers on Table 3 are inputs to SEMOD.

① = Lengthwise beam 1

② = Lengthwise beam 2

③ = Lengthwise beam 3

Ⓢ = Skin
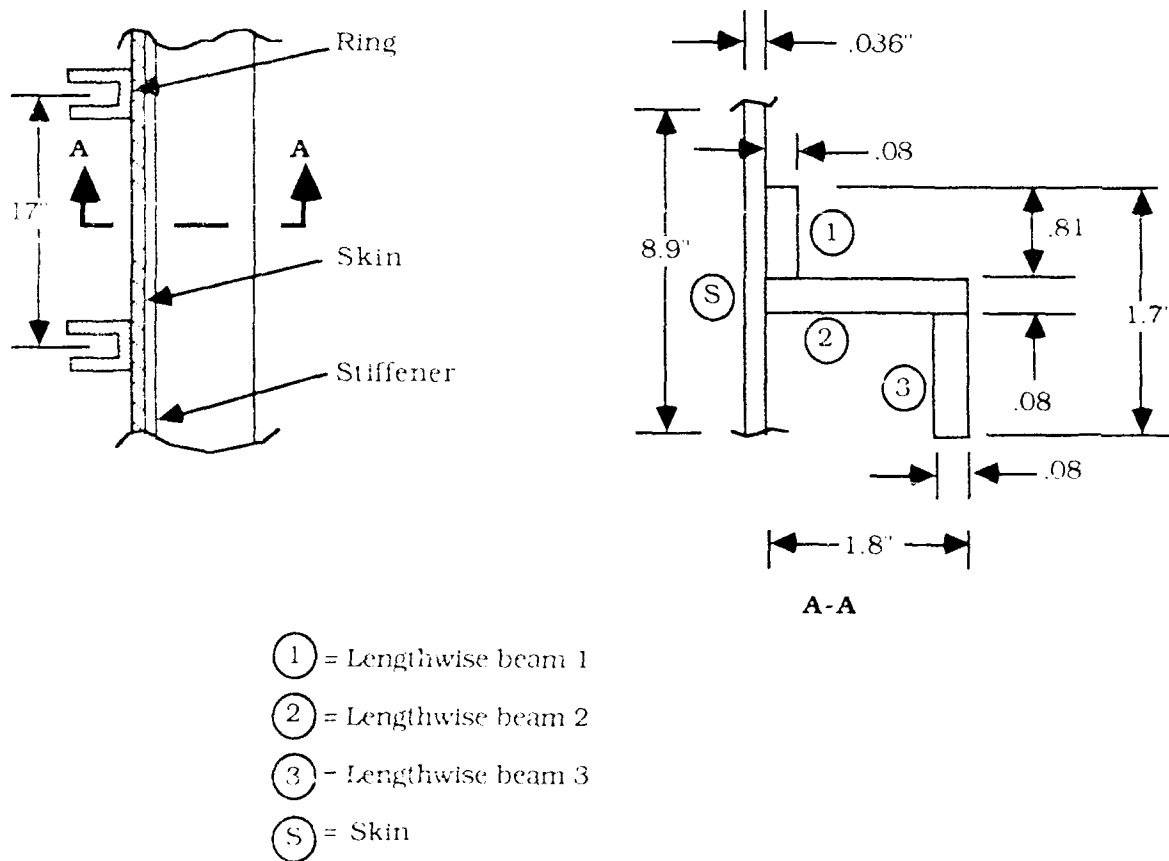
Fig. 6   Interstage Structure Details

Table 2   RUN= EQPL Command File

```
$ ASSIGN EQPL.OUT FOR006  ⎫  Assign output file name
$ RUN VAPEPS                ⎭  Enter VAPEPS
RUN = EQPL, 4, INST            Run equivalent plate
NS = 1                     ⎫
NPL = 5                    ⎪
NBW = 0                    ⎪
BLEN = 17.                 ⎪
WID = 8.9                  ⎬  Enter general parameters
ER   10.6E6               ⎪
RHOR = 2.59E-4            ⎪
CL = 2.01E5               ⎪
DONE                      ⎭
H = .036                  ⎫
CEN = .018                ⎪
E = 10.6E6                ⎬  Enter skin parameters  Ⓢ
RHO = 2.59E-4             ⎪
DONE                      ⎭
H = .08                   ⎫
CEN = .076                ⎪
E = 10.6E6                ⎬  Enter beam  ①  parameters
RHO = 2.59E-4            ⎪
W = .81                   ⎪
DONE                      ⎭
H = 1.8                   ⎫
CEN= .936                 ⎪
E = 10.6E6                ⎬  Enter beam  ②  parameters
RHO = 2.59E-4            ⎪
W = .08                   ⎪
DONE                      ⎭
H = .08                   ⎫
CEN = 1.8                 ⎪
E = 10.6E6                ⎬  Enter beam  ③  parameters
RHO = 2.59E-4            ⎪
W = .81                   ⎪
DONE                      ⎭
TOC 4                         Display Table of Contents DAL 4
PRINT 4, EQPL, INST           Print equivalent plate file
PACK 4                     ⎫  Pack DAL files
PACK 28                    ⎭
END                          Exit VAPEPS
$LASER EQPL.OUT              Print output file
$DEASSIGN FOR006
$EXIT                        Exit command file
```

Table 3   Output File EQPL.OUT

```
VAPL 2 1 07 20 88 07:04:12    1344:0
FOR SPLASHLINE DATED 880418, TYPE  NEWS'
OK
OK
OK
OK
OK
*  Result: 4.EQPL.INST   Size: (9 x 1)
*  Result: 4.SEQP.INST   Size: (6 x 1)


                    Input Specifications

     RLEN= 1.700E-01, WID= 8.900E+00, CL= 2.010E+05

        Layer      H         CEN         E          RHO        W
                              bare skin
          1    3.600E-02  1.800E-02  1.060E-07  2.590E-04    N A


                            lengthwise beams
          1    6.000E-02  7.400E-02  1.060E-07  2.590E-04  8.100E 01
          2    1.800E+00  9.360E-01  1.060E-07  2.590E-04  8.000E 02
          3    6.000E-02  1.800E-00  1.060E-07  2.590E-04  8.100E-01


          +-----------------------------------------------------+
          |               Equivalent Parameters                 |
          |                                                     |
          | H  4.987E-01, E  1.406E-06, RHO= 3.481E-05, RHOS= 9.324E-06 |
          +-----------------------------------------------------+


                 Stress prediction parameters

     H  2.874E-01, E= 1.060E-07, RHO= 3.680E-05, RHOS= 9.324E-06


              Centroid distance =  4.413E-01



TABLE OF CONTENTS FOR DAL UNIT  4     KSC:CS:[VAPEPS]DAL004.DAL:1

SEQ     RR    DATE    TIME   F   WORDS    NR   NC  T ELN    VER   CI
  1     16  880701  7043:  0     4         4    4  1 BARS   INST   0
  2     20  880701  704:   0     15        3    5  1 BEML   INST   0
  3     28  880701  704:         2         5    1  0 GEN3   INST   0
  4     3.  880701  704:   0     5         5    1  1 GENR   INST   0
  5     36  880701  704:.        9         9    1  1 EQPL   INST   0
  6     40  880701  70453  0     6         6    1  1 SEQP   INST   0
PRINT'S EQPL INST(1 9,1 1,'

  R  C     1
     1  4.9800E 01
     2  1.4082E-06
     3  3.4815E 05
     4  9.3240E 06
     5  2.0100E-05
     6  2.6194E 03
     7  1.41 7E  3
     8  1.2347E 03
     9  0.0000E 00
DAL UNIT PACKED TO   6 ELEMENTS
DAL UNIT PACKED TO   41 ELEMENTS
CPU  TOTAL EXECUTION RUN        16.76      1..00      28.71
***CIAU***
```

162

Table 4 presents the command procedure file used to input to SEMOD and to execute SEMOD. The file is annotated to assist the reader.

Table 4   SEMOD Command File DT01.COM

```
$ ASSIGN DT01 OUT FOR006          Assign output file name
$ RUN VAPEPS                      Run VAPEPS
SEMOD 5, DT01                     Run SEMOD
TEXT                          ⎫
MODEL DT01                    ⎪
ELEMENTS EXTA, INST, INTA     ⎪
EXTA IS EXCITATION            ⎬  Comments
FREQUENCY RANGE 50 HZ TO 2,000 HZ ⎪
MODEL BY CLARK BECK           ⎪
DATE 07/20/88                 ⎪
ZZZZ                          ⎭
ELNAME                            Enter ELNAME
EXTA, 1                       ⎫
DESCRIPT=ACOUSTIC-TEST-CELL   ⎪
RHO=1.15E-7                   ⎪
CO=1.34E4                     ⎬  Describe EXTA
VOLUME=1.33E7                 ⎪
AP=2.8E4                      ⎪
AAC=.01                       ⎪
DONE                          ⎭
INTA, 1                       ⎫
DESCRIPT=DTV-INTERSTAGE-VOLUME ⎪
RHO=1.15E-7                   ⎪
CO=1.34E4                     ⎬  Describe INTA
AF=2.13E4                     ⎪
ACC=.01                       ⎪
DONE                          ⎭
INST, 4                       ⎫
DESCRIPT=DTV-INTERSTAGE-STRUCTURE ⎪
RHO=3.481E-5                  ⎪
CL=2.01E5                     ⎪
H=.4965                       ⎪
AP=2.13E4                     ⎪
BL=74.                        ⎪
ALX=17.                       ⎪
ALY=8.9                       ⎪
D=91.5                        ⎬  Describe INST
DLF=.01                       ⎪
E=1.408E6                     ⎪
PATA=25.9                     ⎪
RHOS=9.324E-6                 ⎪
ASMS=0                        ⎪
CO=1.34E4                     ⎪
PIVOTFRQ=300                  ⎪
DONE                          ⎭
DONE                              Exit ELNAME
```

(Continued)

Table 4 (Continued)   SEMOD Command File DT01.COM

```
PATHNAME                                          Enter PATHNAME
EXTA, INST, 2
DONE                                          } Describe path 1
INTA, INST, 2
DONE                                          } Describe path 2
EXTA, INST, INTA, 5
DONE                                          } Describe path 3
DONE                                            Exit PATHNAME
SETEXC EXTA
FREQUENCY 50.,2000.                             Make EXTA the
EXCITATION                                      excitation element and enter
126.8, 130.9, 131.5, 132.5, 132.0, 133.4       1/3 octave band levels
132.0, 132.9, 134.5, 135.4, 133.0, 133.3       (See Table 1)
133.3, 132.5, 131.2, 130.3, 128.9
MDENS                                           Calculate modal density
ATACALC                                         Calculate loss factors
ATACO                                           Calculate coupling factors
CFAC 7, 1, 4                                    Define engineering units
TPRD                                            Predict responses
POWER                                           Calculate power flow
DONE                                            Exit SEMOD
RUN=OVER 5, RESP, DT01 5, OA, DT01           } Calculate overall SPL
RUN=OVER 5, RESP, DT01 5, GRMS DT01 50.,2000 } Calculate overall grms
PRIND 5, TEXT, DT01
PRIND 5, MNAM, DT01                          } Print text and element names
SEMOD 5, DT01                                   Enter SEMOD
LIST RESP
ELNAME
LIST
DONE                                            Print responses,
PATHNAME                                        element names,
LIST                                            pathnames,
DONE                                            power flows,
LIST PCRF                                       loss factors,
LIST ATA                                        critical frequencies,
LIST CRIT                                       modal density,
LIST DENS                                       ring frequencies
LIST RING
DONE                                            Exit SEMOD
PRIND 5, OA, DT01                               Print overall SPL
PRIND 5, GRMS, DT01                             Print overall grms
PACK 5                                          Pack DAL 5
TOC 5                                           Print Table of Contents
END                                             Exit VAPEPS
$LASER DT01.OUT                                 Print output file
$LASER DT01.COM                                 Print comand file
$DEASSIGN FOR006
$EXIT                                           Exit command file
```

SEMOD Output

The command procedure file shown in Table 4 creates an output file, DT01.OUT. The output file serves as documentation for the prediction. An edited version of the output file for this example is contained in the Appendix. The SEMOD Text file has been included to provide a summary description. The excitations and responses of the model elements (RESP) are printed out to provide a tabulation of frequency and level. The overall sound pressure level and overall grms levels are printed out in files OA and GRMS. These files are created by using the VAPEPS command RUN=OVER. The PATHNAME and ELNAME descriptions are shown. Five other SEMOD files are included in the output to assist in evaluation of the model: power flow in each path (PCRF); damping and coupling loss factors (ATA); critical frequency (CRIT); modal densities (DENS); ring frequencies (RING). The final listing in the output file is the table of contents of the VAPEPS DAL file created during the execution of SEMOD.

Model Revision

SEMOD models can be easily revised and executed. This makes the program ideal for preliminary design. The use of a command procedure file makes revision easy. SEMOD execution and data printout time for the analyses presented in this paper required less than five minutes per configuration.

HINT. Execute the VAPEPS commands and SEMOD interactively to become familiar with the program and the command procedures. When you are familiar with how the program executes, then use the command procedure files to expedite analysis.

CONFIGURATIONS ANALYZED

Seven IUS DTV configurations were analyzed. The configurations are described in Table 5.

The interstage model DT01 is described in the example prediction. Model numbers DT02, DT03 and DT13 are the same as DT01 except for the damping (DLF) and mass loading (ASMS) Figure 5 is the SEMOD diagram for DT01, DT02, DT03 and DT13.

Model numbers DT04 and DT05 represent the full IUS DTV. DT04 represents the DTV with unloaded structure while DT05 and DT15 represent loaded structure. Figure 7 is the SEMOD diagram for DT04, DT05 and DT15.

Table 5   Configurations Analyzed

Model Number	Acoustic Element	Vibration Element	Damping (DLF)	Mass (ASMS)
DTO1	EXTA INTA	INST	.01	0
DTO2	EXTA INTA	INST	.10	0
DTO3	EXTA INTA	INST	.01	13.7
DTO4	EXTA INTA INES	INST ESSB ESSC SRM2	.01 .01 .01 .10	0 0 0 15.5
DTO5	EXTA INTA INES	INST ESSB ESSC SRM2	.01 .01 .01 .10	13.7 1.3 13.7 15.5
DT13	EXTA INTA	INST	.01	1.3
DT15	EXTA INTA INES	INST ESSB ESSC SRM2	.01 .01 .01 .10	1.3 1.3 1.3 15.5
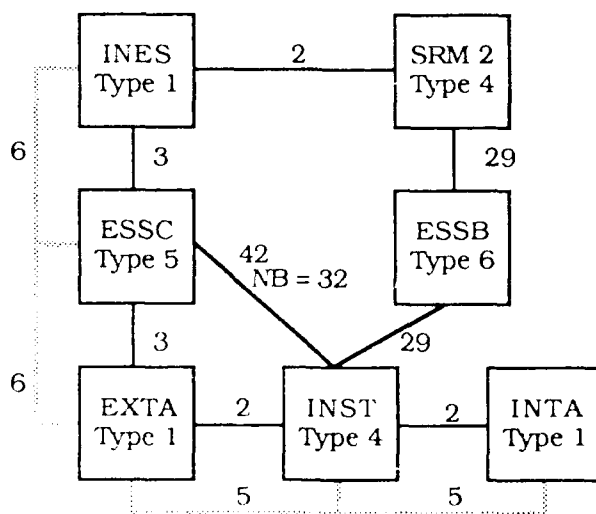
Fig. 7   SEMOD Diagram for DTO4 and DTO5

Table 6 contains a description of Model DT04 element names and path names. Model DT05 and DT15 are the same as DT04 except for DLF values and ASMS values as listed in Table 5.

Table 6   DT04 Description

```
EXTA Type 1
Description = acoustic test cell
RHO = 1.150E-7              CO = 1.340E4         Volume = 1.33E7
AP = 2.8E4                  AAC = .01

INTA Type 1
Description = DTV interstage volume
RHO = 1.150E-7             CO = 1.340E4          Volume = 3.40E5
AP = 2.13E4               AAC = .01

INST Type 4
Description = DTV interstage structure
RHO = 3.481E-5   CL = 2.01E5      H = .4965            AP = 2.13E4
BL = 74.         ALX = 17.        ALY = 8.9            D = 91.5
DLF = .01        E = 1.60E7       PATA = 25.9          RHOS = 9.32E-6
ASMS = 0.        CO = 1.34E4      PIVOTFRQ = 300.


ESSB Type 6
Description = DTV ESS beam
RHO = 2.59E04    CL = 2.0E5       ASMS = 0             DLF = .01
CNT = 32         BL = 17.         B= 1.
H = .71          E = 10.6E6       G = 4.E6

ESSC Type 5
Description = DTV ESS cone
RHO = 8.49E-5    CL = 2.0E5       H = .143             AP = 8.64E3
BL = 26.         ALX = 27.4       ALY = 10.1           D = 109.
DLF = .01        E = 1.06E7       PATA = 37.5          BETA = 18.6
RHOS = 8.29E-6   ASMS = 0.        CO = 1.34E4          PIVOTFRQ = 300.

INES Type 1
Description = DTV  ESS volume
RHO = 1.15E7     CO = 1.34E4          AP = 8.64E3
AAC = .01        Volume = 1.58E5


SRM Type 4
Description = DTV second stage motor
RHO = 2.60E-4    CL = 2.0E5       H = .40              D = 63.
BL = 40.         ALX = 6.2        ALY = 40.            RHOS = 1.E-4
DLF = .01        E = 1.06E7       PATA = 46.2
ASMS = 15.5      CO = 1.34E4      AP = 7.9E3
```

Interstage Model

Figure 8 shows comparisons of the predicted noise spectra inside the interstage (INTA) with an internal noise measurement from the IUS DTV. Predicted noise spectra are shown for two damping values (DLF = .01 and .10). The higher damping lowers the noise level 3 db. Mass loading of the interstage did not change the internal noise level.
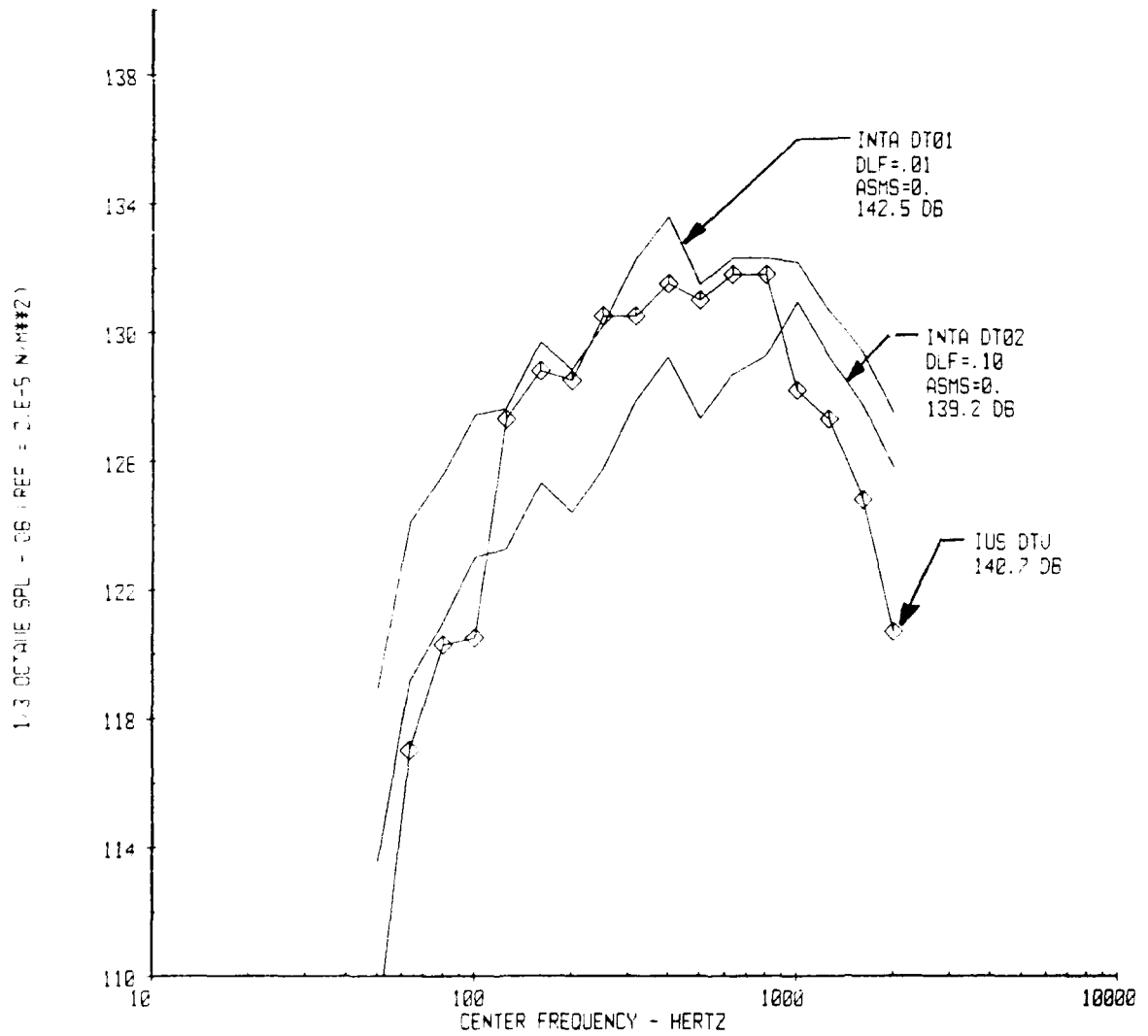

Fig. 8   Prediction/Test Comparison
Interstage Internal Noise
Damping Effect

168

Figure 9 presents the predicted interstage vibration for unloaded structure (ASMS = 0.) Predictions are shown for two damping values, DLF = .01 and .10. The predictions are compared with an envelope of 5 DTV vibration measurements.
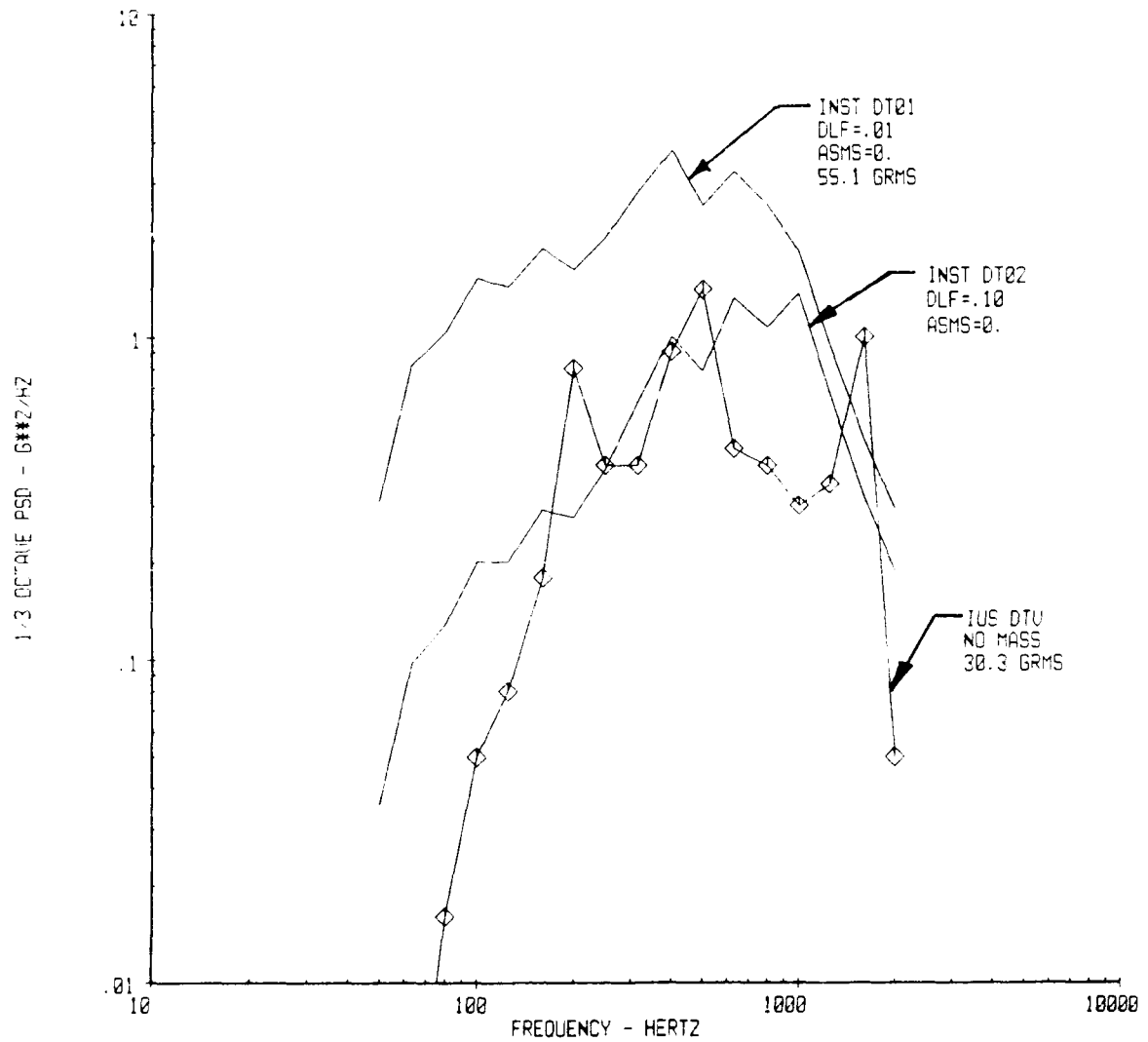
Fig. 9   Prediction/Test Comparison,
Interstage Vibration,
Damping Effect

Figure 10 is a comparison of predicted vibration spectra for mass loaded structure (ASMS = 1.3 and 13.7) with an envelope of 3 vibration spectra from IUS DTV loaded structure. The mass loading value has the units of lbs-sec^2/in. Two values of mass loading were evaluated because the exact mass loading of the structure cannot be accurately included in SEMOD. The masses on the DTV are groups of batteries. The mass loading in SEMOD is one entry, ASMS, for the element, INST.
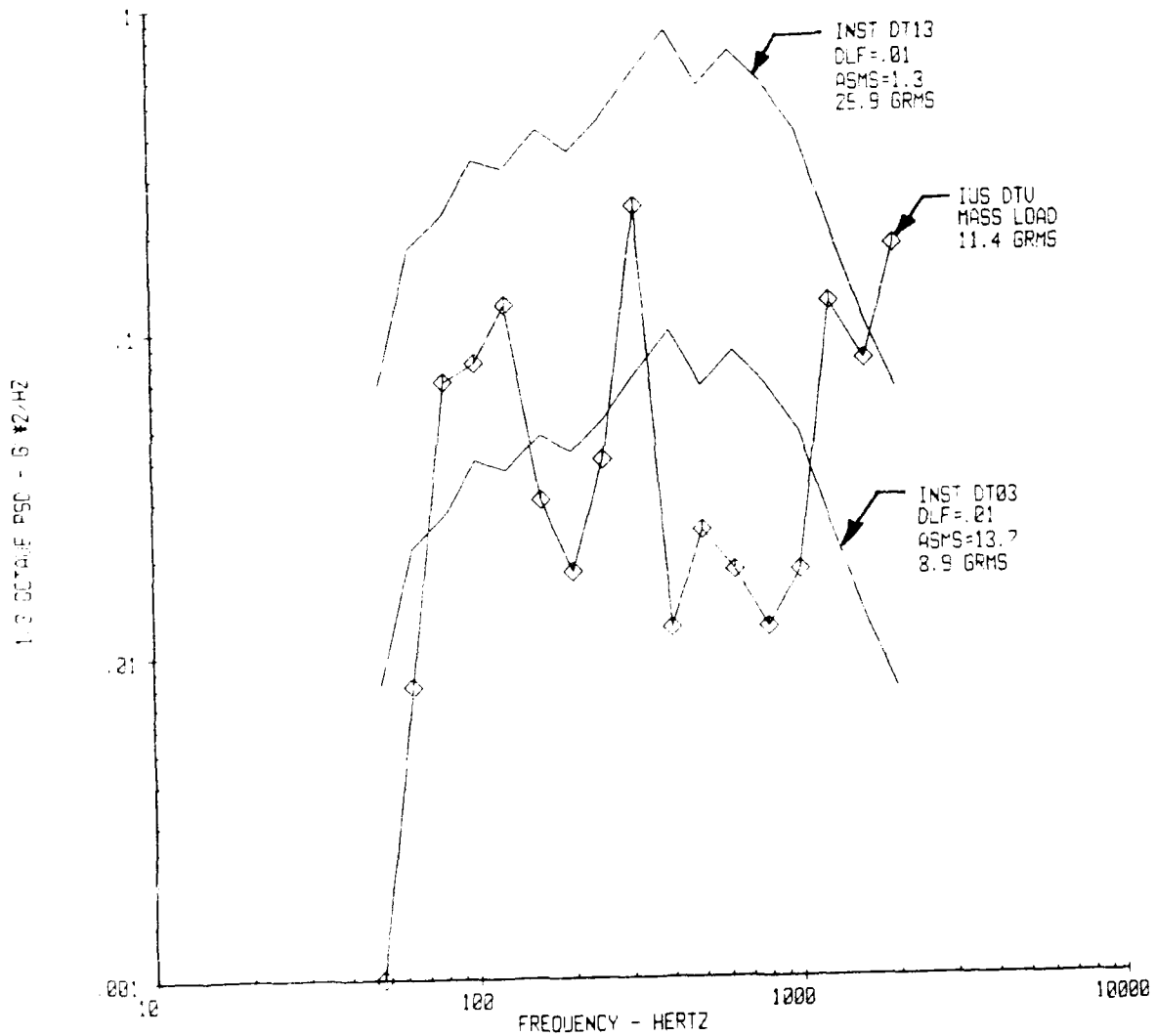
Fig. 10   Prediction/Test Comparison,
Interstage Vibration,
Mass Load Effect

Figure 11 is a prediction of the interstage internal noise for the DTO4 model. The prediction is compared with an interstage internal noise measurement from the DTV.
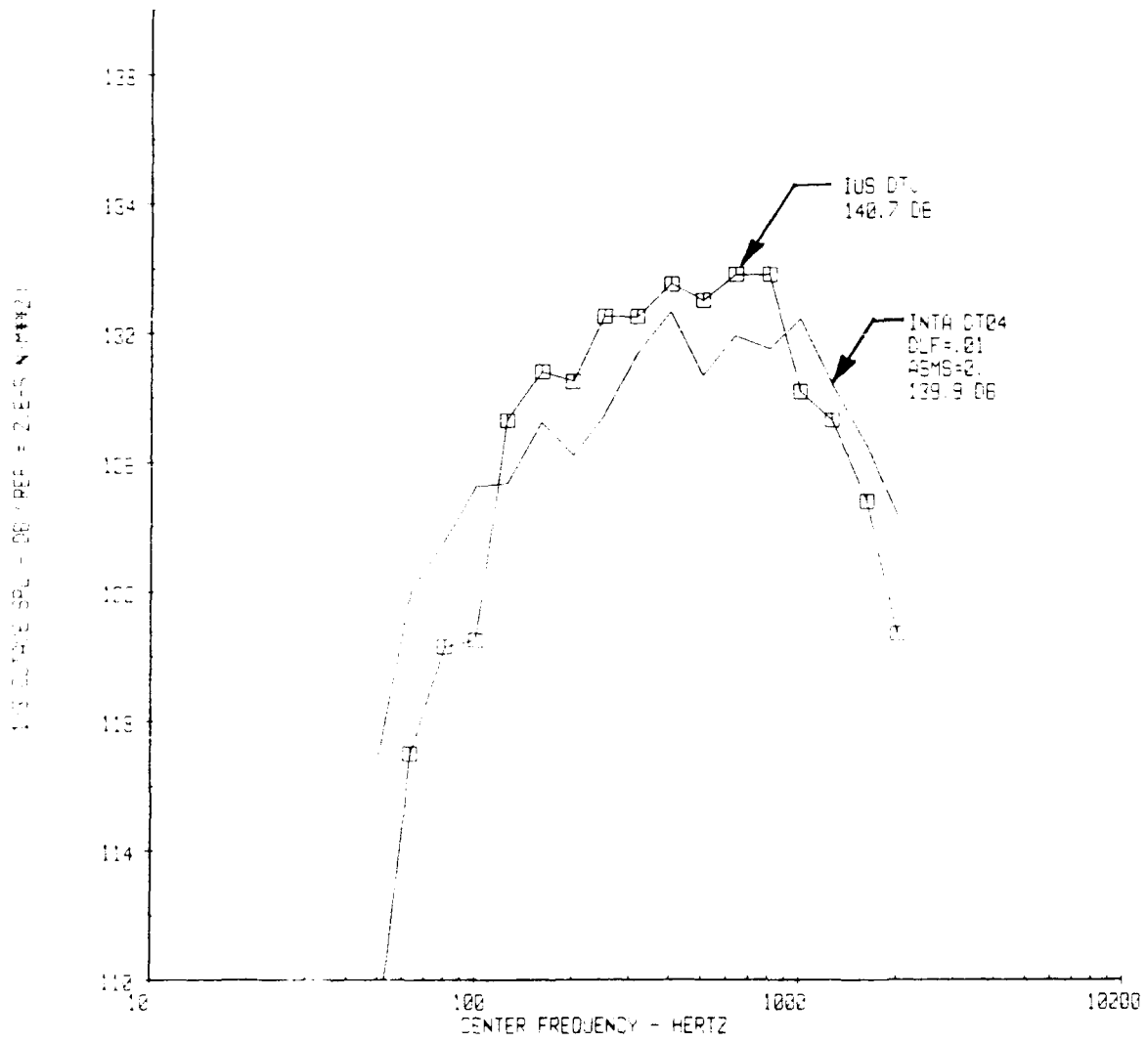
Fig. 11   Prediction/Test Comparison
Interstage Internal Noise
DTO4 Model

Figure 12 contains a comparison of the DTV interstage vibration response with the prediction from the DTO4 model. The DT/ vibration spectrum is the envelope of 5 vibration spectra.
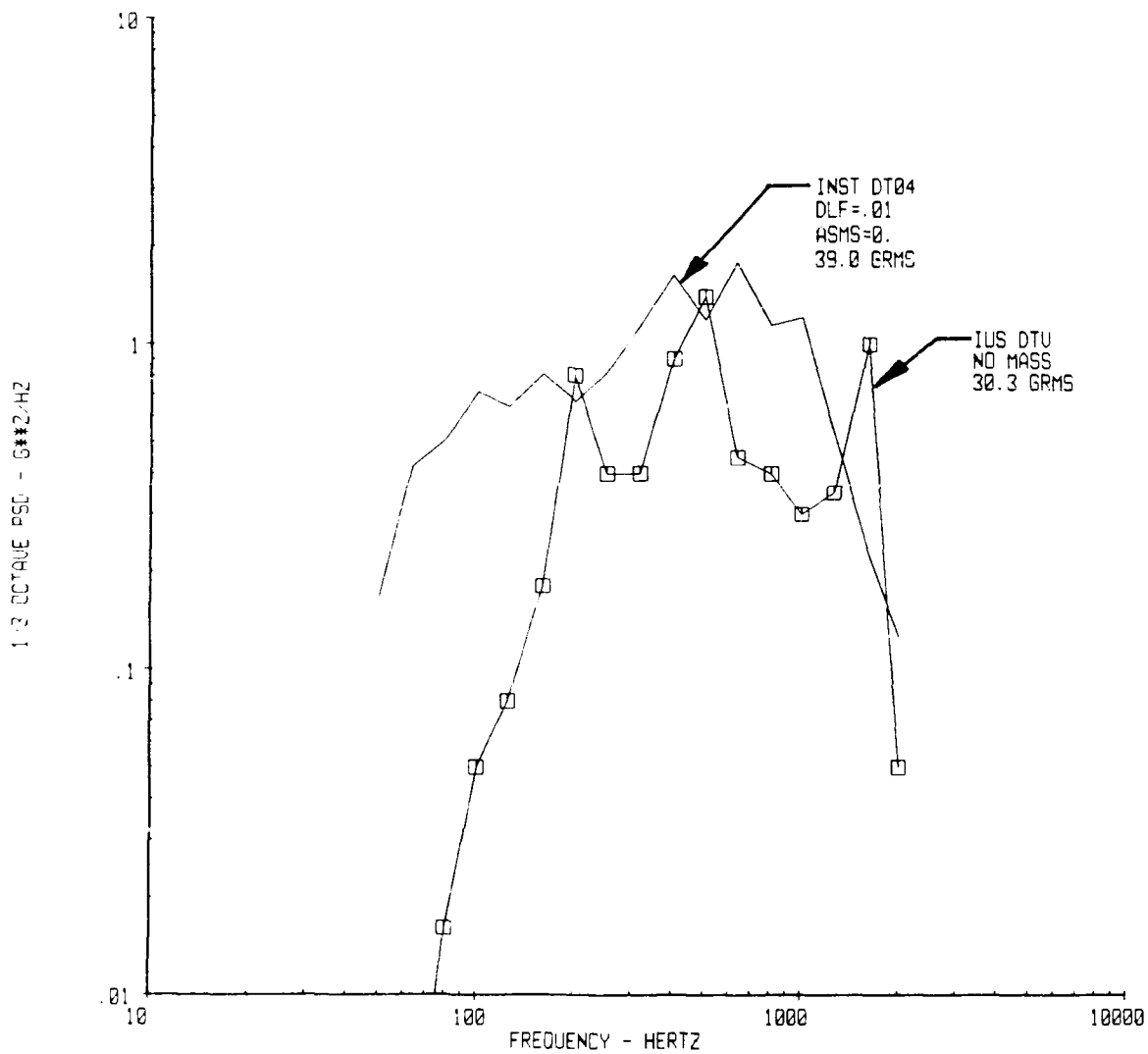
Fig. 12   Prediction/Test Comparison,
          Interstage Vibration,
          No Mass Load

172

Figure 13 shows an envelope of 3 vibration spectra from DTV mass loaded interstage structure. The structure was mass loaded by a group of batteries. The SEMOD predictions are shown for 2 values of ASMS, 13.7 and 1.3.
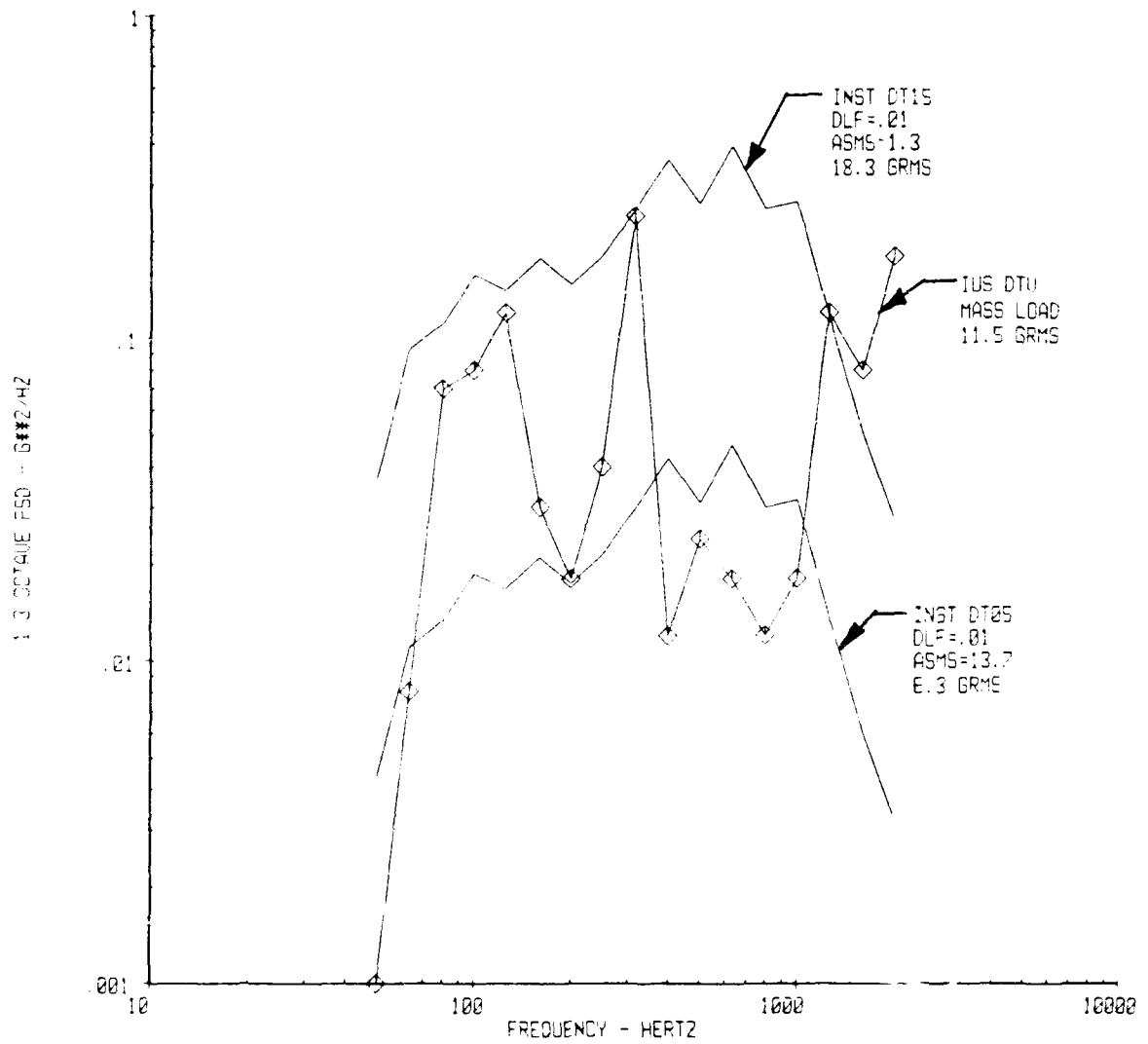
Fig. 13   Prediction/Test Comparison,
          Interstage Vibration,
          Mass Load Effect

173

Figure 14 compares the DTV unloaded equipment support section deck vibration response with the SEMOD prediction. The DTV vibration spectra is the envelope of 42 vibration measurements.
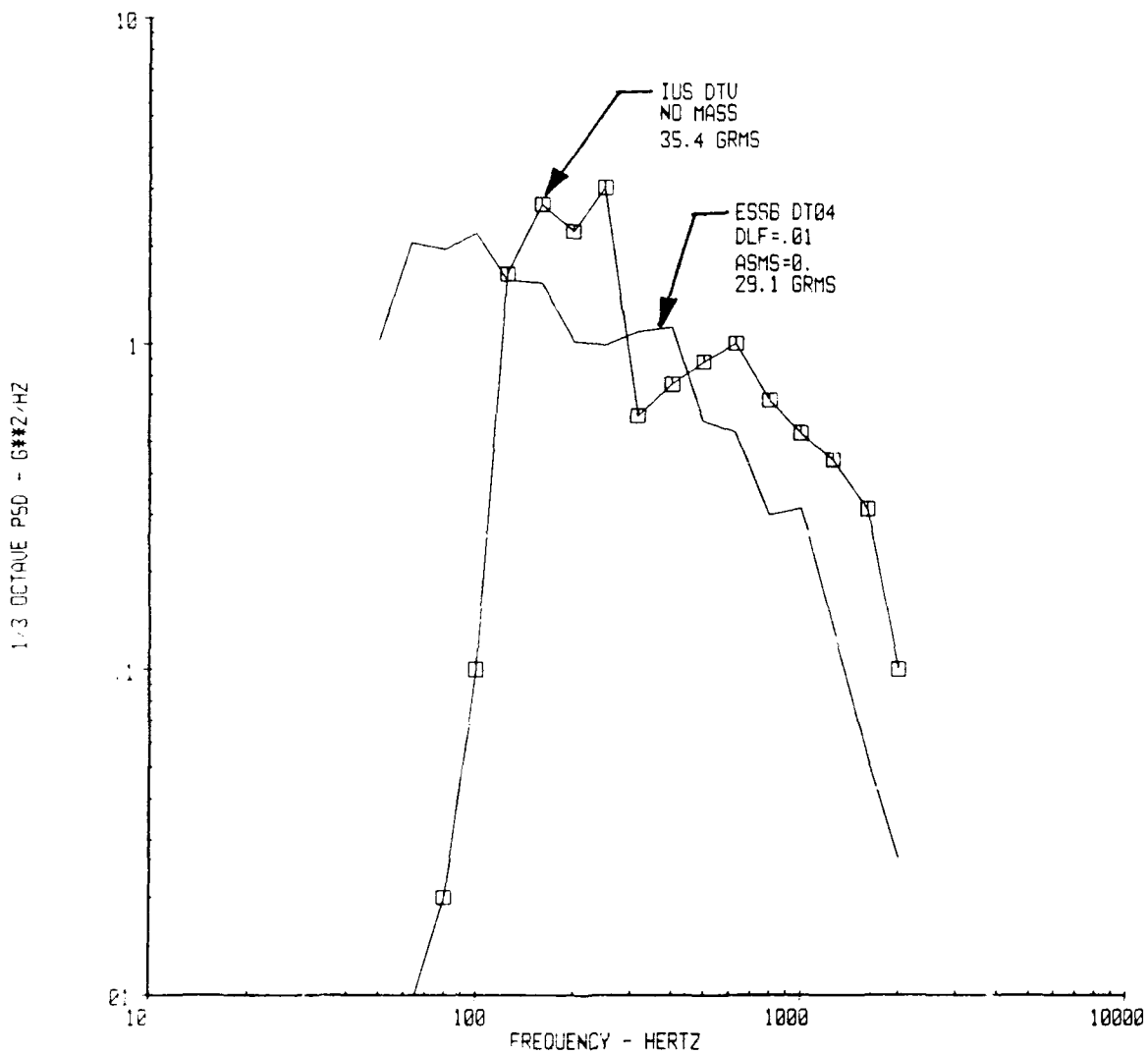
Fig. 14   Prediction/Test Comparison,
ESS Deck Vibration,
No Mass Load

Figure 15 contains a comparison of the SEMOD prediction and the DTV envelope of vibration spectra from the ESS loaded deck.
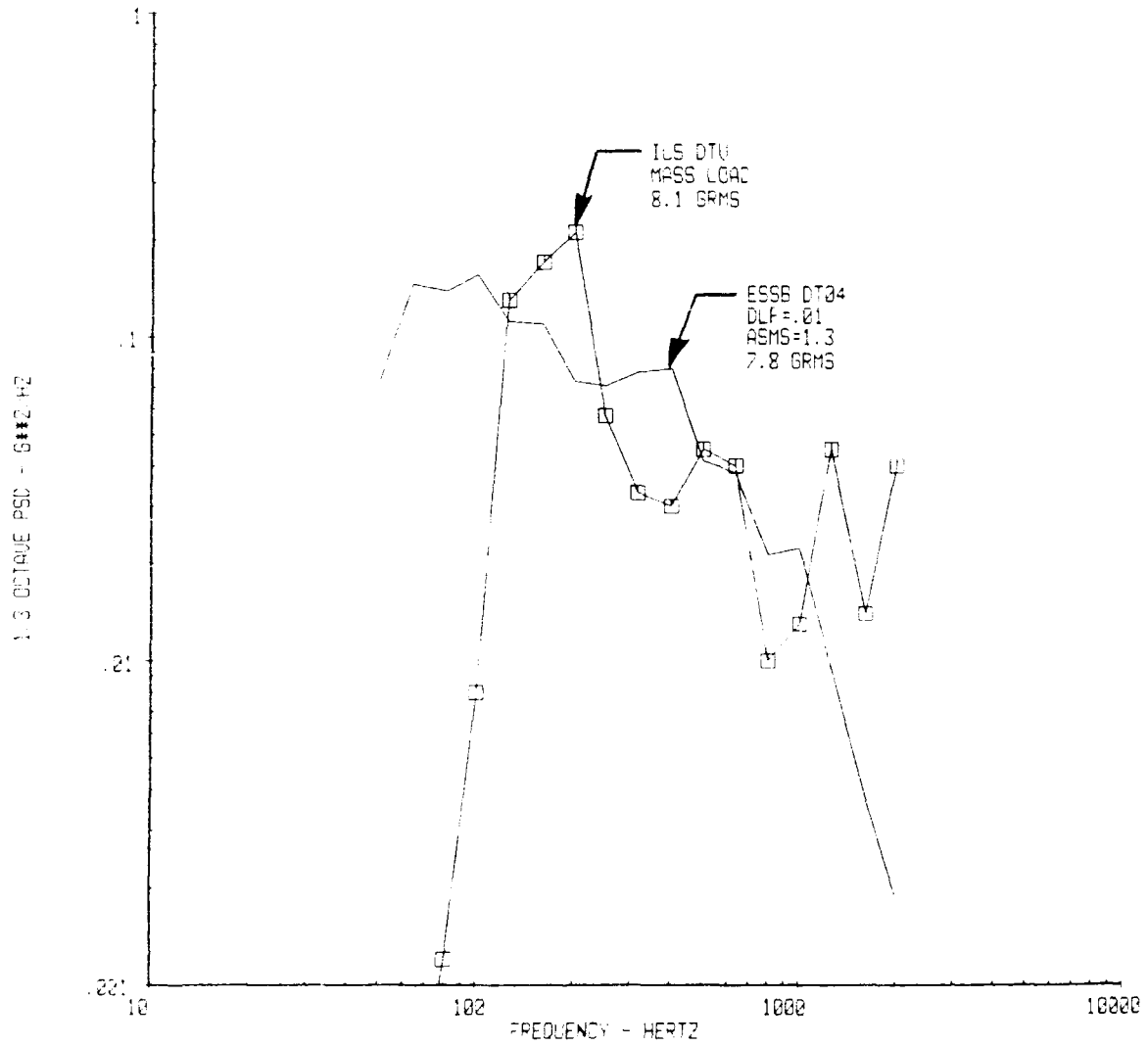
Fig. 15 Prediction/Test Comparison,
ESS Deck Vibration,
Mass Load

Figure 16 shows vibration spectra for unloaded ESS conic structure. The DTV vibration spectra is an envelope of 3 vibration measurements.
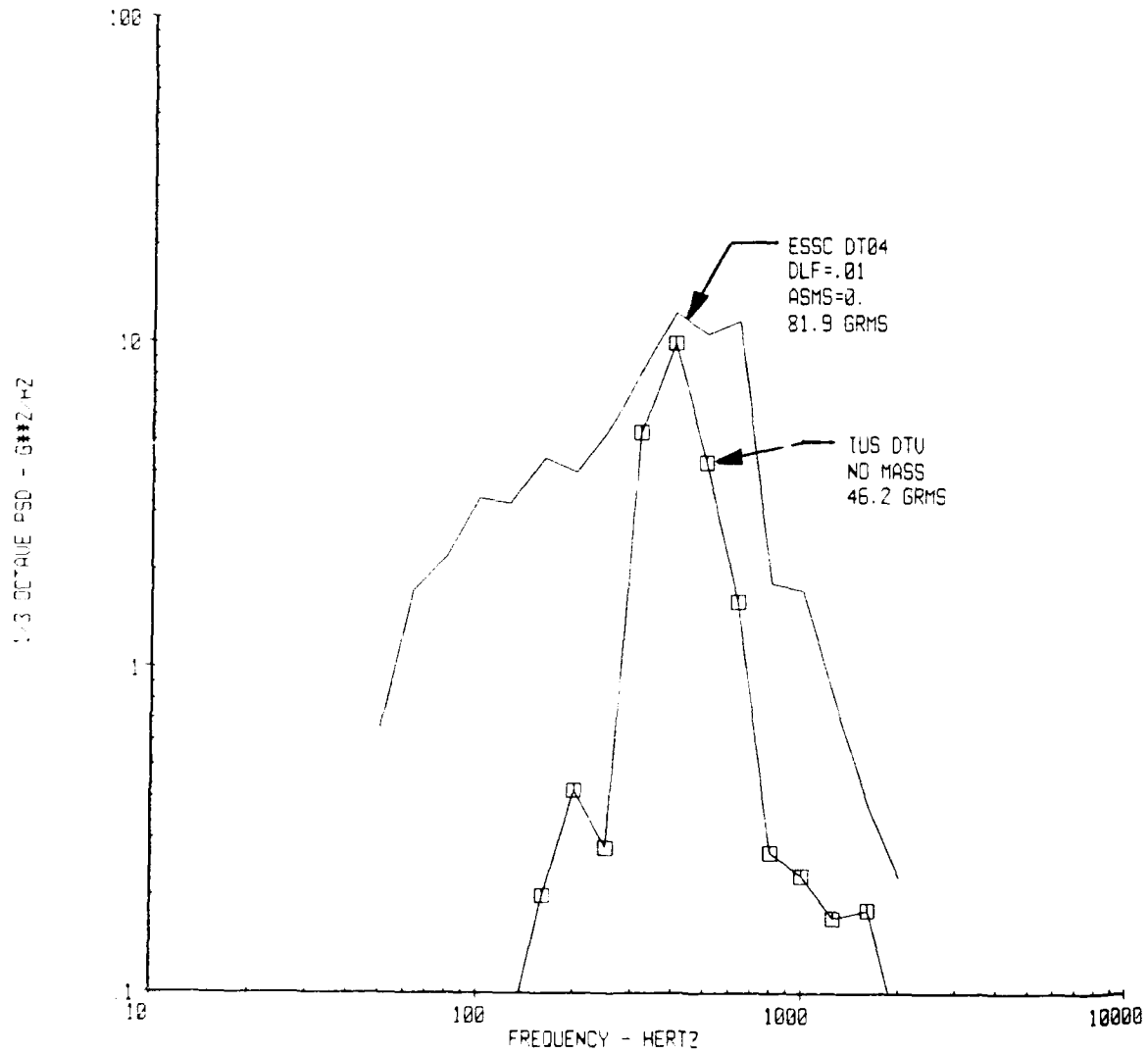
Fig. 16   Prediction/Test Comparison,
            ESS Cone Vibration,
            No Mass Load

Figure 17 presents vibration spectra for loaded ESS conic structure. Predictions are shown for 2 values of mass loading, ASMS = 1.3 and 13.7. The predictions were made for 2 mass loading values because the exact mass loading for the structure cannot be accurately included in SEMOD. The masses on the ESS cone are concentrated loads in the form of avionics packages attached to the shell at irregular intervals. The mass loading in SEMOD, ASMS, is one entry for the entire structure.
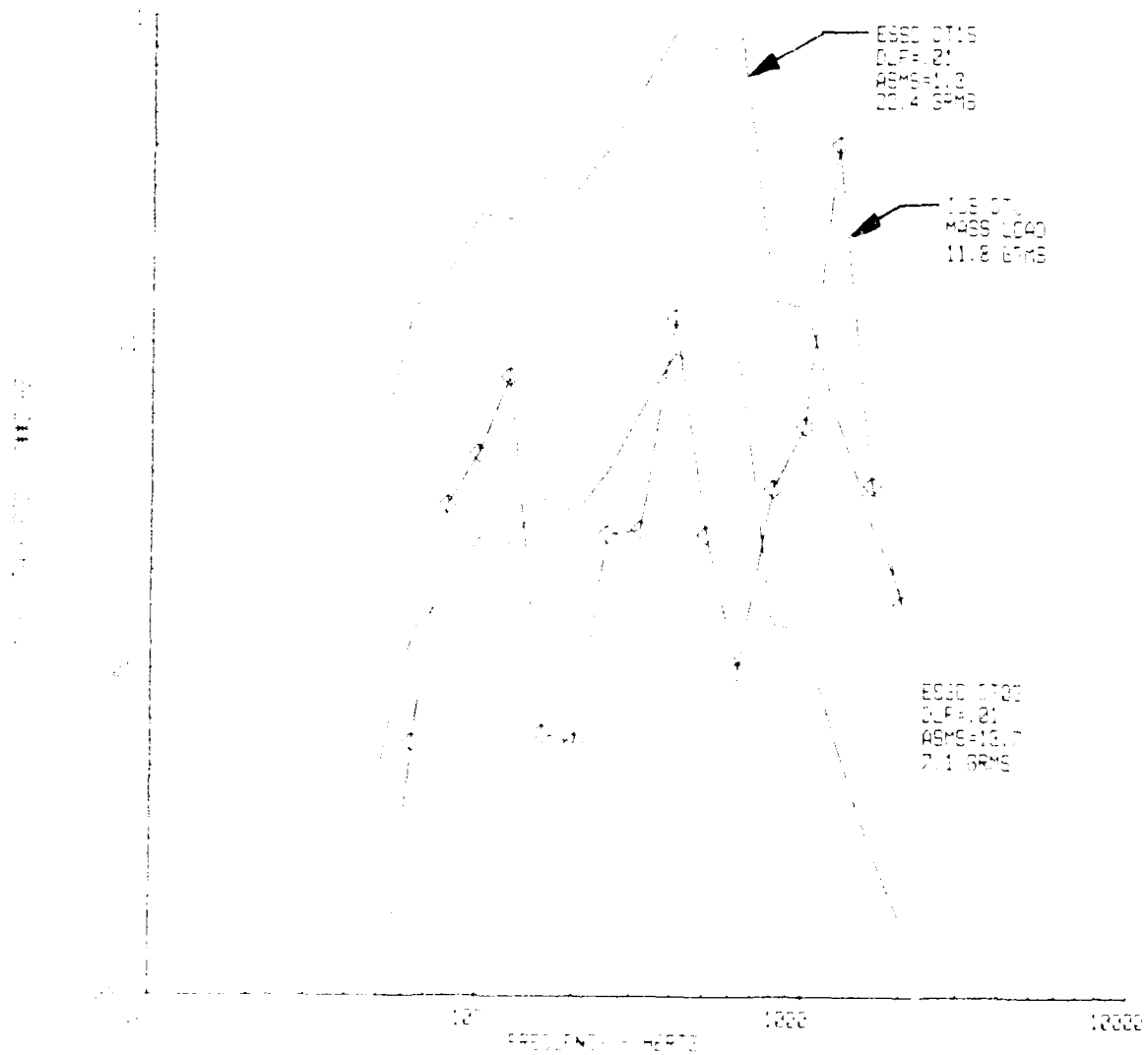

Fig. 17   Prediction/Test Comparison,
ESS Cone Vibration,
Mass Load Effect

Figure 18 compares the predicted vibration response of the second stage solid rocket motor to the measured vibration response from a single DTV motor measurement. The DTV motor measurement was made in a direction normal to the motor surface.
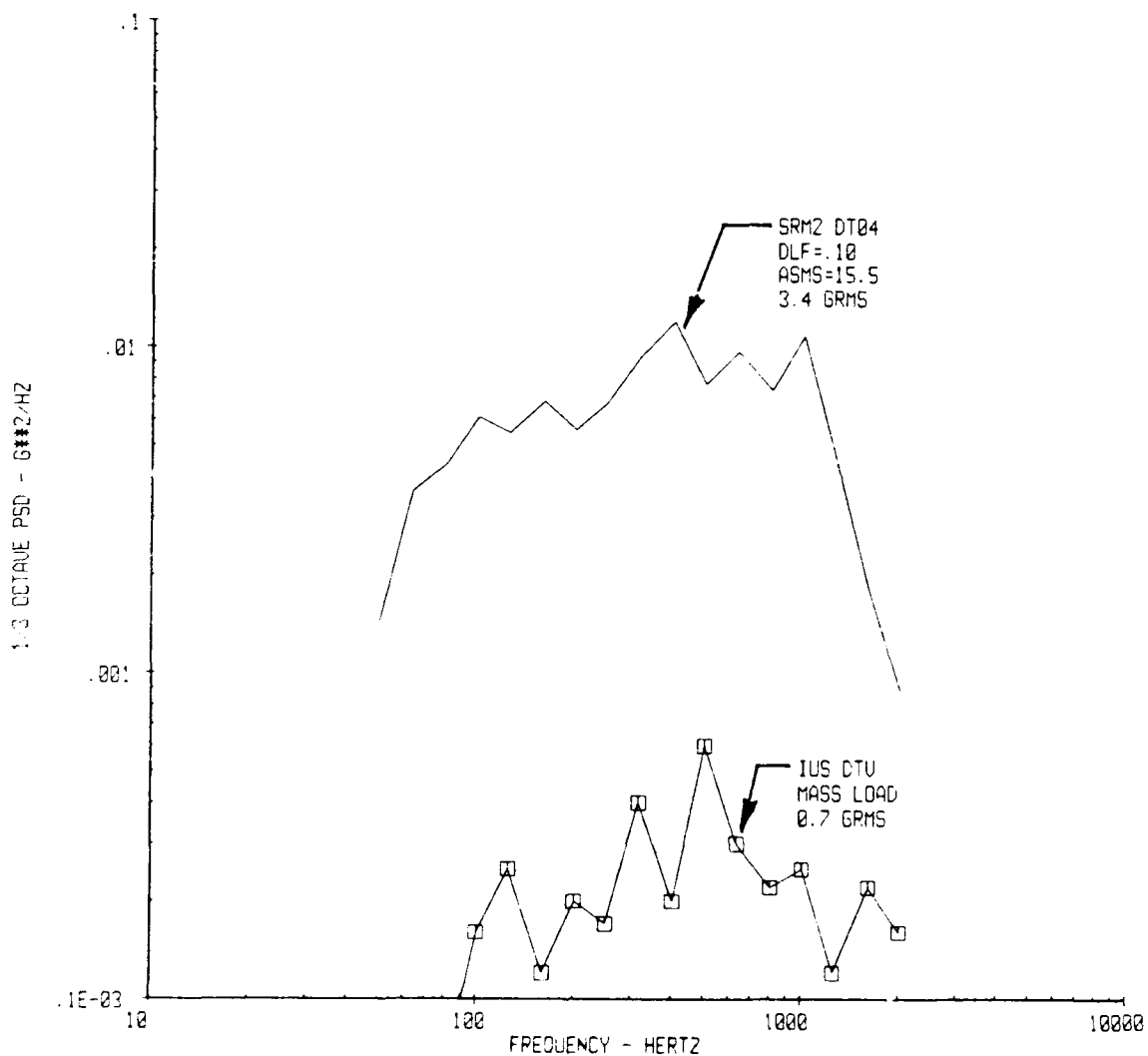

Fig. 18   Prediction/Test Comparison,
Solid Rocket Motor Vibration,
Model DT04

CONCLUSIONS

VAPEPS SEMOD provided reasonable noise and vibration predictions for the IUS DTV vehicle at frequencies greater than 100 Hz.

VAPEPS SEMOD is a useful noise and vibration prediction tool. SEMOD is particularly useful in preliminary design applications. Design concepts can be modeled easily and prediction results can be obtained quickly. The predictor is also useful for solving noise and vibration problems. A model can be defined to simulate the problem and proposed solutions can be evaluated quickly.

RECOMMENDATIONS

Computer command files should be used for model definition and SEMOD execution. The command files can be edited and executed to provide a large number of estimates in a short time.

An automated plot routine should be set up in the command file. Prediction evaluation is enhanced by the use of plotted vibration and noise spectra.

REFERENCE

"Volume II: VAPEPS User's Manual", June 1987. This manual and the VAPEPS computer program is available from:

<div align="center">

VAPEPS DBMC

Jet Propulsion Laboratory

Mail Stop 301-456

4800 Oak Grove Drive

Pasedena, CA 91109

</div>

APPENDIX
OUTPUT FILE FOR MODEL DT01, DT01.OUT

```
VAP5.2 1-07/27/88-13:55:20      134400
Creating new model DT01

     1          MODEL DT01
     2          ELEMENTS EXTA,INST,INTA
     3          EXTA IS EXCITATION
     4          FREQUENCY RANGE 50 HZ TO 2000 HZ
     5          MODEL BY CLARK BECK
     6          DATE 07/20/88
```

Excitations and responses for model DT01

Frequency Hertz	EXTA dB	INTA dB	INST $G^{**}2/Hz$
50.0	126.8	118.9	3.1142E-01
63.0	130.9	124.1	8.1673E-01
80.0	131.5	125.6	1.0344E+00
100.0	132.5	127.4	1.5230E+00
125.0	132.0	127.6	1.4283E+00
160.0	133.4	129.7	1.8797E+00
200.0	132.0	128.8	1.6159E+00
250.0	132.9	130.2	2.0171E+00
315.0	134.5	132.3	2.8146E+00
400.0	135.4	133.6	3.7847E+00
500.0	133.0	131.5	2.5512E+00
630.0	133.3	132.3	3.2541E+00
800.0	133.3	132.3	2.5534E+00
1000.0	132.5	132.2	1.8388E+00
1250.0	131.2	130.7	9.4145E-01
1600.0	130.3	129.4	4.8063E-01
2000.0	128.9	127.5	2.937_ 1

```
OVERALL SPL
    EXTA  1.4473E+02
    INTA  1.4246E+02

OVERALL GRMS
    INST  5.6411E+01
```

Description of elements, ELNAME

```
EXTA
DESCRIPT=ACOUSTIC-TEST-CELL
TYPE       =           1
RHO        = 1.150E-07 CO        = 1.340E+04 VOLUME   = 1.330E+07
AP         = 2.800E+04
AAC        = 1.000E-02


INTA
DESCRIPT=DTV-INTERSTAGE-VOLUME
TYPE       =           1
RHO        = 1.150E-07 CO        = 1.340E+04 VOLUME   = 3.400E+05
AP         = 2.130E+04
AAC        = 1.000E 02


INST
DESCRIPT=DTV-INTERSTAGE-STRUCTURE
TYPE       =           4
RHO        = 3.481E-05 CL        = 2.010E+05 H        = 4.965E-01
AP         =2.130E+04
BL         = 7.400E+01 ALX       = 1.700E+01 ALY      = 8.900E+00
D          = 9.150E+01
DLF        = 1.000E-02 E         = 1.060E+07 PATA     = 2.590E+01
RHOS       = 9.32E-06
ASMS       = 0.000E+00 CO        = 1.340E+04 PIVOTFRQ= 3.000E+02
OK
```


Description of paths, PATHNAME

```
EXTA        INST
TYPE       =           2

INTA        INST
TYPE       -           2

EXTA        INST      INTA
TYPE                  5
OK
```

Percent power flow per path for element INTA   in model DT01

Frequency Hertz	INTA INTA	INTA INST	INST INTA	EXTA INST INTA	INTA INST EXTA
50.0	-3.20%	-93.59%	80.41%	19.59%	-3.21%
63.0	-3.48%	-91.73%	76.98%	23.02%	-4.78%
80.0	-3.78%	-89.64%	74.67%	25.33%	-6.58%
100.0	-4.07%	-87.76%	73.76%	26.24%	-8.18%
125.0	-4.36%	-86.11%	73.94%	26.06%	-9.52%
160.0	-4.69%	-84.72%	75.13%	24.87%	-10.59%
200.0	-4.97%	-83.92%	76.91%	23.09%	-11.11%
250.0	-5.19%	-83.65%	79.25%	20.75%	-11.16%
315.0	-5.27%	-84.13%	82.31%	17.69%	-10.60%
400.0	-4.95%	-85.96%	86.22%	13.78%	-9.09%
500.0	-4.67%	-87.69%	89.17%	10.83%	-7.64%
630.0	-3.04%	-92.82%	94.80%	5.20%	-4.14%
800.0	-4.52%	-84.89%	86.69%	13.31%	-10.59%
1000.0	-1.83%	-95.20%	96.80%	3.20%	-2.97%
1250.0	-3.80%	-91.94%	95.21%	4.79%	-4.26%
1600.0	-8.31%	-85.55%	92.42%	7.58%	-6.13%
2000.0	-14.09%	-78.83%	90.21%	9.79%	-7.09%

Percent power flow per path for element INST in model DT01

Frequency Hertz	INST INST	EXTA INST	INST EXTA	INTA INST	INST INTA
50.0	-75.82%	85.93%	-12.09%	14.07%	-12.09%
63.0	-71.13%	82.79%	-14.44%	17.21%	-14.44%
80.0	-65.67%	79.39%	-17.17%	20.61%	-17.17%
100.0	-60.07%	76.24%	-19.97%	23.76%	-19.97%
125.0	-54.05%	73.24%	-22.97%	26.76%	-22.97%
160.0	-47.03%	70.14%	-26.49%	29.86%	-26.49%
200.0	-40.46%	67.52%	-29.77%	32.48%	-29.77%
250.0	-33.76%	65.04%	-33.12%	34.96%	-33.12%
315.0	-26.66%	62.52%	-36.67%	37.48%	-36.67%
400.0	-20.27%	60.25%	-39.87%	39.75%	-39.87%
500.0	-15.83%	58.62%	-42.08%	41.38%	-42.08%
630.0	-9.47%	55.68%	-45.26%	44.32%	-45.26%
800.0	-9.47%	55.68%	-45.26%	44.32%	-45.26%
1000.0	-2.04%	51.83%	-48.98%	48.17%	-48.98%
1250.0	-2.53%	52.94%	-48.74%	47.06%	-48.74%
1600.0	-3.40%	55.29%	-48.30%	44.71%	-48.30%
2000.0	-3.89%	58.01%	-48.05%	41.99%	-48.05%

Damping and Coupling Loss Factors for Model DT01

Frequency Hertz	EXTA EXTA	INTA INTA	INST INST	EXTA INST	INST EXTA
50.0	2.2452E-04	6.6810E-03	6.0000E-02	4.9970E-03	9.5661E-03
63.0	1.7819E-04	5.3024E-03	4.7619E-02	3.5700E-03	9.6661E-03
80.0	1.4032E-04	4.1756E-03	3.7500E-02	2.5301E-03	9.8026E-03
100.0	1.1226E-04	3.3405E-03	3.0000E-02	1.8418E-03	9.9726E-03
125.0	8.9807E-05	2.6724E-03	2.4000E-02	1.3481E-03	1.0202E-02
160.0	7.0161E-05	2.0878E-03	1.8750E-02	9.6358E-04	1.0559E-02
200.0	5.6129E-05	1.6703E-03	1.5000E-02	7.2063E-04	1.1036E-02
250.0	4.4903E-05	1.3362E-03	1.2000E-02	5.5011E-04	1.1774E-02
315.0	3.5638E-05	1.0605E-03	9.5238E-03	4.3279E-04	1.3101E-02
400.0	2.8065E-05	8.3513E-04	7.5000E-03	3.7095E-04	1.4754E-02
500.0	2.2452E-05	6.6810E-04	6.0000E-03	3.2083E-04	1.5950E-02
630.0	1.7819E-05	5.3024E-04	4.7619E-03	4.1335E-04	2.2756E-02
800.0	1.4032E-05	4.1756E-04	3.7500E-03	2.0062E-04	1.7920E-02
1000.0	1.1226E-05	3.3405E-04	3.0000E-03	4.4448E-04	7.1925E-02
1250.0	8.9807E-06	2.6724E-04	2.4000E-03	1.6527E-04	4.6317E-02
1600.0	7.0161E-06	2.0878E-04	1.8750E-03	5.4916E-05	2.6669E-02
2000.0	5.6129E-06	1.6703E-04	1.5000E-03	2.3893E-05	1.8526E-02

Frequency Hertz	INTA INST	INST INTA	EXTA INST INTA	INTA INST EXTA
50.0	1.9547E-01	9.5661E-03	1.7128E-04	6.7000E-03
63.0	1.3965E-01	9.6661E-03	1.8619E-04	7.2834E-03
80.0	9.8971E-02	9.8026E-03	1.8559E-04	7.2598E-03
100.0	7.2046E-02	9.9726E-03	1.7158E-04	6.7110E-03
125.0	5.2736E-02	1.0202E-02	1.4908E-04	5.8316E-03
160.0	3.7693E-02	1.0559E-02	1.2043E-04	4.7108E-03
200.0	2.8189E-02	1.1036E-02	9.5372E-05	3.7307E-03
250.0	2.1519E-02	1.1774E-02	7.3360E-05	2.8697E-03
315.0	1.6930E-02	1.3101E-02	5.4557E-05	2.1342E-03
400.0	1.4511E-02	1.4754E-02	3.9216E-05	1.5340E-03
500.0	1.2550E-02	1.5950E-02	2.7964E-05	1.0939E-03
630.0	1.6169E-02	2.2756E-02	1.8417E-05	7.2042E-04
800.0	7.8477E-03	1.7920E-02	2.5036E-05	9.7936E-04
1000.0	1.7387E-02	7.1925E-02	1.3887E-05	5.4321E-04
1250.0	6.4648E-03	4.6317E-02	7.6548E-06	2.9944E-04
1600.0	2.1482E-03	2.6669E-02	3.9368E-06	1.5100E-04
2000.0	9.3465E-04	1.8526E-02	2.1480E-06	8.4026E-05

Critcal frequencies for model DT01

Frequency Hertz	EXTA INST	INTA INST
50.0	9.9198E+02	9.9198E+02
63.0	9.9198E+02	9.9198E+02
80.0	9.9198E+02	9.9198E+02
100.0	9.9198E+02	9.9198E+02
125.0	9.9198E+02	9.9198E+02
160.0	9.9198E+02	9.9198E+02
200.0	9.9198E+02	9.9198E+02
250.0	9.9198E+02	9.9198E+02
315.0	9.9198E+02	9.9198E+02
400.0	9.9198E+02	9.9198E+02
500.0	9.9198E+02	9.9198E+02
630.0	9.9198E+02	9.9198E+02
800.0	9.9198E+02	9.9198E+02
1000.0	9.9198E+02	9.9198E+02
1250.0	9.9198E+02	9.9198E+02
1600.0	9.9198E+02	9.9198E+02
2000.0	9.9198E+02	9.9198E+02

Modal densities for model DT01

Frequency Hertz	EXTA	INTA	INST
50.0	1.7366E-01	4.4393E-03	9.0711E-02
63.0	2.7570E-01	7.0478E-03	1.0182E-01
80.0	4.4456E-01	1.1365E-02	1.1474E-01
100.0	6.9462E-01	1.7757E-02	1.2829E-01
125.0	1.0853E+00	2.7746E-02	1.4343E-01
160.0	1.7782E+00	4.5459E-02	1.6227E-01
200.0	2.7785E+00	7.1029E-02	1.8142E-01
250.0	4.3414E+00	1.1098E-01	2.0284E-01
315.0	6.8924E+00	1.7620E-01	2.2768E-01
400.0	1.1114E+01	2.8412E-01	2.7943E-01
500.0	1.7366E+01	4.4393E-01	3.4929E-01
630.0	2.7570E+01	7.0478E-01	5.0079E-01
800.0	4.4456E+01	1.1365E+00	4.9769E-01
1000.0	6.9462E+01	1.7757E+00	4.2926E-01
1250.0	1.0853E+02	2.7746E+00	3.8726E-01
1600.0	1.7782E+02	4.5459E+00	3.6617E-01
2000.0	2.7785E+02	7.1029E+00	3.5835E-01

Ring frequencies for model DT01

Frequency
Hertz   INST

     50.0   6.9924E+02
     63.0   6.9924E+02
     80.0   6.9924E+02
    100.0   6.9924E+02
    125.0   6.9924E+02
    160.0   6.9924E+02
    200.0   6.9924E+02
    250.0   6.9924E+02
    315.0   6.9924E+02
    400.0   6.9924E+02
    500.0   6.9924E+02
    630.0   6.9924E+02
    800.0   6.9924E+02
   1000.0   6.9924E+02
   1250.0   6.9924E+02
   1600.0   6.9924E+02
   2000.0   6.9924E+02

TABLE OF CONTENTS FOR DAL UNIT 5   KSC105:[VAPEPS]DAL005.DAL;1

SEQ	RR	DATE	TIME	E	WORDS	NR	NC	T	ELN	VER	Cl
1	16	880723	125150	0	43	43	1	5	TEXT	DT03	0
2	20	880723	125156	0	1	1	1	0	EXEL	DT03	0
3	24	880723	125156	0	17	17	1	1	FREQ	DT03	0
4	28	880723	125205	0	3	3	1	0	DBFG	DT03	0
5	32	880723	125206	0	51	17	3	1	RESP	DT03	0
6	36	880723	125220	0	6	3	2	4	MNAM	DT03	0
7	40	880727	135523	0	36	36	1	5	TEXT	DT01	0
8	44	880727	135530	0	1	1	1	0	EXEL	DT01	0
9	48	880727	135530	0	17	17	1	1	FREQ	DT01	0
10	52	880727	135530	0	17	17	1	1	EXC	DT01	0
11	56	880727	135532	0	51	17	3	1	DENS	DT01	0
12	60	880727	135535	0	9	9	1	0	PDES	DT01	0
13	64	880727	135535	0	2	2	1	0	CDES	DT01	0
14	68	880727	135535	0	1	1	1	0	RDES	DT01	0
15	72	880727	135535	0	34	17	2	1	CRFR	DT01	0
16	76	880727	135535	0	17	17	1	1	RING	DT01	0
17	80	880727	135535	0	153	17	9	1	ATA	DT01	0
18	92	880727	135536	0	6	6	1	0	IDES	DT01	0
19	96	880727	135536	0	153	9	17	1	CO	DT01	0
20	116	880727	135538	0	68	4	17	1	INCO	DT01	0
21	136	880727	135539	0	34	17	2	1	TRNF	DT01	0
22	140	880727	135540	0	51	17	3	1	CONV	DT01	0
23	144	880727	135541	0	3	3	1	0	DBFG	DT01	0
24	148	880727	135541	0	1	1	1	1	CPOW	DT01	0
25	152	880727	135543	0	51	17	3	1	RESP	DT01	0
26	156	880727	135544	0	153	17	9	1	POWR	DT01	0
27	168	880727	135546	0	10	10	1	0	PCDS	DT01	0
28	172	880727	135546	0	170	17	10	1	PCRF	DT01	0
29	188	880727	135545	0	34	17	2	1	PNET	DT01	0
30	192	880727	135546	0	6	6	1	0	MHM	DT01	0
31	196	880727	135549	0	3	3	1	1	OA	DT01	0
32	200	880727	135552	0	3	3	1	1	GRMS	DT01	0
33	216	880727	135556	0	6	3	2	4	MNAM	DT01	0
34	220	880727	135557	0	140	35	4	0	PIPM	DT01	0
35	228	880727	135602	0	76	19	4	0	PDPM	DT01	0
36	232	880727	135602	0	6	3	2	0	PIPS	DT01	0
37	236	880727	135602	0	19	19	1	4	PISL	DT01	0
38	240	880727	135602	0	29	29	1	1	PIRL	DT01	0
39	244	880727	135602	0	16	16	1	0	PIIL	DT01	0
40	248	880727	135602	0	10	10	1	0	MSTA	DT01	0

CPU: DELTA, EXECUTION. RUN =   15.41   15.41   47.89
CIAU

DYNAMIC MEASUREMENT

PREDICTION AND MEASUREMENT OF THE
ACOUSTIC ENVIRONMENT OF THE AIRBORNE
SEEKER EVALUATION TEST SYSTEM

Leonard L. Shaw and Kenneth R. Wentz
Acoustics and Sonic Fatigue Group
Flight Dynamics Laboratory
Air Force Wright Aeronautical Laboratories
Wright-Patterson Air Force Base. OH 45433

Separated flow behind protuberances on aircraft can result
in acoustic levels high enough to cause structural damage.
The separated flow fluctuating pressure levels must be
predicted and/or measured for a fatigue analysis on the
aircraft structure. The acoustic levels were predicted and
measured for the separated flow behind a large retractable
turret installed on a C-130 aircraft. The predicted levels
agreed well with the measured environment. A maximum
acoustic level of 150 dB was measured. The resulting levels
were used to predict the acoustic fatigue life of the skin
panels behind the turret. A life of over 4000 hours was
predicted for the maximum acoustic levels.

INTRODUCTION

The acoustic environment associated with the separated flow region behind a
large retractable turret was investigated. The large retractable turret comprised
an Airborne Seeker Evaluation Test System (ASETS) which was installed on a C-130
aircraft. The turret is carried inside the fuselage and extended when needed for
testing. It extends fifty inches below the fuselage which is lower than the
ground plane, thus the aircraft could not land with the turret fully extended. A
sketch of the C-130 aircraft with the turret fully extended is shown in Figure 1.
Figures 2 and 3 show the turret in the retracted and extended positions
respectively. Any non-aerodynamic protrusion on the aircraft surface will result
in separated flow. The amplitude of the pressure fluctuations behind the turret
were needed to determine the acoustic fatigue life of the aircraft skin. The
fluctuating pressure levels and the region of separation behind the turret were
predicted using existing prediction methods. An extensive flight test was then
performed during which the fluctuating pressure environment was measured. A total
of twelve B&K model 4068 microphones were used to measure the acoustic
environment. The microphones were located from directly behind the turret to
about six feet down stream as shown in Figure 4. Acoustic data were obtained for
take-off, level cruise, 3g turns, flaps up and at 50 percent, and for the turret
in and at numerous partially extended positions as well as fully extended. All of
the acoustic data were reduced into Power Spectral Densities (PSD). Further
details about the entire measurement program are given in Reference 1.
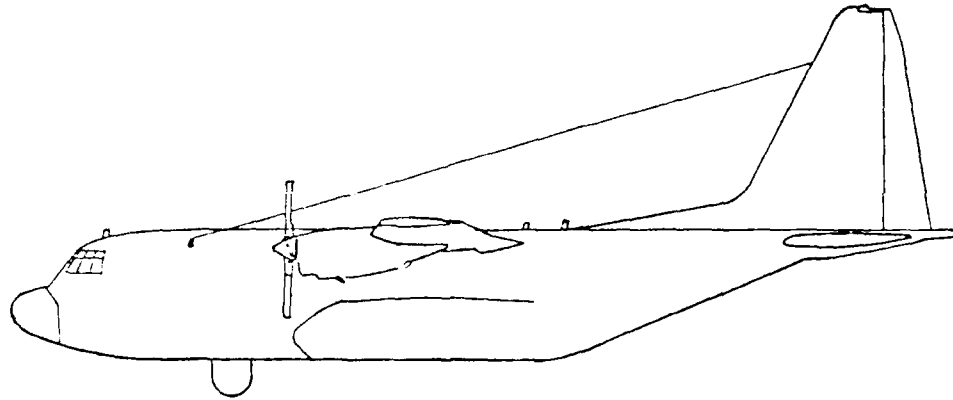
Fig. 1 ASETS Testbed
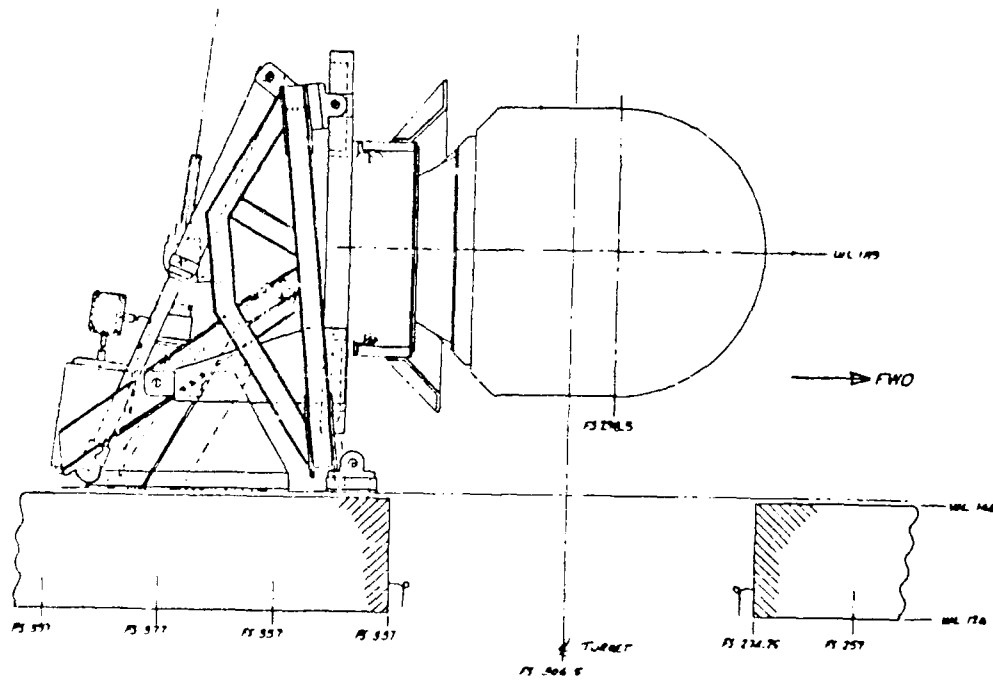
Fig. 2 Retracted Position
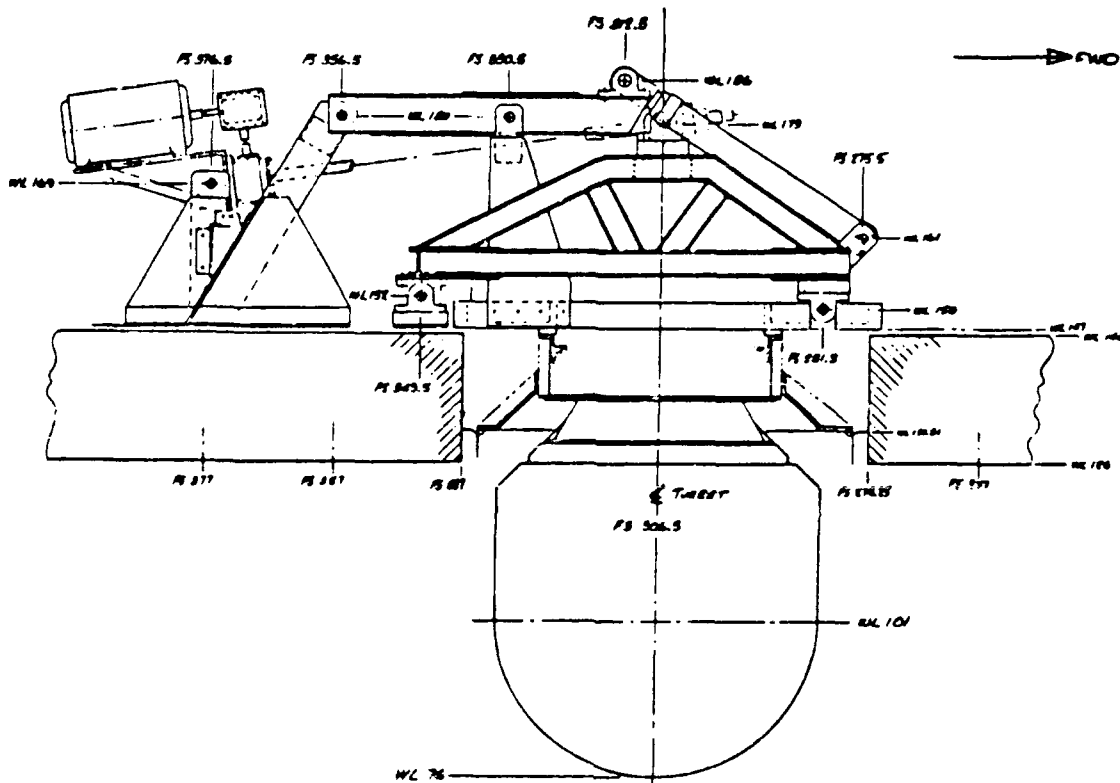
Fig. 3 Extended Position
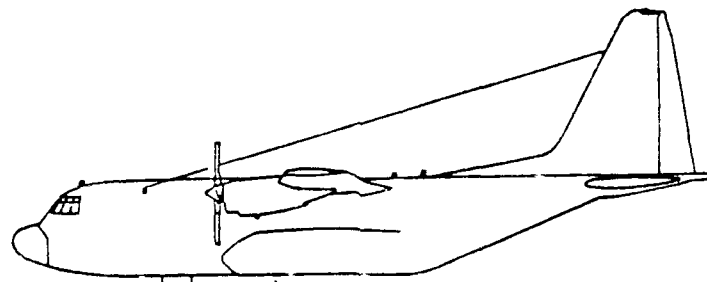
NOTE: Two microphones are located
       inside the cargo compartment.

12   1. Mounted on bulkhead at
         FS 245, 72 inches above the floor

10   2. Mounted on floor centerline
         at FS 270.
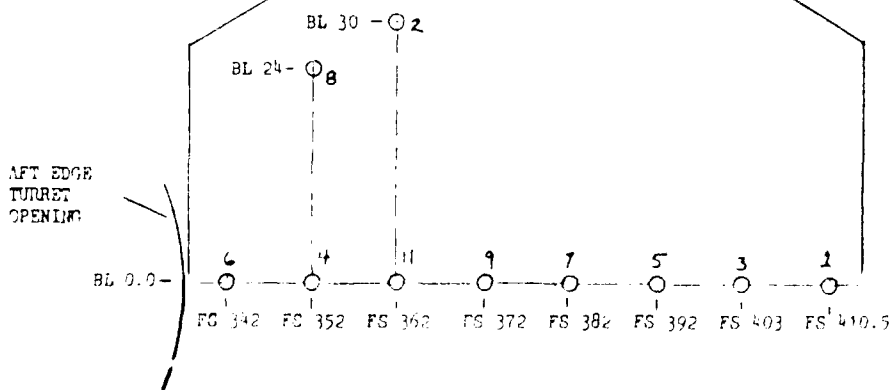
Fig. 4 Acoustic Microphone Locations

PREDICTION

The flow behind the large turret was assumed to be separated. This region of flow separation for blunt bodies can be referred to as base flow. The overall fluctuating pressure level (acoustic level) can be predicted using equation 1 (Ref. 2).

$$\frac{P_{rms}}{q} = 0.045 \tag{1}$$

where, q = free stream dynamic pressure $= \frac{1}{2} \rho V^2$

The turbulence constant 0.045 may be as high as 0.1, depending on the type of separated or base flow. Considering the diameter of the turret (54 inches) fully separated flow was anticipated and thus the higher value of 0.1 was used. The maximum free stream dynamic pressure for the ASETS occurred at 12,000 feet for Mach number 0.4. For these conditions the dynamic pressure is 1.05 psi. Using the 0.1 value for the turbulence constant results in

$$P_{rms} = 0.105 \text{ psi}$$

The sound pressure level is calculated from Equation 2

$$SPL = 20 \log (P_{rms}/P_{ref}) \tag{2}$$

where

$$P_{ref} = 2.9X10^9 \text{ psi}$$

Thus the maximum SPL that should occur behind the turret was predicted to be 151 dB. As shown in the next section the maximum level measured for all flight conditions was 150 dB which verifies the predicted level.

DISCUSSION OF DATA

Acoustic data were obtained for take-off, level cruise, 3g turns, flaps up and at 50 percent, and for the turret in and at numerous partially extended positions as well as fully extended. All of the acoustic data were reduced into Power Spectral Densities (PSD).

Figure 5 shows a typical boundary layer noise spectrum from microphone 9 for a speed of 235 knots and altitude of 12,000 feet. The turret is inside and the doors are closed. All the microphones have nearly the same levels except for the narrowband peak near 68 Hertz. This is the blade passage frequency of the propellers on the C-130 aircraft. Going through a 3g turn did not affect the boundary layer noise levels. Also take off levels are very low, as seen in Figure 6, except the narrowband tones from the propellers.

OASPL - 139 dB
Microphone 9

PSD - dB

Frequency-Hertz
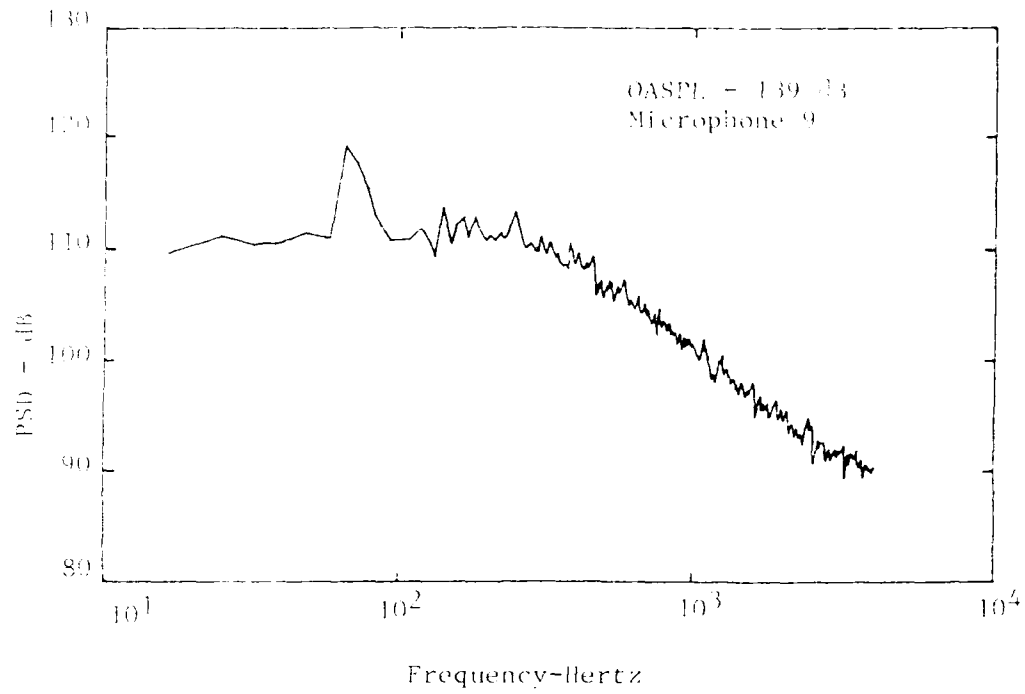
Fig. 5   Typical Boundary Layer Noise Spectrum With The
Turret Inside and the Doors Closed for 235 Knots
and 12,000 Foot Altitude

OASPL - 133 dB
Microphone 9

PSD - dB

Frequency-Hertz
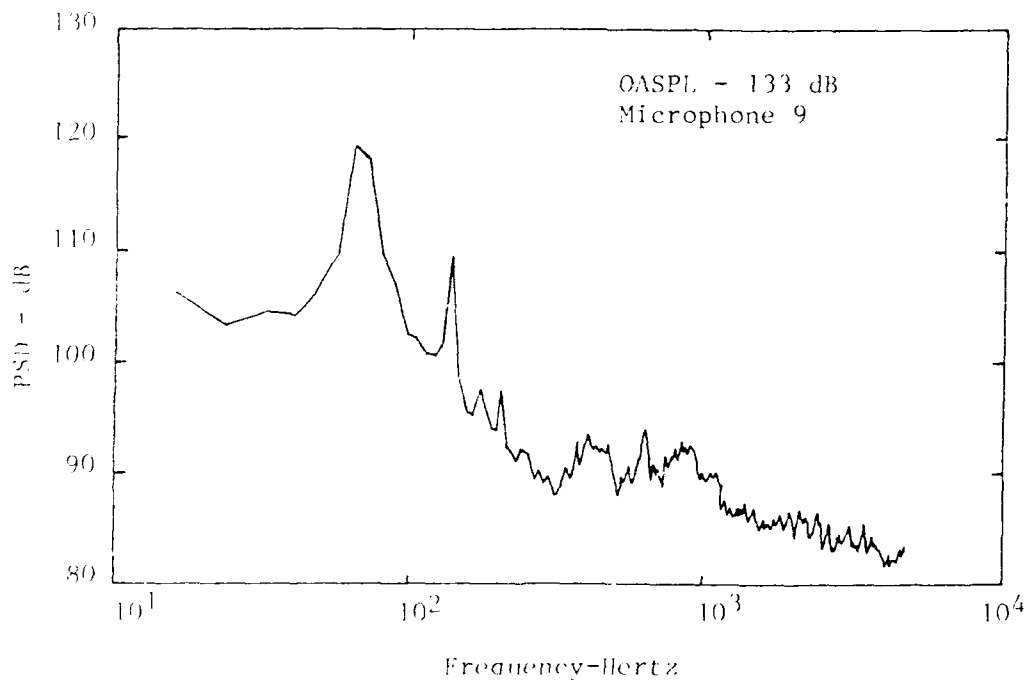
Fig. 6   Typical Take Off Spectrum

193

Figure 7 shows a spectrum from microphone 9 for the turret doors open but the turret inside. This spectrum is for a speed of 170 knots and 9600 foot altitude. It can be compared to the spectrum in Figure 8 which is for the turret fully extended. The low frequencies, less than 50 Hertz, were increased about 10 dB, but the higher frequencies, above 200 Hertz, were not affected. This would be expected since the flow behind the turret should scale with the characteristic dimension of the turret, namely the 54 inch diameter. This results in a characteristic frequency of 240 Hertz which implies that essentially only frequencies below 240 Hertz should be affected by the turret. This indeed was the case.
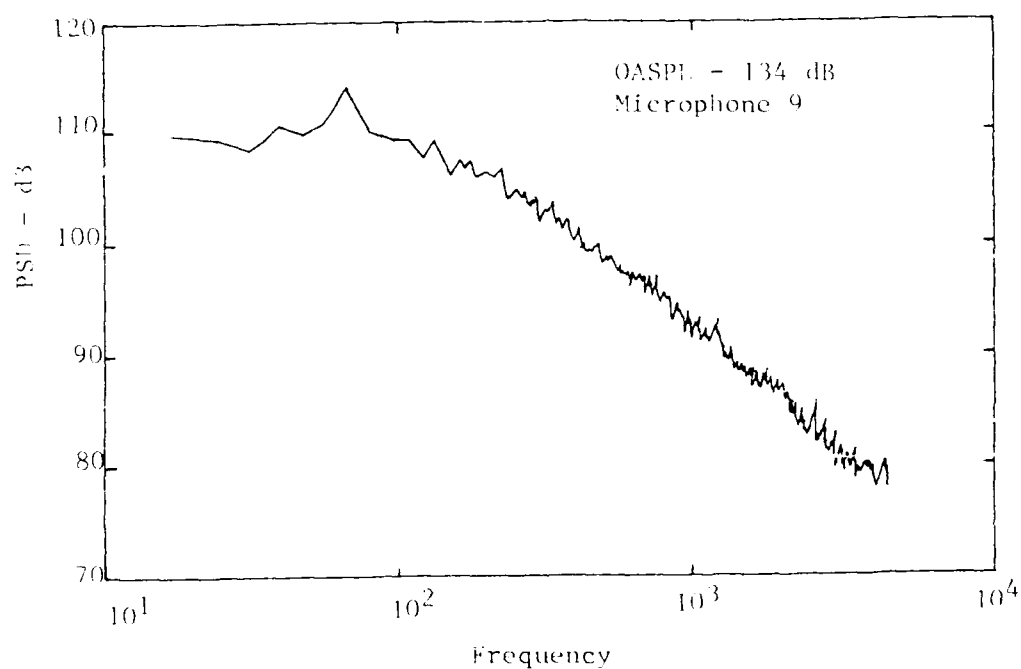
Fig. 7   Spectrum for Doors Open and Turret Inside
          for 170 Knots and 9600 Foot Altitude
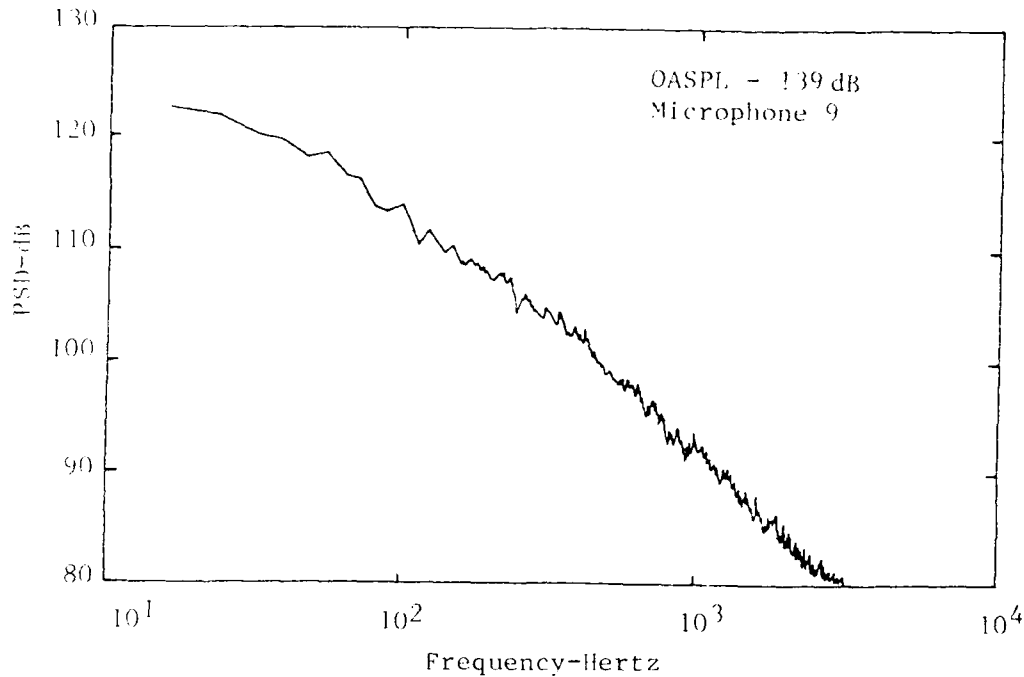
Fig. 8   Spectrum for Turret Fully Extended for 170
Knots and 9600 Foot Altitude

The aircraft flaps were extended to 50 degrees during a flight and acoustic data were obtained. A typical spectrum is shown in Figure 9 and can be directly compared to Figure 8 for flaps up. The two spectra are nearly the same; thus flap settings do not affect the acoustic levels behind the turret.

Since acoustic fatigue was the major reason for the acoustic measurements, the highest levels would result in the shortest fatigue life. The highest levels were recorded for a flight speed of 253 knots at an altitude of 12,000 feet. Figure 10 presents the spectrum for these conditions from microphone 5. The overall level is 150 dB with the maximum PSD level being 133 dB near 30 Hertz. Reviewing all of the data show that the highest levels occur well behind the turret at fuselage stations 382 to 410. The higher levels could extend further aft, but there were no microphones to verify it. Some data were obtained from microphones 2 and 8 for other flights. It showed that the levels at these side locations were generally the same magnitude as microphone locations 1, 3 and 5 (fuselage stations 382 to 410).
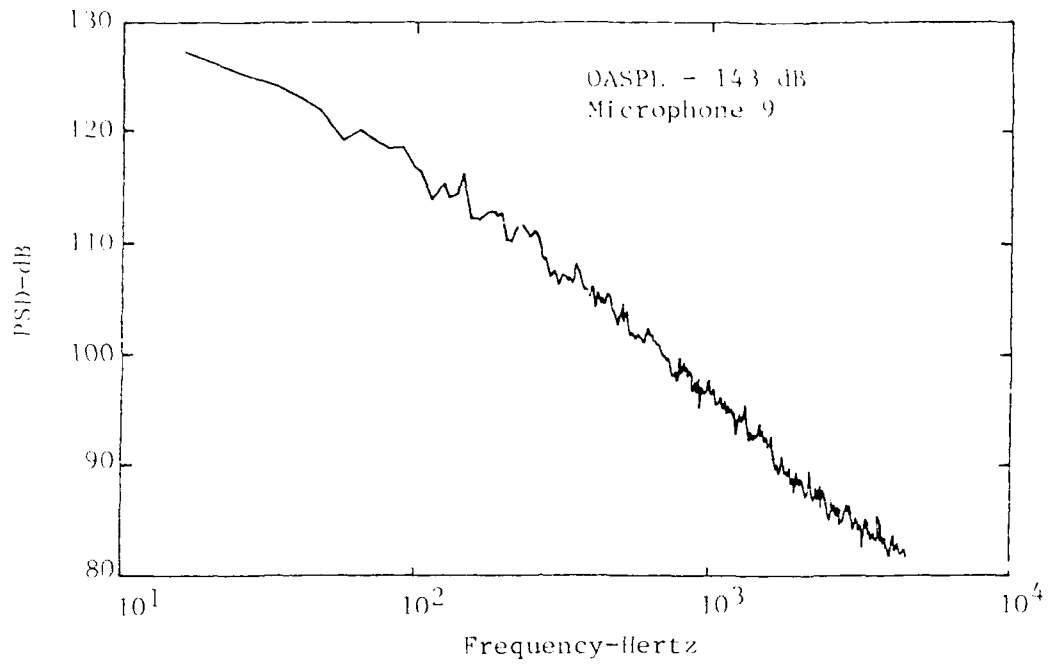
Fig. 9   Spectrum for Turret Fully Extended and Flaps
at 50 Percent for 170 Knots and 9600 Foot Altitude
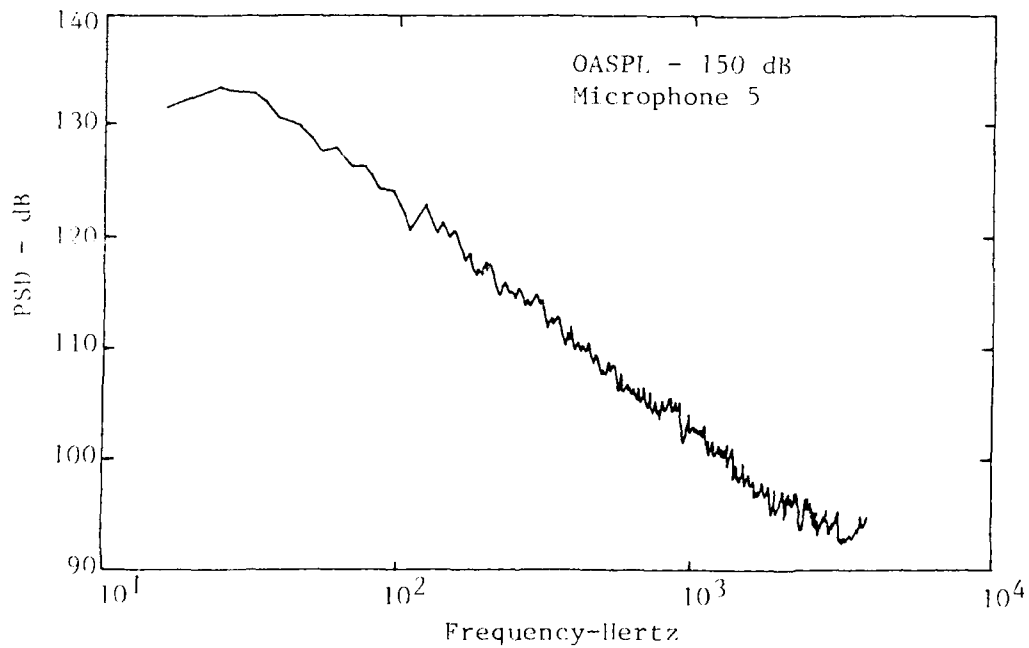
Fig. 10   Spectrum From Microphone 5 for 253 Knots
at 12,000 Foot Altitude

ACOUSTIC FATIGUE ANALYSIS

An acoustic fatigue analysis was performed for the panels located aft of the turret. To perform the analysis the specification of the panels and an acoustic power spectral density (PSD) are needed.

Figure 11 shows the lower fuselage skin of the C-130 aircraft. Typical panel dimensions for the region of interest are 10 x 40 inches. The skin is 0.060 inches thick and made of 7075-T6 clad aluminum. Two equations were used to calculate the resonant frequency of the panel. These equations are for simply-supported (ss) and clamped-clamped (cc) cases [ref 5].
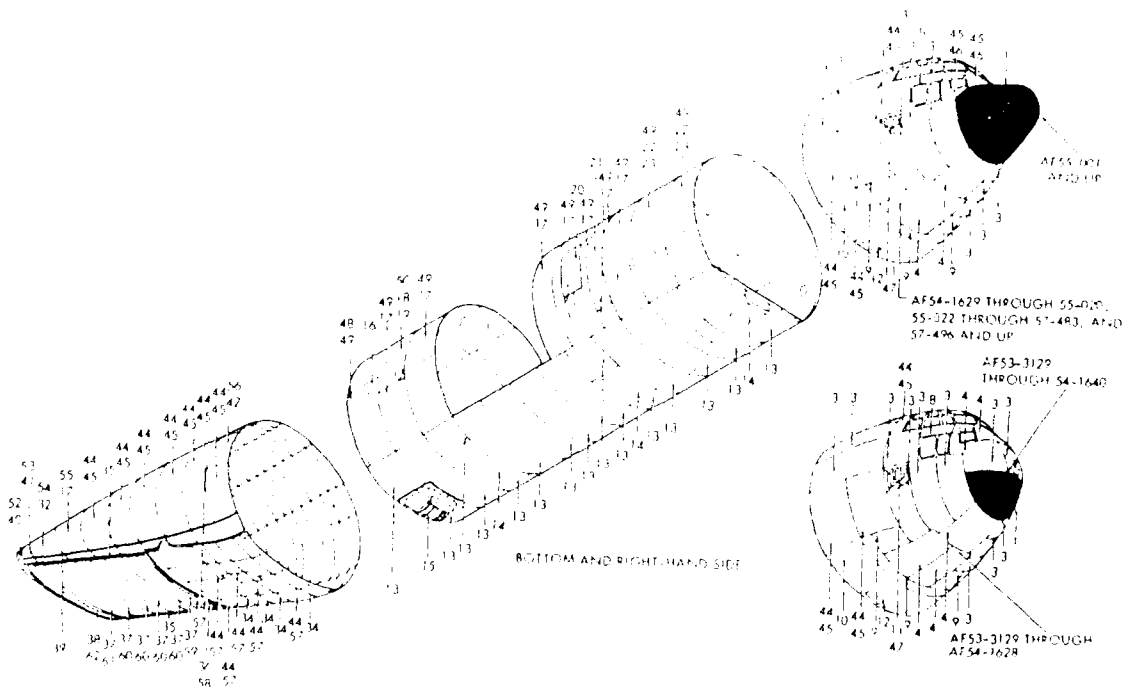
Fig. 11 Fuselage Skin (C-130A/D Airplanes)

$$2\pi f_{ss} = \omega \sqrt{\frac{D}{\rho t}\left[\left(\frac{m\pi}{a}\right)^2 + \left(\frac{n\pi}{b}\right)^2\right]}\qquad(3)$$

$$2\pi f_c = \omega = \sqrt{\frac{\lambda^2 \pi^4 E t^2}{120(1-\nu^2)}}$$

where $\lambda^2 \simeq \left(\frac{Gx}{a}\right)^4 + \left(\frac{Gy}{b}\right)^4 + \frac{2}{a^2 b^2}\left[GxGy\left(Gx - \frac{2}{\pi}\right)\left(Gy - \frac{2}{\pi}\right)\right]$ (4)

where $Gx = m + 1/2$ $Gy = n + 1/2$

a = Length of plate

b = Width of plate

= Angular frequency

D = Isotropic bending stiffness

= Density of material

t = Thickness of plate

m = Number of half sine waves in a direction

n = Number of half sine waves in b direction

f = Frequency

ν = Isotropic poisson's ratio

An average of the two frequencies, f_{ss} and f_{cc}, was used since it is more representative of the actual response of the panel on the aircraft. The resulting frequency is 143 Hertz. The PSD that is used for the analysis is the level at the resonant frequency. Reviewing all the data and selecting the highest level above 100 Hertz (a conservative approach) results in PSD of 125 dB. Using the Modified Miles equation: [Ref. 3]

$$\bar{\sigma}_s = \frac{0.072\, a^{1.25} S_p(f_{11})(b/a)^{1.75}}{h^{1.75}\zeta^{0.56}\left[3(b/a)^2 + 2(a/b)^2 + 2\right]^{0.84}} \quad \text{ksi}$$

(5)

$$S_p(f_{11}) = \sqrt{G_p(f_{11})}$$

where h = skin thickness

       = damping ratio

    G_p = PSD

results in a stress of 2.54 ksi. With the aid of the S-N curve in Figure 12, cycles to failure of 2.1×10^9 is found. For the resonant frequency of 143 Hertz, this results in a sonic fatigue life of 4080 hours. Thus, the skin panels behind the turret will not fail in less than 4000 hours flying in the maximum conditions. The actural life will be longer since much of the flight time will be at slower speeds.
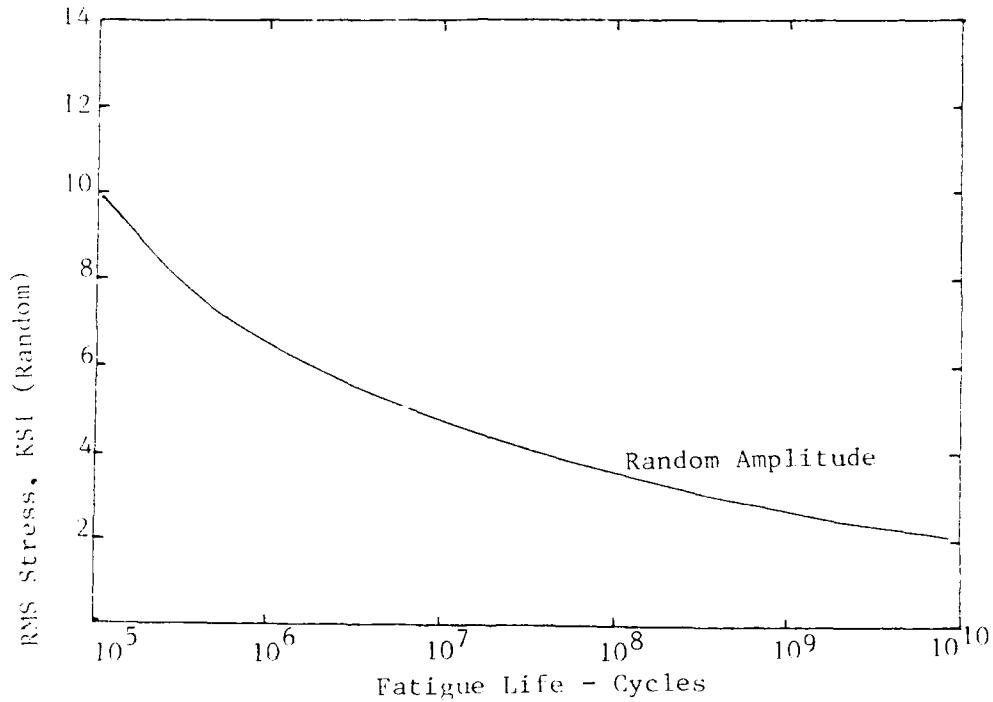
Fig. 12 S-N Curve for 2024-T3 Clad Aluminum

REFERENCES

1. L. Shaw, K. Wentz, and S. Jolliat, "Acoustic Environment of the Airborne Seeker Evaluation Test System," AFWAL-TM-86-242-FIBG, November 1986.

2. Ungar, E.U., "A Guide for Predicting the Vibration of Fighter Aircraft in the Preliminary Design Stages," AFFDL-TR-71-6, April 1973.

3. Rudder, F.F., and Plumbee, H.E., "Sonic Fatigue Design Guide for Military Aircraft," AFFDL-TR-74-1112, May 1975.

PVDF APPLICATIONS IN SHOCK AND VIBRATION MEASUREMENTS AND CONTROL

L. M. Lee
Ktech Corporation.
Albuquerque. NM 87110

J. P. Berhault and J. P. Chambard
Metravib R.S.D.
Ecully. France

F. Bauer
Institute Saint Louis
Saint Louis. France

Piezoelectric polyvinylidene fluoride (PVDF) has
proven to be an excellent transducing material for
a broad range of dynamic measurement applications.
Shock wave measurements have been made up to 46 GPa
providing fast rise time data at shock stress levels
never before measured. Hopkinson bar tests have
provided stress gauge calibration at low stress levels
(0.1 to 1.0 GPa). A new application, use of PVDF in
active vibration control of structures. is also
discussed.

A.   INTRODUCTION

It has been known for many years that appropriately treated polyviny-
lidene fluoride (PVDF) exhibits piezoelectric properties suitable for a wide
variety of applications Some of these applications require a high degree
of reproducibility in material constants because a sensor which functions
under shock-compression loading is destroyed in use. Various studies of
PVDF film by Bauer [1-4] have shown that conventionally available
piezoelectric films do not exhibit sufficient reproducibility for shock
applications. However, PVDF film processed to exacting specifications and
poled with the Bauer method achieves the desired level of reproducibility.

A cooperative effort has been pursued between Institute Saint Louis
(ISL) and Sandia National Laboratories, Albuquerque (SNLA) to provide a
stress gauge for widespread use in shock measurements.   SNLA has been
receiving technical support from Ktech Corporation to develop the Bauer
poling process in the United States, while ISL has been working with
Metravib Corporation in France to develop a commercial source for the stan-
dardized PVDF gauges. Initial efforts in the cooperative program, which was
started in 1982, showed agreement of independent shock wave measurements
made at the two laboratories on PVDF gauges fabricated by ISL [5].   The
initial work was in the stress range from 1.0 to 2.2 GPa. Later work in-
volved setting up specific material film specifications and the Bauer poling
process in the United States and the Metravib Laboratory [6].

Further work showed agreement over a larger stress range. An exacting, controlled impact technique for evaluating PVDF stress gauges has been developed [7].

The ISL Laboratory was the only source for PVDF gauges produced by the Bauer method until very recently. As a result of the cooperative effort between our laboratories, gauge fabrication facilities have been developed in both the United States and France that can produce standardized PVDF shock compression gauges based on the patented Bauer process. The essential ingredients of the standardized gauge are a uniform high quality biaxially stretched PVDF film and the Bauer electrical poling process. The next section of this paper reports the completion of our gauge standardization effort.

Three series of precisely controlled experiments have been conducted to evaluate the shock response of two batches of PVDF gauges made to the same specifications in two separate facilities. Section C of this paper presents our first measurements on shock wave response of PVDF gauges fabricated from different lots of well controlled film and poled in different laboratories using the standardized process.

A recent investigation of the piezoelectric behavior of PVDF ISL gauges placed in a Hopkinson bar, with no internal specimen is presented next. This bar provided lower stress calibration for these gauges.

A new field of PVDF transducer applications (active vibration control) is presented in the fifth section. A general analysis of methods is given and the relative merits of active and passive control are discussed. This section concludes with a description of a computer model for design of active vibration control systems.

B. GAUGE FABRICATION

MATERIAL

The PVDF film used in the United States and France was extruded and biaxially stretched by Rhone Poulenc Films in France from polymer pellets obtained from Kureha, Japan. The special film has a nominal thickness of 26 um. Enough of the PVDF film has been procured for many years of gauge development and applications. This particular film was chosen because of the documented successful poling by Bauer of similar PVDF batches. Also, shock wave measurements on standardized gauges made from different PVDF lots have shown close agreement. Other PVDF films are available, but they are different from the Rhone Poulenc material and none have been subjected to much extensive testing as this material. An essential point of any shock and vibration transducer development project is a material with well defined characteristics to ensure that proper processing can achieve the required end result.

The standardized stress gauge electroding process was developed after evaluating a number of metallization techniques and mask designs. Magnetron sputtering of gold or aluminum over platinum produced electrodes with a very good adhesion. No metal was removed using the Scotch-tape peel test and there was no evidence of film overheating during electroding. Other sputtering and vapor deposition techniques have shown that overheating the film results in detrimental effects on the electrical properties of the gauge. The electrode and sensing area design utilized for the standard gauge is shown in Fig. 1. The sensor area located where the two electrodes overlap is clearly the most important region of the gauge. It is critical to have sharp edge definition for the total electroded area because accurate sensor area measurement is required for accurate shock wave measurements. Masking techniques have been developed which produce the required sharp edge definition at 100x magnification, and also reduce the tendency of the PVDF to crinkle during deposition [8].
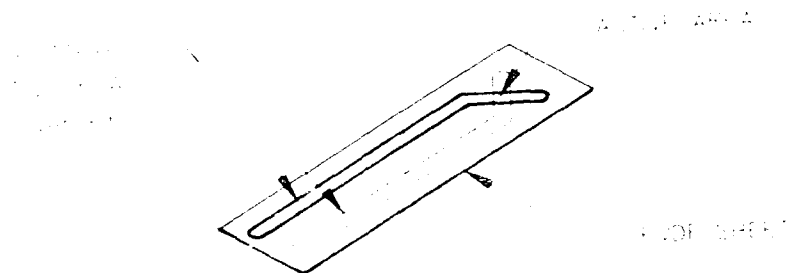
Figure 1. Standardized PVDF shock gauge configuration.

POLING PROCESS

The purpose of the poling process is to induce reproducible piezoelectric polarization in the PVDF and to remove any trapped space charge. Many static, field discharge, and cyclic methods have been tried over the past few years, but only the Bauer process with a specific cyclic poling schedule has been proven by shock-compression tests to condition the PVDF for accurate reproducible output. The poling process incorporates the essential features as described in Bauer's U.S. patent and in the open literature [9].

The Bauer poling procedure is specifically tailored to create a transducing element that produces charge under stress only from the piezoelectric effect and under temperature change only from the pyroelectric effect. The process aligns crystallites, orients dipoles, and migrates ions and space charges out of the film homogeneously throughout the poled region.

A Bauer process poling facility has been developed in Albuquerque, New Mexico, and has been shown to produce routinely high quality gauge elements with high polarization. The remanent polarization of PVDF shock gauges produced with the United States system is the same as produced in France at ISL and Metravib, nominally 9.2 ± 0.2 $\mu C/cm^2$.

C. SHOCK MEASUREMENTS

EXPERIMENTAL METHODS

A standard impact loading experiment for PVDF has been developed for the SNLA 25-meter compressed gas gun which has been used for many previous studies involving precisely controlled impact loading, including quartz and lithium niobate piezoelectric gauge work. The gauge element is placed directly on the impact face of a target of either Kel-F, Z-cut quartz, Z-cut sapphire or tungsten carbide as shown in Fig. 2. The impactor is the same material as the target: hence, the equilibrium particle velocity is known to the precision of the impact velocity measurement, 0.1 percent. The gauge elements are subjected to unusually well behaved shock and release stress pulses because the Z-cut quartz and sapphire target and impactor materials remain elastic up to about 13 and 20 GPa, respectively. The response to release waves can be carefully studied by the use of thin impactors in this arrangement. Tungsten carbide is used for stress greater than 20 GPa with 25 μm thick FEP Teflon film on either side of the gauge to provide electrical insulation. Kel-F is used because of its lower mechanical impedance for stress less than 3 GPa [10].
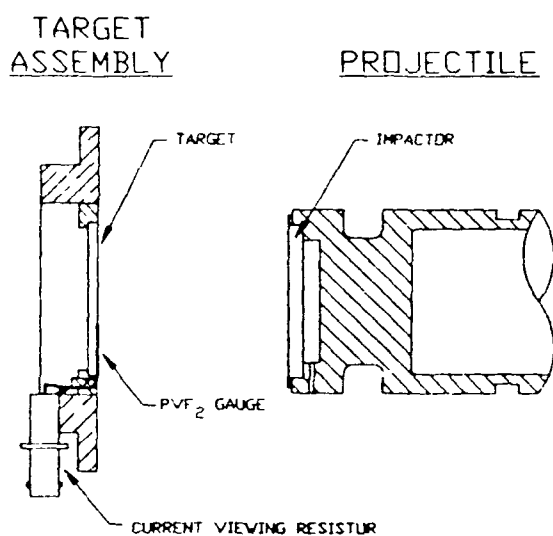
Figure 2. Impact loading configuration for controlled shock loading of standardized PVDF gauges.

Various electronic recording arrangements have been investigated. High speed digitizers provide the best records for ease in data reduction. A high digitizing rate is required to track the detail in the PVDF response because of the very fast loading achieved. LeCroy 6880 digitizers which sample at a rate of 0.742 ns per point and have a recording window of 7.4 μs

were used. The experiment used two separate low-loss coaxial cables to provide recording of the signals at different sensitivities rather than a single cable with a parallel connection to two digitizers.

The electrical currents produced upon impact from electrode areas of about 0.1 cm² range from about 1 to 30 amperes in the most recent experiments. Current-viewing resistors with resistances between 0.025 and 0.2 ohm are connected to the gauge electrodes to reduce the signal levels to acceptable values. Further signal level reduction, if desired, is accomplished with microwave dividers placed at the inputs to the digitizers.

RESULTS

The joint program of PVDF gauge development conducted over the last six years has resulted in a set of quantitative specifications describing the standardized stress gauge. Specifications relative to material, electroding and poling parameters that must be achieved to produce a repeatable, high fidelity, shock wave sensor are shown in Table 1. The normal hysteresis loop listed in Table 1 is shown in Fig. 3 for gauges produced at the three different facilities. The excellent agreement in remanent polarization and hysteresis loop characteristics shows the reproducibility of PVDF gauges made to exacting standards. Although the program is ongoing, the results to date over a wide range of parameters relative to gauge area and shock stress are shown in Table 2. Of primary importance in Table 2 is the fact that the same remanent polarization, which has been shown in previous work to be critical to producing a repeatable shock transducer, has been achieved in the three different laboratories using essentially the same gauge fabrication processes. Also shown in Table 2 is a wide range of shock-compression loading to which the gauges have been exposed. This dynamic range is an order of magnitude larger than any previously available piezoelectric shock gauge.

Table 1. Standardized PVDF Gauge Specifications

Material	Biaxial stretched 25 μm (Rhone Poulenc).
Electrode	Sputtered (2500 A gold over 500 Å platinum).
Poling	Crossed lead strip sensing area. Remanent polarization 9.2 ± 0.2 μC/cm². Normal hysteresis loop.
Physical-Geometric	Quantitative definition of all parameters.
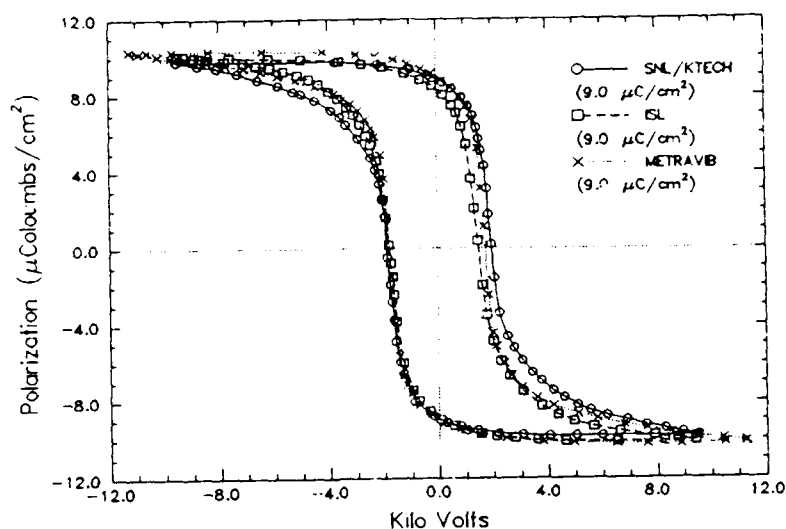
Figure 3. Hysteresis loop comparison for SNLA/Ktech, ISL and Metravib standardized PVDF shock gauges.

Table 2. PVDF Gauge Parameters

Gauge Fabrication	Gauge Area (cm²)	Remanent Polarization (μC/cm²)	Controlled Shock Loading (GPa)
ISL	0.01 1 mm x 1 mm	9.1	7 - 15
SNLA/Ktech	0.09 3 mm x 3 mm	9.1	0.3 - 46
Metravib	0.01 1 mm x 1 mm	9.1	0.7 - 35

A comparison of results from different gauges shock loaded using the controlled impact technique is shown in Fig. 4. The shock compression data shown in Fig. 4 were generated at SNLA ("KTECH DATA" and "SANDIA DATA") and ISL. The results indicate minimal scatter, with similar responses being obtained for the gauges produced in France and the United States. Limited data of this type have been obtained previously; however, in the current study the applicable stress gauge range was expanded up to 46 GPa where the gauge is still functioning properly. The ability to produce repeatable PVDF shock transducers in the different laboratories to exacting specifications now provides the general availability of shock transducers for reliable measurement application.
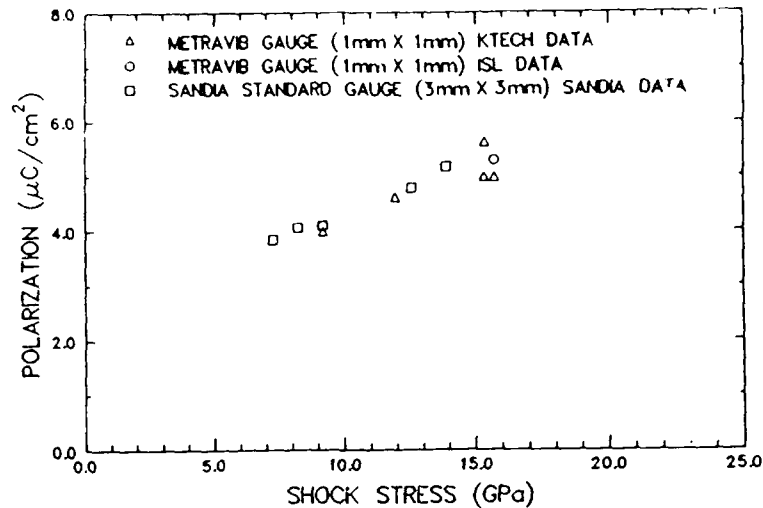
Figure 4.   PVDF gauge charge as a function of shock stress.
            (Preliminary data, detailed data analysis in process).

Some gauges were studied with the negative electrode on the impact surface to investigate the influence of gauge electrical orientation on output current. Data reported here were obtained with the standard orientation used by Bauer in which the positive electrode is placed on the impact surface. It appears there is an electrical polarity effect which has not yet been fully evaluated.

Standardized PVDF gauges have been utilized in pulsed laser experiments which allowed stress measurements to be made within 30 μm of the deposition region with fluxes ranging to 10^8 W/cm^2. Two PVDF records from these experiments are shown in Fig. 5. The large signal to noise ratio combined with the ability to make small sensors in the range of 0.01 cm^2 and the inherent flexibility of the PVDF shock sensor, allow data to be obtained in an extremely harsh electrical environment, which further illustrates the reliability and utility of the PVDF gauge.
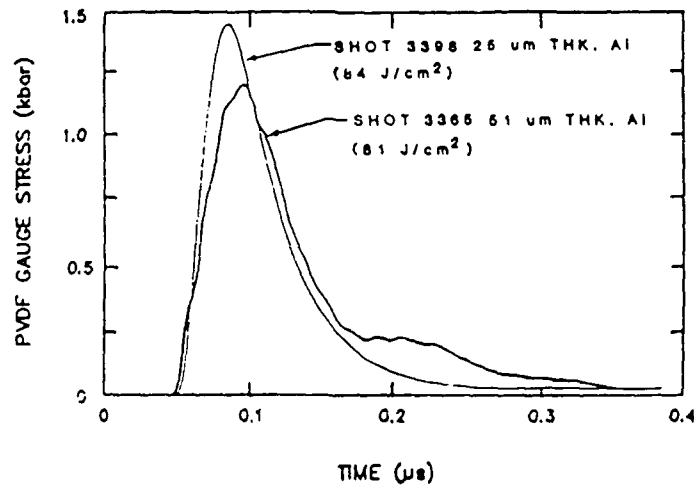
Figure 5.   PVDF stress gauge data from pulsed laser experiments (SPRITE).

207

D. HOPKINSON BAR EXPERIMENTS

The Hopkinson bar used for comparison tests [11] includes a striker bar, the incident and transmitter bars, and the associated instrumentation as detailed in Fig. 6. This generates a square wave of 1.0 μs duration at the impact interface. Propagation to the PVDF gauge location converts this pulse into a uniaxial stress wave with the characteristic Pochhammer-Chree oscillations superimposed on the square wave. A typical stress history adjacent to the gauge is measured by a strain gauge and is shown in Fig. 7.
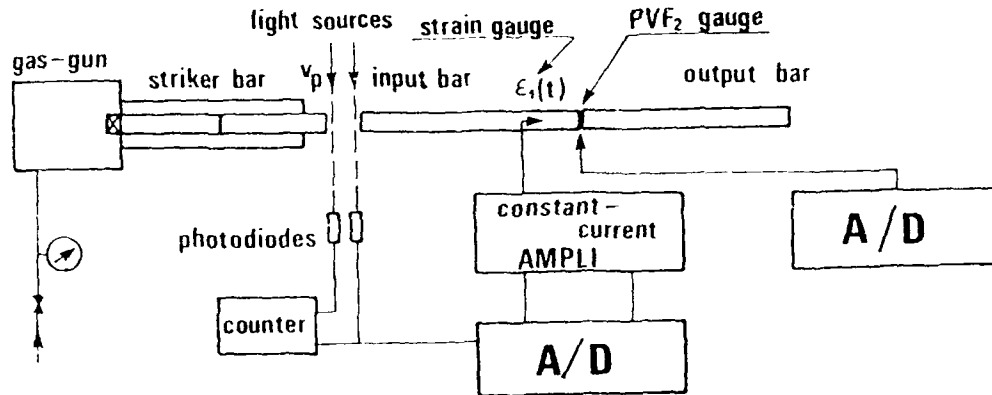
Figure 6.   Schematic apparatus for the Hopkinson bar.
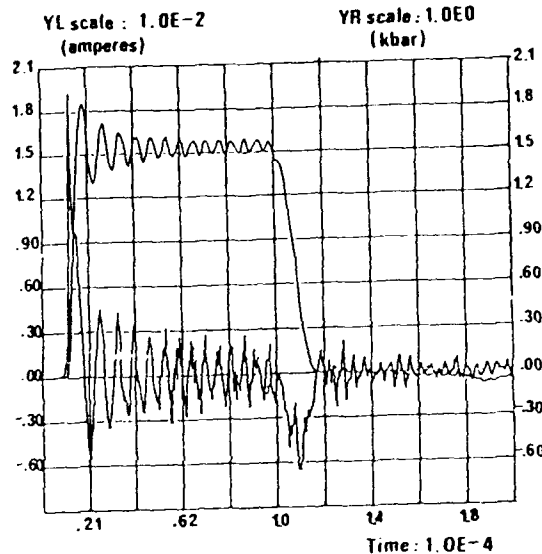
Figure 7.   The incident compressive pulse and measured
            PVDF gauge output.

The gauges for the Hopkinson bar experiments were made of biaxially stretched PVDF 40 μm thick with an active area of 25 mm^2 but were identical to the standard gauges (Table 1) in all other aspects.

If we assume the delivered charge to be proportional to the applied stress, the Q = f(t) (electric charge versus time) should be expected to exhibit the shock wave profile:

$$Q = \int_0^t i(t) \cdot dt \qquad (1)$$

with t = experimental recording time.

EXPERIMENTAL TECHNIQUE AND RESULTS

Hopkinson bar experiments were used to determine the PVDF shock gauge response between 1 and 4 kbar. The gauge was placed in the middle of the bar as indicated in Fig. 6. Two thin sheets of unpoled PVDF (23 μm thick) were placed on each side of the gauge in order to ensure a good insulation without a bonding agent. The current pulses measured with a 7612 Tektronix were integrated digitally to provide electrical charge as a function of time. The charge output of PVDF followed the stress histories and, upon unloading to zero stress, the charge was observed to return to zero. The dynamic compression loading behavior was investigated using several step compressional loading input waves of different amplitudes. Comparison of the stress determined from the measured strain history in the bar (ε(t) in Fig. 6) with the charge obtained from Eqn. (1) results in the calibration curve shown in Fig. 8.
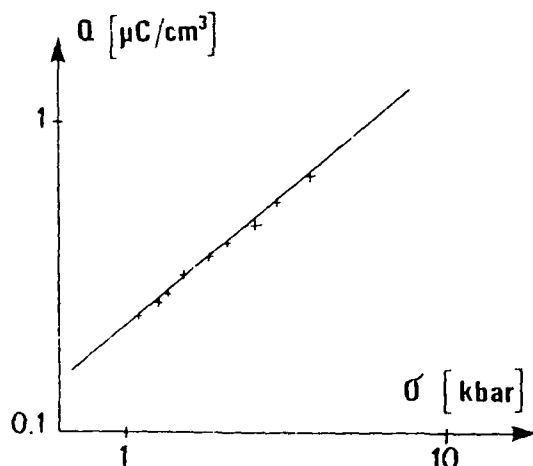
Figure 8. Calibration curve of the ISL PVDF gauge (logarithmic scale).

The law governing the unidimensional axial stress as a function of the electric charge Q released per unit surface can be expressed as follows:

$$\sigma = \alpha \cdot Q^\beta \qquad (2)$$

where Q is the electric charge given in $\mu C/cm^2$, σ is the stress in kbar, and α and β are constants depending on the value of the film and on the piezoelectric coefficients obtained after poling ($\alpha = 6.04$ and $\beta = 1.19$ for 40 μm thick PVDF).

E. USE OF PVDF IN ACTIVE VIBRATION CONTROL

Piezoelectric polymers offer some interesting specific characteristics making them suitable to control the dynamic behavior of light structures: light weight, ease of use, flexibility, and simple assembly. The reliability and long term stability of properly prepared PVDF, poled in an appropriate manner, offer a new field of application for this polymer. Displacement and velocity are the two variables used to control vibrations in structures.

GENERAL PROBLEM DESCRIPTION

Vibration problems are a major concern in specific areas of dynamic engineering such as aerospace or sensor technology. Solar panels and large mirror parts require stable and light weight structures. Optimal structural design usually falls short of these requirements, making active control necessary.

The general concept of active control is diagrammed in Fig. 9. This active control can be accomplished by either the eigenvalue adjustment method or the controlled damping method.
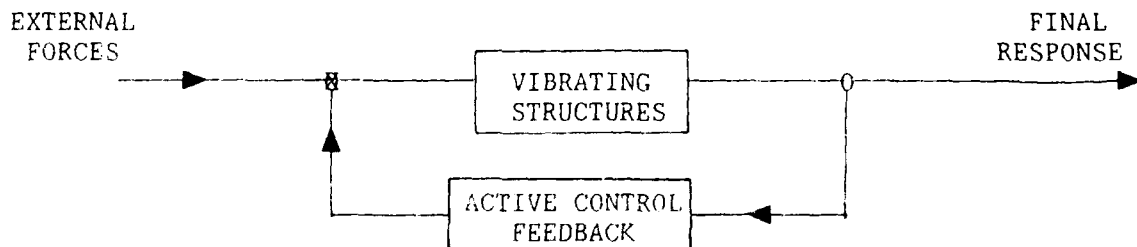
Figure 9. Active control diagram.

ACTIVE VIBRATION CONTROL ANALYSIS

In general, either eigenspace assignment or active damping can be used to modify the structural behavior of any mechanical assembly and both can be implemented with transducers based on PVDF piezoelectric polymer sensors [12].

Eigenvalue adjustment

The active reaction is proportional to the displacement for this method. The control results in a change of eigenvalues of the structural system. In general, the dynamics equation for any system is

$$[M]\; \ddot{y}(t) + [C]\; \dot{y}(t) + [K]\; y(t) = F(t), \tag{3}$$

where $[M]$ $=$ mass matrix
              $[C]$ $=$ damping matrix
              $[K]$ $=$ stiffness matrix
              $F(t)$ $=$ applied vector forces
              $y(t)$ $=$ degree of freedom (d.o.f.) vector

With active control, the applied force term becomes

$$F(t) = B(t) + E(t),$$

where $B(t)$ is the actively generated component of the force and $E(t)$ is the driving force. Eqn. (3) then becomes

$$[M]\; \ddot{y}(t) + [C]\; \dot{y}(t) + [K]\; y(t) = B(t) + E(t) \tag{4}$$

Figure 10. Diagram of eigenvalue adjustment system.

In order to change the eigenvalues of Eqn. (4), we use an actively generated force which is proportional to the d.o.f. displacement vector, $y(t)$, as illustrated in Fig. 10:

$$B(t) = [A]\; y(t) \tag{5}$$

Then, Eqn. (4) can be written as

$$[M]\; \ddot{y}(t) + [C]\; \dot{y}(t) + ([K] - [A])\; y(t) = E(t). \tag{6}$$

The solution to Eqn. (6) can be written as

$$x(t) = \begin{Bmatrix} y(t) \\ \dot{y}(t) \end{Bmatrix} \;\Rightarrow\; \dot{x}(t) = [D]\; x(t) + G(t), \tag{7}$$

where

$$[D] = \begin{bmatrix} [-M^{-1}C] & [-M^{-1}(K-A)] \\ [I] & [0] \end{bmatrix} \tag{8}$$

and
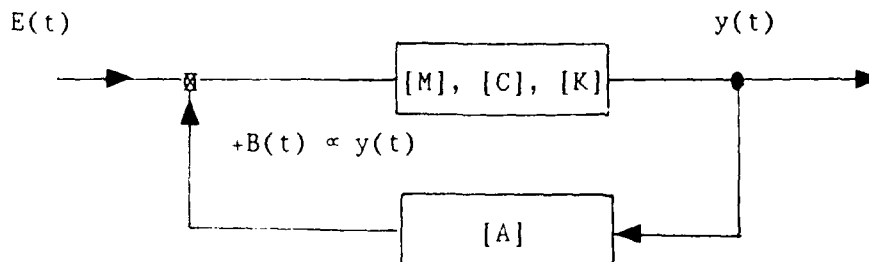
$$G(t) = \left\{ \begin{array}{c} E(t) \\ 0 \end{array} \right\} \qquad (9)$$

For non-vanishing [A] the eigenvalues of Eqn. (6) will differ from the values solving Eqn. (3) as shown in Fig. 11. The change is a shift in both amplitude and resonant frequencies. This shift in the frequency response of the structures can be used to broaden the useful frequency range.
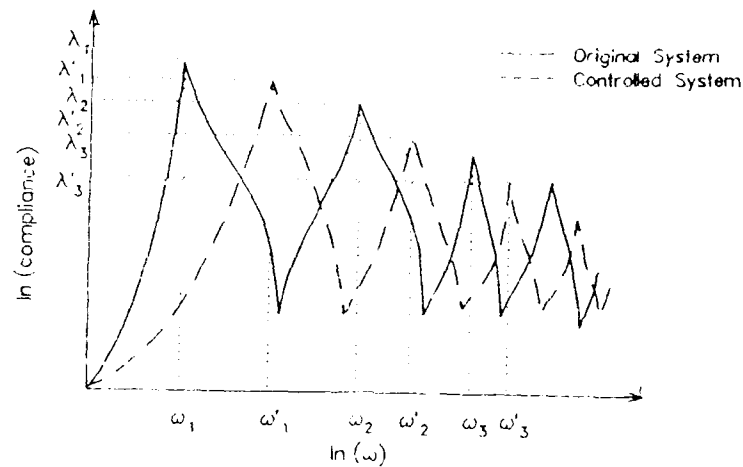
Figure 11. Eigenvalue adjustment response changes.

Controlled damping

An alternative approach to active control relies on changing the amplitude of resonant vibrations instead of modifying the frequency response of the structure. To do this we can use an actively generated force which is proportional to the d.o.f. velocity vector (Fig. 12). In this case Eqn. (5) can be written:

$$B(t) = [A'] \dot{y}(t), \qquad (10)$$

so that Eqn (4) is

$$[M] \ddot{y}(t) + ([C]-[A']) \dot{y}(t) + [K] y(t) = E(t). \qquad (11)$$
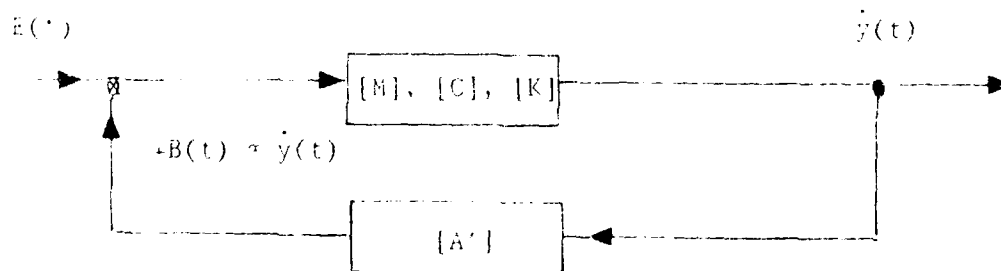
Figure 12. Controlled damping diagram.

The solution to Eqn. (11) is

$$\dot{x}(t) = [D'] \cdot x(t) + G(t) \tag{12}$$

with

$$[D'] = \begin{bmatrix} [-M^{-1}(C-A')] & [-M^{-1}K] \\ [I] & [0] \end{bmatrix} \tag{13}$$

and G(t) given by Eqn. (9).

The eigenvalues of this system are translated on the imaging axis so that the amplitude of the system response is modified, while the frequencies remain the same (Fig. 13).
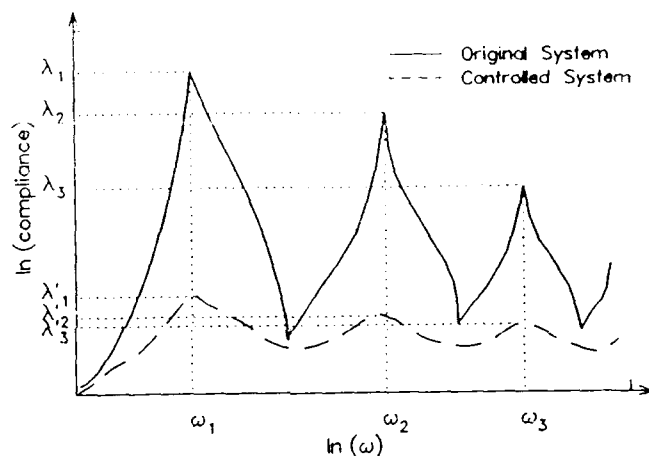
Figure 13. Controlled damping response changes.

ACTIVE DAMPING MODELING

All active control devices are spatially well defined; their corrective action is therefore limited to specific modes. They can, however, excite higher order vibration modes. This problem of space distribution concerns both techniques of active vibration control (eigenvalue adjustment or damping control). However, the negative effects are limited in active damping control and there is no strict need for multiple band pass filtering with this approach.

The general aim of active damping control is to expand the effect of overall damping of the structure (Fig. 14) toward the lower frequency regions in order to reduce the dynamic response over a broader frequency range. Passive damping, with the usual weight limits, is most efficient in

higher frequency engineering applications. Active damping control is useful
for the first few modes too difficult to control by ordinary techniques.
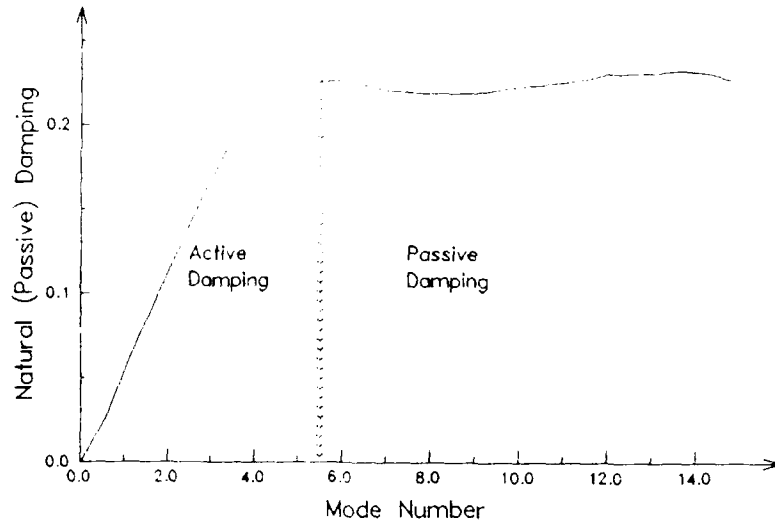
Figure 14.   Diagram of overall damping coefficient of a
             nominal structure as a function of mode number.

A comparative evaluation of advantages and disadvantages is presented
in Table 3.

Table 3.   Advantage and Disadvantage Comparative

	ADVANTAGES	DISADVANTAGES
Active Control	· Improvement of dynamic behavior	· Energy input · Instabilities
Passive Control	· Stability · Ruggedness · Reliability	· Limitations in structures · Weight and space problems
Active and Passive Control	· Reduction of active driving elements · Reduction of energy	· Stability · Space requirement

We have developed a computer model to study the optimization of
active/passive damping in beams under various conditions. This model is
based on single pairs of elements (one sensing, the other providing active
input) as follows:

- a velocity sensor
- a gain control (amplifier)
- a distributed force generator (piezofilm)

The model gives the optimum location and the spatial extent of the sensors. This model makes it possible to identify the modal contamination and to avoid unwanted resonances in the system. It has been used to study potential applications of PVDF piezofilms as well as thin PZT ceramics. Results show that, although PVDF has a lower intrinsic effect, its low density and fast response make it a suitable material for control of low frequency vibrations in light weight structures. The model shows also that the best combination of dipoles is local sensors associated with local actuators as opposed to large area actuators or arrays.

Further work will be required to analyze possible combinations of PVDF distributed sensors and other types of more energetic local actuators to provide a good compromise for active vibration control for general use.

F.   SUMMARY

PVDF has many applications in both measurement and control of shock and vibration.

Recent advances in stretching and poling techniques have resulted in a shock transducer which is reproducible to fast-rising (~ ns) shock waves in its response. Attention to quality control requirements of production and details of calibration tests leads to identical response for gauges produced at separate facilities in France and the U.S.A. These transducers have been used at stresses as high as 46 GPa. Lower stress calibration (0.1 to 0.4 GPa) of similar transducers using a Hopkinson bar is also reported.

PVDF also shows promise in active damping applications where its high polarization per unit mass make it particularly attractive. Techniques are being developed to optimize such systems.

REFERENCES

1. F. Bauer, "Behavior of Ferroelectric Ceramics and PVF_2 Polymers Under Shock Loading," Shock Waves in Condensed Matter - 1981, eds. W.J. Nellis, L. Seaman, R.A. Graham, Amer. Inst. Phy. (1982) p. 251.

2. F. Bauer, "Piezoelectric and Electric Properties of PVF_2 Polymers Under Shock Wave Action: Application to Shock Transducers," Shock Waves in Condensed Matter - 1983, eds. J.R. Asay, R.A. Graham, G.K. Straub, North Holland (1984) p. 225.

3. F. Bauer, "PVF_2 Polymers: Ferroelectric Polarization and Piezoelectric Properties Under Dynamic Pressure and Shock Wave Action," Ferroelectrics, Vol. 49, p. 231, (1983).

4. F. Bauer, "Properties and High Pressure Shock Loading Response of Poled Ferroelectric PVF_2 Polymer Gauges," Techniques and Theory of Stress Measurements for Shock Wave Applications, eds. R.B. Stout, F.R. Norwood, M.E. Fourney, Amer. Soc. Mech. Eng., (1987) pp. 19-28.

5. L.M. Lee, W.D. Williams, R.A. Graham, F. Bauer, "Studies of the Bauer Piezoelectric Polymer Gauge (PVF_2) under Impact Loading," Shock Waves in Condensed Matter, Y.M. Gupta, ed., Plenum Press, New York (1986), p. 497.

6. D.J. Fogelson, L.M. Lee, D.W. Gilbert, W.R. Conley, R.A. Graham, R.P. Reed, and F. Bauer, "Fabrication of Standardized Piezoelectric Polymer Shock Gauges by the Bauer Method," Shock Waves in Condensed Matter - 1987, Elsevier Science Publishers, B.V. (1988) p. 619.

7. R.A. Graham, L.M. Lee and F. Bauer, "Response of Bauer Piezoelectric Polymer Stress Gauges (PVDF) to Shock Loading," Shock Waves in Condensed Matter - 1987, Elsevier Science Publishers, B.V., 1988, p. 619.

8. R.P. Reed, "Recent Developments in Piezoelectric Polymer Stress Gauges," Proceedings The Range Commanders Council, Instrumentation/-Transducer Committee, 14th Transducer Workshop, ed. S.F. Kuehn, Colorado Springs, CO, 16-19 June 1987.

9. F. Bauer, "Method and Device for Polarizing Ferroelectric Materials," U.S. Patent 4,611,260, September 9, 1986.

10. LASL Shock Hugoniot Data, Stanley P. Marsh ed., University of California Press, Berkeley, CA. (1979).

11. F. Bauer and A. Lichtenberger, "Use of PVF_2 Shock Gauges for Stress Measurements in Hopkinson Bar," Shock Waves in Condensed Matter - 1987, Elsevier Science Publishers, B.V. (1988), pp. 631-634.

12. P. Poudant, Study Report FCAM68, Metravib R.D.S., (Private Communication), June 1988.

INERTIAL REFERENCE AND TRACKING SYSTEM
FOR THE MEASUREMENT OF
BLAST INDUCED DISPLACEMENTS

Paul H. Frisch
Applied Physics Inc.
31 Highview Avenue
Nanuet, NY 10954

Richard Pearson
U.S. Army Ballistic Research Laboratory
Aberdeen Proving Ground, MD

One of methods utilized to assess the nuclear survivability of military material (vehicle), is the measurement or determination of the dynamic response to a shock or acceleration environment as simulated during blast tests, in large shock tubes or blast simulators. The ability to effectively track vehicle response utilizing photographic methods is severely limited due to dust and condensation introduced by the simulation. This publication details the methodology, design and fabrication of an Inertial Reference System to measure blast induced linear and angular dynamic response.

The microprocessor-based Inertial Reference System (IRS) is generally illustrated in Figure 1. The system consists of three subassemblies, the primary containing the processor, memory, RS232 communications, and all the analog and digital circuits required to interface with sensors, battery subsystem and processor data bus. The battery assembly houses four custom battery packs consisting of rechargeable NiCAD cells and charging circuits. The sensor assembly provides the precise mounting configuration, orienting the sensors in a predescribed orientation necessary to quantitatively interpolate the precise linear and angular acceleration terms. The system interfaces to a panel mounted control switches enabling the user to manually define channel gains, sampling frequency, filter reference frequency and delay timer. The system interfaces to an IBM based PC via a dedicated RS232 port, off loading post experiment, the acquired sensor data, onto a mass storage disk for processing and analysis.

Introduction/Background:

The effective tracking of inertial coordinate systems is one of the fundamental requirements of kinematic and dynamic response analysis of ridgid bodies to a shock or acceleration environment. The approach demonstrated to be effective and accurate as applied to human analog research is one where accelerometer derived kinematic variables are the best source of both angular and linear acceleration components while angular and displacement components can be obtained directly from photographic data (1). With careful design, calibration and serial conditioning of accelerometers, angular and
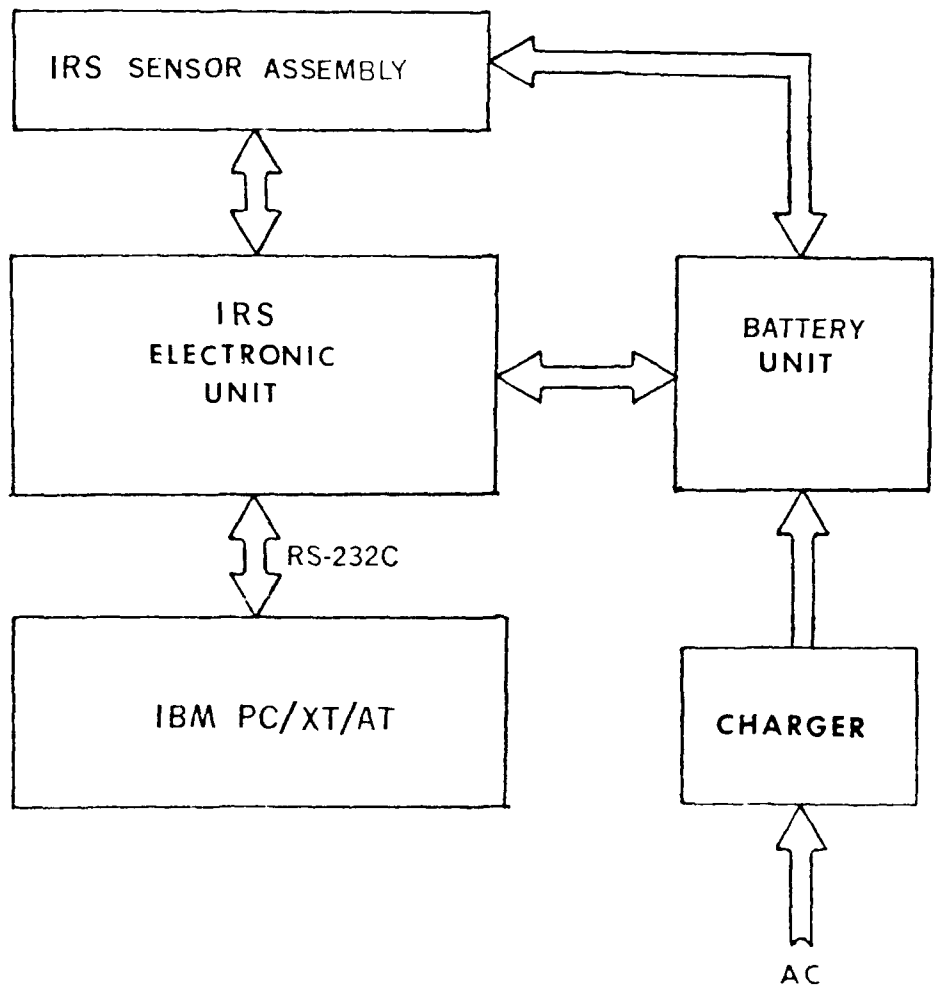
IRS BLOCK DIAGRAM

FIG 1

linear velocity estimates derived from *integration* of accelerometer data have been shown to correlate with those derived from differentiation of photographic data for time durations, typical of shock/impact events.

Both inertial and photographic data collection and analysis problems do exist and must be minimized to obtain accurate and unambiguous results. It is customary that tracking of photographic targets, attached to ridgid bodies be accomplished by at least two cameras, with displacement and orientation determined via a least-squared algorithm of the target locations to compensate for the discrete nature of the data. In order to adequately process photographic data, it is required to have a transformation from points in the object plane to points in the film plane. This of course requires accurate calibration of each camera and precise surveying of the location and orientation of the camera in the inertial reference frame.

Environmental constraints introduced by the blast test or simulated blast complicate the usage of photographic techniques. Resulting dust and condensation make transformation of points from the object plane to the film plane impossible, limiting photographic coverage. Consequently, an alternative technique enabling the 3-dimensional tracking of a vehicle as exposed to a blast is required. The following describe the methodology utilized to implement inertial reference techniques.

Sensor Requirements:

The equation of motion defining the six degree of freedom motion of a ridgid body is best illustrated in Figure #2. The acceleration of a point "P" on the ridgid body (vehicle) is given by equation 1. Typically, point "P" is associated with an instrumentation mounting location, with point "B" defined as the vehicle or ridgid body reference coordinate system. Since system "P" is fixed relative to system "B", based on ridgid body assumptions, the equation of motion reduces that of equation #2. Equation #2 can be represented in component form as shown in equation #3, defining the following required parameters to solve the equation of motion.

- Linear accelerations XYZ
- Angular accelerations
- Angular velocity
- Displacement between coordinate systems.

In order to evaluate the equation of motion, both linear and angular terms have to be measured directly or derived from these measures. It is assumed that initial position is known, so that all relevant parameters of the trajectory can be expressed in the inertial reference frame. There are basically four instrumentation options available to quantify the six degrees of freedom motion of a coordinate system coincident with a ridgid body (Figure 3). The first is a combination of three linear accelerometers (measuring the X, Y, and Z responses) and rate gyros measuring the angular velocities about the respective axes. Differentiation of the angular velocities provide the estimates of angular accelerations required to solve the equations of motion. Interpretation of the angular velocity provides angular orientation. In the second option, in addition to the three linear accelerometers, angular accelerations are monitored directly and the data integrated to obtain angular

$$\bar{A}_p = \bar{A}_b + \bar{\ddot{a}}_p + 2 \otimes \bar{w}_b \otimes \bar{v}_p + \bar{w}_b \otimes (\bar{w}_b \otimes \bar{d}) + \bar{\dot{w}}_b \otimes \bar{d}$$
(1)
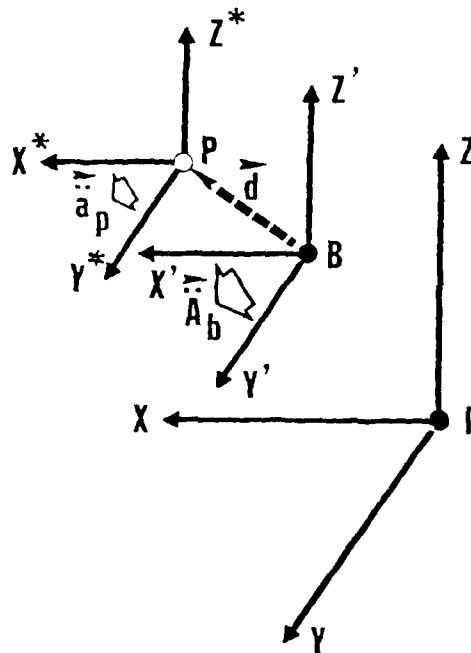
If system P fixed relative to system B then:

$$\bar{\ddot{a}}_p = 0$$

$$\bar{v}_p = 0$$

$$\bar{A}_p = \bar{A}_b + \bar{w}_b \otimes (\bar{w}_b \otimes \bar{d}) + \bar{\dot{w}}_b \otimes \bar{d}$$
(2)

(3)
$$\ddot{A}_{xP} = \ddot{A}_{xB} + w_{pB}(w_{rB}d_y - w_{pB}d_x) - w_{yB}(w_{yB}d_x - w_{rB}d_z) + \dot{w}_{pB}d_z - \dot{w}_{yB}d_y$$

$$\ddot{A}_{yP} = \ddot{A}_{yP} + w_{yB}(w_{pB}d_z - w_{yB}d_y) - w_{rB}(w_{rB}d_y - w_{pB}d_x) + \dot{w}_{yB}d_x - \dot{w}_{rB}d_z$$

$$\ddot{A}_{zP} = \ddot{A}_{zB} + w_{rB}(w_{yB}d_x - w_{rB}d_z) - w_{pB}(w_{pB}d_z - w_{yB}d_y) + \dot{w}_{rB}d_y - \dot{w}_{pB}d_x$$

NEED:

$\ddot{\bar{A}}$

$\dot{\bar{w}}$ or $\bar{w}$

$\bar{d}$

Figure 2   Variables Required to Define 6 DF of Motion.
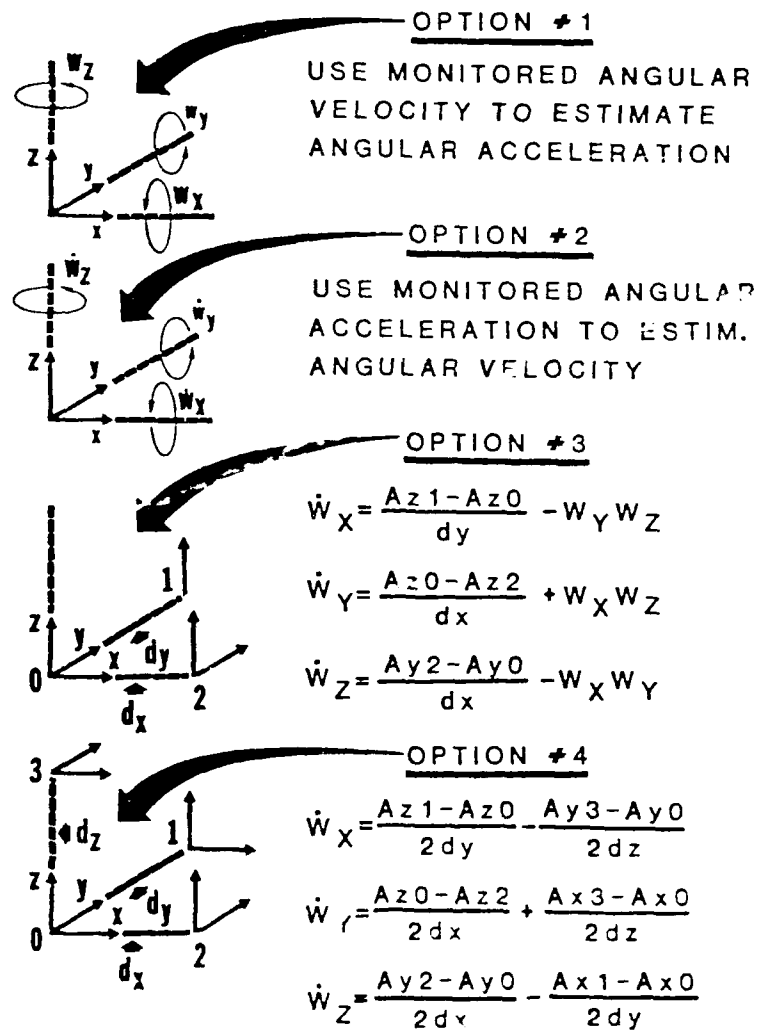
Figure 3   Instrumentation Options.

221

velocity estimates. Option 3 uses an array of six accelerometers, where angular accelerations are derived from the differences in the respective linear accelerations measured, divided by the distance separating them. It should be noted that the cross terms involving the angular velocities are derived from the angular accelerations terms in the previous time interval. Consequently, derivations conducted at time "t" are directly dependent on existing conditions at the "t-1." This has some solution stability implications and instrumentation packages based on such an array should not be employed in long pulse duration events. Finally, under the last option (Option 4), a cluster of nine accelerometers can be used to obtain separate estimates for both the angular accelerations and angular velocity cross terms (needed to solve the equations of motion) and these estimates are functions solely of differences between respective linear acceleration terms existing at the time "t". This provides for increased stability over Option 3. All the aforementioned candidates are presently available as off the shelf technology. The choices of instrumentation configuration options to be taken and the sensors to be utilized will depend on a trade-off between cost, required accuracy as a function of experiment duration, ease of usage in terms of multiplicity of excitation voltages, required size and duration.

The system developed by Applied Physics under the issued SBIR implemented a nine linear accelerometer configuration described by option #4 and illustrated in Figure 4. The sensor assembly consists of one set of triaxial accelerometers and three pairs of biaxial ones. This arrangement makes it possible to directly determine the angular acceleration and velocities at each time interval, without reliance on parameter computed at previous time intervals. The equations for angular acceleration take the form below, as function of only the linear accelerations and separating displacement.

- $\dot{W}_x = (A_{z1} - A_{z0})/2_{dy1} - (A_{y3} - A_{y0})/2_{dz3}$

- $\dot{W}_y = (A_{x3} - A_{x0})/2_{dz3} - (A_{z2} - A_{z0})/2_{dx2}$

- $\dot{W}_z = (A_{y2} - A_{y0})/2_{dx2} - (A_{x1} - A_{x0})/2_{dy1}$

Similarily, the angular velocity components are determined directly from the following set of non-linear algebraic equations:

- $W_y W_z = (A_{z1} - A_{z0})/2_{dy1} + (A_{y3} - A_{y0})/2_{dz3}$

- $W_z W_x = (A_{x3} - Ax0)/2_{dz3} + (A_{z2} - A_{z0})/2_{dx2}$

- $W_x W_y = (A_{y2} - A_{y0})/2_{dx2} + (A_{x1} - A_{x0})/2_{dy1}$

Consequently, all variables necessary to solve the equation of motion are directly measured or derivable from these measures, utilizing the 9 linear accelerometer.

OPTION #4

$$\dot{W}_X = \frac{Az1 - Az0}{2\,dy} - \frac{Ay3 - Ay0}{2\,dz}$$

$$\dot{W}_Y = \frac{Az0 - Az2}{2\,dx} + \frac{Ax3 - Ax0}{2\,dz}$$

$$\dot{W}_Z = \frac{Ay2 - Ay0}{2\,dx} - \frac{Ax1 - Ax0}{2\,dy}$$
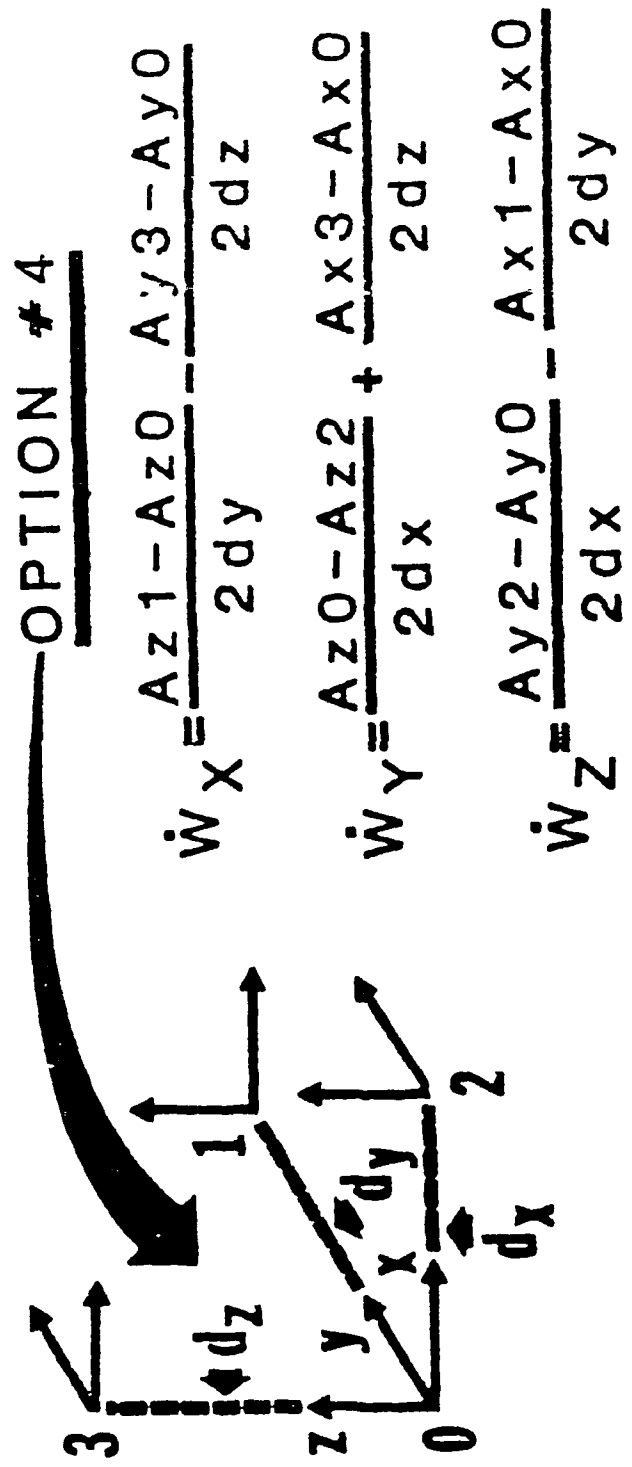
COORDINATE SYSTEM
SENSOR GRID
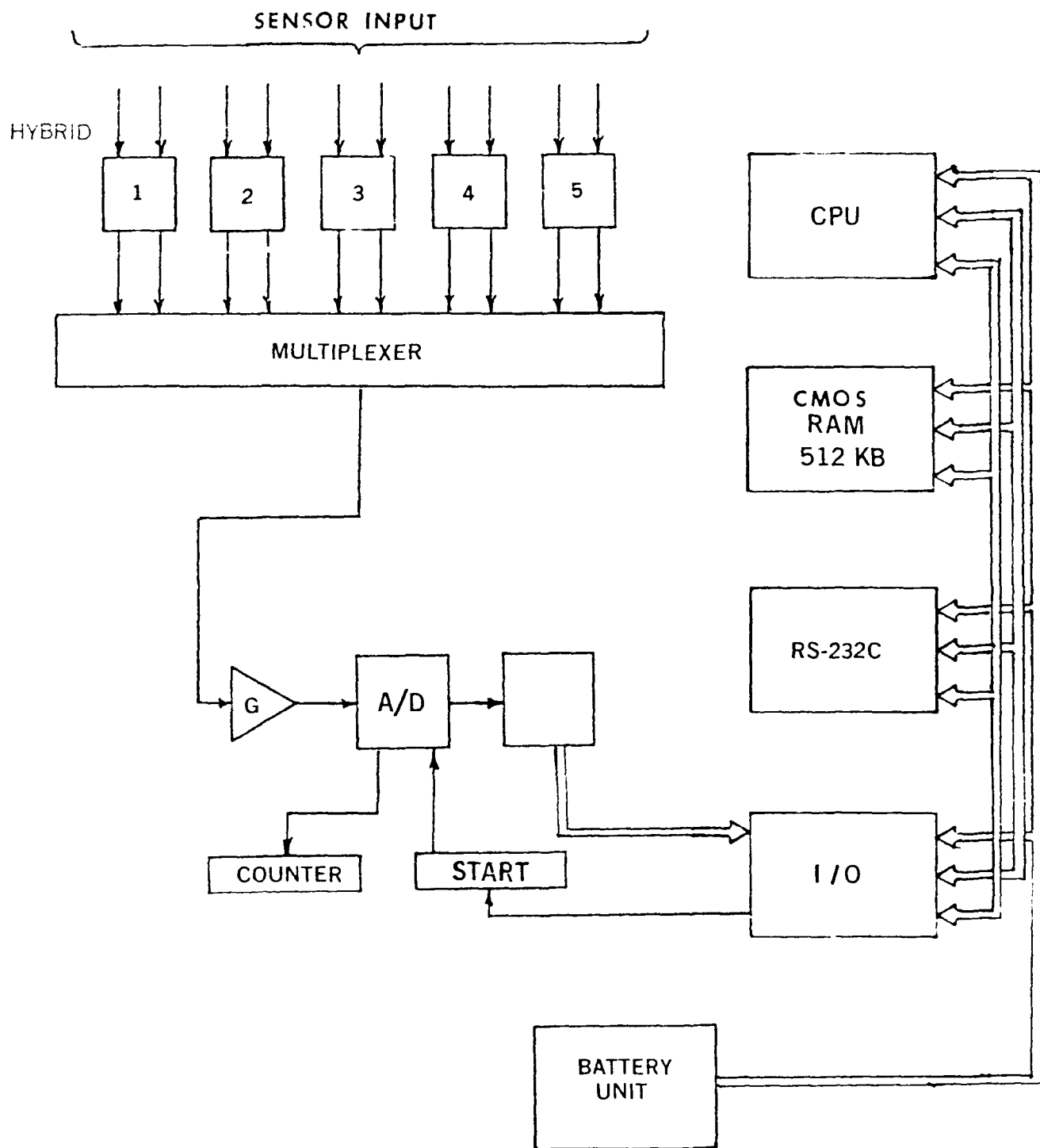
FIG   4

Data Acquisition System Architecture and Design:

The detailed microprocessor-based Inertial Reference System (IRS) as integrated with the miniaturized sensors, and battery assembly is illustrated in Figure 5. The IRS utilizes a dedicated Intel CMOS 8088 CPU, addressing up to 1 Mbyte of battery backed CMOS RAM memory, supporting precision Pheripheral Interface Timers (PIT) and a programmable RS232 port.

The IRS processor and coupled CMOS RAM interface directly to the analog signal conditioning circuits and A/D conversion, timing and bus interface logic. The analog portion of the system consists of an analog card set, where analog A, illustrated in Figure 6 houses all the signal condition circuits, consisting of dedicated custom hybrids, calibration references and offset adjustment circuits. Analog A is designed to support 10 signal conditioned channels maintaining +/- 5VDC input. Analog B, illustrated in Figure 7, provides the A/D conversion network and STD bus interface for the panel switches and A/D output data. Additionally, Analog B, handles the interrupt pulse train or sampling frequency based on the input of the start of the experiment input.

Each analog channel housed on Analog A contains a dedicated analog signal conditioning path as illustrated in Figure 8. Each channel supports a differential instrumentation amplifier with a variable, CPU programmable sampling frequency and gain, maintaining a full scale signal at the A/D converter. Connected to the amplifier is a anti-aliasing filter, providing a CPU adjustable 500 hertz cutoff and a minimum rolloff characteristic of -45 db/octave.

The filter is coupled to a dedicated sample and hold circuit, time synchronized with all other channels. The analog channels are multiplexed to provide dedicated input paths to the A/D converter (Analog B). The A/D is a high speed, bipolar input converter maintaining 12 bit resolution. The converter function and multiplexer addressing (selection of sensor input) is under processor control. The system utilizes a stable clock, count down circuitry, and logic to provide interrupts, hold signals and latching supporting available data sampling frequency. Additionally, the IRS primary unit houses the hardware and software to support parallel input/output lines (for hardware control), and a RS232 asynchronous serial communication interface maintaining communications with the IBM/compatible offload system.

The IRS offload computer and analysis station is a portable IBM compatible unit, communicating with the IRS via an RS232 interface. The IBM or compatible maintains a mass storage media to offload calibration and experimental data from the IRS. The IBM provides all data processing/analysis required to determine and display the time history response of the vehicle to a blast.

IRS SYSTEM DIAGRAM

FIG   5A

PROTECTIVE
COVER

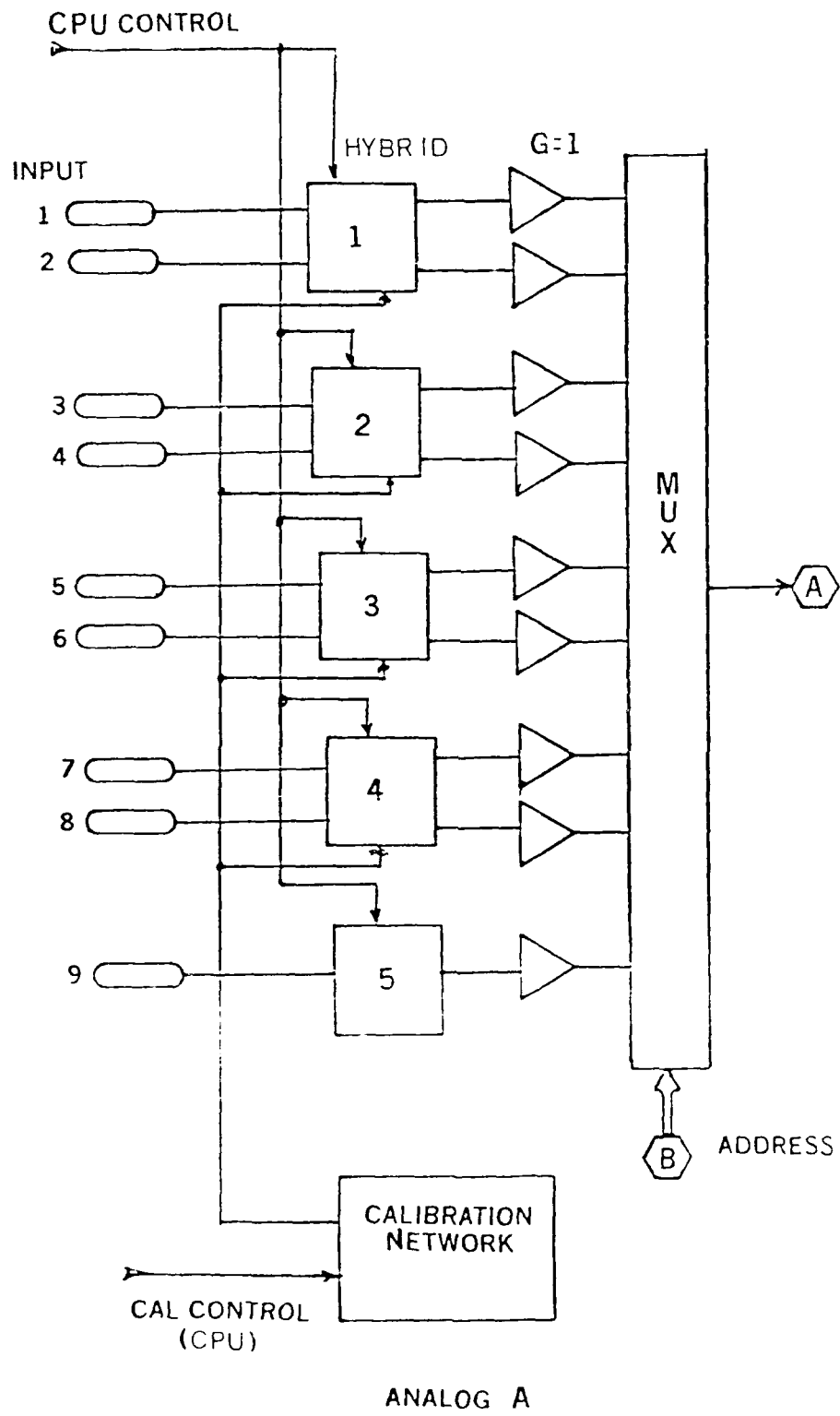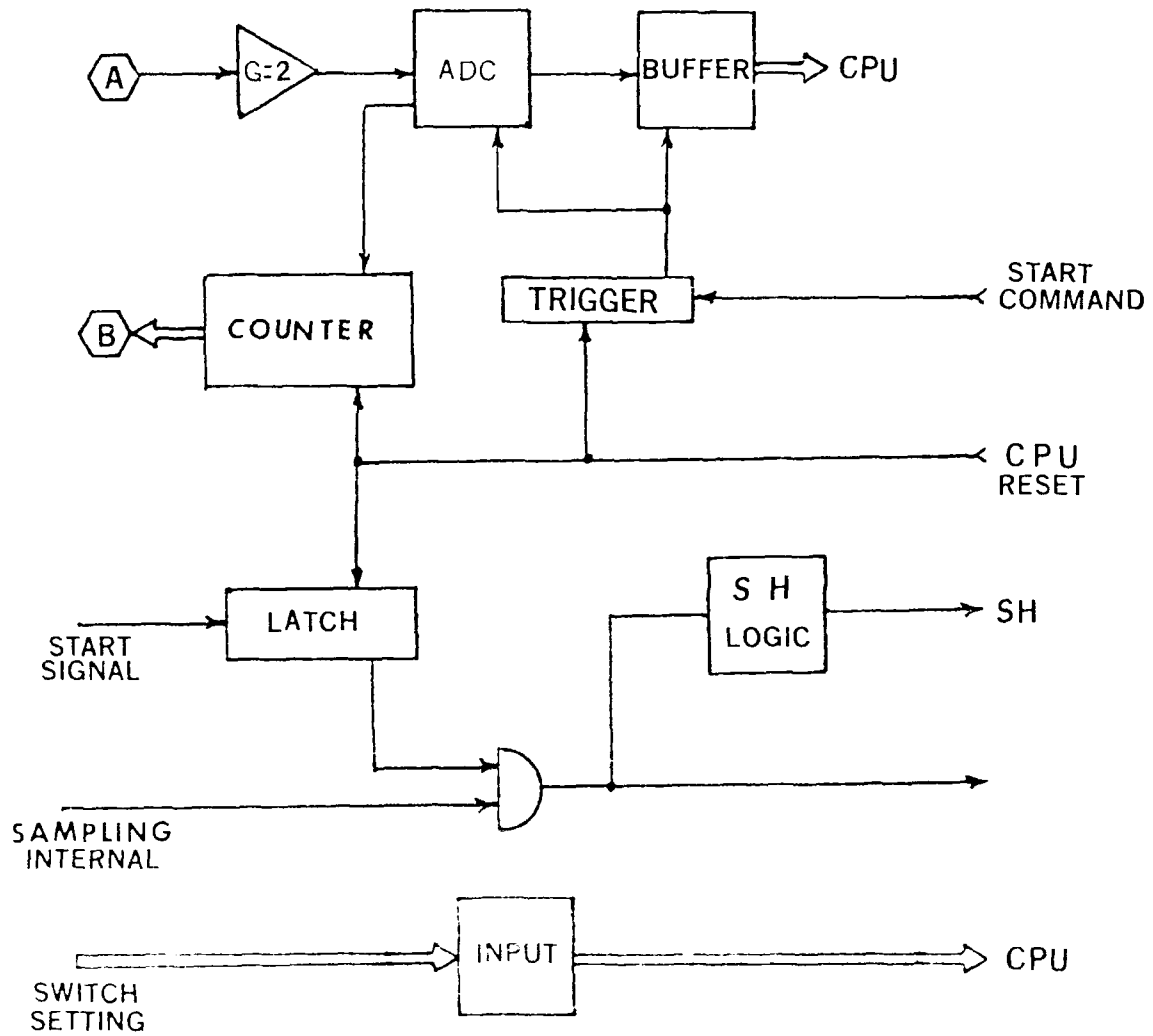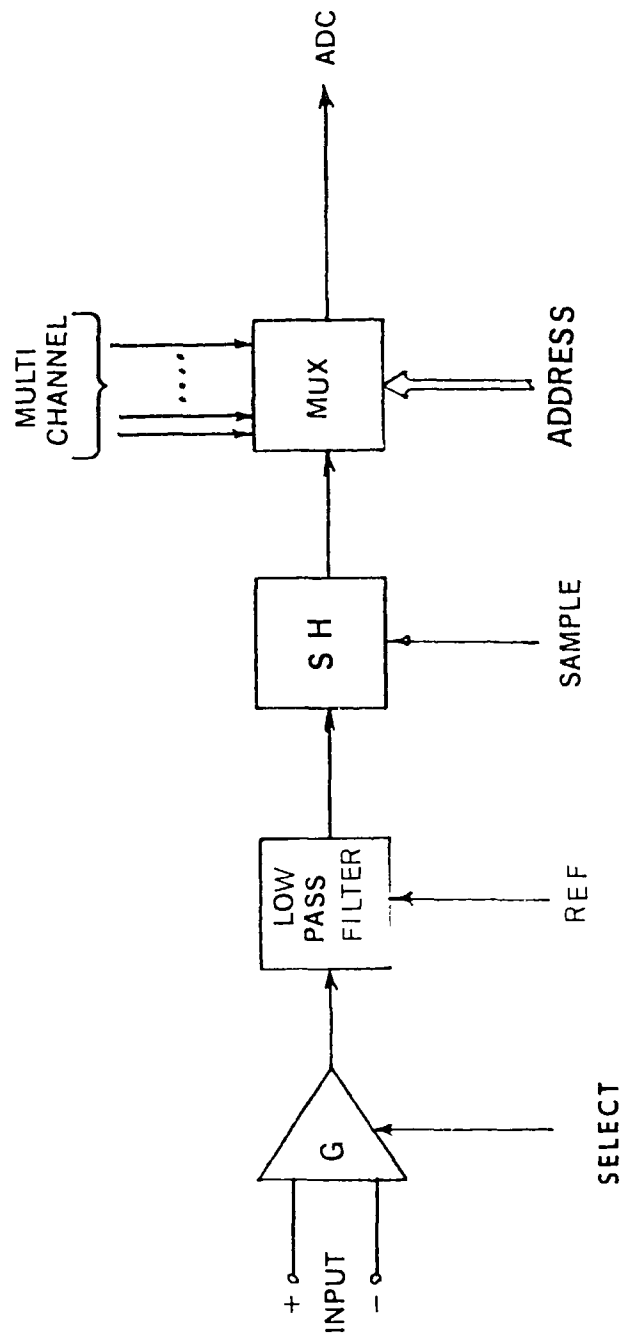CONNECTOR

SENSOR CLUSTER

TRANSDUCER
CHASSIS

ELECTRONIC
CHASSIS

BATTERY
CHASSIS

REMOTE

PWR
INPUT

CHARGER

RS 232

BATTERY
OUTPUT
S

MOUNTING
RAIL

CONTROL

| 1 | 2 | 3 | 4 | 5 | 6 | 7 | 8 |

DISPLAY

KEY
PAD

GAIN SELECT
FREQ SELECT
DELAY SELECT

DATA

XMIT

CAL
DATA
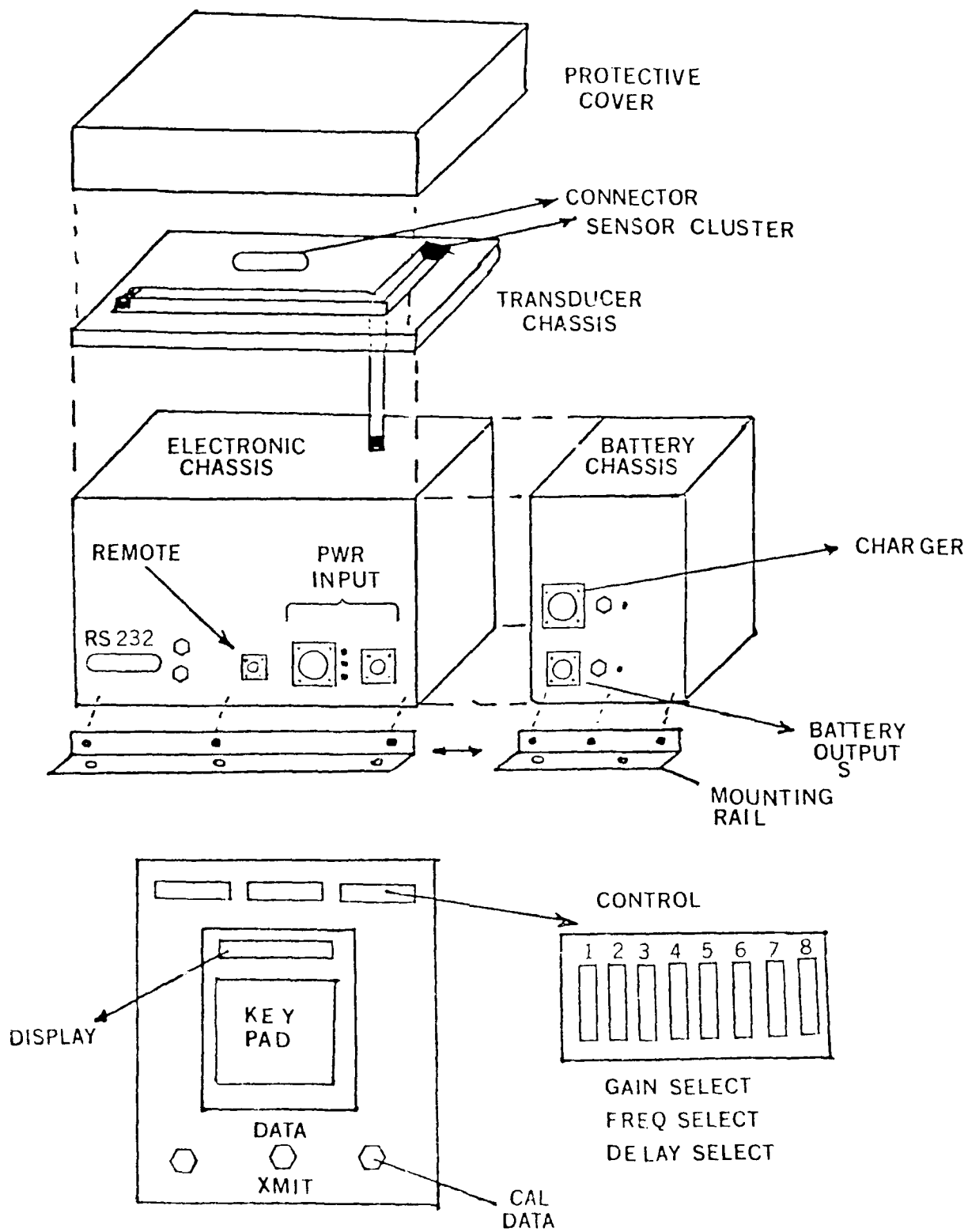
IRS   MECHANICAL   LAYOUT

FIG 5B

CPU CONTROL

INPUT

HYBRID   G=1

CALIBRATION
NETWORK

CAL CONTROL
(CPU)

MUX

A

B ADDRESS

ANALOG A

FIG 6

ANALOG   B

FIG   7

SIGNAL CONDITIONING

FIG 8

The IRS is self-contained and totally powered by rechargeable batteries. The batteries provide sufficient power to maintain system operation for 2.0 hours and data integrity for 4-8 hours. The system contains a power switching network to facilitate use of external DC power for system checkout and maintenance, precluding unnecessary drain of the onboard battery prior to test.

System Operational Theory

The microprocessor-based Inertial Reference System function is defined by the assembly language operating software, structured as illustrated in Figure 9, and divided into the following functional phases:

    Pretest
    Calibration
    Data Offload/Transfer
    Acquisition
    System Monitor

Upon power up, the system enters a pretest mode updating all status registers, memory pointers, communication ports and hardware latches. The pretest software establishes communications with the IBM user interface (RS232) and programs the variable experiment dependent characteristics such as sampling frequency, number of channels, sensor type and the sensor characteristics to their default configuration.

With the system in the PRETEST mode, the software monitors the panel switches for user input in specifying or defining the channel gains, sampling frequency and delay timer frequency. In the normal mode, the system continues onto the automatic calibration procedure. The calibration software provides a means of measuring the errors introduced from the sensor through all components of the system. The system supports two modes of calibration, automatic (voltage substitution) and shunt. In the shunt (RCAL) mode, the processor shunt loads each sensor with a known resistive load, measuring the sensor output at the A/D and storing the results. In the automatic mode, the calibration software provides a voltage substitution scheme simulating a ground analog input into each channel. The system additionally maintains the capability to perform pre and post experiment or test calibrations.

The data acquisition software is based on an interrupt architecture, where an interrupt pulse is generated at the desired data sampling frequency. The interrupt based acquisition is enabled by a start of experiment signal and provides the hold signal to the sample and hold circuits, time synchronizing all channels. Each interrupt triggered acquisition cycle will start the A/D conversion process, and subsequently input data from the A/D converter, storing ... 2 bytes (16 bits), sequentially into memory. The system collects data as 12 bits, with the system automatically loading the 4 most significant
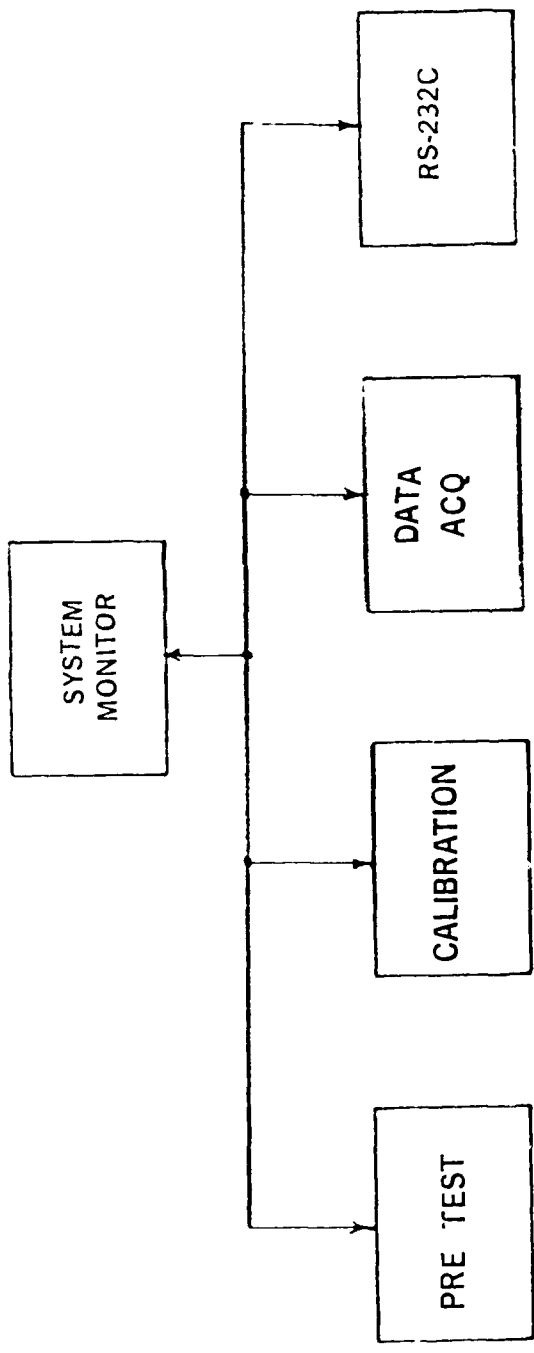
SOFTWARE STRUCTURE

FIG 9

bits with zero, prior to storage, reducing the software overhead necessary for offload of data to the IBM. Each sampling interaction blocks all corresponding channel data with preceding elapsed time data and end of record (EOR) - post data separator. Acquisition is terminated and returns to the system monitor automatically when either the maximum experiment time or available memory has been exceeded.

The communications software provides the link between the IRS and IBM interface, via a serial RS232 port shared by both processors. The data offload, or transmit software, offloads the entire contents of experiment memory (system status, pre/post calibrations, and experimental 'ata), onto the IBM or compatible mass storage device via the RS232 port. The software adheres to all protocols (XON, XOFF, etc) specified by these bus specifications. The PC maintains software to unpack the interleaved binary data and convert the binary into both analog voltage levels or scientific units. The PC Fortran-based software will then process the data providing a quantitative output of the six degree of freedom motion of the vehicle in question.

IBM User Interface and Analysis Software

IBM PC/AT micro-computer provides the user interface, analysis package and data offload media in support of the IRS. The IRS is connected to the IBM via a single RS232 serial communications port and provides the user the capability to define the configuration of the IRS, offload or transfer data to the IBM, translate the data into scientific units and provides an analysis package to quantitatively determine the 6 degree of freedom motion of the vehicle in response to a blast scenario. The analysis package is written in Fortran operating under PC-DOS operating system, while the interface and offload software is coded in "C". The software package provided with the IRS includes all software necessary to compile, link, edit and execute both C and Fortran routines.

The Fortran-based analysis software enables the three-dimensional time history trajectory of the vehicle response to a blast scenario to be computed. Additionally, the software supports 3D graphics software to dynamically display the response profile.

Detailed Data Analysis Procedure

In summary, consider the 3 coordinate systems consisting of the instrumentation system P, the vehicle coordinate system B, and the reference system I (Figure #2). The sensors are mounted in System P in the orientation as illustrated and defined in Figure #4. The analysis software prompts the user for the dx, dy, dz separation between the sensors, which are fixed for the system as delivered. Additionally, the ROLL, PITCH, YAW mounting angles relative to the B coordinate system and the displacement, x, y, z, between the two systems must be entered. These are manually entered from the survey results produced when mounting the system. Additionally, the displacement and angular orientation of the vehicle system relative to the reference coordinate system must be entered at the corresponding prompts. The vehicle coordinate system B may initially coincide with reference coordinate system.

Initially, the accelerations along each axis in the P coordinate system are derived directly from the measured acceleration along those axis, that is

$$Axp = Aox$$
$$Ayp = Aoy$$
$$Azp = Aoz$$

The analysis routine continues by computing the angular velocities and acceleration about the axis in P coordinate system as follows:

$$WpWy = \frac{Az1 - Az0}{2dy} + \frac{Ay3 - Ay0}{2dz}$$

$$WrWy = \frac{Az2 - Az0}{2dx} + \frac{Ax3 - Ax0}{2dz}$$

$$WrWp = \frac{Ax1 - Ax0}{2dy} + \frac{Ay2 - Ay0}{2dy}$$

$$\dot{W}r = \frac{Az1 - Az0}{dy} - WpWy$$

$$\dot{W}p = \frac{Az0 - Az2}{dx} + WrWy$$

$$\dot{W}y = \frac{Ay2 - Ay0}{dx} - WrWp$$

Where: $\dot{W}p$ Analog Acceleration (pitch axis)
$\dot{W}r$ Angular Acceleration (roll axis)
$\dot{W}y$ Angular Acceleration (yaw axis)

The analysis software then computes the transformation cosine matrix, necessary to translate the accelerations, angular velocities and angular accelerations as measured in the P coordinate system to the B coordinate system. This matrix T is fixed for each time iteration and based on the constant geometry between the instrumentation system and vehicle coordinate system. If the two coordinate systems align, the matrix then defaults to the Identity matrix. The transformation matrix is computed as follows:

$$T = \begin{bmatrix} t_1 & t_2 & t_3 \\ t_4 & t_5 & t_6 \\ t_7 & t_8 & t_9 \end{bmatrix}$$

Where:
- t_1 CosP CosY
- t_2 CosP SinY
- t_3 -SinP
- t_4 SinRSinPCosY - CosRSinY
- t_5 SinRSinPSinY + CosRSinY
- t_6 SinRCosP
- t_7 CosYSinPCosR + SinRSinY
- t_8 SinYSinPCosR - CosYSinr
- t_9 CosRCosP

and:

$$P = \text{Pitch Angle}$$
$$Y = \text{Yaw Angle}$$
$$R = \text{Roll Angle}$$

The transformation requires the transpose of matrix T as follows:

Convert accelerations at P to B coordinate system:

$$\begin{bmatrix} AxB \\ AyB \\ AzB \end{bmatrix} = \begin{bmatrix} T^T \end{bmatrix} \begin{bmatrix} AxP \\ AyP \\ AzP \end{bmatrix}$$

Where:

$$T^T = \begin{bmatrix} t_1 & t_4 & t_7 \\ t_2 & t_5 & t_8 \\ t_3 & t_6 & t_9 \end{bmatrix}$$

Convert derived Angular Accelerations at P to B

$$\begin{bmatrix} \dot{W}RB \\ \dot{W}PB \\ \dot{W}YB \end{bmatrix} = \begin{bmatrix} T^T \end{bmatrix} \begin{bmatrix} \dot{W}RP \\ \dot{W}PP \\ \dot{W}YP \end{bmatrix}$$

Convert derived Angular Velocities at P to B

$$\begin{bmatrix} WRB \\ WPB \\ WYB \end{bmatrix} = \begin{bmatrix} T^T \end{bmatrix} \begin{bmatrix} WRP \\ WPP \\ WYP \end{bmatrix}$$

The software then computes the accelerations at the B coordinate system utilizing the translated parameters substituted into the equations of motion:

$$\ddot{\bar{A}}_p = \ddot{\bar{A}}_b + \tilde{w}_b \, \textcircled{x} \, (\tilde{w}_b \, \textcircled{x} \, \bar{d}) + \dot{\bar{w}}_b \, \textcircled{x} \, \bar{d}$$

$$\ddot{A}_{xP} = \ddot{A}_{xB} + W_{pB}(W_{rB}d_y - w_{pB}d_x) - w_{yB}(w_{yB}d_x - w_{rB}d_z) + \dot{w}_{pB}d_z - \dot{w}_{yB}d_y$$

$$\ddot{A}_{yP} = \ddot{A}_{yB} + W_{yB}(w_{pB}d_z - w_{yB}d_y) - w_{rB}(w_{rB}d_y - w_{pB}d_x) + \dot{w}_{yB}d_x - \dot{w}_{rB}d_z$$

$$\ddot{A}_{zP} = \ddot{A}_{zB} + w_{rB}(w_{yb}d_x - w_{rB}d_z) - w_{pB}(w_{pB}d_z - w_{yB}d_y) + \dot{w}_{rB}d_y - \dot{w}_{pB}d_x$$

All of the parameters on both sides of the equation are now known. As previously calculated.

The analysis software continues by calculating the time based direction cosine transformation matrix translating the data from the B coordinate system to the desired reference coordinate system. This matrix is updated for each sampling iteration, utilizing the changing angular and displacement results for each cycle. The determination of this matrix can simply be outlined as follows:

As before, the transpose of the matrix is utilized to translate the data at the B coordinate system to reference system as follows:

$$A_G \quad = \quad D^T A_B$$

$$W_G \quad = \quad D^T W_B$$

$$W_G \quad = \quad D^T W_B$$

As before, equation #1 is utilized to calculate the acceleration at the reference coordinate system accounting for the angular velocities and accelerations. The velocity at the reference coordinate system is based on the integral of the acceleration and the displacement on the second integral as follows:

$$VXG \quad = \quad AXG \quad (tf - ti)$$

$$VYG \quad = \quad AYG \quad (tf - ti)$$

$$VZG \quad = \quad AZG \quad (tf - ti)$$

$$DXG \quad = \quad VXG \quad (tf - ti)$$

$$DYG \quad = \quad VYG \quad (tf - ti)$$

$$DZG \quad = \quad VZG \quad (tf - ti)$$

The displacements become:

$$DX \quad = \quad \sum DXG \quad + \quad dx$$
$$DY \quad = \quad \sum DYG \quad + \quad dy$$
$$DZ \quad = \quad \sum DZG \quad + \quad dz$$

Where dX, dy, and dz are the initial displacement.

The computation of the angles is based on the term of the direction cosine matrix as defined in equatios and simply become:

$$PG \ (Pitch) = -Sin^{-1} \ (D_{13})$$

$$YG \ (Yaw) = tan^{-1} \ (D_{12}/D_{11})$$

$$RG \ (Roll) = tan^{-1} \ (D_{23}/D_{33})$$

The analysis routine stores for each time sampling period the accelerations (AX, AY, AZ), the velocities (VX, VY, VZ), the displacements (DX, DY, DZ) and the angles (R, P, Y) as translated to the ground reference system.

1. Lustik, L.S., Williamson, H.G., Seeman, M.R., and Bartholomew, J.M., "Problems of Measurement in Human Analog Research," Report No. 82R012, Naval Biodynamics Laboratory, New Orleans, LA, 1982.

2. Becker, E.B., "A Photographic Data System for Determination of 3-Dimensional Effects of Multi-Axes Impact Acceleration in Living Humans.." Proceedings, Society of Photo-Optical Instrumentation Engineers, V. 57, 1975.

3. Becker, E.B., Willems, G., "An Experimentally Validated 3-D Inertial Tracking Packing for Application in Biodynamic Research," Proceedings of 13th Stapp Car Crash Conference, Society of Automotive Engineers, Inc., Warrendale, PA, 1975.

4. Ewing, C.L., Thomas, D.J., Lustick, L.S., Muzzy, W.H. III, Willems, G., Majewski, P.L., "Dynamic Response of Human Head and Neck to +Grr Impact Acceleration." Proceedings of the 21st Stapp Car Crash Conference, Society of Automotive Engineers, Inc., Warrendale, PA, 1977.

5. Frisch, G.D., Frisch, P.H., "The Development of a Dynamic Response Sensing and Recording System for Incorporation into a State-of-the-Art Manikin." Proceedings of the 21st Annual Symposium of the SAFE Association, Van Nuys, CA, 1983 and SAFE Journal, Spring Quarter, 1984.

6. Frisch, G.D., Whitley, P.E., Frisch, P.H., "Structural Integrity Tests of a Modified Hybrid III Manikin and Supporting Instrumentation System," Proceedings of the 22nd Annual Symposium of the SAFE Association, Van Nuys, CA, 1984; and the SAFE Journal, Summer Quarter, 1985.

7. Willems, G., "A Detailed Performance Evaluation of Subminiature Piegoresistive Accelerometers." 23rd Intl. Instrumentation Symposium, Instrumentation Society of America, 1977.

8. Willems, G., "A Detailed Evaluation of the Endevco Model 7302 Angular Accelerometer." Technical Report NBDL-83R009, Naval Biodynamics Laboratory, New Orleans, LA, 1983.

9. Frisch, G.D., Whitley, P.H., Wydrie, G., Holdaway, D., "High Speed Ejection Tests of a Modified Hybrid III Manikin." Proceedings of the 23rd Annual Symposium of the SAFE Association, Van Nuys, CA, 1985.

MECHANICAL SHOCK SENSORS
(A FEASIBILITY STUDY)

David Frommer, Michael Gross, and David Heller

Advanced Technology and Research, Inc.
14900 Sweitzer Lane
Laurel, MD 20707

The designs of four mechanical gages for high level shock characterization are proposed and tested. Of the four, the use of an IR heat-sensitive film and the degaussing of a permanent magnet proved to have severe restrictions on their implementation. However, the gages based on copper-ball and pyrotechnic systems showed sufficient promise for continued investigation. The copper-ball system produced a linear measurement of acceleration, exhibited a very high natural frequency, and showed a capability of recording acceleration in the hundred thousand g range. The use of a pyrotechnic device demonstrated consistent results for velocity-change measurement when used as a family of gages. The device serves to bound the velocity change by providing a velocity threshold measure of go/no-go information. By using the peak-reading copper-ball accelerometer together with a sufficient number of pyrotechnic gages, additional information can be inferred about the duration and shape of the shock pulse.

INTRODUCTION

Today's weapons (warheads, projectiles, and attack vehicles) must withstand impacts far beyond the survival capability of on-board, electro-mechanical shock-recording instrumentation. In the sixties and seventies, significant advancement was made in the area of electro-mechanical shock instrumentation which led to a disinterest in the development of mechanical shock (MS) sensors. In recent years shock levels have begun to exceed the survival range of the most advanced electronic shock instrument. A pressing need exists for low-cost, high-g, high-frequency MS sensors that can be mounted with ease on board high velocity impacting- or impacted-vehicles and, on recovery, provide accurate measurement of shock peak levels. While not the best method to defining the weapon-shock environment, MS sensors can, as they have for many years, provide enough shock-correlation information to make it possible to conduct design tests on weapon components in the laboratory under controlled and accurately monitored conditions.

The objectives of this study were the following: determine the feasibility of extending the range, readability, and simplicity of existing MS sensors, while conducting studies on non-conventional materials that may have correlative and

linear response to shock. These objectives were merged by selecting four types of MS sensors to be examined, tested, and developed. Two of these, the copper-ball and pyrotechnic sensors, demonstrate considerable promise. The results and limitations of this study are presented and recommendations made for further developing the proposed gages.

PROCEDURES

SHOCK TESTER

The study called for a shock environment that was high in frequency and acceleration, such as a steel-on-steel impact. To achieve these conditions an air gun was used to launch a steel projectile at a plate to which the test gages were attached. The gages, along with a conventional accelerometer, were mounted on a 3/4-inch radius from the point of impact (Figure 1). To obtain an approximate half-sine pulse duration of approximately 25 microseconds, a 0.025-inch thick, 1-inch square copper pad was placed on top of the plate at the impact point.
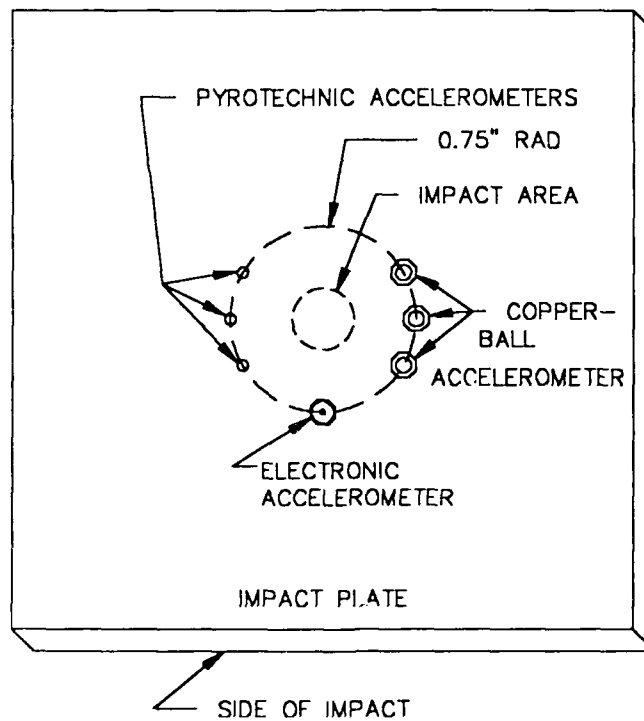
Figure 1: Accelerometer Orientation

DATA ACQUISITION SYSTEM

A conventional accelerometer was used to electronically record the plate response and provide a basis for assessing the performance of the experimental gages. The accelerometers were mounted on a circle centered at the point of projectile impact (theoretically all points on this circle experience identical shock levels). The conventional accelerometer specifications show a linear measurement range of up to 128,000 g and a frequency response of 3 - 50k Hz (+/- 1db). A digital storage scope displayed and transferred the acceleration-time history data to a portable computer from which velocity and a scaled acceleration-time trace were obtained. Figure 2 shows typical plate-response shock data to which the prototype shock sensors were subjected. Table 1 summarizes the tests performed.
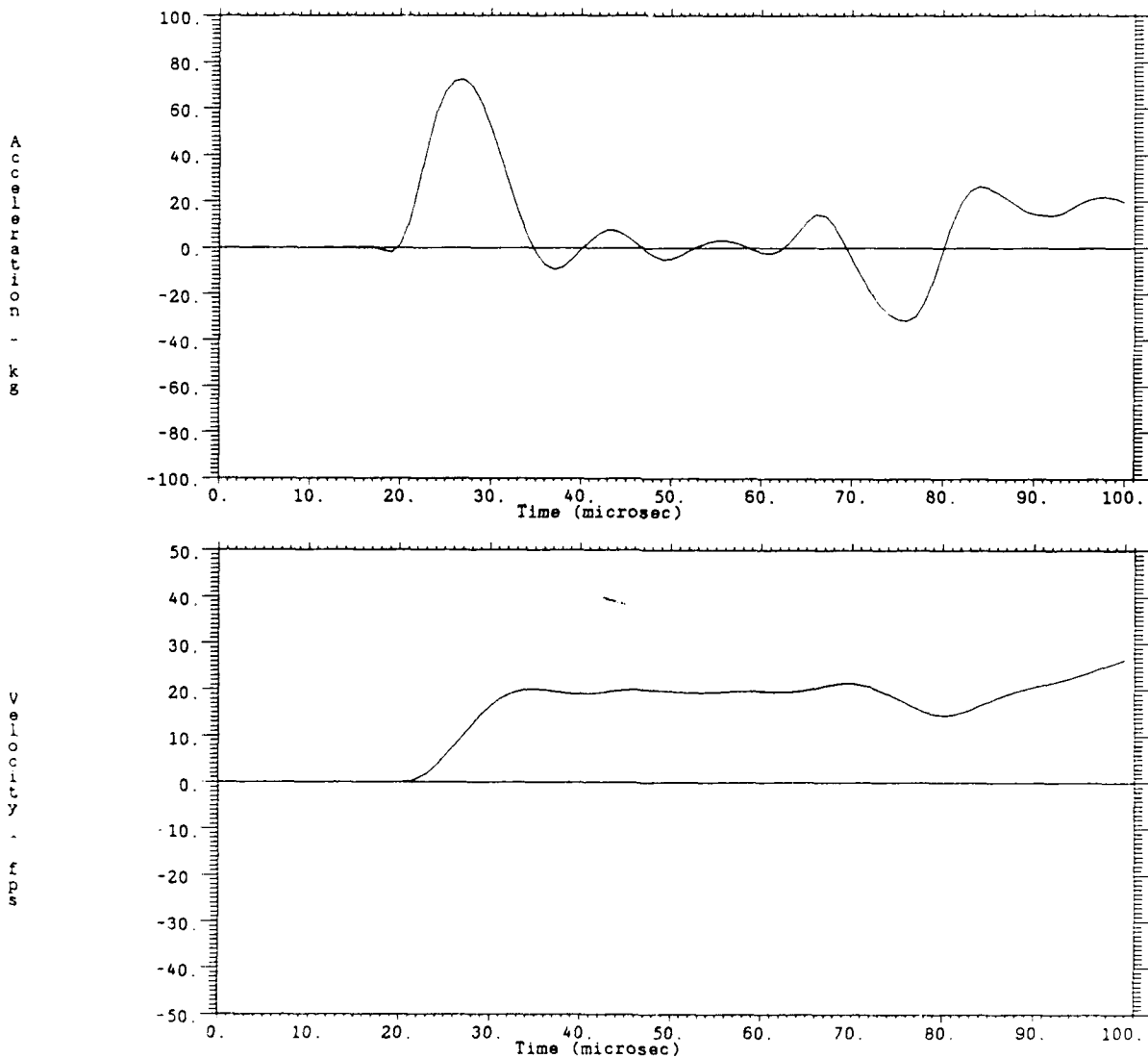
Figure 2: Typical Plate Response

Table 1: Test Summary

Test	Pulse Duration (microsec)	Peak Acceleration (g)	1st Peak Velocity (fps)
331A2	26	143	52
331A1	35	67	28
329A3	28	111	46
329A2	26	122	47
329A1	28	100	37
323A4	58	55	45
323B3	41	80	38
323A2	56	22	24
323A1	50	36	23
322A4	22	96	27
322A3	43	81	36
322A2	43	48	29
322A1	44	37	24
315A3	27	96	39
315A2	24	88	33
315A1	24	63	22
314B3	28	63	23
314A3	27	65	22
314C2	41	29	18
314B2	24	67	23
314A2	27	51	19
314A1	48	12	7
310A3	28	78	29
310A2	22	76	26
310A1	21	66	22
307A4	22	112	36
307B3	18	89	29
307A3	23	76	27
307A2	21	95	33
303B4	18	89	26
303A4	19	90	32
303A3	19	77	24
303A2	22	62	20
303A1	35	15	8
302B4	16	73	20

RESULTS

IR FILM SENSOR AND MAGNETIC SENSORS

The IR Film-based sensor consists of thermosensitive XEROX film sandwiched between the impact plate and an inertial mass. Ideally, a color change occurs in response to the energy associated with accelerating the inertial mass.

Using this arrangement, for the peak acceleration range of 50 to 100 kg, there is no distinguishable film discoloration (discoloration can be achieved under direct impact). An inertial mass considerably larger than those tested is necessary to induce sufficient energy in the film to cause significant discoloration; however, this would result in a lower measurement-system resonant frequency.

A magnetic sensor operates as a stand-alone unit, requiring no inertial mass. When a magnetic material is subjected to a shock environment, the energy product of the magnet is temporarily affected. The change in the flux output from a magnet can therefore be used as an indicator of the severity of the shock environment. Drawbacks to this measurement system include: uncertainty as to the linearity of such a system, the effect of the shock orientation relative to the internal structure of the magnet, the recovery of the original magnetic properties with time, and the brittle nature of the more desirable high energy product magnets.

These difficulties suggest that neither the IR Film nor the Permanent Magnet sensor be recommended as a method of measurement at this level of effort.

COPPER-BALL SENSOR

Conventional copper-ball accelerometers can be used in very high g shock environments through modification of the inertial mass. For this type of system, the measure of acceleration comes from the ''flat'', or indentation, left on the surface of a copper ball from an inertial mass. Since a copper ball deforms in response to force (the result of accelerating the inertial mass), the copper-ball accelerometer offers a peak acceleration measurement.

Copper-ball indentation as an indication of acceleration has been used quite successfully in other shock environments[1]. Extension of this technology to higher acceleration and frequency levels requires the adjustment of the inertial mass to meet the demands of the new environment. Achieving measurements of both higher frequency and acceleration levels requires the use of a light, stiff inertial mass such as Pyrex or other types of glass masses.

Implementation of this type of accelerometer requires special considerations for the fixture of the inertial mass. These include holding the inertial mass in light contact with the copper ball and in the proper orientation relative to the ball at time of measurement. An arrangement which has been found to work well in the laboratory is shown in Figure 3. Here it is seen that the copper ball sits in a socket to minimize deformation due to the fixture. The mass is held against the ball by a small sheet of paper wedged between the coils of the spring and over the top of the mass. This arrangement offers very little additional mass over that of the inertial mass and provides for easy adjustment of the contact force between the mass and the ball.
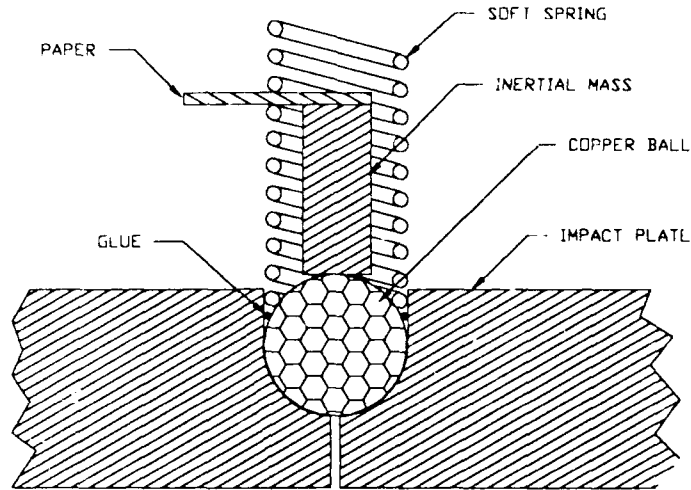
Figure 3: Copper-Ball Accelerometer

When the impact plate accelerates, it applies an accelerating force (via the copper ball) against the stationary inertial mass. This force is recorded as a flat deformation of the copper ball. The flat diameter, for the magnitude of the deformations involved, is much easier to measure than radial deformation. The geometric relation between the two is given in Figure 4.

$$r = 0.0775 \text{ in}$$
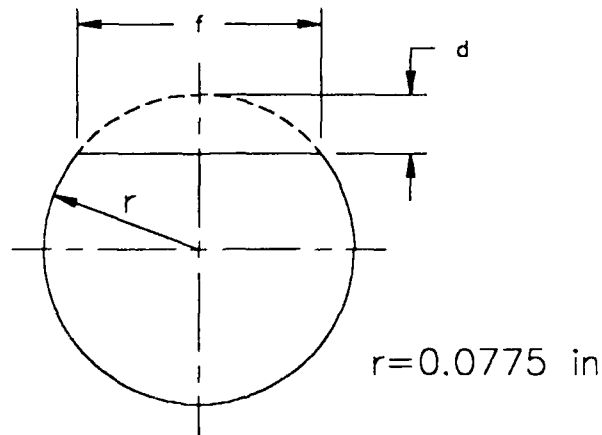
DEFORMATION CALCULATION

$$d = r - \sqrt{r^2 - [f/2]^2}$$

d = radial deformation of ball
r = radius of ball
f = diameter of flat on ball

ACCELERATION CALCULATION

$$a = K_d d / m$$

a = acceleration
m = mass of inertial mass
K_d = dynamic spring rate
        of copper—ball deformation

Figure 4: Copper-Ball Deformation and Acceleration Calculation

Using the dynamic spring rate for the copper ball along with the measured axial deformation gives the applied load necessary to create the deformation. The acceleration in g is therefore given as the applied load divided by the weight of the inertial mass.

The dynamic spring constant of the copper-ball system is also used to calculate the natural frequency of the measurement system. This is done by treating the inertial mass sitting on the copper ball as a free spring-mass system. The natural frequency of this single degree-of-freedom oscillator is given as:

$$wo = (Kd/m)^{1/2}$$
$$= 2(PI)Fn$$

where wo = circular natural freq.
Kd = copper-ball spring rate
m = mass of inertial mass
Fn = natural frequency
PI = 3.14159

The natural frequency of the system is then applied in the conventional manner for dynamic measuring devices.

Table 2 lists a comparison of various copper-ball accelerometers used during the testing. The last column lists some ultimate values which can theoretically be achieved. This is based on an assumed minimum measurable shock input of 25,000 g corresponding to a flat diameter of 0.005 inch. From these two constraints, the mass, size and natural frequency of the copper-ball accelerometer are developed.

During testing, the acceleration of the impact plate is recorded using a conventional accelerometer. Using the method described previously, the flats are used to calculate applied acceleration. Once a preliminary value for acceleration is determined, it is adjusted by the frequency-dependent amplification factor of the measurement system. The ratio of measurement system natural frequency to the primary frequency of the acceleration pulse is used to determine the amplification factor. This is applied to the measured acceleration to arrive at an accurate value for system acceleration. In practice, of course, adjusting the readings according to the dynamics is not possible. The adjustment here is for purposes of investigating the linearity of the copper-ball system.

Table 2: Copper-Ball Accelerometer Capabilities

System	1	2	3	4	Ultimate
Mass (gm)	0.16	0.36	0.45	0.65	0.0271
Material	Glass	Glass	Glass	Steel	Glass
Length (mm)	14	31	39	19	2.334
Diameter (mm)	2.39	2.39	2.39	2.39	2.39
Natural Frequency (hz)	32,000	21,373	19,041	15,876	77,892
Theoretical Diameter Flat based on 25,000 g (in)	0.01215	0.01821	0.02036	0.02444	0.005
Minimum Acceleration (g) based on 0.005" flat	4,225	1,878	1,502	1,040	25,000

Figure 5 is a plot of the dynamically-adjusted, copper-ball measured acceleration (for one particular inertial mass) against the values of acceleration recorded electronically. The data has been regressed and the plot of the best-fit line included. The linear regression finds the relationship between copper-ball measured acceleration and electronically measured acceleration to be:

$$EMA = 1.5817*CBA - 7838.14$$
$$R2 = 0.7627$$

where CBA = copper-ball acceleration
EMA = electronic acceleration
R2 = correlation coefficient
(0=no fit, 1=perfect fit)

The copper-ball accelerometers yield very promising results. Of particular encouragement is the relatively linear relationship between the acceleration measured electronically and that measured using the copper balls.
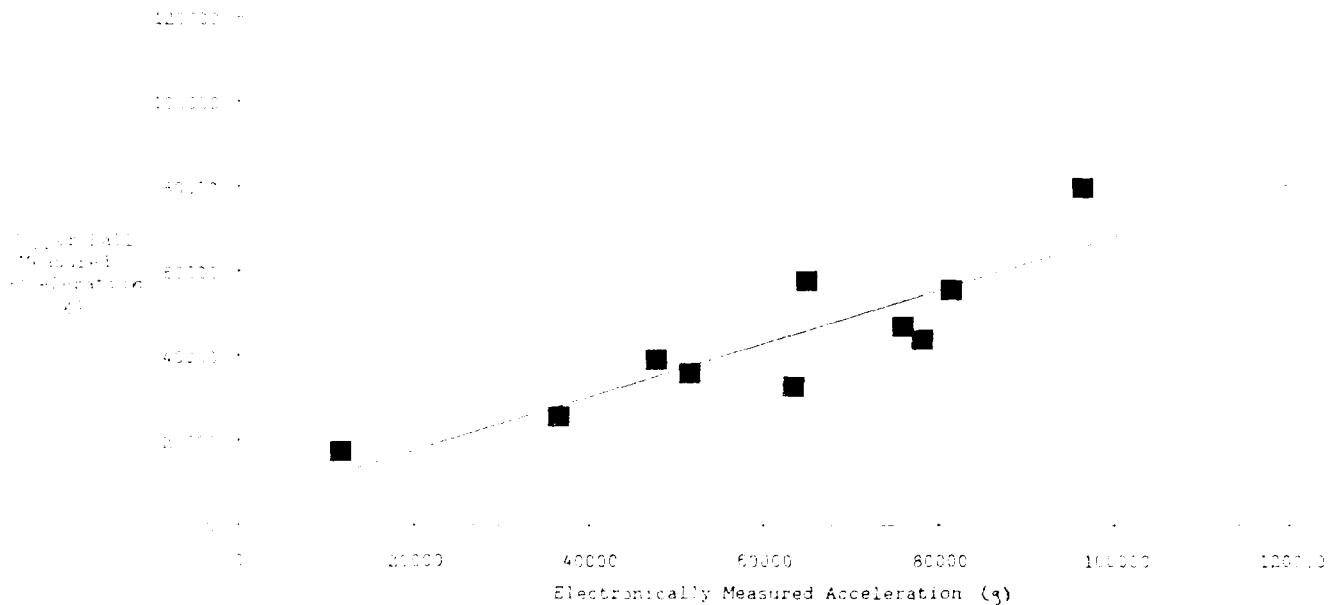
Figure 5: Copper-Ball Acceleration
(0.65gm Ineartial Mass, fn = 15,876)

It is recognized that there is considerable question as to what is the true natural frequency of these copper-ball accelerometers. The weight of the ''mass'' is many times that of the ''spring'' so that the system can not be treated as a true ''mass-spring'' system. However, it is only required that these devices act in a predictably linear fashion over the shock range of interest in order to be of value in determining peak acceleration. It appears that these gages have this inherent capability.

The pyrotechnic shock sensor consists of a small shaped pin (inertial mass) held in place lightly against a pyrotechnic cap by a soft spring (Figure 6). The cap offers a convenient method of holding, mounting and working with a small pyrotechnic material. It is mounted against the impact plate using a drop of glue around the edge. Upon application of sufficient impact-plate velocity, the pyrotechnic ignites through plate and inertial mass interaction. Obviously, this sensor indicates with a go/no-go criterion and is therefore not a peak indicator but a threshold indicator.
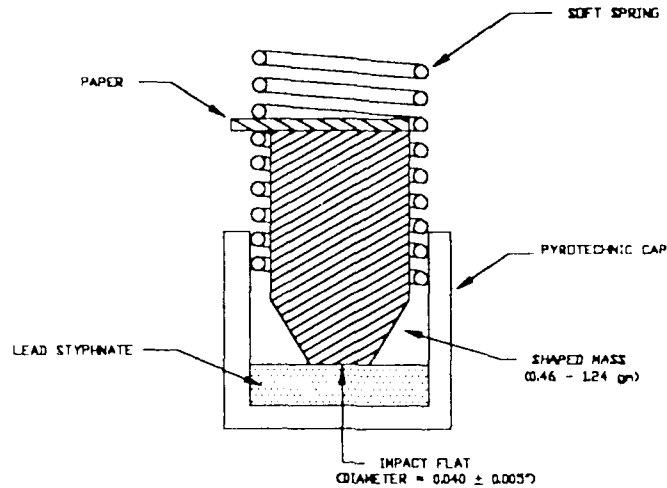
Figure 6: Pyrotechnic Accelerometer

Information obtained from the cap manufacturer lists the active explosives as lead styphnate crystals uniformly distributed within the pyrotechnic paste. The pyrotechnic ignites when sufficient kinetic energy is applied to these crystals. Therefore, the kinetic energy of the inertial mass, as well as its area in contact with the cap, determines whether or not the pyrotechnic will ignite. However, the explosive is temperature sensitive -- less likely to ignite at lower temperatures than higher for the same energy input.

Since detonation of the lead styphnate crystals depends both on kinetic energy and area of contact, an expression called specific energy is used to describe the threshold for detonation. Specific energy is defined as kinetic energy per unit area:

$$\text{Specific Energy (SE)} = \frac{\text{Kinetic Energy}}{\text{Unit Area}}$$

$$= \frac{(0.5) * M * V^2}{PI * (D/2)^2}$$

where M = Shaped Pin Mass
       V = Plate Velocity
       PI = 3.14159
       D = Shaped Pin Flat Diameter

Once the specific energy of detonation is determined it can be used, along with the pin mass and pin flat diameter, to calculate the critical velocity for detonation. Whether detonation occurs determines whether this critical velocity has been exceeded.

The goal of the experimentation was to obtain the specific energy threshold at which the pyrotechnic will ignite. Since specific energy is a function of the shaped pin's mass and geometry (for any plate velocity change, V), the velocity at detonation can be determined by maintaining a constant tip geometry for different masses.

As shown in Figure 1, five pyrotechnic sensors were placed on an equal radius from the impact point. The five sensors had shaped pin masses ranging from 1.24gm to 0.46gm with as uniform-as-possible tip geometry. As expected, the larger mass sensor ignited at the lowest plate peak velocity while the smallest mass ignited at the highest level. Calculating the specific energy ignition level for each system shows a go/no-go threshold of approximately 2200 ft - lb per sq. ft. Figure 7 shows go/no-go, specific energy data calculated for each pin mass. The differences in the threshold levels of detonation may be due to a variety of factors.
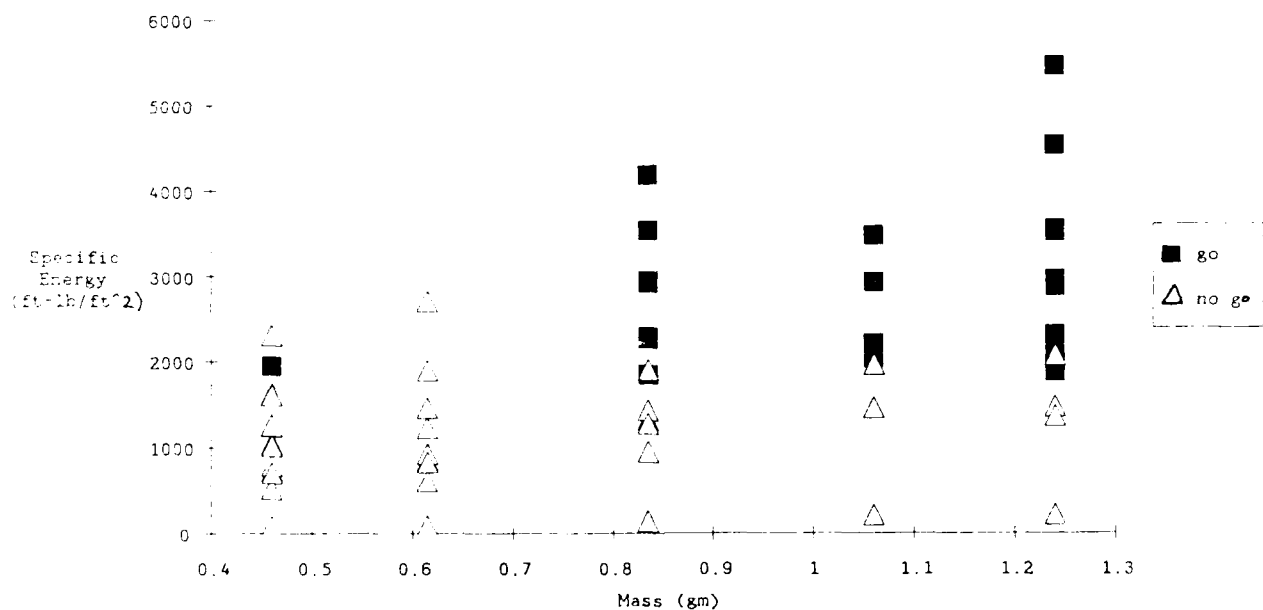
Figure 7: Specific Energy Measurements for Cap Ignition

Some problems with maintaining tip geometry were encountered. The inertial masses were not precision machined pieces, and the variations in tip geometries were found to affect the velocity determination.

Temperature was another uncompensated condition with apparently major effect on cap ignition. The tests were conducted outdoors where there was no control over the pyrotechnic's temperature. For the 0.615gm mass in particular, the specific energy threshold level is higher than for the other four masses. The temperature on the day these tests were made was approximately 20° F which was 20° to 30° F lower than that for the other tests. The effect of humidity on ignition was not determined but could be a factor.

CONCLUSIONS AND RECOMMENDATIONS

The experimental results suggest that two of the shock measurement systems proposed offer encouragement for further investigations. They are the copper-ball accelerometer and pyrotechnic velocity indicator. In contrast, the IR film and permanent magnet accelerometers provided less satisfactory results.

The limitations imposed from both the IR film and the Permanent Magnet accelerometer made these systems impractical to implement during this test series. The conceptual design of both of these accelerometers, however, can not be excluded from possible consideration for future applications, especially at other shock levels.

The copper-ball accelerometer proves quite capable as a peak-acceleration indicator. The measured acceleration (as indicated by the deflections produced from the inertial mass) was reasonably linear with respect to the applied acceleration level, within the limits of the testing environment. Implementation of this system will require a closer investigation into some of the aspects of the accelerometer. First, a more practical fixture method needs to be considered. In addition, the frequency response of the accelerometer requires better characterization. This will also allow for a more detailed investigation into the properties required of the inertial mass. The effects of off-axis loading will also have to be investigated. Finally, if this accelerometer is to be useful for measurement of very high acceleration levels then a closer inspection of the copper ball dynamic spring rate over the entire range of ball deflection will be required.

The pyrotechnic shock sensor shows considerable promise as a severe environment, velocity-change indicator. The results achieved through this testing indicate that with sufficient quality control over the pyrotechnic manufacturing and packaging, the critical energy input from the inertial mass (as measured by the go/no-go condition) appears to be repeatable on a specific energy basis. A working velocity indicator will require a refinement of the inertial mass geometry, an improved fixture arrangement as well as a method for compensating for ambient temperature and humidity.

Concurrent use of the copper-ball accelerometer and pyrotechnic velocity indicator allows for more complete shock environment definition in that other shock parameters may be inferred. The inexpensive, easy to install and read nature of these gages make them attractive for further study.

: DeVost, V.F., ''SHOCK SPECTRA MEASUREMENTS USING MULTIPLE MECHANICAL GAGES (A FEASIBILITY STUDY'', U.S. Naval Ordnance Laboratory, White Oak, Md., NOLTR 67-151, 20 September, 1967

BUILT-IN MECHANICAL FILTER
IN A SHOCK ACCELEROMETER

Anthony S. Chu
Endevco Corporation
San Juan Capistrano, CA

Isolating the sensing element of a transducer from high frequency transient attacks appears to be one of the most effective design improvements in shock accelerometers. An experimental transducer design with integral mechanical filter has allowed the experimenter to record close-range shock excitation without zeroshift, a common linearity error in pyroshock measurement. This piezoelectric accelerometer prototype features both an input mechanical filter and an electronic low-pass filter in order to maximize usable bandwidth. Calibration data indicate flat frequency response to 10kHz with 24 dB per octave roll-off thereafter. Field test results are also shown in this paper.

INTRODUCTION

With all the advances in digital data acquisition equipment and signal processing techniques, the acceleration transducer (accelerometer) is still the weakest link in a pyroshock measurement chain. Current design approaches in accelerometers, such as electronic filtering and high resonance, can not always guaranty the experimenters with repeatable performance and believable results.

The core of the problem has been identified to be the sensing element of the transducer. All sensing mechanisms are vulnerable to high-g excitation at frequencies far above our point of interest. These high frequency, high-g transients, although "invisible" to many recording systems, are present in all close-range pyrotechnic events and metal-to-metal impact testings which are common in many qualification requirements.

The advantage of using a mechanical filter as an isolator is discussed. Isolating the sensing element (piezoelectric or piezoresistive) from high frequency transient attacks appears to be one of the most effective design improvements in shock accelerometer. A shock transducer design with an integral mechanical filter has allowed the experimenter to record pyroshock time history without zeroshift, a common linearity error of the sensor in pyroshock measurement. This piezoelectric accelerometer prototype features both an input mechanical filter and an electronic low-pass filter in order to maximize usable bandwidth. Calibration data indicate flat frequency response to 10kHz with 24 dB per octave roll-off thereafter. A comparison of this unique design with commercially available mechanical filters is also presented. The survivability of transducers in high-g environments has greatly increased due to shock isolation provided by these filters.

PROBLEM IDENTIFICATION

All spring-mass type accelerometers have a finite seismic resonance. To obtain linear response from such a transducer, one must be certain that the input spectrum always stays within its recommended bandwidth. As a general rule-of-thumb, the maximum measured frequency for an undamped accelerometer is to be less than one fifth of the transducer resonance. This rule is generally well observed in the vibration-test community.

Unfortunately, the term maximum measured frequency are often misinterpreted as the upper band of the Shock Response Spectrum in shock measurement. Since most Shock Response Spectra stop at 10kHz or 20 kHz, accelerometers with resonance in the neighborhood of 100 kHz are usually considered adequate for these applications. It is however important to remember that the input spectrum of most high-g shock measurements contains frequency components way above 100 kHz, well beyond the capability of our modern recording devices. These high frequency components are often unnoticeable until something occurs during data acquisition; eg. aliasing of a digital recorder. The most commonly used wide-band analogue tape recorder can only capture time history up to 80 kHz (running at 120 ips), out-of band information is therefore naturally attenuated and "invisible" on playback.

The problem is further confused by the issue of the damage potential of high frequency. It is known that shock inputs above 10 kHz seldom cause any damage to the test article, and they are routinely ignored in most data analysis. These high frequency components, although posing no danger to the article, seriously affect the linear operation of any spring-mass type accelerometer.

Recently, a few papers and articles have been published [1] [2] concerning the effect of ultra-high frequency impulses on shock measurements. This out-of -band transient phenomenon is referred to in the papers as "Pre-Pulse". There are two types of shock simulations capable of generating near true-impulses:

a) Close-Range Pyrotechnic Shock

The process of explosion involves chemical reactions in a substance which convert the explosive material into its gaseous state at very high temperature and pressure. Most explosives, such as Flexible Linear Shaped Charge and pyrotechnic bolts, do not contain as much energy as ordinary fuel, but generate extremely high rate of energy release during explosion. The response of the structure near the immediate region can actually approach a true impulse due to the instantaneous velocity change at the explosive interface. As a result, measuring at the area surrounding a pyrotechnic explosion has always been a nightmare for engineers and scientists.

Depending on the explosive location and the point of measurement, the amount of high frequency energy reaching the transducer is inversely proportion to the distance between them. In a remote sensing location where the shock wave has to propagate through a long path or many joints of dissimilar materials to reach the transducer, high frequency components can be significantly attenuated.

b) Close-Range Metal-to-Metal Impact

Most pyroshock simulation devices, such as drop towers and pneumatic hammers, rely on high velocity metal-to-metal impact to generate the required shock spectrum. When the point of contact allows very little material deformation (like in all reusable machines), the acceleration response of the structure can also approach a true impulse. Again, the response spectrum is highly dependent upon the accelerometer location relative to the point of impact.

EFFECTS OF NEAR TRUE-IMPULSES ON ACCELEROMETER

There are two types of commonly use shock accelerometers, piezoresistive and piezoelectric devices. Each reacts differently under the attack of near true-impulses. Three common failure modes are observed:

a) Sensor Failure

Recent new designs in piezoresistive accelerometer have tremendously improved their usable bandwidth and rigidity. One type of commercially available PR sensor exhibits seismic resonance above 1 MHz [3], leaving quite a margin of safety for the general rule-of-thumb. Under the attack of delta function liked impulses, however, the sensor can still be set into resonance (at 1 MHz) due to the nature of the input signals. Since the gage mechanism is practically undamped, displacement of the elements goes out of control at resonance and eventually cause gage breakdown. The result of this type of failure is complete loss of data.

Piezoelectric sensors are more robust under the same condition. But they fail in other fashions:

b) Zeroshift

This subject has been well examined in many technical papers [4] [5] [6]. A piezoresistive accelerometer generally does not exhibit zeroshift until the gage mechanism has been damaged or is in the process of deterioration. Piezoelectric sensors, on the other hand, account for most of the zeroshift phenomena associated with transducers.

When a piezoelectric element is set into resonance, two things can happen:

1. Relative displacement of the seismic mass can exceed 100 times of the input. The crystal material is overstressed and produces spurious charge outputs due to domain switching. The result of this type of failure is DC offset in the time history.

2. The crystal material is not overstressed but a huge amount of charge output is generated which saturates or damages the subsequent electronics. The result of this type of malfunction is loss of data or gross DC offset in the time history.

Slight amount of zeroshift in the time history can yield unrealistic velocity and displacement during data reduction. The real danger remains that, although data with gross DC offsets are generally discarded, the minor one are accepted as good measurements.

c) Non-Linearity

The output of a transducer at resonance is sometime non-linear and not repeatable. The response of a saturated charge converter is also non-linear and not repeatable. The result of this type of malfunction is poor repeatability in SRS, leading to incorrect definition of the shock environment.

SOLUTION TO THE PROBLEM -- MECHANICAL FILTER

Mechanical Filter

An obvious solution to the accelerometer resonance problem is to isolate the sensor from the high frequency signals. When an appropriate material is placed between the structural mounting surface and the transducer, a mechanical low-pass filter is formed. The filter slope of such an arrangement approaches 12 dB per octave. In order to make the filter effective, the -3 dB corner must be set at a frequency far below the accelerometer resonance to insure adequate attenuation.

There are three critical design parameters in a mechanical filter:

a) First, the filter/accelerometer combination must be robust enough to withstand high level shocks. Many "isolators" rely solely on the strength of spring/damping material to keep the accelerometer in place.

b) Secondly, the Q (amplification) of the mechanical filter must be very low. Otherwise the linearity of the passband data will suffer. Damping characteristic is a critical consideration in matching the accelerometer to the mechanical filter.

c) Thirdly, the relative displacement between the transducer and the mounting surface must not exceed the linear range of the spring/damping material. When the accelerometer "bottoms out", its high frequency isolation characteristic of the filter is lost, and the protection to the sensor fades.

Existing Designs

Although there many shock isolators on the market for machine vibration isolation, they are not designed with linearity in mind, and their applications are quite different. A few foreign and local private institutions have built some experimental devices for their own shock measurements, but none are commercially available. These prototypes were made out of exotic materials, such as rosewood and cloth, for their unique damping and stiffness properties; reliability and repeatability of these external filters are questionable. One of the accelerometer manufacturers does offer an external mechanical filter especially tuned for its own brand of transducers, but it is really intended for a general vibration environment.

One common problem facing external mechanical filters is the resonance of the filter itself. Even with careful selection of spring and damping materials, critical damping is rarely achieved. Any small amount of amplification factor (Q) in an imperfectly damped filter will produce substantial degree of amplitude distortion from a shock input. This distortion manifests itself as ringing (at the filter's corner frequency) superimposed on the accelerometer output signals.

Another problem has to do with accelerometer matching. The corner frequency and the Q of a external filter is highly sensitive to the mass of the attached transducer. Minor deviation on size and weight can result in significantly different response.

Given the physics of the problem discussed above, it seems obvious that if one can design a shock accelerometer to incorporate a tuned internal mechanical filter for sensor isolation, and match it with a built-in electronic low-pass filter to remove unwanted residual ringing of the mechanical filter, many transducer problems in pyroshock measurement can be avoided. A block diagram in Figure 1 depicts this concept.
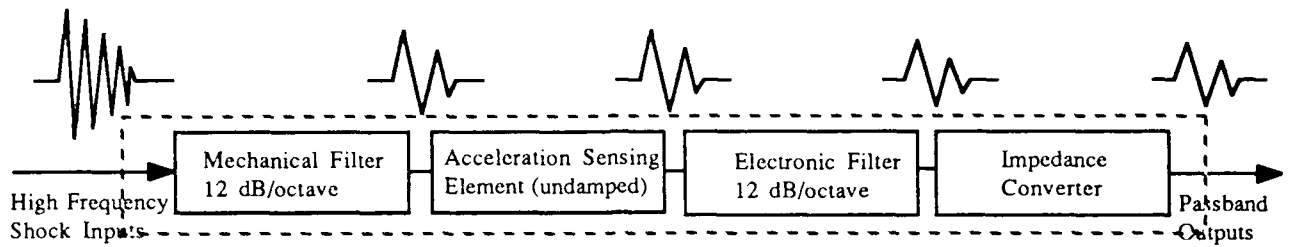
ACCELEROMETER WITH BUILT-IN FILTERS

Figure 1

Built-in Mechanical Filter

An experimental accelerometer with both mechanical and electronic filters was successfully built in our Engineering Lab.

Based on a well established piezoelectric shock sensor, this accelerometer featured a captive mechanical filter arrangement. Compared to the model of an external filter (Figure 2a), this unusual scheme provided the transducer/filter system with added rigidity. (see Figure 2b) The transducer's external housing, which served as an enclosure for the sensor and the isolation material, kept the "guts" together in case of excessive shock input.
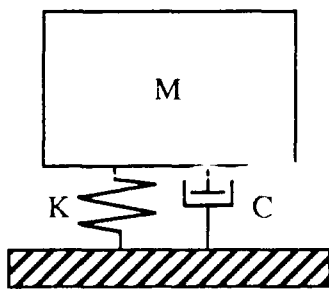
Figure 2a
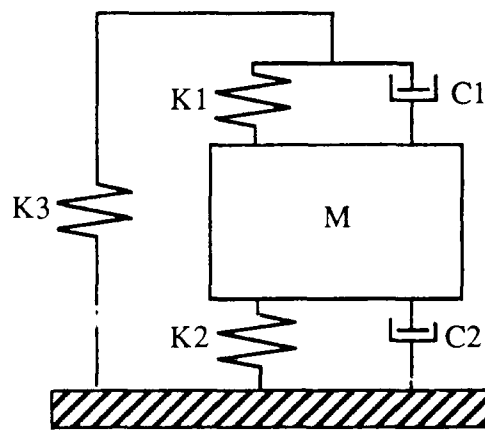
Figure 2b

MECHANICAL FILTER MODELS

The light-weight sensor assembly housed the piezoelectric element and the hybrid microelectronics. The internal electronic filter, a two-pole Butterworth low-pass, provided another 12 dB per octave roll-off after the mechanical filter. The spring/damping material was meticulously chosen and matched to react with the mass of the sensor in a synergistic fashion. This combination yielded a mechanical filter with a damping coefficient of .20 to .15, and a resonant frequency of 15 kHz.

To attenuate the ~5 dB rise at 15 kHz, the corner of the 2-pole low-pass filter was purposely set at 10 kHz in order to compensate for this unwanted peak. The end result is shown in Figure 3 where the solid line represents the combined frequency response of the accelerometer; the single dotted line represents the mechanical filter response, and the double dotted line denotes the electronic filter response. This combination offered a 24 dB per octave roll-off beyond 10 kHz which effectively isolated the piezoelectric element and subsequent electronics from any high frequency transient. Built-in electronics also allowed impedance conversion taking place inside the transducer, a desirable feature for signal transmission.

Accelerometer Performance

A frequency response calibration is shown in Figure 4. The accelerometer has an effective linear amplitude response from 1 Hz to 10 kHz within ±1 dB. Sensitivity of the unit is .11mV/g which equates to a full scale dynamic range of >50,000g. Cross-axis sensitivity up to 50,000 g is less than 5%, and the resonance of the crystal element itself is larger than 130 kHz. The accelerometer weights 3.8 grams and operates from a constant current source.

One of the major concerns regarding the performance of the transducer has been temperature response. Since the material used for damping was basically a polymer, frequency characteristics varied with temperature. An experiment was conducted to investigate the effect of temperature using transient inputs from a Hopkinson bar. The input transient was defined to be about 100,000 g peak, and the corresponding pulse width was ~70 µS. Repeatability of the pulse shape was quite acceptable, but the shock level had a standard deviation of 5,500 g

Figure 5 compares the transient responses of the accelerometer at 75°F and 45°F. The peak response at 75°F is measured to be 86,000 g, and 78,100 g at 45°F (these are median data selected from samples at approximately the same level). The peak level is considerably less than 100,000 g due to filter attenuation. Taking the variability of input level into account, the indicated peak g at 45°F is 9.2% lower than at room temperature.

Figure 6 shows the transient responses at 75°F and 120°F. Here the indicated peak g at 120°F is 83,000 g, and 79,000 g at 75 °F, a +5.0% increase in amplitude response.

Pushing the physical limit of the damping material, the same test was conducted at 150°F. Figure 7 shows the transient responses at 75°F and 150°F. At 150°F, the peak response indicates 100,700 g while the 75°F shows 84,000 g, a +19.9% increase in apparent response.

Our data seems to indicate that, within ±30 F from ambient temperature (75 F), the mechanical filter displays a small amount of variation. Above 120°F, however, some correction factor may be necessary.

Design Limitation

Apart from the temperature constraint mentioned in the preceding section, the accelerometer has another physical limitation. Referring to Figure 2b. The mass M, in our design. is the sensor of the accelerometer, and the mounting surface becomes the boundary of this second order system. The confined springs/dampers are represented in this model by k_1, k_2, c_1 and c_2; the stiffness of the outer case is represented by k_3. As long as the transmitted force F to the sensor does not cause excessive travel in k_1 and k_2, the system will behave in a predictable manner. The practical displacement limit of the existing system is estimated to be > 0.01".

The equation which relates dynamic range of the mechanical filter to the maximum linear travel of the spring material is:

$$\frac{t}{\ddot{x}} = \frac{1}{\omega_n^2 \sqrt{\left[1 - \left(\frac{\omega}{\omega_n}\right)^2\right]^2 + \left(2\zeta\frac{\omega}{\omega_n}\right)^2}}$$

where

t = maximum travel of spring
$\ddot{x}$ = maximum input acceleration
ζ = damping factor
ω = input frequency
ω_n = resonant frequency of mechanical filter

A maximum input shock spectrum derived from this equation (based on 0.01" spring travel) is shown in Figure 8. The weakest spot is understandably at 15 kHz where the filter resonates. The maximum allowable level at that frequency is 67,000 g. Above 67,000 g, the mechanical filter loses its effectiveness (eg. bottoms out), and protection to the sensor ceases.

TEST RESULTS

Several prototypes were sent out for field evaluation. The first group were tested at the U.S. Army Combat Systems Test Activity, Aberdeen Proving Ground, Maryland. The evaluation set-up was a classical close-range shock measurement [7] which involved a 18" x 18" x 1.5" steel plate. All the test transducers were hard mounted on one side (in the middle), while the impacts occurred directly on the other side of the plate. Types of excitation used for shock generation ranged from ball bearing impacts, blasting caps, to C-4 detonation.

Figure 9 shows a comparison between the shock responses of a 200,000 g piezoresistive type accelerometer and the prototype with built-in mechanical filter. A 2" ball bearing was used to strike the plate and produced the input acceleration. The dotted line shows the response of the prototype at about 1,100 g peak, whereas the PR accelerometer shows almost double the peak g level due to its wider bandwidth (1 MHz). Figure 10 shows the same event except that the PR transducer output has been filtered at 10 kHz. Note the closed agreement between the two accelerometers. (the phase shift could be due to different filter characteristics)

Figure 11 shows the response of a typical shock accelerometer measuring the excitation from a DFP-2 non-electric type blasting cap (.05 gram). A classical zeroshift occurred 2 milliseconds after the blast-off. Figure 12 shows the response of the prototype under the same excitation condition; no DC offset was noted.

Figures 13 and 14 show the differences in amplitude response of a typical shock accelerometer and the prototype with mechanical filter. Input excitation was the detonation of a M7 blasting cap (.9 gram) directly behind the sensors. Again the transducer without mechanical filter exhibited a huge amount of DC offset.

Figure 15 shows the killer - 1 oz. of C-4 detonated on the plate. The experimenter reckoned that the input transient could well be in excess of 1 million g. Here the prototype survived the blast, but the DC level has shifted; apparently the mechanical filter bottomed out. In similar tests, other piezoresistive accelerometers had been destroyed due to the high frequency energy content.

Another field test was conducted at McDonnell Douglas, St. Louis, Missouri where three prototypes were mounted on a test article with 28 feet of 18 grain/ft PETN mild detonating cord. This test exhibited tremendous amount of high frequency energy in certain directions. Figure 16 shows the response of one of the prototypes in a mild direction. The Shock Response Spectrum and the velocity were said to be believable.

Figure 17 shows the response in the vicious direction. Although the time history seems normal, integration indictes unrealistic velocity. Note also the rising low end of the SRS due to latent zeroshift. To analyze the data further, the Fourier Spectrum was calculated and is shown in Figure 18. Here an obvious spike dominates the FFT plot at 15 kHz, indicating that the filter is resonating.

FUTURE DEVELOPMENT

There are still many problems to overcome in making a perfect shock accelerometer. Within its limitation, however, this experimental transducer is one step closer to the reality. A patent recently has been applied for this shock transducer design concept , and production units may be available in the near future.

Future development of this experimental accelerometer may include refinement of the mechanical filter for better linearity and higher dynamic range. Different types of sensing elements will be investigated in search of wider frequency response and reduction of sensor non-linearity. Improvement in temperature response of the mechanical filter can also be expected.

REFERENCES

1.   A. E. Galef, "The Pre-Pulse in Pyroshock Measurement and Analysis", Bulletin, 56th Shock & Vibration Symposium, Part III, 1986.

2.   A. E. Galef, "Zero-shifted Accelerometer Outputs", Bulletin, 56th Shock & Vibration Symposium, Part III, 1986.

3.   R. D. Sill, "Shock Calibration of Accelerometers at Amplitudes to 100,000g Using Compression Waves", Proceedings, 29th International Instrumentation Symposium, ISA, 1983.

4.   R. H. Plumlee, "Zeroshift in Piezoelectric Accelerometers", Sandia Corporation Report, SC-RR-70-755, 1971.

5.   D. B. Davis, "Investigation of Zero Shift in Piezoelectric Ceramic Accelerometers", Sandia Corporation Report, 71-631.

6.   A. S. Chu, "Zeroshift of Piezoelectric Accelerometers in Pyroshock Measurements", Bulletin, 57th Shock & Vibration Symposium, Part I, 1987.

7.   W. S. Walton, "Dynamic Response of Armor Plate to Non-Penetrating Projectile Impact", Bulletin, 56th Shock & Vibration Symposium, Part I, 1986.

COMBINED FILTER CHARACTERISTICS

ACCELEROMETER FREQUENCY RESPONSE
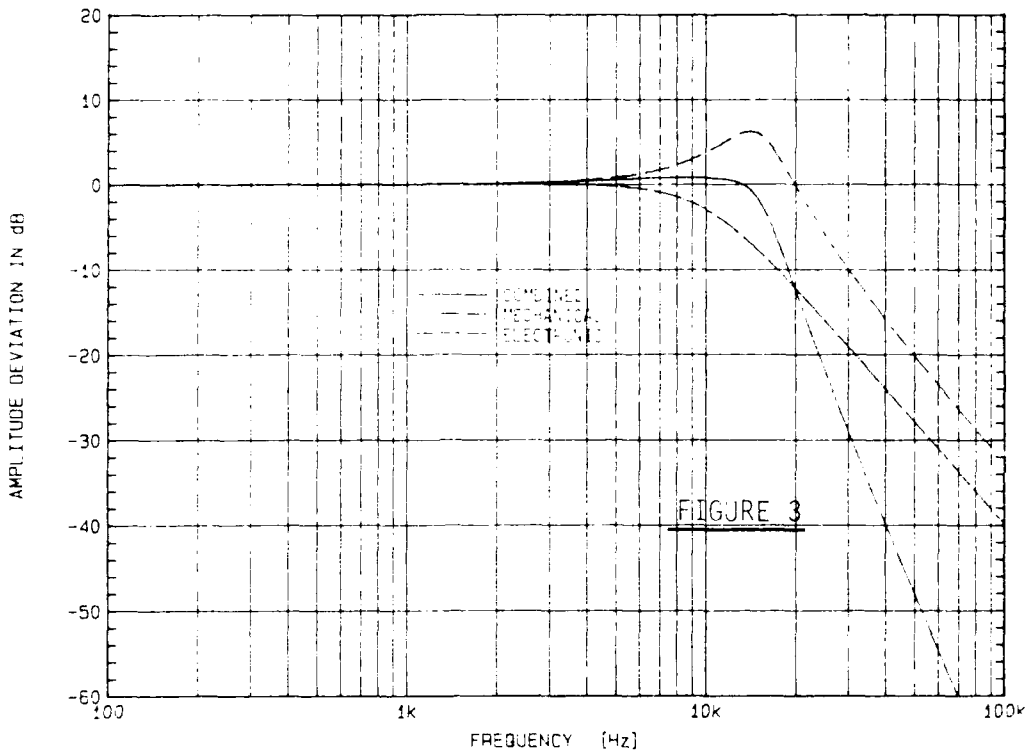
FIGURE 3

Model Number 725S-01 Serial Number XA23

Sensitivity: 0.688 (mV) pC/g @ 100 Hz

System 80 Acceleration Level: 20 g pk

Frequency Limits: 00 Hz to 50K Hz

Vertical Scale: 10 db per major division

Cal. by: AC   Date: 2/24/08
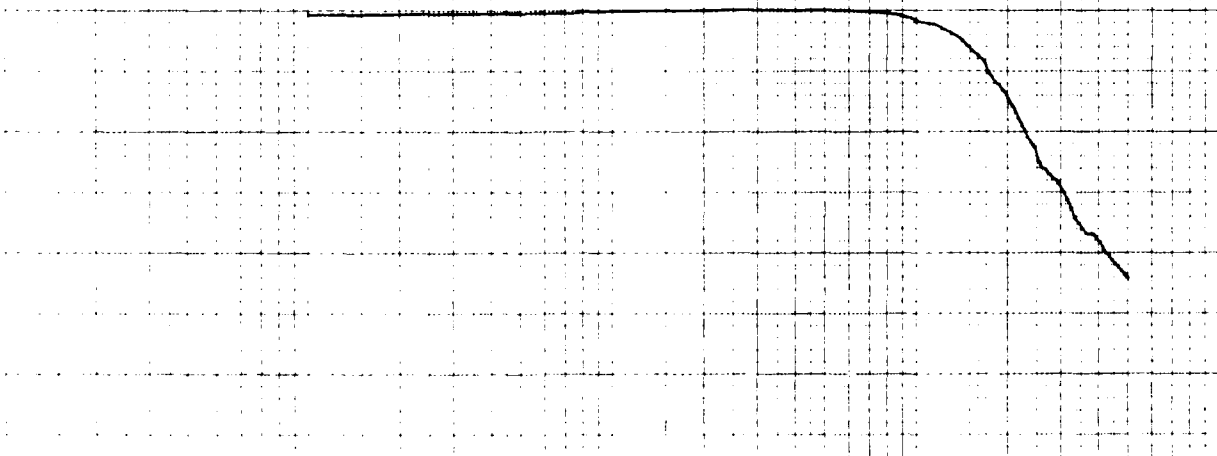
FREQUENCY RESPONSE CALIBRATION

FIGURE 4

MODEL # 7255   REPORT # 45 deg F
SERIAL # PY04   DATE: 5-20-88
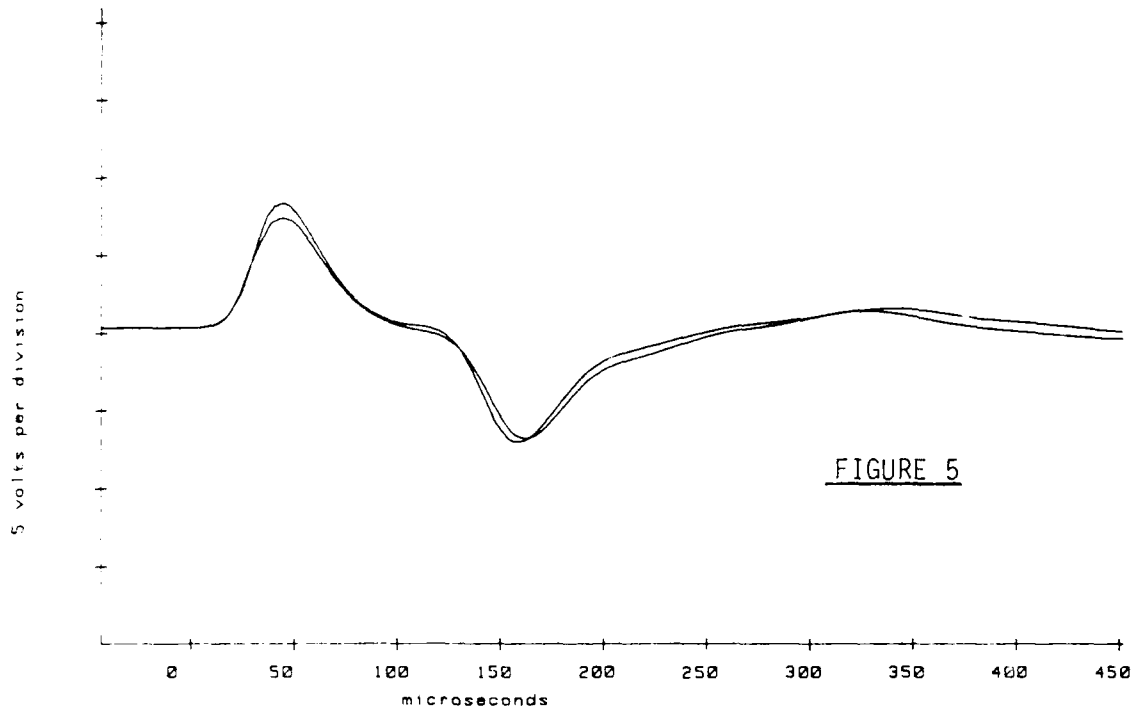
FIGURE 5

TRANSIENT RESPONSE AT TEMPERATURE

MODEL # 7255   REPORT # 120 deg F
SERIAL # PY04   DATE: 5-20-88
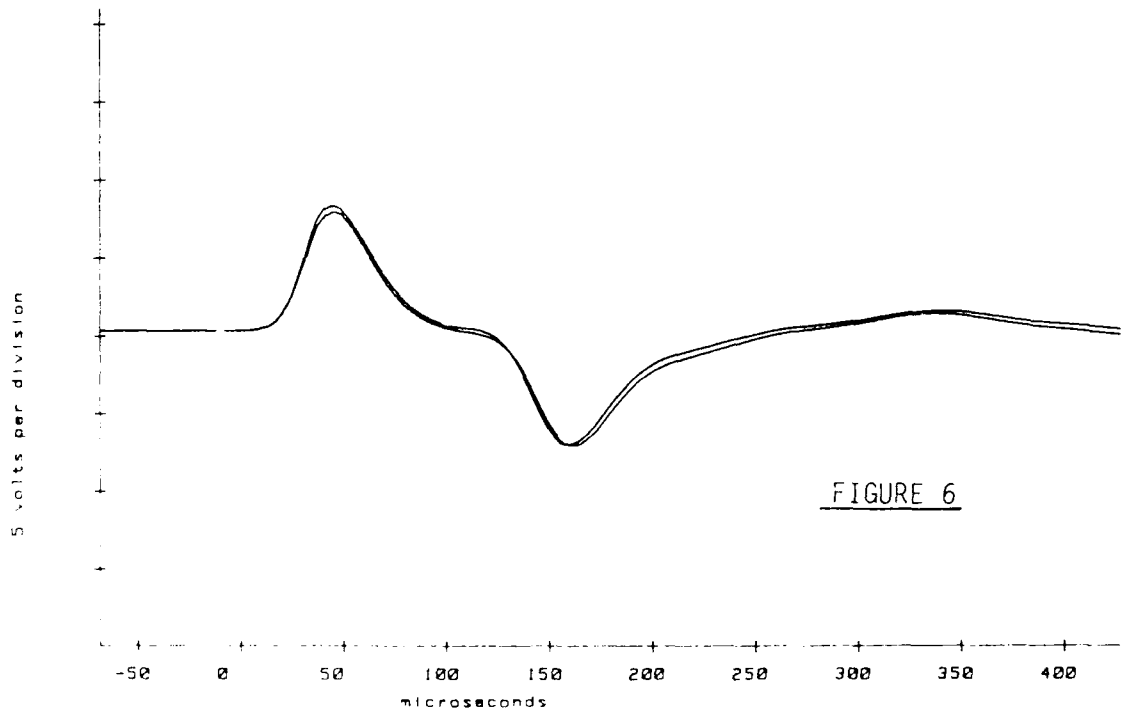
FIGURE 6

TRANSIENT RESPONSE AT TEMPERATURE

FIGURE 7

TRANSIENT RESPONSE AT TEMPERATURE
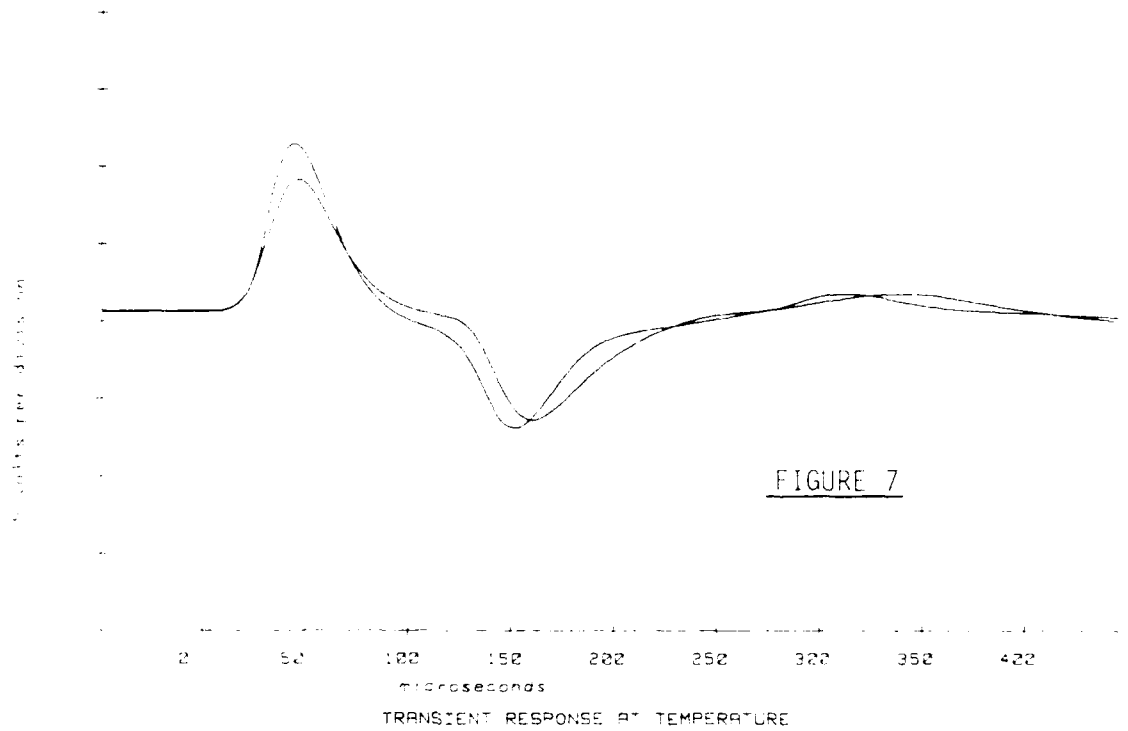
MAXIMUM INPUT SPECTRUM
BUILT-IN FILTERS

FIGURE 8

IMPACT: 2 IN. BALL BRNG
11/30/87   IDBC-01-03
MOUNT: DIRECT PLATE

FIGURE 9

——— PYROTRON #PY04
········ 7270 #AAM76F

TIME IN MILLISECONDS

IMPACT: 2 IN. BALL BRNG
11/30/87   IDBC-01-03
MOUNT: DIRECT ON PLATE

FIGURE 10

——— PYROTRON #PY04
········ 7270 @ 10 KHz

TIME IN MILLISECONDS

FIGURE 11

FIGURE 12

@ 10 KHz

RND# 9 12APR88 014-07

M7 CENTER

FIGURE 13

FIGURE 13 — ACCELERATION IN G'S vs. TIME IN MILLISECONDS

7255 ACCEL DIRECT MOUNT
RND#3 13APR88 017-01
M7 CENTER

FIGURE 14

FIGURE 14 — ACCELERATION IN G'S vs. TIME IN MILLISECONDS

RND 41   CH 26   7255D DIRECT ON PLATE, 60 KHZ   TST 750 22R=587

DPLT2   START (ms) =   5.000 →18
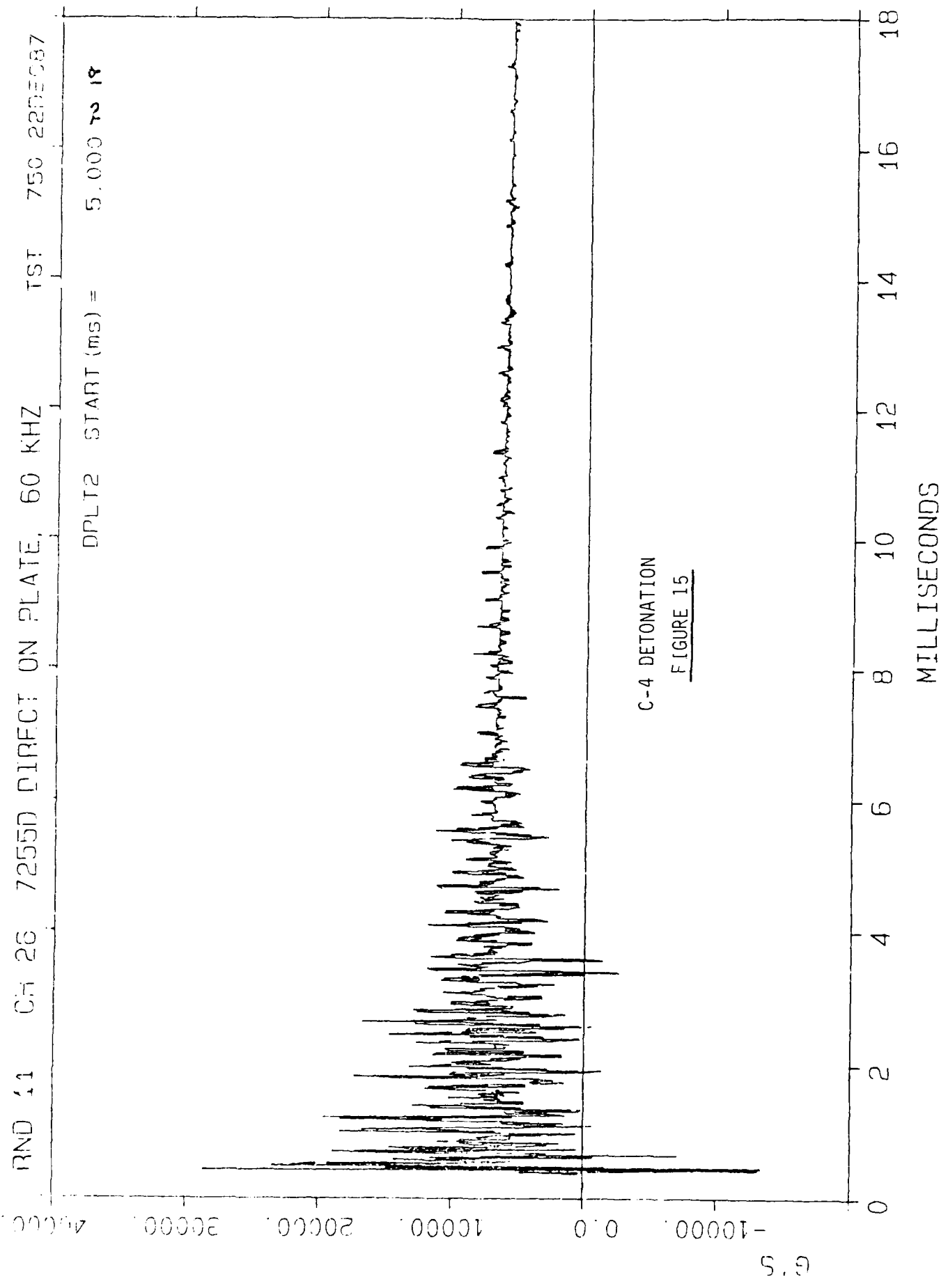
C-4 DETONATION

FIGURE 15
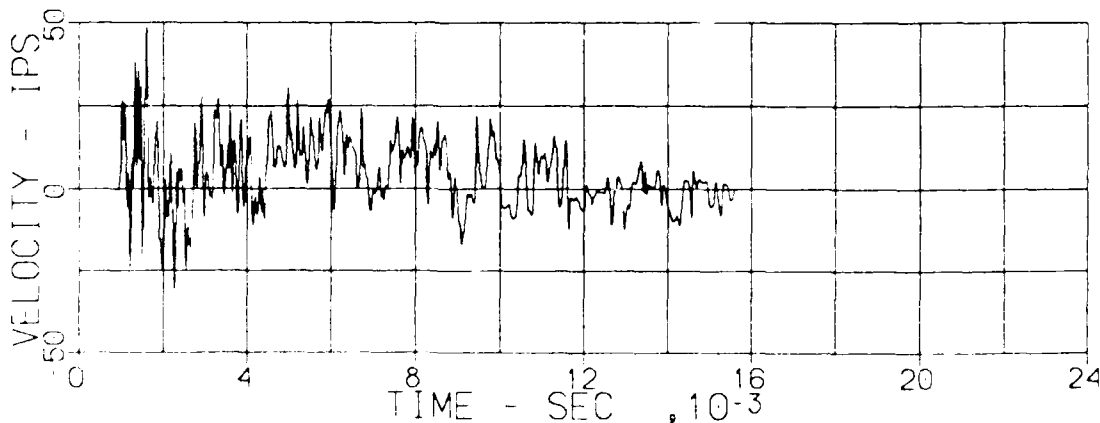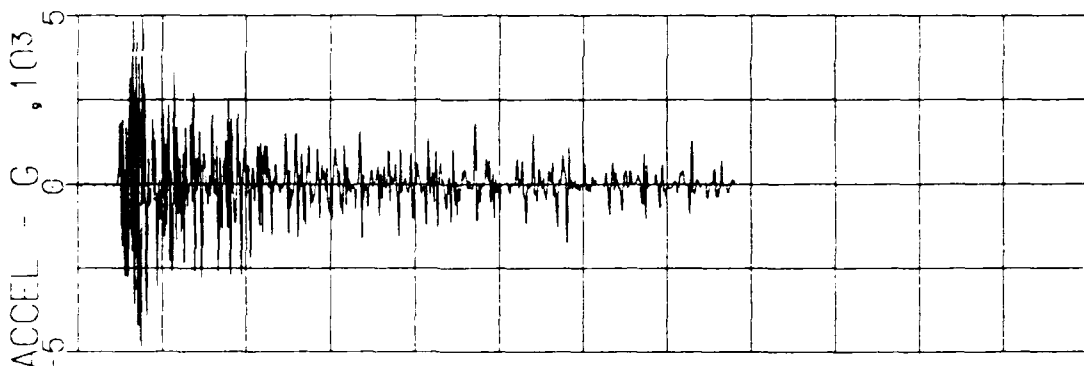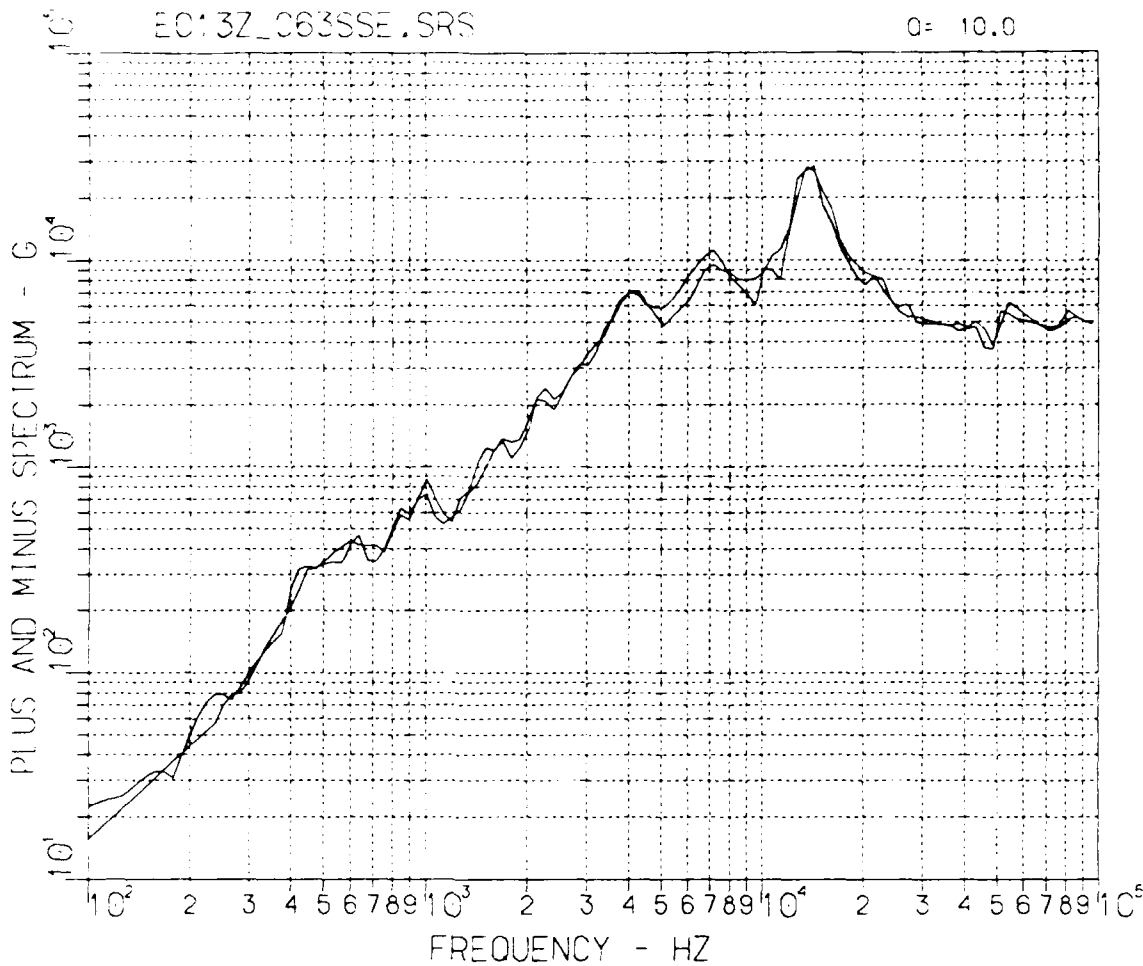
MILLISECONDS

FIGURE 16

EO14X_C61SSE.SRS   Q= 10.0

FIGURE 17

McDonnell Douglas Astronautics Company - St. Louis

268
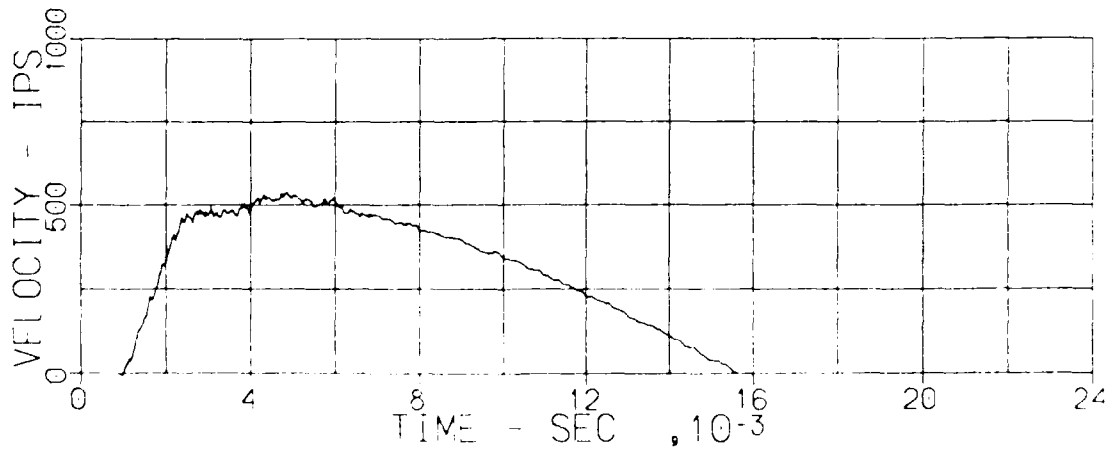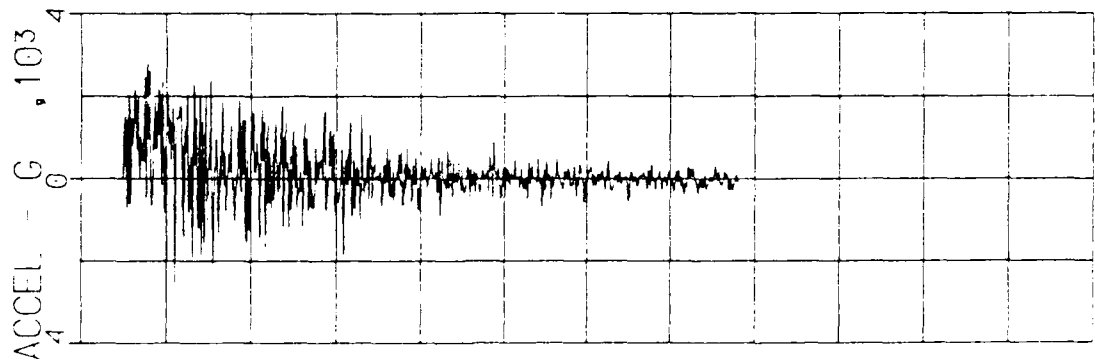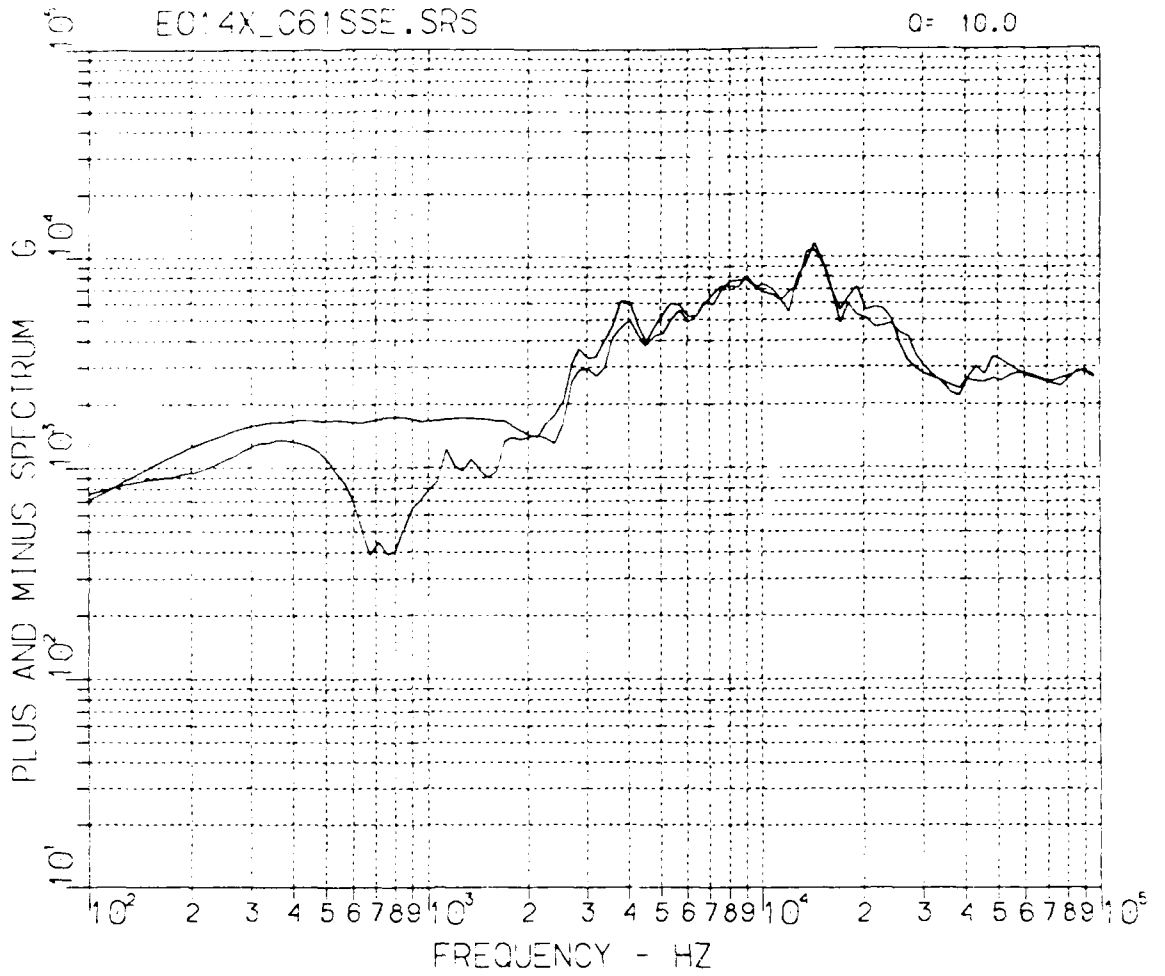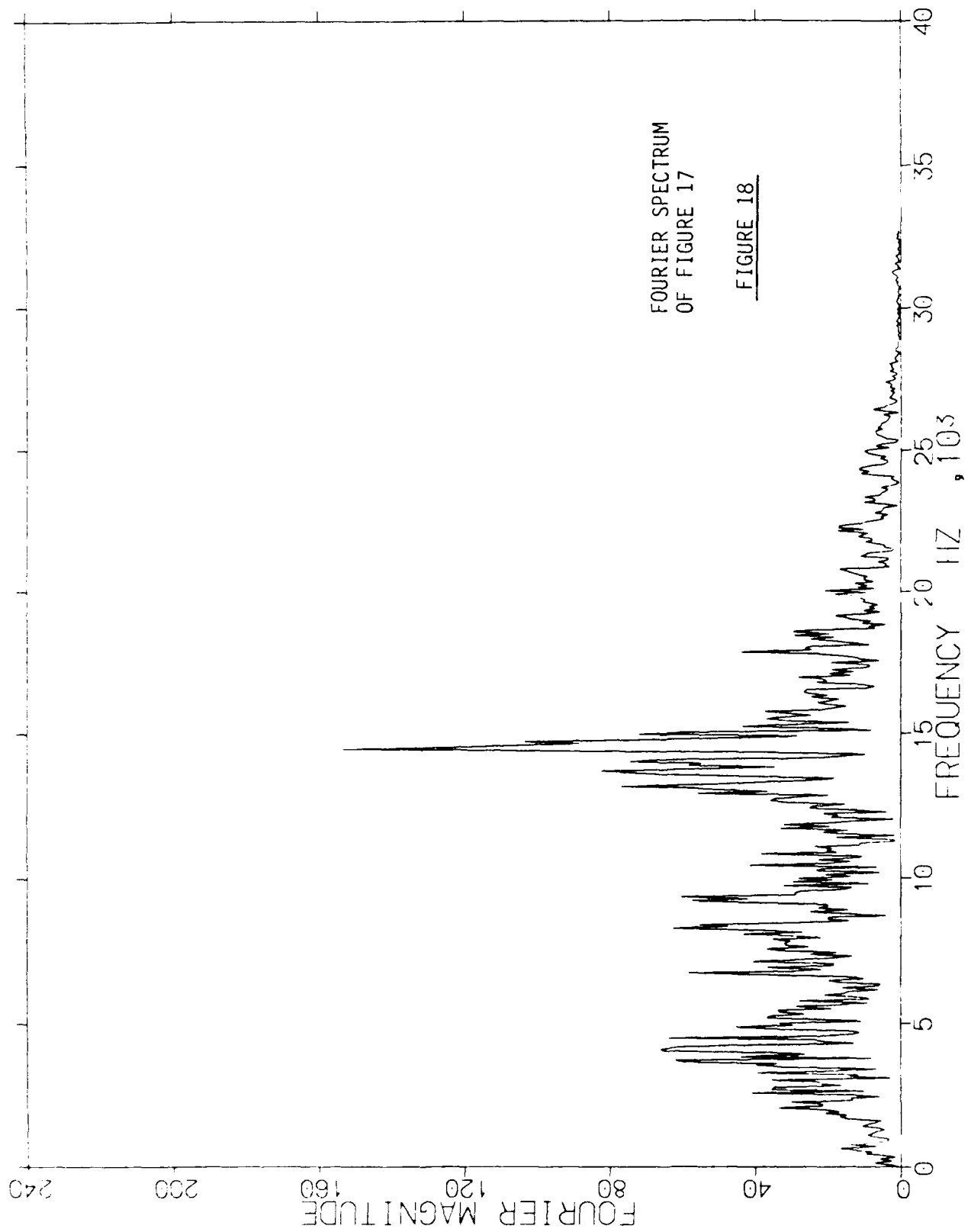
FOURIER SPECTRUM
OF FIGURE 17

FIGURE 18

McDonnell Douglas Astronautics Company - St. Louis

269

MECHANICAL IMPEDANCE MEASUREMENTS
USING OBLIQUE EXCITATION

Larry J. Nucci and Jay R. Reed
Naval Ship Systems Engineering Station
U.S. Naval Base, Philadelphia, PA 19112

It may be necessary to make mechanical impedance measurements
at a point where a driving force cannot be applied in the
direction for which the measurements are required. This paper
describes a method which was developed and implemented to
measure vertical driving point impedance and the orthogonal
axial and transverse transfer impedances due to a vertically
applied force at the same point. Since vertical excitation is
not possible, the structure is excited in the transverse
direction and in a direction 45 degrees to the
vertical-transverse axes. The forces in these directions are
measured along with motion measurements in the vertical, axial
and transverse directions. Relationships were derived from
which the required impedances were calculated. The method was
successfully tried on a test structure where the calculated
results were compared to those obtained by sole vertical
excitation.

INTRODUCTION

It may be necessary to make mechanical impedance measurements at a point where
a driving force cannot be applied in the direction for which the measurements are
required. In this paper the requirement is to measure the vertical driving point
impedance and the orthogonal axial and transverse transfer impedances due to a
vertically applied force at the same point. For the structure in question, because
of space limitations, a shaker can not be positioned to apply this vertical force.
Instead, it is applied in the transverse direction and in a direction 45 degrees to
the vertical-transverse axes. A swept sinusoidal force is applied in each of these
two directions and the vertical, axial and transverse motions are measured. These
data are used to determine equivalent impedances which should duplicate those
obtained from sole vertical excitation.

TEST PROCEDURE

The following course of action was followed to develop a method of measuring the
impedance in the vertical, axial and transverse directions due to a vertical force
using oblique and transverse excitation:

1. A theoretical basis was developed for measuring mechanical impedance using
oblique and transverse excitation.

2. An experiment was conducted to measure mechanical impedance using oblique and
transverse excitation on a large structure.

3. The results were compared to those obtained using vertical excitation.

The impedance in the vertical direction using oblique excitation is derived as follows:

A force as a function of frequency (Fvt) which is applied at an angle of 45 degrees to the vertical and transverse axes v and t will have a directional vector $(1/\sqrt{2})(v+t)$. The vertical response Vv due to this oblique force can be written

$$Vv = Vvv + Vvt \tag{1}$$

where Vvv is the vertical velocity due to the vertical force component Fv and Vvt is the vertical velocity due to the transverse force component Ft. The oblique force Fvt is applied at a 45 degree angle to the v and t axes. Therefore

$$Fv = Ft = Fvt/\sqrt{2} \tag{2}$$

From equations (2) the vertical velocities Vvv and Vvt can be expressed as

$$Vvv = \left(\frac{Vvv}{Fv}\right)\left(\frac{Fvt}{\sqrt{2}}\right) \tag{3}$$

$$Vvt = \left(\frac{Vvt}{Ft}\right)\left(\frac{Fvt}{\sqrt{2}}\right) \tag{4}$$

Substituting equations (3) and (4) into equation (1)

$$Vv = Vvv + Vvt = \left(\frac{Vvv}{Fv}\right)\left(\frac{Fvt}{\sqrt{2}}\right) + \left(\frac{Vvt}{Ft}\right)\left(\frac{Fvt}{\sqrt{2}}\right) \tag{5}$$

Dividing the vertical response (equation (5)) by the oblique excitation Fvt yields the mobility transfer function

$$\frac{Vvv + Vvt}{Fvt} = \frac{1}{\sqrt{2}}\left(\frac{Vvv}{Fv} + \frac{Vvt}{Ft}\right) \tag{6}$$

The vertical mobility becomes

$$\frac{Vvv}{Fv} = \sqrt{2}\left(\frac{Vvv + Vvt}{Fvt}\right) - \left(\frac{Vvt}{Ft}\right) \tag{7}$$

The quantities in parenthesis are the measured forces and vertical velocities. Inverting equation (7) yields the vertical driving point impedance without needing to apply a sole vertical force.

$$\frac{Fv}{Vvv} = \left[\sqrt{2}\left(\frac{Vvv + Vvt}{Fvt}\right) - \left(\frac{Vvt}{Ft}\right)\right]^{-1} \tag{8}$$

Similarly, the driving point transfer impedances in the axial and transverse directions due to a vertical force Fv are

$$\frac{Fv}{Vav} = \left[\sqrt{2}\left(\frac{Vav + Vat}{Fvt}\right) - \left(\frac{Vat}{Ft}\right)\right]^{-1} \tag{9}$$

where Vav and Vat are the axial velocities due to the vertical force component Fv and the transverse force component Ft of the force applied at 45 degrees to the vertical and transverse axes and

$$\frac{Fv}{Vtv} = \left[\sqrt{2} \left(\frac{Vtv + Vtt}{Fvt} \right) - \left(\frac{Vtt}{Ft} \right) \right]^{-1} \tag{10}$$

where Vtv and Vtt are the transverse velocities due to the vertical force compcnent Fv and the transverse force component Ft of the force Fvt applied at 45 degrees to the vertical and transverse axes.

A large structure was excited from 0-256 Hz with an electromechanical shaker and all force and motion measurements were made at the excitation point. A block diagram of the instrumentation system is shown in Figure 1. Figures 2 and 3 compare the oblique and direct measurement of the vertical driving point impedance and mobility. Figure 4 shows the functions measured to obtain oblique vertical mobility. In figures 2 and 3 the dotted function represents the results obtained by the direct method where the force as a function of frequency is applied vertically and the motion is measured vertically. The solid line function is obtained from vertical motion measurements caused by measured forces applied 45 degrees to the vertical and transverse axes and transversely applied forces. The data were processed to yield the vertical driving point impedance and mobility. Figures 5 and 6 compare oblique and direct measurements of axial and transverse driving point transfer impedances.

RESULTS AND DISCUSSION

The impedance in Figures 2, 5 and 6 is presented on log scale. For an alternate method of comparison between oblique and direct method of vertical driving point measurements, the vertical mobility (the inverse of impedance) is plotted on a linear scale in Figure 3. The functions measured to obtain the oblique vertical mobility are also plotted on a linear scale in Figure 4.

It can be seen from the figures that good correlation was achieved between oblique and direct measurements throughout the frequency range of interest. (0-256Hz). The oblique impedance measurement is a valid substitute for direct measurements where a driving force cannot be applied in the direction for which the measurements are required.
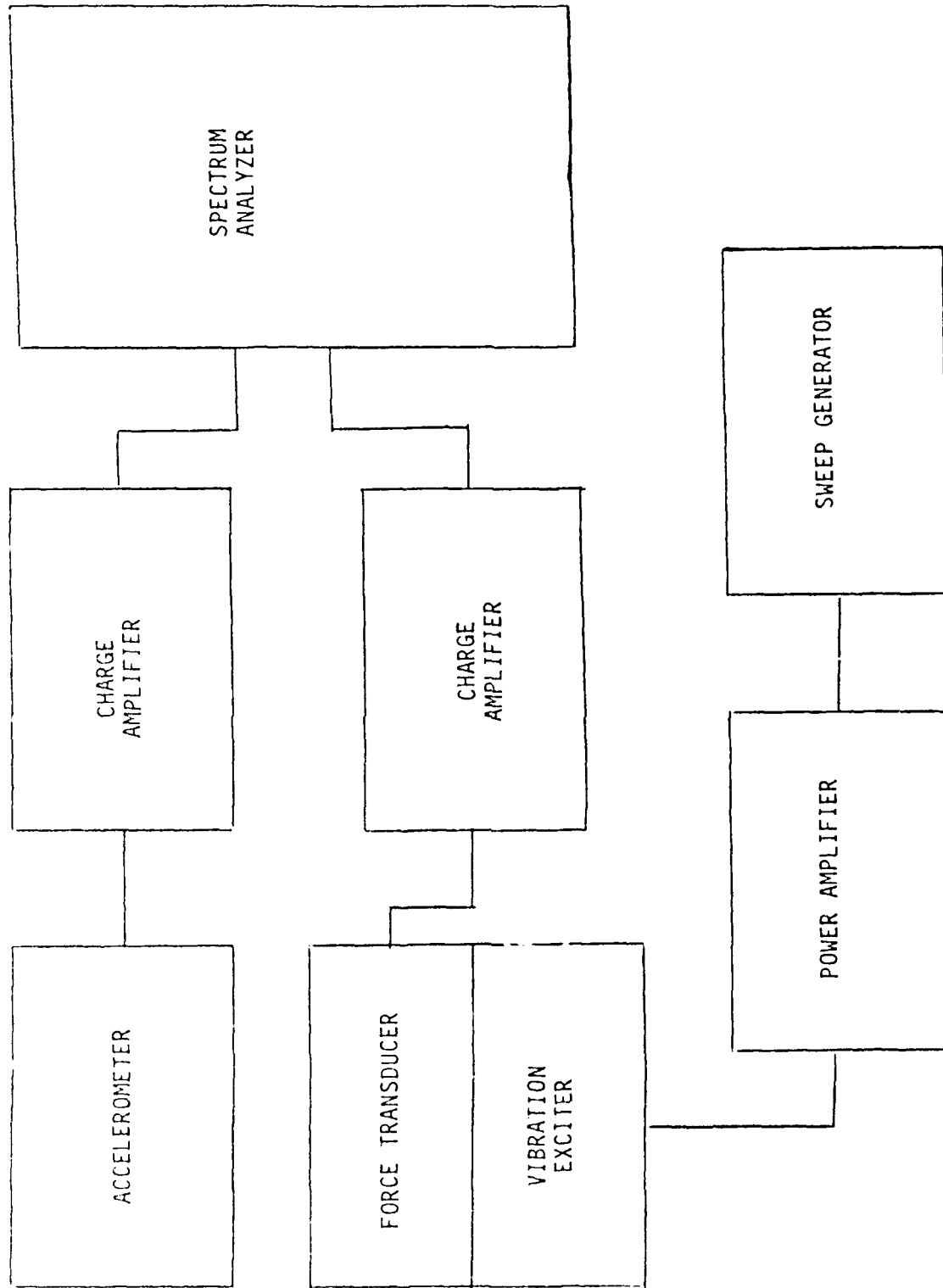
Figure 1 - Instrumentation Diagram

Figure 2 - Comparison of Oblique and Direct Measurements of Vertical Impedance (Fv/Vvv)
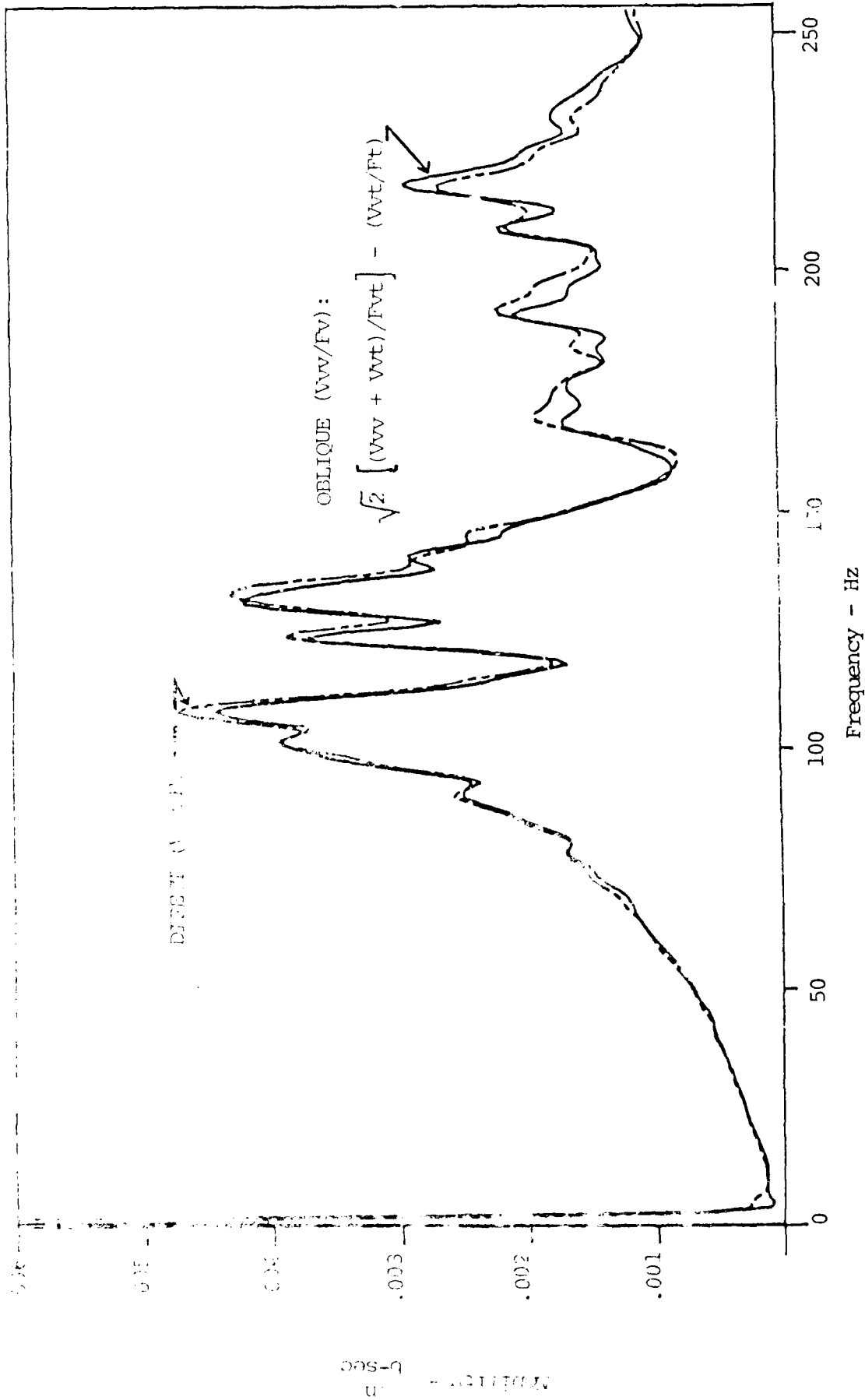
Figure 3 – Comparison of Oblique and Direct Measurements of Vertical Mobility (Vv/Fv)
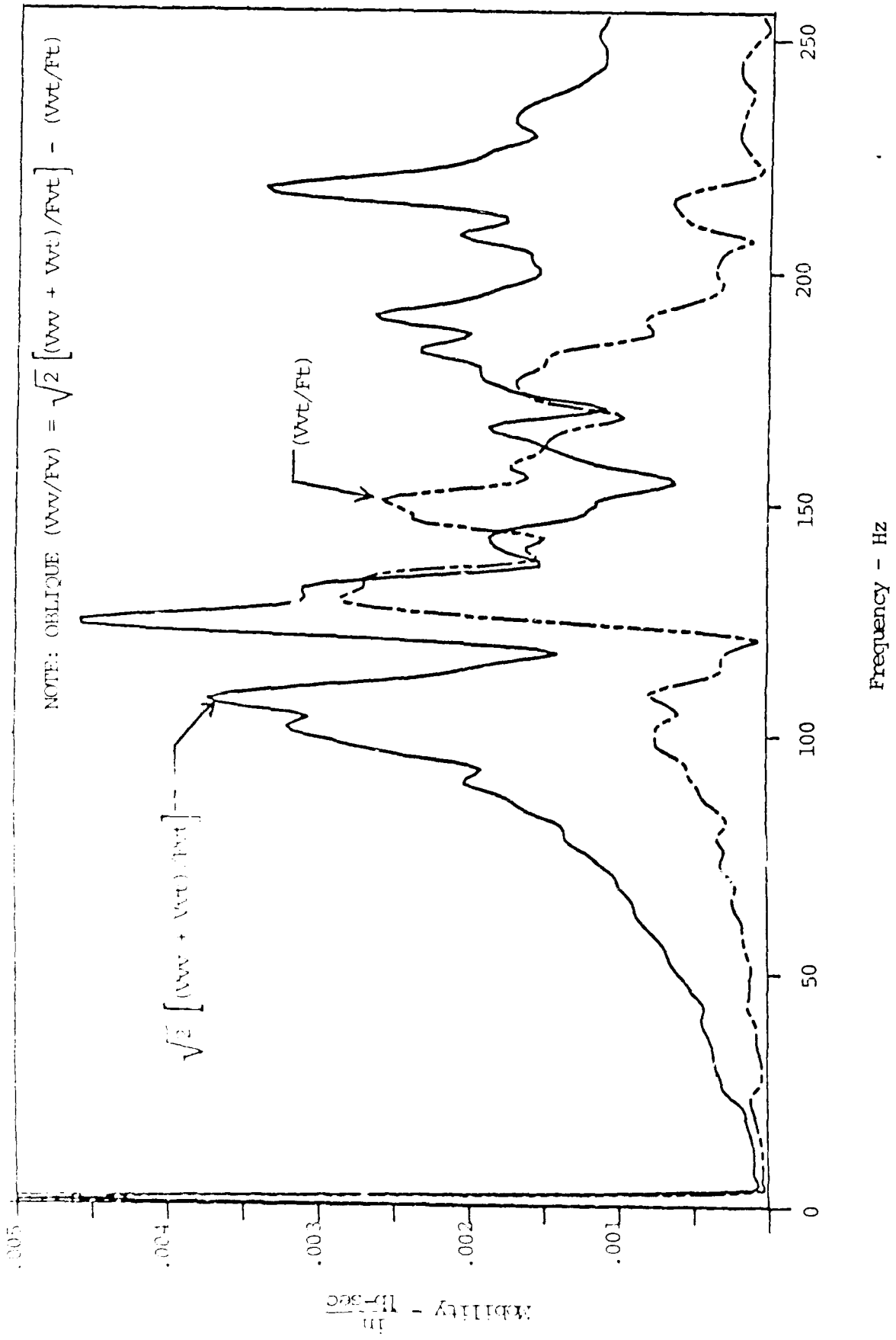
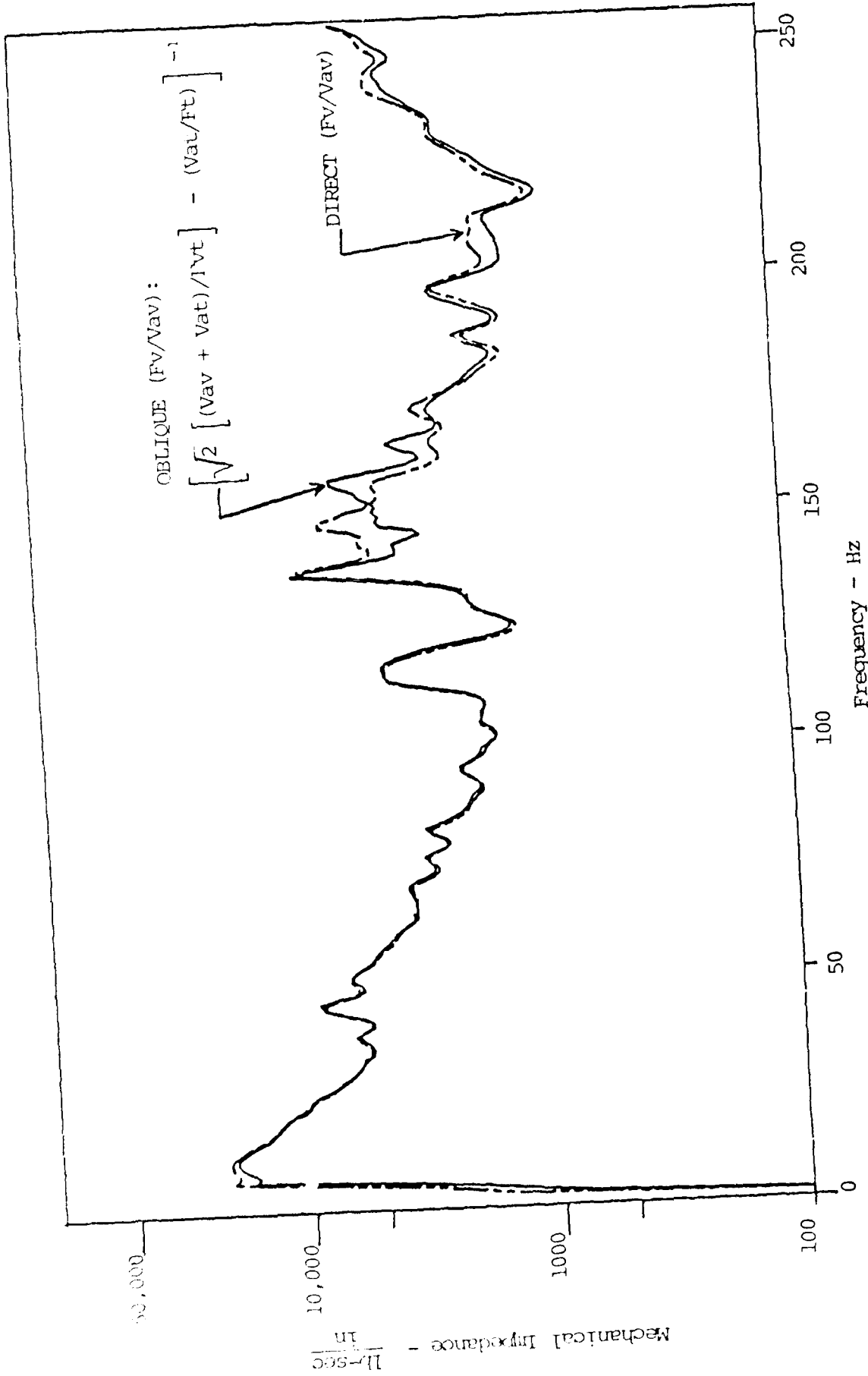Figure 4 - Functions Measured to Obtain Vertical Mobility (Vvv/Fv)

NOTE: OBLIQUE (Vvv/Fv) = $\sqrt{2}\left[(Vvv + Vvt)/Fvt\right] - (Vvt/Ft)$

Figure 5 – Comparison of Oblique and Direct Measurements of Axial Impedance (Fv/Vav)
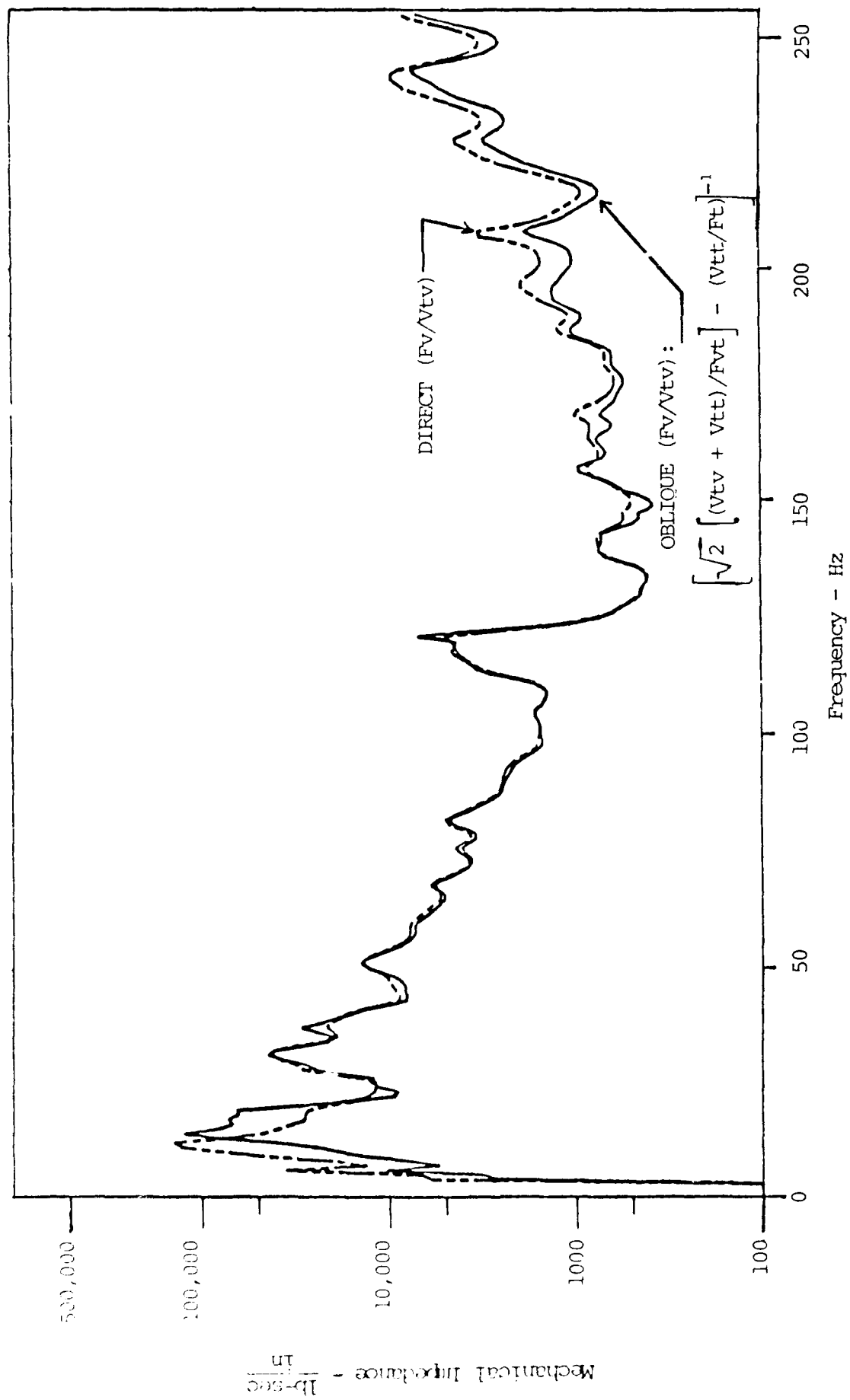
Figure 6 – Comparison of Oblique and Direct Measurements of Transverse Impedance (Fv/Vtv)

The plot axes read:

- Horizontal axis: Frequency – Hz (0, 50, 100, 150, 200, 250)
- Vertical axis: Mechanical Impedance – $\dfrac{\text{lb-sec}}{\text{in}}$ (100, 1000, 10,000, 100,000, 500,000)

Curve labels:

DIRECT (Fv/Vtv)

OBLIQUE (Fv/Vtv) : $\left[\sqrt{2} \left[(Vtv + Vtt)/Fvt \right] - (Vtt/Ft) \right]^{-1}$

DYNAMIC CRITERIA

SIMULATING VEHICLE DYNAMICS:
THE IMPORTANCE OF A VALID FORCING FUNCTION

G. L. Ferguson
Sandia National Laboratories
Albuquerque, NM 87185

The recent evolution of vehicle systems has required they be structurally sound with minimum weight. Historically, a trial and error approach to marketing a vehicle was used. The 1970s saw mainframe computers speed the vehicle design process. In the early 1980s simulating vehicle dynamics became the accepted design procedure. The forcing function used in this technique is also its major drawback. This paper summarizes the results of one sled vehicle used in a detailed study done at the U. S. Air Force's High Speed Test Track. The study concluded that results from simulation studies are valid only if an accurate forcing function is used.

HISTORY OF VEHICLE DYNAMICS

The recent evolution of vehicle systems has required the system to be structurally sound with minimum weight. This requirement has been levied in an effort to extract extra performance safely from an existing, or even smaller, powerplant. The procedures used during the parametric studies of these requirements place further demands on the vehicle system design. These new demands require that the vehicle operate within certain environmental constraints; i.e., deflection, velocity, or acceleration. These constraints are usually placed on the system for payload protection.

The time honored solution sequence has been to build a prototype after some preliminary analysis. Once built, the prototype is then tested. This procedure is then iterated until an acceptable product has been achieved. However, the competitive market place, in both the commercial and defense sectors, has dictated new products reach the customer sooner with less development and testing costs. The advent of powerful mainframe computers and maturing finite element analysis packages in the 1970's assisted the designer in reducing the number of prototype development iterations. The engineer then became able to perform sophisticated transient response analyses on the system to determine its response to loading situations prior to the first prototype having ever been built. Hence, the engineer was closer to final design before ever entering the shop and eliminated many build and test iterations with their associated costs.

Three particular drawbacks exist with using the transient response solution technique. The first drawback is the cost. The program must perform a full modal analysis at each time step for the given loading. This modal extraction, especially for large finite element models, requires large computational machines and significant cpu time. This equates with large costs considering a simple transient analysis can encompass more than one hundred time steps. The second negative aspect of transient response analysis is the problem definition. The designer must have an in-depth knowledge of structural dynamics and the statistical processes used in the formulation of this type of analysis. In other words, the designer must know how to properly define the auto- and cross-correlational terms necessary to relate the various portions of the system. For complicated systems these are generally not known until the system has been built and tested and these quantities have been measured. Finally, transient analysis techniques are not particularly well suited to handle system non-linearities, which have always been prevalent in vehicle design. Because of these reasons, the transient response solution is not a viable option until late in the design phase and generally parallels the first prototype construction.

A second technique is gaining widespread acceptance for the solution of vehicle dynamic response problems. This technique is known as modal reduction, or more commonly as modal synthesis [1,2,3]. The premise behind modal synthesis is that the system response can be decoupled into a rigid body response and an elastic vibration response (see Figure 1). This decoupling allows a generalized suspension system to be defined which delineates the rigid body system response.

The rigid body portion of the system is comprised of masses, springs, and dampers. Typically for an automobile, these would be the tires, springs, and shocks that comprise the suspension system. The ability to define non-linear elements is particularly convenient for this area of the vehicle.

The rest of the vehicle can then be examined as a normal pinned-pinned vibrating system. This assumption requires only one modal extraction to be performed on the vibrating portion of the vehicle. The total vehicle system can then be defined by generalized components of the vibrating system superimposed on the rigid body system.

The process used in this solution technique is to derive the equations of motion, generally through a LaGrangian formulation, and then integrate these through the time domain. The equations are developed by examining a static free-body of the system at a given instant of time. Knowing all the loads subjected to the vehicle, the equivalent inertial forces required to put the system into equilibrium can be found. These acceleration components can then be integrated once into velocity and then again into displacements. Knowing the magnitude of these accelerations, velocities, and displacements at the suspension elements, equivalent inertial, damping, and spring forces can be calculated to modify the static free-body for the next instant of time. System non-linearities can then be introduced by the definition of the suspension properties, usually a non-linear force displacement relationship that represents the spring stiffness. The appeal of this
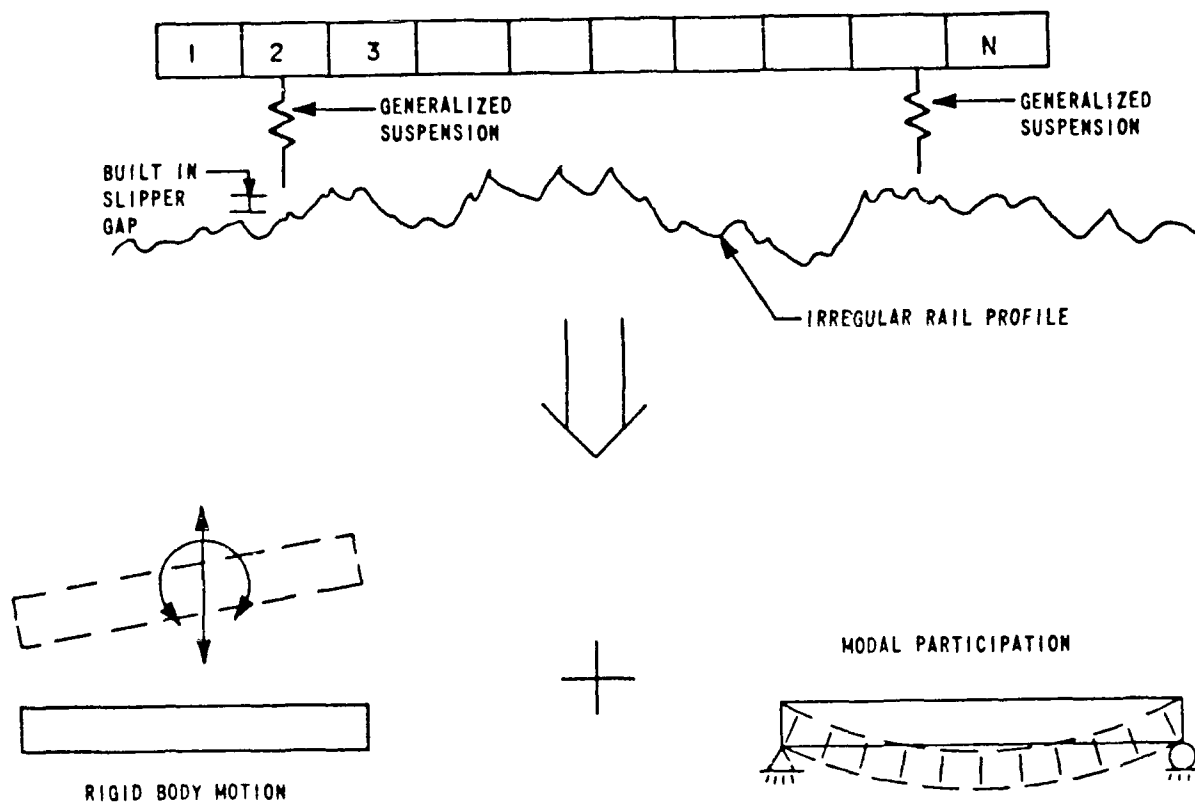
FIGURE I   IDEALIZED SLED MOTION

approach is that a rough design for the suspension can be done early in the process and refined later when the modal parameters of the vehicle structure are defined.

The application of this technique then hinges on the definition of an external forcing function. Typically, this is introduced as a surface irregularity the vehicle travels over and which drives the suspension elements. However, by minor adaptation, this surface irregularity can be expressed as an acceleration, velocity, or load profile as easily as a displacement profile.

FORCING FUNCTION DEFINITION

It is at this point that the various modal synthesis solution sequences differ. The differences hinge on the definition of the irregular surface over which the vehicle must travel. Early work in this field assumed a given profile, and these were generally limited to sine waves of varying amplitude and period length.

Recently, the Air Force has sponsored several studies [4,5] on aircraft landing gear response to runway impacts and to aircraft taxiing on bomb damaged runways. Specific surface roughnesses for these studies are shown in Figures 2 and 3 for the bomb damaged runways. These are shown as step inputs representative of the mats used to repair the runway. The study of Figure 3 was to determine the effectiveness of an actively controlled landing gear responding to

Velocity = 44 ft/sec = constant
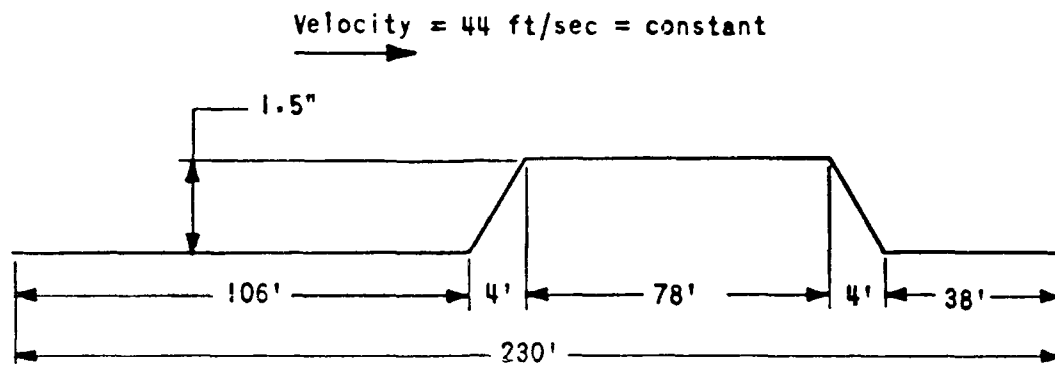
FIGURE 2   RAMP PROFILE FOR DAMAGED RUNWAY

Velocity = 60 ft/sec = constant
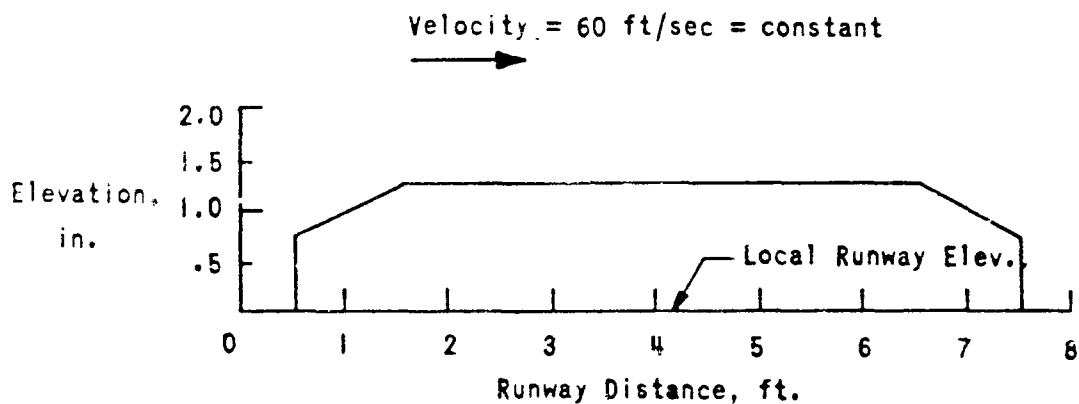
FIGURE 3   STEP PROFILE FOR DAMAGED RUNWAY

Velocity = 120 ft/sec = constant
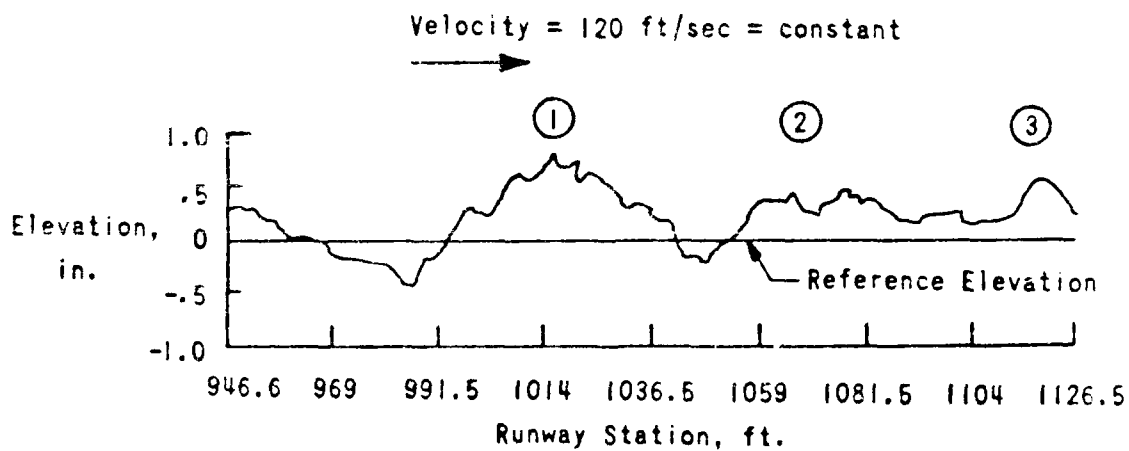
FIGURE 4   ACTUAL RUNWAY PROFILE

this step input. This study was repeated using an actual runway profile shown in Figure 4.

The offshoot of these studies raises the basic question, "Just how important is the definition of the forcing function on the simulation results?" This question took on added significance after a preliminary study of the rail used to guide rocket sleds at the Holloman High Speed Test Track [6]. Final results of this study indicated that the rail could be characterized by any of nine distinct rail profiles.

These profiles were obtained by surveying specific areas of the track at one foot intervals for a minimum distance of 50 feet. Since the rail is supposed to be a straight line, a least squares best fit line was removed from the raw survey data. The residuals after the line removal were classified as "rail roughness". The extent, or rank, of the rail roughness is defined by the standard deviation of the residuals. Two of these nine rail profiles are shown depicted in Figures 5 and 6.

Subsequent frequency domain analysis of the rail roughness data indicated significant power resided at locations repr.sented by physical rail construction details. For example, the ¬ail is comprised of 39 foot sections joined together by welds that have been ground smooth. The entire rail length is aligned vertically and horizontally every 52 inches by tie downs. Each of these distances manifest themselves as the two largest spectral components in the frequency domain. These frequency dependent rail functions then raise the possibility of exciting a sled mode at an appropriate velocity. For instance, if a sled had a fundamental vibration mode of 15 hertz and was traveling at 3000 ft/sec, could a track undulation of 200 feet drive this mode into resonance? This question of long distance rail periodicity drove the need for additional surveys at distances greater than the original 50 foot survey length. Figures 7 and 8 show two profiles that were found to have periodic content of approximately 200 foot.

These questions were answered by examining results of a study performed at the Test Track for sled slipper force predictions. The simulations were performed on an in-house computer program written specifically for the Track called DASTARR [2].

SIMULATIONS AND RESULTS

The simulation series consisted of running constant velocity computer sled runs over a simulated track distance of 4000 feet for each of the nine rail profiles. The 4000 foot simulation distance has been determined to be the optimum distance to travel in order to maximize the slipper loads. In an effort to reduce the permutations available for mixing the nine rail functions, it was decided to use the same function for each rail and stagger the start points by a specified increment.

The simulations were performed using the verified math model of the PAMJET Mission Sled. This sled was a special purpose dual rail sled
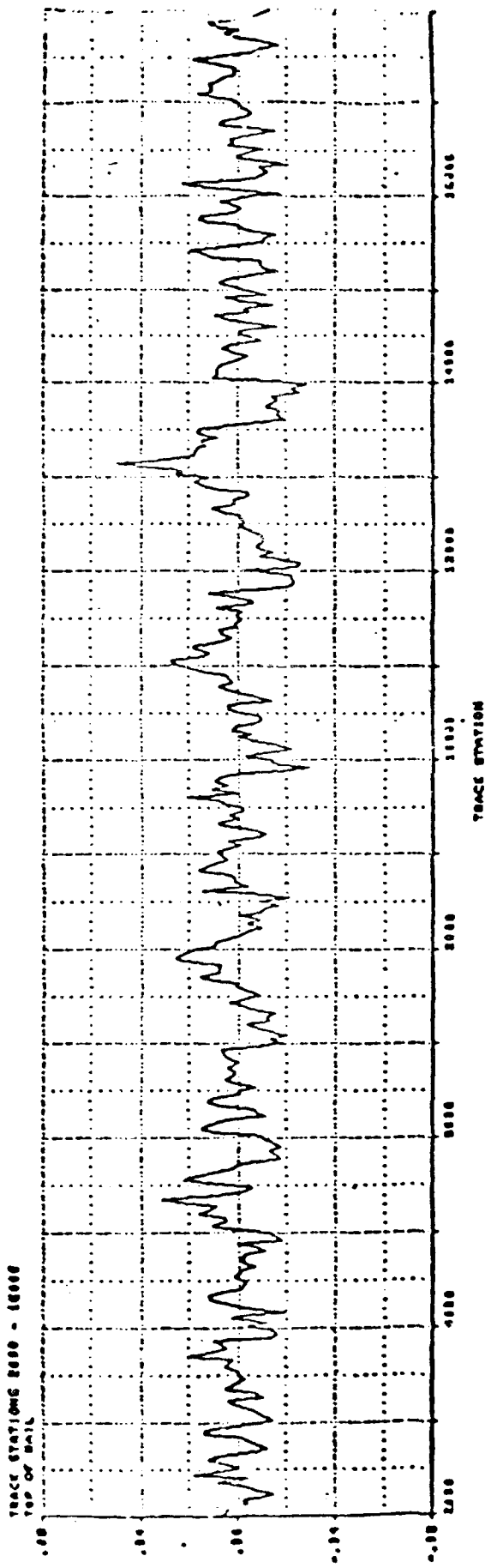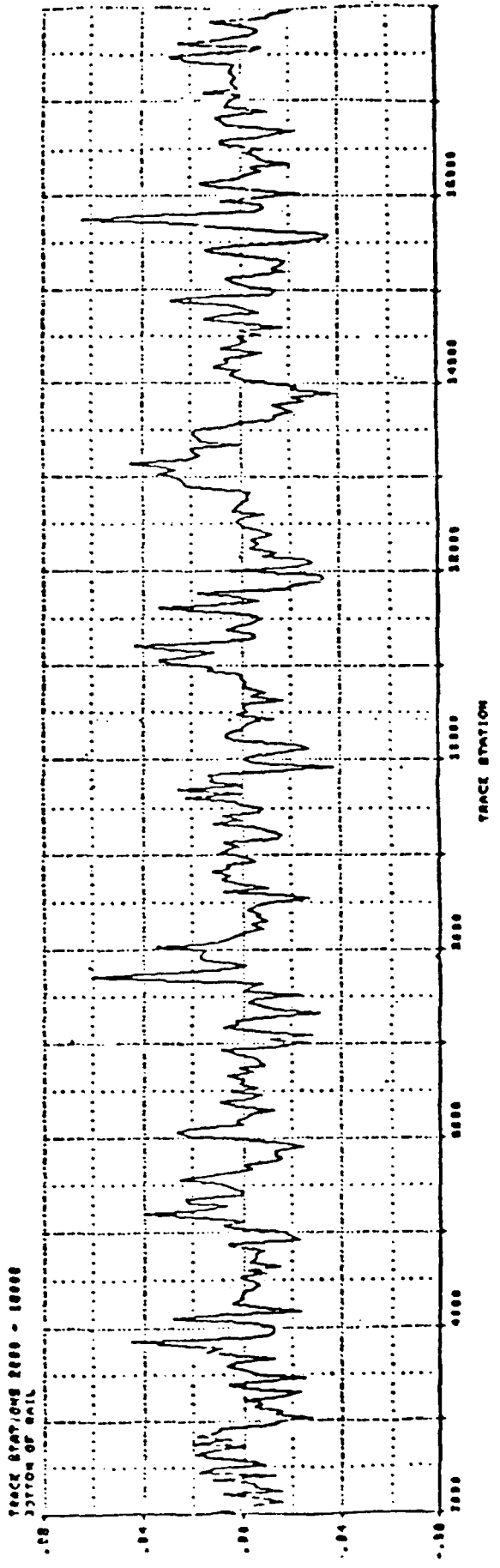
Figure 5   South 15000 Rail Top
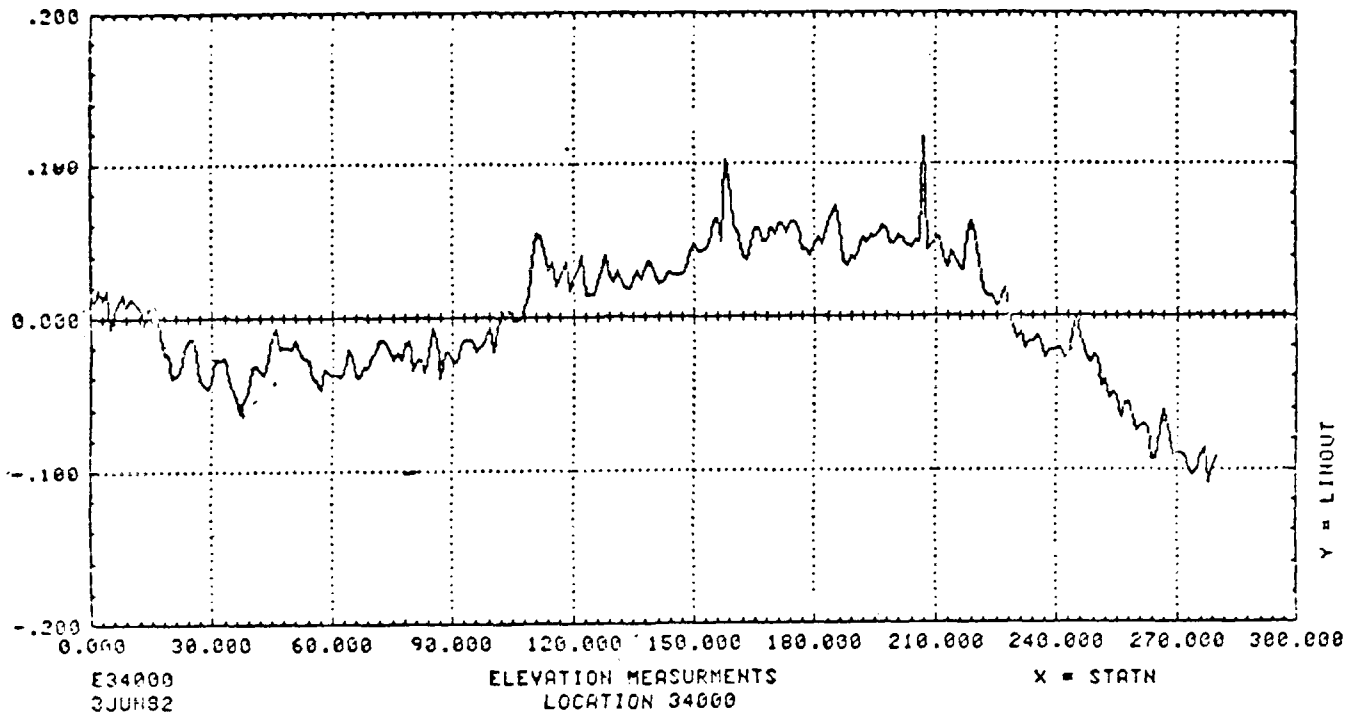

Figure 6   South 15000 Rail Bottom
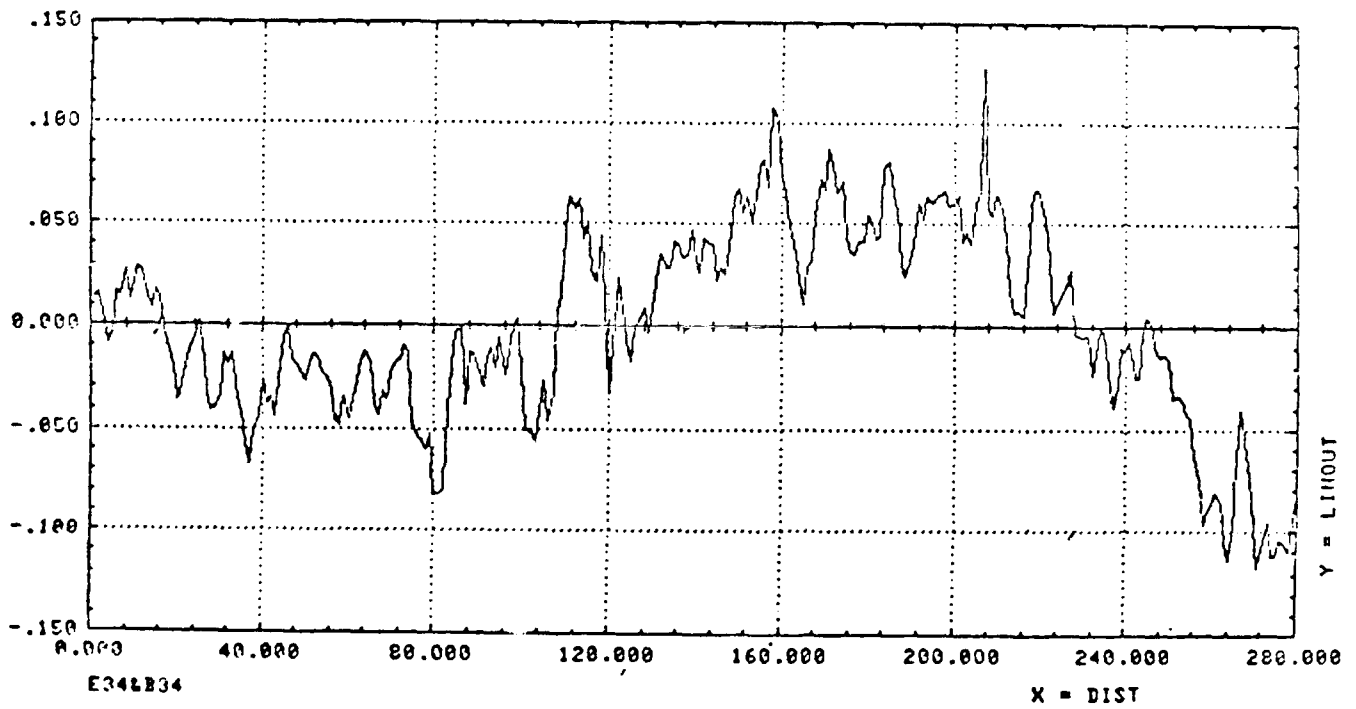
Figure 7   TS 34000 Rail Top

Figure 8   TS 34000 Rail Bottom

(an 84 inch gage between rails) designed to carry either ramjet or scramjet engines at speeds up to Mach 3.5. Special instrumented slipper pins were used to mount the sled to the slippers so the actual slipper forces could be measured. These instrumented slipper pins had previously been statically calibrated to within one percent of known load applications in a lab setting. Several sled runs were made at velocities up to Mach 1.81. Data from these runs were compared for consistency and functionality of the slipper pins in a dynamic environment.

There were a total of 17 velocity conditions examined for the Ramjet sled. These represented conditions from Mach 0.85 to Mach 1.81 under acceleration loads, back through Mach 0.85 coasting. Each of these slipper computer simulation results were compared to actual measured slipper data taken at that velocity condition for this sled. Typical results of this study are shown for one slipper in Figure 9. The solid line represents the actual measured forces, and the symbols represent the various rail profile predicted forces. Notice from the figure that the general trend (regardless of velocity) is the rougher the rail, the larger the force predictions.

The 17 conditions were analyzed statistically to determine the percentage deviation from the actual measured forces for the run as a whole. The standard deviation about the average deviation was also calculated. These results are shown in Figure 10. The conclusions drawn from the statistical results are the same; the average deviation tends to increase with increasing rail roughness. Similarly, the standard deviation increases with rail roughness. The results discussed so far were for the dual rail sled under rigid body motion of the suspension only. These results repeat when modal participation of the sled body is added. This same phenomenon is seen for monorail sleds also.

Results of the actual sled forces and the simulation studies were also analyzed in the frequency domain. Examinations of the PSDs for the actual force data (Figure 11) is almost identical with that of the rigid body simulations (Figure 12). As expected, specific track induced frequency content was manifest in the PSDs. The frequency shown at 42 hertz in both of these figures corresponds to the 39 foot rail length. The 30 hertz frequency is the 50 foot data survey length being looped end-to-end to generate the 4000 foot rail distance the sled travels over. The 52 inch tie down spacing would occur at 370 hertz for this velocity, hence it is not seen in these figures.

An interesting development occurred during this study. At one particular point on the track, a front slipper showed a severe force spike (see Figure 13) that repeated run after run. The project engineer was curious to know whether the spike could be resolved to a specific track location and whether it could be simulated if it fell within one of the defined rail profiles. Using the trajectory analysis, it was determined that the spike occurred somewhere between Track Station (TS) 12020 and 12035. By luck, it happened that this section of track was contained within the rail profile designated south 15000 rail top.
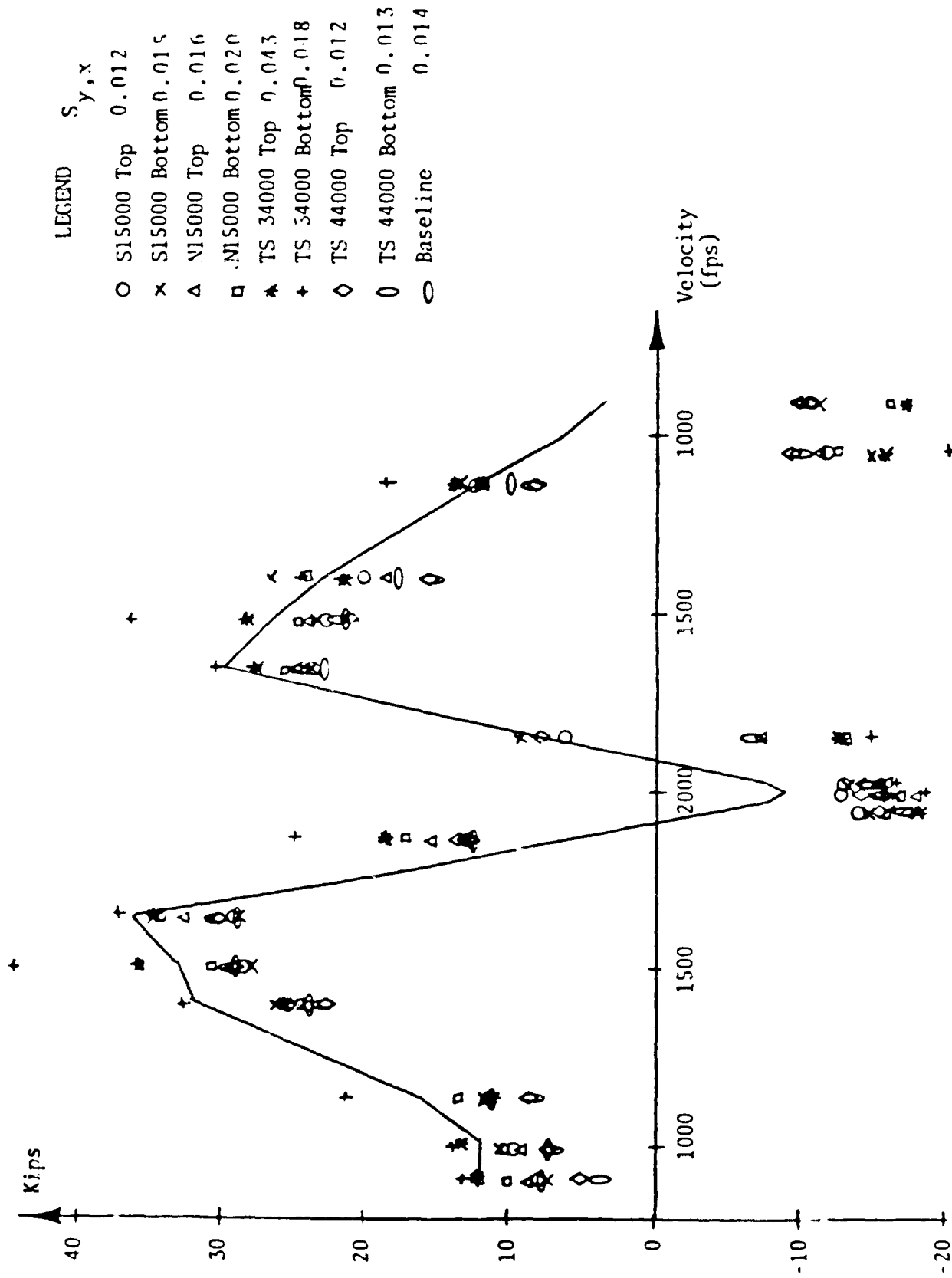
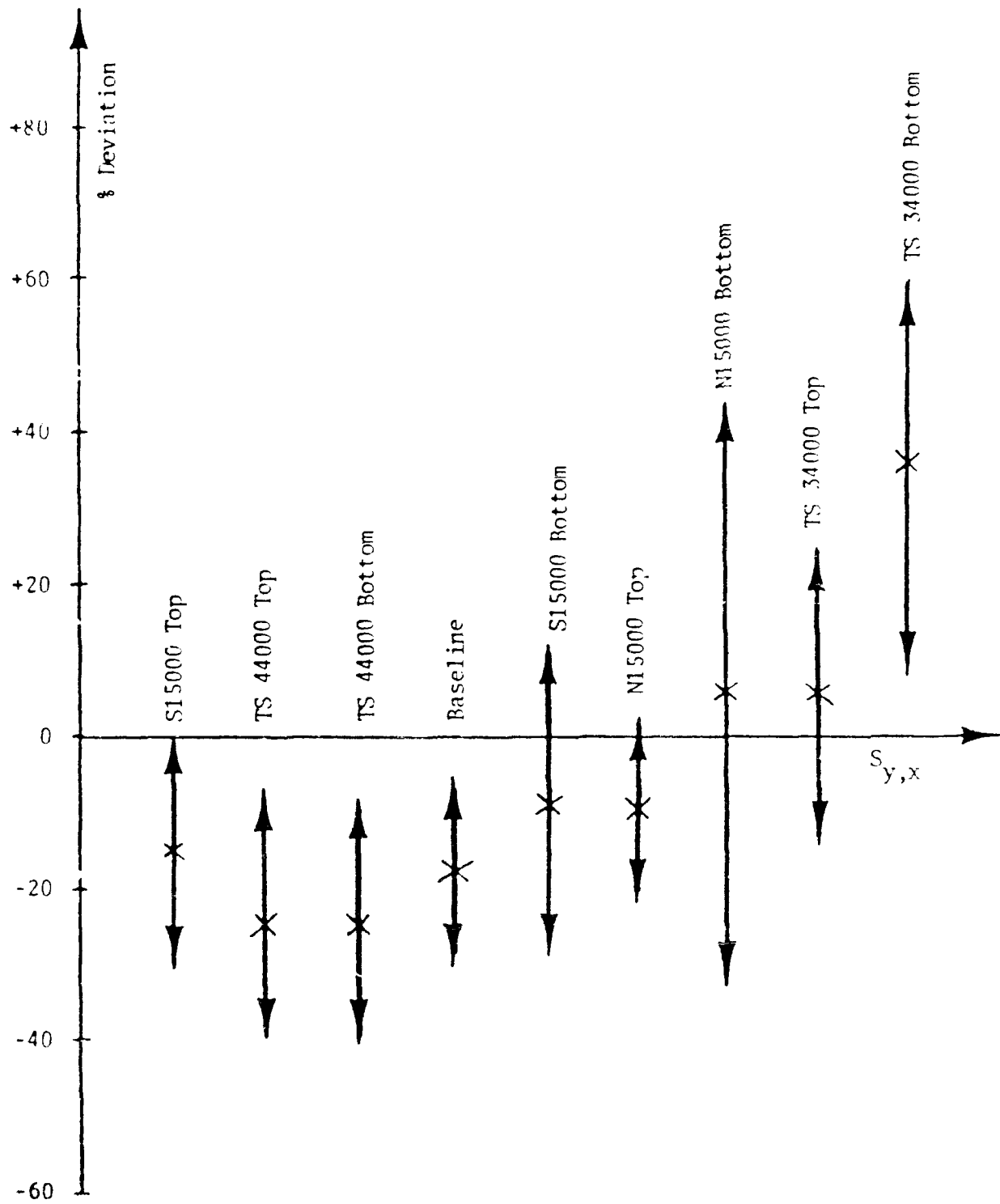Figure 9   Slipper 1 - Peak. Force Vs. Predicted Force

291

Figure 10   Front Beam Statistical Results

SLIPPER FORCE RIGHT FRONT (LBS**2/HZ)

PSD POWER: .4307489E+09
TIME INTERVAL: 11.0 TO 12.0 SEC.

FREQUENCY IN HZ
2 PASS HANNING

DC PSD POWER: .2114339E+09
PLOT NR 4
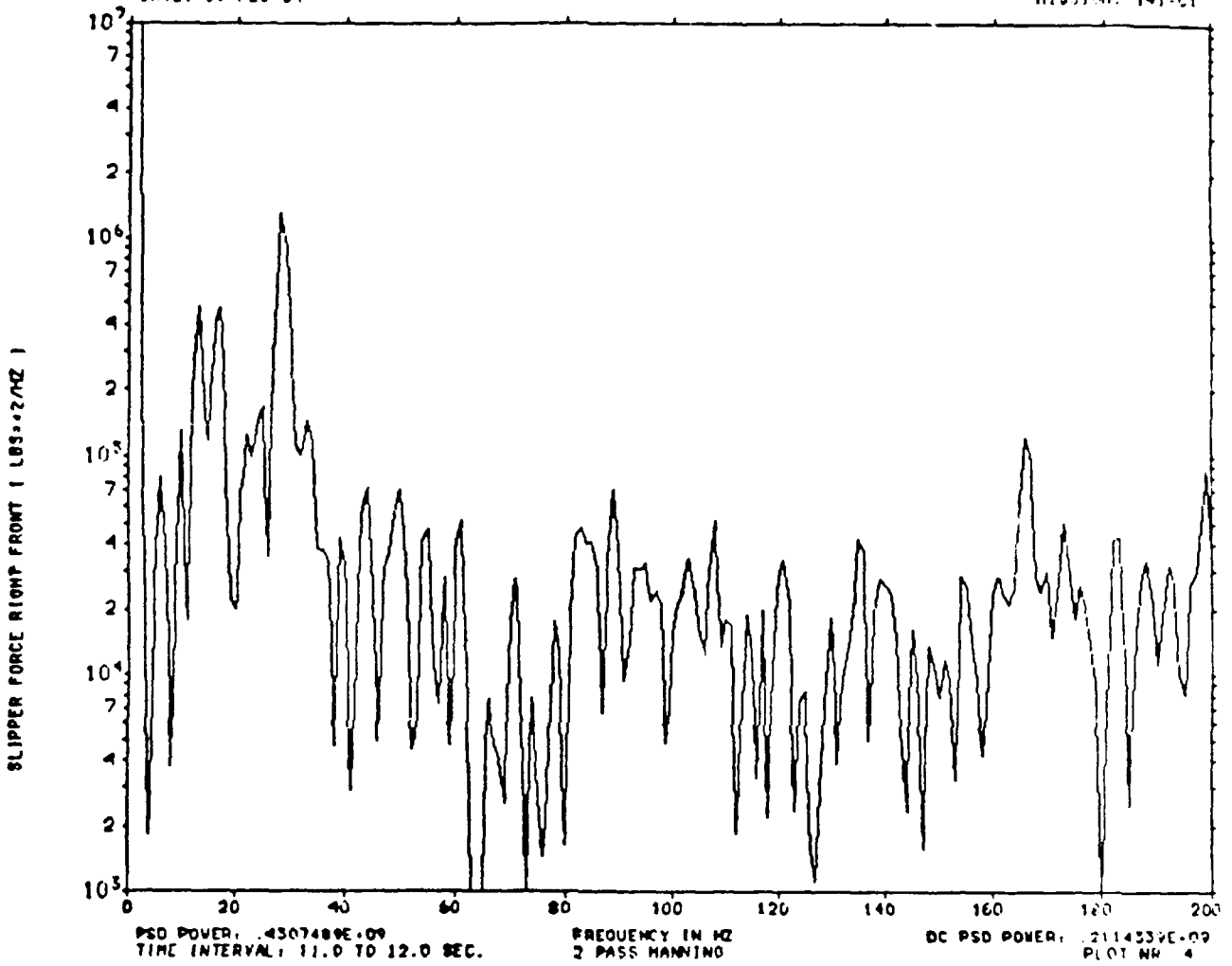
Figure 11   POWER SPECTRAL DENSITY

Y = Y POW

PROC
POWER

Figure 12   PSD SLIPPER FORCES
SLIPPER # 2

X = FREQ

293
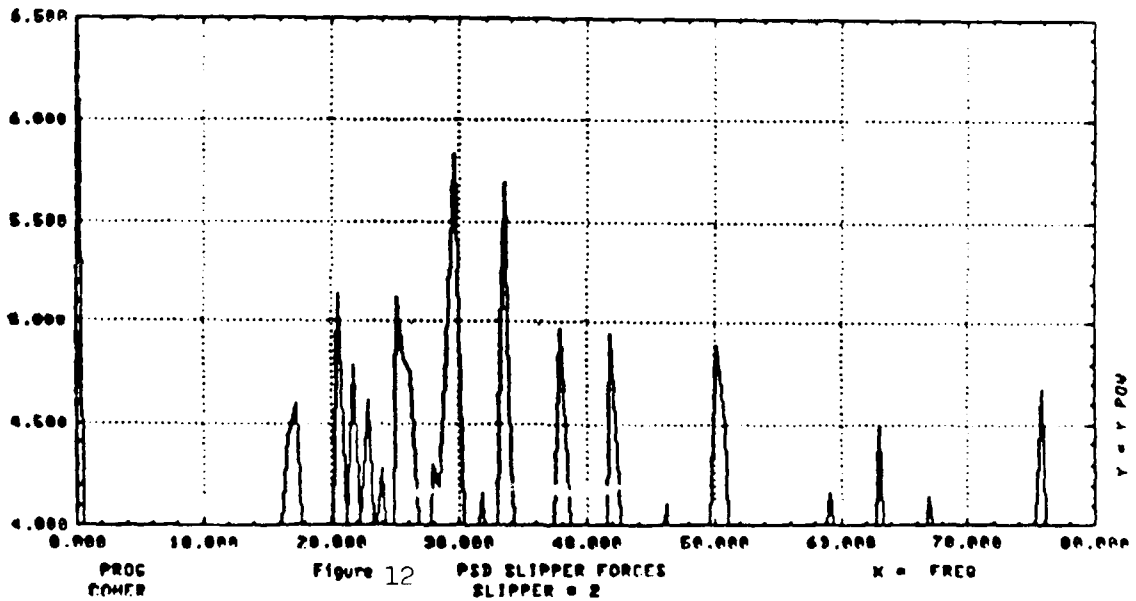
A simulation was made using this rail function at a velocity consistent with the sled velocity that created the force spike. This force time history is shown in Figure 14. Note the twin spikes that recur every quarter second. This time interval corresponds to 400 feet of track at this velocity. This rail profile used a survey distance of 400 feet that was looped to generate the 4000 foot rail. Examining the time into the simulation where the larger spike occurred and comparing this to survey data, it was determined that the spike occurred at TS 12027-12029 (see Figure 5), which is inside the previously ascertained envelope for this occurrence.

CONCLUSIONS

Based on the simulations done for estimating track dynamics for both dual rail and monorail sleds, it is apparent that the program used to simulate the vehicle dynamics yields results that are correlated to actual data both in the amplitude and frequency domain. However, the results of the simulation are strongly dependent on the irregular profile used as the forcing function. Results deviated by as much as 100 percent from that measured; therefore, for accurate simulated results an accurate forcing function must be defined.

Conversely, if an accurate forcing function is known, simulation studies can be performed to assess the effects of artificially smoothing the profile. This is extremely beneficial for the Test Track to decide the benefits of selectively grinding the rail to smoothen it and hence to lessen the dynamic loads that might be transmitted to a test article.

REFERENCES

1. L. Minnetyan, J. A. Lyons, and T. G. Gerardi, "Dynamic Simulation of Structural Systems with Isolated Non-Linear Components," The Shock and Vibration Bulletin, Vol. II, May 1983.

2. G. L. Ferguson, "Dynamic Analysis of a Sled Traveling Along a Rough Rail," AFSC, EAFB, Fl, AD-TR-83-39, May 1985.

3. V. A. Tischler, V. B. Venkayya, and A. N. Palazotto, "Dynamic Analysis of High Speed Rocket Sleds," AFWAL, W-PAFB, Oh, AFWAL-TR-81- , Jan. 1981.

4. D. L. Morris and J. R. McGehee, "Experimental and Analytical Investigation of Active Loads Control for Aircraft Landing Gear," The Shock and Vibration Bulletin, Vol II, May 1983.

5. J. J. Olsen, "A New Look at the Use of Linear Methods to Predict Aircraft Dynamic Response to Taxi Over Bomb-Damaged and Repaired Airfields," The Shock and Vibration Bulletin, Part 4, Jan. 1987.

6. L. C. Mixon, C. B. Evans and W. L. Gilliam, " Rail Roughness Study of the Holloman High Speed Rocket Sled Test Track," AFSC, EAFB, Fl, AD-TR-81-62, Sept. 1981.
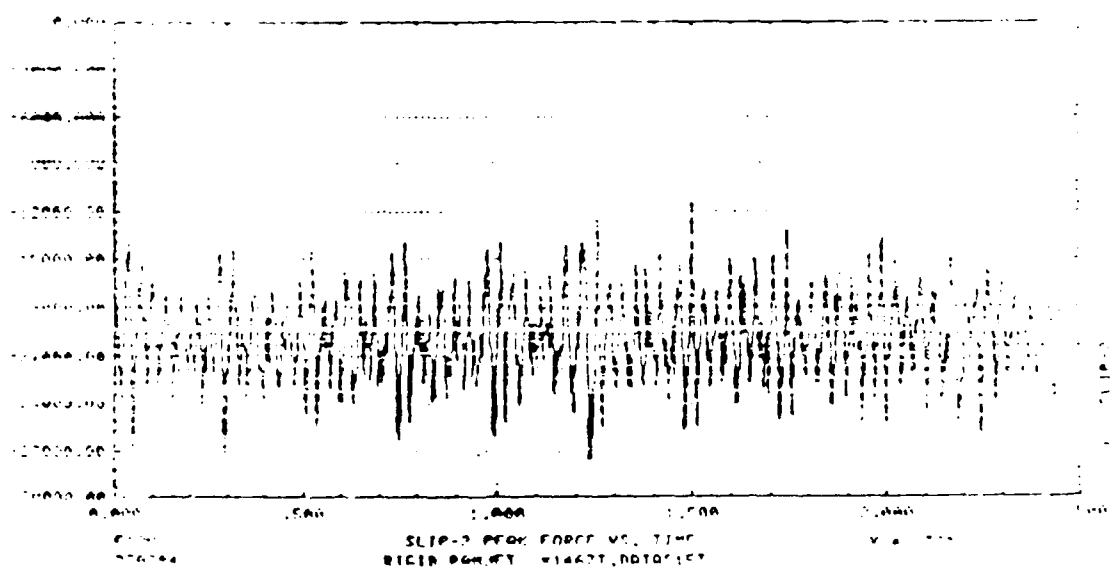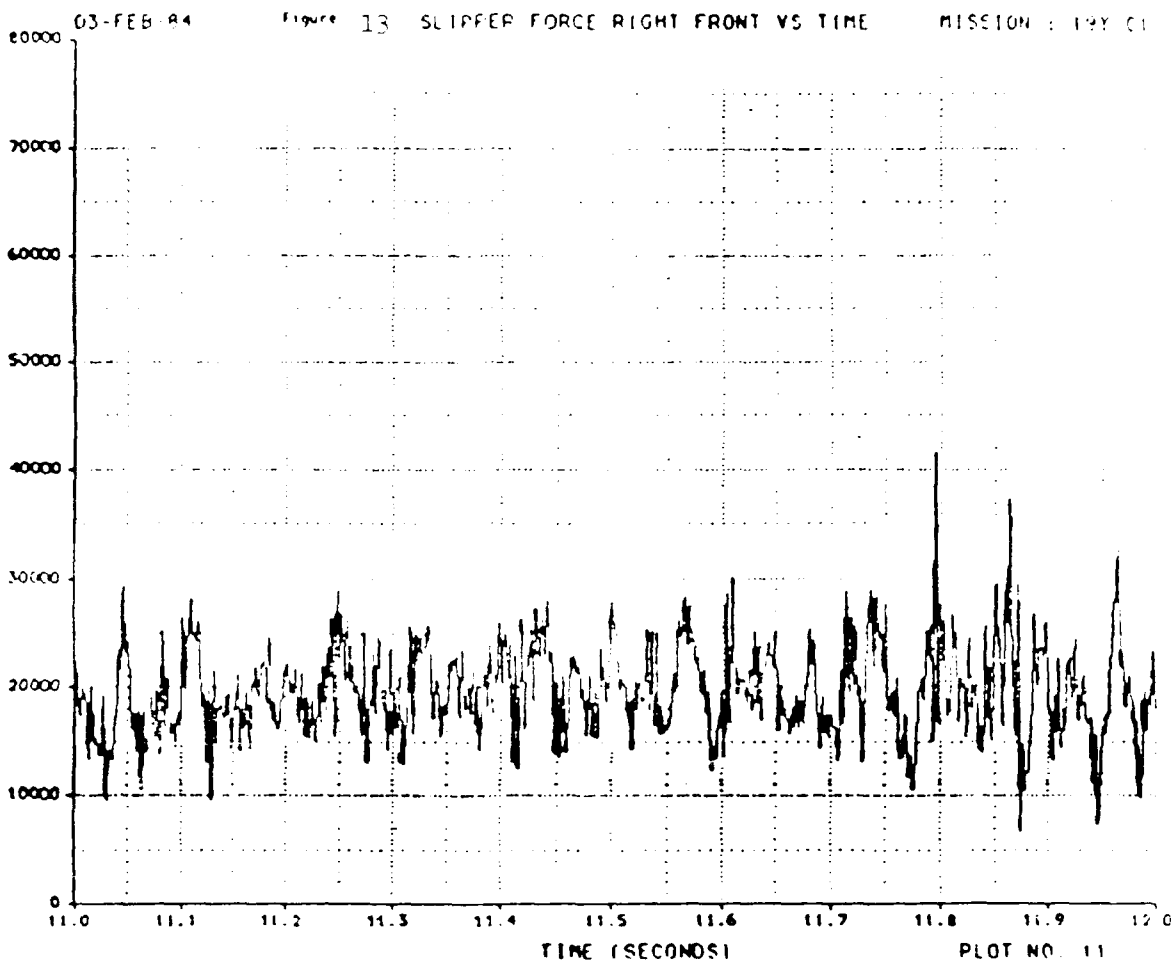
Figure 13 SLIPPER FORCE RIGHT FRONT VS TIME

Figure 14 Rigid Body Dual Rail, S15000 Top

UNDERLYING ASSUMPTIONS IN THE DEVELOPMENT
OF TRACKED VEHICLE VIBRATION SCHEDULES

William H. Connon III
US Army Combat Systems Test Activity
Aberdeen Proving Ground, MD

Because tracked vehicle data has energy concentrated at
certain speed related frequencies, a swept-narrow-band-
random-on-random laboratory test is used to simulate the
entire speed range of operation of the vehicle. As a matter
of test convenience, the data (Power Spectral Densities)
from a small range of speeds are grouped together to form a
phase. The consequence of this grouping process can be an
addition of unintended conservatism to the root mean square
acceleration level of the test and the assumption of a time-
speed distribution which may be unrealistic.

INTRODUCTION

Because tracked vehicle data has energy concentrated at certain speed related
frequencies, a swept-narrow-band-random-on-random laboratory test is used to
simulate the entire speed range of operation of the vehicle. The speed-frequency
relationships are as follows:

$$f1 = k*s$$ (eqn 1)
$$f2 = 2*f1$$
$$f3 = 3*f1$$
$$f4 = 4*f1$$
$$f5 = 5*f1$$

where:

    fi = harmonic frequency
    k = factor related to track pitch (constant for a given vehicle)
    s = speed

Rather than conduct a separate test to simulate each speed independently, it
is convenient to group data (Power Spectral Densities) from a small range of speeds
to form a test phase. When grouping speeds together to create a vibration schedule,
harmonics from higher speeds can overlap higher harmonics from lower speeds creating
control system problems. It can be shown that overlapping will occur if:

$$s(k) >= n/(n-1)*s(i)$$ (eqn 2)

where:
s(k) and s(i) are speeds and s(k) > s(i)
n = number of harmonics present in the data

An example is shown in figure 1.
    A computer program is used to determine where overlapping will occur based on

the above equation and the knowledge of the number of harmonics present at each
speed (from examination of the PSD's). The program checks this harmonic matrix for
the occurrence of overlapping and separates the speeds into test groups without
overlapping. Only speeds with similar numbers of harmonics are placed in the same
group. The technique currently used when grouping is to assign the PSD level of the
average plus one standard deviation of the PSD values used in the grouping of each
of the harmonics limited by the largest PSD value in that harmonic (which normally
has the effect of enveloping the data for small sample sizes such as 3 or 4 speeds).
The bandwidth assigned is the bandwidth from the center frequency of the lowest
speed to the center frequency of the highest speed at each harmonic. An example of
typical tracked vehicle data for three speeds which form a group (test phase) are
shown in figure 2 while the schedule derived from this group is shown in figure 3.
Because of the relationships developed in the first equations, it can be shown that
this technique results in bandwidths at each harmonic which are integer multiples of
the first bandwidth developed.

A smaller bandwidth is selected within each of the harmonic bands and is swept
across the band to simulate changing vehicle speed within the speed range
represented by the test phase. Selection of the width of this swept band has a great
influence on the ability of the control system to update the control spectrum.

DISCUSSION

For the control systems currently in use at USACSTA, the relationship between
the width of the bands, the number of averages per control loop and the sweep rate
for each swept narrow band can be described by: [1]

$$SWRT = (T*df)/(NS*(1.27*NAVLP+6.0)*SWRES) \qquad \text{(eqn 3)}$$

where:
SWRT $=$ number of loops before updating a frequency line
T $=$ test duration in seconds
df $=$ frequency resolution in Blocks/sec
NS $=$ number of narrow band sweeps
NAVLP $=$ number of input averages per control loop
SWRES $=$ number of frequency lines to be changed in a narrow
             band during one sweep (frequency lines/sweep)

The value SWRES can be further defined as:

$$SWRES = (TBW - SBW)/deltaf \qquad \text{(eqn 4)}$$

where:
SWRES $=$ number of frequency lines to be changed
TBW $=$ total width of band to be swept, Hertz
SBW $=$ width of sweeping band within total band, Hertz
deltaf $=$ frequency resolution, Hertz

A requirement of the operating system is that the number of loops before
updating a frequency line (SWRT) must be two or greater to allow time for the drive
to equalize after updating the narrow band spectrum. By assigning a value of 2.1 to
SWRT (any value of 2 or greater is acceptable) and assuming a deltaf (and thus a df)
of 1 Hertz, equation 3 can be rewritten to indicate the required test time as a
function of the number of averages per loop, the number of narrow band sweeps, the

total width of the band to be swept and the width of the sweeping band within the total band as follows:

$$T = 2.1*NS*(TBW-SBW)*(1.27*NAVLP+6.0)$$ (eqn 5)

The effect on the required test time as a function of any of the variables in equation 5 can be computed and plotted, but the relationship between the swept bandwidth and the total bandwidth and that effect on test time are of concern for this paper. Two typical conditions were chosen as examples. The first is a "minimum acceptable" condition of one sweep using six averages per loop. The second chosen was a "desirable" condition of two sweeps and eight averages per loop. The required test time was computed based on the swept bandwidth being 1/2, 1/3, 1/4 or 1/5 of the total bandwidth with the total bandwidth varying between 6 and 72 Hertz. The required test times for the two conditions are shown in figures 4 and 5. It is evident that the required test time is inversely proportional to the ratio of the swept bandwidth to the total bandwidth and, for any given ratio, is a linear function of the total bandwidth. Thus, the sweeping bandwidth normally chosen for test control optimization is one-half the total bandwidth. In addition to requiring the least test time (enabling the number of sweeps or averages per loop to be increased), the use of this ratio and the constraint that the first harmonic total bandwidth be an even number provides an ease of construction of the remainder of the schedule.

Since this bandwidth is chosen as a matter of test convenience and control and is done without regard to the actual bandwidths of the original data, conservatism can be added to the schedule unknowingly. The amount of conservatism is directly proportional to the number of different speeds used to form a test phase and is a result of the test schedule bandwidth being larger than the original data bandwidth. Figure 6 depicts rms values from a typical test schedule (with an exaggeration factor applied) and actual rms values from which the schedule was derived. The same information is shown with symbols rather than solid lines in figure 7 to more easily display the number of speeds used in each test phase. A conservatism ratio can be computed from:

$$CR = (schedule\ rms/actual\ rms)/\sqrt{ef}$$ (eqn 6)

where:
CR   — conservatism ratio
schedule rms — rms value from schedule test phase
actual rms   — maximum rms value from speed group used
                        in test phase
ef   — exaggeration factor used to reduce test time

The conservatism ratio will have a value of 1 if no unintended conservatism has been built into the schedule by speed grouping. The effect of the number of speeds used in a group on the conservatism ratio is shown in figure 8. The increase in the ratio is caused by the increase in the total bandwidth due to the spread of frequencies represented by the speeds and the increase in the swept bandwidth as a function (1/2) of the total bandwidth.

Bandwidth data from several locations of a particular tracked vehicle were analyzed to determine the actual bandwidths which occur during vehicle operation. Bandwidth data from one particular location are plotted as a function of center frequency for each of the harmonics in figures 9 through 12 to show an apparent lack of correlation between bandwidth and the center frequency at which it appears. When the bandwidths are plotted as a function of the harmonic number (figure 13), some scatter is apparent at each of the harmonics, but a trend is apparent. Average

bandwidth data from several locations are shown as a function of the harmonic number in figure 14 illustrating a slight increasing trend with bandwidths ranging from approximately 5 to 7 Hertz. Confidence limits (95%) are shown for the bandwidths of each of the harmonics in figure 15 based on a sample size of 192 for the first and second harmonics down to 13 for the fifth harmonic (which affects the spread of the limit). Although the data presented are from a particular vehicle, the values are typical of tracked vehicles in general and should be considered when schedules are developed.

Another problem associated with speed grouping during the development of vibration schedules is the assumption of a time-speed distribution which may not represent the actual distribution. As an aid to test control, test times for each test phase are identical. Since the test phases represent specific vehicle speeds, a simulated vehicle speed distribution is arbitrarily established. An actual speed distribution taken from speed data measured during operation on a paved road is shown in figure 16 and is superimposed on the speed distribution simulated by a typical schedule in figure 17. It has been shown previously that minimum test times of several minutes are required to achieve reasonable test control (averaging and sweeping); therefore, it is necessary to overuse the data from the lower speeds in a test schedule. It has been standard practice to apply the same exaggeration factor (same time compression) to all phases of a schedule. It is possible to tailor this practice and apply different factors to the various test phases to achieve both a reasonable test time and a realistic time-speed distribution. Awareness of the underlying assumption of speed distribution from speed grouping and test phase duration and an estimation of the actual distribution can produce more reasonable results.

CONCLUSION

It can be concluded that the underlying assumptions made when developing vibration schedules can have a dramatic effect on the ability of the schedule to simulate the real environment and must be considered along with test convenience and control during the development process.

REFERENCES

1.   F. T. Mercer, "Swept Narrow Band Random On Random", Sandia National Laboratories Report SAND80-1534, August 1980.
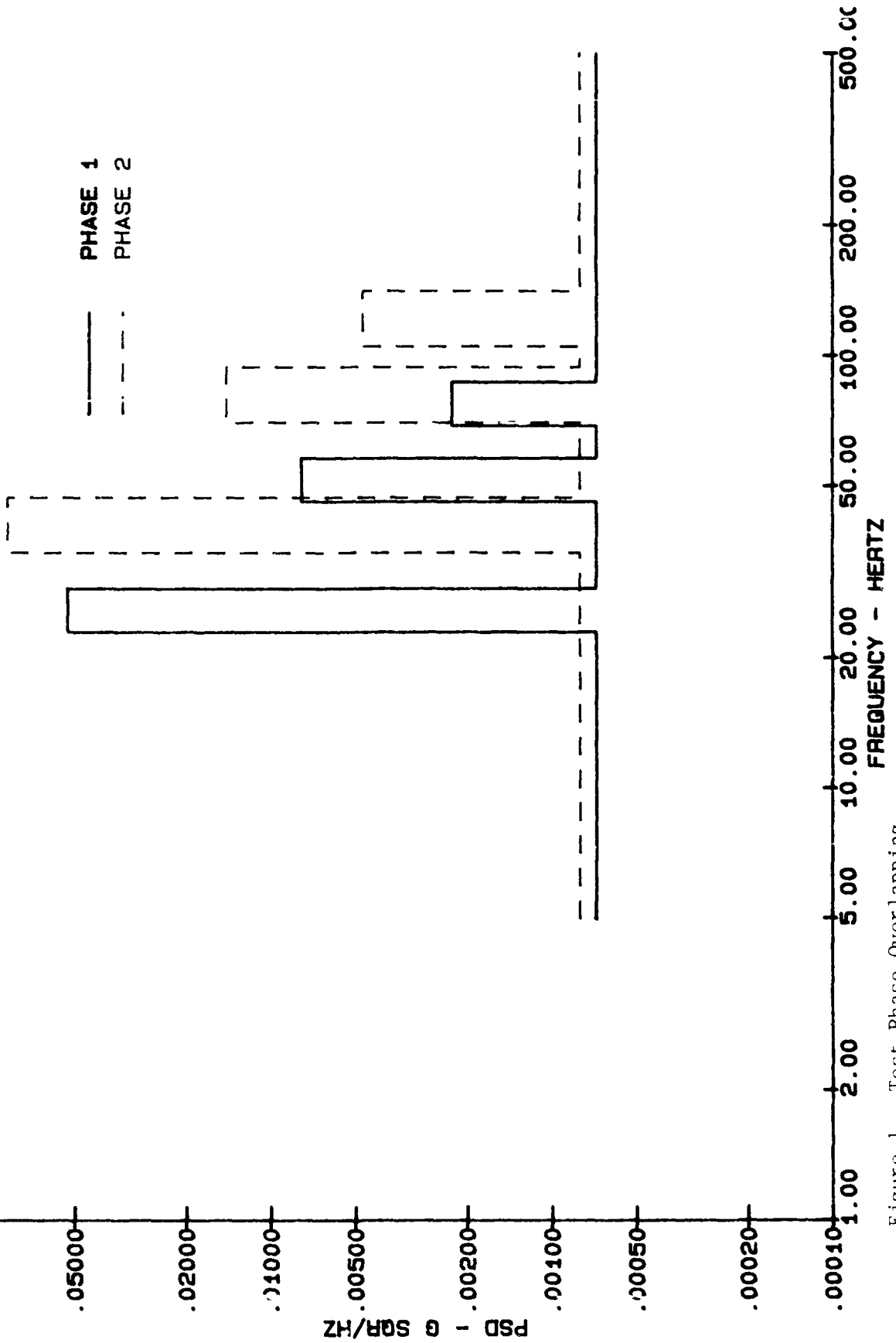
Figure 1. Test Phase Overlapping

TYPICAL TRACKED VEHICLE DATA

Figure 1. Typical Tracked Vehicle Data

12 MPH
14 MPH
16 MPH
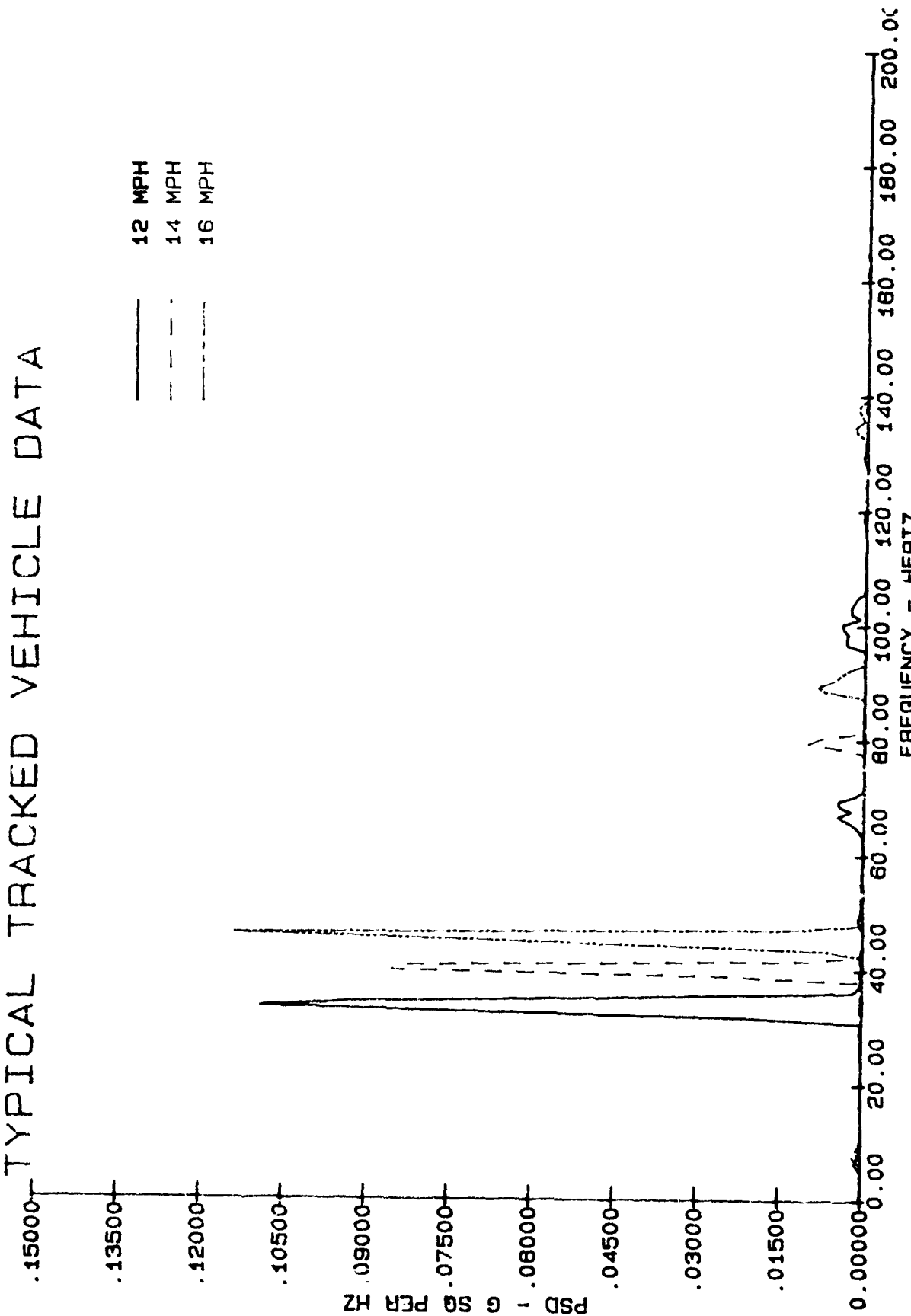
FREQUENCY – HERTZ
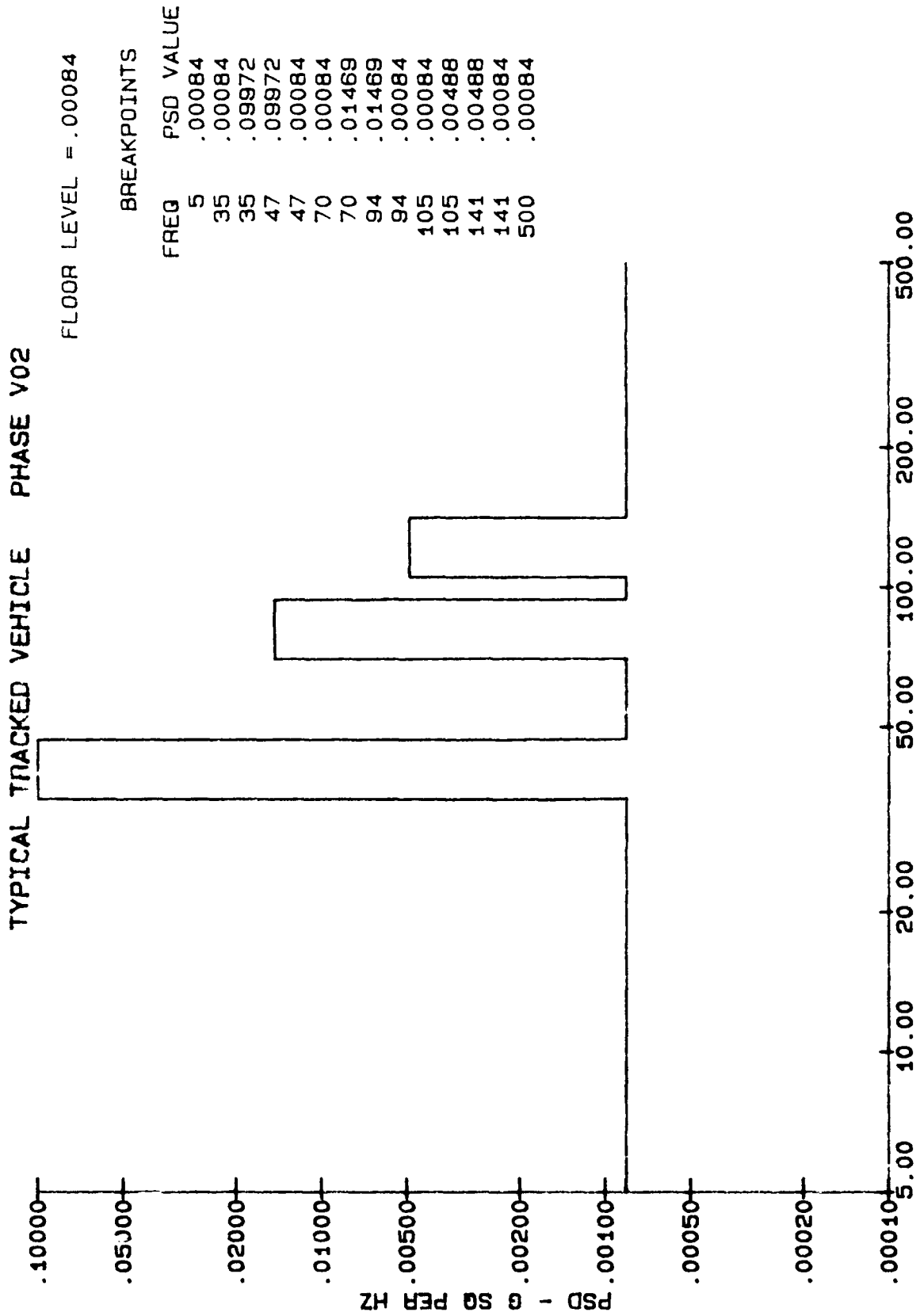
PSD – G SQ PER HZ

TYPICAL TRACKED VEHICLE   PHASE V02

FLOOR LEVEL = .00084

BREAKPOINTS

FREQ	PSD VALUE
5	.00084
35	.00084
35	.09972
47	.09972
47	.00084
70	.00084
70	.01469
94	.01469
94	.00084
105	.00084
105	.00488
141	.00488
141	.00084
500	.00084

Figure 3. Test Schedule

303
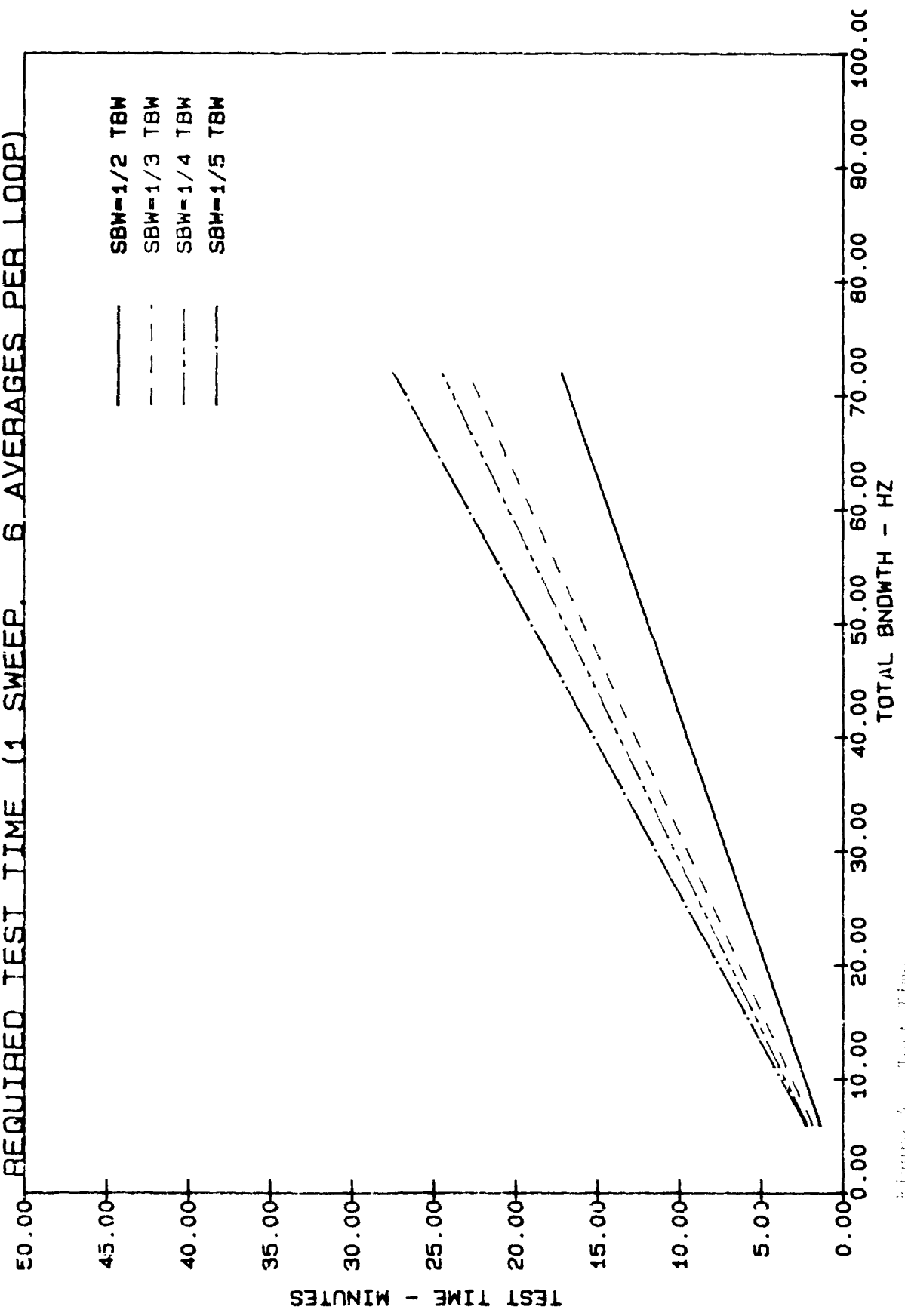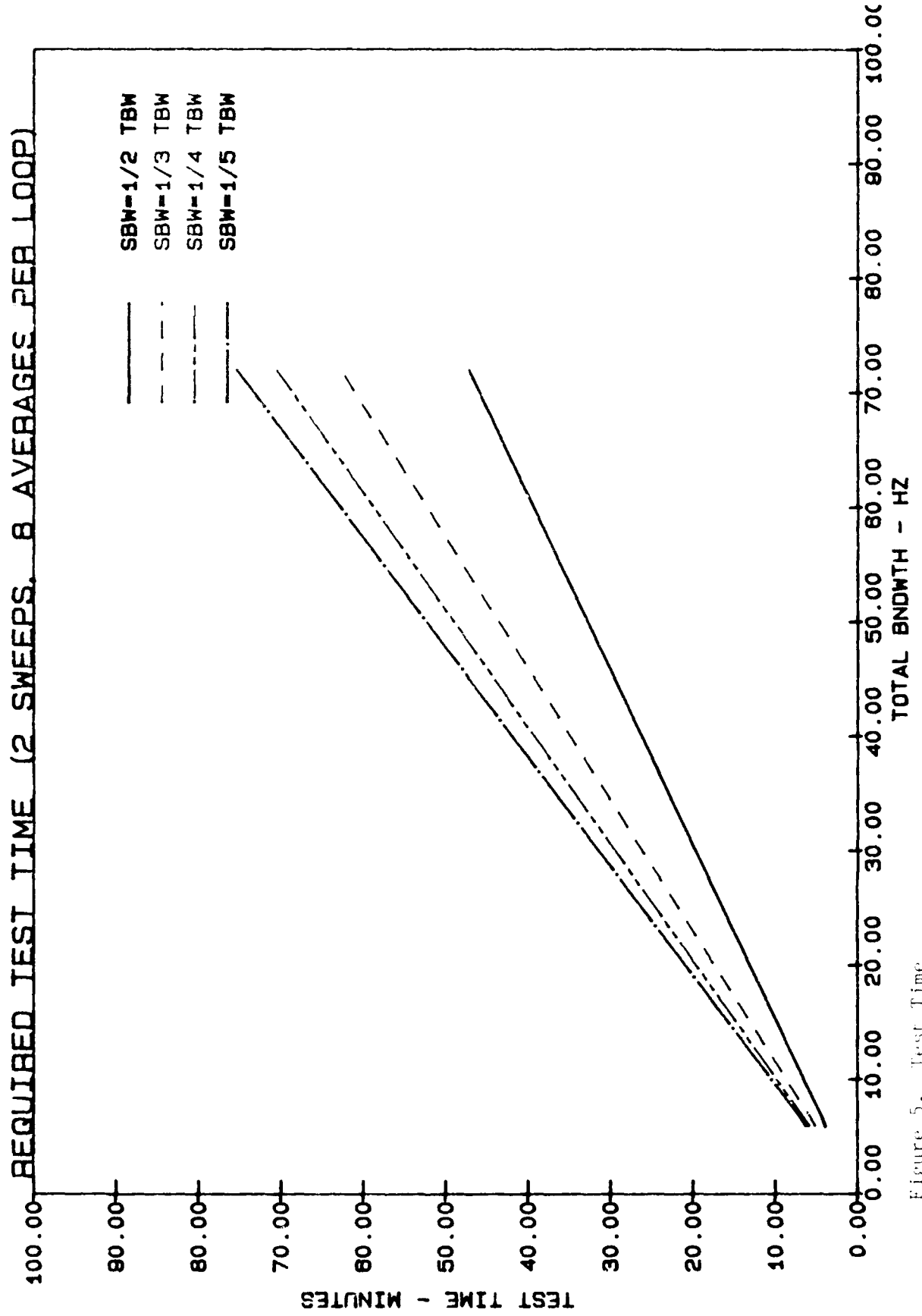
Figure 4. Test Time

Figure 5. Test Time
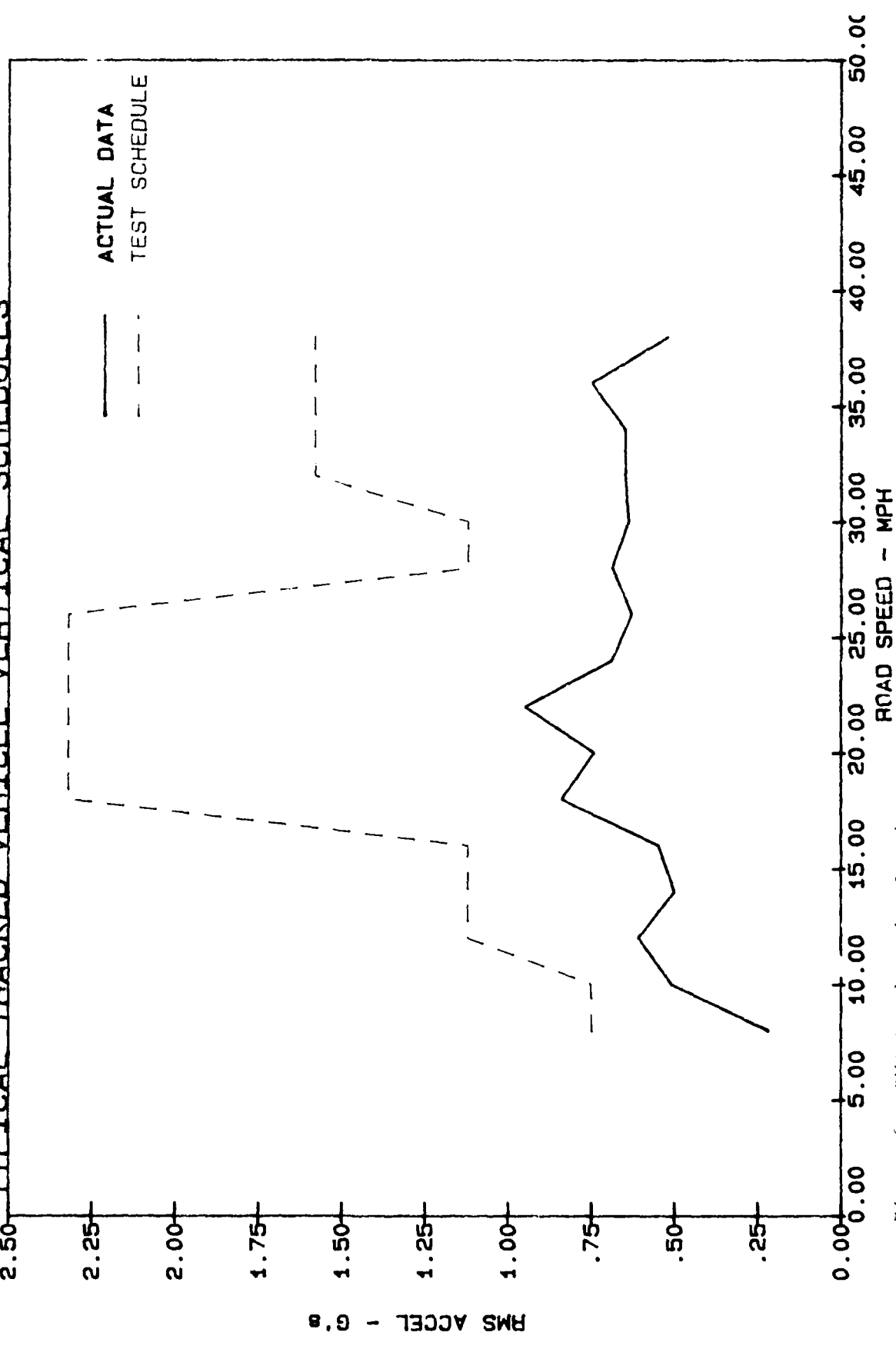
Figure 6. RMS Acceleration Levels
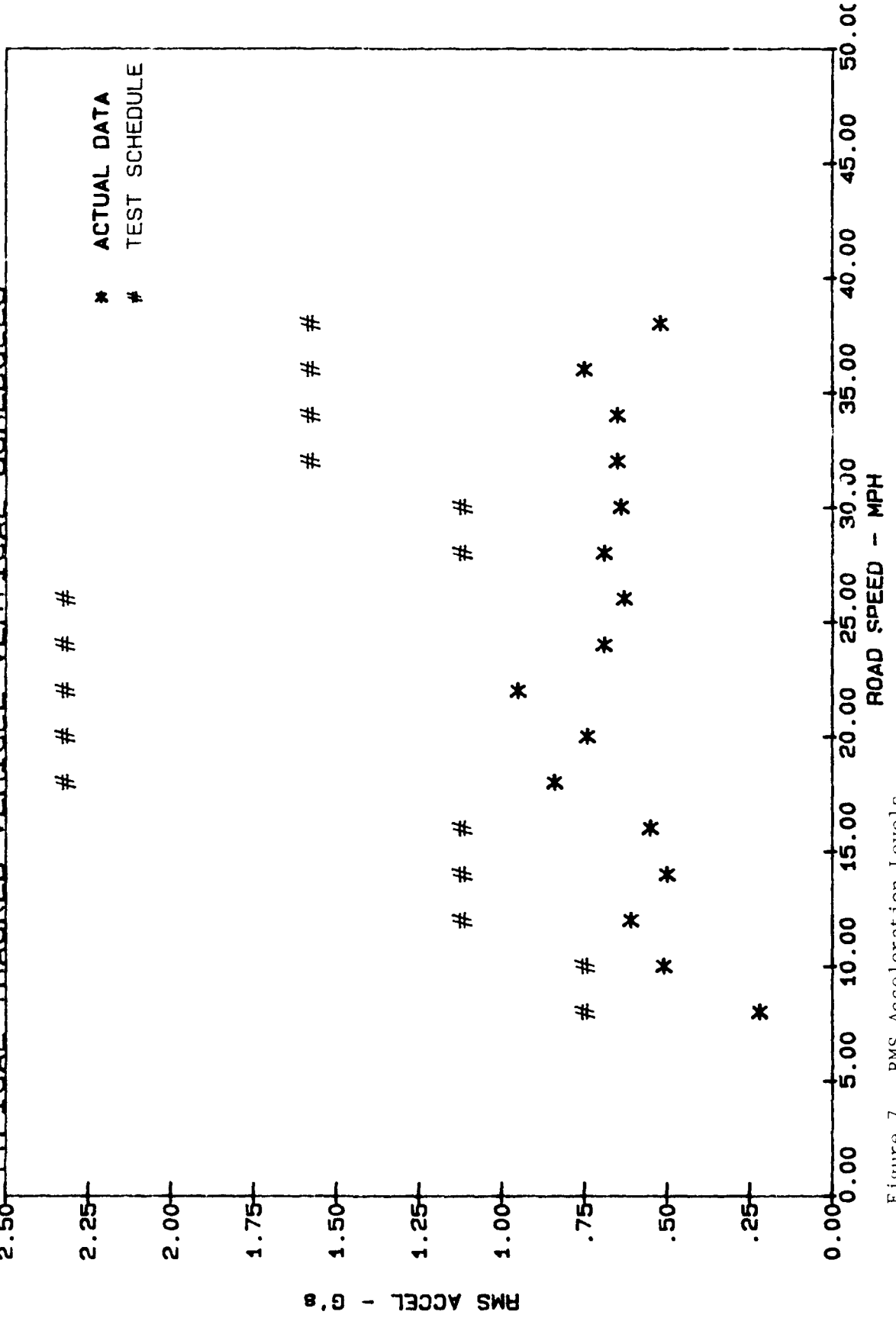
Figure 7. RMS Acceleration Levels
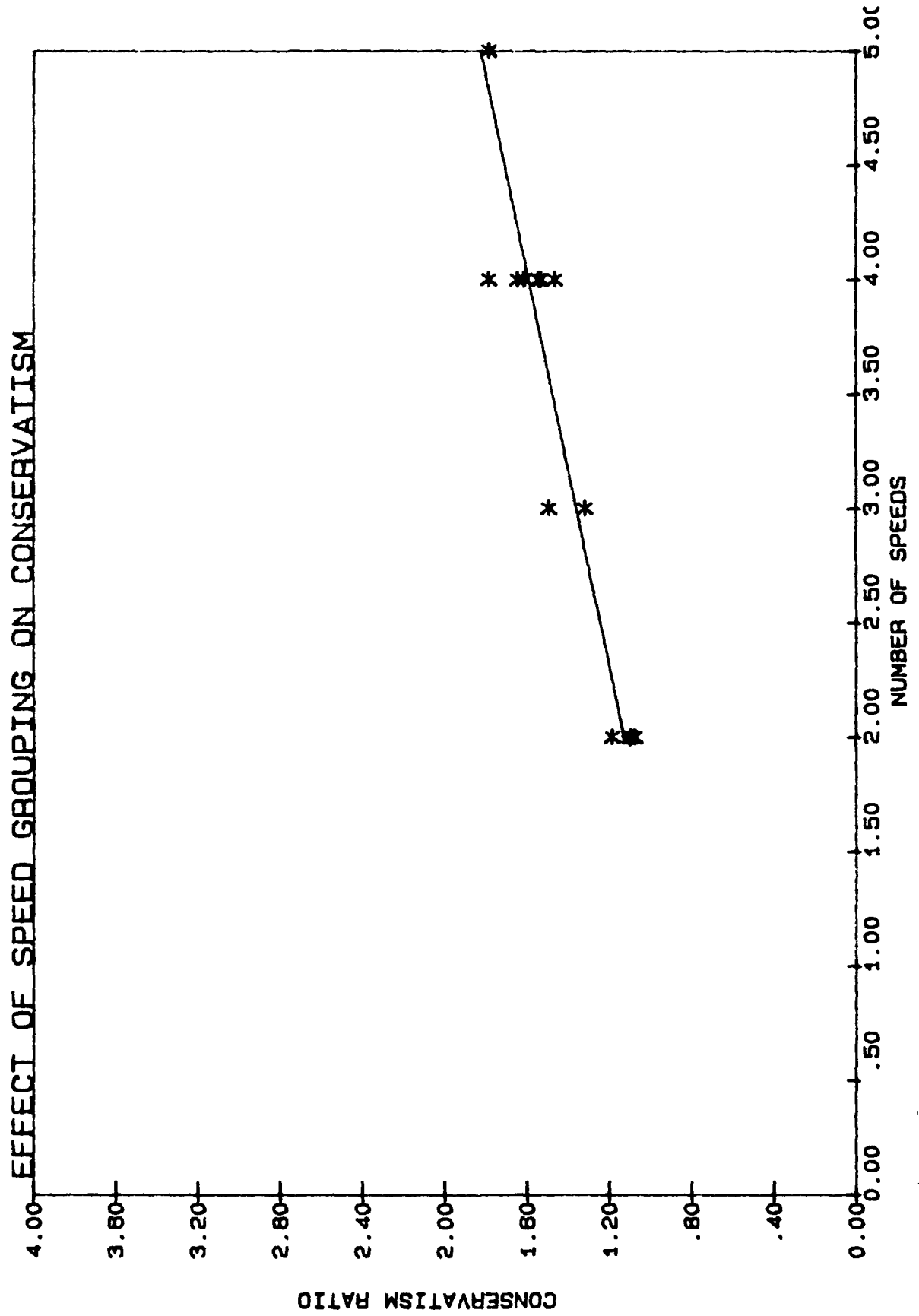
EFFECT OF SPEED GROUPING ON CONSERVATISM

CONSERVATISM RATIO

NUMBER OF SPEEDS
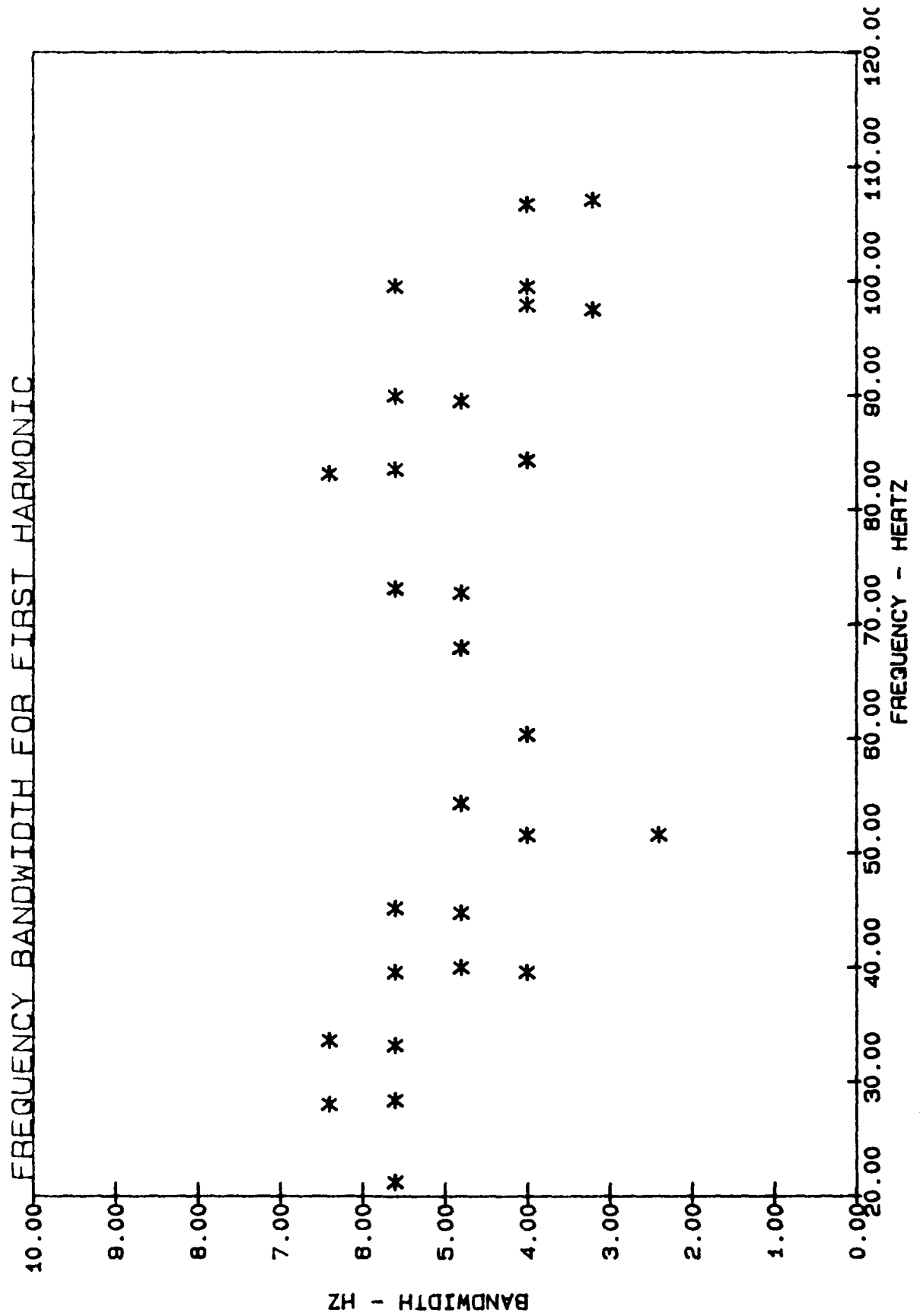
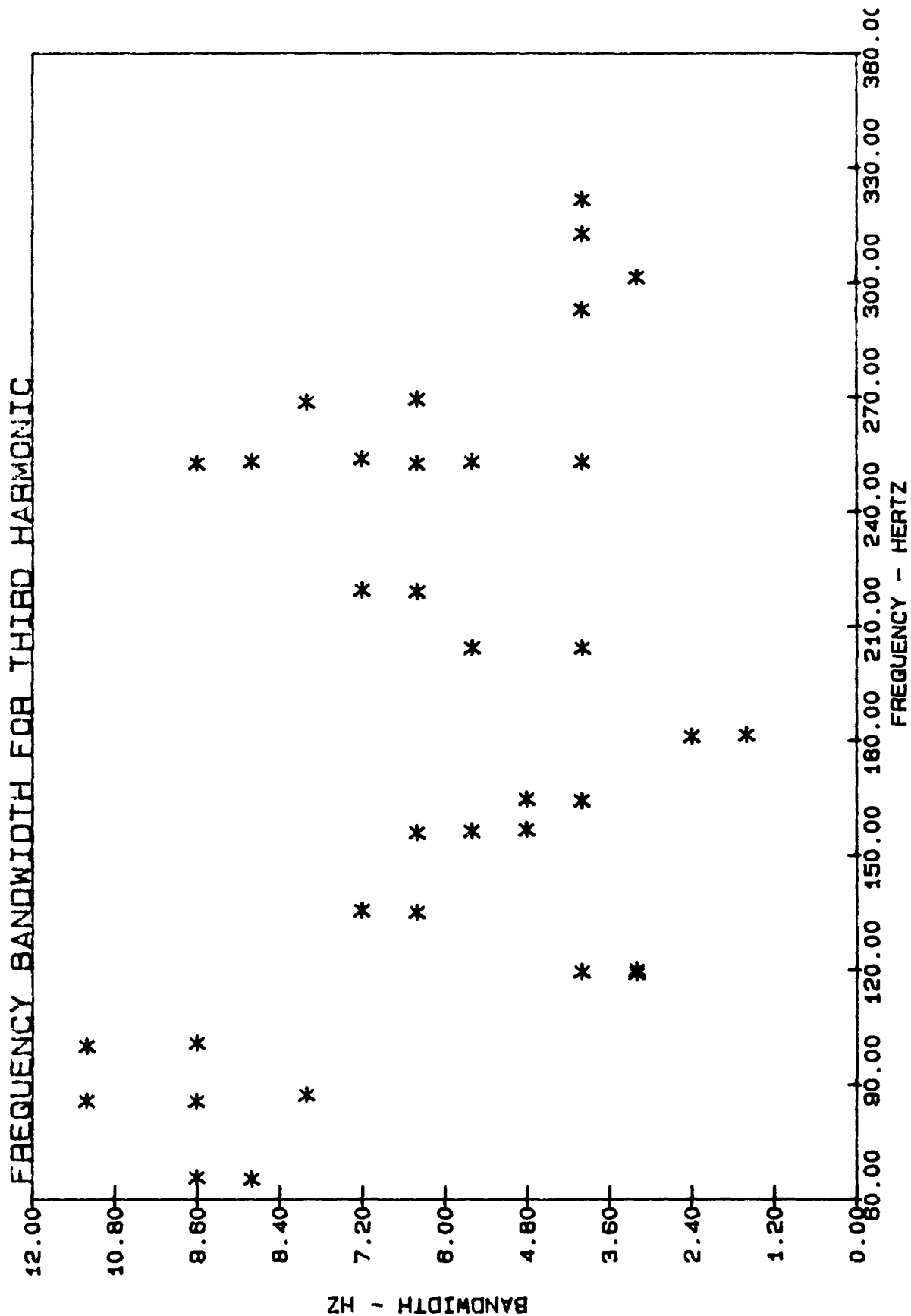Figure 9. Frequency Bandwidth Data
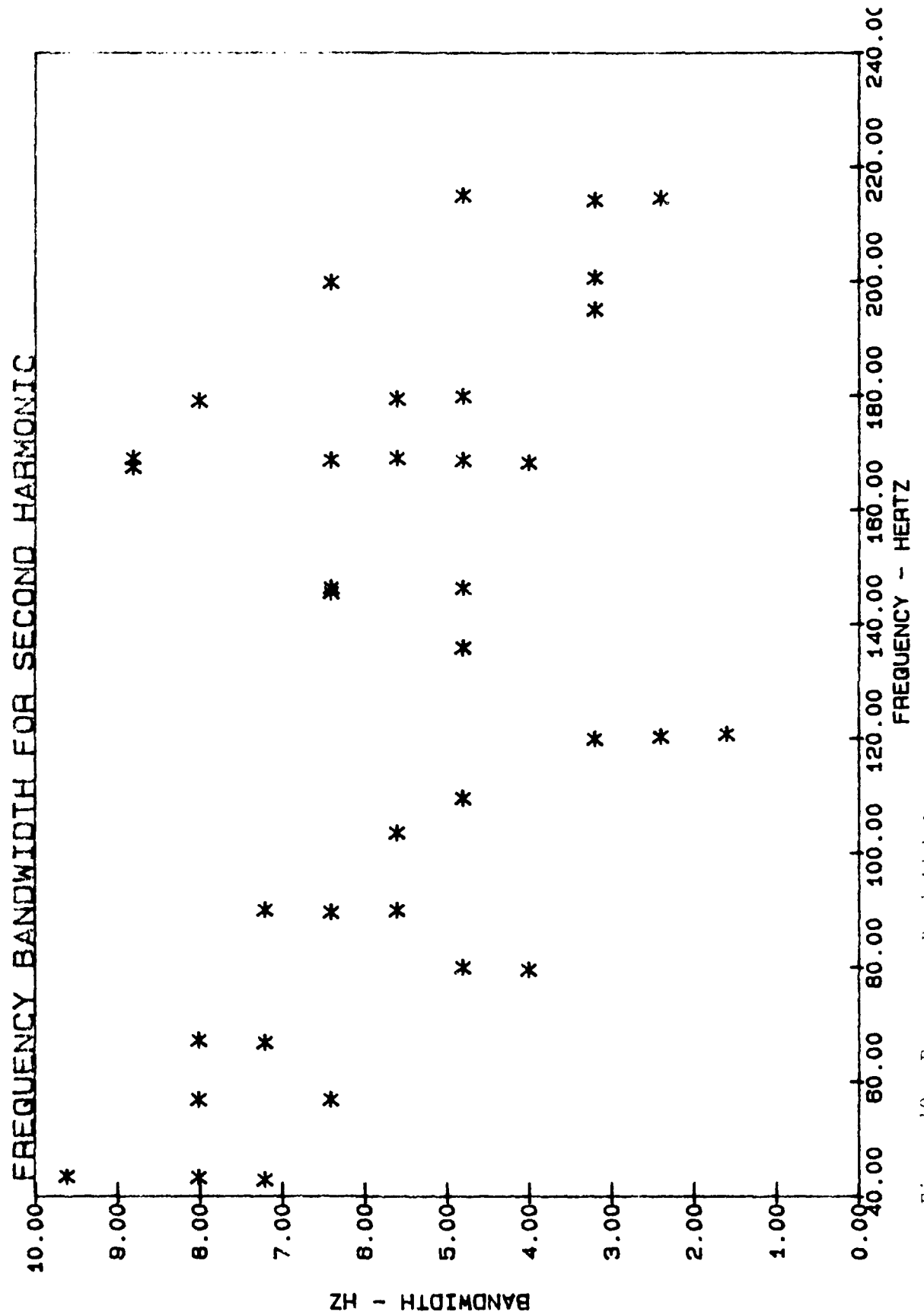
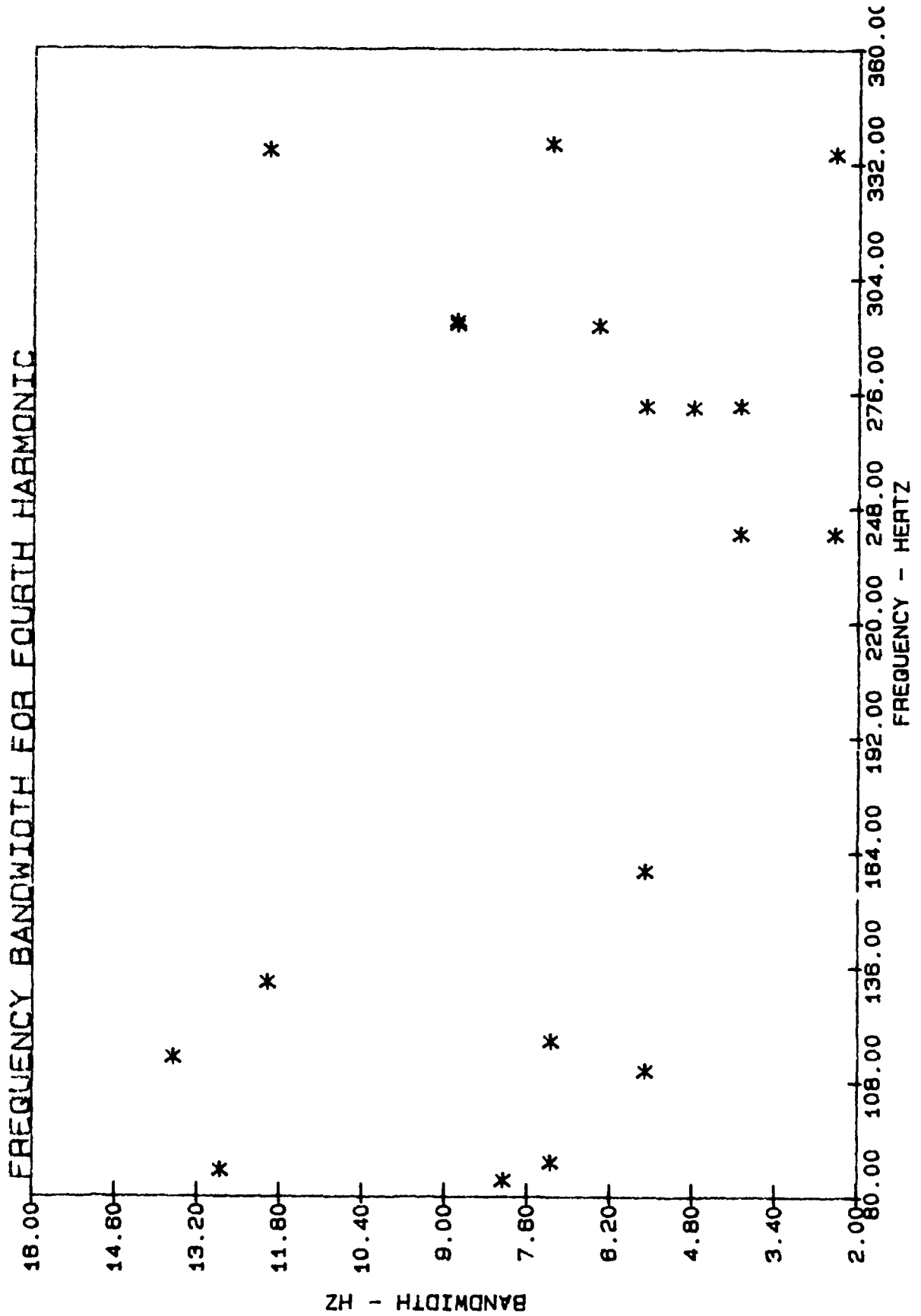Figure 10. Frequency Bandwidth Data

Figure 11. Frequency Bandwidth Data

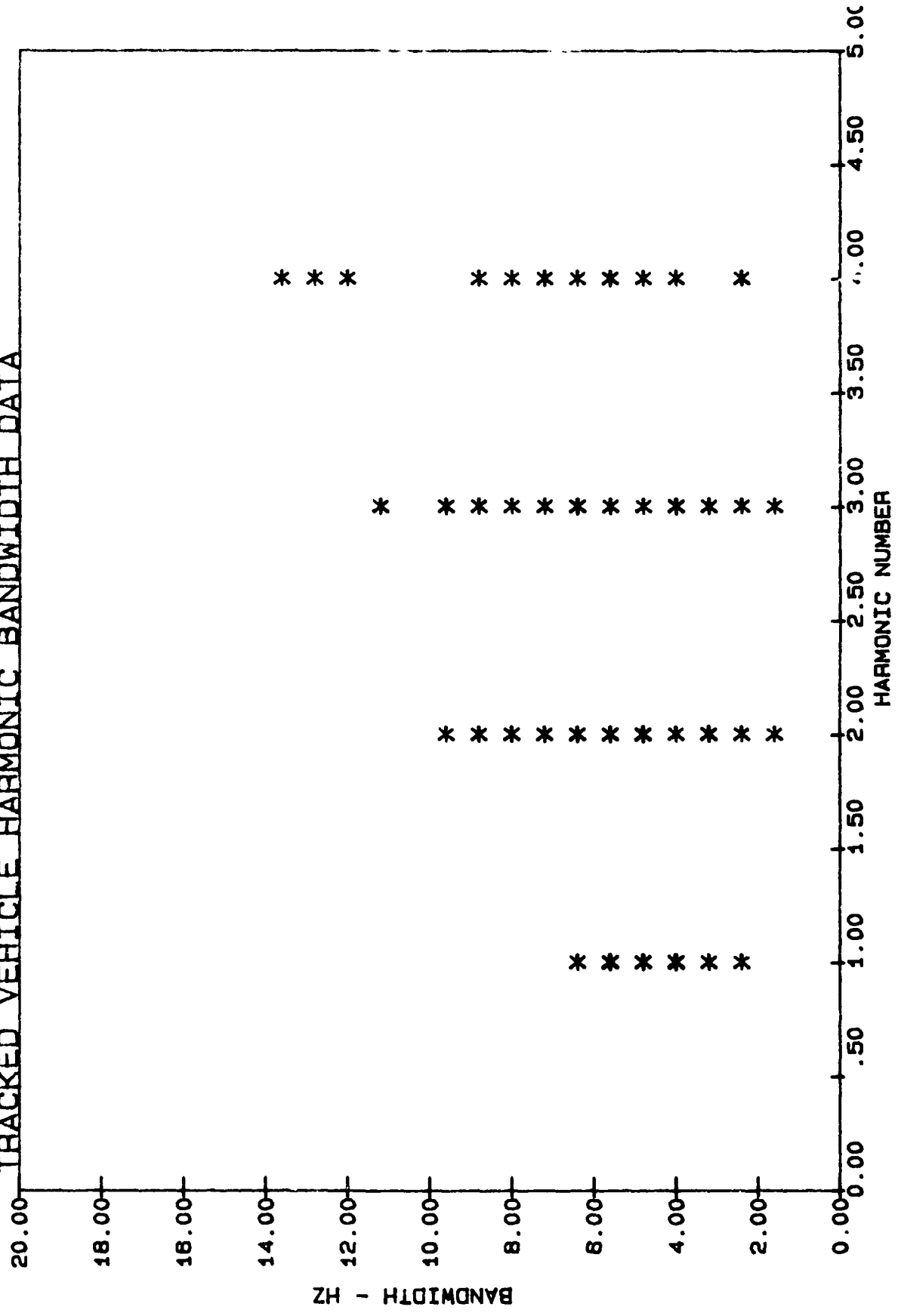Figure 12. Frequency Bandwidth Data
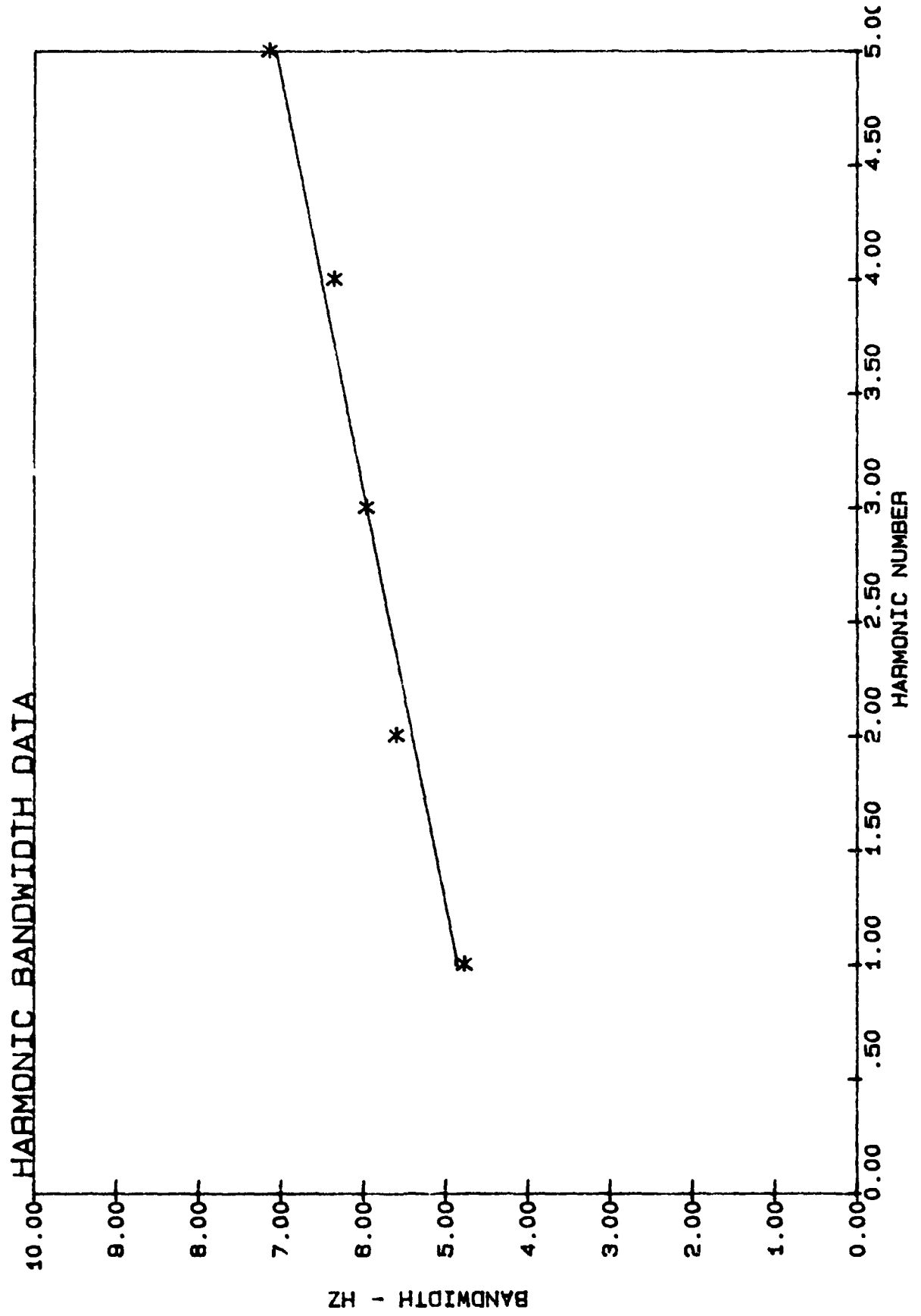
Figure 13. Harmonic Bandwidth Data
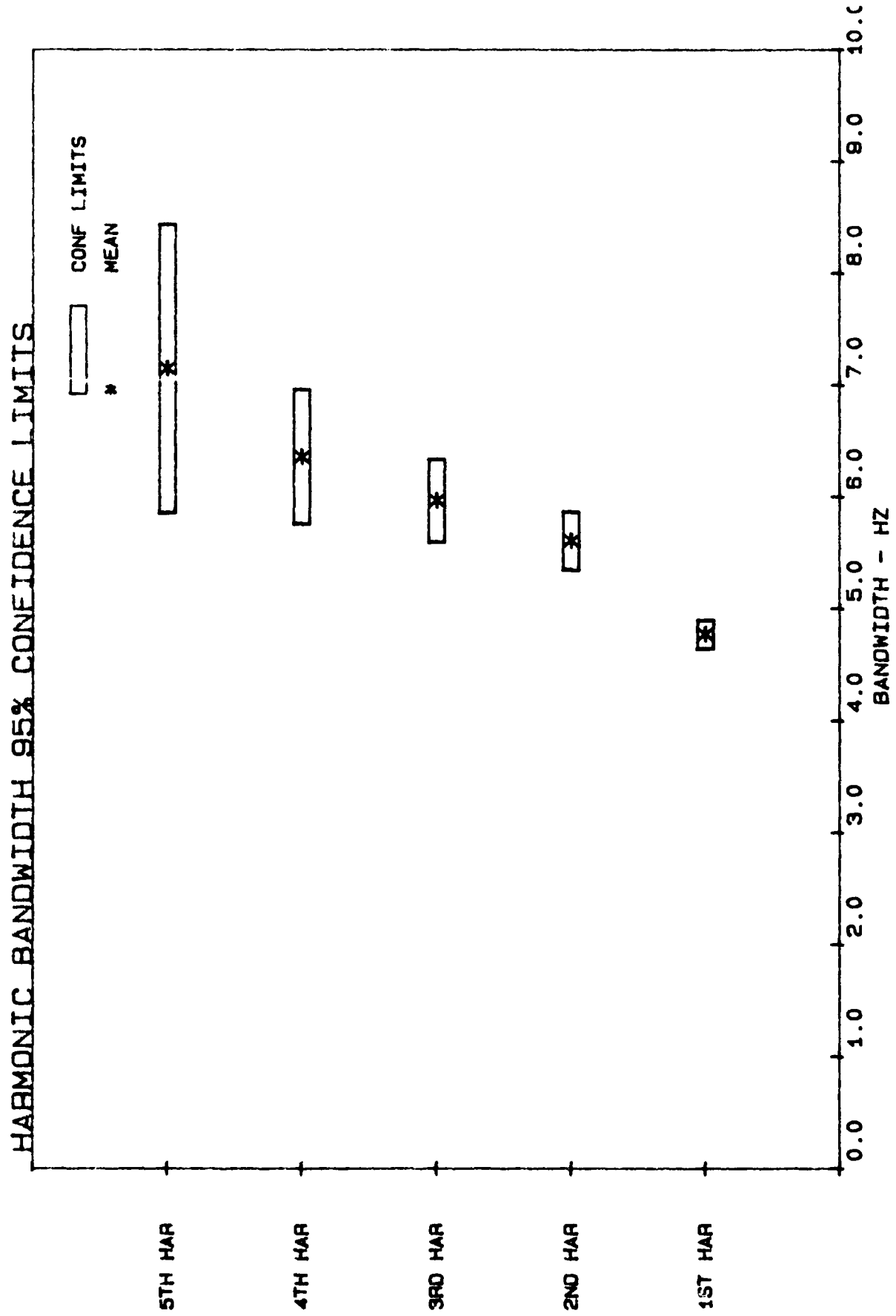
Figure 14. Harmonic Bandwidth Data

314

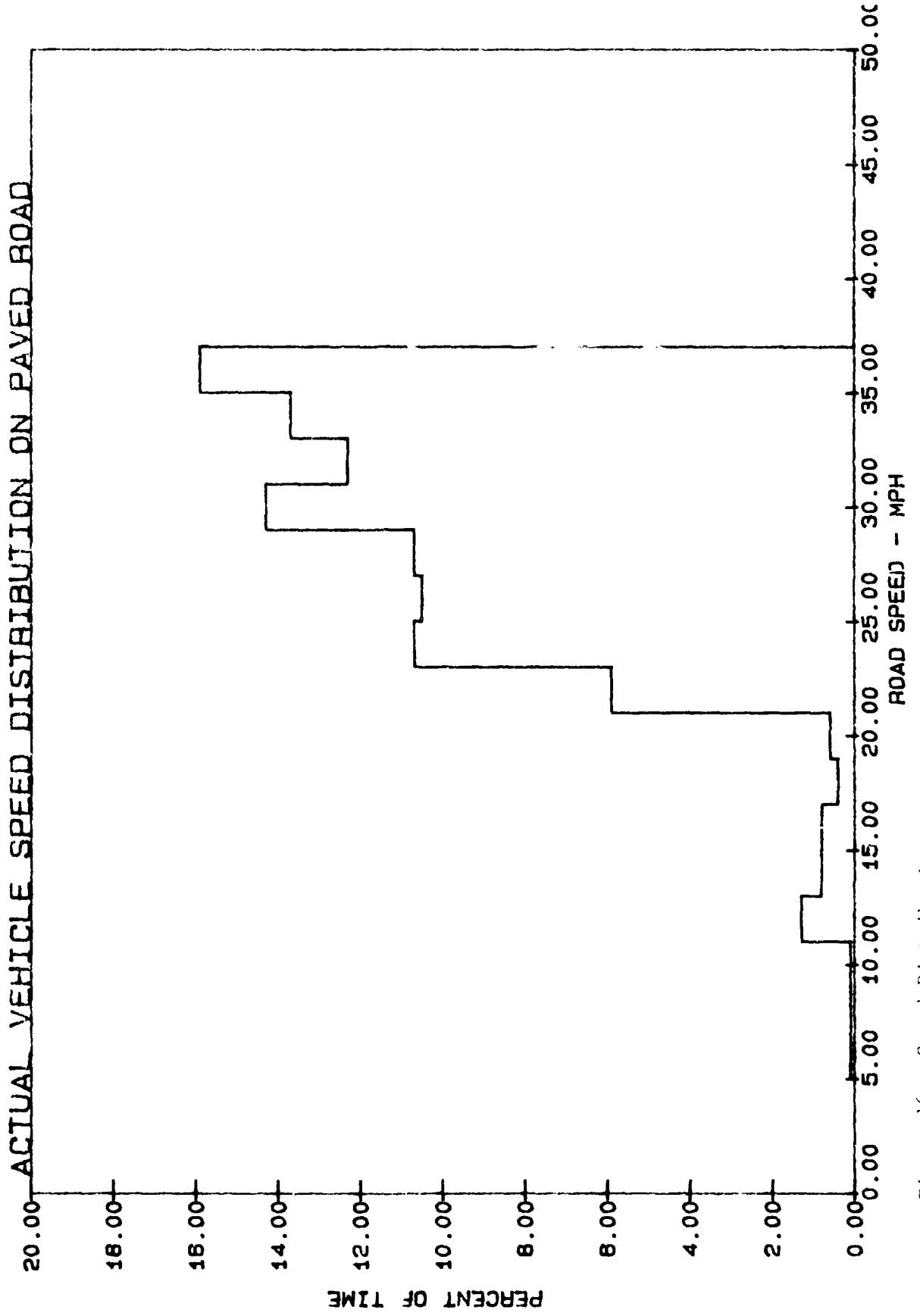Figure 15. Harmonic Bandwidth Confidence Limits
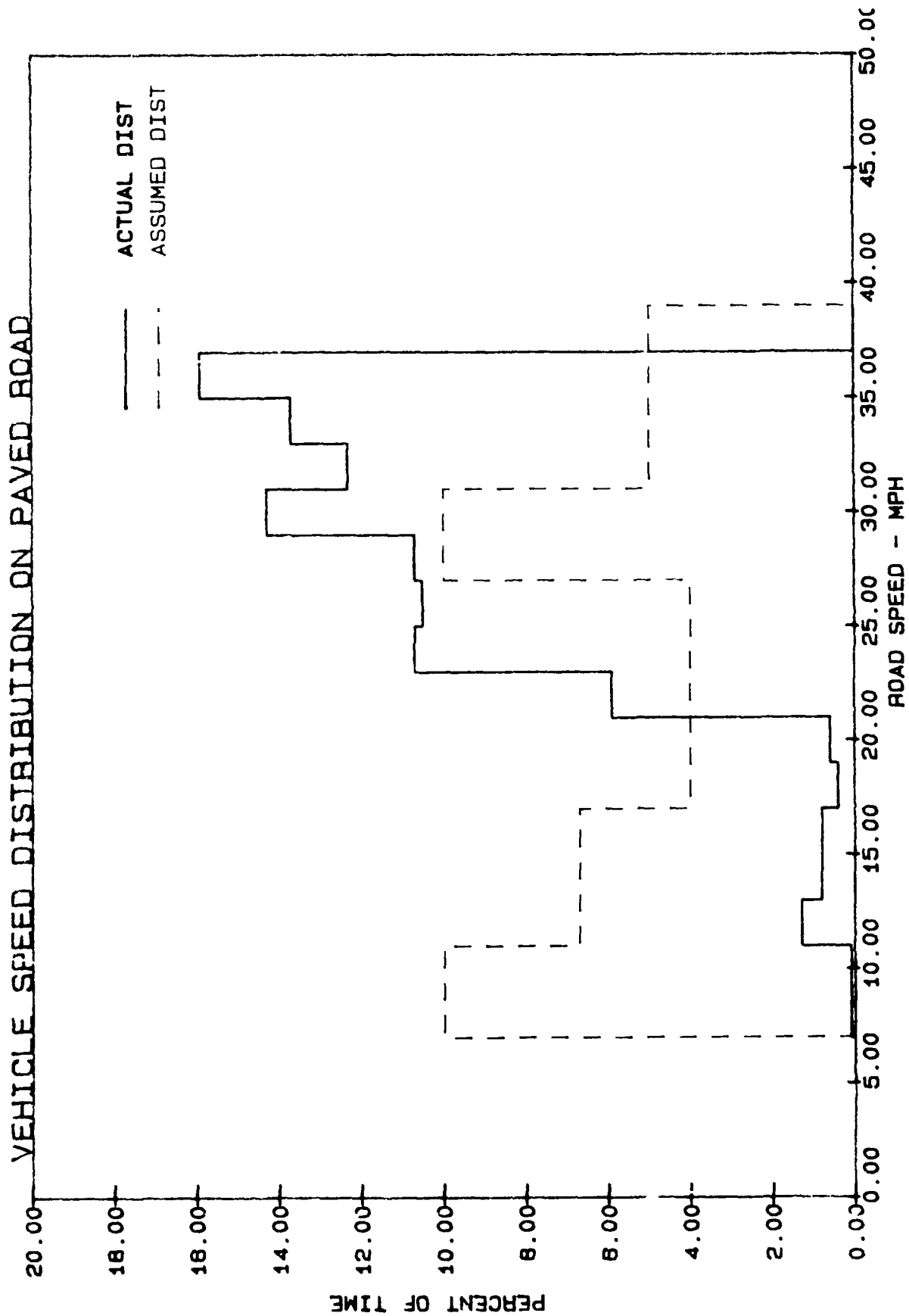
Figure 16. Speed Distribution

Figure 17. Speed Distribution

STRUCTURAL RESPONSE AND COSMETIC CRACKING IN
RESIDENCES FROM SURFACE MINE BLASTING

David E. Siskind and Mark S. Stagg
Twin Cities Research Center
U.S. Bureau of Mines
5629 Minnehaha Avenue South
Minneapolis, MN 55417

The Bureau of Mines studied the problems of blasting-
vibration-induced structural response and cracking of
low-rise residential structures in a series of research
projects between 1976 and 1983. This paper summarizes the
published Bureau findings and presents them from the point
of view of the cracking and failure of the construction
materials used for homes.

The damage data suggest that, for plaster and wallboard
attached to the superstructure, an increase in the rate of
cracking is not likely to result from blasts generating
vibrations of less than 0.5 in/s. Data on cracks in
masonry walls suggest that blast-induced vibration levels of
up to 3.0 in/s may be a threshold for local block-length
cracks. However, additional data are needed to quantify
vibration level effects necessary to generate stair-stepped
cracks in masonry walls, which indicate loss of shear load
capacity.

INTRODUCTION

Ground vibrations from blasting have been a continual problem for the mining
industry, the public living near the mining operations, and the regulatory agencies
responsible for setting environmental standards. Since 1974, when the Bureau of
Mines began to reanalyze the blast damage problem, several field and laboratory
studies have been conducted; the results of the most recent were published in RI
8969, in 1985 [1]. The studies examined blast vibrations with respect to
generation, propagation, structural response, cracking potential, instrumentation,
and fatigue [2-4]. A similar series of studies was conducted for airblast [5-6].

This paper summarizes the material on cracking of construction materials used
in low-rise residential structures; the data excerpted from two comprehensive Bureau
vibration studies, RI 8507 on dynamic response and damage and RI 8896 on fatigue and
long-term influences [3-4]. Specifically, the paper discusses the cracking of
plaster, wallboard, and masonry from blasting and other influences, giving an
overall perspective to the blast vibration impacts as part of the total lifetime
dynamic load for such materials.

CRACKING AND BUILDING PRACTICES

Current residential construction practices address basic human safety and not specifically the occurrence of non-structural minor or cosmetic cracks. Many of these practices were derived from allowable deflection criteria, in which material cracking potential is considered [7-9]. However, cosmetic cracks do develop, and in 1948, Whittmore [10] discussed the lack of guidelines for vibrations of floors and pointed out that "deflection and vibration can be decreased, but only at an increase in price."

LONG-TERM CRACK RATES IN RESIDENTIAL STRUCTURES

Previous Studies

Structures crack naturally over time. Holmberg [11] analyzed blasting inspection reports to estimate a crack rate for apartment buildings in Sweden. Two apartment buildings were inspected for cracks three times between 1968 and 1980. The number of observed cracks is plotted as a function of time in Figure 1. An average of 12 to 13 new cracks per year occurred for these particular structures. Holmberg did not report any specifics on the building construction, although concrete is a reasonable assumption.
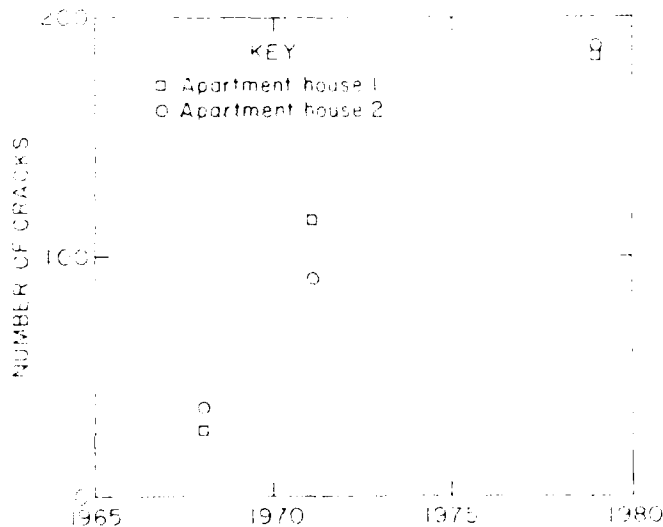

FIGURE 1 Building age versus crack occurrences, after Holmberg (11)

The crack rate depends upon the type of structure. Rates for 11 wood-frame houses that were subjected to 26 weeks of sonic booms and 11 weeks when there were no booms, as reported by Andrews [12], are listed in Table 1. Crack rates at Home 1-1, which were studied during both periods, were generally lower during the no-boom period, which is similar to Bureau findings discussed later. The investigators also found evidence of the possibility that relative humidity and temperature acting together have an effect on the occurrence of cracks.

The rates of 1.3 to 25 cracks per week during the no-boom period are quite comparable to the rate observed by Wall [14] in a study of 44 single-story

concrete block houses over a 26-week period; he reported a crack rate of 2.5 cracks per day for the 43 houses (<1 crack per week per house).

Table 1 Crack rates for houses subjected to sonic booms, after Andrews [12]

House	Number of stories	Area, ft^2	Foundation	Age, yr	Finish		Occu-pied	Number of cracks per week	
					Interior	Exterior		Boom period	Nonboom period
1...	1	1,560	Concrete slab.....	5	Wallboard.	Brick...	Yes..	3.7	1.9
2...	2	1,750	...do.....	New	...do.....	...do....	No....	8.2	3.3
3...	1	1,470	...do.....	8	...do.....	...do....	No....	8.8	1.5
4...	1	1,160	Concrete stem wall	18	...do.....	...do....	No....	6.1	1.8
5...	2	2,870	Masonry stem wall	>50	Plaster and lath	Asbestos siding.	No...	NM	23
6...	1	1,100	Concrete stem wall	25	...do.....	Stone...	Yes..	NM	2.6
7...	1	1,090	...do.....	30	Lath and wallboard	Wood lap	Yes..	NM	1.4
8...	1	1,280	...do.....	30	Plaster and lath.	Brick	Yes..	NM	3.3
9...	2	2,000	Masonry stem wall	40	Paper on plaster and lath	Wood lap	Yes..	NM	3.0
10...	2	2,370	Concrete stem wall	35	Plaster and lath	...do...	Yes..	NM	14
11...	1	1,330	Concrete slab.....	8	Wallboard.	Brick...	Yes..	NM	2.2

NM Not measured.

The large variation in the crack rates reported in the separate studies by Holmberg, Andrews, and Wall is indicative of the wide variation of susceptibility of houses to cracking. The rates ranged from near zero to 23 cracks per week. (The yearly rate reported by Holmberg indicates a cracks-per-week rate of less than none.) None of the investigators reported rates of zero. The large differences in the rates reported are partially a result of the fficulty of defining "cracks." For example, in Wall's report, shrinkage cracks were ignored, and only new cracks in the moderate (easily distinguishable) range were reported.

These data point out that when months pass between preblast and postblast inspections, any postblast inspection is likely to find some new cracks that are the result of natural aging.

Bureau Long-Term Fatigue Study

Blast effects on long-term crack rates were monitored over a 2-year period at a Bureau of Mines test house [4]. Bureau researchers developed two types ... data in terms of the expected damage mechanisms: [1] fatigue damage from accumulated exposure, assessed by periodic inspections, and [2] triggering effects of discrete blast events assessed by inspections immediately before and after blasts, where the

strains from blasting are added to already existing environmental strains. Researchers found that long-term repetition of the low-level blasts (peak particle velocity <0.5 in/s) produced no significant effect; however, blasts with velocities greater than about 1.0 in/s were associated with higher cracking rates, as shown in Table 2.

Table 2 Crack versus vibration [4]

Blast level, in/s	Cracks per week	
	Without corner	Total
<0.5...............	0.28	0.84
>0.5, <1.0........	.33	.89
>1.0...............	1.0	1.8

The crack rate, or number of new cracks per inspection, along with the number of blasts that produced ground vibrations greater than 0.50 in/s and greater than 1.0 in/s, are shown in Figure 2. Sixty shots had levels between 0.5 and 1.0 in/s, while 48 shots had levels above 1 in/s. Some of the crack rates shown in Figure 2 include small hairline corner cracks, and some do not. The majority of corner cracks occurred in the first 8 months. Cracks were found in nearly every corner in the house, but were ignored until inspection period 15. Then it was decided to observe them rigorously despite their miniscule size. Corner cracks are an inevitable consequence of the curing of the tape compound and are enhanced by dynamic strains induced by human activity. The data that exclude corner cracks are more realistic indications of blasting influences for homes other than new construction, i.e., within 6 months.
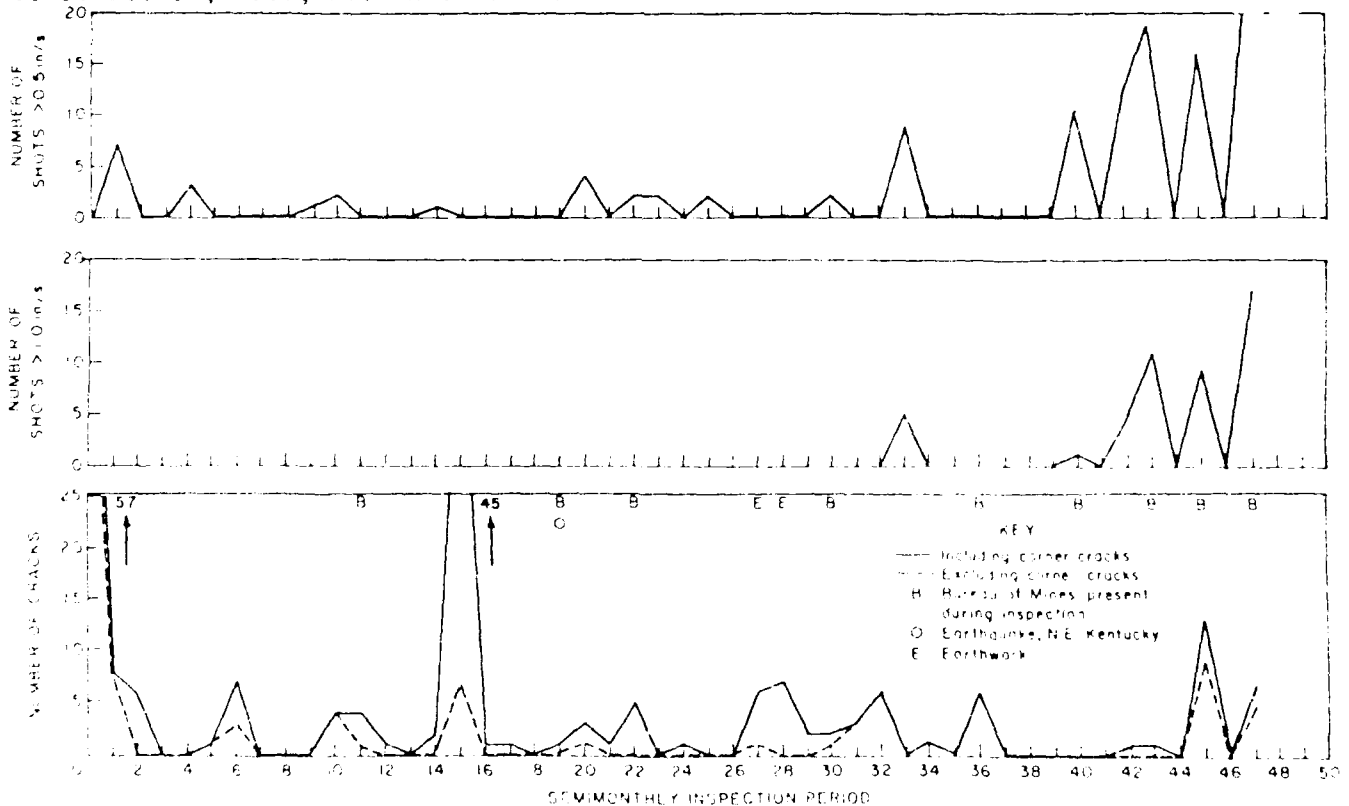

FIGURE 2   Number of cracks and blasts >0.50 in/s and >1.0 in/s versus inspection period

Differences were found in the number of cracks observed by the two teams of inspectors, Vibration Measurement Engineers (VME) and Bureau personnel, during

periods 1, 15, and 36. The most pronounced difference was for period 15. The decision to include small corner cracks was made after VME had completed its inspection for that period but before the Bureau had completed its inspection for period 15. Other than for that period, differences in the number of cracks observed were an inevitable consequence of the difficulty of observing hairline (0.01- to 0.1-mm) cracks. Periods 1, 15, and 36 were omitted in calculations of crack rates. However, periods in which there were unusual external influences, including an earthquake and soil removal by a scraper 40 feet from the test house, were included. The self-triggering seismograph recorded a 0.06-in/s vibration for the scraper activity but did not trigger during the earthquake.

The increase in crack rate with ground vibration level indicates that the blasting produced a triggering strain, at about 1.0 in/s/. The low crack formation rates reported are reasonable since the test house was new, showed no differential settlement, and was not regularly occupied. These conditions resulted in low rates of natural crack formation, which allowed a few blast-related cracks to significantly affect crack formation rates.

CONSTRUCTION MATERIAL CHARACTERISTICS AND CRACKING

Cosmetic cracks result when a dynamic-induced strain (blast vibration or other transient vibration) added to a preexisting strain (static load) exceeds the strain level necessary to initiate a crack. Differential foundation settlement, excessive structural loads, and material shinkage all induce strains that can produce random and/or patterned cracking. For analyzing blasting effects, these strain-inducing forces are considered static and the resulting strains are called "prestrains."

Stress-strain curves are used to describe response of materials under load up to failure (cracking). Most materials, including masonry, plaster and wallboard, respond linearly up to the initial yield point. A linear response means that deformation (strain) is directly proportional to load (stress). Beyond initial yield, plastic deformation or creep occurs until ultimate failure (Fig. 3). The yield point damage is often not visually noticeable because of limited naked-eye resolution of 0.01 to 0.1 mm, particularly in textured surfaces such as masonry.
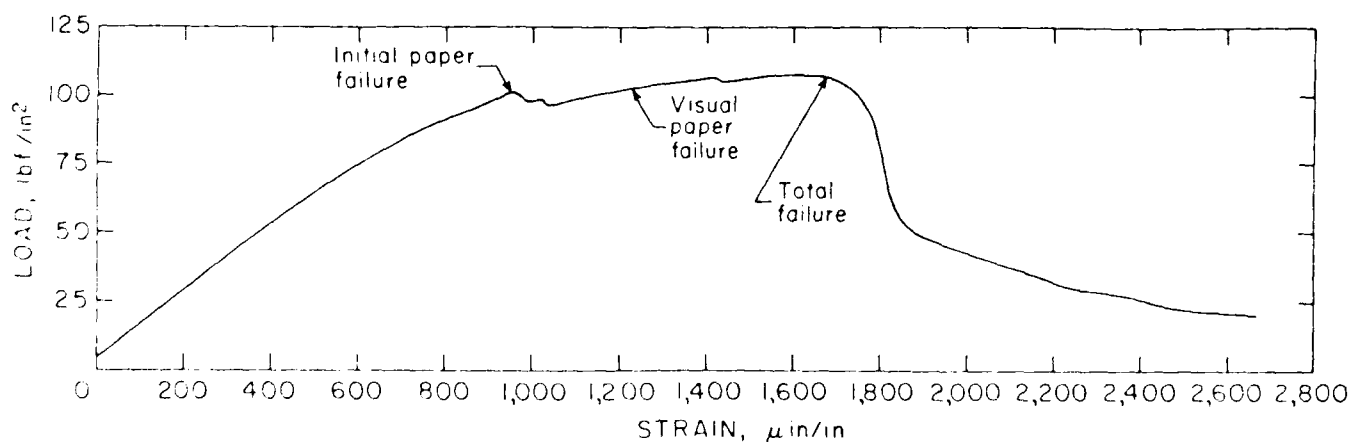

FIGURE 3   Tensile stress-strain curve for 1/2-in-thick wallboard

Plaster

Plaster was not studied extensively because of its widespread replacement by wallboard for modern construction. However, many of the older homes analyzed for RI 8507 [3] were plastered and provided some insight into cracking potential. Also, wallboard is a gypsum plaster faced with paper on both sides. Tests run on stripped wallboard are suggestive of plaster failure [3]. Of all construction materials, plaster is considered most susceptible to damage and exhibits fatigue at stress levels less than 50 percent of the static failure level [14].

Wallboard

The Bureau studied wallboard cracking both in the laboratory and as part of the fatigue study of the test house [4]. For wallboard in the test house, researchers found threshold cracks occurring primarily in the wall corners and around nail heads. They found for wallboard--

1. The gypsum core failed at strains of about 350 μin/in in tension and at about 1,000 μin/in in bending, based on the nonlinear reponse points.
2. For visible cracking, paper failure is the controlling factor. Its nonlinear response point occurred at strains of 1,000 to 1,200 μin/in (Fig. 3). However, visual observation of buckling or cracking was not possible until a slightly higher strain level was reached.
3. Strain rate seemed to affect ultimate or total failure, but the paper yield point was relatively constant. This allows comparison of various loading factors (e.g., blasting versus other activities and environmental factors).
4. Once the wallboard cracked, cyclic opening and closing of the crack of up to 0.1 mm was observed. These movements were unaffected by blasting activities.
5. Data on cyclic loading behavior of wallboard are limited, but results of tests on wood products indicated that fatigue effects can occur at stress (or strain) levels equivalent to 50 percent of static failure conditions, but over 100,000 cycles are required.

Masonry

Bureau researchers also studied the cracking of concrete block walls both at the test structure with its full-size basement and through a series of tests in cooperation with the National Bureau of Standards (NBS) in Gaithersburg, MD [4, 15]. Generally, two types of cracks, local and steplike were identified. Local block-length cracks less than 0.2 mm wide were difficult to discern from existing mortar joint separations and are usually not observed by homeowners. Steplike masonry cracks transverse the wall along the mortar joint interface and, over time, open beyond 0.2 mm in width.

Previous work by Cranston [16], Green [17], and Wroth [18] noted that all brick walls have small, 0.1 mm cracks upon completion. Green stated that 0.1-mm cracks are difficult to see and "therefore, do not cause concern." As reported by Woodward [15], local cracks opened and closed throughout the cyclic and monotonic in-plane shear tests of 5- by 5-feet concrete block walls. It was not until steplike cracks propagated the length of the wall specimens that shear load failure occurred.

Although findings by Bureau researchers on masonry failure provide some insight, further work at the NBS on torsion and out-of-plane loading is recommended. Key findings for tests with masonry are given below.

1. Observations of tensile cracks at strain-monitored sites showed that such cracks are first detected visually at strain levels well above the first nonlinear response point because of naked-eye limitations (~0.01 to 0.1 mm).

2. Strains read at the threshold of visual cracking using different gauge lengths gave different overall strain readings as illustrated below.

Based on the equation $\varepsilon = \frac{\Delta l}{l}$

$$\frac{0.01 \text{ mm}}{13 \text{ mm}} = 770 \quad \mu in/in.$$

but $\frac{0.01 \text{ mm}}{150 \text{ mm}} = 67.0 \quad \mu in/in.$

where 13 and 150 mm are gauge lengths, and the visible crack width is 0.01 mm. Because strain gauge readings can be misleading, crack growth is best described in terms of displacement.

3. Local-site strains across the wall vary considerably from global strains. For in-plane shear failure, global strain is measured or calculated across the wall diagonally.

4. Local cracks can occur at low global strains, and global assessment of these cracks is not recommended. But, for the assessment of steplike cracks that propagate across the entire wall, the global strain approach appears reasonable.

5. Global failure strain levels for steplike cracks are not available. Limited testing to date has shown that in-plane shear failure may not occur in homes because of the relatively light vertical load available to prevent rotation from the shear couple and at least a partial conversion of the shear to tension.

6. For cosmetic cracks that do not affect load-carrying capacity, a crack-width criterion has been proposed [17]. However, the acceptability of crack widths varies with material. For concrete 0.25 mm is the limit of acceptability [19], while 1 mm is the limit of acceptability for brickwork [18].

FACTORS CAUSING STRUCTURE RESPONSE, STRAIN, AND CRACKING

Bureau researchers studied structure responses and cracking associated with blasting vibrations involving a relatively few measurements at each of a wide variety of residential-type structures [3]. Following this, fatigue from repeated loading of one house over a long period of time was studied [4]. For both efforts, measurements were made of wall, floor, and racking responses, and observations of damage were made that could be correlated to specific vibration events. A significant part of the work was done near large surface coal mines with thick soil overburdens and large-diameter blastholes, cases which had not been studied previously. In all, about 900 shots produced useful data on structural responses and damage potential from blast vibrations.

Environmental Strains

Houses are subject to a variety of dynamic loads, in addition to static or slightly variable loads from settlement, soil changes, and aging. Among the dynamic forces considered significant are daily and annual temperature and humidity cycles, wind, and human household activity. Bureau researchers monitored the weather and inside environment during the 2-year test period and, in more detail, for short periods. For one test, they took readings at 3-hour increments for a

2-day period, simultaneously measuring strain at site K_2, over a major doorway (Fig. 4). Because there were at least four factors influencing the strain, researchers used multiple linear regression analyses. Maximum strains from daily environmental changes were found to be a significant fraction of those needed for wallboard core failure or paper cracking. The maximum strain observed at K_2 was +385 μin/in or 39 percent of failure. The total maximum strain calculated from the correlation equation, assuming the worst case for each of the factors, are +675 to -817 μin/in or up to 82 percent of failure. "Failure" is defined as the strain level of 1,000 μin/in found to produce wallboard cracking as previously discussed (Fig. 3).
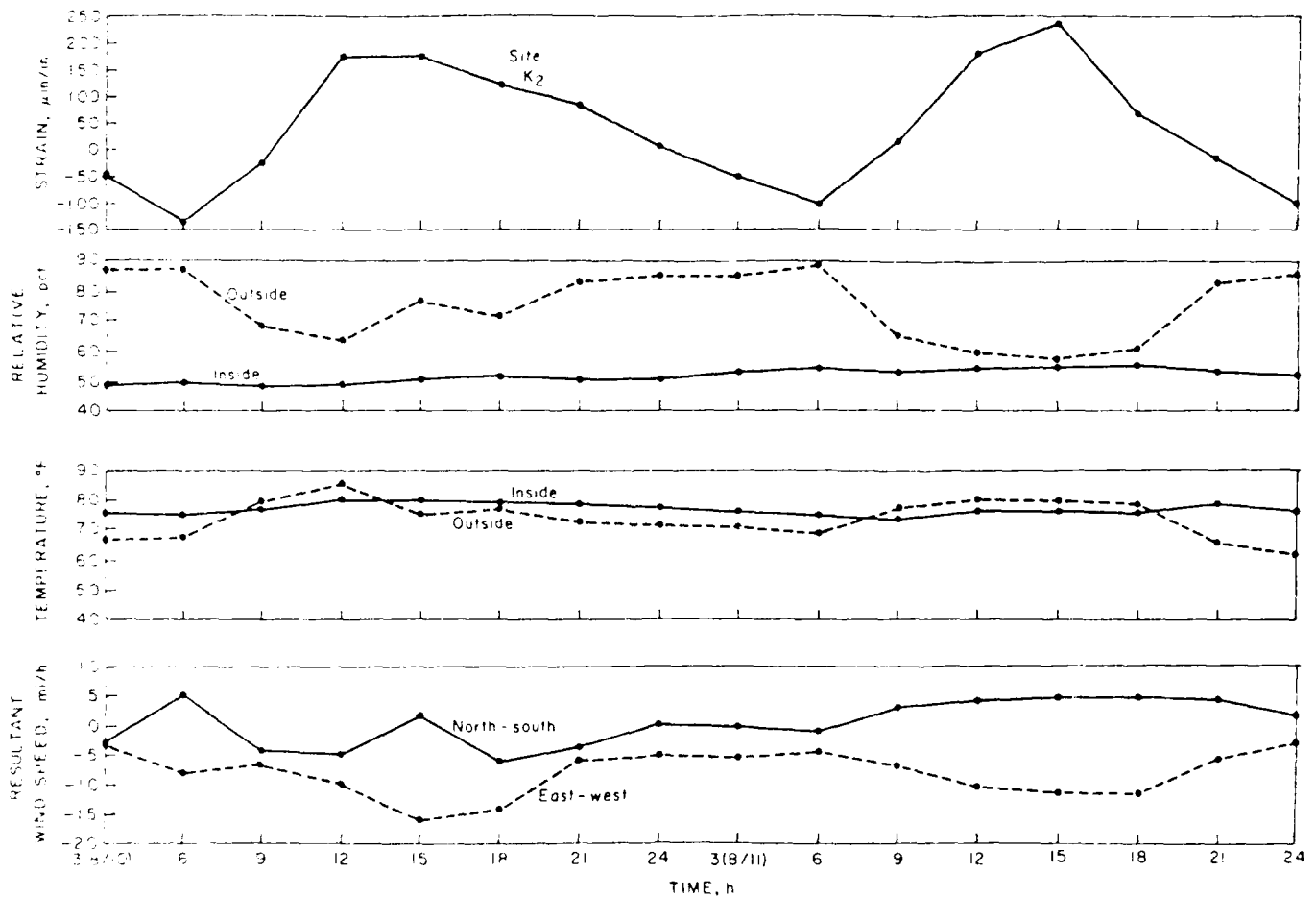

FIGURE 4   Wallboard joint strain and environmental factors versus time, site K_2 over a doorway

Human-Activity-Induced Strains

Activities within the home can produce significant vibration and strain in local structural members [3-4]. In severe cases, such as a hard door slam, the entire superstructure resonates producing strains in every wall, corner, and floor. By contrast, nail pounding produces a strong response only on the wall affected. Strains range up to about 100 μin/in, with typical values being 50 μin/in in critical areas over windows and doorways.

Blasting-Induced Strains and Comparisons

Blasting responses and strains in residential structures were reported in detail in Bureau's RI 8507 and 8896 [3-4]. An example of blast-vibration-induced strains from the fatigue study reported in RI 8896 is shown in Figure 5. Structure vibration responses can be transitional, torsional, vertical uplift, or at times a combination of all three. In blasting, both the superstructure and foundation are typically affected. Non-blasting causes of vibration and strain act only on the superstructure, except for slowly acting soil changes and settlement. Because initial damage involves cosmetic cracks on superstructure interior walls, it is appropriate to compare superstructure stains from blasting and other sources (Table 3). These comparisons are only approximate. A given vibration level does not always produce the same strain even at a single monitoring point, much less throughout the structure, probably because of different response modes for different blast angles, and wave characteristics.

TABLE 3   Comparison of strain levels induced by daily environmental changes, household activities and blasting [4]

Loading phenomena	Site	Induced strain, $\mu in/in$	Corresponding blast vibration level[1], in/s
Daily environmental changes.	Bedroom midwall..	149	1.2
Do....................	Over doorway.....	385	3.0
Household activities:			
Walking............	Over a window....	9	<0.03
Heel drop.........	.......do........	20	.03
Jumping............	.......do........	37	.28
Door slam.........	Over doorway.....	49	.50
Pounding a nail...	Over a window....	89	.88

[1]Vibration velocities are based on highest observation strains for a given velocity. Use of mean or "typical" values from regression analysis gives velocities which are considerably higher. For example, the door slam produces a level of strain typically observed at 1.44 in/s ground-measured particle velocity. See Figure 5.

OBSERVED CRACKING FROM BLASTING

As discussed earlier, environmental factors induce most of the strain necessary for the generation of cracks triggered by household activities or blasting. Crack rates did not increase until blast vibration levels rose above normal threshold levels of 1.0 in/s. It is not surprising then that both wallboard and plaster cracked at low vibration levels, even though failure strain levels for wallboard are about three times those of plaster.

In reviewing both past and newly available data on dynamic vibration response, researchers noticed irregular and sometimes high-amplitude responses when the vibration frequencies matched structure resonances (Fig. 6). A similar effect, noticed for the cracking data, was one of the most significant findings in RI 8507 [3]. Consequently, coal mine and quarry production blasts that are typically 10-25 Hz produce a greater damage risk than smaller scale blasts often used for construction, excavation, and secondary blasting.
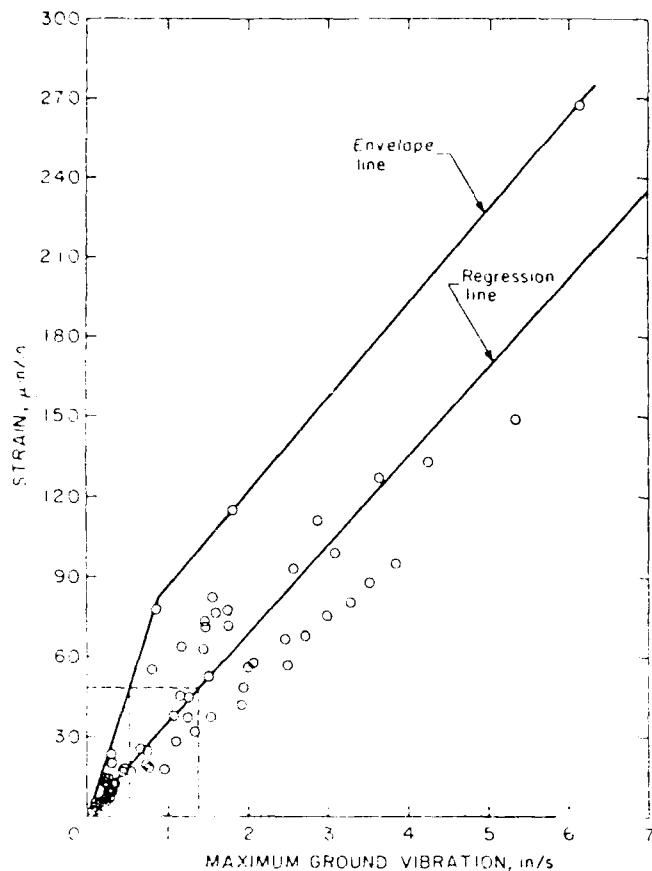
FIGURE 5   Plaster and wallboard strain versus maximum
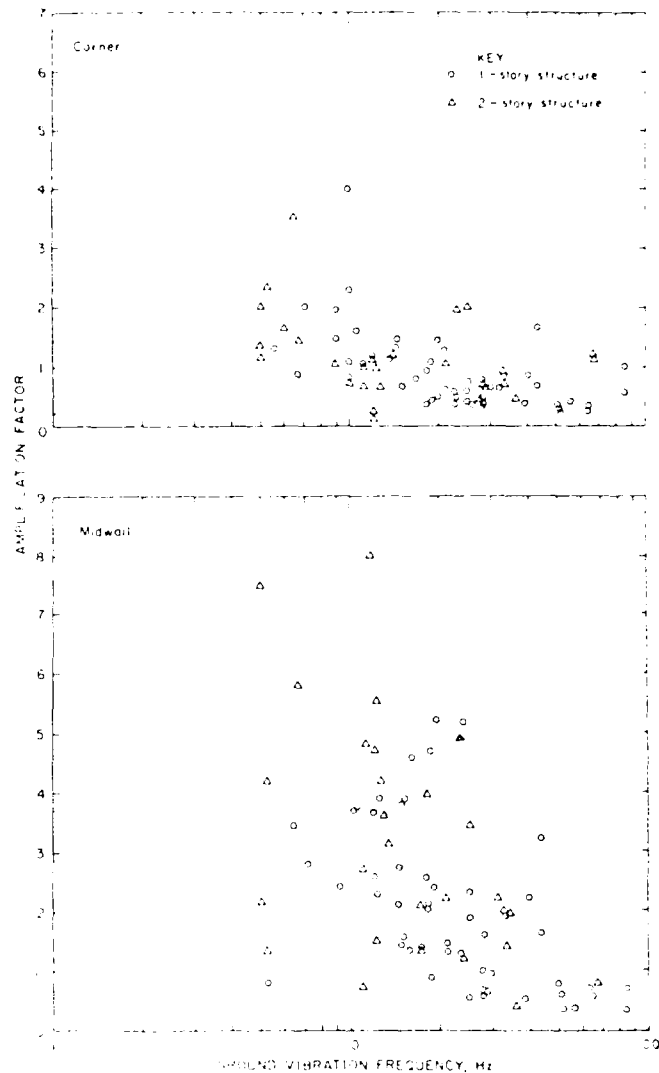ground vibration at site S_1 over a doorway

FIGURE 6   Corner and midwall amplification factors (3)

In a departure from earlier analysis and reports, the following review
quantifies damage separately for each of the three major construction materials:
plaster, wallboard, and concrete block. The reader is directed to the original
reports for procedure and analysis details [3-4, 15].

Plaster Cracks

Threshold and minor cracking data are summarized in Figure 7 for pre-1975
studies and in Figure 8 for recent Bureau research. All these data have been
previously published in RI 8507 [3] and RI 8896 [4]. However, in a departure from
the earlier reports, these figures identify each data point as to source, degree of
cracking damage, and type of material involved.

Langefors [23] presents the only significant amount of high-frequency data.
These data suggest that vibration levels as high as 4 in/s may be safe for
frequencies above about 70 Hz. In the descriptions of damage, in RI 8507's table
10 [3], Langefors did not separate the cracking and fall-of-plaster cases.
Dvorak's study produced observations of cracking at some of the lowest peak
particle velocities, and questions have been raised about data reliability.
However, Dvorak used the same seismic monitoring system as Langefors. Dvorak's

brick structures were likely different from Langefors' unspecified structures (probably concrete), and the vastly different measured frequencies are indicative of a soil versus rock foundation. The lowest vibration level at which cracking was observed was 0.5 in/s with Dvorak's data and about 0.7 in/s without.

Wallboard Cracks

The state of cracking of wallboard is hard to identify because the interior plaster core will crack long before any surface effect is visible. Visible cracking of paper covering occurs at strains about three times those required for core failure. Wallboard cracks are also influenced by how well panels are attached to the superstructure frame. Not being structural elements, they are not always put under in-plane stress when the frame flexes. The core around the nailhead is, at best, partially crushed upon attachment to the studs, and when the studs are uneven major core cracking can occur. The response from superstructure vibration is additional wallboard core crushing around the nailheads, resulting in a "loose" attachment.

At the test house, it was observed that cracks developed primarily at the plastered joints, at wall corners, and in plaster covering coating over nailheads (Table 4). The high rate of naturally occurring cracks was caused primarily from curing of the tape compound. As the tests on the structure continued, a decrease of natural frequency of about 20 percent, e.g., 7.5 to 6 Hz at one location, indicated a loss of rigidity and general flexture-induced loosening [4].

Table 4 Wallboard cracks observed in fatigue test house [4]

Material	Initial cracks, before testing	Cracks developed during testing		Blasting levels, in/s	Mechanical shaker tests[1]	
		Naturally occurring	From blasting		Number of cracks	Number of cycles at cracking
Taped corners	39	35	5	0.88-3.5	ND[2]	NAp
Nail heads...	5	4	3	1.8 -2.2	>3	56,000, 339,500
Taped joints.	2	6	ND	NAp	1	56,000
Wallboard....	3	6	ND	NAp	1	361,500

NAp Not applicable.   ND None detected.
[1]Shakers run at resonant frequency at equivalent vibration levels of 0.3 to 1.0 in/s.
[2]Corners almost completely cracked before shaker study.

The lowest levels of observed blast vibration-induced cracking occurred at a wall corner as crack extensions and when a new crack was observed beneath a window, at amplitudes of 0.79-1.1 in/s (Fig. 8).

Fatigue-induced cracks were observed at 0.3 to 1.0 in/s. However, this cracking required a large number of vibration cycles, such as over 50,000 at a 0.5-in/s equivalent ground vibration. This equates to decades of typical blasting with one blast per day producing 10 cycles per blast.
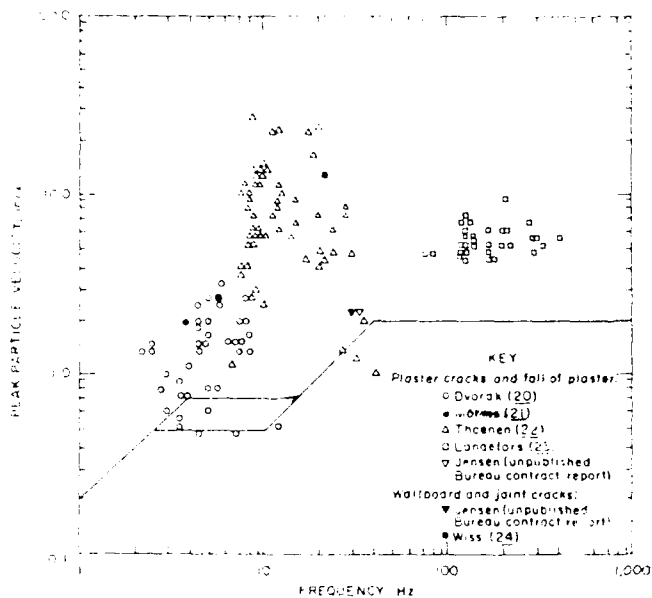
FIGURE 7   Velocity and frequency levels for threshold plaster
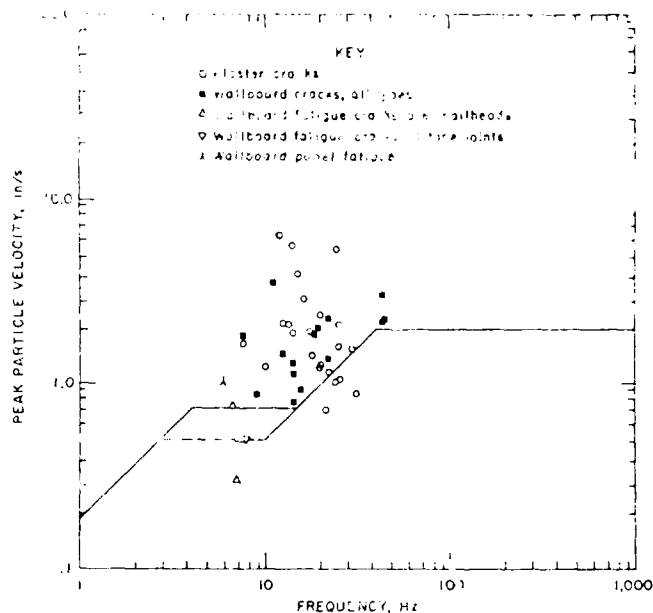and wallboard cracking, pre-1975 studies

FIGURE 8   Velocity and frequency levels for threshold plaster
and wallboard cracking, recent studies (3-4)

Masonry Cracks

Cracks produced in block masonry walls by blasting are given in Figure 9 for
past work, and Figure 10 for recent Bureau studies [3-4]. Most cracks observed
were local, typically shorter than one block length, and about 0.2 mm in width.
Cracks of this magnitude were observed from blast vibrations up to 6.2 in/s and
were not of concern, being indistinguishable from normal construction and shrinkage
effects.   Their observation is difficult, and accounts for the high number of
naturally occurring cracks (Table 5). Also, these local cracks became more
apparent during cyclic test. Differential motion along the block interfaces was
easily observed during continued cyclic motion, which accounts for the low
vibration levels, 0.3 to 1.0 in/s. However, in the test house, a blast vibration
of a 6.9 in/s produced a crack of significant magnitude, widening a crack beyond
the width that was observed the absence of a blast.

TABLE 5   Masonry wall mortar joint cracks observed in fatigue test house [4]

Material	Initial cracks, before testing	Cracks developed during testing		Blasting level, in/s	Mechanical shaker tests[1]	
		Naturally occurring	From blasting		Number of cracks	Number of cycles at cracking
Brick.........	20	28	7	3.4 -6.2	2	229,000, >293,500
Fireplace.....	21	11	1+	-6.9	2	56,000, >103,500
Block:	NA	NA	5+	6.2 -6.9	3+	>339,500
Steplike crack	ND	ND	1	.96-1.5	ND[2]	NAp
Separation....	ND	ND	2	6.9	1	>339,500

NA Not available--see text.   NAp Not applicable.   ND None detected.
[1]Shakers run at resonant frequency at equivalent vibration levels of 0.3 to
1.0 in/s.
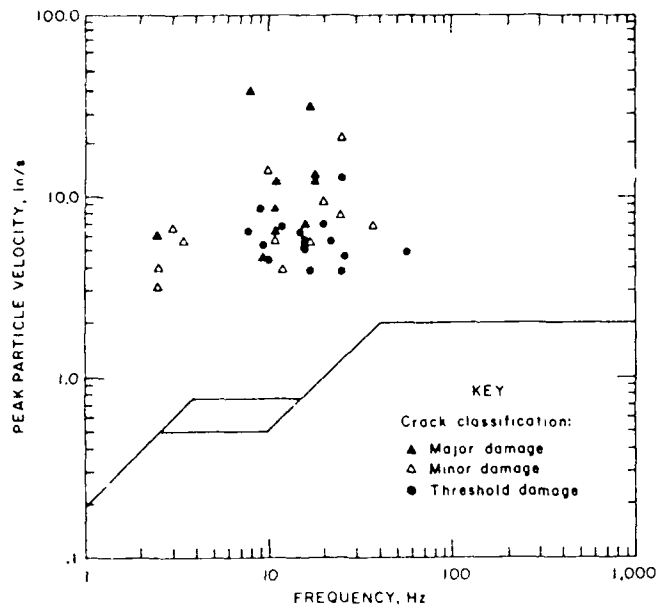[2]Existing steplike crack functioned as an area of stress relief.

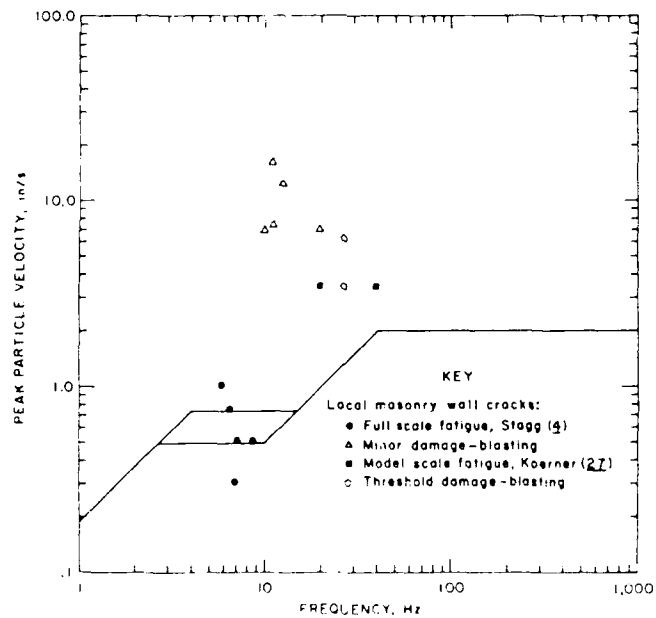**FIGURE 9** Velocity and frequency levels for local masonry wall cracks, pre-1975 studies

FIGURE 10 Velocity and frequency levels for local masonry wall cracks, recent studies (*3-4*)

Shear Load Failure

Shear load failure of the basement wall of the test house was observed after four shots in one day. A diagonal steplike crack propagated in the southwest basement wall, starting at ground level and proceeding upward. When these four shots were detonated, their vibration levels (ranging from 1.0 to 1.5 in/s) were the highest recorded in the study up to that time. But because observation of cracks in masonry is difficult, it remains unknown whether blasting or other events caused this steplike crack. It is noteworthy that no additional steplike crack propagations were observed across brick or block walls. The existing steplike crack functioned as an area of strain relief during shaker runs. Energy transmitted by the shapers into the superstructure and foundation was primarily dissipated in areas of previous cracking.

Observations were also made of chimney and brick veneer responses during cyclic shaker tests. The masonry walls were relatively stationary, with the superstructure cyclically bumping the chimney and a brick veneer wall near the roof line. Mortar joint cracks developed at the chimney-roof interface and horizontally across the brick veneer just above door height.

Crack data from Edwards and Northwood [26] do not specify crack widths. If these crack data correspond to observations exceeding 0.2 mm (excessive crack widths), it would suggest that cracks c_c occur at particle velocity levels of 3 to 7 in/s with no effect of frequency. Additional data are needed to qualify frequency effects and the generation of stairstep crack patterns across the wall signifying shear load failure.

CONCLUSIONS

Bureau studies of the response and cracking of low-rise residential structures from blasting indicated that cracking of plaster and wallboard is not likely below about 0.5 in/s peak particle velocity for the worst case of structure condition and typical vibration frequency.

This safe-level criterion also appears independent of the number of blasting events and their durations. Researchers also noticed that high strains are produced in structure walls by normal weather conditions, such as wind, temperature, and humidity cycling. Dynamic events such as door slams or blasting produce additional strain, can trigger a crack in a structure already under strain. Human activities, such as door slams, can be equivalent to blast vibrations of up to 0.5 in/s. The vibration level of 0.5 in/s thus provides a minimum value of concern for the impact of external transient vibrations on wood-frame, low-rise residential structures typical of those studied by the Bureau.

Data on the response and cracking of masonry walls from blasting indicated that local cracking (block-length) may not be noticeable until particle velocity levels are up to 3.0 in/s. However, additional research is needed to quantify vibration levels that promote the generation of stair-stepped cracks that propagate across the wall and reduce its shear load capacity.

The authors encourage, where possible, direct measurements or assessment of strains or loads on members likely to fail. Alternatively, estimates of responses should be based on realistic transfer functions relating measured vibrations and reasonably expected responses. In particular, applications beyond the scope of the original Bureau studies are to be done only with caution.

REFERENCES

1. Siskind, D. E. and M. S. Stagg. Blast Vibration Measurements Near and on Structure Foundations. BuMines RI 8969, 1985, 20 pp.

2. Stagg, M. S. and A. J. Engler. Measurement of Blast-Induced Ground Vibrations and Seismograph Calibration. BuMines RI 8506, 1980, 62 pp.

3. Siskind, D. E., M. S. Stagg, J. W. Kopp, and C. H. Dowding. Structure Response and Damage Produced by Ground Vibration From Surface Mining Blasting. BuMines RI 8507, 1980, 74 pp.

4. Stagg, M. S., D. E. Siskind, M. G. Stevens, and C. H. Dowding. Effects of Repeated Blasting on a Wood-Frame House. BuMines RI 8896, 1984, 82 pp.

5. Siskind, D. E., V. J. Stachura, M. S. Stagg, and J. W. Kopp. Structure Response and Damage Produced by Airblast From Surface Mining. BuMines RI 8485, 1980, 111 pp.

6. Stachura, V. J., D. E. Siskind, and A. J. Engler. Airblast Instrumentation and Measurement Techniques for Surface Mine Blasting. BuMines RI 8508, 1981, 53 pp.

7. Sabnis, G. M. Vibrations of Concrete Structures. Sec.: Introduction and Background. Am. Concr. Inst., SP 60 1, 1979, pp. 1-12.

8. Tuomi, R. I., and W. J. McCutchen. Testing of a Full-Scale House Under Simulated Snowloads and Windloads. U.S. For. Serv., Res. Paper FPL 234, 1974, 32 pp.

9. Warwaruk, J. Vibrations of Concrete Structures. Sec.: Deflection Requirements--History and Background Related to Vibrations. Am. Concr. Inst., SP 60 2, 1979, pp. 13-41.

10. Whittemore, H. L., J. B. Cotter, A. H. Stang, and V. B. Phelan. Strength of Houses--Application of Engineering Principles to Structural Design. NBS Build. Mater. and Struct. Rep. BMS 109, Apr. 1948, 131 pp.

11. Holmberg, R., N. Lundberg, and G. Rundqvist. Ground Vibration and Damage Criteria. Constr. Res. Counc., Stockholm, Sweden, Rep. R 85:81, 1981, 30 pp.

12. Andrews, D. K., G. W. Zumwalt, R. L. Lowery, J. W. Gillespie, and D. R. Low. Structure Response to Sonic Booms. (U.S. FAA contract FA-64-AC-6-526, Andrews Associates Inc. and Hudgins, Thompson, Ball and Associates, Inc., Oklahoma City, OK). Rep. AD618022, Feb. 5, 1965, 228 pp.; available from Defense Documentation Cent., Alexandria, VA.

13. Wall, J. R., Jr. Seismic-Induced Architectural Damage to Masonry Structures at Mercury, Nevada. Bull. Seismol. Soc. Am., v. 57, No. 5, Oct. 1967, pp. 991-1007.

14. Leigh, B. R. Lifetime Concept of Plaster Panels Subjected to Sonic Boom. Univ. of Toronto, Ontario, Canada, UTIAS-IN-191, July 1947, 78 pp.

15. Woodward, K. A., and F. Rankin. Behavior to Concrete Block Masonry Walls Subjected to Repeated Cyclic Displacement. NBSIR 83-2780, 1983, 178 pp.; NTIS PB 84-122092.

16. Cranston, W. B. Masonry Research and Codes in the United Kingdom. Paper in Earthquake Resistant Masonry Construction: National Workshop (NBS, Boulder, CO, Sept. 13-16, 1976), ed. by R. A. Crist and L. E. Cattaneo. NBS Build. Sci. Series 106, Sept. 1977, pp. 166-176.

17. Green, D. G., I. A. Macleod, and W. G. Stark. Observation and Analysis of Brick Structures on Soft Clay. Paper in Performance of Building Structures (Proc. Int'l Conf., Glasgow Univ., Mar. 31-Apr. 1, 1976). Pentech Press, 1976, pp. 321-336.

18. Wroth, C. P. General Report Session IIIA: Response of the Structure to Foundation Movements. Paper in Performance of Building Structures (Proc. Int. Conf., Glasgow Univ., Mar. 31-April 1, 1976). Pentech Press, 1976, pp. 489-508.

19. Haldane, D. The Importance of Cracking in Reinforced Concrete Members. Paper in Performance of Building Structures (Proc. Int. Conf., Glasgow Univ., Mar. 31-Apr. 1, 1976. Pentech Press, 1976, pp. 99-109.

20. Dvorak, A. Seismic Effects of Blasting on Brick Houses. Pr. Geofys. Ustance Cesk. Akad. Ved. No. 169. Geofys. Sb., 1962, pp. 189-202.

21. Morris G., and R. Westwater. Damage to Structures by Ground Vibrations Due to Blasting. Mine and Quarry Eng., v. 24, Apr. 1958, pp. 116-115.

22. Thoenen, J. R., and S. L. Windes. Seismic Effects of Quarry Blasting. BuMines B 442, 1942, 83 pp.

23. Langefors, U., B. Kihlstrom, and H. Westerberg. Ground Vibrations in Blasting. Water Power, v. 10, 1958, Sept., pp. 335-338; Oct., 390-395; Nov., 421-424.

24. Wiss, J. F., and H. R. Nicholls. A Study of Damage to a Residential Structure from Blast Vibrations. Res. Counc. for Performance of Struct., ASCE, New York, 1974, 73 pp.

25. Stagg, M. S. and D. E. Siskind. Repeated Blasting: Fatigue Damaging or Not? Paper in Proceedings of the 11th Annual Conference on Explosives and Blasting Technique, ed. by C. J. Konya (San Diego, CA, Jan. 27-Feb. 1, 1985) Soc. Explos. Eng., Montville, OH, 1985, pp. 96-110.

26. Edwards, A. T., and T. D. Northwood. Experimental Studies of the Effects of Blasting on Structures. Engineer, v. 210, Sept. 30, 1960, pp. 538-546.

27. Koerner, R. M., and J. L. Rosenfarb. Feasibility of Fatigue Assessment of Block Walls from Laboratory Scale Methods (contract J0285013, Drexel Univ.). BuMines OFR 144-80, 1980, 96 pp.: NTIS PB 81-140139.

MODAL APPLICATIONS

USING MODAL TESTING TO IDENTIFY DYNAMIC CHANGES IN BATTLE DAMAGED F-16 WINGS

Arnel B. Pacia
Flight Dynamics Lab
Air Force Wright Aeronautical Laboratory
AFWAL/FIBG
Wright-Patterson Air Force Base. OH 45433

Modal tests were conducted to determine whether battle damage or battle damage repair significantly change the dynamics of F-16 wings. Two F-16 wing torque boxes were tested while undamaged, damaged, and repaired. A forty channel data acquisition system was assembled for these tests. Three modes were found in the 0-100 Hz bandwidth. Slight changes in modal parameters did occur, increasing in significance with increased damage.

INTRODUCTION

When aircraft structures sustain combat damage, several obvious concerns arise. Most immediate would be whether the damage is catastrophic. If the damage does not result in instant loss, then the concern shifts to vehicle airworthiness and crew safety on the return flight. If the structure does make it to base, can it be repaired? And if repaired, is the repair sufficient? For modal testing to have a role in the battle damage area, it must be part of at least one of the solutions that address these questions.

If damage to the aircraft is catastrophic, the solution lies in aircraft design, i.e., the structure must be designed to withstand a certain amount of damage. However, even though the structure survives, degraded performance seems certain. For example, a damaged aircraft would lose strength, have increased drag and probably have a decreased flutter envelope. Of course, many factors such as fuel capacity, pilot injury, and others also come into play. Furthermore, the question of whether battle damaged structures should be repaired involves additional factors such as the availability of supplies and manpower, required down-time, and extent of damage. Whatever the issues, post-repair inspection is a must.

Modal testing has long been used for troubleshooting vibration problems. Therefore, modal testing has become a valuable tool for determining the extent of damage and for checking repairs. To aid in the survivability of structures, one can extend the current technology in spectrum monitoring and merge it with artificial intelligence and smart structures in the future to diagnose and respond to in-flight structural problems. Once the affects of battle damage to aircraft dynamics is better defined, for example in flutter, modal analysis can be integrated in the design process.

Conceptually, if there is a baseline of modal parameters for a structure, a drop in the natural frequencies of affected modes should indicate the extent of stiffness loss. Mass loss would drive the frequencies higher, and is sometimes

negligible depending on the total mass of the structure. By knowing the amount of strength loss, intelligent decisions on how much repair is needed can be made. For example, would a quick patch suffice and thus have the aircraft operational in short order, or would a more thorough repair be necessary? Just as easily, the modal parameters of the repaired structure can be compared to the baseline to check whether the repair is adequate and complete. In order to put these concepts to use, verification that current modal analysis technology can detect dynamic changes caused by ballistic damage on relatively complex structures like wings is required.

A series of tests were done to identify changes in natural frequencies, modal damping, and the mode shapes of F-15 wings while undamaged, damaged, and repaired. These tests were done in conjunction with the Joint Live Fire program, a DoD effort managed by the Survivability Enhancement Branch of the Wright Aeronautical Laboratories. The Joint Live Fire program's objective was to assess the vulnerability and survivability of aircraft in combat. The program also tested the wings' load carrying capability, aerodynamic integrity, and fire and explosion protection systems.

TEST ARTICLES

In the summer of 1987, two F-15C/D wings, were designated Wing 1 and Wing 2 and tested. These wings were designed for 9g structural load and 13g ultimate load. The main torque box, which also serves as a fuel tank, has eleven spars and four ribs. All internal framework and skins are aluminum alloys. Control surfaces were removed in these tests for logistics reasons.

TEST SITE

Modal tests were conducted in the electronics assembly area in the Aircraft Survivability Research Facility of Wright-Patterson Air Force Base. Originally, these modal tests were planned to be done at Range 3, which is two stories off the ground and open on two sides. Since this potential test site was open, the tests would have been subject to environmental variations. Wind blowing over the accelerometers could have caused transients that would have contaminated the data. Also, modal test equipment had to be safeguarded before the gunrange could be used. Conversely, the assembly area is air-conditioned. This gave some control over the temperature of the test article. This is important because control over changes in the structural dynamic properties due to temperature is critical, and thermal control alleviates the problem of accelerometer temperature sensitivity. Equipment did not have to be safeguarded, was shielded from the weather, and was in a centralized location. This made the testing highly efficient.

TEST FIXTURE

The wings were cantilevered to a vibration test fixture (Fig 1). This fixture was designed to be as low to the ground as possible to minimize the moment on the base. There was only room enough left between the base plate top surface and the wing bottom surface to mount a shaker in case it was necessary to excite inboard. Six stiffness six square steel tubes made up the base fixture vertical supports and six rectangular steel tubes made up the angle supports.

Considerable rocking of the fixture was observed due to the unevenness of the floor. Shaking only induced fixture floating; therefore, foam was laid between the

base and floor to compensate for the unevenness. The foam also acted as a highly damped isolator preventing energy transfer to and from the floor.

Another problem encountered was fixture vibration, the base of the fixture was loaded with lead bags. This added inertial mass and damping to the fixture, which meant most of the motion stayed on the wing and fixture motion was damped by the lead shot bags. Note that the fixture weighed 14000 lb and the wing weighed 800 lb. Ten thousand pounds of lead shot bags were added to the fixture. To keep the boundary conditions consistent, a torque wrench was used to bolt the wing to the fixture, allowing the wing to be bolted with the maximum allowable tension.

INSTRUMENTATION

Thirty-seven lightweight Structcel accelerometers manufactured by the PCB Piezotronics, Inc. measured the acceleration on the wing. Their mounting sockets were hot glued at strong points, i.e. spars or ribs, to avoid local modes. Figure 2 shows the locations of the accelerometers and the grid used for Test Data Analysis System (TDAS) from Structural Dynamics Research Corporation. Figure 3 shows a block diagram of the instrumentation used for the modal test. An alignment tool was used to make sure each accelerometer pointed vertically. A Setra model 141A accelerometer was used as the calibration reference, and to monitor the vibration on the base plate. Figure 1 shows the accelerometers on the wing and the Setra on the fixture base.

FIBG redesigned a 120 channel F-16 ground vibration test system to measure 38 accelerations, 1 force and 1 temperature. Thirty-seven PCB accelerometers were powered, conditioned and amplified by three PCB model 433A Differential Power Supplies. The thirty-seven accelerometer signals at approximately 1 volt/g, the force gage and the Setra signals went through filter cards programmed for 80 Hz cutoff. The filtered signals went into 40 Automatic Gain Changing Amplifiers. The amplifiers select one of eight gains based on the level of the input signal. The analog outputs of each amp connected to the PCM encoder. Also, for each amplifier, a 3-bit binary output proportional to the gain setting went into a digital multiplexer that merged 120 gain bits into two 12-bit word inputs to the PCM encoder. The PCM encoder sampled, digitized and encoded 40 analog signals into 12-bit words, and sampled six 12 bit words containing gain bits, frame counts and time code. The PCM encoder sampled at 200 kbits/sec. Each accelerometer was sampled at 347 2/9 samples/sec.

The Delay Modulation Mark (DMM) PCM data were recorded on one direct record track of a Honeywell 96. A PCM playback system, Fairchild Weston Inc. Model 1786 Universal Telemetry Data System (UTDS), was used to monitor the PCM data in real time. Valuable information on gains and sync lock were provided. Eight digital to analog outputs of the UTDS were used by the modal analysis system, GenRad 2514, to obtain transfer functions, coherence, and autospectrum, to ensure data quality. Analog outputs of the amplifier were also used to monitor data.

TESTS AND RESULTS

To obtain a baseline for comparison, Wing 1 and 2 were tested before they were damaged. The wings were excited at the leading edge wing tip with random noise at 0-100 Hz. Figure 4 shows the frequency response function (FRF) magnitude from the baseline tests of the wings. As expected, the responses are similar. Within the bandwidth, three modes were found: first bending, second bending and first torsion at approximately 12 Hz, 40 Hz, and 60 Hz respectively. Figure 5 shows the mode

[...]

The [...] degrees of freedom polynomial [...] curvefit routine was used to find the natural frequencies and damping. This method was applied because the modes were well separated and looked like normal modes. Figure 6 shows a sample curvefit and Table 1 gives the values of frequencies and damping. IDAS was used to extract frequencies, [...] and mode shapes.

After completing the baseline test on Wing 1, it was damaged by a high explosive incendiary (HEI) round at a relatively harmless location away from spars and ribs. This was shot condition 1. That damage was repaired and Wing 1 was shot according to condition 2 this time damaging a spar and a rib. Figure 7 shows the location of the shots and Figure 8 shows the damage. A modal survey of Wing 1 was conducted. In Figure 9, the FRF of the damaged Wing 1 was overlayed over the undamaged Wing 1. Any frequency shift was less than 1%. Although the wing sustained two damages, there was little change in its dynamic characteristics. Table 1 lists the natural frequencies and damping ratio found for the damaged Wing 1.

The fact that there was little change to these parameters was further verified by comparing modal assurance criterion (MAC) values (Table 2). The MAC is an indication of the relative linear independence between mode shapes; it is similar to the coherence values between mode shapes. Comparing the same modes of the same structure at different stages of structural integrity should give a quantitative value of any change in this dynamic property. The MAC value obtained when the each mode of the damaged Wing 1 was compared to the corresponding mode of the baseline was essentially unity. This means that the mode did not change significantly with the damage.

The damage to Wing 2 was more extensive (Fig 10). This wing was damaged by HEI while full of fuel, so that hydrodynamic ram damage was the leading factor. The top and bottom surfaces were petaled, spar 9 and the rib were severed, and spar 10 was deformed.

Figure 11 shows an overlay of the FRF of the damage over the undamaged Wing 2. The amplitude and damping decreased with the damage. The first mode went down in frequency about 1.5%, the second mode remained relatively unchanged, while the third mode went down in frequency 3 Hz, or about 5%. After Wing 2 was repaired, the modal survey indicated that the stiffness was restored. Figure 12 shows an overlay of the repaired Wing 2 versus the undamaged Wing 2 and Figure 13 is an overlay of the three cases.

There were negligible changes in the frequencies and mode shapes due to the damages to Wing 1. Wing 2 had more significant changes. The first and second modes of Wing 2 did not change drastically. The change was more evident on the third mode. This can be observed by comparing the end view of the third mode of the damaged wing against the undamaged or repaired wing (Fig 14). Note that the trailing edge wing tip changed its phase, indicating that the node line moved. The wing returned to its original mode shape with the repair. The node line for the third mode, Figure 15, shows how it shifted with the damage, and was restored with the repair.

The changes in the third mode were observed only for Wing 2. MAC values in Table 3 confirm that the third mode was most affected by the damage. Note that the MAC returned to a value of 1 with the repair. This means that the stiffness loss by the wing that caused the change in frequency and mode shape was effectively restored by the repair.

CONCLUSIONS

The modal survey conducted on battle damaged F-16 wings showed that current modal analysis methods can detect significant damage to a structure, as was the case with Wing 2. The modal parameters obtained for Wing 2 also seem to verify the adequacy of the repair. However, these modal tests were unable to detect changes in Wing 1. Wing 1 was damaged twice, although neither damage was as severe as that experienced by Wing 2. The damage to Wing 1 was a little forward of that on Wing 2 and thus closer to the node line of the third mode. This could explain why the damage on Wing 1 did not affect its third mode. This suggests that the changes in wing dynamics depend on the location of the damage. It seems clear that a mode will shift if damage occurs in an area stressed by that mode.

As a check for repair adequacy, modal testing may be very useful. The natural frequencies alone can indicate whether the stiffness has been restored to the structure. This test is relatively easy to set up. The MAC can also be useful but is generally more cumbersome to apply. Using modal testing to indicate the extent of damage requires more care. Given a structure, one must identify the modes most critical to structural strength. Once identified, guidelines must be established as to what amount of damage is "significant". Also, since mode changes due to damage depends on the areas stressed, it is very possible that modal testing could be used to locate problems that might go undetected using conventional NDI methods. For example, the Vibration and Acoustic Test Facility at the Johnson Space Center did modal surveys of Shuttle Orbiters and found faults undetected by other means [1,2].

For modal testing to become a useable tool to define the survivability of aircraft structure, more research must be done to determine the affects of ballistic damage to system dynamics. Also since modal surveys can detect dynamic changes due to ballistic damage, it may become a useful check of analytical models seeking to describe this damage. Therefore, modal testing can play a role in determining the survivability and reliability of structures, now and in the future.

REFERENCES

1. Walter M. West, Jr., A.D. Gist, B.W. Holder, "Fault Detection on Orbiter OV-101 Structure and Related Structural Test Specimens," Loads and Structural Dynamics Branch Report, NASA Johnson Space Center, Sept 1984.

2. Walter M. West, Jr., A.D. Gist, "Modal test Report on Orbiter AFA-12, Aft Fuselage Bulkhead," Vibration and Acoustic Test Facility, Loads and Structural Dynamics Branch, NASA Johnson Space Center, June 1985

BIBLIOGRAPHY

1. David Banaszak, "Frequency Response Evaluation of Multiple Accelerometers Using a Modal Data Acquisition System," AFWAL-TM-87-195-FIBG.

2. David Banaszak, Arnel Pacia, "Joint Live Fire F-16 Wing Modal Tests," AFWAL-TM-88-167-FIBG.

3. D.J. Ewins, "Modal Testing: Theory and Practice," Research Studies Press, Letchworth, Hertfordshire, England, 1984.

4. M.H. Richardson, "Detection of Damage in Structures from Changes in Their Dynamic (Modal) Properties - A Survey," NUREG/CR-1431, April 1980.

5. Walter West, A.D. Gist, Alden C. Mackey, "Structural Fault Detection of a Light Aircraft Structure Using Modal Technology," Loads and Structural Dynamics Branch Report, NASA Johnson Space Center, April 1988.

Table 1. Wing 2 and Wing 1 Modal Survey

NATURAL FREQUENCIES (Hz)

| | WING 2 | | | WING 1 | |
	UNDAMAGED	DAMAGED	REPAIRED	UNDAMAGED	DAMAGED
1st Bending	12.161	11.98	12.227	11.985	11.869
2nd Bending	40.684	40.58	40.598	39.994	39.799
1st Torsion	62.140	59.07	61.981	60.365	60.251

DAMPING RATIO (%)

| | WING 2 | | | WING 1 | |
	UNDAMAGED	DAMAGED	REPAIRED	UNDAMAGED	DAMAGED
1st Bending	0.463	0.36	0.400	0.472	0.476
2nd Bending	0.950	0.587	0.628	1.405	1.002
1st Torsion	1.842	1.185	1.988	4.419	3.141

Table 2. Modal Assurance Criterion (MAC) Comparisons of Modes

Natural Frequencies (Hz)

	Undamaged Wing 1	Damaged Wing 1	MAC
1st Bending	11.985	11.862	0.9990
2nd Bending	39.994	39.799	0.9989
1st Torsion	60.365	60.251	0.9948

	Undamaged Wing 2	Damaged Wing 2	MAC
1st Bending	12.161	11.98	1.0000
2nd Bending	40.684	40.58	1.0000
1st Torsion	62.140	59.07	0.9755

	Undamaged Wing 2	Repaired Wing 2	MAC
1st Bending	12.161	12.227	0.9999
2nd Bending	40.684	40.598	1.0000
1st Torsion	62.140	61.981	1.0000
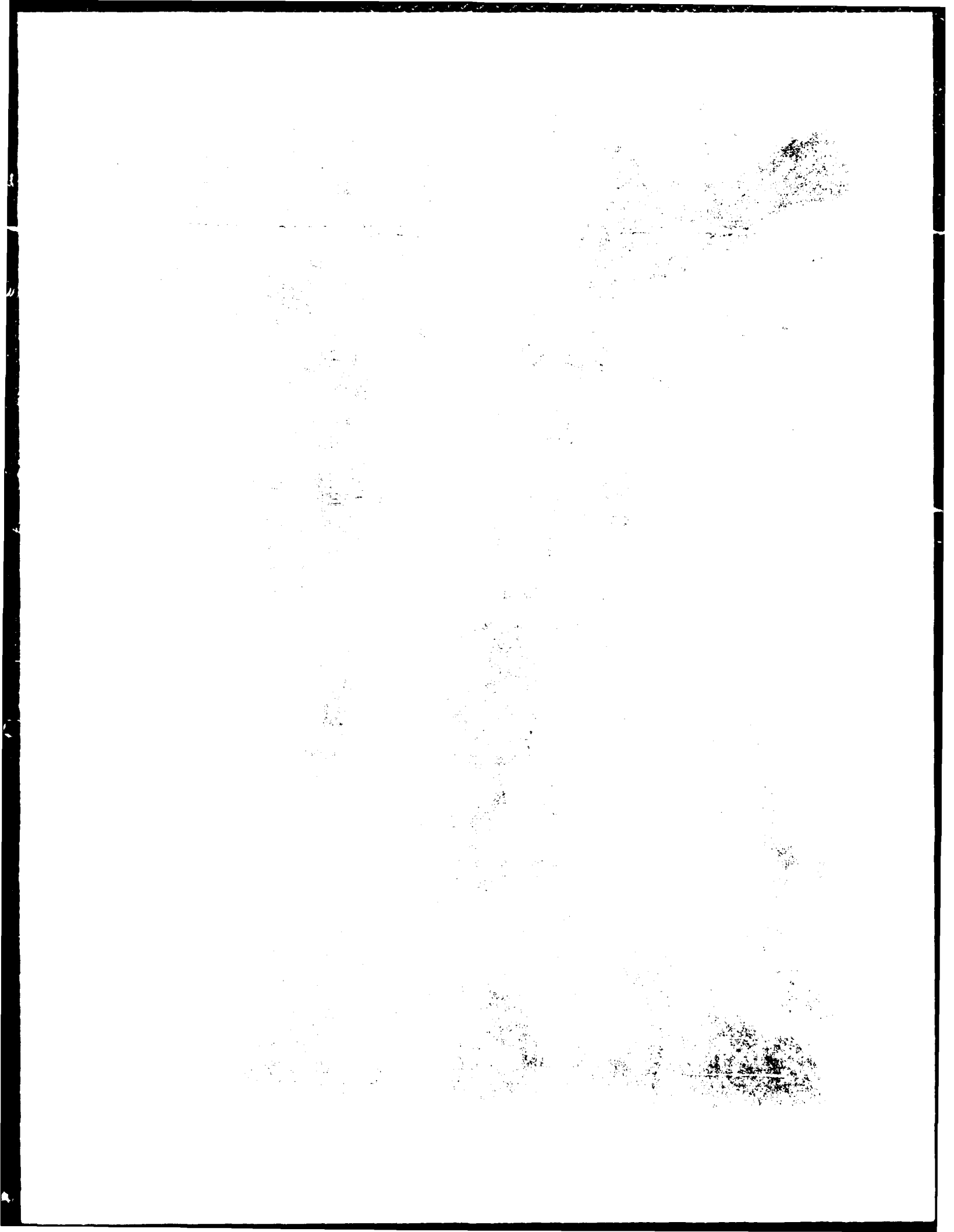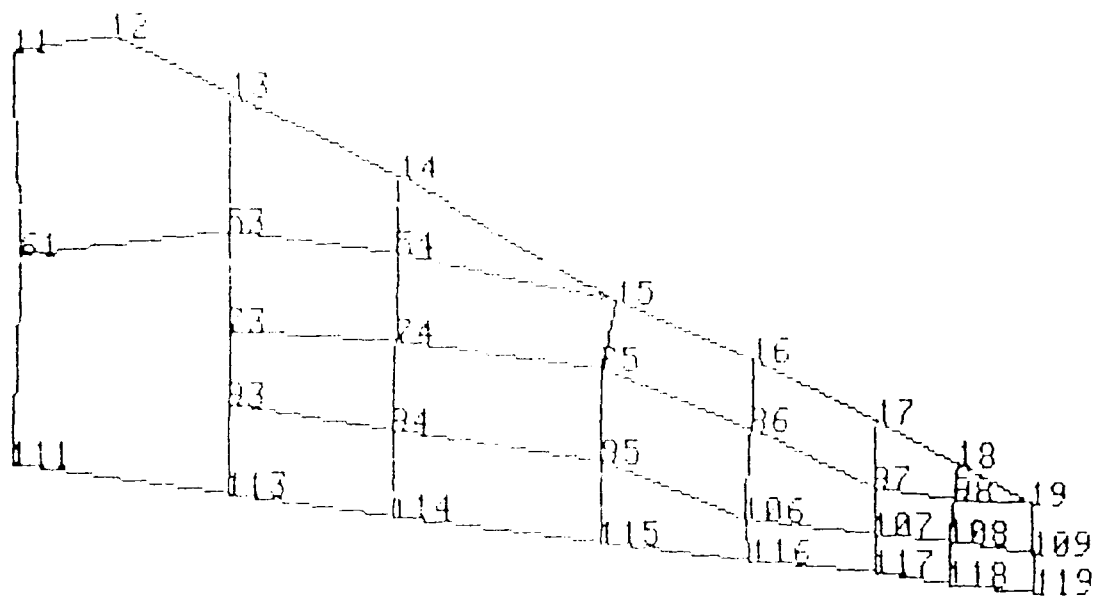
Figure 1. Accelerometer Locations and Numbering Scheme
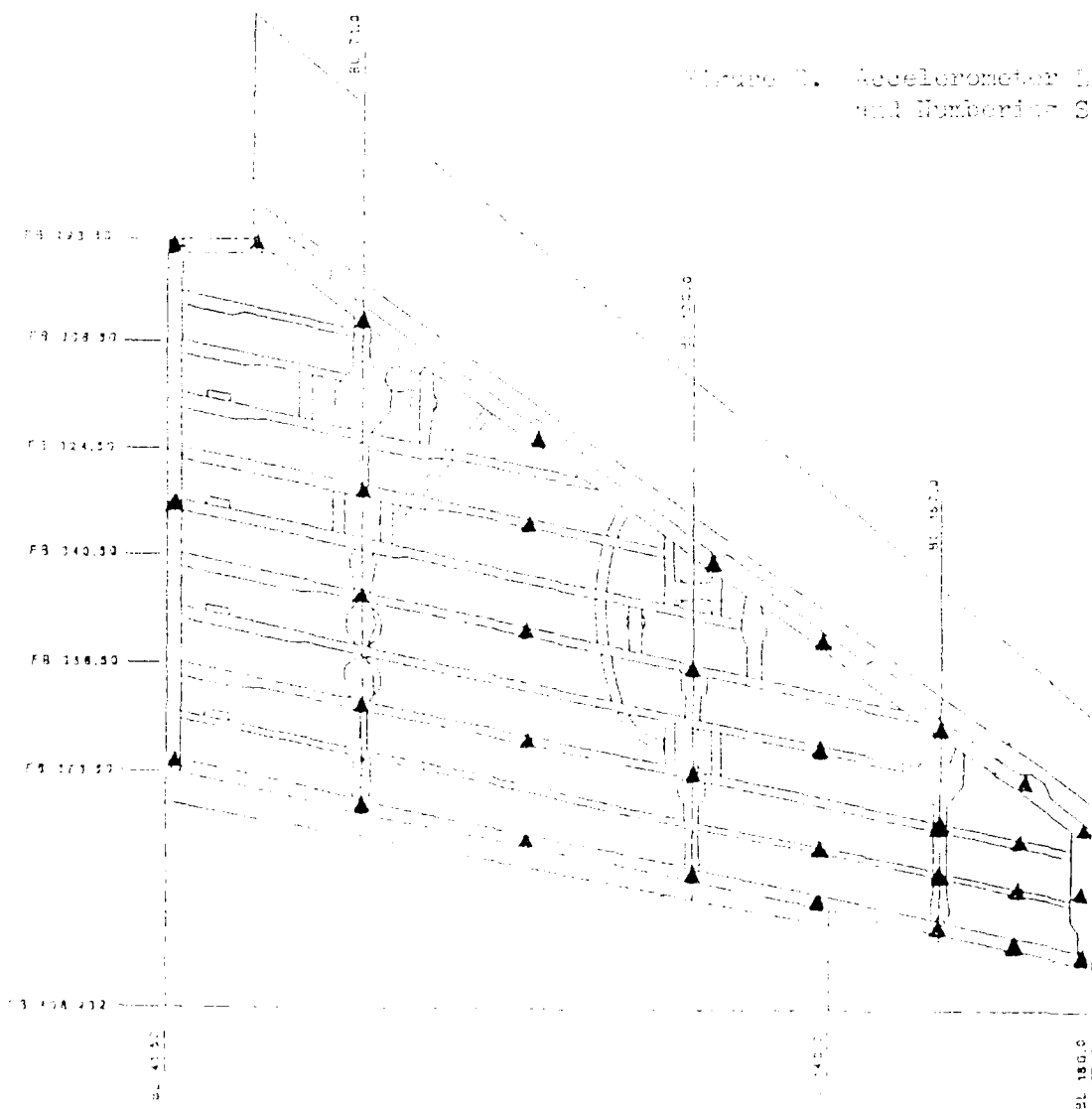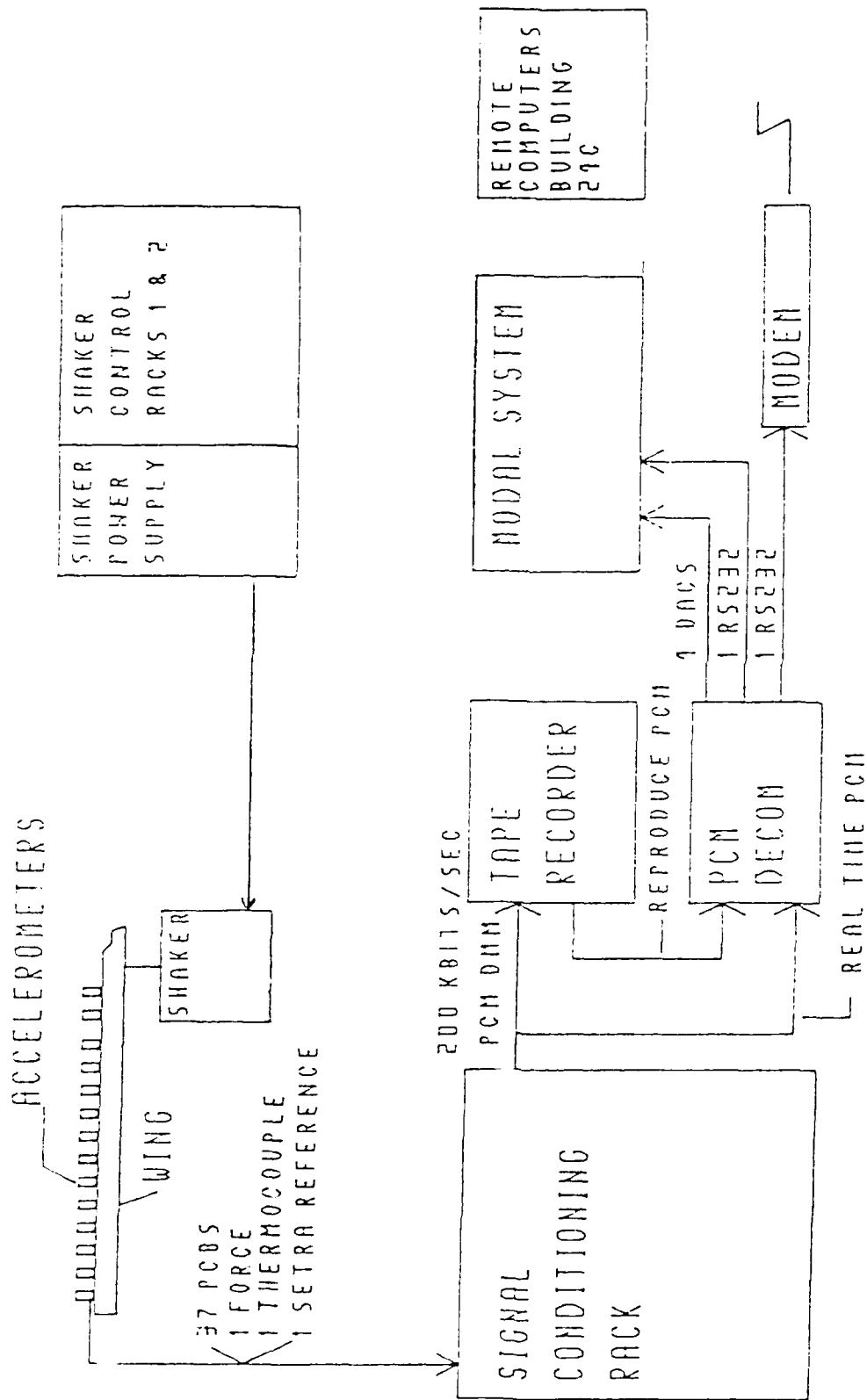
Figure 3. Block Diagram of Joint Live Fire F-16 Wing Modal Survey Instrumentation

347
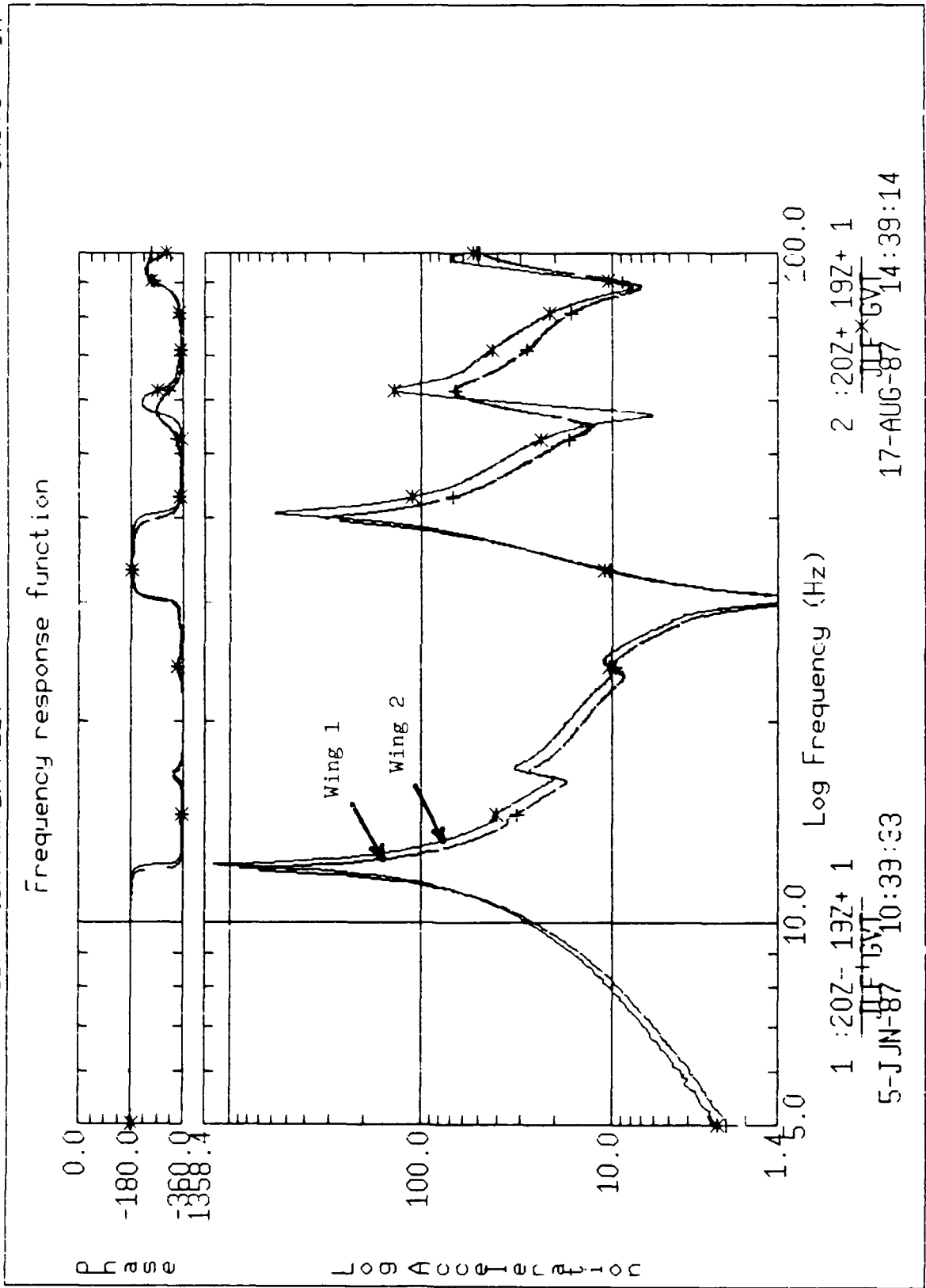
Figure 4. Overlay of Frequency Response Functions of Undamaged Wing 1 and Wing 2

1st Bending
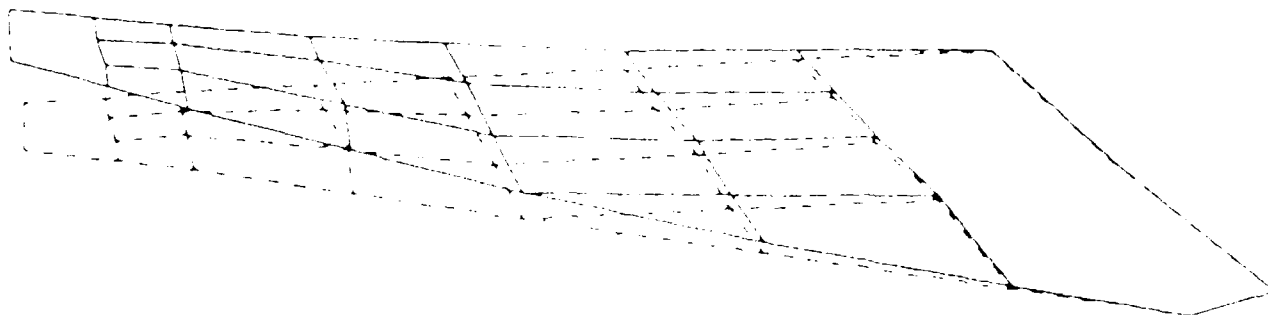
2nd Bending
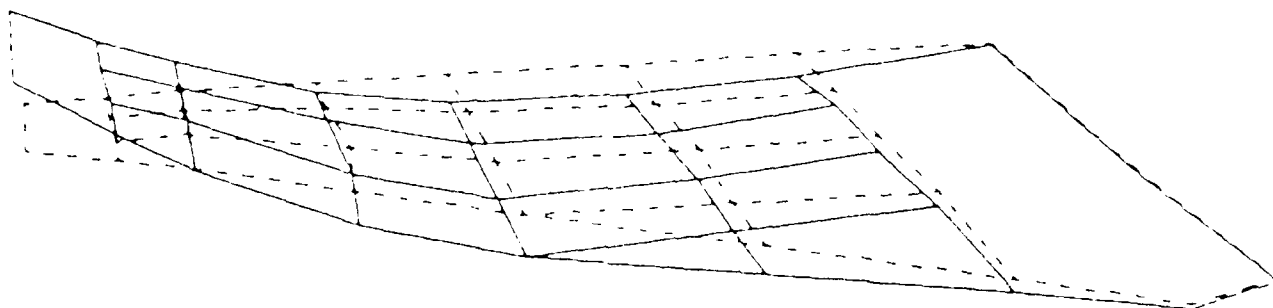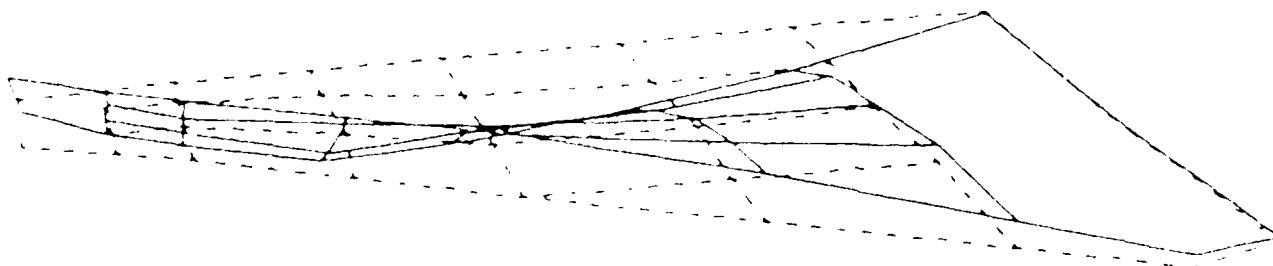
1st Torsion

Figure . Oblique View of the First Bending, Second Bending, and First Torsion of Instrumented Wing 2

SDRC I-DEAS 3.4: Test Data Analysis   28-AUG-87 15:36:56
DATABASE: F-16 WING 2 MODAL TEST   UNITS = IN
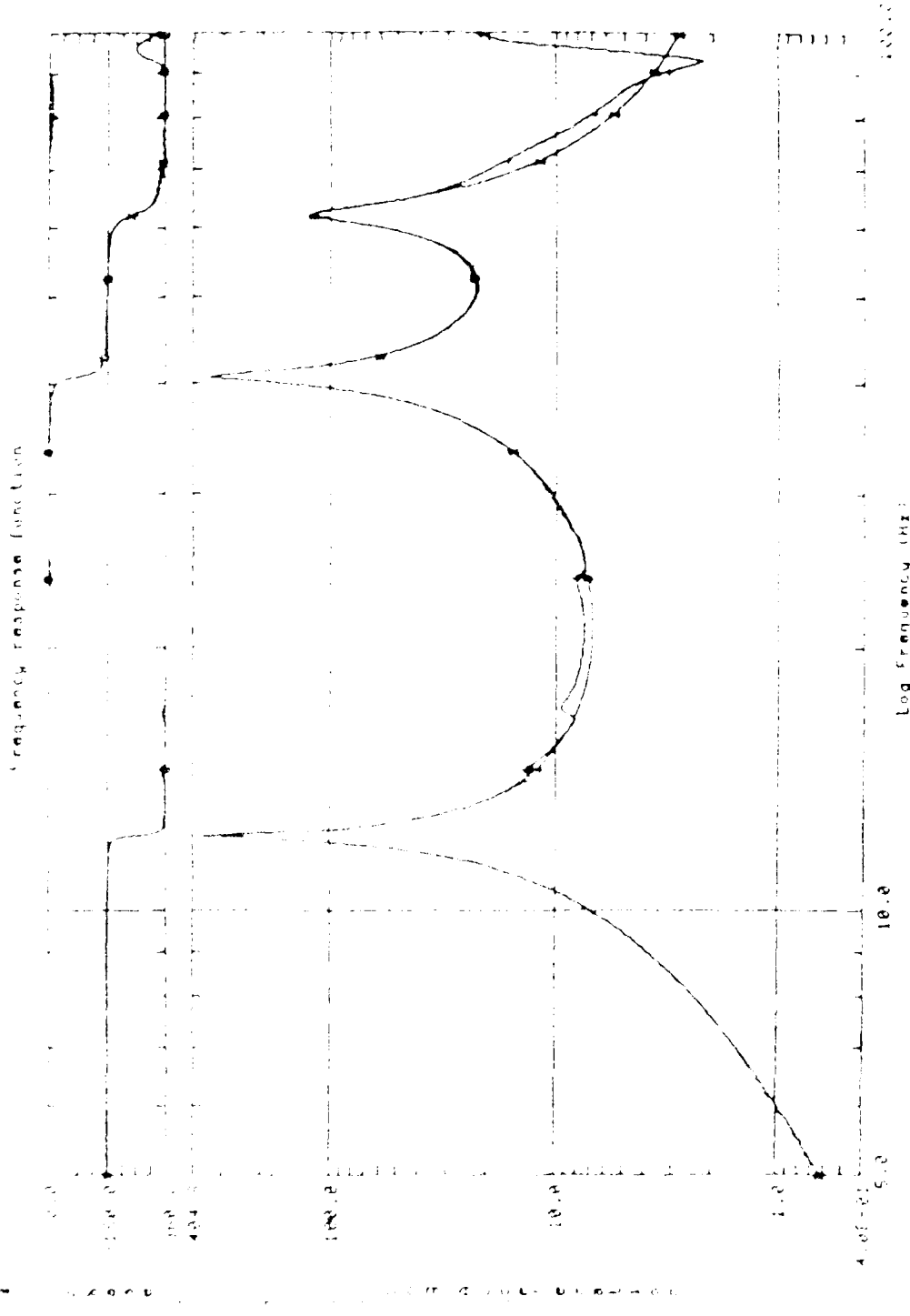
Frequency response function

Log Frequency (Hz)

10.0   5.0

1.202+ 152+ 1   2.1202+ 152+ 1
JLF OUT   JLF OUT
17-AUG-87 14:78:00   28-AUG-87 16:15:16

WING 1

WING 2
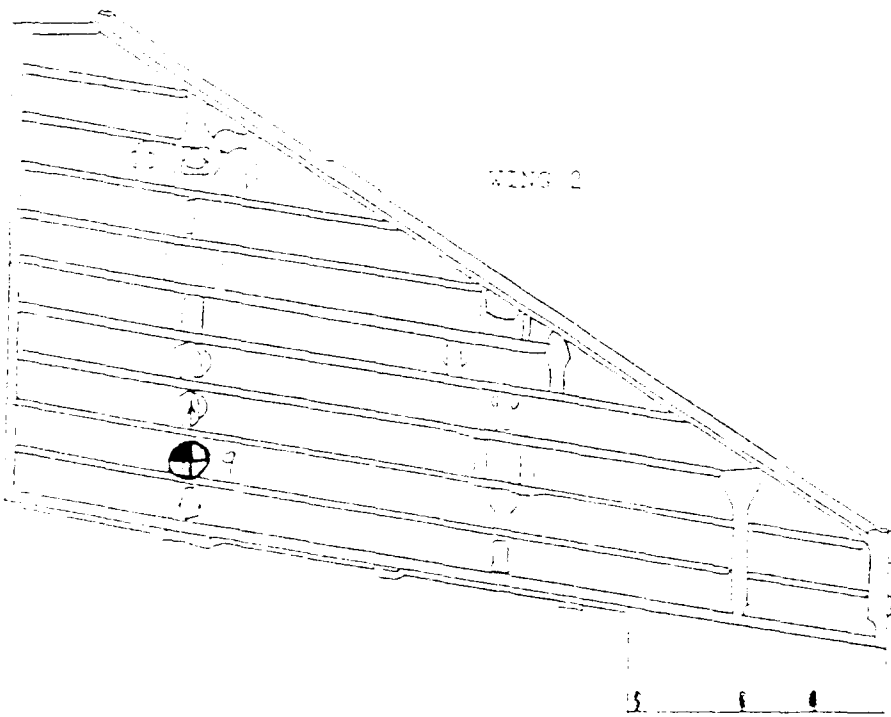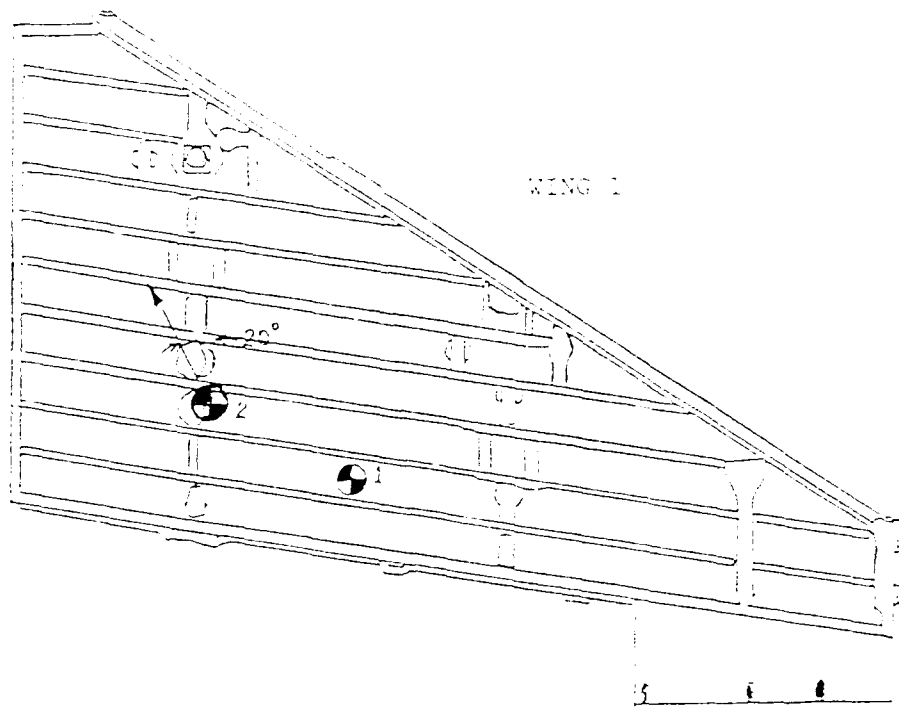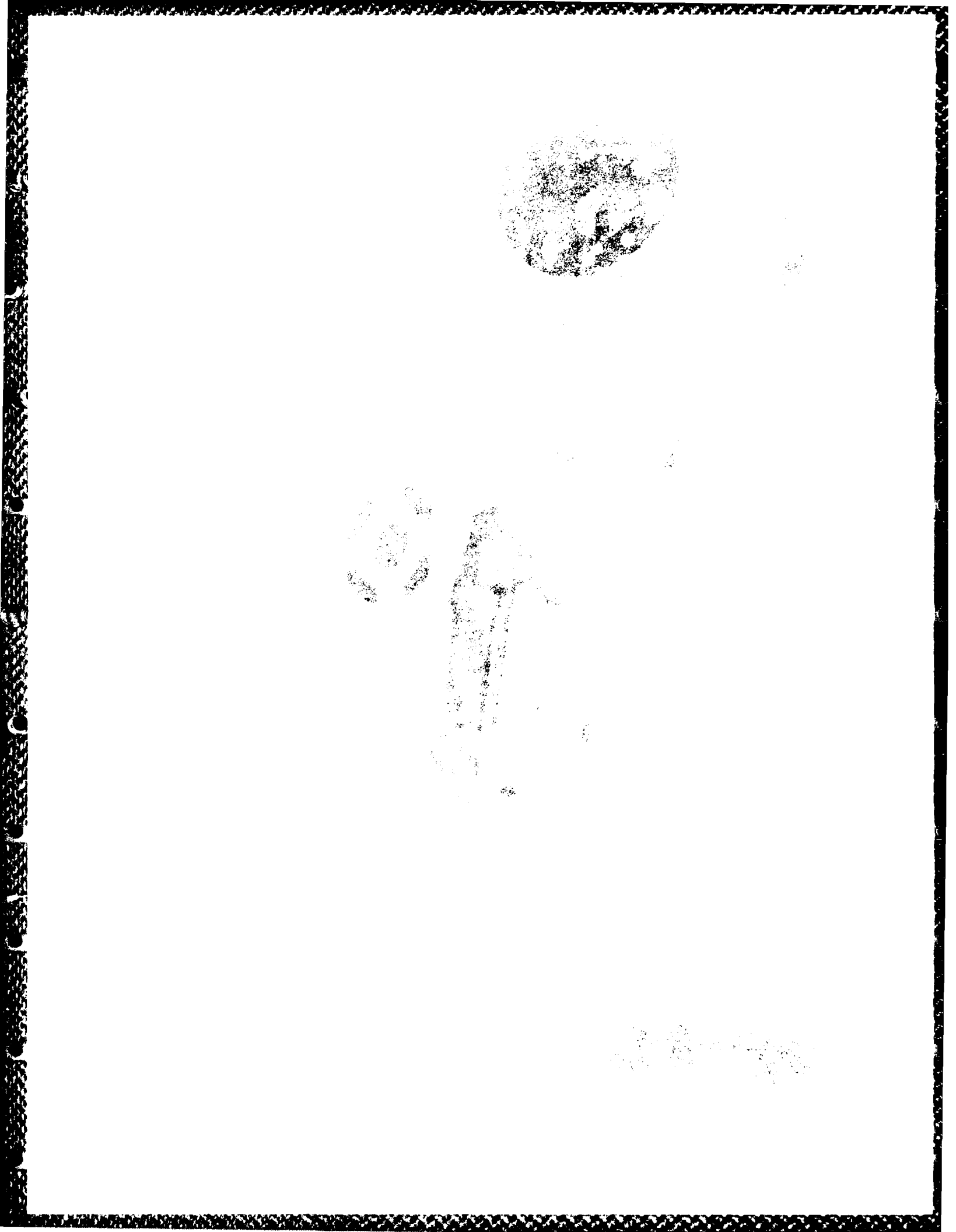
SDRC I-DEAS 3.4: Test Data Analysis   18-AUG-87 16:25:53

DATABASE: WING 1 - BASELINE   UNITS = In

Frequency response function

1X : 11.8
1Y : 252.9
2X : 12.0
2Y : 883.7
3X : 39.8
3Y : 103.2
4X : 39.8
4Y : 168.7
5X : 59.5
5Y : 36.5
6X : 59.5
6Y : 59.6

Undamaged Wing 1

Damaged Wing 1

Log Frequency (Hz)
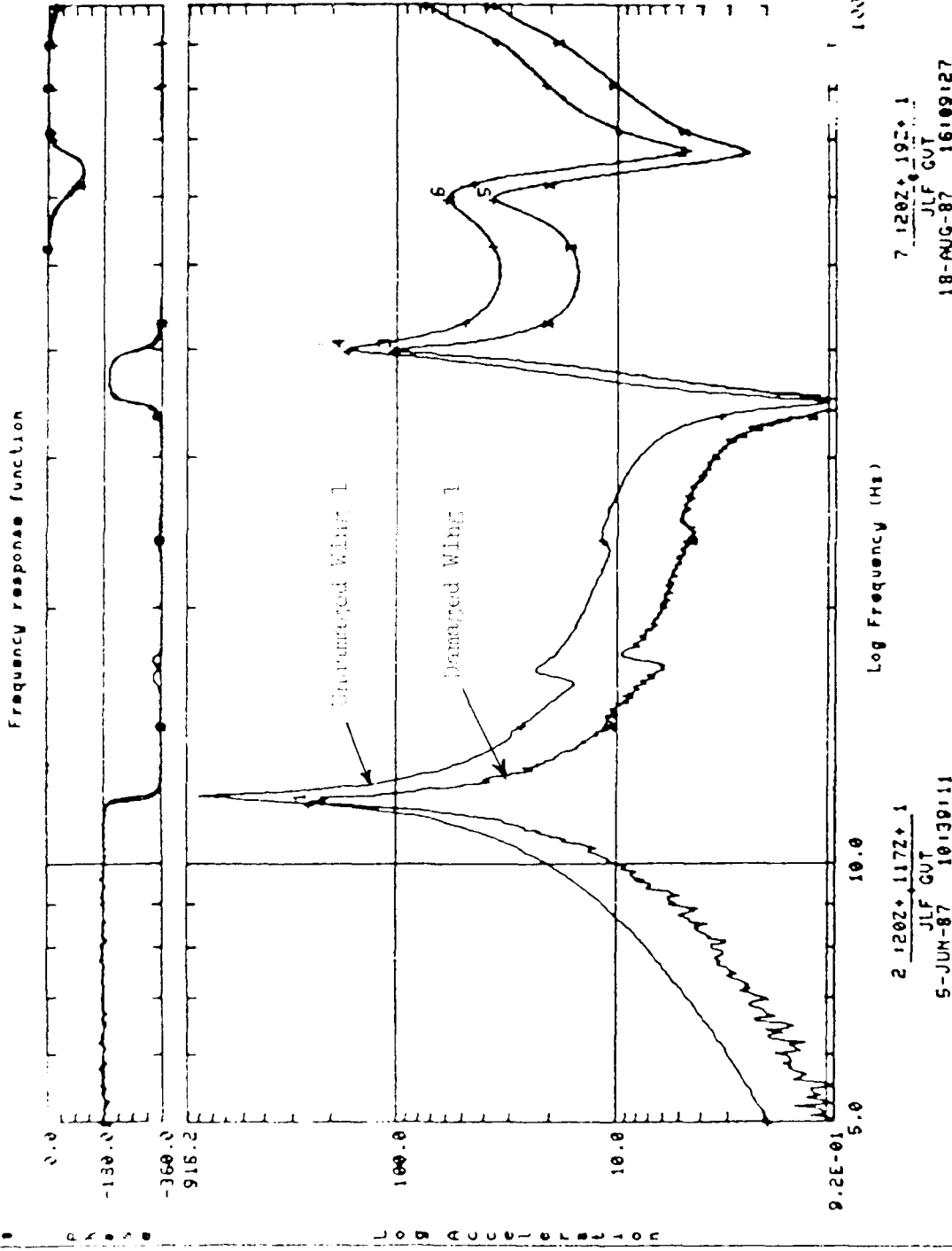
2 :202+ 1172+ 1
JLF GVT
5-JUN-87 10:39:11

7 :202+ 192+ 1
JLF GVT
18-AUG-87 16:09:27

Figure 9. Overlay of the Frequency Response Functions of
the Undamaged Against Damaged Wing 1

347
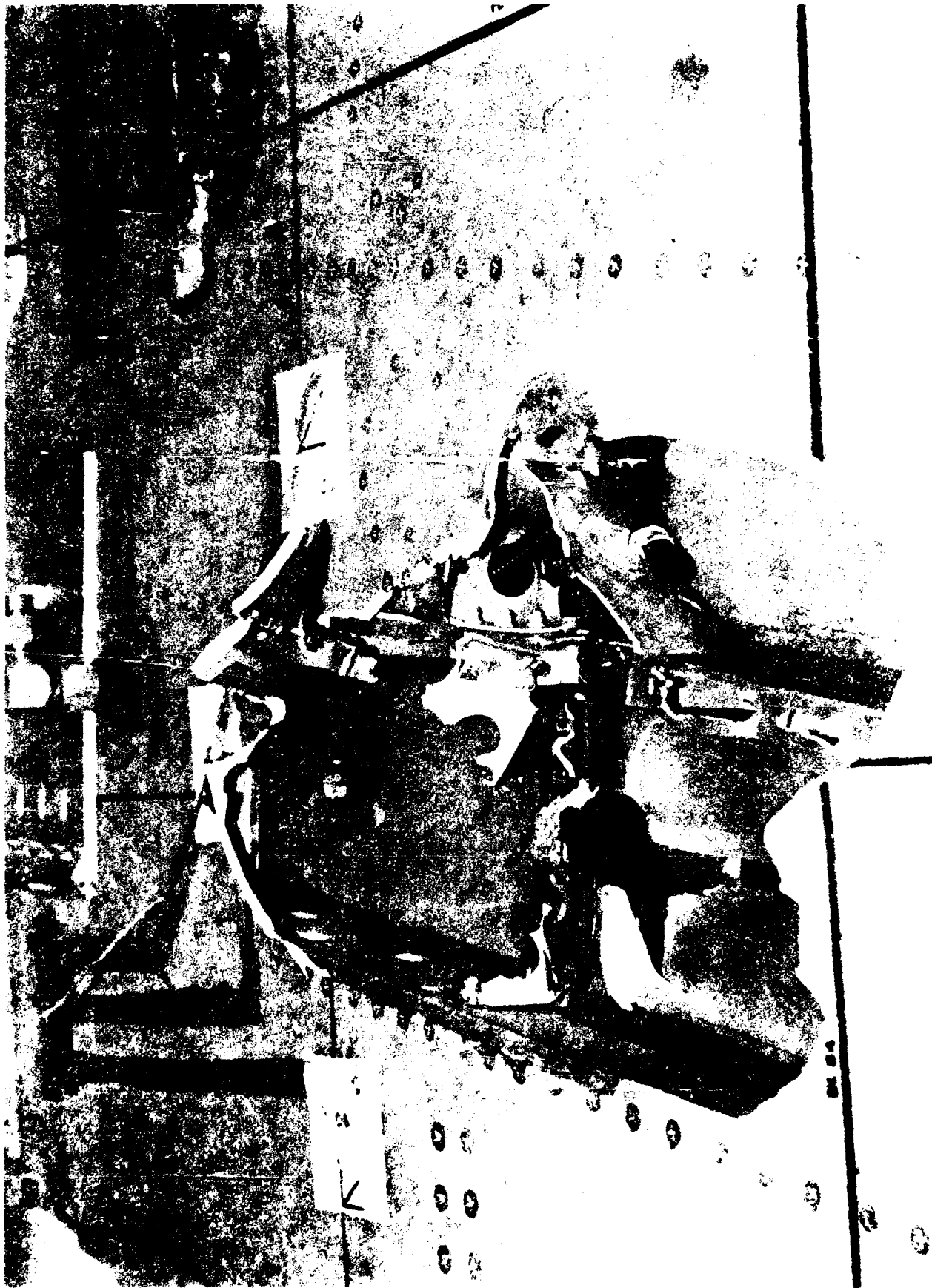
Figure 10. Damage to Wing 2 from Test Condition 9

SDRC I-DEAS 3.4: Test Data Analysis   17-AUG-27 15:11:55

DATABASE: F-16 WING 2 MODAL TEST   UNITS = IN

Frequency response function

1X : 11.3
1Y : 577.2
2X : 12.2
2Y : 1286.3
3X : 40.6
3Y : 353.1
4X : 40.6
4Y : 585.6
5X : 59.0
5Y : 55.5
6X : 62.2
6Y : 134.1
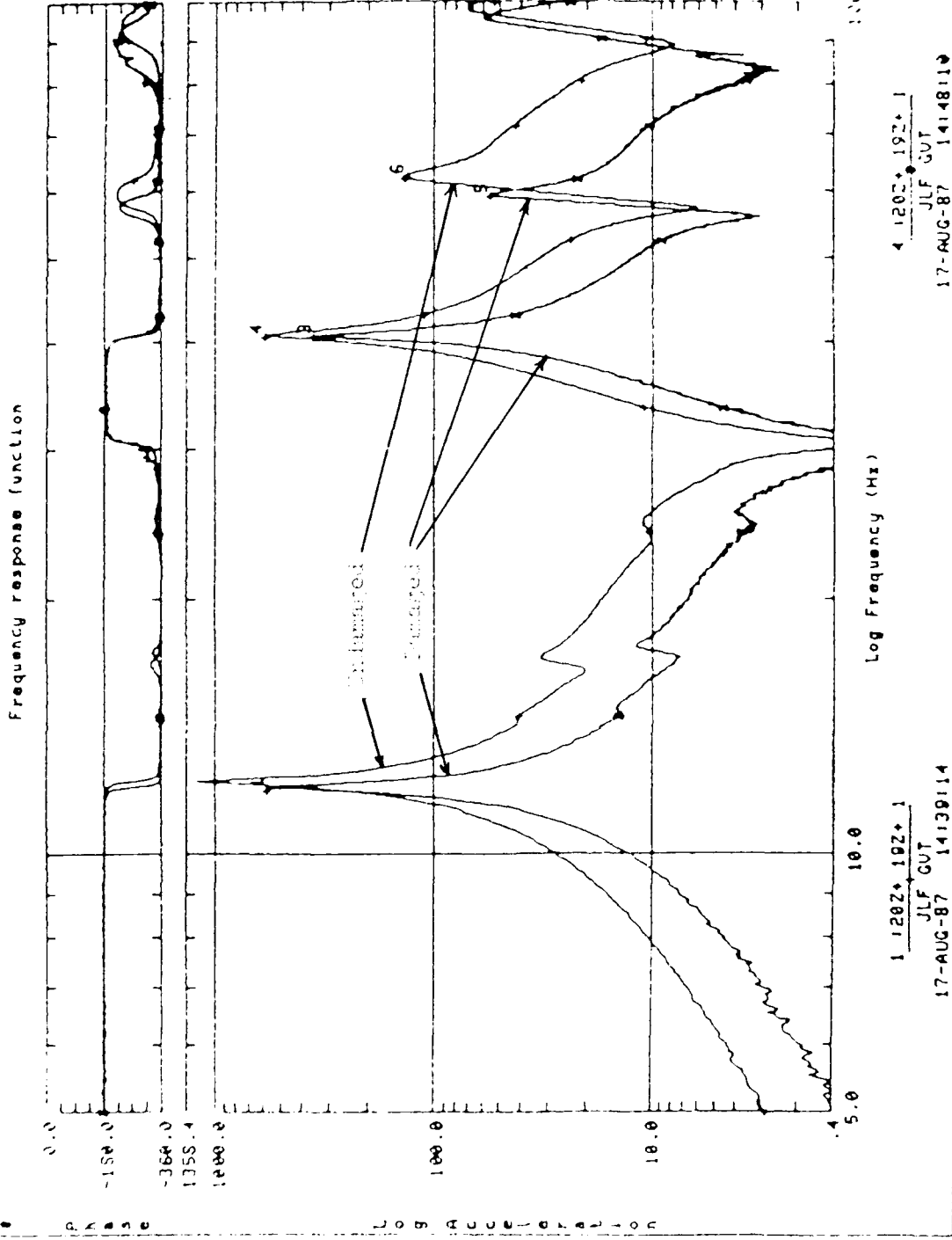
Log Frequency (Hz)
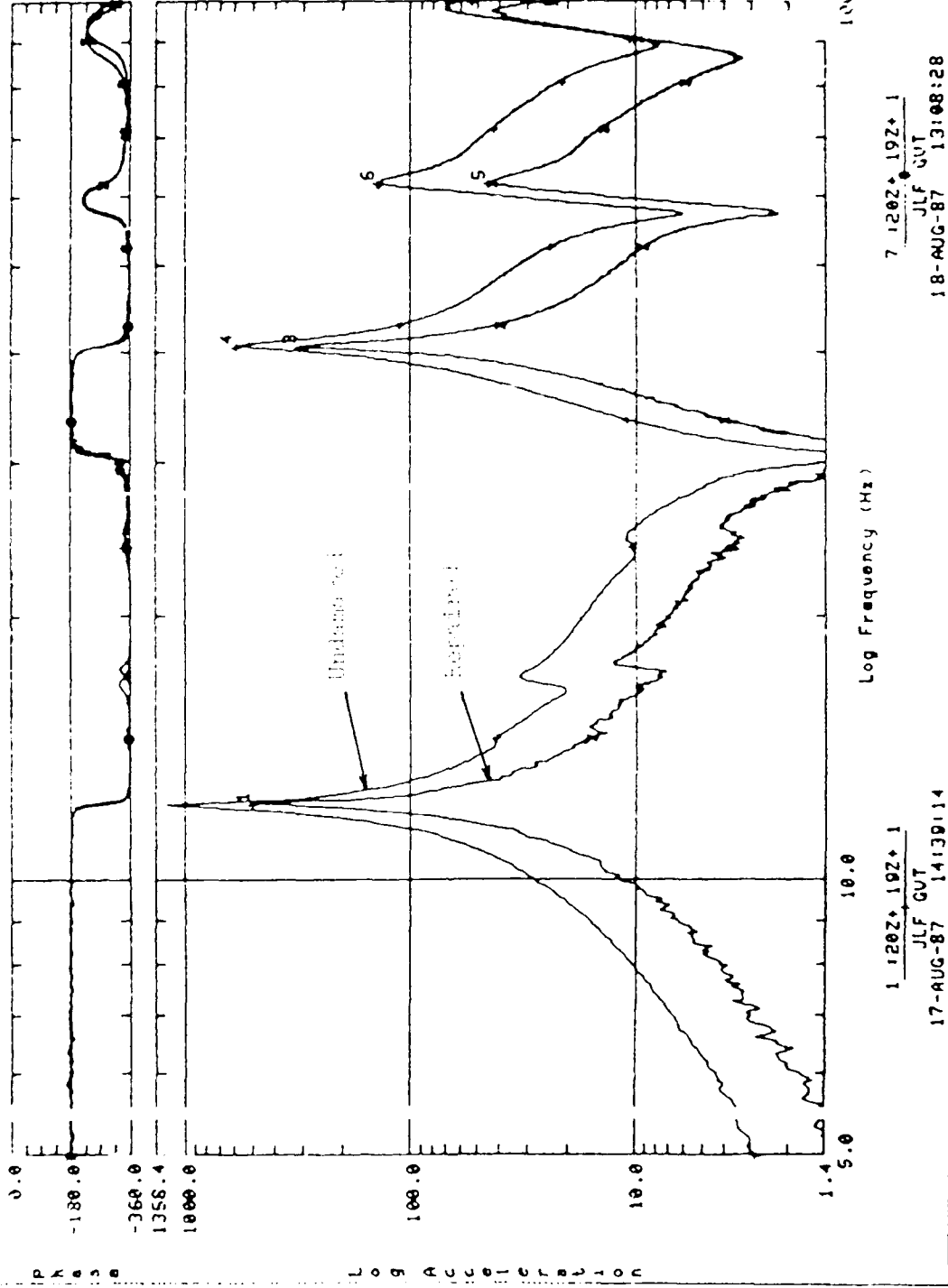
Figure 12. Overlay of THFs of Repaired Against Undamaged Wing 2

SDRC I-DEAS 3.4: Test Data Analysis   18-AUG-87   13:45::2

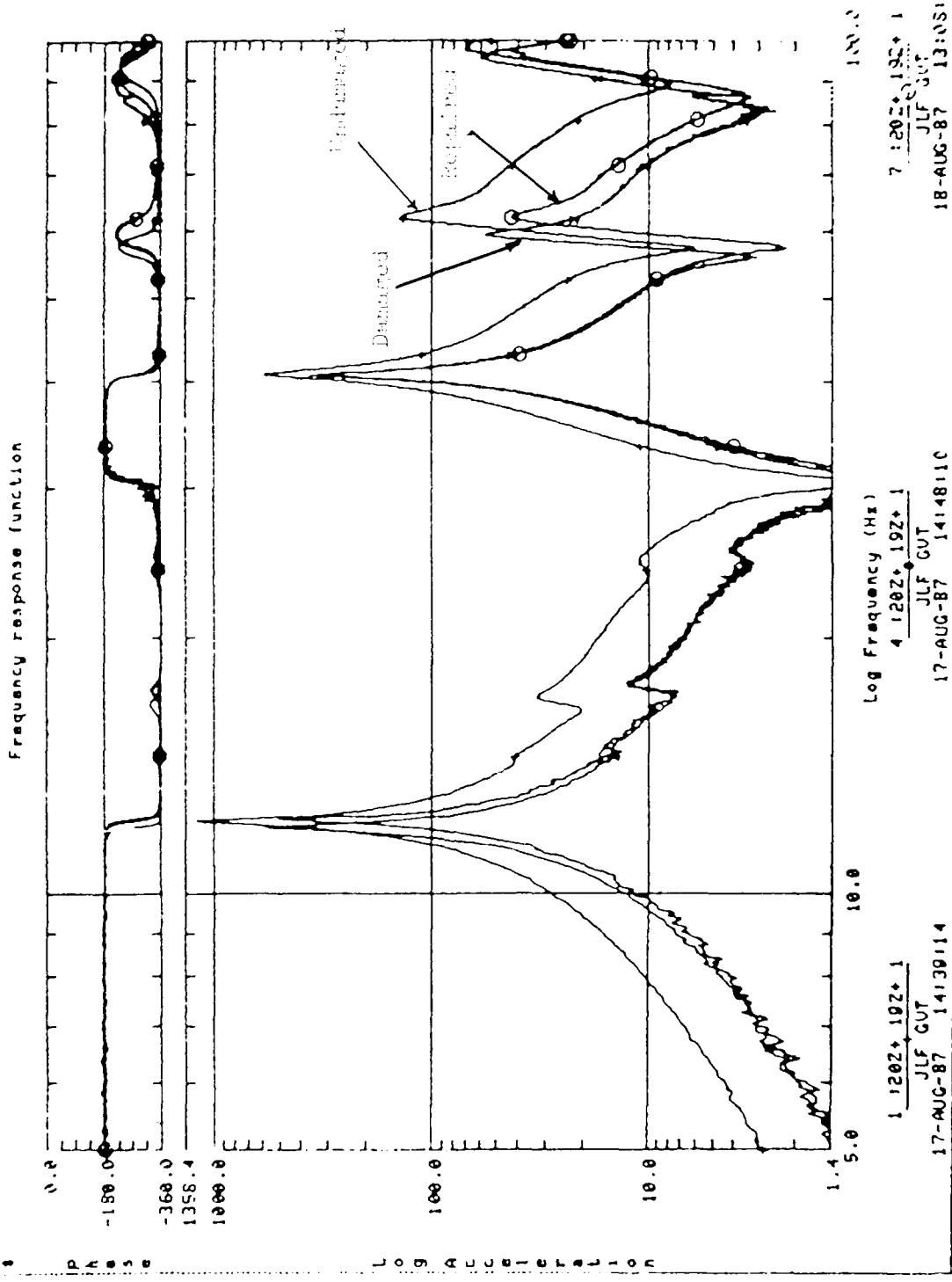DATABASE: F-16 WING 2 MODAL TEST   UNITS : IN
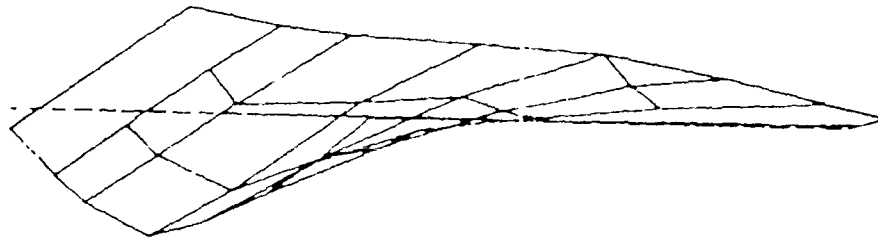
Frequency response function

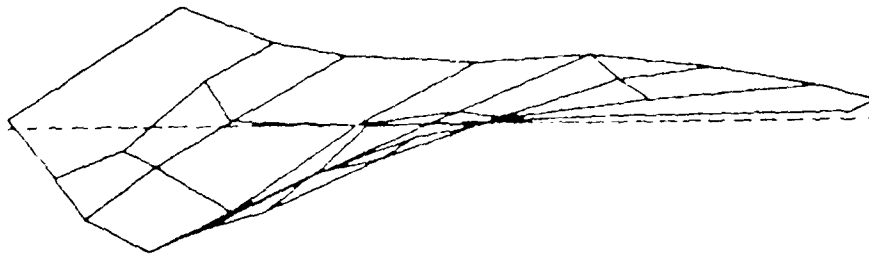Figure 4. RFFs of Undamaged, Damaged and Repaired Wing 2

a)

b)

Figure 84.   End View of First Torsion Mode   a)   Undamaged and Repaired Wing 2
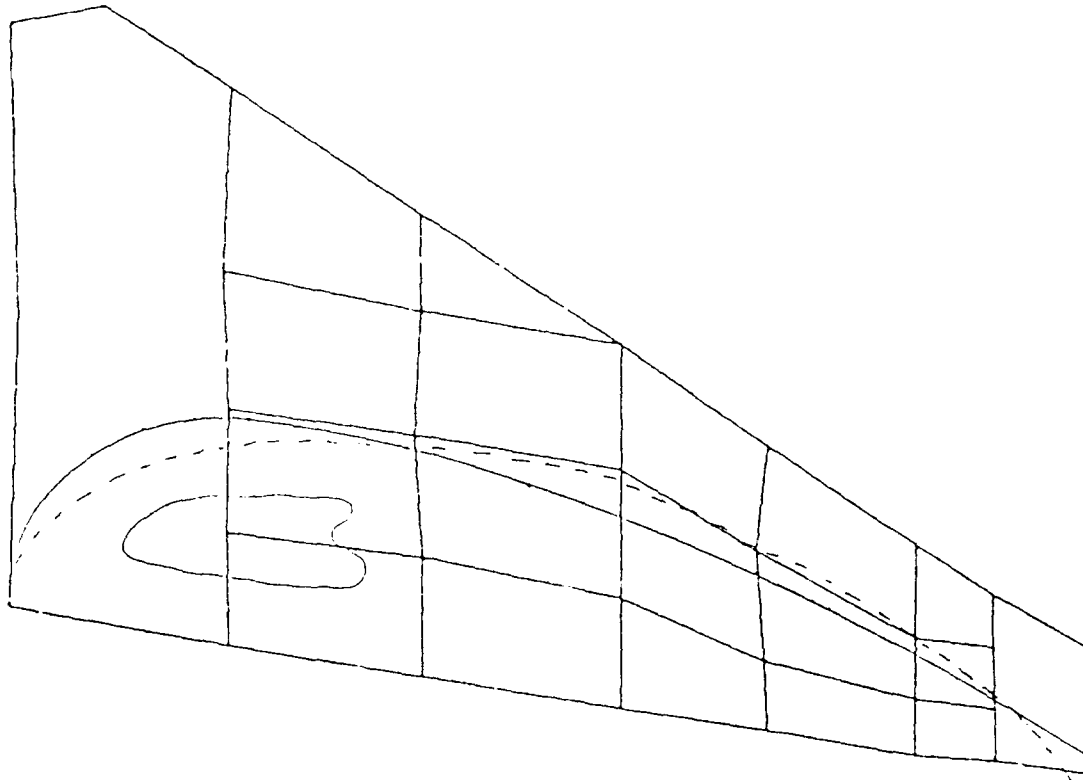
b)   Damaged Wing 2

Figure 15. First Torsion Node Lines

MODAL IDENTIFICATION USING SOLID ROCKET MOTOR STATIC FIRING DATA – A CASE WITHOUT KNOWING THE EXTERNAL EXCITATION

Craig F. Chang and Don Mason
Morton Thiokol, Inc.
Space Operations, P.O. Box 707
Brigham City, UT 84302-0707

The data from full-scale solid rocket motor (SRM) static test
is a valuable resource to assess and analyze the SRM behavior.
An attempt is made in this paper to identify the system
characteristics using the modal approach. In the theory
development, no requirement is necessary on the knowledge of
the input excitations. However, analyses are made based on
the assumption that the system is linear and satisfies the
second order differential equation.

INTRODUCTION

The Space Shuttle Solid Rocket Motor (SRM) manufactured by Morton Thiokol, Inc.
was static-fired in full-scale to test the SRM behavior. Accelerometers were
included among numerous instrumentation to observe the dynamic characteristic
of the SRM. The objective of the current paper is to perform a Space Shuttle SRM
system identification (ID) using static firing data.

In engineering analysis, it is usually necessary to begin with an abstract
mathematical model, which is based on certain assumptions. The accuracy of the
results of the analysis depends to a large extent on the choice of the
mathematical model. It is an unfortunate fact that the current knowledge in
choosing an accurate structural dynamic model seriously lags behind analysis
capabilities. Frequently, the results of the mathematical model are not in
sufficient agreement with the experimental data.

System identification is an attempt to obtain information about the model from
experimental data. This process has been likened to the "black box" problem in
which a mathematical description of the "black box" is sought from observations of
responses to known inputs. It seems to be a strongly intuitive notion that
meaningful information about a correct model for a system can be extracted from
these responses. In fact, it seems obvious that the more test data that can be
made available, the better the information will be provided about the model.

While the concept of attempting to identify a system from observations of its
input and output is an old issue, serious problems arise from the fact that many
input sources are essentially unknown, especially for aerospace structures. For
example, when the SRM is burning, which can be either during static firing or
flight, the dynamic input sources, (i.e., pressure, acoustic wave, etc.), are very
complex. Furthermore, the effects of those input sources and their correlation are

not well understood at our current stage of knowledge. Therefore, the only available information regarding the structural system is the output, which may be referred to as structural response. The question may be raised as to whether we can sucessfully identify the system characteristics, such as modal frequencies and damping values, using only the structural response data.

To answer this question, we first examine the relationships among input, output and the system itself. The conceptional drawing of this relationship is shown in Figure 1.

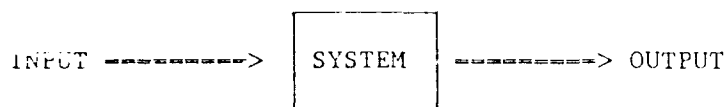INPUT ---------> | SYSTEM | =========> OUTPUT

Fig. 1 Input, Output, and Structural System Relationship.

Intuitively, from Figure 1, we can see that if we did not assume the specific form of the system, we have no way to figure out what the system looks like. The reason is obvious, since, if inputs are unknown and the system does not have any restriction, the output we observed could be arbitrary. The problem would be alleviated if we can restrict the parameters and the form of this system.

It is still a very difficult problem, at the present stage, to identify the system parameters given only the form of the system and the response measurements without knowing the inputs. In this paper, a method is developed to seek the SRM system parameters in the Morton Thiokol T-24 test stand by using only the dynamic response measurements obtained from the Demonstration Motor Number 8 (DM-8) static firing.

At present, numerous research efforts have been studied and presented in the advanced development phase. Nevertheless, most of the investigations were limited to the case where inputs were known. For example, the quite famous paper by Rodeman and Yao [1] gives an indepth discussion of five modal and four non-modal methods. Of particular interest is the discussion by Klosterman [2] which gives a rather complete development of the application of a modal technique. The survey by Hart and Yao [3] contains the most complete list of references in the recent structural dynamics parameter ID literature. They categorized the field into a time domain and frequency domain technique tree. In their general comments on system ID they present three standard approaches for modal parameter estimation defined as follows:

o   Least square - assumes measurements and structural parameters are deterministic.
o   Weighted L. S. - assumes measurements are stochastic (noisy) but structural parameters are deterministic.
o   Statistical Structural Identification - Assumes measuerments and modal parameters are both stochastic.

The method of random-decrement has been used recently for damage ID. [4] The method is mainly based on the ITD method, [5] which is a modal approach. Other papers discussed the modal approach for system ID are Raney, [6] Hasselman, [7] Berman and Flannely, [8] and Ibanez, [9] to name only a few.

MATHEMATICAL MODEL

The matrix differential equation that governs the SRM is given by

$$[m]\{\ddot{x}\} + [c]\{\dot{x}\} + [k]\{x\} = \{f(t)\} \qquad (1)$$

where $[m]$, $[c]$, $[k]$ are the system $N \times N$ mass, damping and stiffness matrices, respectively; the $\{\ddot{x}\}$, $\{\dot{x}\}$, and $\{x\}$ are the SRM acceleration, velocity, and displacement responses respectively; and $\{f(t)\}$ is the excitation forces. To arrive at Eq. (1), an assumption that the SRM behaves linearly during static firing was made. The linearity assumption allows us to use Eq. (1) to analyze the SRM locally as well as globally. Namely, $\{x\}$ can be the combination of either axial or tangential direction measurements.

Generally, the excitations, $\{f(t)\}$, to SRM structure during static firing are in complex nature. For example, the internal pressures, axial thrust, and acoustic field constitute the main excitation sources for SRM. Apparently, all these excitation sources are random. In view of the random characteristic of the excitation source, the force vector, $\{f(t)\}$ may be reasonably assumed as a vector random process. The assumption that the $\{f(t)\}$ is random, which results in $\{x\}$, $\{\dot{x}\}$, $\{x\}$ being random, can be seen from the response measurements. For instance, the radial acceleration measurements at the center field joint (A062) is plotted vs. time as shown in Figure 2. From Figure 2, the acceleration apparently behaves randomly and has a zero mean.
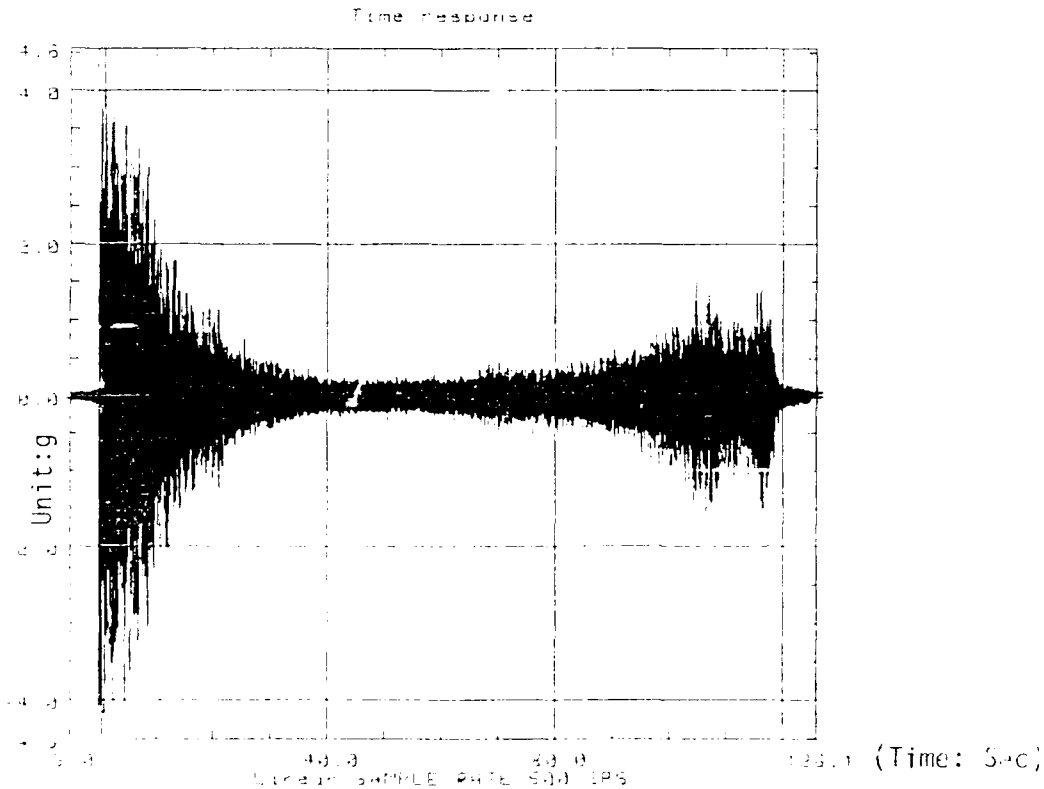

Fig. 2 The Time History for A062

It was mentioned earlier that {x} is mean zero, which will be demonstrated analytically later. The mean zero characteristic makes it convenient to analyze the stochastic differential equation Eq. (1) in a decomposed way. Without loss of generality we can let

$$\{p(t)\} = E[\{f(t)\}], \tag{2a}$$
$$\{u(t)\} = E[\{x(t)\}], \tag{2b}$$

$$\{F(t)\} = \{f(t)\} - E[\{f(t)\}] = \{f(t)\} - \{p(t)\}, \tag{3a}$$
$$\{Z(t)\} = \{x(t)\} - E[\{x(t)\}] = \{x(t)\} - \{u(t)\}, \tag{3a}$$

where $\{p(t)\}$, $\{u(t)\}$ are the mean characteristic of $\{f(t)\}$, $\{x(t)\}$, respectively; and $\{F(t)\}$, $\{Z(t)\}$ are the random component of $\{f(t)\}$, $\{x(t)\}$, respectively. From Eq. (3) it can be seen that $\{F(t)\}$, $\{Z(t)\}$ both are mean zero. Eq. (1) now can be rewritten using Eq. (2) and (3).

$$[m](\{\ddot{u}\}+\{\ddot{z}\})+[c](\{\dot{u}\}+\{\dot{z}\})+[k](\{u\}+\{z\}) = \{F(t)\}+\{P(t)\} \tag{4}$$

Taking the mathematical expectation on the above equation yields

$$[m]\{\ddot{u}\} + [c]\{\dot{u}\} + [k]\{u\} = \{P(t)\} \tag{5}$$

Subtracting Eq. (5) from (4) obtains

$$[m]\{\ddot{z}\} + [c]\{\dot{z}\} + [k]\{z\} = \{F(t)\} \tag{6}$$

It should be noted that Eq. (5) governs the mean response and Eq. (6) governs the random component of the SRM response. It is observed at this point that if $u = \dot{u} = 0$, Eq. (5) is reduced to the static case,

$$[k]\{u\} = \{P(t)\}. \tag{7}$$

The fact that $u = \dot{u} = 0$ is true for many situations. For example, consider a nonlinear oscillator governed by

$$m\ddot{x} + c\dot{x} + R(x) = f(t) \tag{8}$$

where $R(x)$ is the restoring force. If m and c are deterministic constants, the probability density function (PDF) of $\dot{x}$ and x is given by [10]

$$p(\dot{x},x) = C \exp\{-\dot{x}^2/\kappa_1 + \kappa_2 \int_0^x R(\xi)d\xi\} \tag{9}$$

for mean zero Gaussian white type excitation, where κ_1 and κ_2 are constants related to the parameters of m, c, and the correlation coefficient of $f(t)$, and the value of C is subjected to the normalization condition. Apparently, $\dot{x}$ is mean zero Gaussian distribution. This implies x is also mean zero.

We have demonstrated the mean zero characteristic of $\dot{x}$ and x. We will use this characteristic later to develop our model. Next, we need to analyze the random component, Eq. (6). The advantage of using Eq. (6) is that $\{F(t)\}$ is mean zero and is easy to analyze. Remember that [m], [c], and [k] all satisfy Eq. (5) and (6). Therefore, the system identification is preformed based on Equation (6). Since $\{F(t)\}$ now is mean zero, we can use the random-decrement technique to further reduce Eq. (6). The random-decrement technique [4] is discussed as follows.

The concept of random-decrement technique was initially presented by Henry Cole [11]. Consider Eq. (6) which is valid for any time t and any set of initial conditions. Replacing time t with the expression $t_i+\tau$, where the t_i's are selected according to the method of triggering the start of the ensembles for the random-decrement computations, then Equation (6) can be rewritten as

$$[m]\{\ddot{z}(t_i+\tau)\} + [c]\{\dot{z}(t_i+\tau)\} + [k]\{z(t_i+\tau)\} = \{F(t_i+\tau)\}, \quad i = 1,\cdots M \qquad (10)$$

where M is the number of averages intended for use in random-decrement computation. By summing all of the M equations, dividing by M, and replacing $1/M \sum\{z(t_i+\tau)\}$ by $\{y(\tau)\}$, the resulting summation can be written as

$$[m]\{\ddot{y}(\tau)\} + [c]\{\dot{y}(\tau)\} + [k]\{y(\tau)\} = \frac{1}{M} \sum_{i=1}^{M} \{F(t_i+\tau)\} \qquad (11)$$

It should be noted that since the t_i's were selected according to a specific random-decrement triggering criteria, the resulting response $\{y(\tau)\}$ will not average to zero. Now considering the right hand side of Eq. (11). If $\{F(t)\}$ is a stationary random signal, then

$$\frac{1}{M} \sum_{i=1}^{M} \{F(t_i+\tau)\} = 0 \qquad (12)$$

and Eq. (11) becomes

$$[m]\{\ddot{y}(\tau)\} + [c]\{\dot{y}(\tau)\} + [k]\{y(\tau)\} = 0 \qquad (13)$$

Eq. (13) implies that $\{y(\tau)\}$ is a free-decay response that results from applying random-decrement to random response due to a force vector, $\{F(t)\}$, which is a random signal with mean zero. It should be noted that the mass, damping, and stiffness matrices all satisfy Eq. (1), (6), and (13). In obtaining $\{y(\tau)\}$ it should be noted that $\{z(\tau)\}$ is identical to $\{x(\tau)\}$, since $\{u(t)\}$ is zero.

We have shown an important result. Namely, the acceleration measurements obtained from an operational random vibration response satisfy a stochastic equivalent structural system, Eq. 6, which can be reduced to a free vibration system Eq. (13) using random-decrement technique. The system ID then can be performed based on the free vibration response where the excitation is essentially eliminated. Since $\{y(\tau)\}$ is free decay, the system ID can be readily performed by using, for example, Ibrahim time domain (ITD) method.
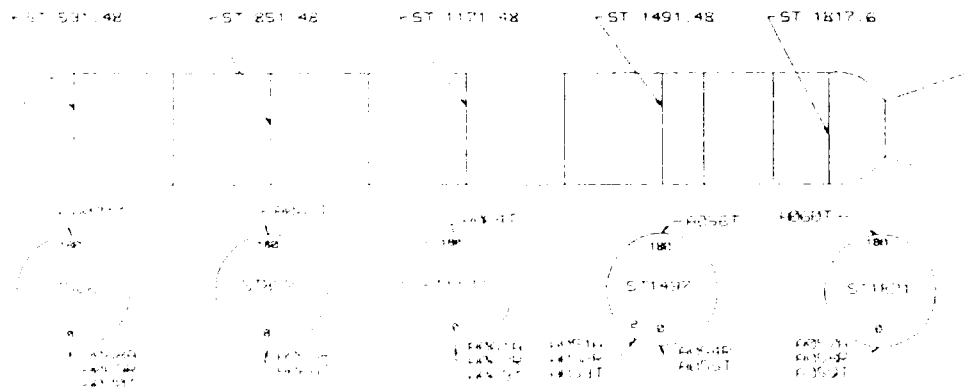

Figure 3 The Location of Accelerometer

CONFRONTING THE STATIC FIRING DATA, DM-8

The theory developed in the previous section is very useful for the study of the dynamic behavior of SRM during firing. There were a total of 18 acceleration channels installed along the case on DM-8. The location of each accelerometer is shown in Figure 3. Those accelerometers enable us to monitor the modal characteristic change during the static firing by using the theory developed previously.

To monitor the vertical bending behavior of the motor, the accelerometers mounted in the radial direction were selected. From Figure 3, these were A054, A058, A062, A065, A069, which enable us to identify the bending modes up to the second order. The data were first read from tapes and then assembled to form the matrix [x]. Three different time periods are chosen. Namely, 0 to 10 sec., 50 to 60 sec., and 110 to 120 sec. The sample rate of the data were 2000 samples/sec. Therefore, the size of matrix [x] was $5 \times 20,000$ for vertical bending.

To form the matrix $\{y(\tau)\}$, the triggering criterion is selected at every positive crossing (from negative to positive) for channel A054. Such selection gives us approximately 1200 of averages. The results of $\{y(\tau)\}$ for Channel A054 were shown in Figures 4 through 6 for three different time intervals as mentioned earlier. It can be seen from those figures that the frequency of $y(\tau)$ during the end of burn is obviously higher than after ignition since the decrease of propellant.

The modal frequencies and damping ratios were then computed using the ITD method. The modal frequencies for the first bending are shown in Figure 7 for three different periods as mentioned earlier. It can be seen that the first bending frequency is about 1.8 Hz, which is close to the frequency before firing (1.86 Hz) obtained from the recent RM-1 modal survey. As time increases, the frequency also increases due to the decrease of propellant. The damping ratio generally shows a large variation by using the ITD method. The result showed that the damping ratio was between 0.5 and 3 percent.

Similar steps are repeated for tangential directions. The result was shown in Figure 8. The first tangential frequency is about 1.9 Hz, which is close to the frequency before firing (1.9 Hz) obtained from the recent RM-1 modal survey.

CONCLUSIONS

The following conclusions can be drawn in accordance with the above analyses and discussions.

(1) The mean displacement responses can be computed using quasi-static analysis.
(2) The random component responses must be analyzed dynamically.
(3) The response time histories show that the SRM responds non-stationarily during the burn. Therefore, analyses were performed by selecting small interval data.
(4) The random characteristics of the SRM, especially the propellant, were ignored. The inclusion of those random characteristics would result in the mean displacement response vector {u} being nonzero [12]. In such case, the force vector cannot be eliminated.
(5) If the locations of the accelerometer were far apart, it would cause the random-decrement response {y(τ)} to have an ill condition. The reason is that

the cross correlation is small if two responses are far apart. Such ill condition causes the tangential bending frequency to have large error.

REFERENCES

1. Rodeman, R., Yao, J. T. P., "Structural Identification Literature Review," School of Civil Engineering, Purdue University, CE-STR-73-3, December 1973.

2. Klosterman, A. L., "On the Experimental Determination and Use of Modal Representatives of Dynamic Characteristics," PH.D. Dissertation, University of Cincinnati, 1971.

3. Hart, G. C., Yao, J. T. P., "System Identification in Structural Dynamics," ASCE Journal of the Engineering Mechanics, Vol. 103, No. EM6, pp. 1089-1104, December 1977.

4. Ibrahim, S. R., "Incipient Failure Detection from Random-Decrement Time Domain," Random Vibration, ASME AMD-VOL. 65, ed. by P. D. Spanos and T. C., Huang, December 1984.

5. Ibrahim, S. D., Mikulcik, E. C., "A Method for the Direct Identification of Vibration Parameters from the Free Response," The Shock and Vibration Bulletin, Bul. 47, 183-198, September 1977.

6. Raney, J. P., "Identification of Complex Structures Using Near-Resonance Testing," The Shock and Vibration Bulletin, No. 38, August 1968, pp. 23-32.

7. Hasselman, T. K., "Method for Constructing a Full Modal Damping Matrix from Experimental Measurements," AIAA Journal, April 1972, pp. 526-528.

8. Berman, A., Flanneley, W. G., "Theory of Incomplete Models of Dynamic Structures," AIAA Journal, Vol. 9, No. 8, September 1971, pp. 1481-1487.

9. Ibanez, P., "Identification of Dynamic Structural Modes from Experimental Data," UCLA Engineering Report, UCLA-ENG-7225, March 1972.

10. Lin, Y. K., Probabilistic Theory of Structural Dynamics, pp. 264, McGraw Hill, Inc., 1967, Published by Robert E. Krieger Publishing Company, Inc.

11. Cole, H. A. Jr., "On-line Failure Detection and Damping Measurements of Aerospace Structures by Random Decrement Signature," NASA Cr. 2205, March 1973.

12. Chang, F. C., Ju, F. D., "On the Correlation Between Energy and Deformation," Advanced Topics in Vibrations, ASME DE-Vol. 8, pp. 67-75, January 1988, ed by T. C. Huang.
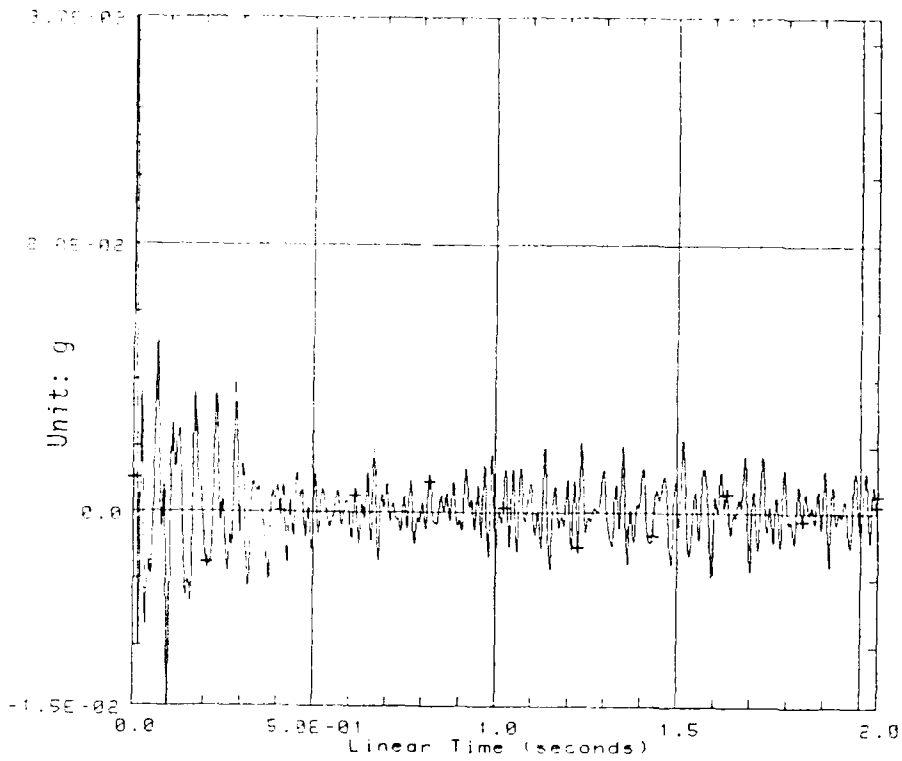
Figure 4 The Random-Decrement Response of A054 Using
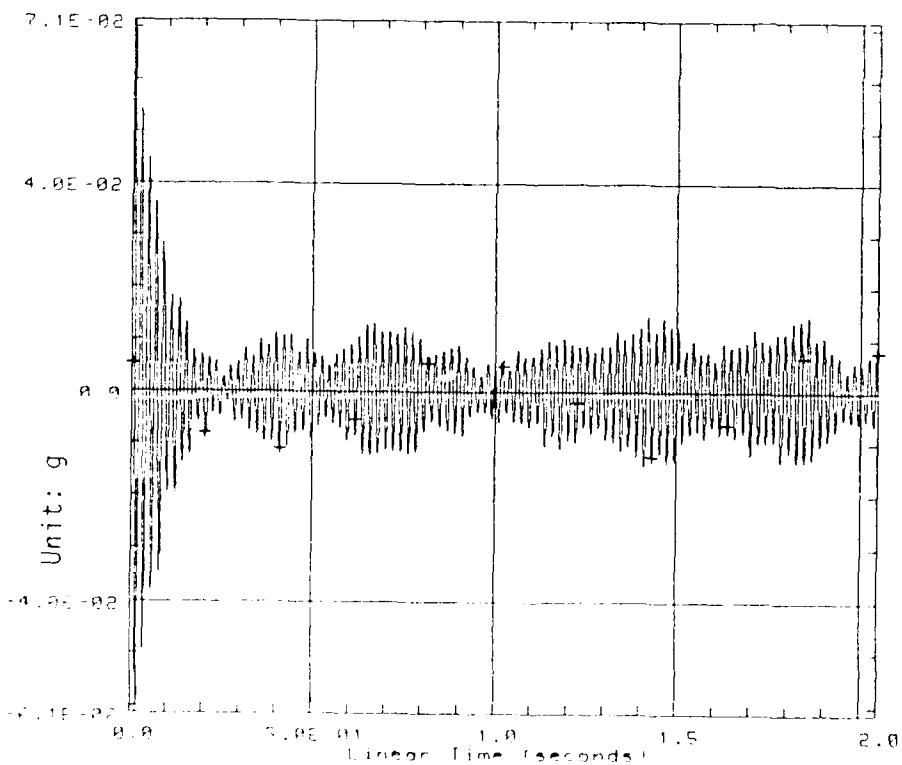Data from Time Interval 0 to 10 second.

Figure 5 The Random-Decrement Response of A054 Using
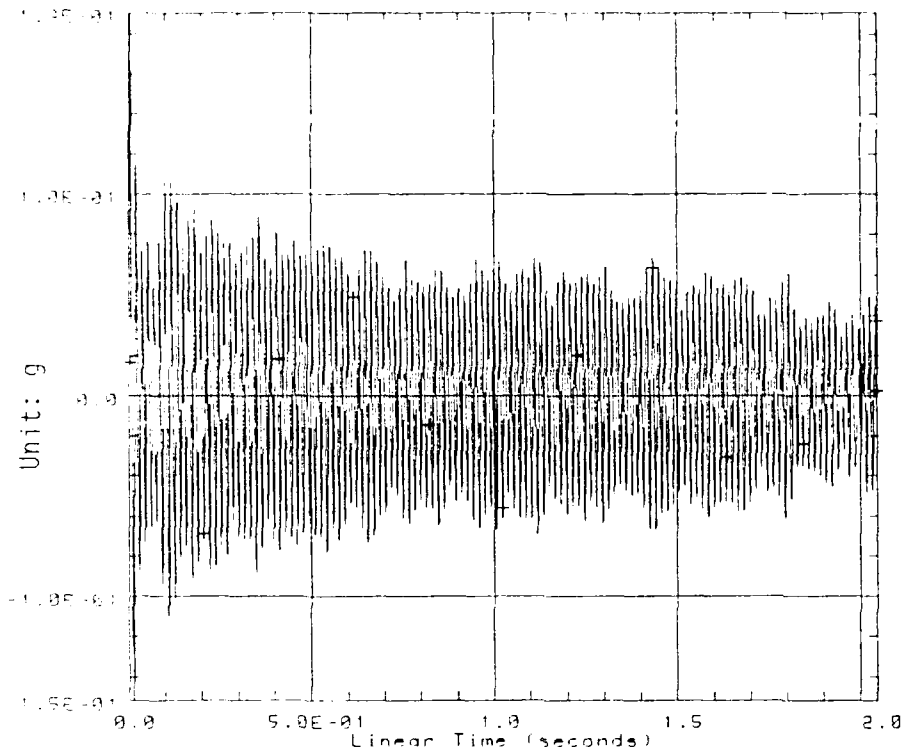Data from Time Interval 50 to 60 Second.

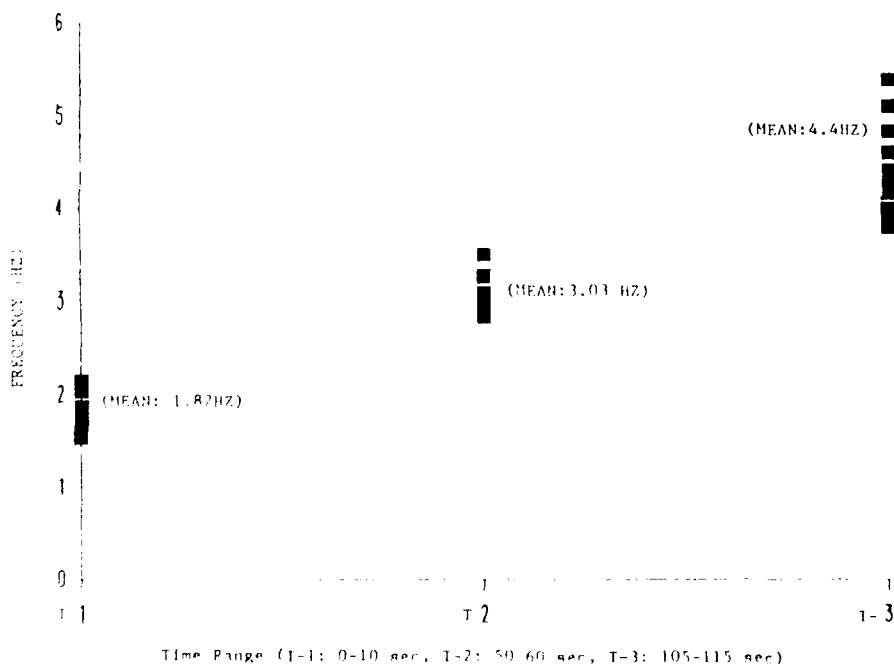Figure 6 The Random-Decrement Response of A054 Using Data from Time Interval 105 to 115 Second.

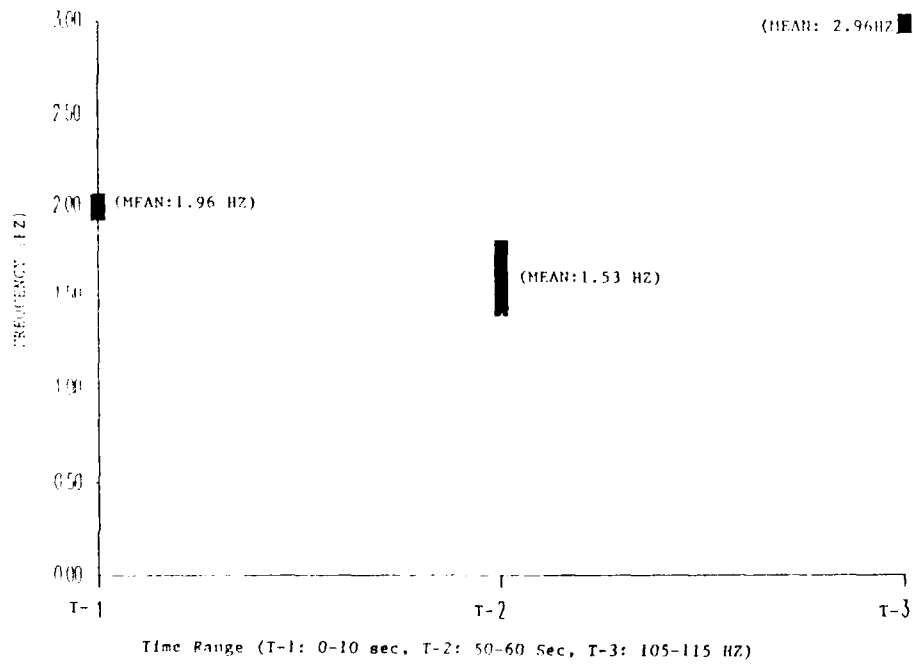Figure 7 The first vertical bending frequency.

Figure 8   The First Tangential Bending Frequency

NONLINEAR SYSTEMS IN VIBRATION

Elton G. Endebrock and Norman F. Hunter, Jr.
Dynamic Testing Section
Group WX-11, Mail Stop C-931
Los Alamos National Laboratory
Los Alamos, NM 87545

Algorithms for the analysis and control
of linear dynamic systems are relatively well
developed. For nonlinear systems similar
algorithms are in a relatively primitive state
of development. This paper reviews the current
state-of-the-art of nonlinear analysis in
several major areas of research, including
state space modelling, force surface mapping,
and higher order spectral estimation.
Applications of these techniques are
illustrated, and suggestions are made for
future work.

INTRODUCTION

The theory and experimental application of vibration
testing concepts is well developed for linear dynamic systems.
While systems that are approximately linear are extremely common
in vibration testing, a significant percentage of the systems
tested exhibit nonlinear characteristics. Methods for the
characterization, analysis, and control of nonlinear systems
have been developed to a limited degree. Nonlinear systems
have a rich spectrum of response characteristics which show
fundamental differences from those of linear systems. Such
characteristics may offer potential design advantages. In this
paper we summarize fundamental characteristics of nonlinear
systems which differ significantly from those of linear systems,
define some analytical and experimental methods of dealing with
nonlinearity in the types of dynamic systems often encountered
in vibrations, and illustrate the application of several of
these techniques with examples of current experimental and
analytical work. We conclude by suggesting directions for
future research.

FUNDAMENTAL SOURCES AND TYPES OF NONLINEARITY

Nonlinear behavior of dynamic systems arises in a variety
of ways. One common source of nonlinearity is nonlinear material
properties. Geometric nonlinearities also occur, where the

nonlinearity is due to geometric properties such as large
deflections. An attempt has been made to classify nonlinear
systems based on the relationship between force and
displacement. In a linear system the restoring force is
proportional to displacement. In nonlinear systems restoring
force is not strictly proportional to displacement.
Nonproportional restoring forces may be caused by nonlinear
damping or nonlinear stiffness terms. The nonlinear stiffness
terms may be elastic or plastic. In a nonlinear elastic system
the force-displacement characteristic follows the same path
whether loading or unloading. In a plastic, or hysteretic,
system, the force-displacement characteristics differ depending
on whether loading or unloading is in process. Typical force-
displacement relationships for linear, nonlinear elastic
hardening, and nonlinear plastic (hysteretic) systems are shown
in Figure 1. Gaps between parts of a dynamic system may cause
nearly instantaneous changes in stiffness as the gaps open and
close (Figure 1d).

(a) Linear System

(b) Elastic Hardening
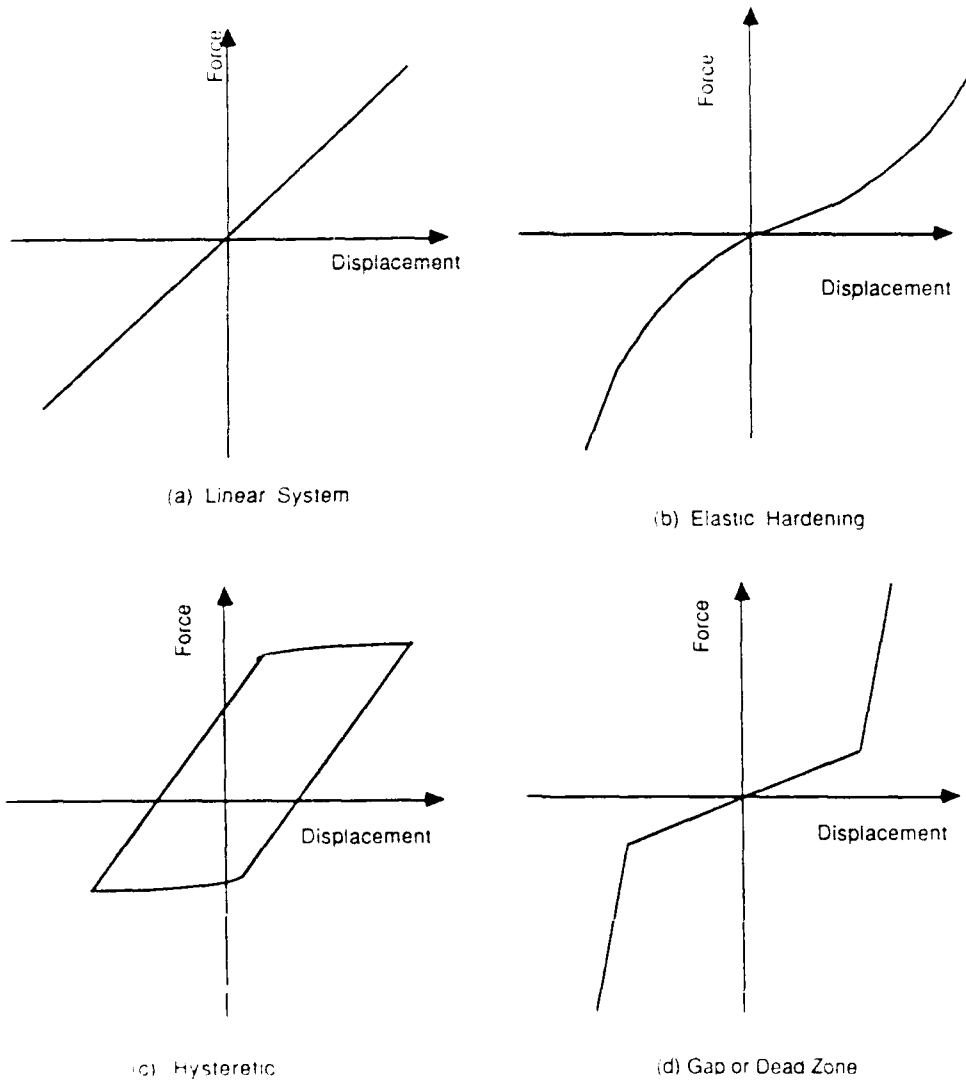
(c) Hysteretic

(d) Gap or Dead Zone

Figure 1
Typical Force-Displacement Characteristics
of Linear and Nonlinear Systems.

Nonlinear behavior may also arise because of relative movements between parts of a system combined with friction as in the case of sliding interfaces or slippage at bolted joints. Friction produces nonlinear behavior in a manner similar to that for a hysteretic system. Nonlinear damping occurs in a variety of contexts and the severity of its effects varies from systems with mildly nonproportional damping to systems with negative damping as described for a second order system by the Van der Pol equation [12].

FUNDAMENTAL PROPERTIES OF NONLINEAR SYSTEMS

A number of the basic properties of nonlinear systems differ fundamentally from those of linear systems [1]. Some of the major characteristics of nonlinear systems, in comparison to those of linear systems are summarized in Table 1:

Table 1
Some Fundamental Characteristics of Linear
and Nonlinear Systems.

Linear Systems	Nonlinear Systems
Described by ordinary or partial differential equations with constant or time varying coefficients.	Described by ordinary or partial differential equations whose coefficients are functions of the independent or dependent variables.
Described by linear difference equations with constant or time varying coefficients.	Described by nonlinear difference equations whose coefficients are functions of the dependent or independent variables.
Steady state sinusoidal excitation implies sinusoidal response at the at the excitation frequency.	Sinusoidal excitation does not imply sinusoidal response
The response at a frequency f_1 is is caused by the input at frequency f_1.	The response at frequency f_1 is caused both by inputs at f_1 and at frequencies other than f_1.
Superposition holds, i.e., if the response due to an input I_1 is R_1 and the response due to a second Input I_2 is R_2 then the response due to both I_1 and I_2 is $R_1 + R_2$.	Superposition does not hold, the response due to $I_1 + I_2$ may drastically differ from $R_1 + R_2$.
Spectral response peaks occur at resonant frequencies.	Spectral response peaks occur in conjunction with limit cycles.

Analysis of systems defined by linear differential or difference equations is well developed [13]. In contrast nonlinear differential or difference equations cannot generally be solved in closed form. Consequently numerical solution techniques are applied to yield estimates of the response. One of the most basic results of numerical analysis, and of experimental work, is the familiar form of the response of a mildly nonlinear system excited by a sine wave shown in Figure 2. Here the system response is primarily composed of the fundamental and the third harmonic of the excitation signal. Harmonic distortion is a common result of nonlinearity but the response of nonlinear systems is not limited to harmonic distortion. Subharmonics of the excitation may occur, as with a parametrically excited beam. Further, nonlinear dynamic systems are capable of exhibiting chaotic behavior[2]. An example of such behavior is shown in Figure 3, where a single-degree-of-freedom nonlinear system responds chaotically to a sinusoidal input. Nonlinear systems are capable of generating band limited white noise when driven with a sinusoidal input.
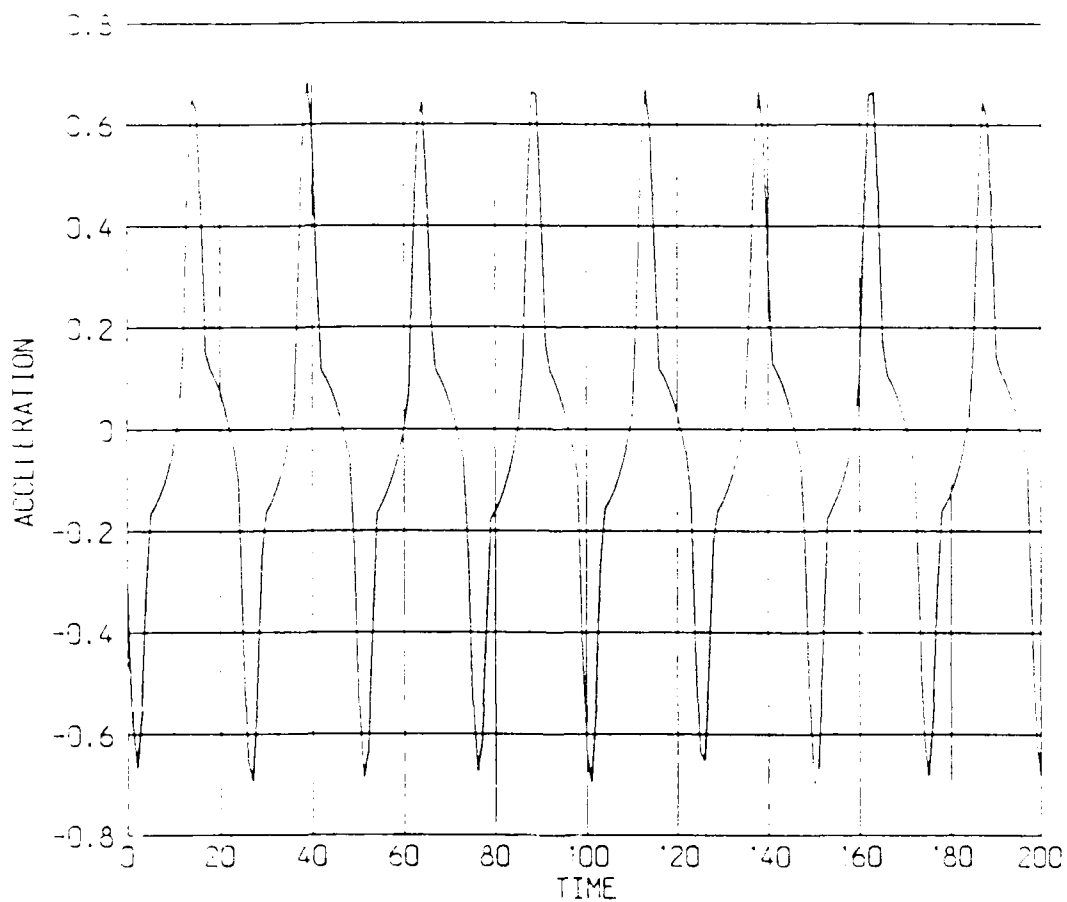

Figure 2

Response Time History of a Nonlinear System
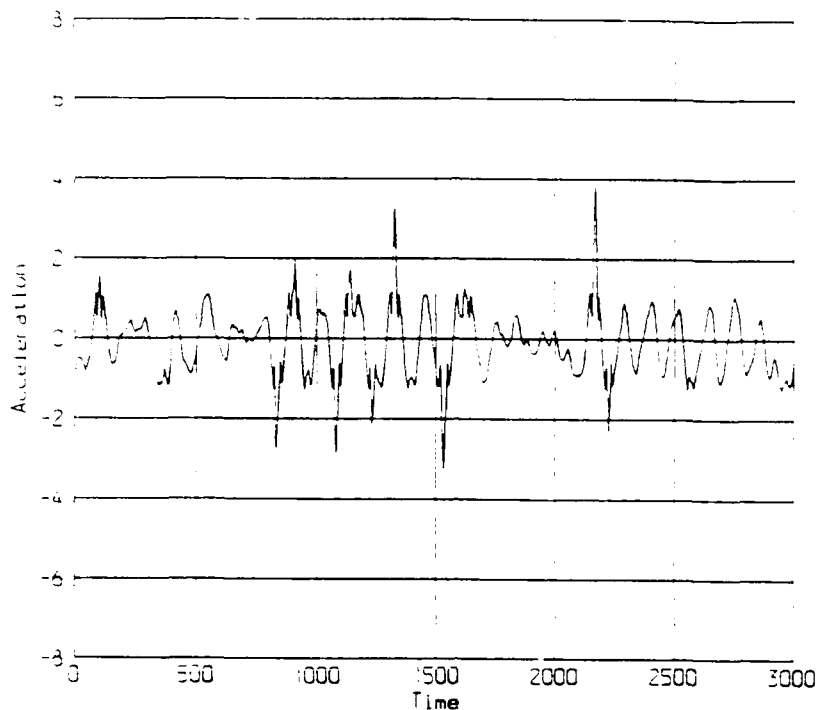Excited by a Sinusoidal Input.

Figure 3

Response Time History of a Chaotic System
to a Sinusoidal Input.

The harmonic generating properties of nonlinear systems have
led to time domain representations such as the Volterra and
Weiner series [14] and to multidimensional frequency domain
representations like the bispectrum [4] , Volterra Functions, or
Harmonic Generating Transfer Functions [3].   All of these
techniques quantify the amount of spectral energy transferred
from an input frequency to a response frequency.   As illustrated
in Figure 4, for a linear system, at a given frequency, the
response and input are related by the expression:

$$R_i = H_1 X_i \tag{1}$$

For a nonlinear system, the response and input are related
through expressions of the form:

$$R_i = \sum_{j=0}^{i=N} H_{1,j} X_j \tag{2}$$

Here X is the input frequency and R is the response frequency. For the nonlinear system the magnitude and phase of the response frequency is represented as a summation of contributions from many input frequencies. Typically Volterra systems are based on an expansion of the systems stiffness in a polynomial form. When this form of stiffness is transformed into the frequency domain it results in a convolution of Fourier Transforms [14]. For a Volterra system, the response at R is caused by sets of input frequencies whose sum equals the response frequency. In a harmonic generating transfer function (HGTF) model the response at a given frequency may be caused by any combination of input frequencies, without restriction. At this time no clear proofs are available to distinguish between cases where one or the other model is to be preferred.

$$R_i = H_1 X_1 \qquad\qquad R_i = \sum_{j=0}^{j=N} H_{1j} X_j$$
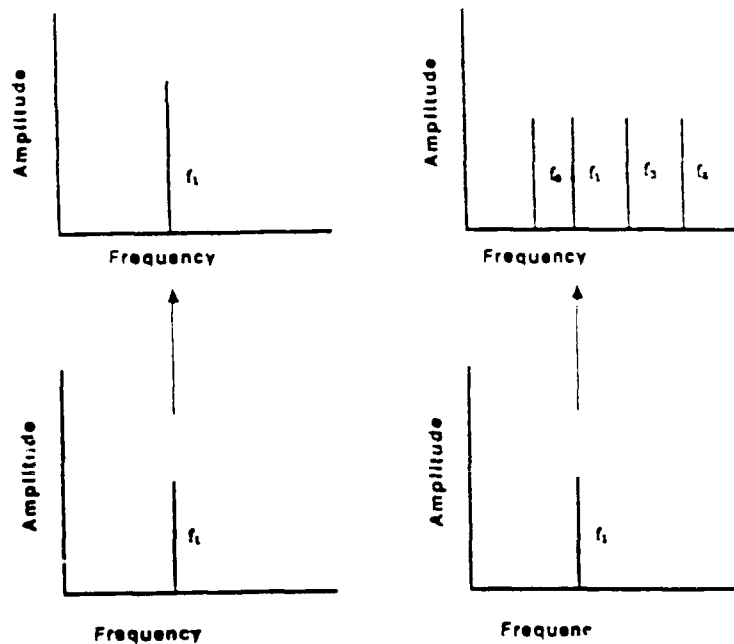
(a) Linear System   (b) Nonlinear System

Figure 4

Frequency Generating Characteristics of
Linear and Nonlinear Systems.

One of the most subtle features of nonlinear systems is the failure of superposition. Whenever analysis of a nonlinear system is attempted, care is required to avoid inadvertent use of the principle of superpositon. It is very natural (and incorrect) to imply that the response of a nonlinear system to a combined excitation at 10 Hz. and 30 Hz. is the sum of the responses of the system to the individual applications of the inputs at these frequencies.

Resonances occur in a linear system. In a nonlinear system resonant behavior may occur, but in addition, a phenomena known as a limit cycle may appear. A limit cycle is best represented in a state space formulation and may occur at frequencies not directly related to a ratio of mass and stiffness.

INVESTIGATIONS OF NONLINEAR SYSTEMS

Objectives

The general objectives of investigations into nonlinear behavior of systems are quite similar to those for linear systems and may be classified as follows:

1. Characterization- The goal of system characterization is the classification a given system's behavior as belonging to a certain category, i.e., nonlinear elastic hardening, plastic softening, etc.

2. Modeling and Prediction- Given a nonlinear system and its response to a certain class of inputs, the goals of modeling and prediction require building a conceptual quantitative model which describes the system, including prediction of the systems response to future inputs. Such modeling may also involve determination of the number of parameters necessary to optimally describe the systems behavior and subsequent calculation of parameter values.

3. Control- In vibration testing the control of a nonlinear system implies synthesis of the input required to produce a given response waveshape or a given response spectral density at a defined system response point.

Each of these objectives is currently a topic of extensive research. Some progress has been made on each of these three problems, particularly problems 1 and 2, but optimal methods of approach are far from clear.

Methods of Modeling Nonlinear Systems

Numerous techniques for dealing with nonlinear systems exist. A summary of these methods includes:

1. Empirical approaches.

2. Modeling of the differential equations.

3. Force State Mapping.

4. Hilbert Transforms.

5. Methods based on state space models.

6. Spectral Methods based on higher order frequency response functions.

In empirical approaches, we simply pick a quantative representation of some type of nonlinearity, numerically solve the differential equation(s) describing the systems behavior, and attempt to generalize the results to some classes of systems driven by certain forms of excitation[6]. Such methods may provide useful insight but do not in general allow quantiative response prediction, system modeling, or control.

Determination of the parameters of the differential equation is currently a very active field of research. A form of the systems differential equation is assumed and various techniques are used to fit parameters to the model[7,8]. This approach provides quantiative information regarding the systems behavior and may be adaptable to system control. A disadvantage is that the form of the differential equation or equations must be assumed prior to estimation.

In force state mapping, system acceleration responses are integrated to obtain relative velocities and displacements. Restoring forces are plotted as a function of velocities and displacements to define surfaces whose parameters define the systems damping and stiffness[8]. In the author's opinion this technique is approaching a viable model for many types of nonlinear systems. This model may be extended to provide system response predictions.

Hilbert Transforms[9] rely on the relationship between the real and imaginary parts of a frequency response function of a causal system as a means of detecting nonlinearity. When the transfer function of a nonlinear system is determined using sinusoidal excitation, a distortion occurs where energy is discarded at points of harmonic generation. This distortion introduces an apparent noncausality in the impulse response function which may be detected through use of Hilbert Transforms. The particular form of this distortion serves as the basis for a classification scheme of nonlinear systems.

Higher order frequency response functions have been described above. Their use potentially quantifies the response of nonlinear systems in the frequency domain and can lead to methods of response prediction and response control.

State Space Models have been investigated extensively in control theory and are currently a very active field of research [5,15]. Generally such models attempt to describe a systems behavior (whether linear or nonlinear) as a function of current and past inputs and past outputs. This is essentially a difference equation formulation. As such they are well adapted to computer modeling and offer some promise for the development of prediction and control methods.

In some sense, all of the above methods are related, as the state space models and higher order frequency response functions are derived from the differential equations defining the system. Some specific examples of these methods which are currently active fields of research in the Dynamic Testing Section at Los Alamos National Laboratory will now be described.

Empirical Methods

As an example of an empirical method, consider a single-degree-of freedom system with a bilinear spring. The differential equation describing such a system is of the form:

$$(3)$$

$$MX'' + CX' + K(X) X = F(t)$$

    where M = the system mass.
          C = system damping coefficient.
          K(x) = the restoring force matrix as a function of X.
          F(t) = the applied force.

In the bilinear case, as defined in this paper, the restoring force in tension differs from that in compression. A typical restoring force-displacement curve for a bilinear spring is shown in Figure 5 where, C' defines the ratio of restoring force in tension to that in compression.
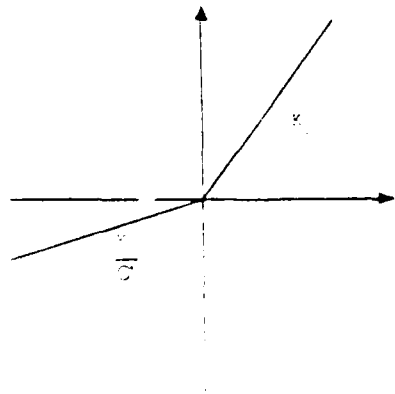
Force-Displacement Relationship for a Bilinear Spring.

Figure 5

The time history responses of a four-degree-of-freedom base
excited system in which only the base stiffness is bilinear is
shown in Figure 6 for different values of C'. Distortion of the
time history for large values of C' (C' =20.0) is evident in
Figure 6. Note that for moderate values of C' (between 1.0 and
2.0, 1.0 being a linear system) that no drastic effects appear
in the time history response. The frequency response functions
for the bilinear system are shown in Figure 7.

Figure 6

Time History Responses of a Multi-Degree-
of-freedom System with a Bilinear Spring
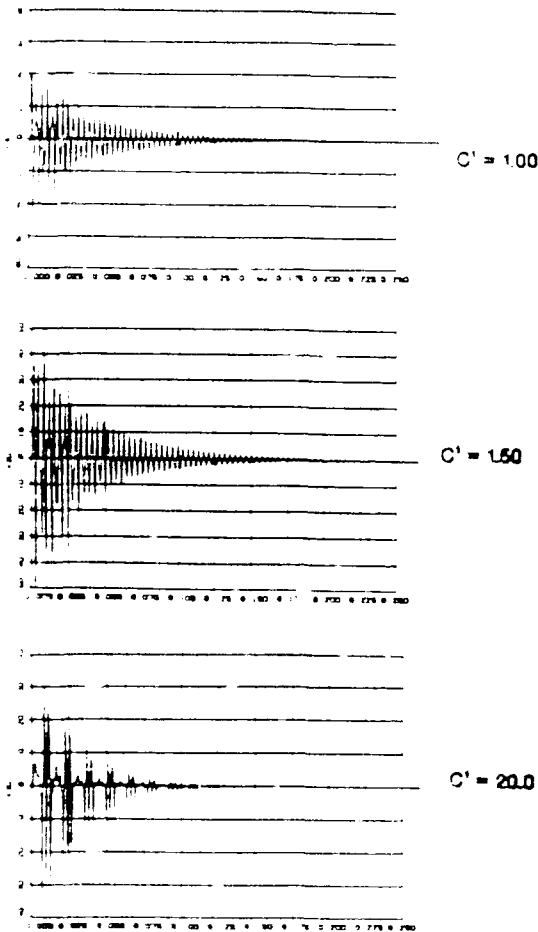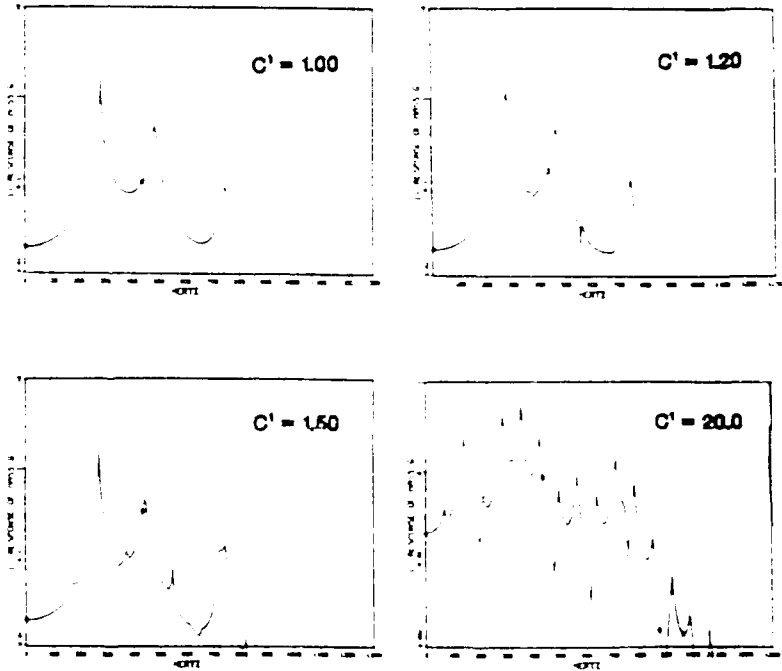Excited by a Force Impulse.

C' = 1.00

C' = 1.50

C' = 20.0

Figure 7

Frequency Response Functions
for a Bilinear System.

C' = 1.00

C' = 1.20

C' = 1.50

C' = 20.0

These frequency response functions show analomies which become progressively more prominent as the value of C' increases. Note that a single bilinear stiffness in a multi-degree-of-freedom system changes all of the systems resonant frequencies as it changes from tension to compression since a change in the value of a single stiffness term changes the eigenvalues of the entire system.

A typical time history and frequency response function are shown in Figure 8 for a system with a dead zone excited by a force impulse.
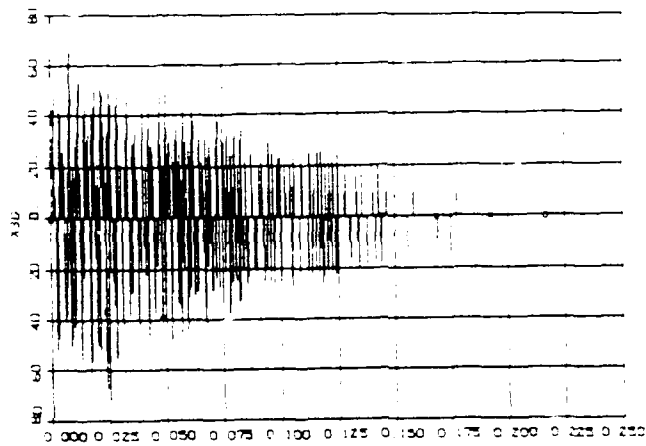

Figure 8a

Impulse Response Time History of a System
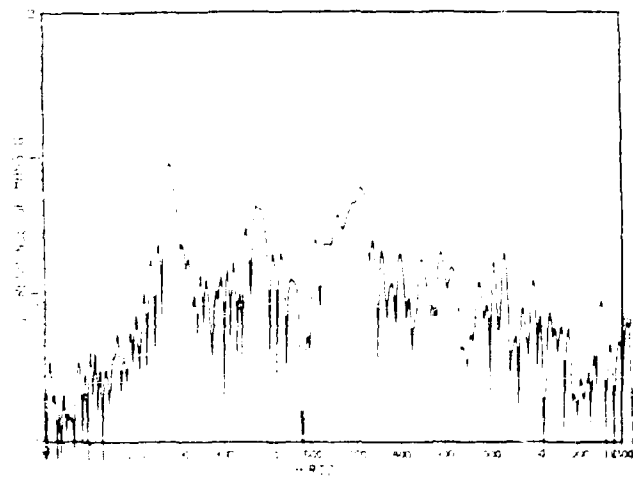with a Dead Zone.

Figure 8b

Frequency Response Function of a System
with a Dead Zone.

Similar studies have been made on systems with hysteretic
characteristics. Some limited conclusions may be drawn from
these types of studies [6], including:

1. Time history acceleration responses of systems with gaps may
show large, seemingly unpredictable acceleration spikes.
Frequency response functions of such systems typically exhibit a
lobed appearance.

2. Hysteretic systems typically show a nonproportionality in the
Fourier transform of the systems impulse response function in
which increasing the input does not produce a corresponding
increase in the output.

3. In Bilinear Systems all modes of the system are affected as
the bilinear spring switches from tension to compression.

Certainly such phenomena as shifts in resonant frequency with
input force level and nonproportional increase in response with
input force are common in vibration testing and are typically
attributed to some form of nonlinearities such as those noted
above.

Another empirical technique is based on observation of the
probability density function of the response of a nonlinear
system excited by broadband, Gaussian random noise. For a
linear system the response probability density must also be
Gaussian but a nonlinear system will produce non-Gaussian
responses. An example of a non-Gaussian probability density
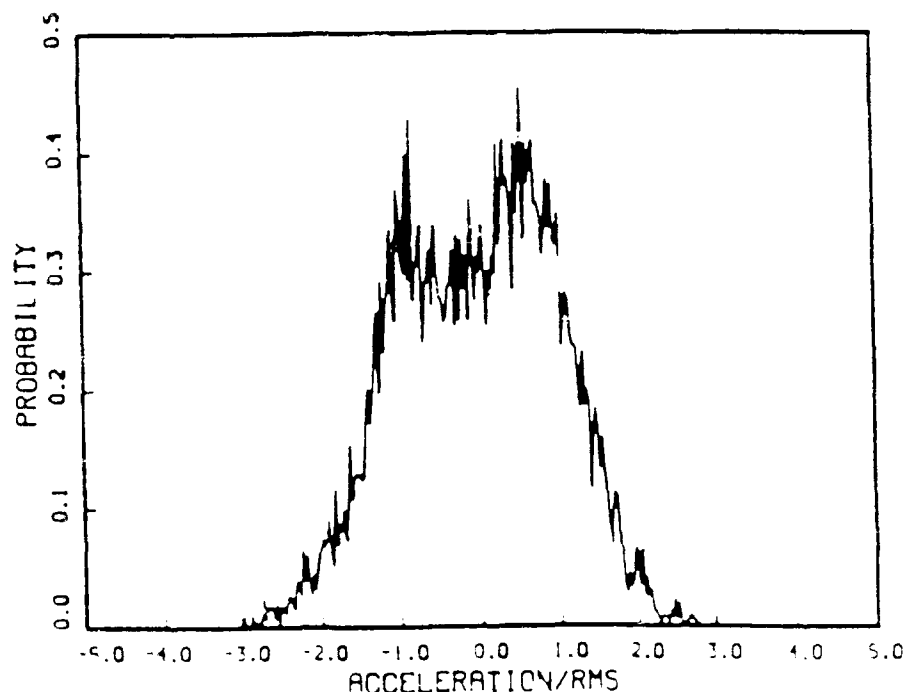function produced by a hysteretic system is shown in Figure 9.

Figure 9

Probability Density Function of the Acceleration Response
of a Hysteretic System excited by Gaussian random noise.

Force State Mapping

In force state mapping the system restoring force is plotted in three dimensional space as a function of velocity and displacement. Consider the differential equation of a second order system:

$$M\,Y'' + C\,Y' + K\,Y = F(t)$$

Dividing by M and solving for F(t)/M yields

$$\frac{F(t)}{M} - Y'' = \frac{C}{M}\,Y' - \frac{K}{M}\,Y$$

where :
    $F(t)$ = force applied to the system.
    M = system mass.
    C = system damping.
    Y'' = response acceleration.
    Y' = response velocity.
    Y = displacement response.

Measurement of signals proportional to F(t) and Y" is done using appropriate transducers. Then Y" is integrated to determine Y' and Y. A plot of the restoring force F/M -Y" versus Y' and Y defines a surface in three dimensional space. For a linear system this surface will be a plane as shown in Figure 10A. Various nonplanar surface shapes will occur for nonlinear systems. The surface for a cubic stiffening system is shown in Figure 10B.
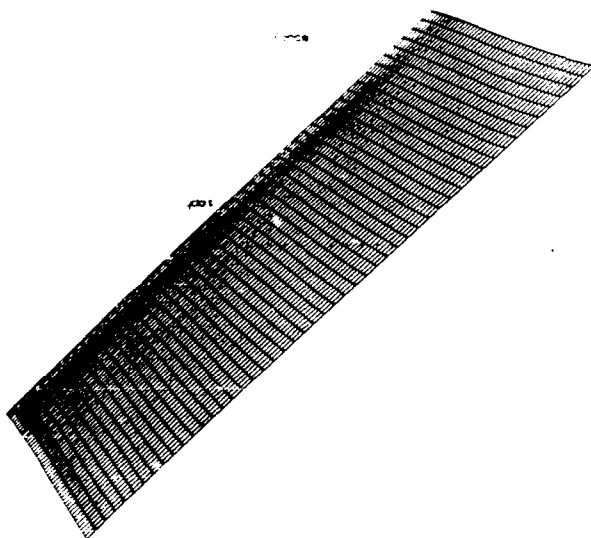

Figure 10(a)

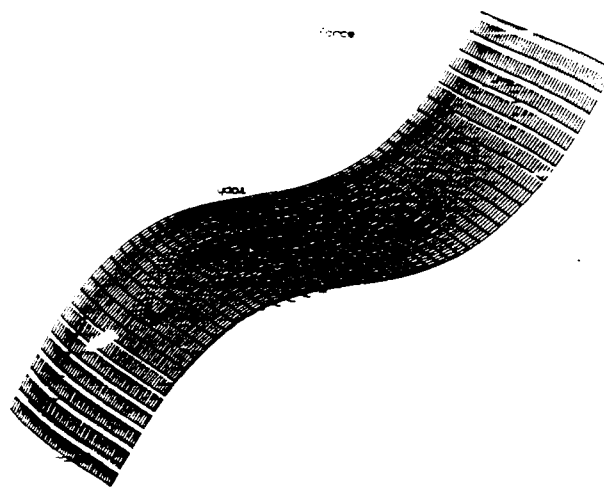Restoring Force Surface
for a Linear System.

Figure 10(b)

Restoring Force Surface for a System With
a Cubic Stiffness Characteristic.

A parametric model based on the restoring surface technique fits the parameters of a surface to the experimentally determined surface plot. In Figure 10B a general cubic surface in Y and Y' has been fitted to the measured data. The actual restoring force and the restoring force predicted from the surface fit are shown in Figure 10B where the points represent digitized measured data and the surface grid is defined by the fitted parametric surface. Once the parameters for the differential equation have been determined the equation may be solved numerically to determine a predicted system response. Potentially, this method can lead to characterization, response prediction, and control of some classes of nonlinear systems. Problems in the formulation that need to be addressed include determination of the mass associated with the Y" term, estimating parameters for multi-degree-of-freedom systems, and determining the number of equations which optimally describe a given test system. Another problem is the difficulty of measuring angular acceleration in test environments and the potential effects on the form of the differential equations caused by the lack of angular acceleration terms.

A variant of Force State Mapping developed by one of the authors (Endebrock) uses sampled adjacent time points to determine the local mass, stiffness, and damping associated with points in a given time region. This is similar to measuring the local slope of the surface. This type of measurement relies on differences between point values in a local region as does the difference equation technique.

State Space and Difference Equation Models

In one formulation of state space modeling the system is represented by an input-output difference equation model of the form.

$$y(t) = a_0 + a_1 u(t) + a_2 u(t-t_s) + a_3 u(t-2t_s) + \ldots + a_n u(t-(n-1)t_s) +$$
$$b_1 y(t-t_s) + b_2 y(t-2t_s) + \ldots + b_m (t-mt_s) \tag{6}$$

for a linear system or,

$$\tag{7}$$
$$y(t) = F(u(t), u(t-t_s), \ldots, u(t-(n-1)t_s), y(t-t_s), \ldots, y(t-mt_s))$$

for a general system. The u's represent current and past system inputs separated by a sampling interval ts and the y's represent current and past system responses. Such systems have been studied extensively[15,13,16,5].

In the case of a linear system the a's and b's are constants. For time varying systems the a's and b's are functions of time and for nonlinear systems they are functions of the u's and y's. For linear systems measured data may be used to formulate a system of equations based on responses y as a function of current and past inputs u and past outputs y. Singular value decomposition or orthogonal regression are then used to produce a mean square solution for the a's and b's. The resultant coefficients, along with the input, form a parametric system model which can be used to predict the system response to a general input. An example of a predicted and measured output for the acceleration response of an aluminum beam excited by random noise is shown in Figure 11. This is a linear system. Z transform techniques may be used to determine the system frequency response function (transfer function) from the coefficients of this form of parametric model[10].
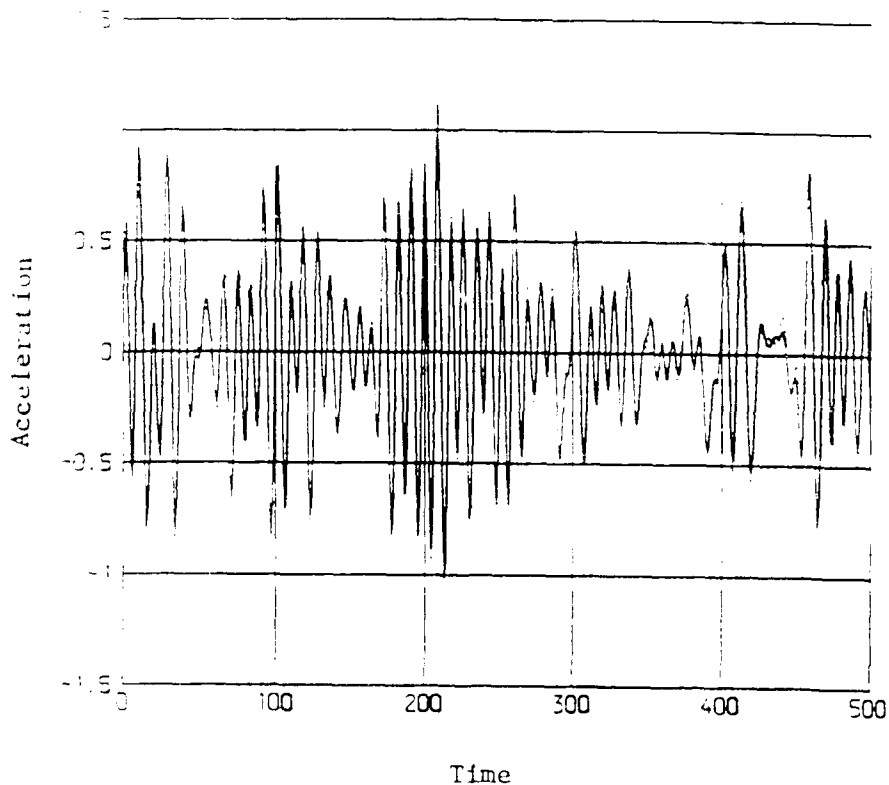

Time

Figure 11

Predicted ....
Measured ———

Predicted and Measured Response Time Histories
of an Aluminum Beam Excited by Random Noise.

For a nonlinear system numerous functions may be used as trial functional forms. Polynomial functions are one obvious choice where the output is represented as a truncated power series in the u's and y's[10]. Rational or orthogonal polynomials may also be used[11, 5]. Alternatively local fits may be preformed in regions of the space defined by various ranges of the u's and y's to allow more variety of functional form than is possible using a predefined global function[5].

In all of these methods there is the possibility of predicting the output of the system due to a new input provided that the frequency and amplitude range of the test input is chosen in a manner which properly exercises the system. The control problem is much more difficult. In principle for some systems, solution of a polynomial equation for the current input u(t) could be sufficient to allow control over a limited amplitude and frequency range.

Methods Based on Higher Order Spectra

Higher Order Spectra are, as noted above, based on a relationship between an input at a frequency f1 and response at a frequency f2. In general a response spectrum can be described as:

$$Y(k) = H_{k;k}^{(0)} + \sum_{k1=0}^{N} H_{k1;k}^{(1)} X(k_1) + \sum_{k1=0}^{N} \sum_{k2=0}^{N} H_{k1,k2;k}^{(2)} X(k1)X(k2) +$$

$$\sum_{k1=0}^{N} \sum_{k2=0}^{N} \sum_{k3=0}^{N} H_{k1,k2,k3;k}^{(3)} X(k1)X(k2)X(k3) + \ldots$$

(8)

where: $Y(k)$ = system spectral response at frequency index k.
H^r = system transfer function of order i.
$X(k)$= system spectral input at frequency index k.

For a linear system the response at frequency index k is caused by the input at frequency index k. For nonlinear systems progressively more complex representations of the frequency response are represented by transfer functions H^r where the response at frequency index k is caused by r inputs at frequencies k1, k2, .., kr. For an HGTF model [3] any combination of input frequencies may transfer energy to the response frequency whereas in a volterra model the input frequencies must sum to equal the response frequency. The H^r's may be determined through either time or frequency domain estimation procedures[10,11].

Use of higher order spectra and transfer functions form a natural extension of the widely used Fourier methods used in the analysis of linear systems. However the estimation procedures are considerably more complex and a relatively large number of parameters may be required to define the transfer functions, especially for transfer functions exceeding third order. The method is potentially adaptable to both characterization and control of nonlinear systems. In fact, controlling the spectral density of the response of a nonlinear system may well prove to

be more tractable than controlling the response time history of such a system.

Conclusions and Summary

It is clear that the analysis of nonlinear systems is in a state much more primitive than the analysis of linear systems. From our investigations of the literature and our experimental research we submit the following conclusions:

1. Superposition is not valid for nonlinear systems.

2. The specific types of responses produced by nonlinear systems strongly depend on the type of nonlinearity involved.

3. Nonlinear systems are frequency creative.

4. Nonlinear systems may exhibit chaotic responses.

5. Gaussian Input implies Gaussian response for a Linear System. A nonlinear system excited by Gaussian noise will generally not produce Gaussian responses.

6. The determination of the existence/and or degree of system nonlinearity should be made on the basis of inputs at several different levels. Specific tests for nonlinearity may be made based on statistical properties of the input and response. A single frequency response function is not a good method of determining system linearity or nonlinearity.

7. Methods of analyzing nonlinear systems include higher order spectral methods, difference equation formulations, and force state mapping.

    In summary, if one suspects nonlinear responses, it is relatively easy to verify nonlinear behavior. Some methods exist for source identification and parametric modeling of nonlinear vibration systems. To our knowledge no extensive formulation and application of control methods to nonlinear vibration systems has been made.

Figure Titles:

Figure 1:   Typical Force-Displacement Characteristics of Linear and Nonlinear Systems.

Figure 2:   Response Time History of a Nonlinear System Excited by a Sinusoidal Input.

Figure 3:   Response Time History of a Chaotic System to a Sinusoidal Input.

Figure 4:   Frequency Generating Characteristics of Linear and Nonlinear Systems.

Figure 5:   Force-Displacement Relationship for a Bilinear Spring.

Figure 6:   Time History Responses of a Multi-Degree-of-Freedom System with a Bilinear Spring Excited by a Force Impulse.

Figure 7:   Frequency Response Functions for a Bilinear System.

Figure 8(a):   Impulse Response Time History of a System with a Dead Zone.   8(b):   Frequency Response Function of a System with a Dead Zone.

Figure 9:   Probability Density Function of the Acceleration Response of a Hysteretic System Excited by Gaussian Random Noise.

Figure 10(a):   Restoring Force Surface for a Linear System. 10(b):   Restoring Force Surface for a System with a Cubic Stiffness Characteristic.

Figure 11:   Predicted and Measured Response Time Histories of an Aluminum Beam Excited by Random Noise.

References

Reports

1. Tomlinson, G.R., Detection, Identification, and Quantification of Nonlinearity in Modal Analysis - A Review. Proceeding of the 4th International Modal Analysis Conference, 1984.

2. Crutchfield, J.P., Farmer, J. D., and Packard, N. H., and Shaw, R. S., "Chaos", Scientific American, 254(12):46-57, 1986.

3. Paez, Thomas J., "Nonlinear Structural System Modeling", Proceedings of the SDM, 1987.

4. Choi, D. W., Bispectral Identification of Non-linear Mode Interactions, Proceedings of the First International Modal Analysis Conference, 1983.

5. Farmer, J.D. and Sidorowich, John J. "Exploiting Chaos to Predict the Future and Reduce Noise", LA-UR-88-901. Los Alamos National Laboratory Report, 1988.

6. Hunter, Norman F., Jr. "An Investigation of the Time History and Modal Responses of Some Typical Linear and Nonlinear Systems", Proceedings of the Third International Modal Analysis Conference, 1985.

7. Hammond, J.K., Yar, M., Lo, H.R., "The Analysis of Hysteretic Systems with Reference to a Particular Model", Proceedings of the 4th International Modal Analysis Conference, 1986.

8. Tomlinson, G.R. and Worden, K., "Developments in Force State Mapping for Nonlinear Systems", Proceedings of the 6th International Modal Analysis Conference, 1988.

9. Tomlinson, G.R., "Using the Hilbert Transform with Linear and Non-Linear Multi-Mode Systems", Proceedings of the 3rd International Modal Analysis Conference, 1985.

10. Billings, S.A., Tsang, K.M., and Tomlinson, G.R., "Application of the Narmax Method to Frequency Response Function Estimation", Proceedings of the 6th International Modal Analysis Conference, 1988.

11. Paez, Thomas J., and Hunter, Norman F. Jr. "Experimental Identification of Nonlinear Structural Models", Proceedings of the 6th International Modal Analysis Conference, 1988.

Books

12. Chaotic Vibrations, Moon.

13. Stearns, Samuel D., _Digital Signal Analysis_, Hayden Book Company, 1975.

14. Schetzen, Martin, _The Volterra and Weiner Theories of Nonlinear Systems_, Wylie, 1980.

15. Eykhoff, _System Identification, Parameter and State Estimation_, Wylie, 1974.

16. Stearns, Samuel D., and David, Ruth, _Algorithms for Digital Signal Analysis_, Prentice-Hall, 1988.

17. Sontag, E.D., Polynomial Response Maps, _Lecture Notes in Control and Information Sciences_, Springer Verlag, Berlin, 1979.